

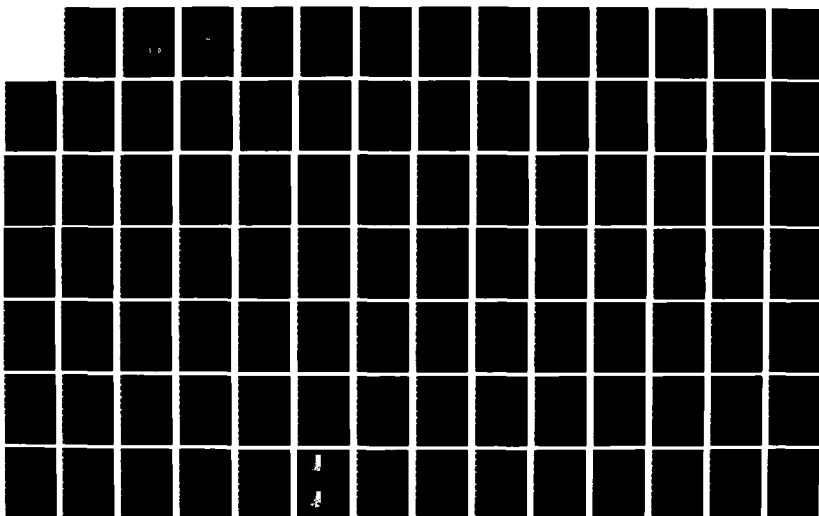
AD-A171 688

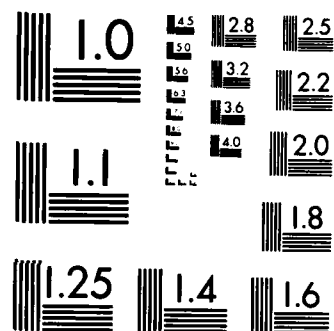
GEOPHYSICAL PLASMAS AND ATMOSPHERIC MODELING(U) SCIENCE 1/8  
APPLICATIONS INTERNATIONAL CORP MCLEAN VA  
E HYMAN ET AL JUL 86 SAIC-86/1781 N00014-85-C-2018

UNCLASSIFIED

F/G 4/1

NL





MICROCOPY RESOLUTION TEST CHART  
NATIONAL BUREAU OF STANDARDS-1963-A

AD-A171 688

GEOPHYSICAL PLASMAS  
AND ATMOSPHERIC MODELING

SAIC FINAL REPORT 86/1781

July 1986

**SAIC**

Science Applications International Corporation

DTIC  
ELECTE  
SEP 11 1986  
S D

DTIC FILE COPY

86 815 019

DISTRIBUTION STATEMENT A  
Approved for public release  
Distribution Unlimited

12

**GEOPHYSICAL PLASMAS  
AND ATMOSPHERIC MODELING  
SAIC FINAL REPORT 86/1781**

**July 1986**



*Science Applications International Corporation*

**DTIC  
ELECTE  
SEP 1 1 1986  
S D**

**DISTRIBUTION STATEMENT A**  
**Approved for public release**  
**Distribution Unlimited**



## **DISCLAIMER NOTICE**

**THIS DOCUMENT IS BEST QUALITY  
PRACTICABLE. THE COPY FURNISHED  
TO DTIC CONTAINED A SIGNIFICANT  
NUMBER OF PAGES WHICH DO NOT  
REPRODUCE LEGIBLY.**

**GEOPHYSICAL PLASMAS  
AND ATMOSPHERIC MODELING**

**FINAL REPORT**

**SAIC 86/1781**

**July 1986**

**Dr. Joseph Huba  
Geophysical and Plasma Dynamics Branch  
Plasma Physics Division  
Naval Research Laboratory  
Washington, D.C. 20375**

**Prepared by:**

**Ellis Hyman with  
James Drake, Gurudas Ganguli, Supriya Ganguli,  
Charles Goodrich, Adil Hassam, Y.C. Lee, Horace Mitchell,  
Dennis Papadopoulos, Harvey Rowland, Keith Sashegyi,  
Punyamurthula Satyanarayana, and Darrell Strobel**

**Prepared Under:**

**Contract No. N00014-85-C-2018**

**SCIENCE APPLICATIONS INTERNATIONAL CORPORATION**

**1710 GOODRIDGE DRIVE, MCLEAN, VA 22102 (703) 734-5840**

# TABLE OF CONTENTS

SECTION	PAGE
I. TECHNICAL DISCUSSION . . . . .	1
A. Magnetospheric Physics: High Frequency Waves.	2
B. Whistler Growth in a Cold Plasma Injection Experiment. . . . .	4
C. Collective Particle Accelerator Studies. . . . .	5
D. Magnetosphere-Ionosphere Coupling. . . . .	6
E. High Latitude Ionospheric Investigations . . . . .	12
F. Plasma Transport in the Auroral Return Current Region . . . . .	21
G. Ion Cyclotron Wave Turbulence in the Auroral Ionosphere . . . . .	25
H. Preferred Scale Size in the Structuring of Barium Clouds. . . . .	26
I. Spectral Characteristics of Interchange Turbulence in the Ionosphere . . . . .	29
J. Debris-Air Coupling in HANE and in the NRL Laser Experiment . . . . .	31
K. Power Spectral Density of Radiating Plasma Clouds. . . . .	38
L. Debris Charge States in HANE and in the NRL Laser Experiment. . . . .	41
M. Low Frequency Instabilities in HANE . . . . .	48
N. Numerical Studies of the Dynamics of the Summer Monsoon. . . . .	51
O. Middle Atmosphere Transport and Chemistry Studies . . . . .	56



ltc. on f

Availability Codes	
101	Avail and/or Special
A-1	23

## TABLE OF CONTENTS (Continued)

APPENDIX A. . . . .	A-1
"Electrostatic Ion Cyclotron Instability Caused by a Nonuniform Electric Field Perpendicular to the External Magnetic Field"	
APPENDIX B. . . . .	B-1
"Temporal Evolution of Whistler Growth in a Cold Plasma Injection Experiment"	
APPENDIX C. . . . .	C-1
"Stochasticity of Particle Orbits in a Collective Particle Accelerator"	
APPENDIX D. . . . .	D-1
"A Simulation of High Latitude F-Layer Instabilities in the Presence of Magnetosphere- Ionosphere Coupling"	
APPENDIX E. . . . .	E-1
"Transverse Motion of High-Speed Barium Clouds in the Ionosphere"	
APPENDIX F. . . . .	F-1
"Theory of the Current-Driven Ion Cyclotron Instability in the Bottomside Ionosphere"	
APPENDIX G. . . . .	G-1
"Excitation of Lower-Hybrid Instability by Longitudinal Currents"	
APPENDIX H. . . . .	H-1
"Parallel Current Effects on Auroral E-Region Plasma Instabilities"	
APPENDIX I. . . . .	I-1
"On the Stability of a Stratified Shear Layer"	
APPENDIX J. . . . .	J-1
"Dynamics of the Large Scale Return Currents on Auroral Field Lines"	
APPENDIX K. . . . .	K-1
"Plasma Transport in the Auroral Return Current Region"	

TABLE OF CONTENTS (continued)

APPENDIX L. . . . .	L-1
"ICW Turbulence and Auroral E Fields"	
APPENDIX M. . . . .	M-1
"Convective Stabilization of Ionospheric Plasma Clouds"	
APPENDIX N. . . . .	N-1
"Spectral Characteristics of Interchange Turbulence"	
APPENDIX O. . . . .	O-1
"Early Time Coupling Studies Using a 1D Hybrid Code"	
APPENDIX P. . . . .	P-1
"Collisionless Coupling in the AMPTE Artificial Comet"	
APPENDIX Q. . . . .	Q-1
"Projections of Plasma Cloud Structures and Their Spectra"	
APPENDIX R. . . . .	R-1
"A Striation Model and Spectral Characteristics of Optical-IR Emission from HANE"	
APPENDIX S. . . . .	S-1
"Low Frequency Instabilities Driven by an Ion Temperature Anisotropy"	
APPENDIX T. . . . .	T-1
"A Linear Model Study of Cross-Equatorial Flow Forced by Summer Monsoon Heat Sources"	

## SECTION I

### TECHNICAL DISCUSSION

The work performed by Science Applications International Corporation (SAIC) on this contract, "Geophysical Plasmas and Atmospheric Modeling," Contract Number N00014-85-C-2018, SAIC Project Number 1-157-17-197, encompasses a wide range of topics in space plasma physics and atmospheric modeling support of the programs of the Geophysical and Plasma Dynamics Branch of the Naval Research Laboratory (NRL). This report covers the period 1 February 1985 to 1 June 1986. In this section we will summarize the various subjects studied and the results obtained. Details will be included in Appendices which will document reports and publications resulting from our work.

In the following subsections we will describe the major accomplishments in each of the following research efforts:

(A) magnetospheric physics: high frequency waves, (B) whistler growth in a cold plasma injection experiment, (C) collective particle accelerator studies, (D) magnetosphere-ionosphere coupling (E) high latitude ionospheric investigations, (F) plasma transport in the auroral return current region, (G) ion cyclotron wave turbulence in the auroral ionosphere, (H) preferred scale size in the structuring of barium clouds, (I) spectral characteristics of interchange turbulence in the ionosphere, (J) debris-air

coupling in HANE and the NRL laser experiment, (K) power spectral density of radiating plasma clouds, (L) debris charge state in HANE and in the NRL laser experiment, (M) low frequency instabilities in HANE, (N) numerical studies of the dynamics of the summer monsoon, and (O) middle atmosphere transport and chemistry studies.

#### A. Magnetospheric Physics: High Frequency Waves

Recently high frequency ( $\omega \sim \Omega_{ci}$ ) waves have been reported in connection with transverse inhomogeneous electric fields in a magnetoplasma in (1) laboratory plasmas [Nakamura et.al., Proceedings of the Second Symposium on Plasma Double Layers and Related Topics, Innsbruck, Austria, 1984, p. 171; Alport et. al., J. Geophys. Res. 91, 1599, (1986)], (2) space plasmas [Mozer et.al., Phys. Rev. Lett. 38, 292, 1977; Temorin, et al., Phys. Rev. Lett. 48, 1175, 1982; Yau et. al., J. Geophys. Res. 88, 341, 1983], as well as in (3) barium cloud release experiments [Koons and Pongratz, J. Geophys. Res. 86, 1437, 1981]. Clearly, there is a strong indication that the transverse electric field is linked with the high frequency waves. It is well known that a transverse inhomogeneous electric field can give rise to the low frequency and long wavelength Kelvin-Helmholtz instability but the generation of the short wavelength and

high frequency waves near the ion cyclotron frequency remains somewhat mysterious. In order to investigate the origin of the high frequency short wavelength waves we have developed a kinetic formalism for a magnetoplasma immersed in a transverse inhomogeneous electric field.

We have discovered a new mechanism capable of exciting high frequency waves. To illustrate the mechanism, we first choose an ideal external electric field profile  $E_0(x) = E$  for  $|x| \leq x_0$  and 0, otherwise. The energy density of the Bernstein modes for  $|x| > x_0$  is positive while for  $|x| < x_0$  it is negative. Thus a flow of energy from  $|x| < x_0$  towards  $|x| > x_0$  leads to a growth of the Bernstein modes. The same principle may provide growth to other waves eg. lower hybrid waves, etc. We were asked by the American Geophysical Union to give an invited talk describing this new mechanism, at the Spring Meeting in Baltimore, 1985. The abstract follows.

A New Excitation Mechanism for Waves in a Magnetoplasma  
G. GANGULI, Y.C. LEE (Science Applications International Corporation, 1710 Goodridge Drive, McLean, VA, 22102)  
P. PALMADESSO (Plasma Physics Division, Naval Research Laboratory, Washington, D.C. 20375)

We discuss a new mechanism for excitation of waves (ion cyclotron, lower hybrid, etc.) in a magnetoplasma with a localized electric field perpendicular to the external magnetic field. In the absence of the electric field the mode energy is positive while in the presence of a uniform electric field perpendicular to the magnetic field the wave energy can be negative. However, when the electric field is nonuniform, it is possible for a finite region of space (over which the



electric field is localized) to be of negative wave energy density. A nonlocal wave packet couples the two regions so that a flow of energy from the region of negative wave energy to the region of positive wave energy will cause the mode to grow. This gives rise to the instability. We demonstrate the mechanism and its features by considering the kinetic ion cyclotron waves as an example. Various applications of this instability and comments on its nonlinear behavior will be given. The relationship of this process to the Kelvin-Helmholtz instability will also be discussed.

This work is supported by ONR and NASA.

For further details refer to the paper, Ganguli et al., Phys. Fluids 28, 761, 1985. This paper is included in this report as Appendix A entitled "Electrostatic Ion Cyclotron Instability Caused by a Nonuniform Electric Field Perpendicular to the External Magnetic Field. It also is available as NRL Memo Report 5549. The formalism is currently being improved and various applications are under consideration.

#### B. Whistler Growth in a Cold Plasma Injection Experiment

As a part of the Active Magnetospheric Particle Tracer Explorer (AMPTE) program we have investigated the evolution of whistler mode turbulence and particle precipitation in a cold plasma release experiment. We have used a cold plasma density model for a typical ambient radiation belt environment. It is known from earlier work that the release of cold lithium ions can significantly lower the critical electric field,  $E_c$ , above which the resonant radiation belt

electrons can pitch angle scatter. We have studied the time evolution of the one pass gain factor for a whistler wave packet and find that for parameters accessible to AMPTE type experiments the gain factor is large enough to ensure strong whistler turbulence and strong pitch angle diffusion of radiation belt particles with energies in the range between the ambient value of  $E_c$  and the reduced value of  $E_c$ . Estimates for the total power input to the ionospheric footprint of the release are of the order of an erg/cm<sup>2</sup>/s. We conclude that this precipitated energy should produce a patch of visible aurora and the effect should persist for many hours. This work has been described in detail in a paper, Ganguli et al., "Temporal Evolution of Whistler Growth in a Cold Plasma Injection Experiment," J. Geophys. Res. 89, 7351 (1984) and appears here in Appendix B.

#### C. Collective Particle Accelerator Studies

From our earlier studies of the stability of the plasma in a Collective Particle Accelerator (CPA) we concluded that the transverse oscillations considered fatal (Uhm, Phys. Fluids 25, 1908 (1982)) are not totally harmful [Ganguli and Palmadesso, J. Appl. Phys. 55, 2715 (1984)]. It is always possible to successfully accelerate a few meters of a solid electron beam. Thus the next question of interest is the particle dynamics i.e. the particle orbits and their

stability in a typical CPA field configuration. A detailed investigation of the behavior of the particle orbits in the simultaneous presence of three large amplitude waves much as those encountered in the collective particle accelerator experiment at the Naval Research Laboratory has been completed [Ganguli et. al., J. Appl. Phys. 59, 365, 1986]. This paper, entitled "Stochasticity of Particle Orbits in a Collective Particle Accelerator," is included here as Appendix C. It also is available as NRL Memo Report 5664 (1985). We conclude that the stochasticity arising out of the resonance overlap of the waves can influence the particle dynamics significantly and thereby affect the outcome of the experimental result. Choice of initial phase and energy for successful operation is identified and discussed.

#### D. Magnetosphere-Ionosphere Coupling

In high latitudes the ionospheric and magnetospheric plasmas are strongly coupled by the vertical magnetic field lines which thread the two regions. Electric fields perpendicular to these field lines map rapidly from one region to the other and currents flow with little or no resistance parallel to the field. As a result, the dynamics of the plasmas in both the high-latitude ionosphere and the polar magnetosphere are highly dependent on each other. For

several years, we have been investigating this coupling phenomenon with a numerical simulation of these regions. This simulation consists of multiple two-dimensional layers perpendicular to the magnetic field. Each layer has a dynamic behavior characteristic of one of the regions along the field, e.g., the magnetospheric plasma, the F-region ionospheric plasma, the E-region plasma, etc., and the separate layers are coupled by the perpendicular electric field mapping and the parallel currents flowing between layers. By altering the characteristics and initial conditions of the simulation layers many different physical aspects of magnetosphere-ionosphere coupling dynamics may be investigated.

Our primary simulations with this model have concerned the non-linear evolution of high-latitude irregularities. Simulations of high-latitude structuring have previously not taken into account the fact that structuring electric fields have to move the coupled magnetospheric plasma which is along the magnetic field above the ionospheric plasma. Simulations performed with our model suggest that this coupling not only slows the development of these instabilities by increasing the effective inertia of the plasma, but also isotropizes the wave spectra of the irregularities. This effect can interfere with the coherent non-linear behavior of the structured fields, leading to a

more isotropic small-scale irregularity structure. These effects have been reported in an article entitled "A Simulation of High Latitude F-Layer Instabilities in the Presence of Magnetosphere-Ionosphere Coupling" in Geophysical Research Letters (H.G. Mitchell, Jr., et. al., Geophys. Res. Lett. 12, 283-286, 1985.) and are included in this report in Appendix D. This report is also available as NRL Memo Report 5597 (1985).

It is also possible to model the effects of ionospheric conductivity on the development of magnetospheric instabilities with this simulation. Many magnetospheric configurations involve boundary layers between regions of differing plasma flow velocities. Such a layer may be unstable to the Kelvin-Helmholtz instability, leading to vortex formation at the velocity shear interface. The movement and formation of the shapes of auroral arcs may be one manifestation of such behavior in the magnetosphere. However, if such a shear is perpendicular to magnetic field lines which are connected to the ionosphere, then the instability electric fields tend to be shorted out by currents which flow down to the ionosphere and across the field there due to the ionospheric conductivity. Our simulations of this configuration show that the primary effect of the ionospheric conductivity is to damp the instability. In parameter regimes for which the velocity

shear is still unstable, the conductivity also has the effect of interfering with the formation of Kelvin-Helmholtz vortices, leading to configurations along the shear interface which have the appearance of breaking waves rather than vortices. These results have been reported at both the Fall 1985 and the Spring 1986 meetings of the American Geophysical Union. These four abstracts are included below. We are at the present time preparing a detailed report of these results for journal publication.

Nonlinear Simulations and Theory of the Kelvin-Helmholtz Instability in the High Latitude Ionosphere\*

P. SATYANARAYANA and H. MITCHELL (Science Applications International Corporation, McLean, VA 22102) M. KESKINEN, J. FEDDER, S. ZALESK, and J.D. HUBA (Naval Research Laboratory, Washington, D.C. 20375)

Numerical and analytical studies of the nonlinear evolution of the Kelvin-Helmholtz instability in the high latitude ionosphere are presented. In our numerical simulations we solve a simple set of plasma fluid equations, on a highly resolved grid, in the electrostatic approximation under a variety of initial conditions. We include particle collisions in our analysis. In the nonlinear regime we compute numerically the power spectrum of velocity and density fluctuations and compare with theoretical estimates. Finally, we compare our results with DE and Hikat satellite observations.

\*Work supported by ONR, NASA, and DNA.

Multilevel Numerical Simulations of High Latitude Ionospheric Instabilities\*

S.T. ZALESK, J.A. FEDDER, M.J. KESKINEN, J.D. HUBA (Naval Research Laboratory, Washington, D.C. 20375-5000) H.G. MITCHELL (Science Applications International Corporation, McLean, VA 22102)

Numerical simulations of high latitude ionosphere instabilities are presented. These simulations account

for the compressibility and active chemistry of the high latitude E-region by treating the region as a separate computational layer from the F-region. Ion inertial effects are neglected, as are parallel resistivity effects. The physics of the instability is found to be dominated by the large E-region Pedersen and Hall conductivities. To first order, the E-region is found to severely reduce the growth rate of the gradient drift/ $E \times B$  instability, but "imaging" due to E-region plasma compressibility, and the dynamics of chemical production and loss, are found to have significant effects on the nonlinear plasma evolution.

\*Research supported by ONR, NASA, and DNA.

Kelvin-Helmholtz Instability in the High Latitude Ionosphere: Nonlinear Evolution\*

H.G. MITCHELL and P. SATYANARAYANA (Science Applications International Corporation, McLean, VA 22102)

M. KESKINEN, J. FEDDER, S. ZALESK, and J.D. HUBA (Naval Research Laboratory, Washington, D.C. 20375-5000)

We study the behavior of the Kelvin-Helmholtz instability in the presence of ion-neutral collisions which is relevant to the high latitude ionosphere. We perform numerical simulations of collisionless Kelvin-Helmholtz instability and compare them to simulations with increased Pedersen conductivity in the linear and nonlinear regimes. We find that collisions imply the existence of a coupling between the electrostatic field and density gradients through the divergence of the Pedersen currents, which, in addition to reducing the growth rate of the instability, also leads to the breakup of the coherent vortex structure characteristic of the Kelvin-Helmholtz instability. We will show the results of these simulations in detail.

\*Research supported by ONR, NASA, and DNA.

Kelvin-Helmholtz Instability in the High Latitude Ionosphere: Power Spectra\*

M.J. KESKINEN, J.A. FEDDER, S.T. ZALESK, J.D. HUBA (Naval Research Laboratory, Washington, D.C. 20375-5000)

H.G. MITCHELL and P. SATYANARAYANA (Science Applications International Corporation, McLean, VA 22102)

The electrostatic Kelvin-Helmholtz instability resulting from velocity-sheared plasma flows perpendicular to a magnetic field, has been studied including self-consistent Pedersen conductivity coupling

effects. We find that the Kelvin-Helmholtz instability develops in a fundamentally different manner with Pedersen (ionospheric) coupling. Specifically, we show that Pedersen coupling (1) inhibits Kelvin-Helmholtz vortex formation and leads to nonlinear structures which can be described as "breaking waves", (2) generates, in the nonlinear regime, small scale structures by means of secondary instabilities growing on the primary waves, and (3) results in a much increased time for Kelvin-Helmholtz instability wave growth. We compute the power spectra associated with the density and field fluctuations associated with the Kelvin-Helmholtz instability with and without Pedersen conductivity. Finally, we compare our results with recent observations of velocity sheared plasma flows in the high latitude space plasma.

\*Work supported by ONR, NASA, and DNA.

We have also used our simulation to predict the behavior of large ion clouds injected at very high velocity perpendicular to the magnetic field. In theoretical support of the forthcoming CRRES (Combined Release and Radiation Effects Satellite) missions, we have modelled the effects of magnetic field line coupling on the movement of high speed barium clouds. This work is important in that it will be necessary for observational purposes to have a good idea of the motion of such a cloud before the actual experiment is performed. Our results show that, in certain parameter regimes of cloud and background density and velocity, a cloud injected in such a manner will 'skid' across the magnetic field until the ion cloud and the neutral source cloud are not coincident, at which time the cloud will stop skidding. Our preliminary results on this simulation have



been published in the Journal of Geophysical Research entitled "Transverse Motion of High-Speed Barium Clouds in the Ionosphere" (H.G. Mitchell, Jr., et. al., J. Geophys. Res., 90, 11091-11095, 1985) and appear here in Appendix E. It is also available as NRL Memo Report 5626 (1985). We are at present refining this simulation in terms of physical parameters and neutral cloud behavior in order to obtain results as close as possible to the actual physical experiments to be performed.

## E. High Latitude Ionospheric Investigations

### 1. Introduction

The theoretical and numerical investigations undertaken during the past year are basically related to high latitude ionospheric phenomena. The research is directed toward understanding the mechanisms that lead to large scale structure in the ionosphere. Smaller scale phenomena due to instabilities feeding on the free energy source are available in the high latitude ionosphere; the work is in direct support of the DNA HILAT theory program at NRL. The sources of free energy generally are shears in the equilibrium velocity or electric fields, field-aligned currents, and inhomogeneities in other equilibrium quantities such as density, temperature, etc. Some of the

outstanding problems as seen from the data supplied by HILAT and DE-2 satellites are the following:

(1) Observations of electrostatic ion cyclotron waves and lower hybrid waves at low altitudes, in the E-region and bottomside F-region of the ionosphere.

(2) Observations of upflowing ion events, the ions being of ionospheric origin.

(3) Observation of transversely heated ions at altitudes as low as 300 km.

(4) Sporadic observation of ion conics in the ionosphere.

(5) Observation of strong velocity shears and moderate field aligned currents localized in a region 100's of kilometers in the transverse direction to the magnetic field and large current structures localized in a few 10's of kilometers.

As a first step in solving these problems a linear stability analysis is performed to identify the instabilities and their dispersion characteristics, and then, in the case of velocity shear driven turbulence, a nonlinear fluid simulation is performed involving inhomogeneous plasmas. The latter problem has applications in the F-region large scale structure and magnetosphere-ionosphere coupling. With the observations in mind the following problems are considered:

(a) Current driven instabilities with wavelengths of the order of the local ion gyroradius in the collisionless topside and collisional bottomside ionosphere using a model Fokker-Planck collision operator for ion-ion collisions,

(b) Current driven instabilities with wavelengths shorter than the local ion gyroradius and with real frequency of the order of the lower hybrid frequency,

(c) Possible heavy ion heating by collisional ion cyclotron waves and isotropization in the collisional plasma leading to threshold altitudes for ion conic observations,

(d) Modified Farley-Buneman instability that arises due to the coupling of magnetic field-aligned currents and the transverse electrojet currents in the ionospheric E-region,

(e) Nonlinear evolution of transverse Kelvin-Helmholtz instability driven by equilibrium shear flows in an inhomogeneous plasma with magnetosphere-ionosphere coupling, a neutral wind, and ion-neutral collisions,

(f) Effects of electron parallel dynamics on the Kelvin-Helmholtz instability,

(g) Analysis of the collisional Kelvin-Helmholtz instability in the ionosphere,

(h) Stability boundaries of a stratified shear layer with arbitrary density gradients.

## 2. Description and Results

### 2.1 Theory of collisional current-driven ion cyclotron instability in the bottomside ionosphere

A kinetic theory of the electrostatic ion cyclotron (EIC) instability in collisional plasmas has been developed using a BGK model for electron collisions and ion neutral collisions. We show that EIC waves can be excited in the bottomside ionosphere, where the electron collisions are strong enough to destabilize the EIC instability even in the presence of moderate ion-neutral collisional damping. Details of the analysis are given in a paper published in the Journal of Geophysical Research (90, 12,209 (1985) and here in Appendix F). It is also available in NRL Memo Report 5656 (1985). Currently a Fokker-Planck model is used to represent the ion-ion collision and applied to study the current driven ion cyclotron instability; a manuscript is being prepared for publication in the Physics of Fluids.

### 2.2 Excitation of lower hybrid instability by longitudinal currents

In this brief paper a local theory of a homogeneous plasma with currents along the magnetic field is presented. We find that the electrons streaming along the magnetic field relative to a stationary ion background, constituting a current along the magnetic field, can excite the

lower-hybrid instability. It is found that when the drift velocity exceeds the parallel phase velocity of the wave at the lower hybrid frequency, the modes become unstable. This condition is found to hold in the collisionless topside of the ionosphere and collisional bottomside of the ionosphere. Since the ionospheric E-region is highly collisional, the ion collisions demagnetize the ions, thus making it possible for the collisional LHD to be excited. The details are given in Appendix G (Satyanarayana, P., et. al., Phys. Fluids, 29 (1986)). Currently, the Fokker-Planck model used in 2.1 is being applied to show the transition of EIC waves to the LHD instability for large enough ion-ion collisions.

### 2.3 Ion heating by the collisional ion cyclotron instability

Recent observations from the DNA HILAT satellite show evidence of upflowing ions in the high latitude ionosphere and rocket observations indicate ion cyclotron wave activity or sometimes lower hybrid waves during ion heating processes in the ionosphere. The so called ion conic distributions have been interpreted as resulting from heating of ions at low altitudes followed by adiabatic motion due to the magnetic mirror force. In this brief report, we apply the results of section 2.1 and discuss the effects of collisions on ion heating by the current driven ion cyclotron instability in the high latitude ionosphere and identify

regions in the ionosphere where possible ion conic distributions can be observed. Details of the calculations will be reported in a paper entitled "Ion Heating by the Collisional Ion Cyclotron Instability" in preparation.

#### 2.4 Parallel current effects on E-region plasma instabilities

In this paper, field-aligned currents that close in the ionosphere are shown to affect the development of plasma instabilities in the auroral electrojet. We consider the Farley-Buneman and ion-acoustic instabilities and include the parallel motion of electrons. It is found that inclusion of parallel current modifies the threshold criteria for the onset of the Farley-Buneman instability, and may cause excitation of oblique ion sound waves. We apply these results to the auroral E-Region and show that they may explain some observations of auroral irregularities, for example, the presence of type I irregularities for sub-threshold conditions (when the electron Hall drift is less than the ion-sound speed), and the observation of irregularities which are not highly field-aligned. The details of the calculations and applications are given in Appendix H, entitled "Parallel Current Effects on Auroral E-Region Plasma Instabilities" which has been submitted to the Journal of Geophysical

Research and is in preparation, also, as an NRL Memo Report.

## 2.5 Effects of parallel electron dynamics on the Kelvin-Helmholtz instability

The Kelvin-Helmholtz instability driven by velocity shears is a common phenomenon in the auroral ionosphere and numerous observations showing the large scale wave-like structures typical of the Kelvin-Helmholtz instability have been recorded by various authors. The instability manifests in swirling flows with scale sizes of the order of the shear layer thickness. In classical treatments of the Kelvin-Helmholtz instability, often the parallel electron motion is ignored while considering only the transverse motion of the ions and the  $E \times B$  motion of electrons. Thompson (J. Geophys. Res. 88, 4805 (1983)) recently considered the effects of parallel electric fields and showed that the parallel motion of electrons could be stabilizing. In our investigations we quantify the above conclusions and show that if the ratio of parallel to perpendicular wavelengths is larger than 0.25 the Kelvin-Helmholtz modes are stabilized. The following abstract outlines the presentation given at the AGU Spring Meeting 1986.

### Kelvin-Helmholtz Instability\*

P. SATYANARAYANA\*\*, Y.C. LEE\*\*, and J.D. HUBA (Naval Research Laboratory, Washington, D.C. 20375-5000)

The nature of the transverse velocity shear driven Kelvin-Helmholtz instability is studied by including the electron motion along the magnetic field. This parallel electron dynamics introduces new kinetic effects by imposing constraints on the finite parallel extent of the system ( $\kappa_{\parallel}/\kappa_{\perp}$ ), on the  $\mathbf{E} \times \mathbf{B}$  drift speed as compared to the electron thermal speed ( $V_E/V_e$ ), and on the extent of the shear layer in relation to the ion gyroradius ( $L/\rho_i$ ). Preliminary numerical results indicate that parallel electron dynamics produce a sharp lower cutoff in the perpendicular wavenumber (instability for  $\kappa_{\perp} < \kappa_{\perp} < 1$ ) and alter the nature of the eigenfunctions.

\*Work supported by ONR, NASA, and DNA.

\*\*Science Applications International Corporation, McLean, VA 22102

## 2.6 Analysis of the collisional Kelvin-Helmholtz instability in the ionosphere

Ion-neutral collisions play an important role in the lower ionosphere and produce drastic effects on the Kelvin-Helmholtz instability. In the work reported in Section D, it was shown that in the large wavelength limit the instability has a small but finite growth rate that is inversely proportional to the ion-neutral collision frequency. However, the analysis breaks down for shorter wavelengths, i.e., for  $\kappa L$  of order 1. In this report, we develop an analytical method by considering a quasi-equilibrium situation and show that the growth rate does depend inversely on the ion-neutral collision frequency and also show its dependence on the wavenumber. These analytical methods will be used in the future to determine



the growth rate and stability boundaries for velocity shear driven instabilities for the equilibrium considered in the Section D discussion including the effects on gravity. The details of the analytical methods will be presented in a paper currently in preparation.

## 2.7 On the stability boundaries of a stratified shear layer

In order to study the effects of strong density gradients which are often observed along with velocity shears in the auroral ionosphere, we examine a frequently made assumption, the Boussinesq approximation, which ignores all the density gradient terms except those that appear in the driving term of the interchange process. Using the Boussinesq approximation Drazin [J. Fluid Mech., 4, 214, (1958)] showed that for a Richardson number larger than  $1/4$  the modes are stable. We examine the exact equation including all the density gradient terms and show that as the ratio  $L_n/L_v$  is increased the restrictions on the Richardson number become severe thus making the conditions not suitable for a Kelvin-Helmholtz-like instability. In fact, the Kelvin-Helmholtz instability is stabilized for  $L_n$  less than  $0.5 L_v$ . Furthermore, for strong density gradients we show that the gravity driven interchange process is more likely to be active rather than the velocity shear driven Kelvin-Helmholtz instability. The analytical details are

given in Appendix I, entitled "On the Stability of a Stratified Shear Layer" which has been submitted to Physics of Fluids and is in preparation, also, as an NRL Memo Report.

#### F. Plasma Transport in the Auroral Return Current Region

Multimoment time dependent and steady state multifluid plasma simulations have been performed to study the dynamics of auroral field line plasma in the presence of large scale field-aligned return currents. This work is intended to contribute to the development of improved fluid models for use in the study of large scale magnetospheric-ionospheric dynamics. Also, substantial investigation of the upward current region has been performed but the physics of plasma transport in the return current regions has not been thoroughly explored. The theoretical formulations are based on the 13 and 16-moment systems of transport equations. In the polar wind an electron temperature anisotropy develops above 2500 km altitude with  $T_{\perp} > T_{\parallel}$ . The hydrogen ion temperature shows reverse anisotropy, i.e.,  $T_{\parallel} > T_{\perp}$ . Our results are in good agreement with previous theoretical studies of the polar wind and recent experimental observations. The time dependent simulations show the effects of changes on the polar wind plasma dynamics after the sudden application of a current. The electron velocity

and temperatures have a rapid response to a sudden change in conditions with a time constant of a few minutes. The  $H^+$  ion temperatures change on a much longer time scale. The application of return currents to steady state plasma (with a hot electron upper boundary and downward heat flow) reverses the electron temperature anisotropy. Our simulations show that the electron drift velocity corresponding to a current of  $-0.65 \mu A/m^2$  is above the threshold for electrostatic ion cyclotron (EIC) waves. The EIC instability heats the hydrogen ions in the perpendicular direction. The instability also produces anomalous resistivity which heats the electrons. The downward electron heat flow or thermal conduction competes with the upward convection effects to determine the direction of the electron temperature anisotropy. When the resistivity is strong the heating effects dominate. To our knowledge, this is the first successful solution to the 16-moment system of transport equations for the polar wind and the first fluid model to investigate simultaneous interaction of ion cyclotron heating, anomalous resistivity and fluid transport processes in the auroral return current region.

Aspects of this work have been presented at the AGU Spring Meeting 1985, APS Meeting 1985, AGU Fall Meeting 1985, and the AGU Spring Meeting 1986. Abstracts of these presentations are given below. Additional documentation

appears in Appendix J (Ganguli, S.B., H.G. Mitchell, Jr., and P.J. Palmadesso, "Dynamics of Large Scale Return Currents on Auroral Field Lines," NRL Memo Report 5673 (1985)) and in Appendix K (Ganguli, S.B., "Plasma Transport in the Auroral Return Current Region," Ph.D. Thesis, Boston College, Physics Department, 2 April 1986).

#### Studies of Auroral Field Line Equilibria Including the Effects of Return Currents

SUPRIYA B. GANGULI (Science Applications International Corporation, McLean, VA 22102) P.J. PALMADESSO (Naval Research Laboratory, Washington, D.C. 20375)

A numerical model has been developed to study the steady state behavior of a fully ionized plasma ( $H^+$ ,  $O^+$  and the electrons) encompassing the geomagnetic field lines extending from 1500 km to 10 earth radii. For theoretical formulation we have used the 16-moment system of transport equations of Schunk et al. [1982]. The electron gas is collision dominated below 1500 km. Above this altitude electron temperature anisotropy develops with temperature perpendicular to the field line being higher than that parallel to the field line. The  $H^+$  ion temperature anisotropy shows  $H^+$  temperature parallel to the field line being higher than that perpendicular to the field line.  $H^+$  ion temperature also exhibits adiabatic cooling as the supersonic ion gas cools down as it expands in a diverging magnetic field. Our results are in good agreement with the previous theoretical polar wind studies of Schunk et al. Using the same model we studied the auroral field line equilibria including the effects of return currents. With the introduction of the current the electron velocity increases significantly over its polar wind value. The direction of electron temperature anisotropy remains the same but the total electron temperature decreases. These results will be discussed in detail.

This work is sponsored by NASA and ONR.

Schunk, R.W., "Mathematical Structure of Transport Equations for Multispecies Flows," Rev. Geophys. Space Phys. 15, 429-445, 1977.

A Simulation of the Auroral Field Line Plasma Including the Effects of Return Current\*, S.B. GANGULI, Science Applications International Corporation, and P.J. PALMADESSO, Naval Research Laboratory--The importance of field-aligned

currents in magnetosphere ionosphere coupling process is well established. Multimoment fluid plasma simulations have been performed to study the auroral field line equilibria in the presence of large scale field-aligned return currents. Preliminary results indicate that the application of return currents to steady state plasma reverses the electron temperature anisotropy, the electron temperature decreases and the electron velocity increases. The  $H^+$  ion temperature increases as  $H^+$  ion velocity decreases. Various instabilities can arise due to field-aligned currents. Kindel and Kennel [1971] examined several current driven instabilities and showed that electrostatic ion cyclotron instability has the lowest threshold. Our simulations show that the electron drift velocity corresponding to a current of  $-1.0 \mu A/m^2$  is above the threshold for electrostatic ion cyclotron waves. The effects of anomalous resistivity and anisotropic ion heating arising due to EIC instability will be discussed.

\*Work supported by NASA and ONR.

#### Anisotropic Ion Heating in Auroral Return Current Region\*

SUPRIYA B. GANGULI (Science Applications International Corporation, McLean, VA 22102)

P.J. PALMADESSO (Naval Research Laboratory, Washington, DC 20375-5000)

The importance of field-aligned currents in magnetosphere ionosphere coupling process is well established. Multimoment fluid plasma simulations have been performed to study the auroral field line equilibria in the presence of large scale field-aligned return currents.

Various instabilities can arise due to field-aligned currents. Kindel and Kennel [1971] examined several current driven instabilities and showed that electrostatic ion cyclotron instability has the lowest threshold. Our simulations show that the electron drift velocity corresponding to a current of  $-1.0 \mu A/m^2$  is above the threshold for electrostatic ion cyclotron waves. The effects of anomalous resistivity and anisotropic ion heating arising due to EIC instability excited by return currents will be discussed.

\*Work supported by NASA and ONR.

#### Dynamics of Return Currents on Auroral Field Lines\*

H.G. MITCHELL and SUPRIYA B. GANGULI (Science Applications International Corporation, McLean, VA 22102)

P.J. PALMADESSO (Naval Research Laboratory, Washington, DC 20375-5000)

Multimoment fluid plasma simulations have been performed to investigate the plasma dynamics in the presence

of large scale field aligned return currents. The flux tube plasma has a rapid initial response to the onset of the current. The electron velocity and temperature have rapid response to sudden change in conditions with a time constant of about a few minutes. Also, the behavior of the energy transport in the collisionless region determines the time scales on which the flux tube plasma reaches equilibrium. The results from two sets of studies will be discussed: (1) cold electrons of ionospheric origin (13-moment system of transport equations used) and (2) hot magnetospheric electrons at the upper boundary (16-moment system used).

\*Work supported by NASA and ONR.

Anomalous Resistivity in the Auroral Return Current Region\*  
SUPRIYA B. GANGULI (Science Applications International Corporation, McLean, VA 22102)

P.J. PALMADESSO (Naval Research Laboratory, Washington, D.C. 20375-5000)

Multimoment fluid plasma simulations have been performed to study the effects of EIC instability and anomalous resistivity in the auroral return current region. The hydrogen ions are heated transversely due to EIC waves and the anomalous resistivity heats the electrons. The electron heating reverses the electron temperature anisotropy of the return currents. A simple model for the transverse distribution of return currents is discussed. Shapes of the return current profiles can be correlated with the field-aligned transport parameters. Model results are compared with experimental observations of the return currents.

\*Work supported by NASA and ONR.

#### G. Ion Cyclotron Wave Turbulence in the Auroral Ionosphere

We have performed a study on the effects of ion cyclotron wave turbulence on the acceleration and heating of auroral electrons. We showed that large amplitude ion cyclotron waves cause the formation of very localized, spikey parallel d.c. electric fields when a potential drop is applied to a plasma. These structures are in good agreement with the parallel fields observed in the aurora.

A report detailing this work is given in Appendix L entitled "ICW Turbulence and Auroral E Fields". One of the major limitations of this work is that we have to use a fixed model for the ion cyclotron waves. This is due to the large difference between the electron and ion time scales. To remedy this and to provide a tool to study other low frequency phenomena we are exploring with Dr. J. Lyon (NRL) the feasibility of developing other simulation models such as multiple time scale or hybrid codes.

#### H. Preferred Scale Size in the Structuring of Barium Clouds

The development of mathematical models to describe the structuring of barium clouds has been an important topic of record for many years. In the past most of this work has been based on two-dimensional models in which the dynamics of the cloud along the ambient magnetic field  $B$  (third dimension) is unimportant. In the limit in which the parallel conductivity of the plasma is infinite this 2-D model is reasonable. The magnetic field lines in this case are equipotential surfaces so that all the plasma on a given magnetic field moves as a whole. In this 2D model the fundamental equations describing the nonlinear cloud dynamics can be cast in dimensionless form in which no preferred scale size exists. The phenomenon of freezing, in which the continued bifurcation of the cloud ceases once a

critical minimum scale size is reached, therefore, can not be explained within this model.

On the other hand, the parallel conductivity of any real plasma is finite and the potentials which develop within the cloud do not map perfectly along the magnetic field. In the real 3D situation the nonlinear equations describing the cloud dynamics can again be cast in dimensionless form by isotropizing the conductivity tensor. A single new dimensionless parameter

$$g = \frac{cT}{eB} \frac{1}{r_c V_n}$$

now enters the equations, where  $T$  is the temperature,  $B$  is the magnetic field strength,  $V_n$  is the neutral wind velocity and  $r_c$  is the scale size of the cloud perpendicular to  $B$ . Thus, in 3-D the preferred scale size is given by

$$r_c = \frac{cT}{eB} \frac{1}{V_n} ,$$

which is consistent with observed scale lengths of "frozen" barium clouds.

The details of how the parameter  $g$  modifies the cloud dynamics are currently being pursued. In calculations



reported earlier [J.F. Drake, J.D. Huba and S.T. Zalesak, "Finite Temperature Stabilization of the Gradient Drift Instability in Barium Clouds," J. Geophys. Res. 90, 5227 (1985) and NRL Memo Report 5566 (1985)] of a slab plasma cloud with finite extent along B, the gradient drift mode propagates at the diamagnetic frequency,  $\omega_k$ , when  $g \neq 0$ . For  $g > 1$  the propagation frequency exceeds the local growth rate of the instability. However, stabilization occurs only at rather short wavelengths and is not consistent with freezing scale sizes.

Stability calculations of the gradient drift instability have now been extended to more realistic geometries. A set of exact equations have been derived which govern the stability of a cylindrical waterbag of infinite extent along B. When the parallel wave vector,  $k_z$ , is nonzero, diamagnetic propagation again becomes important for  $g > 1$ . In this case the role of the finite diamagnetic propagation is much more important than in the slab geometry. When the diamagnetic velocity exceeds the fluid flow velocity past the cloud ( $g > 1$ ), the perturbations convect from the unstable "backside" of the cloud to the stable "frontside" so that there is no instability. Continued bifurcation of the cloud occurs only for  $g < 1$  or  $r_c > cT/eBV_n$ . This explains the phenomenon of "freezing" and represents a fundamental breakthrough in our understanding of this

important long standing problem. Published work to date appears in the manuscript "Convective Stabilization of Ionospheric Plasma Clouds" which will appear shortly in the Journal of Geophysical Research (see Appendix M). It is also available as NRL Memo Report 5722 (1986).

#### I. Spectral Characteristics of Interchange Turbulence in the Ionosphere

Given the generally accepted notion that ionospheric irregularities, particularly Equatorial Spread F, result from gravitational or wind-driven interchange instabilities, it is important to appreciate a basic difference in interchange physics above and below the altitude of 500 km: below 500 km, ion-neutral collisions,  $\nu_{in}$ , are so strong that the interchanging flute-like flows are heavily damped by the friction and so are always at "terminal velocity". In contrast, above 500 km the friction is weak-the flows can now accelerate or decelerate, create swirls and mix disparate wavelengths.

This simple fact, i.e., the size of the ratio of  $\gamma_g$ , the classical interchange growth rate, to  $\nu_{in}$  has fundamental consequences for the electric field spectra of interchange turbulence. Below 500 km the friction inhibits inertial overshoots and results in the instability being finger-like in the direction of  $\hat{g}$  (see Fig. 7a of Appendix N); in

contrast, above 500 km the swirls mix the flows and create isotropic turbulent fields (Fig. 7b, Appendix N). Consequently, the collisional spectrum is anisotropic (Fig. 5a, Appendix N) while the inertial spectrum is isotropic (Fig. 5b, Appendix N). As a matter of fact, more can be said about the inertial spectrum, namely that it is Kolmogorov-like ( $V_k^2 \propto k^{-8/3}$  as theoretically predicted).

Our numerical simulation, relying on pseudo spectral methods for a model problem, has produced these time results. We believe these results are of a general nature: for example, they are borne out by the 2-D simulation of Mitchell et al (1985, see Appendix D). Thus, an assessment of the nature of ionospheric irregularities must draw a distinction between low and high altitudes and expect fingerlike irregularities below but Kolmogorov turbulence above 500 km.

This work is described in detail in Appendix N, entitled "Spectral Characteristics of Interchange Turbulence" by A.B. Hassam, W. Hall, J.D. Huba, and M.J. Keskinen. It has appeared as NRL Memorandum Report 5793 (1986) and has been submitted for publication in the Journal for Geophysical Research.

## J. Debris-Air Coupling in HANE and in the NRL Laser Experiment

We have investigated debris-air coupling processes relevant to HANE's (High Altitude Nuclear Explosions) and to the NRL laser experiment. The coupling occurs in three stages, loosely labeled as, magnetic field compression, piston formation, and shock formation. During the initial phase the magnetic flux piles up in front of the debris ions impinging on the ambient air plasma with no significant debris-air momentum coupling. The coupling is accomplished in the next stage, the piston formation stage. Finally, a shock is generated by the piston that propagates into the ambient plasma. To determine the dominant physical processes at each stage, we performed numerical simulations using a one dimensional hybrid code. The code includes a self-consistent kinetic treatment for the ions but treats the electrons as a massless fluid and is particularly appropriate to the study of the ion processes involved in the piston and shock formation stages. We focused our work on these later stages of the interaction, while the field compression stage was investigated within the limits of the hybrid numeric scheme. In addition, our understanding of the microphysics involved in the coupling was benchmarked against in situ measurements during the AMPTE releases in the magnetosphere.

## 1. Piston Formation

We performed several simulations to clarify the physics of the piston formation stage, i.e., for times less than an ion gyrotime. These simulations were initialized with various plausible models for the field compression; the results were relatively insensitive to the specific model. We find that several mechanisms can be effective at different times of the debris expansion: specifically turbulent coupling, laminar pickup, and Larmor coupling. A strong electric field is set up in the region of field compression and electron heating occurs near the leading edge of the debris, which is convected into the ambient plasma. The bulk of the ambient plasma is accelerated to approximately the debris speed by this electric field while a small fraction of the ions are reflected and flow upstream with about 3 times the original debris velocity,  $V_d$ . Due to the debris thermal spread, a fraction of the debris overtakes the electric field and is accelerated also to about  $V_d$ . The flow of the accelerated debris and ambient ions through the upstream ambient plasma is unstable; electric turbulence is produced that results in significant heating of the ambient plasma upstream.

Within the magnetic field compression, there is turbulent coupling between the debris and ambient plasmas. While significant heating occurs here, the coupling is

incomplete and at later times Larmor coupling becomes important. The latter two results, however, depend on the initialization model; specifically on the assumptions concerning the width of the field compression and the amount of ambient plasma penetration into the debris. Our results are described in more detail in Goodrich et al. (1985) entitled "Early Time Coupling Studies Using a 1D Hybrid Code," NRL Memo Report 5553 (1985) which appears here as Appendix O.

We investigated further aspects of the piston formation problem. Due to the importance of the laminar electric field pushed ahead of the debris, and its dependence on electron heating, we examined the effects of several electron heating models on our results including: ohmic heating due to anomalous resistivity, adiabatic heating only, constant electron temperature, and zero temperature. We find that the amount of both debris and ambient ions accelerated decreases as the amount of electron heating allowed decreases, i.e. for the electron models in the order listed above. This result has important implications to the simulations that Berkeley Research, MRC, and we have performed for DNA since the electron models vary widely in the codes used. We have also performed simulations in which the debris was composed of several different charge states. We find, as expected, qualitatively similar results in

which, however, the ions with the highest charge per mass receive the greatest acceleration.

## 2. Shock Formation

We have performed a small number of very large hybrid simulations of the full coupling process with the specific goals of: documenting the existence of the compression, piston formation, and shock formation stages, studying the transitions among them, and investigating the conditions and time required for a shock to form. Only a small number of runs could be made, due to the cost in computation and memory resources required to run the simulations for the several ion gyrotimes needed to probe shock formation with sufficient spatial resolution to reasonably treat the compression stage. These runs were initialized by impinging a debris beam onto uniformly magnetized ambient plasma; no initial field compression was assumed. We find that interaction of the debris and ambient plasmas does indeed separate into the above three distinct stages described below, with  $\omega_{ci}$  = ion gyrofrequency.

### 2.1 Magnetic compression ( $t < 1/\omega_{ci}$ ):

Initially the magnetic field is compressed just ahead of the debris with little effect on diffusion of the field compression into the debris beam. Later some debris ions are accelerated by the laminar electric field due to the compression, reaching approximately twice their initial

velocities. After the magnetic compression becomes large enough it stops any debris ions from entering it (via thermal motion) and being accelerated.

#### 2.2 Piston formation ( $t > 1/\omega_{ci}$ ):

Coupling occurs between the debris and ambient plasmas. The ambient plasma is compressed and accelerated (to about 80% of the initial debris speed) by the fields at the leading edge of the debris beam. A fraction of the ambient ions are reflected by these fields and flow upstream with velocities of about  $2V_d$ . The bulk of the debris is compressed (to twice the original density) and decelerated to  $0.8V_d$  at the "piston", the debris-ambient plasma interface, while a few of the debris ions are reflected.

#### 2.3 Shock formation ( $t > 6/\omega_{ci}$ ):

After about  $t = 1/\omega_{ci}$ , a region of heated ambient plasma extends increasingly far ahead of the piston. Roughly  $5/\omega_{ci}$  later, the reflected ambient ions are returned, due to Larmor coupling, to this heated region. The reflection and return of these ions is characteristic of supercritical perpendicular shock waves (Leroy et al., Geophys. Res. Lett. 8, 1269, 1981). However, the gyroradii of these ions are large enough to penetrate through the piston and are lost to the heated ambient plasma region. Thus a shock does not yet fully form and cannot until the leading edge of the heated region extends more than a gyroradius (of the reflected



ions) beyond the piston. More details describing this work appear in a classified report: K. Papadopoulos, C. Goodrich, H. G. Mitchell, and J. D. Huba "Time Scale for Shock Formation Following a HANE(U)", NRL Memo Report 5712, July 1985 (SECRET). The unclassified abstract of this paper follows.

#### Abstract

We present a simple model to determine the minimum time to form a high Mach number ( $M_A$ ) shock following the formation of the piston which drives the shock. We find that the time scale is controlled primarily by the time scale for piston formation. For  $M_A > 2$  the time scale for shock formation is  $t_0 \sim 4-6 M_A / \Omega_i$  where  $\Omega_i$  is the upstream ion gyrofrequency. We discuss the relevance of this result to the modeling of debris patches following a HANE.

### 3. Simulations of the NRL Laser Experiment

We performed a series of simulations to study the expansion of the target debris in the NRL laser experiment.<sup>(1)</sup> While similar to those described in Section 2.2, these runs involved much lower debris velocities and total mass. We find that first ( $t < 2$  nsec) the debris ( $A1^{+3}$ ,  $A1^{+5}$ ) forms a leaky piston; coupling via turbulent electric fields occurs with the ambient ( $N^+$ ) plasma that penetrates into the debris. A shock is launched into the ambient plasma that propagates away from the piston. We find that the key observables in the experiment, the peak electron density and peak magnetic field, are associated with the piston and

shock respectively; we thus predict that the peak field should be seen spatially displaced from the peak density. This result is consistent with the experimental results and directly contradicts simulation results obtained by MRC using the MACRO code for the same parameters. At later times, we find that the debris is stopped in roughly 0.6-0.8cm, about an equal mass distance. The shock (and peak field value) weakens as it propagates through the ambient plasma.

#### 4. HANE Coupling Microphysics Revealed by AMPTE Measurements

The in situ measurements of the plasma parameters from the AMPTE (Active Magnetospheric Particle Tracer Explorers) artificial comet releases in the solar wind has provided us with a unique set of data to test the available theories on the subject of collisionless coupling of magnetized plasma streams under high Mach number conditions ( $M_a \gg 1$ ). Understanding of the subject is critical to the debris-air momentum coupling following HANE's and subsequent energization of the plasma. We performed a theoretical analysis which compares the in situ observations of the plasma parameters and wave signatures against the theoretical concepts currently applied to the HANE early time problem. The analysis demonstrates that the coupling

occurred in two stages. In front of the interaction and before the final magnetic field compression the coupling can be attributed to the magnetized counterstreaming ion instability between the solar wind and the released ions. The observations of the slowing down and of the wave amplitude and spectrum are consistent with the instability criteria and the nonlinear analysis of the saturated spectra. During this stage more than 80% of the solar wind momentum couples to the release. During the second stage, the field compression reached a value in excess of ambient, while its width became comparable to the  $Ba^+$  gyroradius. At this point, Larmor coupling dominated and completed the coupling process. An interesting effect is the fact that the  $Ba^+$  cloud was observed to skid in a direction transverse to the magnetic field reminiscent of the Starfish jets. An analysis of this phenomenon is in progress. This work has been documented in a report by K. Papadopoulos, J.D. Huba, and A.T.Y. Lui, "Collisionless Coupling in the AMPTE Artificial Comet" which has been submitted to the Journal of Geophysical Research (1986) and appears, also, as NRL Memo Report 5835 (1986). This report appear here as Appendix P.

#### K. Power Spectral Density of Radiating Plasma Clouds

We have investigated the spatial spectral properties of radiating plasma clouds. We first consider the general

relationship between properties of the cloud and the power spectral density (PSD) of a scan of its photographic image. We then model a HANE-like striation, using this theory, and compare with HANE data. To concentrate on essential properties, in relating cloud to scan measurements, we focus on the uncertainties associated with geometrical aspects, assuming idealized conditions, namely, optically thin clouds, no parallax effects, and no distortion due to camera, lenses, and film grain. We consider clouds with piecewise constant (pc) and power law radiating intensities. We do not attempt to correlate this radiant intensity with the ion density.

For pc clouds, where the one-dimensional asymptotic spectrum of the power is proportional to  $k^{-2}$ , we show that the asymptotic spectrum of the scan depends upon the character of the contour at the point where it is tangent to the extremal ray. If the contour at  $(x_0, y_0)$  behaves like  $y - y_0 = \gamma(x - x_0)^\tau$ , then the asymptotic spectral envelope of the PSD of the scan varies as  $k^{-2(\tau+1)}$ . In addition, if the radiating intensity in a cloud flank varies with a power law  $\mu$ , then the asymptotic spectral envelope of the scan's PSD varies as  $k^{-2(1+\tau+\mu)}$ .

We apply these considerations to data from PLACES events IRIS and GAIL. We show that the good data of highest  $K$  are associated with a transitional region and are not associated

with the asymptotic spectral index that arises in nonlinear turbulent or wave-steepening dynamical processes. Details of this work, entitled "Projections of Plasma Cloud Structures and Their Spectra," have been published in J. Geophys. Res. 91, 5851(1986) and appear in this report as Appendix Q.

As to the HANE striation modeling, there is good reason to believe that substantial regions of the ionosphere following HANE events will be characterized by a highly structured plasma and that the structuring will persist for hours. Since defense detectors typically operate in the ir and are sensitive to the nature of the structuring, it is important to be able to predict the spatial characteristics of ir emissions. We present a simple analytical model which embodies current knowledge of late-time high altitude striations, based on theory and the simulations being performed at NRL. Those properties still uncertain are parameterized. Using this model we are able to predict the PSD characteristics that result from striations as a function of shape parameters, edge sizes, and the angle of observation.

These results are preliminary. First, there is still imperfect knowledge of some aspects of the physics incorporated in the simulations. Second, simulations to date have been more appropriate to the barium release

scenario and need to be repeated for parameters more relevant to the HANE case. Finally, HANE data in the ir is essentially non-existent and available visible data (photographic) has insufficient range to distinguish among alternative models. This work, by Hyman, et al, entitled "A Striation Model and Spectral Characteristics of Optical-IR Emission from HANE," has been published as NRL Memo Report 5568 (1985) and appears here as Appendix R.

#### L. Debris Charge States in HANE and in the NRL Laser Experiment

It is reasonably well established that the charge state,  $z$ , of HANE debris drops from very high values to  $z \sim 1$  on disassembly time scales. Measurements of debris spectra from STARFISH<sup>(2)</sup> detect neutral aluminum,  $Al^{+1}$ , and  $Al^{+2}$  but nothing higher. Disassembly calculations also predict this result. A calculation by Clark and Jacobs at NRL<sup>(3)</sup> estimates that the charge state drops to  $z \sim 1$  by the time the burst has expanded to  $\sim 200$  meters radius, at which point the charge state is frozen in. That is, by this time the density has dropped to the point that recombination is too slow to be important. Let us investigate the charge state of aluminum in the laser experiment.

Code results at NRL predict very high charge states ( $z \sim 10$ ) on the front side, persisting for times  $> 100$  nsec. On

the back side, because of much lower temperatures, charge states never get above  $z \sim 1$ . We will first show why the high charge states on the front side do not recombine in the laser experiment and then present an argument to explain in what way the bomb and the laser are different.

At 10 nsec, shortly after the laser pulse shuts off, the average charge state of the aluminum ions is  $\sim 10$  and  $T_e \approx 300$  ev,  $N_i \sim 10^{19} \text{ cm}^{-3}$ ,  $N_e \sim 10^{20} \text{ cm}^{-3}$  according to code results. The radiative recombination rate coefficient,  $\alpha_R$ , for 10 times ionized aluminum is

$$\alpha_R = 10^{-10} T_e^{-0.8} = 10^{-10} (300)^{-0.8} = 1 \times 10^{-12} \text{ cm}^3/\text{sec}.$$

Under the above conditions 3 body recombination is more than 2 orders of magnitude slower and can be neglected. The recombination time scale is then,  $\tau$ ,

$$\tau = \frac{1}{\alpha_R N_e} = \frac{1}{(10^{-12})(10^{20})} = 10^{-8} \text{ sec} = 10 \text{ nsec}$$

Thus, the recombination e-folding time is 10 nsec. However, the electron density drops 2 orders of magnitude in the next 10 nsec because of hydrodynamic expansion. The aluminum ions, therefore, become frozen at the high charge states that exist at 10 nsec.

Why does the charge state in the bomb freeze out with  $z \sim 1$  and the laser experiment with  $z \sim 10$ ? It is useful to consider the dimensionless quantity,  $\xi$ , defined by

$$\xi = N_e \alpha_R \delta t$$

where  $\delta t$  is a time interval of interest. When  $\xi$  is much greater than unity recombination will be important on that time scale. When  $\xi \leq 1$ , those charge states that exist at that time will be frozen in. We will calculate  $\xi$  for the bomb ( $\xi_B$ ) and for the laser ( $\xi_L$ ). For simplicity we will approximate the recombination coefficient by  $\alpha = z^{1.5} \alpha_0 / T_e$  which simplifies the analysis and does not materially affect the conclusion. Then for adiabatic expansion at constant velocity with  $\gamma = 5/3$

$$n = n_0 \left( \frac{r_0}{R} \right)^3$$

$$T = T_0 \left( \frac{r_0}{R} \right)^2$$

$$R = vt$$

$$N_e = \bar{z} n$$



Here,  $n_0$ ,  $r_0$ ,  $T_0$ , and  $v$  are the density, radius, temperature, and expansion velocity, respectively, at the time zero as the expansion begins.  $\bar{z}$  is the average charge. Then,

$$\begin{aligned} \xi &= \bar{z} n \frac{\alpha_0 z^{1.5}}{T} = \bar{z} n_0 \left[ \frac{r_0}{R} \right]^3 \frac{\alpha_0 z^{1.5}}{T_0} \left[ \frac{R}{r_0} \right]^2 \delta t \\ &= \bar{z} n_0 \alpha_0 z^{1.5} \left[ \frac{r_0}{v t} \right] \frac{\delta t}{T_0} \end{aligned} \quad (1)$$

For the laser we have  $n_{0L} = 10^{23} \text{ cm}^{-3}$ , i.e., solid density.  $T_{0L} = 10^3 \text{ ev}$ ,  $r_0 \sim 2 \times 10^{-3} \text{ cm}$ ,  $R_L = v_L t_L$ , where  $v_L$  is the expansion velocity in the laser experiment,  $\sim 3 \times 10^7 \text{ cm/sec}$ , and  $t_L$  is the time elapsed. Thus,

$$\xi_L = \bar{z} [10^{23}] z^{1.5} \alpha_0 \frac{[2 \times 10^{-3}]}{[3 \times 10^7 t_L]} \frac{\delta t_L}{[10^3]} \sim 7 \times 10^9 \alpha_0 \bar{z} z^{1.5}$$

where we have taken  $\delta t_L = t_L$ .

For the bomb we have  $n_{0B} = 10^{23} \text{ cm}^{-3}$ ,  $r_{0B} = 10^2 \text{ cm}$ ,  $R_B = v_B t_B = (1 \times 10^8 \text{ cm/sec}) t_B$ , and  $T_{0B} = 10^5 \text{ ev}$ . Then

$$\xi_B = \bar{z} [10^{23}] \alpha_0 z^{1.5} \frac{[10^2]}{[1 \times 10^8 t_B]} \frac{\delta t_B}{[10^5]} = 1 \times 10^{12} \alpha_0 \bar{z} z^{1.5}$$

with  $\delta t_B = t_B$ . For  $\alpha_0 \sim 10^{-12}$ ,  $\xi_L \rightarrow 1$ , with the charge state at a high level, whereas  $\xi_B$  does not drop to unity until the charge state  $\sim 1$ . For equal charge states the ratio  $\xi_L/\xi_B \sim 0.007$ . That is, the bomb and laser experiment give rise to values of  $\xi$  which differ by more than 2 orders of magnitude. The fundamental difference is in the scaling of the weapon mass and size. Since the masses scale like  $M_L/M_B = 10^{-12}$  and the densities are initially the same,  $r_0^3 \sim M$ . Then  $r_{0L}/r_{0B} = 10^{-4}$ . Thus, the  $\xi$ 's, which scale like  $r_0$  (see (1)), differ inherently by a factor of  $10^{-4}$ . A second subtler difference is the energization time and is not accounted for in the above discussion.

It is possible that charge exchange between aluminum ions and the background nitrogen gas will rapidly reduce the average aluminum charge and restore a greater similarity between the experiment and the bomb. We consider this now.

The charge exchange cross section for aluminum ions of charge  $z$  on neutral nitrogen is given to a good approximation by (4)

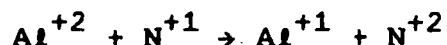
$$\sigma = 1.5 \times 10^{-16} [1 + 4z^{1/2} + 4z] \text{ cm}^2$$

About 75% of the reactions result in  $N^+$  and the rest produce mostly  $N^{++}$  and some  $N^{+++}$ . At  $z = 10$  this gives a cross section of  $8 \times 10^{-15} \text{ cm}^2$ . The time constant for charge exchange, assuming  $2 \times 10^{16} \text{ cm}^{-3}$  neutral N, is  $\tau = 1/(\sigma v [N]) = [(8 \times 10^{-15})(4 \times 10^7)(2 \times 10^{16})]^{-1} = 2 \times 10^{-10} \text{ sec}$ . Thus, as long as the  $Al^{+10}$  can mix effectively with the neutrals it will rapidly charge exchange. The cross section drops as  $z$  drops but it is still quite large ( $\sigma = 3.8 \times 10^{-15} \text{ cm}^2$  for  $Al^{+4}$ ) for moderately charged aluminum. However, what happens is the neutral nitrogen gets used up. Now, we need to rely on the charge exchange reaction between highly charged aluminum ( $Al^{+10}$ , eg.) and singly ionized nitrogen, and then doubly ionized, etc. These rates are lower by, perhaps, a couple of orders of magnitude<sup>(4)</sup> from the neutral charge exchange. They are not really known well and we are currently investigating these cross sections.

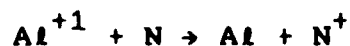
Code calculations at NRL<sup>(5)</sup> show that charge exchange does reduce the aluminum charge state but primarily in the boundary region. An aluminum cavity with  $z \sim 10$  still persists out to times  $\sim 100 \text{ nsec}$ . In the boundary region as one moves out of the cavity the charge drops from  $z \sim 10$  down to  $z \sim 3$  or 4. It is likely that if some low-lying excited states of N and  $N^+$  were incorporated in the model the charge state of aluminum would drop further. For example,



is endothermic by 1.15 ev. However,  $\text{N}^{+1}$  has a low lying excited state at 1.9 ev above the ground state that will be highly populated at the existing plasma temperature. This will significantly increase the  $\text{Al}^{+2}$  density over current results. Similarly,



is endothermic by 10.8 ev. But there is an excited state of  $\text{N}^{+1}$  at 11.4 ev, above ground. At temperatures ~ 5 ev this state would be significantly populated. Finally,



is endothermic by 8.5 ev. But, again, there are levels at ~10 ev above ground that will have substantial population at temperatures ~ 5 ev. Thus, it is not out of the question that states of aluminum down to and including neutral aluminum could be produced via charge exchange with the background. It is difficult to estimate number densities at

this time without looking in more detail at the possible excited state reactions and their cross sections.

#### M. Low Frequency Instabilities in HANE

It is well known that HANE's can have deleterious effects on C<sup>3</sup>I systems (for example, by disrupting satellite communications and radar systems) and it is therefore important to the Defense Nuclear Agency to understand the atmospheric effects of HANE's. The primary cause of these negative effects is the production of long-lasting, large-scale, ionization irregularities in the ionosphere. In order to understand the cause and evolution of these irregularities, SAIC in collaboration with NRL has developed and is continuing to develop detailed theoretical and computational models of HANE's. Of recent interest to the Defense Nuclear Agency is a thorough re-examination of early time phenomena ( $t < 1$  sec) which are primarily associated with the deposition of weapon energy in the atmosphere. Aside from radiation processes, the conversion of the kinetic energy of the debris into thermal energy of both the debris and air ions, and its ultimate deposition in the conjugate patches, is of particular importance. The important issues involved are debris-air coupling length and time scales, and thermalization processes. Underlying these issues are a host of complicated plasma physics processes.

The ensuing turbulence which results from plasma instabilities can act as a mechanism to thermalize the various ion species and to pitch angle scatter ions.

To date, the most intense effort to understand the role of plasma instabilities in early time HANE evolution has been directed at debris-air coupling. In this regard, NRL performed a series of investigations in the 70's to determine the anomalous transport properties of instabilities which could occur at the debris-air interface<sup>(6)</sup>. The effects of these instabilities on the evolution of the coupling shell were determined by incorporating the appropriate anomalous transport coefficients in a multi-fluid code. Subsequently, further advances have been made in this area through the use of a one dimensional hybrid code. This code treats the electrons as a fluid but the ions as particles. This permits the instabilities, and their effects on the plasma, to be studied self-consistently (see Appendix O). It has also been recently suggested that microturbulence could impact the evolution of structure causing instabilities.<sup>(7)</sup> Thus, the point to be made is that plasma turbulence can have a significant impact on the early time evolution of a HANE.

The aforementioned studies of plasma instabilities have dealt with high frequency turbulence, i.e.,  $\omega \gg \Omega_i$  where  $\omega$  is the wave frequency and  $\Omega_i = eB/m_i c$  is the ion cyclotron

frequency. These instabilities impact very early time processes such as debris-air coupling and plasma thermalization. However, there are many low frequency instabilities (i.e.,  $\omega \leq \Omega_i$ ) that can be excited which may be important to early time HANE evolution. We present a detailed linear analysis of low frequency ( $\omega \leq \Omega_i$ ) instabilities driven by an ion temperature anisotropy ( $T_{\perp i} \neq T_{\parallel i}$ ). In particular we investigate the electromagnetic ion cyclotron instability, the mirror instability, and the firehose instability. These instabilities require a high  $\beta$  plasma (i.e.,  $\beta > 1$ ) which is typical of an early time HANE plasma. The electromagnetic ion cyclotron and mirror instabilities also require  $T_{\perp i} > T_{\parallel i}$ , while the firehose instability requires  $T_{\parallel i} > T_{\perp i}$ . In general, we expect the early time coupling shell to have  $T_{\perp i} > T_{\parallel i}$  so that the firehose instability is not obviously relevant to HANE situations but is included for the sake of completeness. We have also included an analysis of the influence of an electron temperature anisotropy on the MHD instability. This is an extension and correction of the work of Basu and Coppi<sup>(8)</sup>. We discuss the application of this research to HANE phenomena.

This work is described in more detail in a report by Y.C. Lee and J.D. Huba entitled "Low Frequency Instabilities

Driven by an Ion Temperature Anisotropy," NRL Memo Report 5552 (1985) and appears here as Appendix S.

#### N. Numerical Studies of the Dynamics of the Summer Monsoon

The summer monsoon circulation is dominated at low levels by the East African Jet (EAJ), which is a cross equatorial jet running along the East African topography and across the Arabian Sea to India. Models of the jet have not satisfactorily explained the source of mass for the jet, the wind maximum off the Somali coast or the curvature of the flow in the region.

The linear model study of Sashegyi and Geisler, included here as Appendix T, examined the linear response of a stratified atmosphere to diabatic heating associated with the large scale summer monsoon convection. The study showed that the summer monsoon heat source forces a cross-equatorial meridional circulation which is about half as strong as the dominant zonal circulation to the west of the heat source. The imposition of a meridional wall concentrates the cross-equatorial flow in the meridional cell into a western boundary jet. For representative summer monsoon heating the northward mass transport in this linear jet is comparable to what is observed. The cross-equatorial flow pattern forced by low-level diabatic heating along the African coast consists of a western boundary jet near the



equator that turns into a geostrophically balanced sea breeze in low latitudes away from the equator. The northward mass flux in this locally forced jet is about an order of magnitude smaller than that which is forced by the summer monsoon heat source. This locally forced jet is of very small vertical scale with a maximum wind speed comparable to that in the monsoon-heating jet. This suggests that the flow in the lowest few hundred meters of the EAJ can be strongly influenced by a flow driven by low-level differential heating. For further details, refer to the paper in Appendix T entitled "A Linear Model Study of Cross-Equatorial Flow Forced by Summer Monsoon Heat Sources" which has been provisionally accepted (June 1986) for publication in The Journal of the Atmospheric Sciences.

In a study motivated by the linear model results, we have adapted NRL's Regional Numerical Weather Prediction model to study the various influences of realistic topography, convective heating and sensible heating on the structure of the EAJ. The model is a three dimensional, hydrostatic primitive equations model which incorporates topography and physical parameterizations of the planetary boundary layer, horizontal mixing and precipitation processes. In this study, the regional model is integrated for six days from an initial zonally averaged wind field. Cases have been run with and without prescribed convective

heating, surface sensible heating and topography for average July conditions. The details are described in a report by Sashegyi and Chang (in preparation).

In the study of Sashegyi and Chang, the strength of the East African Jet (EAJ) and the structure of the monsoon circulation are found to be very sensitive to the terrain, the convective heating and the strength of the zonal flow. They are less sensitive to the sensible heating and the effects of nonlinear advection. With topographic forcing only, the response is largely confined to the lower troposphere. The South-East trades are deflected across the equator by the East African topography, as a shallow low level jet, lying below 850 mb. The jet doesn't penetrate farther north than 8°N, curving southward on its eastward path over the Arabian Sea and crossing the extreme southern tip of India. A wind maximum of 7 m/s is found over the northern tip of Madagascar and a further maximum of 5 m/s is found at 4°N. The trades are not maintained during the integration, weakening to some 5 m/s. Some  $9 \times 10^{12}$  g/s (or 78%) of the flow incident on the topographic barrier is deflected across the equator in the low level jet. The horizontal structure of the jet is strongly inertially controlled as in the barotropic model of Hart.<sup>(9)</sup> Above 850 mb, the response is weak and flows mostly over the topographic barrier.

With forcing by the monsoon cumulus heat source included, the low level cross equatorial flow is much stronger and the low level jet penetrates farther north to 16°N in a broad stream of southwesterly flow across the Arabian Sea. The cross equatorial mass flux is increased to some  $34.0 \times 10^{12}$  g/s, most of which (some  $27.6 \times 10^{12}$  g/s) occurs in the model low level "East African" Jet (EAJ). A wind maximum of 8.7 m/s is produced over the central Arabian Sea, in a region of confluence of strong Arabian northwesterlies with the cross-equatorial flow as in Bannon's<sup>(10)</sup> barotropic model. However, as he stated, the position of this maximum is too far to the east compared to the observations. This wind maximum is only weakly influenced by nonlinear advection. The trade winds in the Southern Hemisphere are stronger, reaching 8 m/s. In the upper troposphere, a high is centered over NW India and the Tibetan Plateau, with a strong easterly jet on its equatorward side. A strong southward flow emanates from the easterly jet to cross the equator and subside in the region east of southern Africa, providing a feedback to the low level trade winds. Without the presence of topography, the response to monsoon cumulus heating shows a southwesterly jet, weaker cross equatorial flow and no East African jet.

In a final set of experiments, the effects of surface sensible heating were included with the use of prescribed

surface air temperatures. In the first case the surface air temperature is given by the initial zonal temperature field and in the second case, observed average surface air temperatures for July are used. With topography, monsoon convective heating and surface sensible heating due to the initial surface air temperatures, the trade winds in the Southern Hemisphere are maintained through the integration period to a maximum of 11.4 m/s. The wind maximum in the low level EAJ is stronger and its position shifted somewhat westward. Stronger Arabian northerlies (reaching 10.8 m/s) are also found. However, only a small 2.5% increase in the cross-equatorial mass flux is found in the EAJ. Little change is observed in the upper tropospheric response. Using observed July surface air temperatures, the low level EAJ is stronger with a maximum of 14 m/s over the Arabian Sea, oriented along the coastline of Somalia and Saudi-Arabia at the confluence line of the Arabian northerlies and the cross-equatorial flow, in agreement with the observations. Non-linear advection of momentum does not play an important role in this jet maximum. The cross equatorial mass flux in the EAJ is only increased by some  $4.4 \times 10^{12}$  g/s to  $32.7 \times 10^{12}$  g/s. The Arabian northerlies have weakened to 7.2 m/s and upslope winds are found on the slopes of the Tibetan Plateau in response to the surface heating.

The study demonstrates that the summer monsoon circulation is primarily driven by the large scale convective heating contrast in the presence of topography. In the Northern Hemisphere the geometry of the lower tropospheric monsoon flow forced by the convective heating is controlled by the topography in this region. The cross-equatorial flow forced by the monsoon convective heating is concentrated to form the EAJ by the East African topographic barrier. The deflection of the trade winds by the barrier appears to be a smaller contribution than that due to the monsoon convective heating. The low level wind maximum off the coast of Somalia is dynamically related to the confluence of the Arabian northerlies with the cross-equatorial flow. Its position and intensity are controlled jointly by monsoon convective heating in the presence of topography, the north-south temperature gradient and the sensible heating contrast across the coastline.

#### O. Middle Atmosphere Transport and Chemistry Studies

On the basis of our model calculations in support of the NRL Middle Atmosphere Program we conclude that mesospheric water vapor measurements provide the most definitive clue to vertical mixing in the mesosphere. The low  $H_2O$  mixing ratio and resultant odd hydrogen densities indicated in Bevilacqua et al.<sup>(11,12)</sup> lead to substantial reductions in the loss of

odd oxygen and CO at the mesopause. The calculated O, O<sub>3</sub>, and CO concentrations are in reasonable agreement with mesopause data. Below the mesopause the O and O<sub>3</sub> density profiles are insensitive to vertical mixing and the inference of K<sub>zz</sub> from their profiles is poorly constrained. Although chemical acceleration of vertical transport is substantial for O and O<sub>3</sub> below 80 km, it is not sufficient to overcome the chemical control of their density structure. The importance or significance of chemical acceleration is subtle, because one must distinguish which species have accelerated transport and which are most sensitive and diagnostic of vertical transport. Chemical acceleration produces large increases in K<sub>zz</sub> but only modest, at most factor of 2, effects on the concentrations of O and O<sub>3</sub>. Our calculations show conclusively with our present understanding of O, O<sub>3</sub>, H<sub>2</sub>O, and CO that only the H<sub>2</sub>O profile reveals the correct magnitude of background vertical mixing (D<sub>H</sub>) in the mesosphere, which for early summer in the Northern Hemisphere at mid-latitudes is  $\sim(1-2) \times 10^5 \text{ cm}^2 \text{ s}^{-1}$ . From Strobel et al.<sup>(13)</sup> the associated cooling due to breaking gravity waves is  $\sim 0.75-1.5 \text{ }^\circ\text{Kd}^{-1}$ . Thus, to lowest order the mesosphere is in radiative equilibrium. Although it can not be proved from this research, it appears that the consensus is the momentum diffusion coefficient, D<sub>M</sub>  $\sim 10^6 \text{ cm}^2 \text{ s}^{-1}$ <sup>(14,15,16,17)</sup> and hence the eddy Prandtl number must

be greater than 1. Fritts and Dunkerton<sup>(18)</sup> have analytically demonstrated why in the wave breaking process  $P_r > 1$ .

## REFERENCES

1. Ripin, B.H., A.W. Ali, H.R. Griem, J. Grun, S.T. Kacenjar, C.K. Manka, E.A. McLean, A.N. Mostovych, S.P. Obenschain, and J.A. Stamper, "Physics of Laser-Produced Interstreaming Plasmas", in Laser Interaction and Related Plasma Phenomena, Vol. 7, edited by G. Miley and H. Hora (Plenum Press), in press, 1986.
2. Sappenfield, D., M. Peek, H. Hoerlin, "Dominic Spectroscopy by LASL: Starfish" (U), LA03943-MS (1968) SRD.
3. Clark, R. and V. Jacobs, unpublished.
4. Olson, R.E., private communication.
5. Hyman, E., M. Mulbrandon, and J. Giuliani, presentation at DNA Laser HANE meeting, NRL, January 1986.
6. Lampe, M., W. M. Manheimer, and K. Papadopoulos, "Anomalous Transport Coefficients for HANE Applications Due to Plasma Micro-Instabilities," NRL Memo Report 3076, 1975.
7. Huba, J.D., "Influence of Microturbulence on Early Time HANE Structure", NRL Memo Report 5305, 1984.
8. Basu, B. and B. Coppi, "Field-Swelling Instability in Anisotropic Plasmas," Phys. Rev. Lett. 48, 799 (1982).
9. Hart, J.E., "On the Theory of the East African Low-Level Jet Stream," Pure Appl. Geophys. 115, 1263-1282 (1977).
10. Bannon, P.R., "On the Dynamics of the East African Jet. III, Arabian Sea Branch", J. Atmos. Sci. 39, 2267-2278 (1982).
11. Bevilacqua, R.M., J. J. Olivero, P. R. Schwartz, C.J. Gibbins, J. M. Bologna, and D. L. Thacker, "An Observational Study of Water Vapor in the Mid-Latitude Mesosphere Using Ground-Based Microwave Techniques," J. Geophys. Res., 88, 8523-8534, 1983.
12. Bevilacqua, R.M., W. J. Wilson, W. B. Ricketts, P. R. Schwartz, and R. J. Howard, "Possible Seasonal Variability of Mesospheric Water Vapor," Geophys. Res. Lett., 12, 391-400, 1985.



13. Strobel, D.F., J. P. Apruzese, and M. R. Schoeberl, "Energy Balance Constraints on Gravity Wave Induced Eddy Diffusion in the Mesosphere and Lower Thermosphere, J. Geophys. Res., 90, 13,067-13,072, 1985.
14. Lindzen, R.S., "Turbulence and Stress Owing to Gravity Wave and Tidal Breakdown," J. Geophys. Res., 86, 9707-9714, 1981.
15. Holton, J.R., "The Role of Gravity Wave-Induced Drag and Diffusion in the Momentum Budget of the Mesosphere," J. Atmos. Sci., 39, 791-799, 1982.
16. Holton, J.R., "The Influence of Gravity Wave Breaking on the General Circulation of the Middle Atmosphere," J. Atmos. Sci., 40, 2497-2507, 1983.
17. Garcia, R.R., and S. Solomon, "The Effect of Breaking Gravity Waves on the Dynamics and Chemical Composition of the Mesosphere and Lower Thermosphere," J. Geophys. Res., 90, 3850-3868, 1985.
18. Fritts, D.C., and T. J. Dunkerton, "Fluxes of Heat and Constituents Due to Convectively Unstable Gravity Waves," J. Atmos. Sci., 42, 549-556, 1985.

## **APPENDIX A**

### **Electrostatic Ion-Cyclotron Instability Caused by a Nonuniform Electric Field Perpendicular to the External Magnetic Field**

**G. Ganguli and Y.C. Lee  
Science Applications International Corporation**

**P. Palmadesso  
Naval Research Laboratory**

# Electrostatic ion-cyclotron instability caused by a nonuniform electric field perpendicular to the external magnetic field

G. Ganguli and Y. C. Lee<sup>a)</sup>

Science Applications International Corporation, McLean, Virginia 22102

P. Palmadesso

Plasma Physics Division, Naval Research Laboratory, Washington, D.C. 20375

(Received 6 November 1984, accepted 6 January 1985)

A new mechanism that can destabilize kinetic ion-cyclotron waves in the presence of a nonuniform electric field perpendicular to the uniform ambient magnetic field is given. In the absence of the electric field, the mode energy is positive, while in the presence of a uniform electric field the mode energy could be negative. However, when the electric field is nonuniform, it is possible for a finite region to be of negative wave energy surrounded by regions of positive wave energy. A nonlocal wave packet couples the two regions so that a flow of energy from the region of negative wave energy to the region of positive wave energy will cause the mode to grow. This gives rise to the instability.

The ion-cyclotron instability has been of importance to both space and laboratory plasmas. In most previous studies, field-aligned currents or ion beams have been cited as the driving mechanism.<sup>1</sup> Recently some laboratory experiments<sup>2</sup> have reported ion-cyclotron instability in circumstances in which neither of the above mechanisms provides a satisfactory free energy source, and the existence of a two-dimensional electric field is conjectured to play a role. Further, unstable ion-cyclotron waves have been reported in connection with double layers<sup>3</sup> and electrostatic shocks.<sup>4</sup> In all these cases, a localized electric field perpendicular to the external magnetic field is an intrinsic feature of the equilibrium. The purpose of this letter is to report a new kinetic ion-cyclotron instability driven by a nonuniform electric field perpendicular to the external magnetic field, which could be of importance to the situations referred to above.<sup>2-4</sup>

Using physical arguments we first establish that an equilibrium characterized by an external uniform magnetic field  $B_0$  (in the  $z$  direction) perpendicular to an external nonuniform electric field  $E_0(x)$  (in the  $x$  direction) is unstable to the electrostatic ion-cyclotron waves. The local dispersion relation of the electrostatic ion-cyclotron waves<sup>5</sup> is given by

$$D(\omega, k) = 1 + \tau + \sum \Gamma_n(b_1) \left( \frac{\omega}{|k_{\parallel}| v_i} \right) Z \left( \frac{\omega - n\Omega_i}{|k_{\parallel}| v_i} \right) + \tau \left( \frac{\omega}{|k_{\parallel}| v_e} \right) Z \left( \frac{\omega}{|k_{\parallel}| v_e} \right) = 0, \quad (1)$$

where  $(k\lambda_i)^2 \ll 1$  is assumed. Also  $\tau = T_i/T_e$ ,  $v_{i,e}$  are the ion and electron thermal velocities,  $\Omega_i = eB_0/m_i c$  is the ion gyro-radius,  $k_{\parallel}$  and  $k_{\perp}$  are the parallel and perpendicular components of the wave vector (with respect to  $B_0$ ),  $\Gamma_n(b_1) = I_n(b_1) \exp(-b_1^2)$ ,  $b_1 = k_{\perp}^2 \rho_i^2/2$ ,  $\rho_i = v_i/\Omega_i$ , and  $I_n$  are the modified Bessel functions. Setting  $k_{\parallel} \rightarrow 0$ , one obtains the dispersion relation for the Bernstein modes (BM),

$$D_{\text{BM}}(\omega, k) = 1 - \Gamma_0 - \sum_{n>0} \frac{2\omega^2}{\omega^2 - n^2\Omega^2} \Gamma_n = 0, \quad (2)$$

and if  $(\omega/v_e) \ll k_{\parallel} \ll (\omega - n\Omega_i)/v_i$ , then one gets the corresponding expression for the ion-cyclotron modes (IC),

$$D_{\text{IC}}(\omega, k) = 1 + \tau - \Gamma_0 - \sum_{n>0} \frac{2\omega^2 \Gamma_n}{\omega^2 - n^2\Omega^2} = 0. \quad (3)$$

For the time being we neglect all the natural dampings. In the local approximation the energy density of the electrostatic waves is proportional to  $\partial(\omega D)/\partial\omega = \omega \partial D/\partial\omega$ . Thus the energy density  $U$  of both the BM and IC waves is given by

$$U \propto \omega \left( \frac{\partial D}{\partial\omega} \right) = \omega \left( \sum_{n>0} \frac{4\Gamma_n n^2 \Omega^2}{(\omega^2 - n^2\Omega^2)^2} \right) = \omega^2 \sigma(\omega), \quad \sigma > 0. \quad (4)$$

Clearly  $U$  is positive definite and thus the waves are positive energy waves.

We now introduce a uniform electric field  $E_0$  in the  $x$  direction. This initiates a drift of magnitude  $V_E = cE/B$  in the  $y$  direction. Thus, other than a Doppler shift (i.e.,  $\omega \rightarrow \omega_1 = \omega - k_y V_E$ ), there is no change in the dispersion relations given in (2) and (3). The energy density of the Doppler shifted waves  $U'$ , is given by

$$U' = \omega \omega_1 \sigma(\omega_1). \quad (5)$$

While  $U$  is positive definite,  $U'$  can be negative provided  $0 < \omega < k_y V_E$ , thereby giving the waves a negative energy density.

Clearly, a uniform electric field perpendicular to the external magnetic field can convert the positive energy waves into negative energy waves. However, as long as the electric field is uniform, a transformation to another frame moving with a velocity  $V_E$  will enable the waves to get back the positive energy character. This is no longer possible once the electric field is nonuniform. For example consider a specific model for the external electric field,

$$E_0(x) = \begin{cases} E_0 & -L/2 \leq x \leq L/2, \\ 0, & \text{otherwise.} \end{cases}$$

As the main objective of this letter is to demonstrate and discuss the new instability, we have chosen a somewhat idealized electric field profile for relative ease in computation and transparency of the physics involved. Since  $E$  is localized in  $x$  over a distance  $L$  ( $L > \rho_i$ ), one finds that a negative wave energy region I is surrounded by positive wave energy

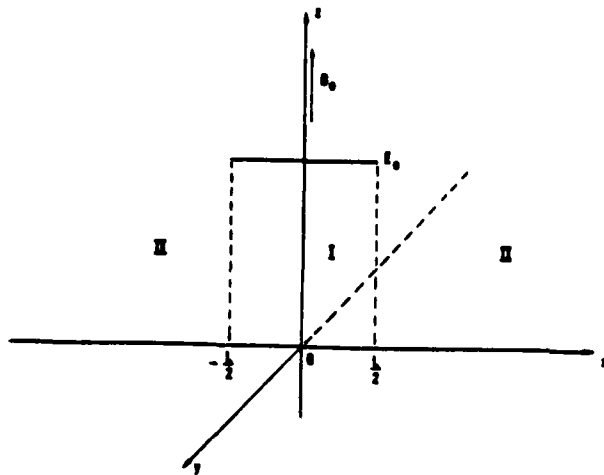


FIG. 1. A sketch of the electric field model.

regions II (see Fig. 1). A nonlocal wave packet can couple these regions, and a flow of energy from region I to region II can enable the mode to grow. This gives rise to the instability. This is essentially a nonlocal instability with no local limit. The negative energy wave framework has been previously used<sup>6</sup> to explain other plasma instabilities at a local level. Ours is a nonlocal instability similar in concept with Lau *et al.*,<sup>7</sup> who apply this concept to an astrophysical problem.

Since the  $x$  direction is nonuniform we use nonlocal differential equations<sup>3</sup> in regions I and II to analyze this case. Dissipation processes such as Landau damping are now included.

Region I:

$$\left(\frac{\partial^2}{\partial \xi^2} + \kappa_1^2\right) \Phi_1(\xi) = 0, \quad (6)$$

Region II:

$$\left(\frac{\partial^2}{\partial \xi^2} + \kappa_2^2\right) \Phi_2(\xi) = 0, \quad (7)$$

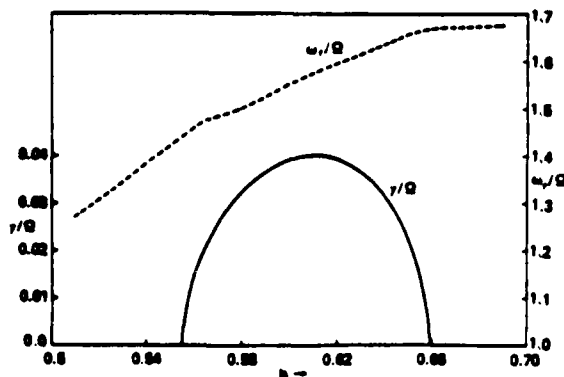


FIG. 2. A plot of the real and imaginary part of the wave frequency  $\omega_r/\Omega_i$  and  $\gamma/\Omega_i$  vs  $b(=mk_1^2 \rho_i^2/2)$ . Here  $\tau = 0$ ,  $\epsilon(=m\rho_i/L) = 0.3$ ,  $\mu(=m_i/m_e) = 1837$ ,  $u(=mk_1/k_e) = 10^{-3}$ , and  $V(=V_E/v_i) = 2.9$ ;  $V_E = cE/B$ , the drift velocity, and  $v_i$ , the ion thermal velocity.

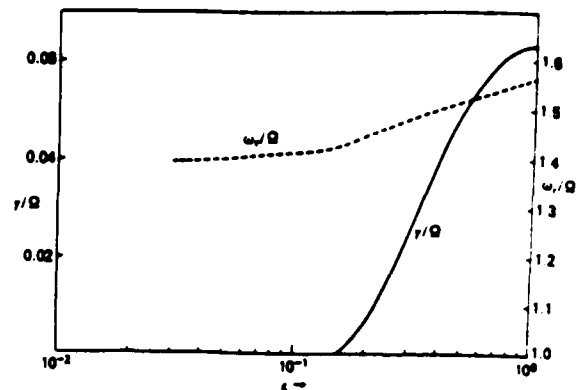


FIG. 3. A plot of  $\omega_r/\Omega_i$  and  $\gamma/\Omega_i$  vs  $\epsilon(=m\rho_i/L)$ . Other parameters are similar to Fig. 2.

where  $\xi = x/\rho_i$ ,  $\kappa_1^2 = Q_i/A_i$ , and

$$Q_i = 1 + \tau + \sum \Gamma_n \left( \frac{\omega_1}{|k_{\parallel}|v_i} \right) Z \left( \frac{\omega_1 - n\Omega_i}{|k_{\parallel}|v_i} \right) + \tau \left( \frac{\omega_1}{|k_{\parallel}|v_e} \right) Z \left( \frac{\omega_1}{|k_{\parallel}|v_e} \right), \quad (8)$$

$$A_i = -\frac{1}{2} \sum_n \Gamma_n \left( \frac{\omega_1}{|k_{\parallel}|v_i} \right) Z \left( \frac{\omega_1 - n\Omega_i}{|k_{\parallel}|v_i} \right), \quad (9)$$

$$\Gamma_n = \frac{\partial}{\partial b} \Gamma_n, \quad b = \frac{k_{\perp}^2 \rho_i^2}{2}.$$

Here  $\kappa_{11}^2$  is identical to  $\kappa_1^2$  if  $\omega_1$  is replaced by  $\omega$ . The solution in region I is

$$\Phi_1(\xi) = \Phi_{01} \cos(\kappa_1 \xi), \quad (10)$$

while in region II it is

$$\Phi_2(\xi) = \Phi_{02} \exp(i\kappa_2 \xi + i\delta), \quad (11)$$

where  $\Phi_{01}$ ,  $\Phi_{02}$ , and  $\delta$  are constants. Demanding that the logarithmic derivative of the solutions be continuous at  $\xi = L/2\rho_i$ , we obtain the nonlocal dispersion relation,

$$-\kappa_1 \tan(\kappa_1/2\epsilon) = i\kappa_2, \quad (12)$$

where  $\epsilon = \rho_i/L$ . Given the parameters, we use a numerical root finder to solve (12) for the complex frequency  $\omega$ . As a boundary condition we demand that the solution vanish at  $\infty$ , i.e.,  $\text{Im}(\kappa_2) > 0$ . It should be remarked that since the electric field has a sharp profile our treatment at the second-order differential equation level can be improved by employing an integral equation formulation. However, such a formulation is mathematically cumbersome and does not provide a simple and clear interpretation of the physics involved. Thus, for the time being, we stress simplicity and clarity over greater accuracy which will be provided in the future.

Figure 2 is a plot of the real and imaginary parts of the frequency,  $\omega_r/\Omega_i$  and  $\gamma/\Omega_i$ , against  $b$  for  $\tau = 0$ ,  $V_E = 2.9v_i$ ,  $\epsilon = 0.3$ ,  $u = k_{\perp}/k_e = 0.001$ , and  $\mu = m_i/m_e = 1837$ . The instability exists only for a very narrow band of  $k_{\perp}$ , thereby making it very coherent. The real part of the frequency is large ( $\omega \sim 1.60\Omega_i$ ) compared to the first harmonic. Also, the instability peaks for  $k\rho_i \sim O(1)$  and  $u \approx 0$ . These features are

in keeping with the observations of Mozer *et al.*<sup>4</sup> We also note that for sufficiently small  $u$  ( $< 10^{-2}$ ) the growth rate is insensitive to the value of the temperature ratio.

Figure 3 is a plot of  $\omega$  against  $\epsilon$  for  $u = 10^{-4}$  and other parameters similar to Fig. 2. Our theory at the second-order differential equation level is valid for  $\epsilon < 1$  (i.e.,  $\rho_i < L$ ). For  $\rho_i > L$  situations an integral equation formulation will become necessary. For most of the laboratory experiments  $L \sim (2 \text{ to } 3)\rho_i$ , for which our theory holds. Figure 3 indicates that the instability is more severe for smaller  $L$  (i.e., for strongly localized electric fields) and disappears for  $L > 7\rho_i$ , for the given parameter range. Holding  $\epsilon = 0.3$  we find that the instability occurs when  $\bar{V}_E (\equiv V_E/v_i)$  is greater than 2.8 but less than 3.2, peaking around 3. Further,  $\omega_i \approx -\Omega_i$  is necessary for the onset.

In this letter we give a new mechanism that can explain the occurrence of the short-wavelength ( $k\rho_i \sim 1$ ) turbulence around the ion-cyclotron frequency in the presence of a non-uniform electric field perpendicular to the external magnetic field. This instability is driven by the coupling of the positive and negative energy ion-cyclotron waves. Ion-cyclotron turbulence has been observed associated with shocks<sup>4</sup> in the magnetosphere and with double layers<sup>3</sup> both in laboratory and space plasmas, where a strongly localized electric field perpendicular to the magnetic field is present. Thus the instability mechanism described in this letter could play a significant role in such situations. We would also like to note that the mechanism of the instability given here is general and can be applied to other instabilities as well. For example, a study of lower-hybrid wave excitation by this mechanism is in progress and will be the subject of a future article.

## ACKNOWLEDGMENTS

We would like to thank Dr. J. J. Rasmussen of Risø National Laboratory, Denmark, and Dr. P. Satyanarayana of Science Applications International Corporation for useful discussions, and Dr. R. L. Merlino of the University of Iowa for providing useful information regarding the Iowa double layer experiment.

This work is supported by the National Aeronautics and Space Administration and the Office of Naval Research.

<sup>4</sup> Present address: University of Maryland, College Park, Maryland 20740.

<sup>1</sup> W. E. Drummond and M. N. Rosenbluth, *Phys. Fluids* **5**, 1507 (1962).

<sup>2</sup> R. Hatakeyama and N. Sato, *Proceedings of the Plasma Conference*, Institute of Electrical Engineers, Japan, 1981, p. 31; M. Nakamura, R. Hatakeyama, and N. Sato, *Proceedings of the Second Symposium on Plasma Double Layers and Related Topics*, Innsbruck, Austria, 1984, p. 171.

<sup>3</sup> R. L. Merlino, S. L. Cartier, M. Alport, and G. Knorr, *Proceedings of the Second Symposium on Plasma Double Layers and Related Topics*, Innsbruck, Austria, 1984, p. 224.

<sup>4</sup> F. S. Mozer, C. W. Carlson, M. K. Hudson, R. B. Torbet, B. Parady, J. Yatteau, and M. C. Kelly, *Phys. Rev. Lett.* **38**, 292 (1977); M. Temerin, C. Cattell, R. Lysak, M. Hudson, R. B. Torbert, F. S. Mozer, R. D. Sharp, and P. M. Kintner, *J. Geophys. Res.* **86**, 11278 (1981).

<sup>5</sup> G. Ganguli and P. Bakshi, *Phys. Fluids* **25**, 1830 (1982).

<sup>6</sup> B. B. Kadomtsev, A. B. Mikhailovskii, and A. V. Timofeev, *Sov. Phys. JETP* **20**, 1517 (1965); L. S. Hall and W. Heckrotte, *Phys. Fluids* **9**, 1496 (1966); A. Bers and S. Gruber, *Appl. Phys. Lett.* **6**, 27 (1965).

<sup>7</sup> Y. Y. Lau, C. C. Lin, and J. W.-K. Mark, *Proc. Natl. Acad. Sci. USA* **73**, 1379 (1976).

**APPENDIX B**

**Temporal Evolution of Whistler Growth in a Cold Plasma  
Injection Experiment**

**G. Ganguli  
Science Applications, Inc.**

**P. Palmadesso and J. Fedder  
Naval Research Laboratory**

## Temporal Evolution of Whistler Growth in a Cold Plasma Injection Experiment

G. GANGULI

*Science Applications, Inc., McLean, Virginia*

P. PALMADESSO AND J. FEDDER

*Geophysical and Plasma Dynamics Branch, Plasma Physics Division  
Naval Research Laboratory, Washington, D. C.*

Using a simple time dependent cold plasma density model and assuming a typical ambient radiation belt environment, we study the evolution of the whistler mode turbulence and particle precipitation in a cold plasma release experiment similar to one that may be conducted as part of the Active Magnetospheric Particle Tracer Explorers (AMPTE) program. It is known from earlier work that the release of cold lithium ions can significantly lower the critical energy  $E_c$  above which the resonant radiation belt electrons can pitch angle scatter. We study the time evolution of the one pass gain factor for a whistler wave packet and find that for parameters accessible to AMPTE type experiments the gain factor is large enough to ensure strong whistler turbulence and strong pitch angle diffusion of radiation belt particles with energies in the range between the ambient value of  $E_c$  and the reduced value of  $E_c$ . Estimates for the total power input to the ionospheric footprint of the release are of the order of an erg/cm<sup>2</sup>/s. This precipitated energy should produce a patch of visible aurora. This effect should also persist for many hours.

## INTRODUCTION

Energetic electron precipitation has been of considerable interest for over two decades. Bursts of precipitation were observed by balloon X ray bremsstrahlung measurements as early as 1963 [Winckler *et al.*, 1962; Anderson and Milton, 1964] and in situ measurements of greater than 40-keV electron fluxes were made by Injun 3 [O'Brien, 1964]. The importance of loss cone electromagnetic cyclotron (EMC) instabilities in the magnetosphere and the relevance of such instabilities to particle precipitation processes was first pointed out by Cornwall [1965] and, independently, by Obayashi [1965]. An attempt to formulate a theory of particle trapping and precipitation under the influence of EMC instabilities was made by Kennel and Petschek [1966]. Kennel and Petschek studied the wave growth and loss rates of whistler, ion cyclotron and magnetosonic waves in a finite plasma (i.e., magnetosphere) and derived a limit on the stably trapped particle fluxes in the radiation belts. Subsequently, more rigorous and self-consistent studies of these processes have been conducted, with the result that some of the conclusions of Kennel and Petschek must be modified [Etcheto *et al.*, 1973]. Cocke and Cornwall [1967] suggested that cold plasma played an important role in controlling the wave particle interactions in the radiation belts within the plasmasphere. Later Brice [1970] pointed out that cold plasma injected from the ionosphere into the magnetosphere could produce enhanced whistler mode turbulence and associated precipitation of energetic electrons, while Cornwall *et al.* [1970] recognized a parallel process for the ion cyclotron waves and ion precipitation.

Brice [1970] and Brice and Lucas [1971] have suggested that a substantial increase in the energetic electron precipitation could be achieved by injection of very modest amounts of cold plasma into the radiation belts. A hypothetical experiment in which ULF EMC noise and proton precipitation could be enhanced by lithium injection was analyzed by Cornwall [1974]. Similarly, enhancement of VLF EMC noise and

electron precipitation by barium injection was studied by Liemohn [1974].

Under certain conditions the injection can introduce a new limit to the number of stably trapped particles [Kennel and Petschek, 1966]. Electrons with energies below a certain threshold energy  $E_c$  will continue to be trapped and those with energies higher than  $E_c$  may be precipitated provided conditions regarding their degree of anisotropy and relative abundance are satisfied. For ambient cold plasma densities the threshold energy  $E_{c1}$  is greater than the thermal energy of the hot particles, and the energetic electron density can increase to a large value. With the injection of additional cold plasma, the threshold energy is reduced from  $E_{c1}$  and  $E_{c2}$  and electrons with energies between  $E_{c1}$  and  $E_{c2}$  create growing waves, are pitch angle scattered, and precipitate into the atmosphere. This precipitation may produce an artificial aurora that is observable from the ground.

Cuperman and Landau [1974] have studied the theory of the electromagnetic electron cyclotron (whistler) instability produced by addition of cold plasma to an infinite uniform anisotropic plasma. Their formalism disregards the finite size of the region of cold plasma enhancement in the magnetosphere and used a stationary model for the cold plasma density. We extend the Cuperman and Landau model to study a time varying cold plasma density injection  $n_c(t)$  and take into account the finite size of the flux tube by studying the wave gain as a function of both the spatial and the temporal growth rates of the waves.

The purpose of this brief report is to make semiquantitative estimates of the magnitude and the duration of the enhancement of VLF EMC noise and electron precipitation effects that might be produced by a cold lithium release experiment in the parameter range accessible to AMPTE.

## MODEL

We assume a point injection of neutral lithium gas. The neutral lithium has a Maxwellian distribution and is allowed to expand radially into the vacuum. Solar radiation ionizes the expanding lithium gas with a time scale of 3000 s. After ionization the cold plasma is frozen to the geomagnetic field

Copyright 1984 by the American Geophysical Union.

Paper number 4A0698.

0148-0227/84/004A-0698\$05.00

and its volume increases in time as a geomagnetic field aligned cylinder (see Figure 1). The cylinder has a radius  $R_0$  and its length is a function of time  $L(t)$ , so that its volume is  $\pi R_0^2 L(t)$ .

To estimate the number of cold lithium ions in this field aligned cylinder, we also modeled the evolution of the neutral lithium injection cloud. We assume a release of 100 kg of neutral lithium and a yield of 6% so that the total number of vaporized lithium atoms is  $\sim 1.2 \times 10^{26}$ . The initial distribution of neutral atoms injected at a point  $R_1$  is

$$f_0(v, R, 0) = \frac{N_0}{(\pi v_0^2)^{3/2}} \delta(R - R_1) \exp(-v^2/v_0^2) \quad (1)$$

with thermal velocity  $v_0 \sim 4.5$  km/s. Integrating over the initial distribution, with  $R$  replaced by  $R - vt$ , gives the neutral lithium density as a function of radius from the release point and time

$$n_0(R, t) = e^{-t/\tau_i} \iiint f_0(v, R - vt, 0) d^3v, \quad (2)$$

where  $\tau_i$  is the ionization time for neutral lithium atoms. Initially we are interested only in the total number of ions in the flux tube and not their position in the tube, so we neglect transport of ionized lithium. The rate at which lithium ions are created is given by

$$\frac{d}{dt} n_i(R, t) = \frac{1}{\tau_i} n_0(R, t) \quad (3)$$

Assuming a finite extent of the whistler wave packet across the magnetic field of  $R_0 \sim \alpha(\lambda_\perp)$  ( $\sim 50$  km) we integrate (3) from 0 to  $R_0$  and in time from 0 to  $\infty$  to estimate the total number of lithium ions deposited within a sphere of radius  $R_0$  ( $N_i \sim 5 \times 10^{23} \text{ cm}^{-3}$ ) that becomes a field-aligned flux tube since the ions are trapped by the magnetic field. The actual rate of appearance of the lithium ions in the flux tube is  $N_i(1 - e^{-t/\tau_i})$ . Additional ions are created outside the flux tube that have much lower density and are not accounted for in this estimate. Estimating the effects of ion transport we find that the cylindrical length  $L(t)$  increases linearly in time at a velocity  $v_0$  in both directions along the flux tube. Thus the time dependent model for the cold ion density is given by

$$n_c(t) = \frac{N_i}{(2V_0 t)(\pi R_0^2)} (1 - e^{-t/\tau_i}) \\ = 12.8 \times 10^6 (R_0/L_0) \left( \frac{1 - e^{-T}}{T} \right) \text{ m}^{-3} \quad (5)$$

where  $L_0 = 2V_0\tau_i$  and  $T = t/\tau_i$ . Figure 2 shows the decay of the cold lithium density as a function of the normalized time  $T$ . However, the ionized lithium also is magnetically trapped along the field lines by the mirror force. The condition for the low-energy lithium ions to be mirrored above the ionosphere after being released at the equator in the altitude range of 5–8  $R_E$  is  $\frac{1}{2} m v_{\perp 0}^2 \geq 0.02 \text{ eV}$  (see appendix). Since the thermal energy is much greater than 0.02 eV the majority of the lithium ions will remain trapped at high altitudes in the magnetosphere and will be unable to leak into the ionosphere. This will ensure a saturation of the cold lithium ions for large  $T$  at a value larger than the lowest value shown in Figure 2. On the basis of the presence of magnetic trapping, we expect the cold density will saturate around  $T \sim 2$  at a value of around  $1.0 \text{ cm}^{-3}$ .

We now discuss the critical resonance energy criterion in the presence of a time dependent cold plasma density. It is

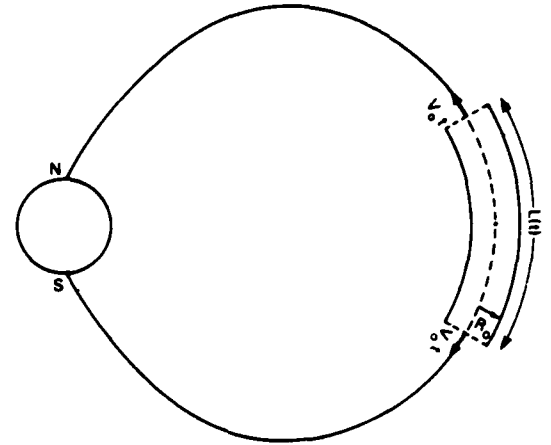


Fig. 1. A schematic representation of the cylindrical cold plasma volume.

well known that wave particle interaction can occur when the resonance energy  $E_R$  is greater than or equal to the threshold energy  $E_c$ .  $E_R$  was defined by Kennel and Petschek [1966] as

$$E_R = \frac{1}{2} m V_R^2 \quad (6)$$

where  $V_R = \omega - \Omega/k_{\parallel}$  is the resonance velocity. Taking into account the dispersion relation for the wave, Cornwall [1972] calculated a minimum energy condition for resonance given by

$$E \geq E_c = \frac{B^2}{8\pi N} A_c^{-1} (1 + A_c)^{-2} \quad (7)$$

where  $A_c \equiv (\Omega_e/\omega - 1)^{-1}$ . Using the dispersion relation as given in the work of Cupperman and Landau [1974] we can write

$$A_c = \frac{a^2}{\alpha(t)\beta} \quad (8)$$

where  $a = k\rho$ ,  $\rho = v_{th}/\Omega_e$ ,  $\alpha = 1 + n_c(t)/n_w$ ,  $n_w$  is the energetic electron density, and  $\beta = n_w K T / (B^2/8\pi)$ , where  $K$  is the Boltzmann constant. Thus we can rewrite (7) as

$$\frac{E_c}{E_{th}} = \frac{1}{\alpha(t)\beta A(1 + A)^2} \quad (9)$$

where  $E_{th}$  is the thermal energy of the energetic electrons.

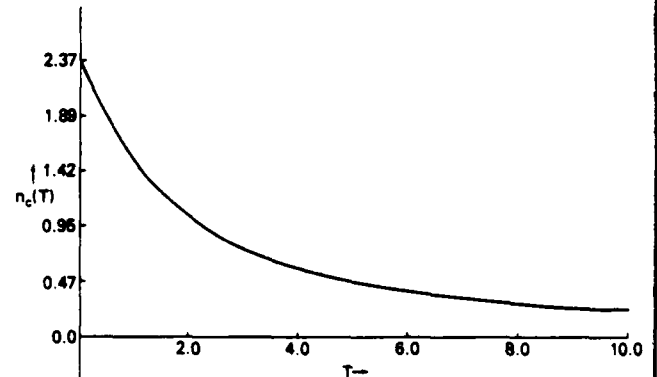


Fig. 2. A plot of  $n_c(T)$  against  $T$ .



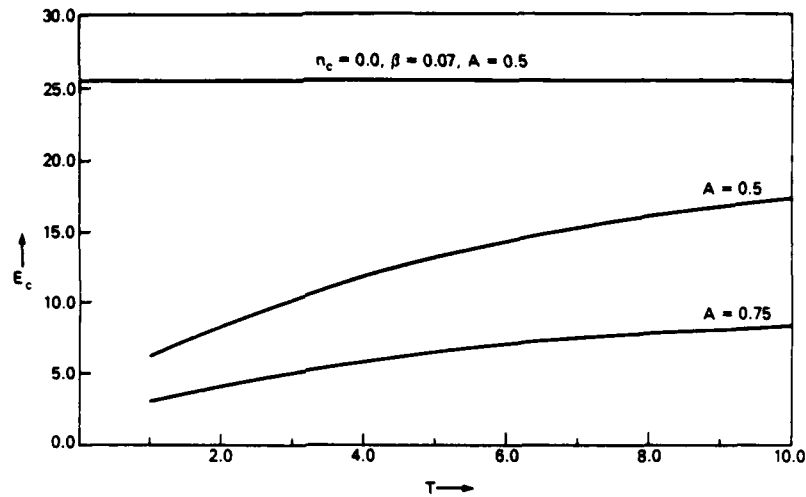


Fig. 3. A plot of the ratio of the critical energy to the background warm electron energy,  $E_c$ , against  $T$ . The top line corresponds to  $n_c = 0$ ,  $\beta = 0.07$  and  $A = 0.5$ . The lower curves are for  $A = 0.5$  and  $0.75$ , with  $\beta = 0.07$  and  $n_c(T)$ .

In the absence of cold plasma  $\alpha = 1$  and  $E_c$  is a constant. This is indicated in Figure 3, top line. Here we took the density of the ambient electrons to be 0.5 per cubic centimeter, their thermal energy  $E_{th} \sim 2.0$  keV, a magnetic field of  $10^{-3}$  G, the degree of anisotropy  $A \sim 0.50$  and  $\beta \sim 0.07$ . With the addition of cold plasma,  $E_c$  is sharply reduced, especially at early times, thereby enabling a very large population of energetic electrons to interact with the waves, enhancing the whistler mode turbulence, and thus as a consequence of pitch angle scattering precipitating electrons into the atmosphere. Although  $E_c$  does increase somewhat at later times it is still much lower than in the absence of the injected cold plasma. Further, as described earlier, magnetic trapping of the cold lithium ions will not allow the cold plasma density to fall as rapidly as indicated in Figure 2, thereby ensuring a low  $E_c$  for a considerable length of time.

### RESULTS

In the previous section we saw that the introduction of the cold plasma considerably lowers the threshold energy and thus enhances the growth of whistler noise turbulence. Since the flux tube where the cold plasma is enhancing wave particle interaction has a finite length, the temporal growth rate alone cannot determine the extent of the wave growth because the waves propagate away from the region of rapid growth. Therefore, we consider the spatial growth rates and finally calculate the net gain  $G$ , of the wave during a single pass through the flux tube. The condition for a large effect is  $GR > 1$  where  $R$  is the reflection coefficient for the wave at the ionosphere. The waves with  $\ln G \gg 1$ , a more severe condition, will experience a significant gain in the wave amplitude independent of  $R$ , leading to strong whistler turbulence and considerable pitch angle scattering of the electrons interacting with the waves. The gain  $G$  of the wave is defined as

$$G = e^g \quad (10)$$

$$g = \frac{\gamma(\omega, k)L(t)}{V_g(\omega, k)} \quad L(t) < 4R_E \quad (11)$$

$$g = 4 \frac{\gamma}{V_g} R_E \quad L(t) > 4R_E$$

where  $\gamma(\omega, k)$  is the temporal growth rate of the whistler mode

instability,  $V_g = \partial\omega/\partial k$ , is the group velocity of the whistler mode and  $R_E$  is one earth radius. Since the whistler mode is excited primarily in the equatorial region where the magnetic field is nearly uniform and straight, we have limited the length  $L(t)$  in (11) to  $4R_E$ .

In order to evaluate  $\gamma(\omega, k)$  and  $V_g(\omega, k)$  for the resonant energy we solve the expression (32) of *Cuperman and Landau* [1974]

$$\frac{a^2}{x\beta} = \frac{\bar{\omega}}{1 - \bar{\omega}} \quad \bar{\omega} = \omega/\Omega_e \quad (12)$$

and the resonance condition

$$\bar{\omega} = 1 + a\bar{v}_R \quad \bar{v}_R = \frac{v_R}{v_{th}} \quad (13)$$

simultaneously. Eliminating  $\bar{\omega}$  from (12) and (13) we obtain a cubic equation for  $a$  given by

$$a^3 + x\beta a + \frac{x\beta}{\bar{v}_R} = 0 \quad (14)$$

We solve (14) using a numerical root finder for  $a$ . The  $a$  is used to evaluate the group velocity  $V_g$  from (12) and the temporal growth rate  $\gamma/\Omega_e$  from the expression (33) of *Cuperman and Landau* [1974]. With these quantities  $g$  is evaluated for the resonant waves.

The observed differential flux for radiation belt electrons is not a Maxwellian for energies higher than 30 keV, which is a typical value of  $E_c$  with ambient cold plasma distributions between 5 and 8  $R_E$ . The observed flux is given by a power law of the form

$$j = C_{11} E^{-\sigma} \text{ electrons/cm}^2 \text{ sr s keV} \quad (15)$$

which corresponds to the energy distribution function given by

$$f(E) = C_{2,\sigma} E^{-(1+\sigma)} \quad (16)$$

We have considered two distributions of the following form for the energetic electrons corresponding to quiet and disturbed magnetospheric conditions, respectively:

$$f_{\omega} = n_{\omega} \left( \frac{m_e}{2\pi k T} \right)^{3/2} \exp(-E/E_{th}) + C_{2,\sigma} E^{-(1+\sigma)} \quad (17)$$

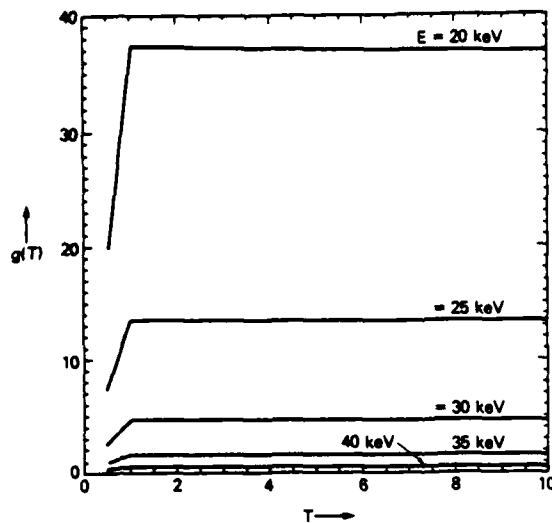


Fig. 4. A plot of  $g(T)$  against  $T$  for  $\sigma = 3/2$  for typical particle energy varying from 20 to 40 keV. Here  $A = 0.75$ ,  $\beta = 0.07$ ,  $n_w = 0.5/\text{cm}^3$  and  $E_{th}$  for the electrons is 2 keV.

where  $\sigma$  is either  $3/2$  or  $3$  and  $C_{2,3/2} = 4.72 \times 10^{31}$ ,  $C_{2,3} = 6.7 \times 10^{34}$  (D. Williams, private communication, 1983). We note that the power law applies only for particle energies in excess of 30 keV. Above  $E_c$  the stable flux is limited as shown by Kennel and Petschek [1966] and others. Below  $E_c$  the ambient flux is not limited by the wave processes and can therefore be larger. For ease of calculation we make a conservative estimate of the flux in this energy range by extending the power law to lower energies.

Figure 4 is a plot of  $g(T)$ , which is  $\ln G(T)$ , as a function of  $T$  for  $\sigma = 3/2$  for characteristic particle energies spanning from 20 to 40 keV in steps of 5 keV. We chose plasma parameters such that  $A = 0.75$ ,  $\beta = 0.07$ ,  $E_{th} = 2$  keV and the density of energetic electrons  $n_w = 0.5/\text{cm}^3$ . The gain curves rapidly increase until the injected electrons fill a flux tube of length  $4 R_E$  and thereafter show a very mild decrease owing to the decrease in the temporal growth rate. The group velocity shows very little variation with time.

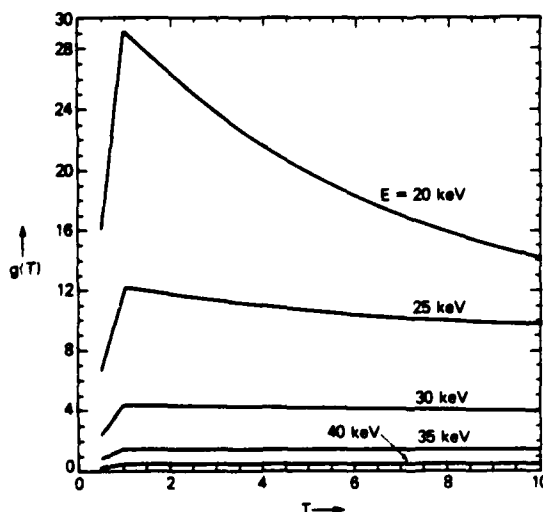


Fig. 5. A plot similar to Figure 4 but with  $\sigma = 3$ .

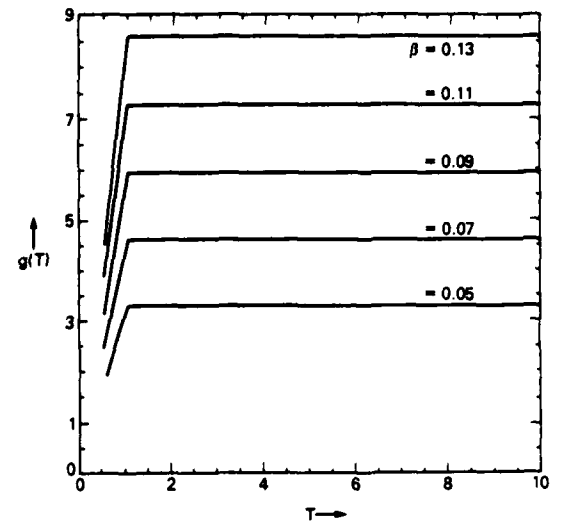


Fig. 6. A plot similar to Figure 4. Here the resonant particle energy is 30 keV. We vary the value of  $\beta$  from 0.05 to 0.13 to demonstrate the sensitivity of  $g(T)$  on  $\beta$ . Other parameters are identical to Figure 4.

Figure 5 is a plot similar to Figure 4 except here  $\sigma = 3$ . The overall behavior of both Figures 4 and 5 are similar.

Figure 6 is a plot of  $g$  against time for a typical energetic particle energy of 30 keV for various values of  $\beta$ . It shows that the wave gain is quite sensitive to the value of  $\beta$ . For higher  $\beta$  the gain increases. Therefore if magnetic fluctuations are taken into account  $\beta$  will fluctuate and with it the wave gain.

Overall, we find a significant wave gain for a single pass through the flux tube especially for lower energy particles. Nevertheless, at 25 keV the gain factor is already large enough to ensure strong turbulence and strong pitch angle diffusion. For lower energies the gain factor becomes too large for the linear theory to be meaningful; this indicates that nonlinear processes (i.e., strong pitch angle scattering) are important at these energies. Figure 7 shows a gain versus time plot for lower energies (4–12 keV). The gain  $g(T)$  increases to a very large number as the energy decreases until the particle energy

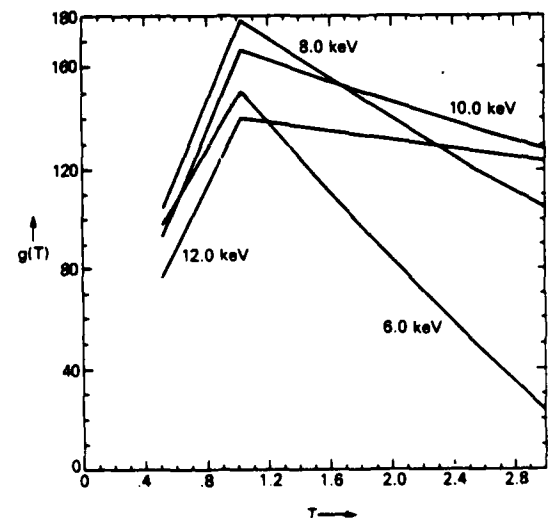


Fig. 7. A plot of  $g(T)$  against  $T$  for lower energies.

is around 8 to 10 keV, while for still lower energies the gain is reduced. This decrease occurs for particle energy near  $E_c$ .

### CONCLUSION

Using a simple time dependent cold plasma density model we have shown that a cold lithium injection in the AMPTE parameter range can give rise to whistler mode turbulence with significant gain to the wave amplitude in a single pass through the flux tube. Whistler mode growth gives rise to pitch angle diffusion of the energetic electrons, which then precipitate. As energetic electrons are removed by precipitation new electrons drift into the flux tube via gradient and curvature drift motion. An equilibrium can be established in which newly supplied radiation belt electrons in excess of the new stable trapping limit are continuously precipitated. The rate of power input into the ionosphere can thus be estimated roughly as follows:

$$\frac{\text{Power Input to Flux Tube}}{\text{Area of Ionospheric Foot}} = n_{\omega}^{\text{eff}} k T^{\text{eff}} V_{\text{drift}} \frac{A_{\text{side}}}{A_{\text{foot}}} \quad (18)$$

In (18), the ionospheric cross section of the flux tube,  $A_{\text{foot}} \sim (\pi R_0^2) B_M / B_1$  ( $B_1$  and  $B_M$  are the magnetic fields in the ionosphere and the magnetosphere) and the meridional cross section of the flux tube,  $A_{\text{side}} \sim R_0 L(t)$  give a typical value for the ratio  $A_{\text{side}}/A_{\text{foot}} \sim 5 \times 10^4$ . Using a reasonable distribution for the energetic electrons we estimate  $n_{\omega}^{\text{eff}} \sim 10^{-2} \text{ cm}^{-3}$ . Very large wave gain occurs for particles of energy 10 keV which have  $KT^{\text{eff}} \sim 10^{-9}$  ergs and a  $V_{\text{drift}} \sim 5 \times 10^3 \text{ cm}^{-2} \text{ s}^{-1}$ . Using these numbers in (18), we find a precipitated power of  $2 \text{ ergs cm}^{-2} \text{ s}^{-1}$ . This value of the precipitated power is large enough to produce a visible aurora. The precipitation would be expected to continue producing a visible aurora until the injected cold plasma in the flux tube is lost or destroyed by magnetospheric convection or other processes.

### APPENDIX

Here we calculate the minimum perpendicular energy for lithium ions in the magnetosphere to be trapped at high altitude by the magnetic mirror force. The total energy of the lithium ions is given by

$$E = \frac{1}{2} m v_{\perp}^2 + \mu B - \frac{G M m}{r} \quad (A1)$$

where  $\mu = \frac{1}{2} m v_{\perp}^2 / B$ , and  $G$  is the gravitational constant. Requiring conservation of energy, the net energy in the magnetosphere must be equal to the net energy in the ionosphere,

$$E_M = E_I \quad (A2)$$

In order to be magnetically trapped in the magnetosphere, the ions must have  $v_{\parallel} = 0$ . Thus

$$\frac{1}{2} m v_{\perp M}^2 \geq \frac{-G M m \left[ \frac{1}{r_1} - \frac{1}{r_M} \right] - \frac{1}{2} m V_{\parallel M}^2}{1 - \frac{B_1}{B_M}} \quad (A3)$$

Taking 6 eV for the net gravitational energy, 0.5 eV for the parallel thermal energy in the magnetosphere, and  $1 - B_1/B_M \sim 287$ , we find,

$$\frac{1}{2} m v_{\perp M}^2 \geq 0.02 \text{ eV}$$

for trapping to occur.

**Acknowledgments.** The authors would like to acknowledge important discussions with D. Williams and S. M. Krimigis. This work was supported by the Office of Naval Research and the National Aeronautics and Space Administration.

The Editor thanks S. Cuperman and J. M. Cornwall for their assistance in evaluating this paper.

### REFERENCES

- Anderson, K. A., and D. W. Milton, Balloon observations of X rays in the auroral zone, 3. High time resolution studies, *J. Geophys. Res.*, 69, 1964.
- Brice, N. M., Artificial enhancement of energetic particle precipitation through cold plasma injection: A technique for seeding substorms?, *J. Geophys. Res.*, 75, 4890, 1970.
- Brice, N. M., and C. Lucas, Influence of magnetospheric convection and polar wind loss of electrons from the outer radiation belt, *J. Geophys. Res.*, 76, 900, 1971.
- Cocke, W. J., and J. M. Cornwall, Theoretical simulation of micropulsations, *J. Geophys. Res.*, 42, 2843, 1967.
- Cornwall, J. M., Cyclotron instabilities and electromagnetic emission in the ultra low frequency and very low frequency ranges, *J. Geophys. Res.*, 70, 61, 1965.
- Cornwall, J. M., Magnetosphere dynamics with artificial plasma clouds, *Space Sci. Rev.*, 15, 841, 1974.
- Cornwall, J. M., Precipitation of auroral and ring current particles by artificial plasma injection, *Rev. Geophys. Space Phys.*, 10, 993, 1972.
- Cornwall, J. M., F. V. Coroniti, and R. H. Thorne, Turbulent loss of ring current protons (abstract), *Eos Trans. AGU*, 51, 378, 1970.
- Cuperman, S., and R. W. Landau, On the enhancement of the whistler mode instability in magnetosphere by cold plasma injection, *J. Geophys. Res.*, 79, 128, 1974.
- Etcheto, J., R. Gendrin, J. Solomon, and A. Roux, A self-consistent theory of magnetospheric ELF hiss, *J. Geophys. Res.*, 78, 8150, 1973.
- Kennel, C. F., and H. E. Petschek, Limit on stably trapped particles, *J. Geophys. Res.*, 71, 1, 1966.
- Liemohn, H. B., Simulation of VLF amplification in the magnetosphere, *Space Sci. Rev.*, 15, 861, 1974.
- Obayashi, T., Hydromagnetic whistlers, *J. Geophys. Res.*, 70, 1069, 1965.
- O'Brian, B. J., High-latitude geophysical studies with satellite Injun 3, 3. Precipitation of the electrons into the atmosphere, *J. Geophys. Res.*, 69, 13, 1964.
- Winckler, J. R., P. D. Bhavsar, and R. A. Anderson, A study of the precipitation of energetic electrons from the geomagnetic field during magnetic storms, *J. Geophys. Res.*, 67, 3717, 1962.
- J. Fedder and P. Palmadesso, Geophysical and Plasma Dynamics Branch, Plasma Physics Division, Naval Research Laboratory, Code 4780, Washington, D. C. 20375.
- G. Ganguli, Science Application, Inc., 8301 Greensboro Drive, McLean, VA 22102.

(Received February 8, 1984;  
revised April 27, 1984;  
accepted April 30, 1984.)

**APPENDIX C**

**Stochasticity of Particle Orbits in a  
Collective Particle Accelerator**

**G. Ganguli and H.G. Mitchell  
Science Applications International Corporation**

**P. Palmadesso  
Naval Research Laboratory**

# Stochasticity of particle orbits in a collective particle accelerator

G. Ganguli and H. G. Mitchell

*Science Applications International Corporation, McLean, Virginia 22012*

P. Palmadesso

*Plasma Physics Division, Naval Research Laboratory, Washington, DC 20375-5000*

(Received 13 August 1985; accepted for publication 1 October 1985)

A detailed investigation of the behavior of particle orbits in the simultaneous presence of three large amplitude waves such as those encountered in the collective particle accelerator experiment at the Naval Research Laboratory is undertaken. Stochasticity arising out of the resonance overlap of the waves can influence the particle dynamics significantly and thereby affect the outcome of the experimental results. Choice of initial phase and energy for successful operation is identified and discussed.

## 1. INTRODUCTION

High-energy and high-density beams have been of considerable interest in recent years. A novel method to achieve such a high-density, high-energy particle beam was proposed by Friedman<sup>1</sup> in 1978 in a device called the collective particle accelerator (CPA). Briefly, the device is a traveling wave accelerator with a novel feature: the traveling wave (TW) which does the accelerating is generated on the axis of a cylindrical drift tube as a consequence of the interaction between (1) a periodically bunched annular electron beam injected near the drift tube wall, and (2) a periodically rippled axial magnetic field. The advantage of this as compared to conventional traveling wave devices, in which the TW is a cavity mode, arises from the fact that the phase velocity in the CPA may be chosen to be as slow or fast as desired, within limits to be discussed below, and may be easily varied as a function of distance along the drift tube by varying the wavelength of the magnetic ripple. Thus ions may, in principle, be accelerated along the axis either coparallel or antiparallel to the motion of the annular beam, or electrons may be accelerated in the antiparallel direction. An important side effect of this method of generating the TW is the fact that three large amplitude waves are simultaneously generated in the device: a forward (i.e., co-parallel with the annular beam velocity) TW; a backward TW; and a stationary-wave pattern.

The first experiments in support of the CPA concept were conducted around 1976. A relativistic annular electron beam was propagated a distance of 7 m, without bunching and with straight magnetic field lines. In the next phase the beam was bunched and again 7-m propagation was achieved. Addition of the magnetic field ripple in the third stage of the effort was similarly successful. Next, a solid beam with current  $\sim 10\%$  of the annular beam current was successfully propagated along the axis in the absence of the annular beam. The full experiment, solid beam plus bunched annular beam with rippled  $B$  field was then tried. The solid beam did not come out at the end opposite to which it was injected, and diagnosis of this beam through the annular beam was difficult, so a simpler experiment was tried. A solid beam was injected into an annular beam without bunched or  $B$  field ripples, but was not detected near the other end, al-

though a magnetic field disturbance attributed to the solid beam was detected close to the solid beam emitter. Note that without bunches and ripples no acceleration can take place, in which case the solid beam cannot overcome the potential hill near the annular beam cathode, so in the full experiment one does not expect the solid beam to hit the opposite end even if it propagated. A number of variations of these experiments were attempted in 1979; e.g., the solid beam was carried to a point well inside the drift tube via a smaller radius drift tube projecting inside the annular beam, but still the solid beam was not observed to propagate the remaining distance. Again we emphasize that observation of the weak solid beam through the strong annular beam is difficult, and the negative result in the unmodulated case cannot be regarded as definitive.

Various theoretical analyses for the stability properties of the dual beam system were undertaken in order to understand the experimental results. Chen and Palmadesso<sup>2</sup> studied the diocotron instability in the CPA in an attempt to understand the sensitivity to small misalignments of the annular beam encountered in the first experiment. The  $l = 1$  diocotron mode can be excited by a shift of the annular beam axis off the drift tube axis, and was shown to have a growth length comparable to the device length for the parameters used. The growth of the instability is not significant if the beam is very accurately centered initially, but is enough to cause the beam to hit the wall if the initial displacement is within an  $e$  fold or two of the distance between the beam and the wall.

Uhm<sup>3</sup> showed that the transverse oscillation instability has a growth time  $\sim 1/5$  of the beam transit time for the CPA parameters used. However, Ganguli and Palmadesso<sup>4</sup> used the wave kinetic equations in a finite length device to show that the transverse oscillation instability behaves like a backward convective instability in the rest frame of the solid beam, i.e., in this frame the growth is spatial rather than temporal and vanishes at the beam head. The implication is that the front part of the beam (about 5 m worth in this case) would make it across the device even though the tail end of the beam was being torn up as the head completed its transit.

Thus the theoretical models analyzed so far do not account for the failure of the solid beam to emerge from the end

of device, in the case where an accelerating TW is present. These theoretical models did not investigate the role of the important second and third large amplitude waves generated and the influence of these waves on the particle dynamics. The purpose of this paper is to study the role of these waves in determining the particle dynamics of the CPA and hence influencing the experimental outcome. In Sec. II we describe our theoretical model, provide the equation of motion governing the CPA system, and describe the method of solution. In Sec. III we give the results of the calculations and discuss the ramifications of these, and, finally, in Sec. IV we provide concluding remarks.

## II. THEORY

As discussed earlier an important side effect of the way that the traveling waves are generated in the CPA is the simultaneous presence of three large amplitude waves in the device. It is well known that if a particle is under the influence of two or more waves with resonance widths broad enough to bridge (or nearly bridge) the gap between the wave phase velocities, then the multiple resonance can make the particle orbits stochastic.<sup>5</sup> With the onset of stochasticity the predictability of the particle motion is lost. This is a possible scenario taking place inside the CPA. The expression for the axial electric fields generated by the bunched beam and rippled  $B$  field is (see Appendix)

$$E_z(z, t) = -E_{\infty} \left\{ \cos \left[ 2\pi z \left( \frac{1}{\lambda} - \frac{1}{L} \right) - 2\pi f t \right] - \cos \left[ -2\pi z \left( \frac{1}{L} + \frac{1}{\lambda} \right) + 2\pi f t \right] - 2 \sin \frac{2\pi z}{L} \right\}, \quad (1)$$

where  $L$  is the wavelength of the rippled magnetic field,  $f$  and  $\lambda$  are the frequency and the wavelength of the modulation.  $E_{\infty} = (Q/4\epsilon_0)(r_1/r_0L)$ , where  $r_0, r_1$  are the equilibrium radius of the annular electron beam (AEB) and the amplitude of the oscillations of the AEB due to the ripples of the magnetic field, and  $Q$  is charge/length. Equation (1) represents the superposition of a forward wave with a phase velocity given by

$$v_{\text{eff}} = v[L/(L + \lambda)], \quad (2)$$

where  $v = f\lambda$ , a backward wave with a phase velocity of

$$v_{\text{bb}} = -v[L/(\lambda - L)], \quad (3)$$

and a stationary wave pattern.

Both traveling waves can accelerate ions but only the backward wave can accelerate the electrons since it can have a phase velocity approaching  $c$  (the velocity of light) which happens to be approximately the velocity of the electrons parallel to the magnetic field.

A particle subjected to the field given in Eq. (1) experiences the potential of both the forward and the backward waves along with the standing wave simultaneously. These are large amplitude waves whose resonance widths in velocity space scale as

$$\frac{\Delta\omega}{k} = \frac{1}{k} \left( \frac{eE_{\infty}k}{\gamma m_0} \right)^{1/2} \propto (\gamma m_0)^{-1/2}, \quad (4)$$

where  $\Delta\omega$  is the resonance width in the frequency space,  $k$  is the wave number, and  $\gamma = (1 - V^2/c^2)^{-1/2}$ . For the typical CPA parameters,  $(eE_{\infty}k/m_0)^{1/2}/k \sim 0(c)$ ; for low  $\gamma$  this implies an overlap of resonance leading to stochastic motion. As a consequence of the stochasticity in the orbits, the particles (electrons in our case) spend a longer time inside the device thereby increasing the space charge and decreasing the value of the critical current. However, Eq. (4) also implies that for a sufficiently large injection energy (initial value of  $\gamma$ ) the resonance widths will be small enough so that stochastic motions will not occur. In view of the results of the CPA experiments we must investigate the role of stochasticity and estimate injection energy thresholds.

The equation of motion for the electrons in the CPA is given by

$$\frac{dp}{dt} = -eE_z(z, t), \quad (5)$$

$$\frac{dz}{dt} = v(p) = \frac{1}{m_0} \frac{p}{\sqrt{1 + p^2/m_0^2 c^2}}, \quad (6)$$

where  $p$  is the momentum in the  $z$  direction,  $e$  is the magnitude of electronic charge, and  $E_z$  given by Eq. (1) can be expressed as

$$E_z = -4E_{\infty} \sin(2\pi\alpha\zeta) \cos^2[\pi(\zeta - \tau)]. \quad (7)$$

Here,  $\zeta = z/\lambda$ ,  $\alpha = \lambda/L$ , and  $\tau = ft + 1/4$ . The equations of motion can be rewritten in dimensionless form as

$$\frac{d\zeta}{d\tau} = \frac{\bar{p}}{\sqrt{1 + \bar{p}^2/\sigma^2}} \quad (8)$$

and

$$\frac{d\bar{p}}{d\tau} = \left( \frac{4eE_{\infty}}{\lambda f^2 m_0} \right) \sin(2\pi\alpha\zeta) \cos^2[\pi(\zeta - \tau)], \quad (9)$$

where  $\sigma = c/f\lambda$ ,  $\bar{p} = p/f\lambda m_0$ , and  $m_0$  is the rest mass of the electrons.

We shall first study an infinitely long system by means of surface-of-section plots. After injecting a single particle at  $\tau = 0$  we shall let the system represented by Eqs. (8) and (9) run in time, and plot  $\bar{p}$  and  $\zeta$  for  $\tau = 1, 2, 3 \dots$  etc., given the initial momentum  $\bar{p}_0$  and position  $\zeta_0$ . We take  $E_{\infty} = 15$  MV/m,  $\alpha = 2$ ,  $f = 0.995 \times 10^9$  Hz, and  $\lambda = 0.3$  m. These parameters are typical of the experiment.<sup>1</sup> Note that the system is periodic in  $\zeta$  and hence we shall plot  $\zeta$  modulo 1. The results will be discussed in the following section.

After examining the infinite device to gain general insights we will study a finite device of 7 m. Accumulation of electrons in the device is detrimental to its operation and may be caused by delays in time of flight. This enhances the electron density inside the device and decreases the critical current. In order to estimate the lag time of electrons we plot

$$S = (\tau_t/\tau_{\text{min}}) - 1 \quad (10)$$

as a function of injection phase. Here  $\tau_t$  is the transit time of the electrons through the device and  $\tau_{\text{min}} = 7/c$  is the minimum time that the electron needs to travel the device of 7 m when the electron velocity remains close to the speed of light  $c$ . Thus orbits with small  $S$  do not contribute to charge accu-

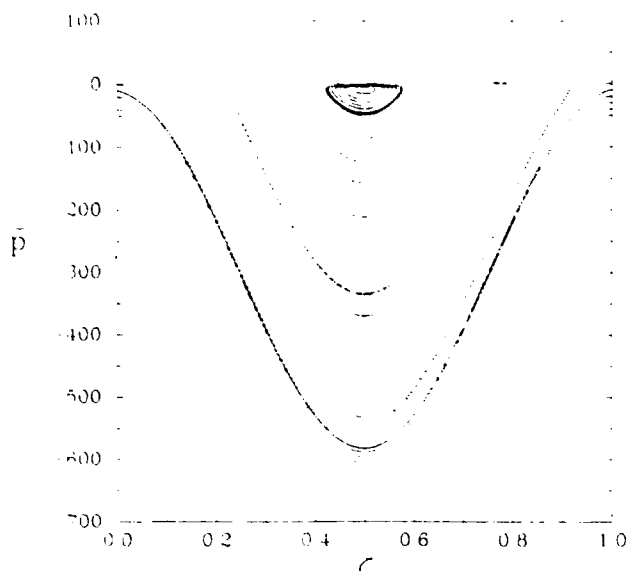


FIG. 1. Surface of section plot. Here  $E_{\infty} = 15 \text{ MV/m}$ ,  $\alpha = 2$ ,  $\lambda = 0.3$ . The magnitude of the normalized momentum  $\bar{p}$  is approximately equal to  $\gamma$ .

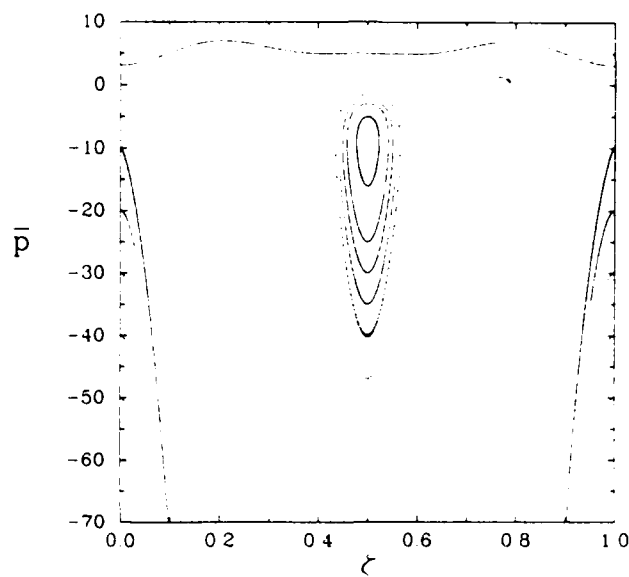


FIG. 2. An enlarged version of the low-energy part of the stochasticity region of Fig. 1.

mulation in the device while the higher values of  $S$  indicate highly disturbed electron orbits which contribute to an enhancement of the space-charge cloud and a decrease in the limiting current.

Also, experimentally it is not possible to launch all the particles at the same phase initially. We shall study  $S$  as a function of  $\Phi_0 = -2\pi(\zeta_0 + \tau_0 - 1/4)$ , the value at injection of the backward (accelerating) wave phase, for various injection energies  $\gamma_0$ . The results are discussed in the following section.

### III. RESULTS AND DISCUSSION

We find two kinds of orbits exhibited on the surface of section plot. "Integrable" orbits are indicative of the existence of a well-behaved constant of the motion which confines the motion of the particle through phase space to a subspace of reduced dimension. The intersection of an integrable orbit with a two-dimensional surface of section such as that in Fig. 1 takes the form of a sequence of points  $[\bar{p}(\tau_n), \zeta(\tau_n)]$  for  $\tau_n = 0, 1, 2, \dots$ , which lie on a simple one-dimensional curve or, in special cases, on a single "fixed" point. In general, the obvious global constants of the motion are exploited to reduce the dimension of the system of motion equations before one constructs a surface of section plot, so that the additional constants associated with integrable orbits exist only in local regions of phase space, and it is rarely possible to express them analytically. Each of the nested closed curves near  $\zeta \bmod 1 \sim 0.5$ ,  $\gamma < 40$  in Figs. 1 and 2 represents an integrable orbit corresponding to a different initial condition. At the center of this group of nested orbits is a fixed point, which corresponds to periodic motion passing through the stable force null of the backward wave at integer values of  $\tau$ , i.e., the electron returns to the point  $\zeta = 0.5 \bmod 1$  at  $\tau = 1, 2, 3$ , etc.

The four or five outermost curves which pass through  $\zeta$

$\bmod 1 = 0$  with  $p \leq -10$  (i.e.,  $\gamma \gtrsim 10$ ) also represent distinct integrable orbits. No calculations were made in the blank regions at higher values of  $\gamma$ , but it is believed that all orbits in this region are integrable. At high energies the resonance widths of the three waves are small, the resonances are well separated, and solid beam electrons ( $v \sim -c$ ) interact strongly only with the backward wave. The electron velocity exceeds the backward wave phase speed when  $\gamma > 10$ , so that an accelerated electron cannot maintain a constant phase relationship with the wave. Electrons gain energy, slip smoothly out of the phase interval in which the force due to the electric field is coparallel with the velocity, then decelerate while continuing to advance in phase. As the particle loses energy the resonances broaden. If the electron in this idealized infinite system has sufficient energy, it will slide forward in phase to the next accelerating region before its speed decreases to the point where it matches the phase speed of the backward TW, and before resonance overlap occurs. The lowest energy integrable orbit of this group of orbits slows down until its speed is infinitesimally greater than the backward wave phase velocity at the point it reaches the unstable (hyperbolic) force null of the backward TW at  $2\pi(\zeta + \tau) = 0$  ( $\zeta \bmod 1 = 0$  on the surface of section plots); thus  $\gamma$  never falls below 10 on this orbit. There is also a set of integrable orbits representing high energy particles with positive velocities which are outside the resonances of all three waves. These orbits are not physically meaningful for the CPA and will not be discussed further here.

"Stochastic" orbits occupy regions in which no such local well behaved constants of the motion exist, and these orbits meander through the entire phase space allowed by the global constants of the motion, with the restriction that they may not cross the "KAM" surfaces<sup>6</sup> (roughly speaking, these are surfaces in phase space traced out by integrable orbits). In the 2D surface of section plots, a single stochastic orbit accounts for all the points between the integrable re-

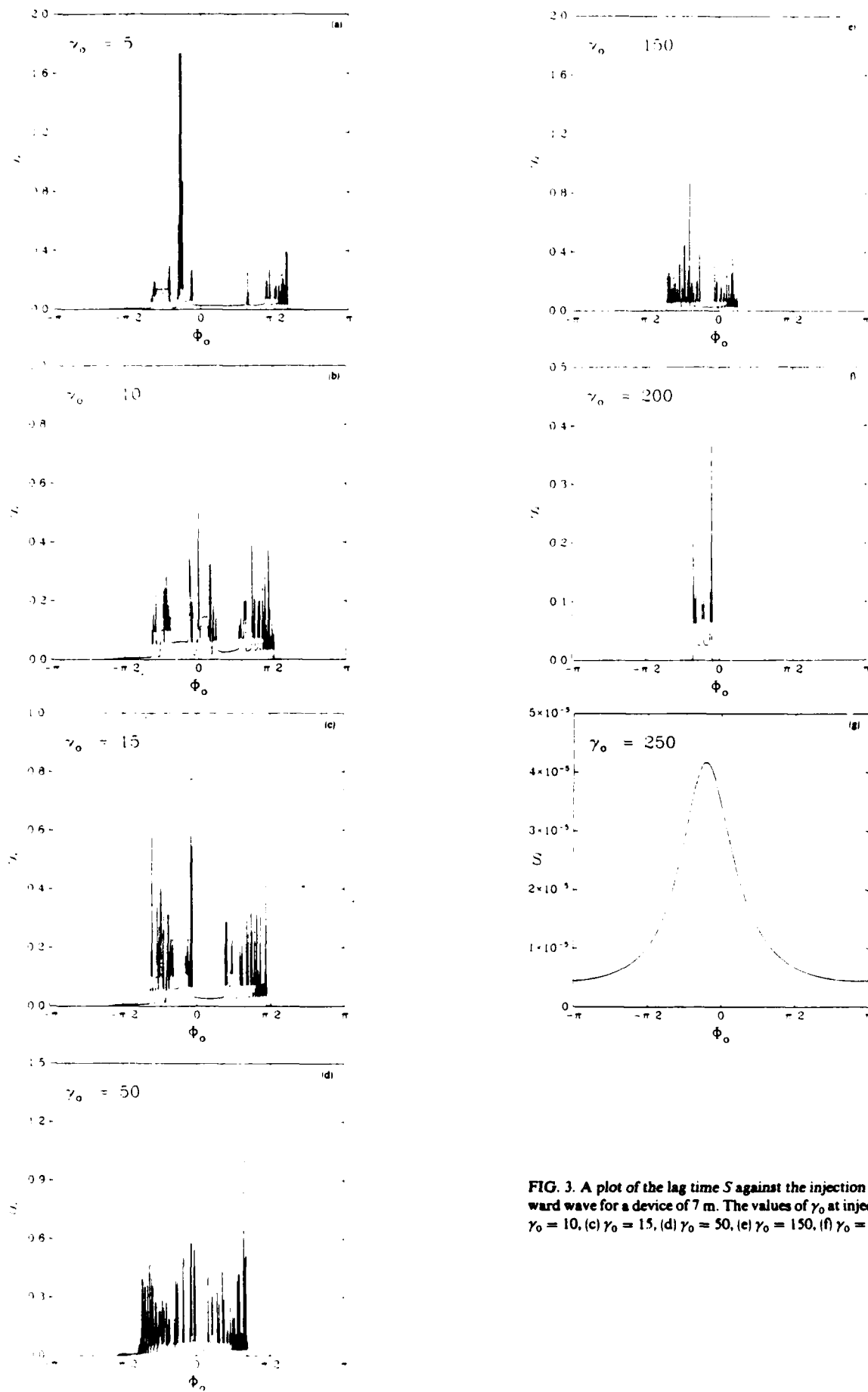


FIG. 3. A plot of the lag time  $S$  against the injection phase  $\Phi_0$  of the backward wave for a device of 7 m. The values of  $\gamma_0$  at injection are (a)  $\gamma_0 = 5$ , (b)  $\gamma_0 = 10$ , (c)  $\gamma_0 = 15$ , (d)  $\gamma_0 = 50$ , (e)  $\gamma_0 = 150$ , (f)  $\gamma_0 = 200$ , and (g)  $\gamma_0 = 250$ .



gions discussed above. This orbit behaves in a chaotic manner at low energies ( $\gamma$  less than about 10), but catches the accelerating phase of the backward wave at random intervals and then gains energy in an orderly way. Segments of the stochastic orbit with  $\gamma$  above about 10 rise and fall in energy in much the same manner as the high-energy integrable orbits, but the electron speed falls below the backward TW phase speed ( $\gamma \sim 10$ ) while the particle is still in the deceleration phase, so that the particle continues to lose speed and energy and slips in phase with respect to the backward TW at an increasing rate. Finally the motion ceases to be dominated by the backward TW and the particle falls back into the chaotic resonance overlap region below  $\gamma \sim 10$ .

A rough calculation of the electron orbits for  $\gamma > 10$  may be performed by assuming that the particles have a constant velocity of  $-c$  and are only affected by the backward wave, in which case the momentum equation takes the form

$$\frac{d\bar{p}}{d\tau} = \left( \frac{eE_x}{\lambda f^2 m_0} \right) \cos\{-2\pi[\zeta_0 + (1-\sigma)(\tau - 1/4)]\}, \quad (11)$$

where  $\zeta_0$  is the injection value of  $\zeta$ . This equation may be solved to give an analytic expression for the energy  $\gamma$  of the particle as a function of the phase  $\Phi$  of the particle relative to the backward wave, the injection energy  $\gamma_0$ , and the injection phase  $\Phi_0$ :

$$\begin{aligned} \gamma - \gamma_0 + \left( \frac{eE_x}{cfm_0} \right) \frac{1}{2\pi(\sigma - 1)} [\sin(\Phi_0) - \sin(\Phi)] \\ = \gamma_0 + 280[\sin(\Phi_0) - \sin(\Phi)], \end{aligned} \quad (12)$$

where the CPA parameters have been used. An electron injected at the unstable force null ( $\Phi_0 = \pi/2$ ) at the speed of the backward wave ( $\gamma_0 = 10$ ) achieves its maximum energy at phase  $\Phi = -\pi/2$ . This energy is  $\gamma = 570$ , which is in good agreement with Fig. 1 for the threshold energy above which all electrons have integrable orbits. In a finite length device, the electron stays with the backward wave only for a finite time and the phase slippage is limited in size. Thus, not all particles below the threshold will become stochastic in a finite length device. For a device of length 7 m, a particle traveling at the speed of light will remain in the device for  $2.3 \times 10^{-8}$  s, which implies that  $\Delta\tau = 23$  for this choice of the parameters  $f$  and  $\lambda$ , and that the maximum phase shift that the particle can undergo is  $2\pi(1-\sigma)\Delta\tau \sim -\pi/4$ . From Eq. (12), this means that if  $\gamma_0 \gtrsim 10 + 280[\sin(\pi/8) - \sin(-\pi/8)] \sim 224$ , a particle cannot become stochastic in a 7-m device with these parameters.

In Figs. 3(a)–3(g) we display plots of the normalized lag time  $S$  against the injection phase of  $\Phi_0$  of the backward wave for seven different injection energies from  $\gamma_0 = 5$  to  $\gamma_0 = 250$ . These plots are pertinent to a finite device of 7 m. We learn two very important features of the CPA operation from this figure. First and foremost, it is seen that as the injection energy  $\gamma_0$  increases from  $\gamma_0 = 5$  to  $\gamma_0 = 250$  the mean value of  $S$  decreases steadily. This implies that for high enough injection energies there is uniform motion no matter what the initial phase is. For lower energies the mean value of  $S$  increases significantly indicating that the electrons are spending longer times inside the device. This implies an electron space-charge cloud buildup inside the device and conse-

quently a decrease in the limiting current. The value of the injection energy in the experiment for the solid beam was on the order of  $\gamma_0 = 5$ , and hence it is not surprising to find the absence of the accelerated solid beam in the experiment, which was conducted with injected current very close to the critical current as traditionally calculated.

Along with the decrease in the mean value of  $S$ , we also notice a shrinkage of the interval  $\Delta\Phi_0$  over which  $S$  is significant as the injection energy  $\gamma_0$  is increased. If this interval of injection phases is avoided, then uniform motion could be achieved even at lower energies. For example, if  $\gamma_0 = 5$  and  $\Phi_0 = \pi$ , Fig. 3(a) shows no significant lag time. On the other hand, even for high energy, say  $\gamma_0 = 150$  [Fig. 3(e)], if the initial phase is around zero we can expect stochastic behavior. As noted earlier we find that the optimum phase for acceleration is  $\Phi_0 = \pi$ . Figure 3(a) indicates that particles launched with an injection phase  $\Phi_0 = \pi$  can be accelerated even for injection energies lower than the  $\gamma$  of the background wave since the particles cannot shift into the chaotic region before leaving the finite device. When a uniformly solid beam is injected, particles of all phases will simultaneously occupy the drift tube. Thus the charge buildup associated with the particles with phases in the stochastic range can be detrimental to successful acceleration of those particles which have the optimum phase.

#### IV. CONCLUSION

We have studied the influence of the three large amplitude waves that arise due to the CPA wave generation scheme on the particle dynamics in the CPA. For typical CPA parameters the resonance width of the waves are broad enough to overlap for low-energy electrons. This gives rise to stochasticity in the particle orbits if the initial phase is not properly chosen. The stochasticity enhances the transit time of the electrons consequently giving rise to an electron cloud buildup inside the device. The charge buildup inside the device decreases the critical current and could prevent the propagation of the solid beam. Further, we conclude that in the CPA experiment those particles of the solid beam that were launched at the optimum phase must not have caused any problems. Since the solid beam was unmodulated, there was a continuous range of injection phases and the particles in the stochastic range contributed to the charge buildup in the device, which in turn may have prevented propagation and acceleration of the optimum phase locked particles. To avoid these effects for a continuous solid beam an injection  $\gamma > 225$  is necessary. However, if the solid beam is injected in small pulses around the optimum phase it should be possible to achieve successful acceleration even for low injection energies.

We have studied the lag time as a function of the phase of the backward wave. It seems that by properly choosing the injection phases (pulsed solid beam) it is possible to avoid the stochasticity and minimize the transit time.

#### ACKNOWLEDGMENTS

Discussions with Professor George Schmidt are gratefully acknowledged. This work was supported by the Office of Naval Research.

## APPENDIX

Here we reproduce the derivation as given by Friedman<sup>1</sup> leading to Eq. (1). The axial electric field, on axis, produced by an annular unneutralized magnetically focused intense relativistic electron beam (IREB) propagating through a drift tube of radius  $R$ , is

$$E_z \approx - \left( \frac{1}{2\pi\epsilon_0} \frac{\partial Q}{\partial z} \right) \ln \frac{R}{r_b} - \left( \frac{\mu}{2\pi} \frac{\partial I}{\partial t} \right) \ln \frac{R}{r_b} + \frac{Q}{2\pi\epsilon_0 r_b} \frac{\partial r_b}{\partial z}, \quad (\text{A1})$$

where  $Q$  is the charge/length,  $Q = I/v$ ,  $I$  is the beam current,  $r_b$  is the beam radius, and  $v$  is the electron velocity. Equation (A1) was obtained from Maxwell equations under the assumption that the characteristic length is greater than the radius of the drift tube. By covering the drift tube walls with a thin dielectric layer of thickness  $\delta R$  and permeability  $\epsilon$  one gets from Eq. (A1) (after some rearranging)

$$E_z \approx - \frac{\mu}{2\pi} \frac{1}{\beta^2 \gamma^2} \frac{\partial I}{\partial t} \ln \frac{R}{r_b} + \frac{\mu}{2\pi\beta^2} \frac{\epsilon}{\epsilon - 1} \frac{\delta R}{R} \frac{\partial I}{\partial t} + \frac{Q}{2\pi\epsilon_0 r_b} \frac{\partial r_b}{\partial z}; \quad (\text{A2})$$

by choosing

$$\frac{\delta R}{R} \approx \frac{\epsilon}{\epsilon - 1} \frac{1}{\gamma^2} \ln \frac{R}{r_b}, \quad (\text{A3})$$

one gets

$$E_z \approx \frac{Q}{2\pi\epsilon_0 r_b} \frac{\partial r_b}{\partial z}. \quad (\text{A4})$$

In a case where a modulated IREB is propagating through a rippled magnetic field<sup>7</sup> one inserts in Eq. (A4) the following:

$$Q = \frac{Q_0}{2} \left[ \sin \left( \frac{2\pi}{\lambda} z - 2\pi f t \right) + 1 \right] \quad (\text{A5})$$

and

$$r_b = r_0 + r_1 \cos(2\pi z/L); \quad r_1 < r_0, \quad (\text{A6})$$

where  $f$  and  $\lambda$  are the frequency and wavelength of the modulation  $\lambda f = v$ ,  $r_0$  is the equilibrium radius of the IREB,  $r_1$  is the amplitude of the oscillations of the IREB due to the influence of the ripple magnetic field, and  $L$  is the wavelength of the rippled magnetic field. Here we assume that the parallel velocity of the electrons is  $v = c$ :

$$E_z \approx - \frac{Q_0}{4\pi\epsilon_0} \left( \frac{r_1}{r_0} \right) \frac{2\pi}{L} \sin \frac{2\pi z}{L} \left[ \sin \left( \frac{2\pi z}{\lambda} - 2\pi f t \right) + 1 \right]. \quad (\text{A7})$$

Rearranging the terms in Eq. (A7) we can obtain Eq. (1).

<sup>1</sup>M. Friedman, NRL Memorandum Report No. 3724 (1978).

<sup>2</sup>R. Chen and P. Palmadesso, *Phys. Fluids* **24**, 357 (1981).

<sup>3</sup>H. S. Uhm, *Phys. Fluids* **25**, 1908 (1982).

<sup>4</sup>G. Ganguli and P. Palmadesso, *J. Appl. Phys.* **55**, 2715 (1984).

<sup>5</sup>B. V. Chirikov, *Plasma Phys.* **1**, 253 (1960).

<sup>6</sup>H. G. Shuster *Deterministic Chaos: An Introduction* (Physik, Weinheim, 1984).

<sup>7</sup>M. Friedman, *Appl. Phys. Lett.* **24**, 303 (1974).

## **APPENDIX D**

### **A Simulation of High Latitude F-Layer Instabilities in the Presence of Magnetosphere-Ionosphere Coupling**

**H.G. Mitchell, Jr., J.A. Fedder, M.J. Keskinen  
and S.T. Zalesak**

A SIMULATION OF HIGH LATITUDE F-LAYER INSTABILITIES  
IN THE PRESENCE OF MAGNETOSPHERE-IONOSPHERE COUPLING

H.G.Mitchell, Jr.<sup>1</sup>, J.A.Fedder<sup>2</sup>, M.J.Keskinen<sup>2</sup>, and S.T.Zalesak<sup>2</sup>

<sup>1</sup>Science Applications International Corporation,  
1710 Goodridge Drive, McLean, VA 22102

<sup>2</sup>Geophysical and Plasma Dynamics Branch, Plasma Physics Division,  
Naval Research Laboratory, Washington, DC 20375

**Abstract.** A magnetic-field-line-integrated model of plasma interchange instabilities is developed for the high latitude ionosphere including magnetospheric coupling effects. We show that the primary magnetosphere-ionosphere coupling effect is to incorporate the inertia of the magnetospheric plasma in the analysis. As a specific example, we present the first simulation of the  $\mathbf{E} \times \mathbf{B}$  instability in the inertial regime, i.e.,  $v_i \ll \omega$  where  $v_i$  is the ion-neutral collision frequency and  $\omega$  is the wave frequency. We find that the inertial  $\mathbf{E} \times \mathbf{B}$  instability develops in a fundamentally different manner than in the collisional case ( $v_i \gg \omega$ ). Our results show that striations produced in the inertial regime are spread and retarded by ion inertial effects, and result in more isotropic irregularities than those seen in the collisional case.

Introduction

Recent experimental ground-based, rocket, and satellite (HILAT, DYNAMICS EXPLORER, AUREOL-3) observations in the auroral zone and polar cap ionosphere have indicated the existence of both large [Weber et al., 1984; Basu et al., 1984; Bythrow et al., 1984; Cerisier et al., 1984; Vickrey et al., 1980] and small [Manuise et al., 1981; Baker et al., 1983] scale density structures and irregularities. Different mechanisms, have been proposed to account for high latitude ionospheric irregularities, e.g., particle precipitation, plasma instabilities, and neutral fluid turbulence [Keskinen and Ossakow, 1983]. Considerable quantitative progress has been made in explaining ionospheric structure using plasma interchange instabilities, e.g., the Rayleigh-Taylor instability [Balsley et al., 1972; Ossakow, 1981] in equatorial spread F, and the  $\mathbf{E} \times \mathbf{B}$  and current-convective instabilities in the high latitude ionosphere [Ossakow and Chaturvedi, 1979; Keskinen and Ossakow, 1983]. Recently, Weber et al. (1984) and Cerisier et al. (1984) have invoked the  $\mathbf{E} \times \mathbf{B}$  instability to explain large scale density fluctuations in the high latitude ionosphere.

A shortcoming of most past research on the nonlinear theory of the  $\mathbf{E} \times \mathbf{B}$  instability as it applies to ionospheric structure is that it has been restricted to the collisional (or non-inertial) regime, i.e.,  $v_i \gg \omega$  where  $v_i$  is the ion-neutral collision frequency and  $\omega$  is the

wave frequency. One exception is the recent work of Huba et al. (1985) who studied the nonlinear evolution of interchange instabilities in both the inertial and non-inertial regimes. However, their work was limited to short wavelength turbulence, i.e.,  $kL \gg 1$  where  $k$  is the wavenumber and  $L$  is the density gradient scale length, which is not applicable to large scale ionospheric structures.

In this letter, we present the first simulation of inertial high latitude ionospheric interchange instabilities (e.g., the  $\mathbf{E} \times \mathbf{B}$  instability) with inclusion of magnetospheric coupling effects. The basic conclusions of this study are (1) magnetospheric coupling effects reduce the growth rate of the  $\mathbf{E} \times \mathbf{B}$  instability, (2) striations produced by the inertial  $\mathbf{E} \times \mathbf{B}$  instability develop in a different manner than in the non-inertial ( $v_i \gg \omega$ ) regime, (3) in configuration space, the striations in the inertial regime are more isotropic and spread out resulting in irregularities oriented perpendicular to those produced in the non-inertial case.

Model

The physical configuration and assumptions of our model are described as follows. We only consider structure in the plane transverse to the ambient magnetic field, i.e., the xy plane. The F-layer is initially characterized by a 6 to 1 density enhancement with a Gaussian profile of scale size 12 km in the x-direction and uniform in the y-direction, a uniform magnetic field in the z-direction ( $B_z = 0.5$  G), and a background electric field in the y-direction ( $E_y = .025$  V/m). The entire enhancement  $\mathbf{E} \times \mathbf{B}$  drifts in the x-direction at a velocity  $v_x = 0.5$  km/sec. A uniform horizontal magnetosphere is assumed above the F-layer linked by the vertical magnetic field lines. The back edge of the F-layer enhancement, relative to the drift, is unstable to the  $\mathbf{E} \times \mathbf{B}$  instability, which drives ion Pedersen currents in the F-layer and ion polarization drift currents in the magnetosphere due to the perpendicular electric field mapping along the geomagnetic field. These currents close along the magnetic field via parallel electron currents. Assuming that all ion drifts associated with the perpendicular currents are negligible compared to the  $\mathbf{E} \times \mathbf{B}$  drift and that  $\mathbf{E}_\perp = -\nabla_\perp \phi$ , the equations describing this system are

$$\frac{\partial n}{\partial t} + \nabla_\perp \cdot n \mathbf{v}_\perp = 0 \quad (1)$$

Copyright 1985 by American Geophysical Union.

Paper number 5L6469.  
0094-8276/85/005L-6469 \$03.00

$$\mathbf{v} = \mathbf{v} - \frac{c \nabla_{\perp} \phi}{B} \times \mathbf{z} \quad (2)$$

$$\mathbf{j}_{F\perp} = - \left( \frac{c n e v_{i\perp}}{B \Omega_i} \right) \nabla_{\perp} \phi = - \sigma_p \nabla_{\perp} \phi \quad (3)$$

$$\mathbf{j}_{M\perp} = - \frac{1}{4\pi} \left( \frac{c^2}{V_A^2} \right) \left[ \frac{\partial}{\partial t} + \mathbf{v}_{i\perp} \cdot \nabla_{\perp} \right] \nabla_{\perp} \phi \quad (4)$$

$$0 = \int_F dz (\nabla_{\perp} \cdot \mathbf{j}_{F\perp}) + \int_M dz (\nabla_{\perp} \cdot \mathbf{j}_{M\perp}) \quad (5)$$

where  $n$  is the ion (and electron) density,  $\mathbf{v}_{e(i)\perp}$  is the perpendicular electron (ion) velocity,  $\mathbf{j}_{F\perp}$  and  $\mathbf{j}_{M\perp}$  are the F-layer Pedersen and the magnetospheric polarization drift current densities, respectively,  $\sigma_p$  is the F-layer Pedersen conductivity,  $V_A = B / (4\pi n m_i)^{1/2}$  is the Alfvén velocity, and  $v_i$  and  $\Omega_i$  are the ion-neutral collision frequency and ion gyrofrequency, respectively. Using (2)-(4) in (5) yields the potential equation,

$$0 = \nabla_{\perp} \cdot \left[ \Sigma_p + C_M \left( \frac{\partial}{\partial t} - \left( \frac{c \nabla_{\perp} \phi}{B} \times \mathbf{z} \right) \cdot \nabla_{\perp} \right) \right] \nabla_{\perp} \phi \quad (6)$$

where the field-line integrated F-layer Pedersen conductivity is

$$\Sigma_p = \int_F dz \sigma_p \quad (7)$$

and the field-line integrated magnetospheric inertial capacitance is

$$C_M = \frac{1}{4\pi} \int_M dz (c^2 / V_A^2) \quad (8)$$

Since the magnetospheric layer is uniform and the ion flow given by (2) is incompressible, the magnetosphere remains uniform and the continuity equation for this layer may be neglected. The F-layer continuity equation for  $n$  may be written as a continuity equation for  $\Sigma_p$ ,

$$\frac{\partial}{\partial t} \Sigma_p + \nabla_{\perp} \cdot (\Sigma_p \mathbf{v}_{i\perp}) = 0 \quad (9)$$

Therefore, the system is completely described by (2), (6) and (9) in the variables  $\Sigma_p$  and  $\phi$ , with  $C_M$  a constant capacitance describing the magnitude of magnetosphere-ionosphere coupling.

The numerical methods used to simulate the model equations are described in Zalesak et al. [1982]. The continuity equation (9) is solved numerically using the multidimensional flux-corrected techniques of Zalesak [1979], while the potential equation (6) is solved with the incomplete Cholesky conjugate gradient algorithm of Hain [1980]. The simulations are performed on an  $100 \times 80$  cell grid ( $x, y$ ) with a cell size of  $1.0 \text{ km} \times .25 \text{ km}$  which is drifting with the enhancement at the  $E_y \times B$  velocity. Periodic boundary conditions are assumed in the  $y$ -direction, and the grid is initialized with a random 1% density fluctuation.

If  $\Sigma_p$  has scale length  $L^{-1} = (1/\Sigma_p) \partial \Sigma_p / \partial x$ ,

the non-inertial ( $C_M = 0$ ) growth rate for a wave with wave vector  $\mathbf{k}$  parallel to  $\mathbf{y}$  is  $\gamma_0 = c E_y / BL$  in the regime  $kL \gg 1$ . For the parameters of our simulation, the maximum (non-inertial) growth rate is  $\gamma_0 = 0.05 \text{ sec}^{-1}$ . The e-folding distance of  $E_{\perp}$  parallel to  $B$  for this wave is about  $\lambda_{\perp} = (\sigma_i / \sigma_p)^{1/2} k_{\perp}^{-1}$  [Volk and Haerendel, 1971], implying that a wave with  $k_{\perp}^{-1} = 1 \text{ km}$  has an e-folding distance of  $10^3 \text{ km}$  parallel to the field and that  $E_{\perp}$  maps well up into the magnetosphere where the e-folding distance is much greater due to the rapid decrease in  $\sigma_p$ . The Alfvén speed is  $V_A \sim 10^3 \text{ km/sec}$  so that electric fields of a wave with a growth time of 20 sec map upwards on the order of  $10^4 \text{ km}$  into the magnetosphere, and  $C_M$  has a value of roughly  $10^{13} \text{ cm}$  (or  $\sim 10$  farad).

The effect of ion inertia on the  $E \times B$  instability has previously been studied by Ossakow et al. [1978] in the linear regime. Although their results were for Pedersen and polarization drifts at the same altitude, the linear growth rates are effectively the same for our model equations. A non-zero inertia implies the existence of an inertial relaxation rate,  $\gamma_i = \Sigma_p / C_M$ . The growth rate in the presence of inertia for the short wavelength approximation has two regions of interest, the non-inertial regime

$$\gamma = \gamma_0 \quad \text{for} \quad 4\gamma_0 \ll \gamma_i \quad (10)$$

and the inertial regime

$$\gamma = (\gamma_0 \gamma_i)^{1/2} \quad \text{for} \quad 4\gamma_0 \gg \gamma_i \quad (11)$$

Assuming a  $\Sigma_p$  for the F-layer of  $8 \times 10^{10} \text{ cm/sec}$  ( $\sim 0.1 \text{ mho}$ ), a typical value of  $\gamma_i$  for the simulation is  $.008 \text{ sec}^{-1}$ , which is in the inertial regime and which reduces the growth rate of the instability from  $.05 \text{ sec}^{-1}$  to  $.02 \text{ sec}^{-1}$ . For our simulation, two cases were run: a non-inertial case for which  $\gamma_i = 1.00 \text{ sec}^{-1}$ , and an inertial case for which  $\gamma_i = 0.01 \text{ sec}^{-1}$ .

## Results

The results of the two simulations are shown in Figures 1 and 2. The four panels in each simulation show approximately equal times relative to the linear growth time of the instability. Figure 1 shows the results for the non-inertial  $E \times B$  instability, while Figure 2 shows the results for the inertial case. It is clear that the results of the two cases are very different at later times.

The behavior of the plasma in Figure 1 is typical of that observed in previous  $E \times B$  instability simulations [Keskinen and Ossakow, 1982]. In panel 2, at 104 seconds, we see that early in the nonlinear stage a set of "fingers" has clearly formed. The high density fingers grow outward into the low density plasma while the low density fingers penetrate into the high density cloud. Subsequent nonlinear evolution involves the continued elongation of these fingers with very little apparent change in the size of the structures perpendicular to their long dimension as seen in panels 3 and 4. The original density enhancement has effectively

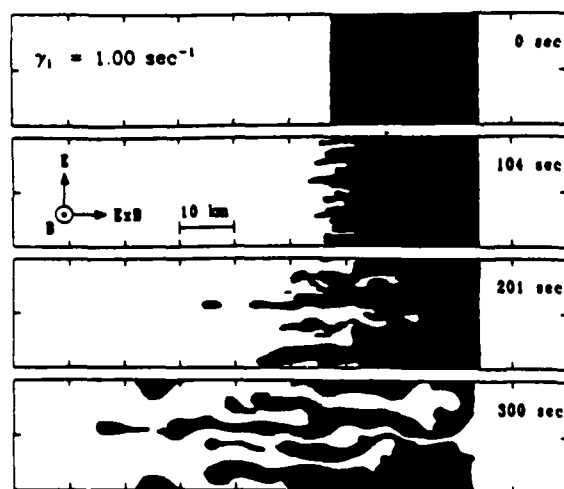


Fig. 1. A plot of density for four times for the case of  $\gamma_i = 1.00 \text{ sec}^{-1}$  (the non-inertial case). The shaded region represents those areas whose density is greater than 2.5 times the background density. The simulation grid is periodic in the direction of  $\mathbf{E} \times \mathbf{B}$  and is moving with the  $\mathbf{E} \times \mathbf{B}$  velocity.

been sliced into a group of sheets parallel to the initial density gradient.

The behavior of plasma and structure formation in Figure 2, the inertial case, is very different. During the time period between panel 1 and panel 2, before 300 seconds, the growth of the instability closely resembles that in Figure 1. There is nonlinear development of long narrow high and low density fingers which move in opposite directions. However, after 300 seconds, the behavior changes radically. In panels 3 and 4, we see that the fingers form mushroom-like heads and tend to thicken. No

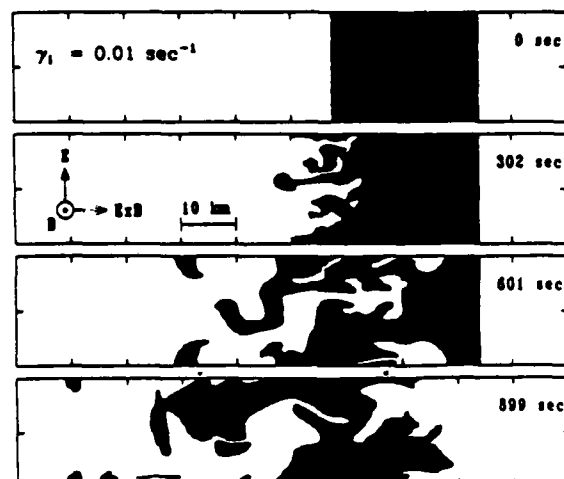


Fig. 2. A plot of density for four times for the case of  $\gamma_i = 0.01 \text{ sec}^{-1}$  (the inertial case). The shaded region and the simulation grid are the same as in Fig. 1. The times shown in the two figures are roughly equal multiples of the linear growth time for the instability in the two cases.

longer are there long thin interpenetrating fingers, rather they are fat interpenetrating blobs. Any narrow fingers which begin to form quickly go to a mushroom shape and then spread out. In a number of simulations we have noted a tendency for the structure in the  $y$  direction to undergo an inverse cascade to the longest mode which will fit in the system. This feature can clearly be seen in panel 4, where the structured state throughout most of the simulation region shows two blobs; one of high density, the other of low density.

The non-inertial simulation, shown in Figure 1, is characterized by striations with a large value of  $k_y$ , which grow in the  $x$ -direction without hindrance, completely destroying the initial orientation of the density enhancement in the  $y$ -direction. The inertial simulation, shown in Figure 2, is characterized initially by striations with a large value of  $k_y$ , which are hindered in their growth in the  $x$ -direction. The plasma at the leading edge of the striation finger is swept to either side and around the striation forming the characteristic mushroom shape. Further evolution involves an inverse cascade in  $k_y$  to the minimum value allowed on the numerical grid while simultaneously, the typical value of  $k_x$  increases. Consequently, individual enhancements tend to an orientation similar to the original  $x$ -directed orientation. Furthermore, the individual enhancements appear to be stabilized to further  $\mathbf{E} \times \mathbf{B}$  structuring owing to velocity shear along their apparently unstable faces (Perkins and Doles, 1975; Huba et al., 1983).

Interestingly, Rino et al. (1979), Livingston et al. (1982), and Rino and Vickrey (1982) have reported sheet-like structures in the night side auroral region which are aligned perpendicular to the large scale  $F$  region ionospheric density gradient. This alignment perpendicular to the density gradient is not easily explained by the traditional instability theory. However, the alignment is similar to the final alignment observed in the inertial simulations.

#### Concluding Remarks

Several conclusions can be drawn from our simulations. First, instability-generated electric fields in the high-latitude  $F$ -layer may map well up into the magnetosphere, resulting in a much reduced linear growth rate due to the effectively increased ion inertia. Second, the nonlinear development of the instability is fundamentally different in the presence of this coupling; the striations produced are spread and retarded by ion-inertial effects resulting in more isotropic irregularities than in the non-inertial case. The inertial effects may even tend to stabilize the final nonlinear state by producing a velocity shear across normally unstable gradients. The simulation results demonstrate some interesting features which may have been observed in the high latitude nighttime ionosphere.

**Acknowledgments.** We thank Dr. J.D. Huba for helpful discussions and a critical reading of the manuscript. This research was supported by the Defense Nuclear Agency, the National

Aeronautics and Space Administration, and the Office of Naval Research.

# References

- Baker, K.B., R.A. Greenwald, and R.T. Tsunoda, Very high latitude F-region irregularities observed by HF-radar backscatter, Geophys. Res. Lett., **10**, 904, 1983.
- Balsley, B.B., G. Haerendel, and R.A. Greenwald, Equatorial spread F: recent observations and a new interpretation, J. Geophys. Res., **77**, 5625, 1972.
- Basu, S., S. Basu, E. MacKenzie, W.R. Coley, W.B. Hanson, and C.S. Lin, F region electron density irregularity spectra near auroral acceleration and shear regions, J. Geophys. Res., **89**, 5554, 1984.
- Bythrow, P.F., T.A. Potemra, W.B. Hanson, L.J. Zanetti, C.I. Meng, R.E. Huffman, F.J. Rich, and D.H. Hardy, Earthward directed high-density Birkeland currents observed by Hilat, J. Geophys. Res., **89**, 9114, 1984.
- Cerisier, J.C., J.J. Berthelier, and C. Beghin, Unstable density gradients in the high latitude ionosphere, Radio Sci., 1985, in press.
- Hain, K., A non-recursive incomplete Cholesky decomposition method for the solution of linear equations with a sparse matrix, NRL Memorandum Report 4264, Naval Research Laboratory, Washington, D.C. 1980.
- Hanuise, C., J.P. Villain, and M. Crochet, Spectral studies of F region irregularities in the auroral zone, Geophys. Res. Lett., **8**, 1083, 1981.
- Huba, J.D., S.L. Ossakow, P. Satyanarayana, and P.N. Guzdar, Linear theory of the  $E \times B$  instability with an inhomogeneous electric field, J. Geophys. Res., **88**, 425, 1983.
- Huba, J.D., A.B. Hassam, I.B. Schwartz, and M.J. Keskinen, Ionospheric turbulence: Interchange instabilities and chaotic fluid behavior, Geophys. Res. Lett., **12**, 65, 1985.
- Keskinen, M.J. and S.L. Ossakow, Nonlinear evolution of plasma enhancements in the auroral ionosphere. I, Long wavelength irregularities, J. Geophys. Res., **87**, 144, 1982.
- Keskinen, M.J. and S.L. Ossakow, Theories of high-latitude ionospheric irregularities: a review, Radio Sci., **18**, 1077, 1983.
- Livingston, R.C., C.L. Rino, J. Owen, and R.T. Tsunoda, The anisotropy of high-latitude nighttime F region irregularities, J. Geophys. Res., **87**, 10519, 1982.
- Ossakow, S.L., Spread F theories - a review, J. Atm. Terr. Phys., **43**, 437, 1981.
- Ossakow, S.L. and P.K. Chaturvedi, Current convective instability in the diffuse aurora, Geophys. Res. Lett., **6**, 332, 1979.
- Ossakow, S.L., P.K. Chaturvedi, and J.B. Workman, High altitude limit of the gradient drift instability, J. Geophys. Res., **83**, 2691, 1978.
- Perkins, F.W. and J.D. Doles, III, Velocity shear and the  $E \times B$  instability, J. Geophys. Res., **80**, 211, 1975.
- Rino, C.L., R.C. Livingston, and S.J. Matthews, Evidence for sheet like auroral ionospheric irregularities, Geophys. Res. Lett., **5**, 1034, 1978.
- Rino, C.L. and J.F. Vickrey, Recent results in auroral-zone scintillation studies, J. Atmos. Terr. Phys., **44**, 875, 1982.
- Vickrey, J.F., C.L. Rino, and T.A. Potemra, Chatanika/Triad observations of unstable ionization enhancement in the auroral F region, Geophys. Res. Lett., **7**, 789, 1980.
- Volk, H.J. and G. Haerendel, Striations in ionospheric ion clouds, J. Geophys. Res., **76**, 4541, 1971.
- Weber, E.J., J. Buchau, J.G. Moore, J.R. Sharber, R.C. Livingston, J.D. Winningham, and B.W. Reinisch, F layer ionization patches in the polar cap, J. Geophys. Res., **89**, 1683, 1984.
- Zalesak, S.T., Fully multi-dimensional flux-corrected transport algorithms for fluids, J. Comp. Phys., **31**, 335, 1979.
- Zalesak, S.T., S.L. Ossakow, and P.K. Chaturvedi, Nonlinear equatorial spread F: the effect of neutral winds and background Pedersen conductivity, J. Geophys. Res., **87**, 151, 1982.

H.G. Mitchell, Science Applications International Corporation, McLean, VA 22102.  
J.A. Fedder, M.J. Keskinen, and S.T. Zalesak, Naval Research Laboratory, Washington, D.C. 20375-5000.

(Received February 7, 1985;  
revised March 14, 1985;  
accepted March 15, 1985)

**APPENDIX E**

**Transverse Motion of High-Speed Barium  
Clouds in the Ionosphere**

**H.G. Mitchell, Jr.  
Science Applications International Corporation**

**J.A. Fedder, J.D. Huba and S.T. Zalesak  
Naval Research Laboratory**



## Transverse Motion of High-Speed Barium Clouds in the Ionosphere

H. G. MITCHELL, JR.

Science Applications International Corporation, McLean, Virginia

J. A. FEDDER, J. D. HUBA, AND S. T. ZALESK

Geophysical and Plasma Dynamics Branch, Plasma Physics Division, Naval Research Laboratory, Washington, D. C.

Simulation results, based on a field-line-integrated, two-dimensional, electrostatic model, are presented for the motion of a barium cloud injected transverse to the geomagnetic field in the ionosphere at high speeds. It is found that the gross evaluation of injected plasma clouds depends on the initial conditions, as well as the nature of the background coupling. For a massive ( $M_0 \sim 10$  kg), orbital ( $V_0 \sim 5$  km/s) release in the F region (350–450 km), we find that plasma clouds can drift tens of kilometers across the magnetic field in tens of seconds after ionization. This type of release is similar to those which are planned for the Combined Release and Radiation Effects Satellite (CRRES) mission.

## INTRODUCTION

The evolution of artificial plasma clouds in the earth's ionosphere has been under scientific investigation for more than two decades. A variety of experimental, theoretical, and computational research programs have been carried out, and research in this area remains active. One interesting problem that requires further investigation is the dynamics of a high-speed plasma cloud moving transverse to the ambient geomagnetic field. Experimentally, this phenomenon has been studied using shaped charge barium releases [Wescott *et al.*, 1980; Simons *et al.*, 1980; Koons and Pongratz, 1981] and rocket barium releases [Mende, 1973; Brence *et al.*, 1973; Heppner *et al.*, 1981], and it will be a major part of the scientific studies for the upcoming CRRES mission (Combined Release and Radiation Effects Satellite) sponsored by NASA and the U.S. Air Force. It should be noted that the high-speed releases to date have been relatively small (barium vapor less than 1 kg) in comparison to those planned for the CRRES mission (up to 10 kg of barium vapor). Theoretically, this problem has been addressed by Scholer [1970] for magnetospheric releases and by Sperling [1983] for ionospheric releases using simple, idealized cloud models. However, to our knowledge, no studies or simulations have been performed to study this phenomenon for more realistic two-dimensional cloud models.

In this paper we present results of numerical simulations based on a two-dimensional, electrostatic model which describe the gross motion of a massive barium release injected transverse to the geomagnetic field at a high velocity. Since our model is electrostatic, we limit our attention to small kinetic beta clouds, i.e.,  $\beta_k \ll 1$  where  $\beta_k = \frac{1}{2} n m_i V^2 / (B^2 / 8\pi)$ , and neglect any MHD perturbations generated by the injected cloud. Our primary interest is to determine whether or not injected plasma clouds can "skid" across the magnetic field, and if so, what physical processes control this behavior. We find that the gross motion of injected clouds depends on initial conditions, as well as the nature of the background coupling. For the case of a massive barium release ( $M_0 \sim 10$  kg) in the F region (350–450 km) at orbital velocity ( $V_0 \lesssim 5$  km/s), we

predict that the plasma cloud can drift tens of kilometers on a time scale of tens of seconds after ionization.

## MODEL AND EQUATIONS

We use a slab geometry such that the ambient geomagnetic field is in the  $z$  direction ( $\mathbf{B} = B_0 \mathbf{e}_z$ ) and a neutral barium cloud is injected transverse to  $\mathbf{B}$  in the  $y$  direction ( $\mathbf{V}_a = V_0 \mathbf{e}_y$ ). The barium subsequently becomes ionized by either photoionization or Alfvén's critical velocity ionization mechanism; we only consider the former in this brief report. We now describe the neutral and plasma cloud models in more detail.

## Neutral Cloud Evolution

The model we use to describe the evolution of the neutral cloud transverse to  $\mathbf{B}$  is relatively simple. The basic processes we consider are self-diffusion of the neutral barium cloud, slowing down of the cloud because of collisions with the background ionosphere, and a neutral loss due to photoionization. Assuming that the neutral cloud initially has a Gaussian density profile, the time evolution of the field-line-integrated density is approximately described by

$$n_n(r, t) = \frac{M_0}{m\pi r_D^2(t)} \exp \left\{ -\frac{[r - x(t)]^2}{r_D^2(t)} - \sigma_i t \right\} \quad (1)$$

where

$$v(t) = V_a \exp(-v_i t) \quad (2)$$

$$x(t) = x_0 + [1 - \exp(-v_i t)] V_a / v_i \quad (3)$$

$$r_D(t) = (r_0^2 + 4Dt)^{1/2} \quad (4)$$

Here  $r$ ,  $x$ , and  $v$  refer only to the perpendicular components, the subscript  $n$  denotes neutrals,  $M_0$  is the initial total mass,  $\sigma_i$  is the ionization loss rate,  $v_i$  is the collision frequency associated with the slowing down of the cloud,  $V_a = V_0 \mathbf{e}_y$  is the injection velocity at  $t = 0$ ,  $r_0$  is the cloud radius at  $t = 0$ ,  $x_0$  is the cloud center position at  $t = 0$ , and  $D$  is the diffusion coefficient ( $D = T/mv_D$ , where  $T$  is temperature,  $m$  is the mass, and  $v_D$  is the collision frequency for diffusion). In deriving (1)–(4) we have made the assumption that the slowing down process and the self-diffusion process are independent of each other. Although this assumption is certainly an oversimplification of the neutral dynamics, we have made it because we are primarily interested in the ion cloud dynamics and it leads to a relatively simple description of the neutral cloud.

Copyright 1985 by the American Geophysical Union.

Paper number 5A8729.  
0148-0227/85/005A-8729\$02.00

### Plasma Cloud Evolution

We assume that the plasma cloud is generated by photoionization of the neutral cloud. This ionization contributes a source term of the form  $\sigma_i n_n$  to the ion continuity equation and one of the form  $m_i \sigma_i n_n (\mathbf{v} - \mathbf{v}_i)$  to the ion momentum equation, where  $\sigma_i$  is the ionization production rate. Upon ionization, the ions and electrons have a large initial velocity and gyrate about the ambient magnetic field in opposite directions, leading to a source Pedersen current density  $\mathbf{j}_s$ . This causes excess charge to pile up on the edges of the cloud and produces a polarization electric field across the cloud. This field leads to an  $\mathbf{E} \times \mathbf{B}$  drift of the plasma cloud in the direction of the neutral cloud motion.

In order to describe this behavior quantitatively we use a field-line-integrated, two-layer, electrostatic model. We consider a cloud layer and a background ionosphere layer which are coupled by the ambient magnetic field lines, assumed to be equipotentials. Note that we neglect any MHD perturbations that may have been generated by the ion cloud. The equations which describe this model are the following:

$$\frac{\partial n_c}{\partial t} + \nabla \cdot (n_c \mathbf{v}_i) = \sigma n_n \quad (5)$$

$$\mathbf{v}_i = \mathbf{v}_e = -\frac{c \nabla \phi}{B} \times \mathbf{e}_z \quad (6)$$

$$\mathbf{j}_s = -\sigma_{ps} \nabla \phi + \frac{B}{c} \sigma_{ps} \mathbf{v} \times \mathbf{e}_z \quad (7)$$

$$\mathbf{j}_c = -\sigma_{pc} \nabla \phi - \frac{1}{4\pi} \frac{c^2}{V_{Ac}^2} \left( \frac{\partial}{\partial t} + \mathbf{v}_i \cdot \nabla \right) \nabla \phi \quad (8)$$

$$\mathbf{j}_b = -\sigma_{pb} \nabla \phi - \frac{1}{4\pi} \frac{c^2}{V_{Ab}^2} \left( \frac{\partial}{\partial t} + \mathbf{v}_i \cdot \nabla \right) \nabla \phi \quad (9)$$

where  $\sigma_{pc(b)} = (ce/B)(n_i v_{in}/\Omega_i)_{c(b)}$  is the Pedersen conductivity of the cloud (background),  $\sigma_{ps} = (ce/B)(n_n \sigma_i/\Omega_i)$  is the source function for Pedersen conductivity caused by ionization,  $v_{in}$  is the ion-neutral collision frequency,  $V_{Ac(b)} = B/(4\pi n m_i)^{1/2}$  is the Alfvén velocity in the cloud (background),  $\Omega_i$  is the ion cyclotron frequency, and  $\nabla$  refers to only the perpendicular components. The perpendicular currents in the cloud ( $\mathbf{j}_c$ ) and background ( $\mathbf{j}_b$ ) are assumed to close via parallel electron currents.

Making use of (5)–(9), we assume that the source Pedersen currents close by Pedersen and polarization currents in the cloud and in the background, and so we integrate  $\nabla \cdot \mathbf{j} = 0$  along the field lines to obtain the potential equation

$$\begin{aligned} \nabla \cdot \left\{ \Sigma_{pc} \left[ 1 + v_{in}^{-1} \left( \frac{\partial}{\partial t} + \mathbf{v}_i \cdot \nabla \right) \right] \nabla \phi + \Sigma_{pb} \nabla \phi \right. \\ \left. + C_b \left( \frac{\partial}{\partial t} + \mathbf{v}_i \cdot \nabla \right) \nabla \phi \right\} = -\nabla \cdot \left\{ \Sigma_{ps} \left( \nabla \phi - \frac{B}{c} \mathbf{v} \times \mathbf{e}_z \right) \right\} \end{aligned} \quad (10)$$

where  $\Sigma_{pc}$ ,  $\Sigma_{ps}$ , and  $\Sigma_{pb}$  are the integrated Pedersen conductivities associated with the cloud, source, and background, respectively, and  $C_b$  is the integrated inertial capacitance associated with the background, i.e.,

$$C_b = \frac{1}{4\pi} \int dz (c^2/V_{Ab}^2)$$

We also rewrite (5) as a continuity equation for  $\Sigma_{pc}$ :

$$\frac{\partial \Sigma_{pc}}{\partial t} + \nabla \cdot (\Sigma_{pc} \mathbf{v}_i) = v_{in} \Sigma_{ps} \quad (11)$$

The background layer is assumed incompressible so that its continuity equation can be neglected. Thus the system is completely described by (1)–(4), (6), (10), and (11) in the variables  $\Sigma_{pc}$  and  $\phi$ . It should be noted that these equations have not been used in large-scale simulation codes to study plasma cloud motion in the ionosphere to date. The new feature in these equations is ion inertia, i.e., the terms that are associated with  $(\partial/\partial t + \mathbf{v} \cdot \nabla)$  in (10) and which lead to polarization currents. Previous studies neglected these terms to study plasma cloud evolution because the time scales of interest were such that  $v_{in} \gg (\partial/\partial t + \mathbf{v} \cdot \nabla)$  and inertial effects could be safely neglected [McDonald *et al.*, 1981; Zalesak *et al.*, 1985]. However, this approximation is not valid for the releases of interest (e.g., CRRES releases), and ion inertia must be considered.

### SIMULATION RESULTS

The numerical methods used to simulate the model equations are described by Zalesak *et al.* [1982] and Mitchell *et al.* [1985]. The continuity equation (11) is solved numerically using the multidimensional flux-corrected techniques of Zalesak [1979], while the potential equation (10) is solved with the incomplete Cholesky conjugate gradient algorithm of Hain [1980]. The simulations are performed on a  $80 \times 100$  cell grid ( $x, y$ ) with a cell size of  $1 \text{ km} \times 1 \text{ km}$ .

We present the results of two simulations. The parameters used are the following:  $B_0 = 0.4 \text{ G}$ ,  $v_D = v_s = v_{in} = \sigma_i = 0.04 \text{ s}^{-1}$ ,  $r_0 = 2 \text{ km}$ ,  $T = 0.1 \text{ eV}$ ,  $M_0 = 10 \text{ kg}$ ,  $V_0 = 5 \text{ km/s}$ , and  $m_i = 137 m_p$  (barium). These parameters are appropriate for a 350- to 450-km-altitude release at mid-latitudes. The integrated Pedersen conductivity of the background is taken to be  $\Sigma_{pb} = 1 \text{ mho}$ , and two values of the integrated inertial capacitance are chosen,  $C_b = 0$  (case 1) and  $C_b = 10 \text{ farads (F)}$  (case 2).

Figure 1 shows the results for the case where  $C_b = 0$ . Physically, this corresponds to source region currents closing via Pedersen currents. Figure 1a shows the integrated Pedersen conductance and velocity flow field for the ion cloud, and Figure 1b shows the corresponding electrostatic potential at times  $t = 1, 9, 19$ , and  $25 \text{ s}$  after initialization. We also show the location of the neutral vapor by a heavily outlined circle of radius  $r_D$ . Note that the velocity vectors are normalized to the maximum velocity at each time step, and comparisons in the magnitude of the velocity at different times can only be made from the potentials. Two features are immediately apparent. First, at early times ( $t \leq 3 \text{ s}$ ) the plasma and neutral clouds are nearly collocated, but the plasma decelerates more quickly than the neutral vapor. By  $25 \text{ s}$  the high-density portion of the plasma cloud has almost stopped drifting after traversing  $\sim 38 \text{ km}$  across the field. Second, the region of strong electric fields remains in the source region, the neutral vapor cloud, and at later times only the low-density leading edge of the plasma continues to drift rapidly. Moreover, the electric field strength in the source region monotonically decreases as the plasma production weakens and the cloud conductance increases.

Figure 2 shows the results for the case where  $C_b = 10 \text{ F}$ . Physically, this case has the source region currents close via Pedersen currents and polarization currents in the background plasma. Again, the Pedersen conductance and velocity field of the ion cloud, and the electrostatic potential are shown in Figures 2a and 2b, respectively, at the same times as in Figure 1. In comparing Figure 2 to Figure 1, three differences immediately stand out. First, the ion cloud in Figure 2 lags further behind the neutral vapor cloud than in Figure 1.

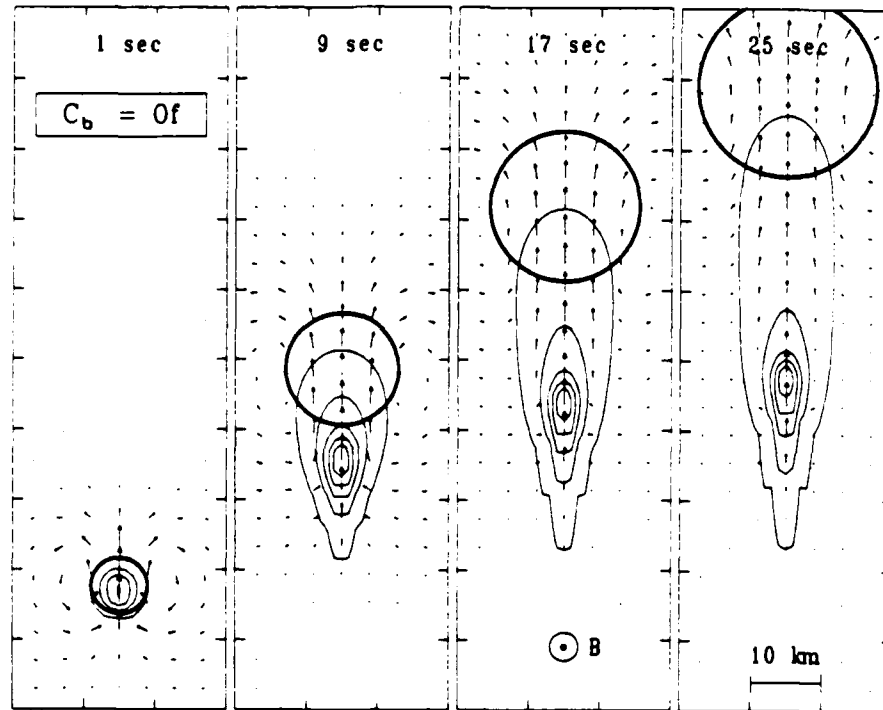


Fig. 1a. Contours of constant  $\Sigma_e$  and velocity flow vectors for  $t = 1, 9, 17$ , and  $25$  s after initialization. The contour separation is  $0.2$  mho with the minimum contour at  $0.1$  mho, and the vectors are independently normalized for each time. The heavily outlined circle represents the location of the neutral vapor and has radius  $r_D$ .

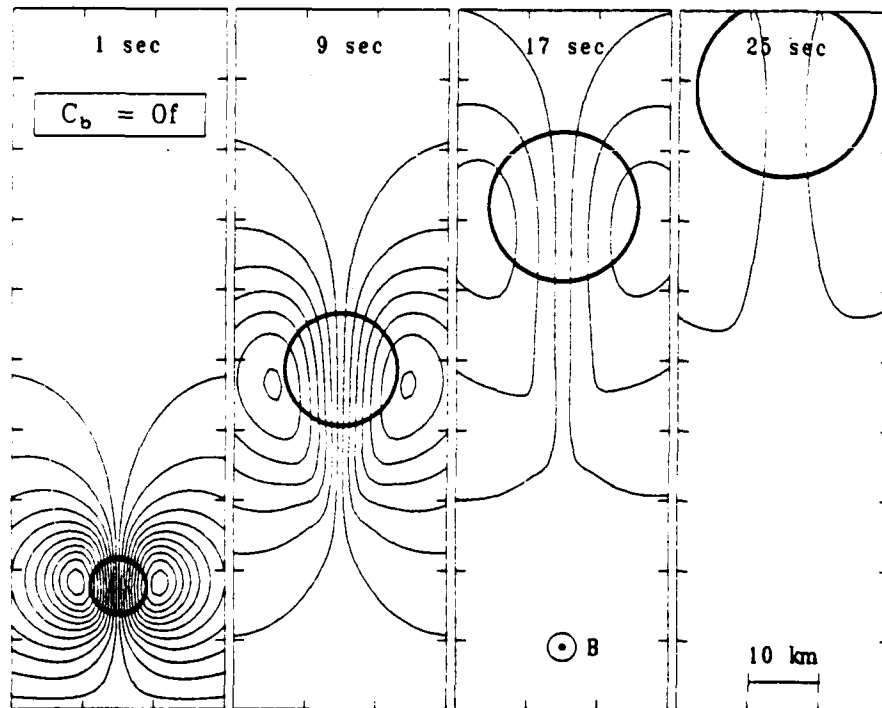


Fig. 1b. Electrostatic potential contours for the times in Figure 1a. The potential difference between contours is  $60$  V.

Fig. 1. Contours of constant  $\Sigma_e$ , velocity flow vectors, and electrostatic potential for the case  $C_b = 0$  F.

Second, at later times, the potential for the second case decays more slowly in the dense portion of the ion cloud than it did in the first case. Third, the plasma cloud in the second case is bifurcated on its trailing edge. The differences between Figures

1 and 2 are the direct results of the inclusion of the background plasma inertia in case 2.

The evolution of the electric field and the ion cloud drift can be understood by consideration of (10). If we neglect inertial

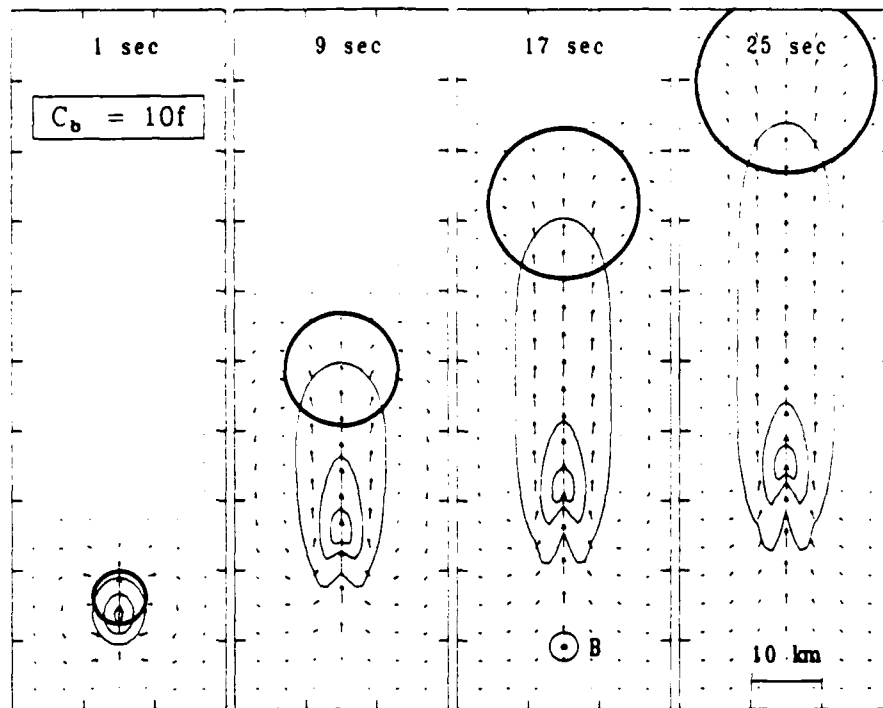
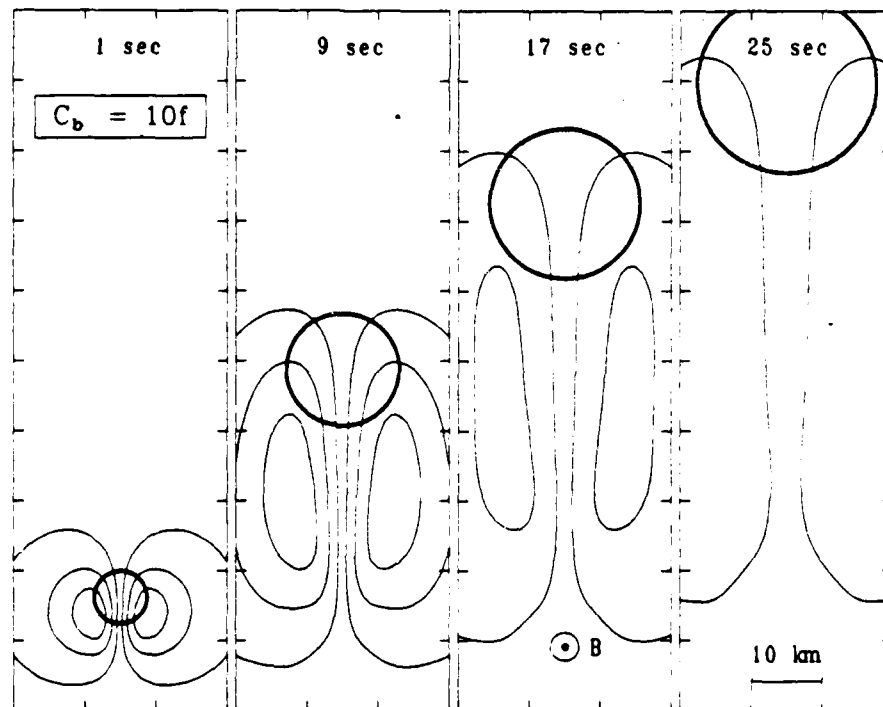
Fig. 2a. Contours of constant  $\Sigma_{pr}$  and velocity flow vectors.

Fig. 2b. Electrostatic potential contours.

Fig. 2. Same as Figure 1 for the case  $C_b = 10 F$ .

effects, as in case 1, the electric field in the production region is approximately

$$E = \Sigma_{pr} / (\Sigma_{pr} + \Sigma_{pb} + \Sigma_{pi}) V_a \times B / c$$

At early times the electric field in the source region is strong ( $\sim 0.96 V_a \times B / c$ ) but decreases rapidly as  $\Sigma_{pr}$  decreases and

$\Sigma_{pr}$  increases. The primary effect of the inertial terms is to cause the electric field in the dense portion of the cloud to decay with a time constant  $\Sigma_{pr} / v_{ia} (\Sigma_{pr} + \Sigma_{pb}) \sim 12$  s. The ion cloud is decelerated in relation to the neutral cloud because the background Pedersen currents (i.e., "line tying" currents) couple the ion cloud momentum to the higher-density, low-

altitude neutral atmosphere. For case 2, the inertial terms in (10) cannot be neglected. The source currents, in addition to closing via Pedersen conduction current, must now also close via polarization currents which set the background plasma into motion along with the ion cloud. The newly produced ions share their momentum with the background, and therefore the electric field in the source region is less than in case 1 (initially  $E_2 \sim 0.6E_1$ ). Additionally, the background ionization inertia leads to a slower decay of plasma momentum outside the source region. The decay time constant for case 2 is

$$(C_b + \Sigma_{pc} v_{ia}) / (\Sigma_{pc} + \Sigma_{pb}) \sim 16 \text{ s}$$

Thus at later times the electric field in the dense portion of the ion cloud for case 2 can be greater than that for case 1. The bifurcation of the trailing portion of the case 2 plasma cloud is the direct result of the spatial variation of the longer decay time constant. The denser portion of the ion cloud travels faster for a longer period of time than the less dense portion. This is clearly shown by comparing the regions of maximum velocity between case 1 and case 2.

#### SUMMARY

We have presented a two-dimensional, electrostatic model and simulation results for a plasma cloud injected transverse to the ambient geomagnetic field at high velocities (e.g., orbital velocity). Such a model is relevant to shaped charge and satellite barium releases and to the proposed chemical release for the upcoming CRRES mission. From the results shown here and from other simulations of releases we have performed for different parameters, we find that the gross evolution of the plasma cloud depends on the initial conditions (i.e.,  $M_0$ ,  $V_0$ , etc.), as well as the nature of the background coupling. Plasma clouds that generate currents which close via Pedersen currents in the background ionosphere tend to drift further across the ambient field than those which have currents which also close via polarization currents. In either case though, it is predicted that the plasma clouds can drift tens of kilometers across the geomagnetic field after ionization for a massive barium release in the *F* region. In fact, recent analysis of the Buaro shaped charge release indicates that barium injected perpendicular to *B* at a velocity of  $\sim 10$  km/s "skidded"  $\sim 50$  km across the magnetic field (M. B. Pongratz, private communication, 1985), which is consistent with our simulations.

The problem studied here is similar in many respects to a previous investigation of the interaction of Io with its plasma torus by Goertz [1980]. Goertz' paper was directed toward obtaining solutions for Alfvén wave generation and propagation for acceleration of ambient plasma on magnetic field lines which pass near Io, while using an approximation for the source region plasma and electric potential. Here, we are concerned with obtaining an accurate description for the source region plasma density and electric potential, while approximating the interaction with the ambient geomagnetic field line connected plasma. The two sets of results are complementary and are consistent with each other.

The results shown and discussed above are not presented as

a detailed, precise prediction of plasma cloud release behavior for a particular experiment. They do, however, demonstrate processes which are physically important for high-velocity plasma cloud releases and must be considered in planning for future experiments such as those planned for the upcoming CRRES mission.

**Acknowledgments.** This research has been sponsored by NASA. The Editor thanks S. H. Brecht for his assistance in evaluating this paper.

#### REFERENCES

- Brence, W. A., R. E. Carr, J. C. Gerlach, and H. Neuss, NASA Max Planck Institute barium ion cloud experiment, *J. Geophys. Res.*, **78**, 5726, 1973.
- Goertz, C. K., Io's interaction with the plasma torus, *J. Geophys. Res.*, **85**, 2949, 1980.
- Hain, K., A non-recursive incomplete Cholesky decomposition method for the solution of linear equations with a sparse matrix, *NRL Memo. Rep. 4264*, Nav. Res. Lab., Washington, D. C., 1980.
- Heppner, J. P., M. L. Miller, M. B. Pongratz, G. M. Smith, L. L. Smith, S. B. Mende, and N. R. Nath, The Cameo barium releases:  $E_1$  fields over the polar cap, *J. Geophys. Res.*, **86**, 3519, 1981.
- Koons, H. C., and M. B. Pongratz, Electric fields and plasma waves resulting from a barium injection experiment, *J. Geophys. Res.*, **86**, 1437, 1981.
- McDonald, B. E., S. L. Ossakow, S. T. Zalesak, and N. J. Zabusky, Scale sizes and lifetimes of *F* region plasma cloud striations as determined by the condition of marginal stability, *J. Geophys. Res.*, **86**, 5775, 1981.
- Mende, S. B., Morphology of the magnetospheric barium release, *J. Geophys. Res.*, **78**, 5751, 1973.
- Mitchell, H. G., J. A. Fedder, M. J. Keskinen, and S. T. Zalesak, A simulation of high latitude *F*-layer instabilities in the presence of magnetosphere-ionosphere coupling, *Geophys. Res. Lett.*, **12**, 283, 1985.
- Scholer, M., On the motion of artificial ion clouds in the magnetosphere, *Planet. Space Sci.*, **18**, 977, 1970.
- Simons, D. J., M. B. Pongratz, and P. Gary, Prompt striations in ionospheric barium clouds due to a velocity space instability, *J. Geophys. Res.*, **85**, 671, 1980.
- Sperling, J. L., Ion Pedersen drift and parallel electric field effects on plasma jetting, *J. Geophys. Res.*, **88**, 7095, 1983.
- Wescott, E. M., H. C. Stenbaek-Nielsen, T. J. Hallinan, C. S. Deehr, G. J. Romick, J. V. Olson, J. G. Roederer, and R. Sydora, A high-altitude barium radial injection experiment, *Geophys. Res. Lett.*, **7**, 1037, 1980.
- Zalesak, S. T., Fully multidimensional flux-corrected transport algorithms for fluids, *J. Comput. Phys.*, **31**, 335, 1979.
- Zalesak, S. T., S. L. Ossakow, and P. K. Chaturvedi, Nonlinear equatorial spread *F*: The effect of neutral winds and background Pedersen conductivity, *J. Geophys. Res.*, **87**, 151, 1982.
- Zalesak, S. T., P. K. Chaturvedi, S. L. Ossakow, and J. A. Fedder, Finite temperature effects on the evolution of ionospheric barium clouds in the presence of a conducting background ionosphere. I. A high altitude incompressible background ionosphere, *J. Geophys. Res.*, **90**, 4299, 1985.
- J. A. Fedder, J. D. Huba, and S. T. Zalesak, Naval Research Laboratory, Code 4780, Washington, DC 20375.
- H. G. Mitchell, Jr., Science Applications International Corporation, 1710 Goodrich Drive, McLean, VA 22102.

(Received June 20, 1985;  
revised August 15, 1985;  
accepted August 20, 1985.)

## **APPENDIX F**

### **Theory of the Current-Driven Ion Cyclotron Instability in the Bottomside Ionosphere**

**P. Satyanarayana and P.K. Chaturvedi  
Science Applications International Corporation**

**M.J. Keskinen, J.D. Huba and S.L. Ossakow  
Naval Research Laboratory**



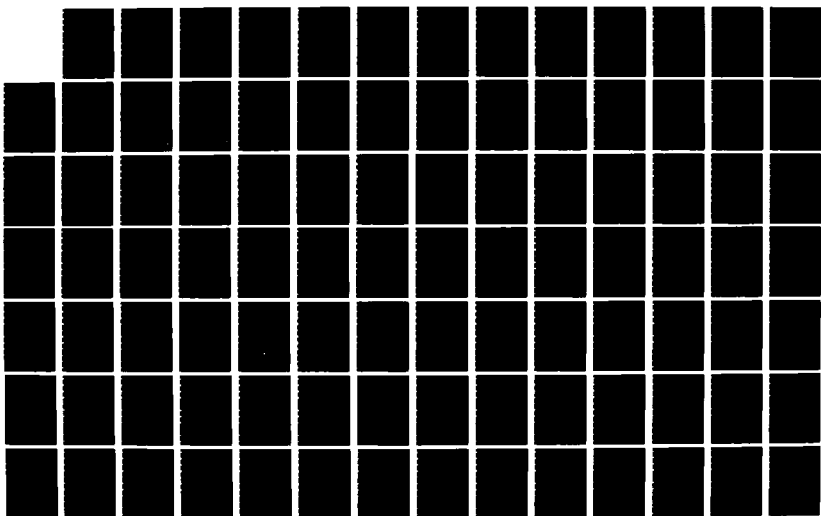
AD-A171 688

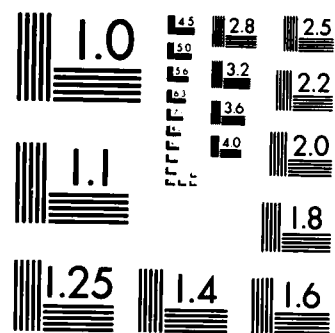
GEOPHYSICAL PLASMAS AND ATMOSPHERIC MOEELING(U) SCIENCE 2/8  
APPLICATIONS INTERNATIONAL CORP MCLEAN VA  
E HYMAN ET AL. JUL 86 SAIC-86/1781 N00014-85-C-2018

UNCLASSIFIED

F/G 4/1

NL





MICROCOPY RESOLUTION TEST CHART  
NATIONAL BUREAU OF STANDARDS-1963-A



# Theory of the Current-Driven Ion Cyclotron Instability in the Bottomside Ionosphere

P. SATYANARAYANA AND P. K. CHATURVEDI<sup>1</sup>

Science Applications International Corporation, McLean, Virginia

M. J. KESKINEN, J. D. HUBA, AND S. L. OSSAKOW

Naval Research Laboratory, Washington, D. C.

PREVIOUS PAGE  
IS BLANK

A theory of the current-driven electrostatic ion cyclotron (EIC) instability in the collisional bottomside ionosphere is presented. It is found that electron collisions are destabilizing and are crucial for the excitation of the EIC instability in the collisional bottomside ionosphere. Furthermore, the growth rates of the ion cyclotron instability in the bottomside ionosphere maximize for  $k_{\perp}\rho_i \geq 1$ , where  $2\pi/k_{\perp}$  is the mode scale size perpendicular to the magnetic field and  $\rho_i$  the ion gyroradius. Realistic plasma density and temperature profiles typical of the high-latitude ionosphere are used to compute the altitude dependence of the linear growth rate of the maximally growing modes and critical drift velocity of the EIC instability. The maximally growing modes correspond to observed tens of meter size irregularities, and the threshold drift velocity required for the excitation of EIC instability is lower for heavier ions ( $\text{NO}^+$ ,  $\text{O}^+$ ) than that for the lighter ions ( $\text{H}^+$ ). Dupree's resonance-broadening theory is used to estimate nonlinear saturated amplitudes for the ion cyclotron instability in the high-latitude ionosphere. Comparison with experimental observations is also made. It is conjectured that the EIC instability in the bottomside ionosphere could be a source of transversely accelerated heavier ions and energetic heavy-ion conic distributions at higher altitudes.

## 1. INTRODUCTION

Electrostatic ion cyclotron (EIC) waves are one of the more important plasma wave modes in the near-earth space plasma environment. Recently, EIC waves have been invoked to explain, among other effects, strong perpendicular ion heating leading to the formation of ion conics [Okuda and Ashour-Abdalla, 1981]. Ion cyclotron wave phenomena have been observed both at high (several earth radii) and low ( $< 1000$  km) altitudes along auroral field lines. Kintner *et al.* [1978, 1979] have reported  $\text{H}^+$  EIC wave observations using S3-3 satellite data at high altitudes in the auroral zone. At low altitudes,  $\text{O}^+$  EIC waves have been observed [Ogawa *et al.*, 1981] on a sounding rocket equatorward of a discrete auroral arc. Yau *et al.* [1983], also using sounding rocket data, have reported particle and wave observations of low-altitude (400–600 km) ionospheric ion acceleration events consistent with ion cyclotron wave phenomena. Bering [1984] has given indirect, but compelling, evidence of short-wavelength ( $k_{\perp}\rho_i \geq 1$ , where  $2\pi/k_{\perp}$  is the density fluctuation scale size perpendicular to the magnetic field and  $\rho_i$  is the ion gyroradius) ion cyclotron wave activity at low altitudes ( $< 350$  km) in the diffuse aurora, using sounding rocket data. Evidence for short-wavelength ( $k_{\perp}\rho_i \geq 1$ ) ion cyclotron wave emissions in the auroral *E* region has been presented by Fejer *et al.* [1984] using backscatter radar observations. Photometric observations in the bright auroras at  $\sim 130$ -km altitude by Martelli *et al.* [1977] indicated excitation of EIC waves at frequencies lying between 25 and 32 Hz, corresponding to gyrofrequencies of  $\text{NO}^+$  and  $\text{O}_2^+$ . Bythrow *et al.* [1984], using Hilat satellite data, have concluded that the very large earthward directed currents seen

near the equatorward edge of the diffuse aurora exceed the threshold for the excitation of ion cyclotron waves.

Kindel and Kennel [1971] first discussed the ion cyclotron instability in a space plasma context by showing that the electrostatic ion cyclotron instability has the lowest threshold among various current-driven instabilities in the high-latitude auroral space plasma. They only briefly discussed the role of weak collisional effects on the evolution of the EIC wave instability. They did note, however, in the context of the EIC instability, that electron collisions were destabilizing and ion collisions were stabilizing. Physically, the ion cyclotron instability is due to the dissipative effect on electrons in their parallel motion which impedes the "instantaneous" redistribution of the electron fluid to a Boltzman-like distribution in the wave potential. In the collisionless limit the dissipation is due to the wave-particle (Landau) resonance, while in the collisional case, it is caused by the electron collisions with ions (or neutrals). The results of Kindel and Kennel [1971] are only applicable to the collisionless and weakly collisional topside ionosphere [Chaturvedi *et al.*, 1984]. Recently, Ganguli *et al.* [1985] have proposed a mechanism that depends on the inhomogeneity of the transverse electric fields to generate ion cyclotron waves in a collisionless plasma in the absence of field-aligned currents. Thus most of the theoretical work described so far has dealt mainly with the collisionless situation. However, several of the aforementioned experimental studies have indicated ion cyclotron wave emissions can occur at low altitudes in the collisional bottomside ionosphere. D'Angelo [1973], using the work of Varma and Bhadra [1964] and Levine and Kuckes [1966], has suggested that the current-driven EIC instability might be excited in *E* region down to 120 km altitudes, where the ion-neutral collision frequency is comparable to the ion cyclotron frequency. This work has been extended to the collisional auroral *F* region altitudes by Chaturvedi [1976], based on the analyses of Chaturvedi and Kaw [1975] and Milić [1972]. However, Chaturvedi [1976] considers collisional effects on the ion cyclotron instability

<sup>1</sup>Now at Naval Research Laboratory, Washington, D. C.

using a fluid approximation ( $k_{\perp} \rho_i < 1$ ). This analysis is not applicable to the recent experimental observations which indicate  $k_{\perp} \rho_i \geq 1$ . For example, *Bering* [1984] and *Fejer et al.* [1984] have reported observations of tens of meter size irregularities corresponding to  $k_{\perp} \rho_i \approx 1$ . Indeed, the transition between collisionless and collisional excitation of the ion cyclotron instability, the approximate altitude of this transition, and the dependence of growth rate of the ion cyclotron instability on ambient high-latitude ionospheric plasma parameters is not well defined. We address these issues in the 130–600 km region in this paper.

In addition to observations indicating existence of EIC waves in the bottomside ionosphere the presence of energetic heavy ions at 1400-km altitude was first documented by *Hoffman et al.* [1974]. Energy and pitch angle distributions of various ion species obtained by S3-3 and PROGNOZ 7 satellite measurements provide evidence for the presence of energetic heavier-ion species ( $\text{NO}^+$  and  $\text{O}^+$ , for example) at altitudes of a few thousand kilometers or more [*Hultqvist*, 1983; *Yau et al.*, 1984]. The pitch angle distributions of ions ranged from being field aligned (ion beams) to conical, in which case the flux peaks at an angle to the geomagnetic field. The pitch angle distributions measured at energies less than 650 eV are relatively field aligned, while those at 1 keV and above have a conical distribution with no field-aligned component [*Klumpp et al.*, 1984]. Recent data from DE 1 also showed that the high-altitude polar cap region contains upflowing heavy molecular ions such as  $\text{NO}^+$ ,  $\text{O}_2^+$ , and  $\text{N}_2^+$  [*Craven et al.*, 1985]. These data suggest that the source for these energetic heavy ions might be located in the ionosphere [*Hultqvist*, 1983]. On the basis of our linear theoretical analysis we conjecture that the current-driven EIC waves at the ion (heavy) cyclotron frequency could selectively accelerate the heavier ions, such as  $\text{NO}^+$ ,  $\text{O}_2^+$  and  $\text{O}^+$ , in the transverse direction. Thus the bottomside ionosphere can act as a source for the heavier-ion conics observed at magnetospheric altitudes.

In this paper we study the EIC instability in the bottomside collisional ionosphere. We find that the growth rates of the EIC instability in the bottomside ionosphere maximize for  $k_{\perp} \rho_i \approx 1$ . In section 2 we present the general dispersion relation for EIC waves in a collisional plasma, which we solve analytically both in the collisionless, weakly collisional, and strongly collisional limits. We also solve the full dispersion relation numerically, using the plasma density and temperature profiles obtained from the Sondrestrom radar [*Kelly*, 1983]. The dispersion relation is solved for the maximally growing modes for which  $k_{\perp} \rho_i \approx 1.4$ , corresponding to observed tens of meter size irregularities. In section 3 we compute expected nonlinear saturation amplitudes of the electrostatic ion cyclotron instability in a collisional plasma based upon *Dupree's* [1966] resonance-broadening theory and compare with experimental observations. Finally, in section 4 we summarize and discuss our results.

## 2. LINEAR THEORY

We consider a homogeneous plasma in a uniform magnetic field along the  $z$  direction,  $\mathbf{B} = B\hat{z}$ . The plasma is collisional, and the main source of free energy is due to the magnetic-field-aligned currents. In this paper we ignore inhomogeneous effects, for example, density and temperature gradients, and as a result, use local theory. Furthermore, we assume the scale height in the high-latitude ionosphere to be much larger than the parallel wavelengths involved. In our attempt to understand ion cyclotron instabilities in the bottomside ionosphere

we include collisional effects and use the general dispersion relation derived by *Clemmow and Dougherty* [1969]. In order to include collisional effects we use a number-conserving Bhatnagar-Gross-Krook (BGK) collision model. This model can also be shown to conserve momentum if the electrons are assumed to carry the bulk of the current and the ions are considered to be at rest. Under these conditions the BGK model reproduces the effects of electron-neutral  $\nu_{en}$ , electron-ion  $\nu_{ei}$ , and ion-neutral  $\nu_{in}$  collisions. However, the BGK model does not model well ion-ion  $\nu_{ii}$  or electron-electron collisions and a different collision model, for example, Fokker-Planck approximation, must be used. Since we will be considering bottomside  $F$  region altitudes ( $z \leq 600$  km),  $v_{ii} \leq v_{in}$  is satisfied. Electron viscous effects  $\nu_{ee}$  are negligible because the electron Larmor radius is much smaller than the perpendicular wavelengths of interest. In section 2.2 we do include a phenomenological model for  $\nu_{ii}$  in our numerical computation of growth rates and marginal stability criteria for the electrostatic ion cyclotron instability.

We utilize the dispersion relation derived by *Clemmow and Dougherty* [1969]. We list only the salient features of the derivation here. The equilibrium function is a drifting Maxwellian

$$f_{0j} = N_{0j} \left( \frac{m_j}{2\pi T_j} \right)^{3/2} \exp \{ -[V_{\perp}^2 + (V_{\parallel} - V_{dj})^2]/V_j^2 \} \quad (1)$$

where  $N_{0j}$ ,  $m_j$ ,  $T_j$ ,  $V_{dj}$ , and  $V_j$  are the density, mass, temperature, drift, and thermal velocities of the  $j$ th species, respectively. The perturbed distribution function (where  $f_j = f_{0j} + f_{1j}$ ), using a BGK collision model, is given as,

$$\begin{aligned} \frac{\partial f_{1j}}{\partial t} + \mathbf{v} \cdot \frac{\partial f_{1j}}{\partial \mathbf{x}} + \frac{e}{mc} (\mathbf{v} \times \mathbf{B}) \cdot \frac{\partial f_{1j}}{\partial \mathbf{v}} \\ = \sum_j \nu_j [f_{1j} - (N_{1j}/N_{0j}) f_{0j}] \end{aligned} \quad (2)$$

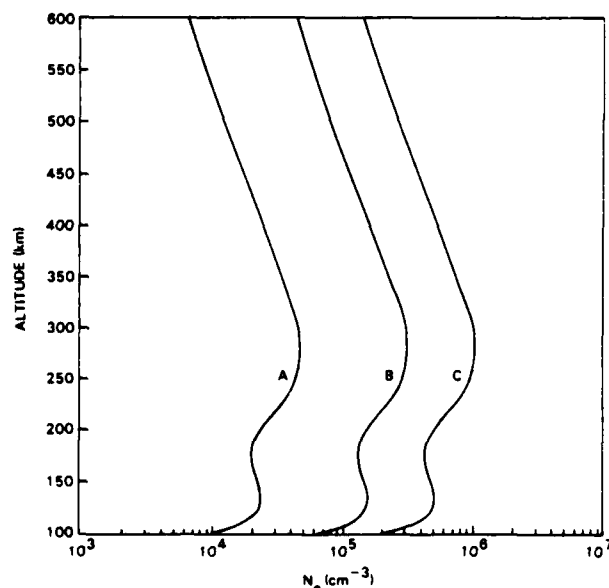


Fig. 1. Typical ionospheric electron density profiles valid in the region 130–600 km, based on Sondrestrom incoherent scatter radar data. Curve A represents a quiet condition, curve B an intermediate electron density, and curve C a disturbed condition.

where

$$N_{1j} = -(e/m)\nabla\phi_1 \int D^{-1} \partial f_0 / \partial V d^3V \cdot \left[ 1 - (v_j/N_0) \int D^{-1} f_0 d^3V \right]^{-1}$$

and

$$D \equiv i(\omega - iv_j - \mathbf{k} \cdot \mathbf{V})$$

For a low  $\beta$  ( $8\pi nkT/B^2 \ll 1$ ) plasma and perturbations of the form  $f_1 \propto \exp[-i(\omega t - \mathbf{k} \cdot \mathbf{x})]$  the dispersion relation is given as [Kindel and Kennel, 1971]

$$-k_{\perp}^2 = \sum_j \left\{ \sum_{n=-\infty}^{\infty} \left[ \frac{\Gamma_n(b_j)}{\lambda_{dj}^2} \right] \left[ 1 + \frac{\tilde{\omega}_j}{k_{\parallel} V_j} Z(\xi_j) \right] \cdot \left[ 1 + \left( \frac{iv_j}{k_{\parallel} V_j} \right) \sum_{n=-\infty}^{\infty} \Gamma_n(b_j) Z(\xi_j) \right]^{-1} \right\} \quad (3)$$

where

$$\begin{aligned} b_j &= k_{\perp}^2 \rho_j^2 / 2 \\ \rho_j &= V_j / \Omega_j \\ \Omega_j &= q_j B / m_j c \\ \lambda_{dj} &= (T_j / 4\pi n_j q_j^2)^{1/2} \\ V_j^2 &= 2T_j / m_j \\ \tilde{\omega}_j &= \omega - k_{\parallel} V_{dj} + iv_j \\ \xi_j &= \frac{\tilde{\omega}_j + n\Omega_j}{k_{\parallel} V_j} \\ \Gamma_n &= I_n(b_j) e^{-b_j} \end{aligned}$$

where  $I_n(b)$  is the modified Bessel function of  $n$ th order,  $Z(\xi)$  is the plasma dispersion function,  $v_j = v_{jn}$  is the collision fre-

quency of the  $j$ th species with neutrals, and  $q_j$  is the charge of the species ( $\pm e$ ). In the case of electrons, Coulomb collisions can also be included, and we define  $v_e = v_{ei} + v_{en}$ .

The effects of collisions are reflected in the shifted frequency  $\tilde{\omega}$  (by  $iv_j$ ) and, more importantly, in the additional term proportional to  $v_j/k_{\parallel} V_j$  in the denominator of (3). In fact, this term gives rise to instability in the collisional domain. This local dispersion relation is assumed to describe both the collisional bottomside and collisionless topside ionosphere. We assume quasi-neutrality and solve (3) analytically in the collisionless, weakly collisional, and strongly collisional (fluid) limits.

### 2.1. Collisionless Domain

By setting  $v_j = 0$  in (3) we immediately recover the collisionless dispersion relation [Drummond and Rosenbluth, 1962; Kindel and Kennel, 1971]. Furthermore, if we set  $n = 0$  for electrons and  $n = 1$  for ions and expand the plasma dispersion function  $Z(\xi)$  such that the electrons are treated kinetically and the ions are treated in the fluid limit, ( $\xi_e \ll 1$  and  $\xi_i \gg 1$ , respectively) we obtain their results:

$$\omega_r / \Omega_i \approx 1 + \tau \Gamma_1(b_i) \quad (4)$$

$$\gamma / \Omega_i \approx -\tau (\pi/2)^{1/2} \Gamma_1(b_i) \frac{(\omega_r - k_{\parallel} V_d)}{k_{\parallel} V_e} \quad (5)$$

where  $\tau = T_e/T_i$  and  $V_d = V_{de} - V_{di}$ . We note here that as will be shown in section 2.2, the numerical solution of (3) agrees with (4) and (5) if  $n = 1$  for ions.

### 2.2. Weakly Collisional Limit

The analysis in this limit was also attempted by Kindel and Kennel [1971]. We expand the electron  $Z$  function in the small argument limit,  $\xi_e \ll 1$ , and retain only  $n = 0$  terms in the electron part of the dispersion relation. The electron contribution to (3) is given as

$$\begin{aligned} D_e &\approx \frac{1}{\tau} \frac{1 + i(\pi)^{1/2} \xi_e}{1 - (\pi)^{1/2} (v_e/k_{\parallel} V_e) \xi_e} \\ &= \frac{1}{\tau} \left\{ 1 + i(\pi)^{1/2} \frac{(\omega - k_{\parallel} V_d)}{k_{\parallel} V_e [1 - (\pi)^{1/2} v_e/k_{\parallel} V_e]} \right\} \quad (6) \end{aligned}$$

Here we have assumed  $b_e \ll 1$ , which gives  $\Gamma_0(b_e) \approx 1$ . We expand the ion  $Z$  function in the large argument limit,  $\xi_i \gg 1$ . The ion contribution of (3) is given as

$$D_i = -\sum_n \frac{\omega + iv_i}{\omega + n\Omega + iv_i} \Gamma_n(b_i) \left[ 1 - iv_i \sum_n \frac{\Gamma_n(b_i)}{\omega + n\Omega + iv_i} \right]^{-1} \quad (7)$$

For  $v_i/\Omega_i < 1$  the ion contribution becomes

$$D_i = -f_n [(\omega - v_i^2 f_n) + iv_i (1 + \omega f_n)] \quad (8)$$

where

$$f_n \equiv \sum \frac{\Gamma_n}{\omega + n\Omega + iv_i} \quad (9)$$

For  $v_i/\omega < 1$  the dispersion relation then becomes  $D = D_e + D_i = 0$  or

$$\frac{1}{\tau} \left[ 1 + i\pi \Gamma \frac{(\omega - k_{\parallel} V_d)}{k_{\parallel} V_e (1 - \Gamma_1 v_e/k_{\parallel} V_e)} \right] = -f_n (\omega + iv_i + \omega v_i f_n) \quad (10)$$

From the real part of (10) we obtain the usual result for  $n = 1$ .

$$\omega_r \approx \Omega_i [1 + \tau \Gamma_1(b_i)] \quad (11)$$

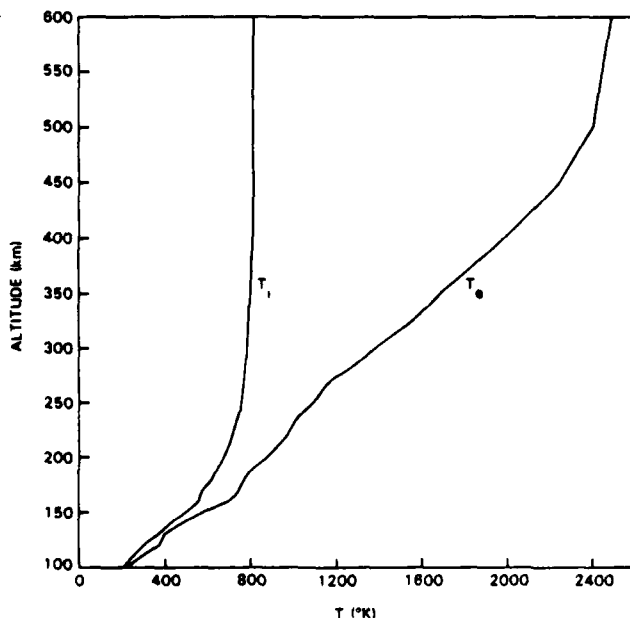


Fig. 2. Typical temperature profiles for  $T_e$  and  $T_i$  versus altitude valid in the region 130–600 km, based on Sondrestrom data.

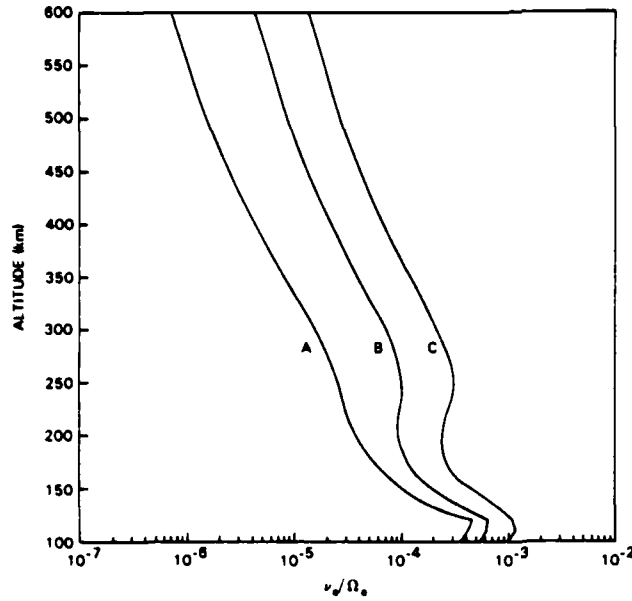


Fig. 3. Total normalized ion collision frequencies  $\nu_i/\Omega_i$ , where  $\nu_i = \nu_{ie} + \nu_{ii}$  as a function of altitude, valid in the region 130–600 km.

and from the imaginary part we obtain

$$\gamma/\omega_r \approx -2(\pi)^{1/2} \tau \Gamma_1(b_i) \frac{(\omega_r - k_{\parallel} V_e)}{k_{\parallel} V_e} \left[ 1 + (\pi)^{1/2} \frac{v_e}{k_{\parallel} V_e} \right] - \nu_i/\Omega_i \left( 1 + \frac{1}{\tau} \right) \quad (12)$$

which leads to the collisionless result of *Drummond and Rosenbluth* [1962] and *Kindel and Kennel* [1971] in (5), when  $v_e = v_i = 0$ . Equation (12) shows that the electron collisions have a destabilizing influence, whereas the ion collisions are stabilizing. In the short-wavelength limit,  $v_e/k_{\parallel} V_e \ll 1$ , the ion collisions override the destabilizing influence of electron collisions. However, we show in the section 2.3 that the electron collisions dominate the ion collisions in the fluid limit,  $v_e/k_{\parallel} V_e \gg 1$ .

### 2.3. Strongly Collisional Limit

In this limit the electron mean free path  $\lambda_e \ll \lambda_{\parallel}$  and thus  $v_e/k_{\parallel} V_e \gg 1$ . For  $v_e/k_{\parallel} V_e \gg 1$  we can expand the electron Z function in the large argument limit while still satisfying  $V_i < V_e \leq V_c$ , obtaining

$$D_e = -\frac{1}{2\tau} \frac{\Gamma_0(b_e)}{\xi_e^2 - (iv_e/k_{\parallel}^2 V_e^2) \tilde{\omega} (1 + 1/2\xi_e^2) \Gamma_0(b_e)} \quad (13)$$

The ion contribution is obtained, as before, by expanding the Z function in the large argument limit  $\xi_i \gg 1$ , as

$$D_i \approx G - \Gamma_1(b_i) \frac{\omega}{\omega - \Omega_i} \quad (14)$$

where

$$G = 1 - \frac{1 - \Gamma_0(b_i)}{b_i}$$

Now the dispersion relation becomes

$$D = D_e + D_i \approx 0$$

from which the growth rate and real frequency can be written as

$$\frac{\omega_r}{\Omega_i} \approx 1 + \tau \Gamma_1(b_i) (1 - \tau G)^{-1} \left[ 1 - \frac{(\Omega_i - k_{\parallel} V_e)^2}{k_{\parallel}^2 V_e^2} \frac{1}{\Gamma_0(b_e) + \alpha} \right] \quad (16)$$

$$\frac{\gamma}{\omega_r} \approx \frac{-2\tau \Gamma_1(b_i) (1 - \tau G)^{-1} (\omega_r - k_{\parallel} V_e) v_e}{(\Gamma_0(b_e) + \alpha) k_{\parallel}^2 V_e^2} \quad (17)$$

where  $\alpha = (v_e^2/\Omega_e^2)(k_{\perp}^2/k_{\parallel}^2)$ . For  $b_i \ll 1$  and  $v_e/\Omega_e \ll 1$ , (16) and (17) reduce to those obtained by *Chaturvedi* [1976], who used a fluid analysis. We see from (16) and (17) that the real frequency is not significantly different from the collisionless result (see equation (4)) and the growth rate is directly proportional to  $v_e$  and  $V_e$  but has a peak in  $v_e$  at  $v_e = \Omega_e(k_{\parallel}/k_{\perp})[\Gamma_0(b_e)]^{1/2}$ . Since  $v_e \propto T_e^{-3/2}$  for Coulomb collisions, we see from (17) that initially the growth rate decreases with  $T_e$  as  $T_e^{-3/2}$ , and for strong collisions the growth rate increases as  $T_e^{3/2}$ , indicating a minimum as a function of  $\tau$  (for a fixed  $T_i$ ). This is in sharp contrast to the collisionless case where the growth rate increases as a function of  $\tau$  (equation (5)).

### 2.4. Marginal Stability Analysis

In the collisionless domain, several authors have estimated the drift velocity thresholds for the onset of the ion cyclotron instability (see, for example, *Drummond and Rosenbluth* [1962] and *Kindel and Kennel* [1971]). *Kindel and Kennel* [1971] have examined briefly the effects of ion-neutral collisions and weak electron-neutral collisions. Their expression for threshold drift velocity shows that while the electron-neutral collisions could destabilize the EIC instability, the ion-neutral collisions strongly stabilize the EIC instability.

In the weakly collisional limit  $v_e/k_{\parallel} V_e \ll 1$  we expand the electron Z function in the small argument limit. The electron part of the dispersion relation in the above limit together with the ion part in the large argument limit yield the dispersion relation given in (10). The imaginary part of (10) yields, for  $\gamma = 0$ ,

$$\omega_r - k_{\parallel} V_c = -\frac{\tau}{(\pi)^{1/2}} (k_{\parallel} V_e - (\pi)^{1/2} v_e) \frac{f_n v_i (1 + \omega_r f_n)}{(1 - v_i^2 f_n^2)} \quad (18)$$

where  $V_c$  is the threshold drift velocity. Considering the resonance at the first harmonic, we obtain from (18)

$$\frac{V_c}{V_e} = \frac{\omega_r}{k_{\parallel} V_e} + \frac{\tau \Gamma_1}{(\pi)^{1/2}} \left[ 1 - \frac{v_e (\pi)^{1/2}}{k_{\parallel} V_e} \right] \left( \frac{v_i}{\omega - \Omega} \right) \left( 1 + \frac{\omega_r \Gamma_1}{\omega - \Omega} \right) \quad (19)$$

which agrees with that of *Kindel and Kennel* [1971]. Equation (19) shows that in a weakly collisional limit the critical drift velocity is reduced by electron collisions and is increased by ion collisions. For a given ion temperature, increasing the electron temperature increases the critical drift velocity; however, electron collisions reduce the influence of ion collisions.

In the strongly collisional limit  $v_e/k_{\parallel} V_e \gg 1$  and  $v_e \geq \omega$  the large argument expansion of the electron and ion Z functions yield the dispersion relation (equation (15)) from which

$$\frac{\Gamma_0(b_e) + \alpha}{[\Gamma_0(b_e) + \alpha] - 2(\tilde{\omega}_e \omega - k_{\parallel} V_e)/k_{\parallel}^2 V_e^2} + \tau \left\{ 1 + \Gamma_1 \left[ -\frac{\tilde{\omega}}{\tilde{\omega} - \Omega_i} + i(\pi)^{1/2} \frac{\tilde{\omega}}{k_{\parallel} V_e} e^{-\tilde{\omega}^2} \right] \right\} = 0 \quad (20)$$

where  $\Gamma_1 = \Gamma_1(b_i)(1 + \tau G)$  and  $\tilde{\omega} = \omega + iv_i$ . From the imagi-

nary part of (20) we obtain for  $(\omega - k_{\parallel} V_e)/k_{\parallel} V_e \ll 1$ ,

$$\frac{V_e}{V_e} \approx \frac{\omega_r}{k_{\parallel} V_e} - \tau \Gamma_1 (\Gamma_0 + d) \frac{k_{\parallel} V_e}{v_e} \left[ \frac{v_i \Omega_i}{(\omega_r - \Omega_i)^2 + v_i^2} + (\pi)^{1/2} \frac{\omega_r}{k_{\parallel} V_i} e^{-|\zeta|^2} \right] \quad (21)$$

where  $\omega_r$  is obtained from the real part as

$$\omega_r \approx \Omega_i [1 + \tau \Gamma_1 / (1 + \tau)] \quad (22)$$

Equation (21) shows that in the strongly collisional limit the critical drift velocity has a markedly different behaviour than in the weakly collisional or collisionless limit. Even for  $v_i = 0$  the electron collisions reduce the critical drift velocity, which is not the case in the weakly collisional limit (equation (19)). Furthermore, ion collisions affect the collisional result differently depending on how strong the collision frequency is compared to  $(\omega_r - \Omega_i)$ , as can be seen from the second term on the right-hand side of equation (21). More importantly, the critical drift velocity has a different behavior as a function of  $\tau$ , showing a minimum in some domains, compared to the collisionless case, where it was shown to increase linearly with  $\tau$  [Drummond and Rosenbluth, 1962].

## 2.5. Numerical Results Applied to Auroral F Region

The dispersion relation given in (3) describes the obliquely propagating ion cyclotron instability and the ion acoustic instability as well ( $k_{\perp} = 0$ ,  $\tau > 1$ ). In this paper we confine ourselves to the analysis of the ion cyclotron instability. We illustrate the properties of the EIC instability by solving the dispersion relation numerically, using parameters typical of the high-latitude ionosphere, and compare the numerical results with the analytical results in various regimes of collisionality where possible. We find that the growth rate of the collisional ion cyclotron instability maximizes at  $k_{\perp} \rho_i \approx 1$ . Furthermore,  $k_{\perp} \rho_i \approx 1$  also corresponds to modes with  $\lambda_{\perp} \approx 11$  m ( $\rho_i \approx 2.56$  m for  $O^+$ ), which is of the order of typically observed scale size [Fejer et al., 1984; Bering, 1984].

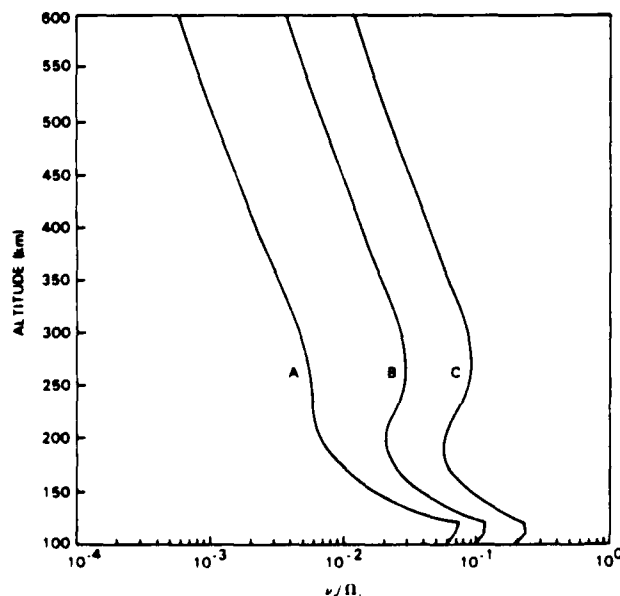


Fig. 4. Total normalized electron collision frequencies  $\nu_e / \Omega_e$ , where  $\nu_e = \nu_{en} + \nu_{ei}$ , as a function of altitude, valid in the region 130–600 km.

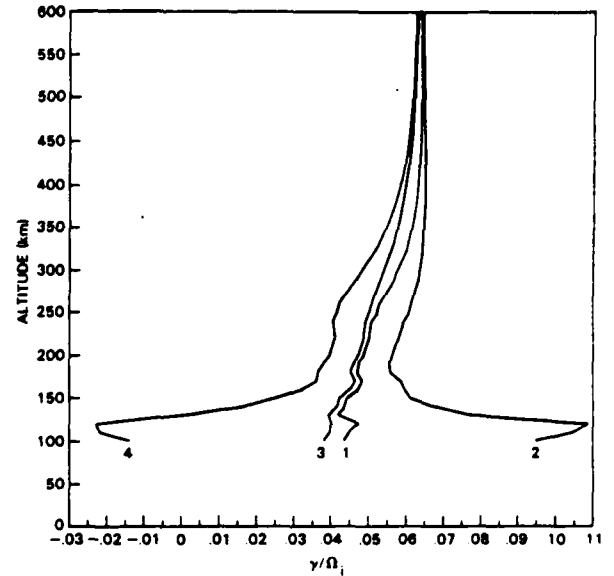


Fig. 5. Growth rate  $\gamma / \Omega_i$  of electrostatic ion cyclotron instability versus altitude for  $O^+$  ion plasma using curve B of Figure 1 and taking  $\tau$  as varying with altitude and  $v_e = v_i = 0$  (curve 1);  $v_e = v_e(z)$ ,  $v_i = 0$  (curve 2);  $v_e = v_e(z)$ ,  $v_i = v_i(z)$  (curve 3); and  $v_e = 0$ ,  $v_i = v_i(z)$  (curve 4). Here  $k_{\parallel} / k_{\perp} = 0.06$ ,  $k_{\perp} \rho_i = (2)^{1/2}$  and  $V_d / V_e = 0.3$ .

Typical bottomside auroral zone ionospheric electron density and temperature profiles based on Sondrestrom incoherent scatter radar data [Kelly, 1983; C. L. Rino, private communication, 1984] are shown in Figures 1 and 2, respectively. Curve B is taken from Kelly [1983], the data being simply extrapolated to 600 km. The two electron density profiles (A and C) are expected to bracket both quiet and disturbed conditions with corresponding  $F$  peak densities of roughly  $10^4$  and  $10^6$   $\text{cm}^{-3}$ , respectively. The electron-neutral  $\nu_{en}$ , electron ion  $\nu_{ei}$ , ion-ion  $\nu_{ii}$ , and ion-neutral  $\nu_{in}$  collisions based upon the data in Figures 1 and 2 are calculated using standard expressions [Spitzer, 1962; Banks and Kockarts, 1973]. Figure 3 gives the total electron collision frequency  $\nu_e = \nu_{en} + \nu_{ei}$ , while Figure 4 displays the ion collision  $\nu_i = \nu_{in} + \nu_{ii}$  frequency. These collision frequencies are calculated using the electron density profiles of Figure 1 [Kelly, 1983]. Neutral particle density profiles are taken from Banks and Kockarts [1973] and fall off exponentially with altitude. We note that the  $E$  region (100–130 km) is not accurately modeled here. We do not intend to apply our theory to this region because the ion-neutral collision frequency in the  $E$  region becomes of the order or greater than the ion gyrofrequency, thus demagnetizing the ions.

In order to illustrate the destabilizing effects of electron-neutral and electron-ion collisions on the ion cyclotron instability, we solve the dispersion relation (3) numerically, varying  $\nu_e = \nu_{en} + \nu_{ei}$  and keeping other parameters fixed. To illustrate the effect of collisionality of the plasma, we show in Figure 5 the growth rate of the electrostatic ion cyclotron instability (equation (3)) as a function of altitude for profile B of Figure 1, assuming a pure  $O^+$  and an  $e^-$  plasma and taking  $k_{\parallel} / k_{\perp} = 0.06$ ,  $V_d / V_e = 0.3$ . The growth rate shown is based on  $b_{\perp} = k_{\perp}^2 \rho_i^2 / 2 = 1$ , which gives maximum growth. Curve 1 represents the collisionless growth rate  $\nu_e = 0 = \nu_i$ . The decrease in growth rate is due to the decrease in  $\tau$  as one goes down in altitude. Curve 2 (where  $\nu_e \neq 0$ ,  $\nu_i = 0$ ), however, displays the strong destabilization in the 130- to 150-km region and mild

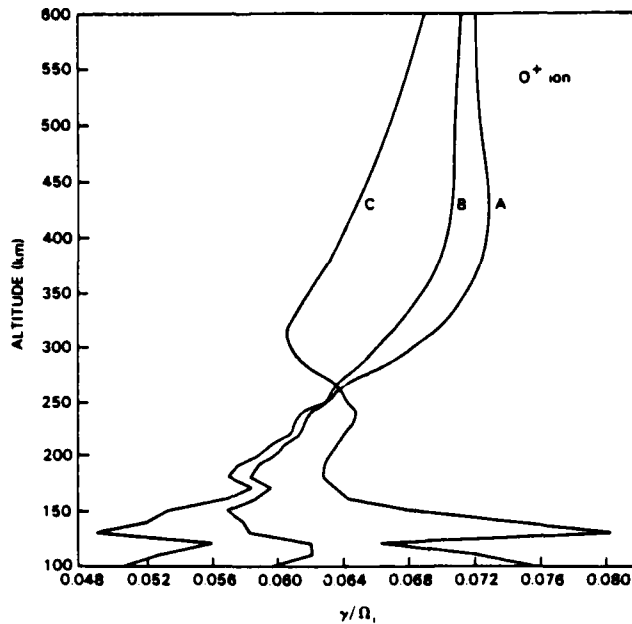


Fig. 6. Growth rate  $\gamma/\Omega_i$  of electrostatic ion cyclotron instability versus altitude of  $O^+$  ion plasma using curves A–C of Figure 1, with fixed parameters  $k_{\parallel}/k_{\perp} = 0.06$ ,  $k_{\perp}\rho_i = (2)^{1/2}$  and  $V_d/V_e = 0.3$ .

destabilization around 300 km. Curve 3 (where  $v_e \neq 0$ ,  $v_i \neq 0$ ), on the other hand, shows the stabilizing influence of ion collisions. The damping influence of ion-ion collisions is phenomenologically represented by  $(v_{ii}b_i)/(1 + b_i)$ , as discussed in the next paragraph. As a comparison, we show in curve 4 the collisionless growth with only ion damping included ( $v_i \neq 0$ ,  $v_e = 0$ ). Curve 3 represents the growth rate for completely realistic ionospheric conditions for which parameters such as plasma density, electron and ion temperatures, and neutral density vary with altitude. Curves 3 and 4 clearly establish the importance of the electron collisions, which overcome the ion damping in the region  $130 < z < 150$  and significantly enhance the growth rate in the region  $150 < z < 300$  km.

Figure 6 displays the growth rate of the electrostatic ion cyclotron instability, including both electron and ion collisions for the three electron density profiles in Figure 1 and temperatures shown in Figure 2, assuming an  $O^+$  ion plasma. Although not explicitly calculated in (3), the ion-ion collisional damping  $v_{ii}$  is included in the calculation of the growth rates of Figure 6 by modeling this damping with the expression  $-v_{ii}k_{\perp}^2\rho_i^2/(1 + k_{\perp}^2\rho_i^2)$  (Y. C. Lee, private communication, 1984). This expression reduces to the appropriate viscous damping in both the magnetized ( $k_{\perp}\rho_i < 1$ ) and unmagnetized ( $k_{\perp}\rho_i \gg 1$ ) limits. Since we are concerned with bottomside characteristics of EIC waves ( $v_{ii} \leq v_{in}$ ), the growth rates will not be extremely sensitive to  $v_{ii}$  in any case. The ion-neutral collisions were treated by BGK model with  $v_{in} \propto n_0 T_i^{1/2}$ , where  $n_0$  is the neutral density. Finally, for Figure 6 the following parameters,  $k_{\parallel}/k_{\perp} = 0.06$ ,  $k_{\perp}\rho_i = (2)^{1/2}$ , and  $V_d/V_e = 0.3$  are used. Curves A, B, and C correspond to the profiles given in Figure 1. It can be seen from curve A that the growth rate maximizes around 400 km and progressively decreases at lower altitudes as a result of increased damping by ion-neutral and ion-ion collisions and a decrease in the electron temperature ( $\tau$  decreases with decreasing altitude; see Figure 2). Curve B, representing a typical ionosphere, has a smaller growth rate than curve A above 250 km and a slightly higher

growth rate than curve A below 250 km. Although electron collisions lead to higher growth, the decrease in  $\tau$  has a greater effect on the collisional instability than on the collisionless instability; hence, the decrease in the growth rate above 250 km. The increase in the growth rate at lower altitudes is mainly due to increased electron collisions. Curve C, representative of a disturbed ionosphere, has peak growth at  $\sim 250$  km in the F region, the decrease in the growth rate at higher altitudes being mainly due to increased ion-ion collisional damping. Eventually, the ion damping decreases at higher altitudes where the collisionless theory is valid, in which case the growth rate increases due to increasing  $\tau$ .

Figure 7 gives the threshold drift velocities ( $V_d/V_e$ ) for the EIC instability for the three electron density profiles of Figure 1, assuming an  $O^+$  ion plasma taking  $k_{\parallel}/k_{\perp} = 0.06$ , and for maximally growing modes with  $k_{\perp}\rho_i = (2)^{1/2}$ . For profile B the electrostatic ion cyclotron instability could be destabilized in the bottomside ionosphere ( $\leq 300$  km) for current drift velocities of the order of a tenth of electron thermal velocities,  $V_d \leq 0.1 V_e$ . Curves A, B, and C again are obtained using the density profiles given in Figure 1. Comparing Figure 1 with Figure 6, we see that lower drift velocities are needed at larger growth rates.

Figure 8 shows the growth rate of the EIC instability, including both electron and ion collision for the three electron density profiles in Figure 1, assuming an  $NO^+$  ion plasma. The growth rates of the EIC instability for an  $NO^+$  plasma are similar to (though slightly lower than) the growth rate for the  $O^+$  plasma (Figure 6). This is consistent with (5), (12), and (17), which indicate that the  $\gamma/\Omega_i$  is not a strong function of ion mass. Note that the growth rate is normalized to respective gyrofrequencies in each case.

Figure 9 displays the threshold drift velocities  $V_c/V_e$  for the EIC instability, including both electron and ion collisions, using the density profiles of Figure 1 and assuming  $NO^+$  ion plasma. Comparing Figure 9 with Figure 7 ( $O^+$  plasma), one notes a slight decrease in the threshold drift velocity as one

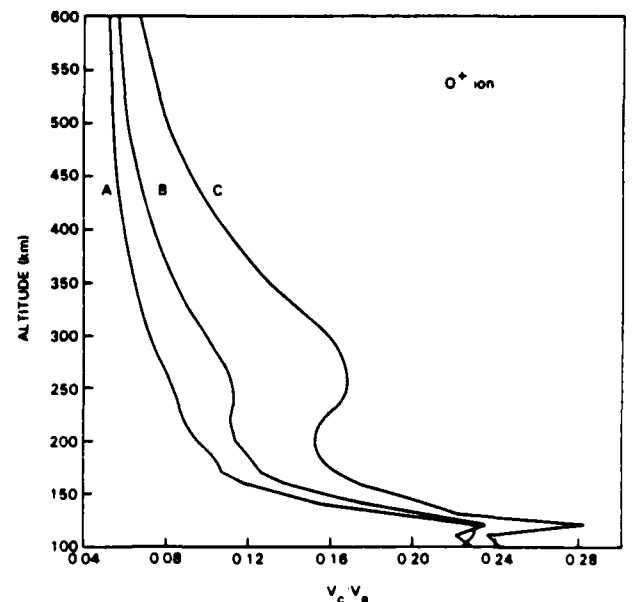


Fig. 7. Critical current drift velocity  $V_c/V_e$  for excitation of electrostatic ion cyclotron instability versus altitude for curves A–C of Figure 1 for  $O^+$  ion plasma and  $k_{\parallel}/k_{\perp} = 0.06$ ,  $k_{\perp}\rho_i = (2)^{1/2}$ .

goes from  $O^+$  to  $NO^+$ . This is also consistent with previous studies [Drummond and Rosenbluth, 1962; Kindel and Kennel, 1971] which have shown that increasing the ion mass decreases the threshold current drift velocity at all  $T_e/T_i$  to excite the EIC instability. We have also calculated the growth rates and the critical drift velocities for the hydrogen plasma. We find the growth rates of  $H^+$  EIC waves to be smaller and the critical drift velocities for excitation of  $H^+$  EIC waves to be much higher; for instance,  $V_c/V_e = 0.4$  for  $H^+$  EIC wave excitation for the typical parameters used for  $O^+$  calculations, as compared to  $V_c/V_e = 0.1$  for  $O^+$  excitation. These critical drift velocities correspond to extremely large currents, and thus we can conclude that the  $H^+$  EIC waves are not likely to be excited in the bottomside ionosphere. For this reason we do not present the detailed results of  $H^+$  EIC wave calculations.

To emphasize further the heavy-ion EIC excitation in the  $F$  region, we show the threshold currents in the altitude region 100–600 km. We use the density profile  $n_e$  from curve A of Figure 1,  $T_e$  from Figure 2, and  $V_c/V_e$  from Figures 7 and 9 to calculate the threshold current  $J = n_e e V_c$ . Figure 10 shows the threshold currents required to excite  $O^+$  EIC and  $NO^+$  EIC in  $O^+$  and  $NO^+$  plasmas, respectively, for  $k_{\perp} \rho_i = (2)^{1/2}$  and  $k_{\parallel}/k_{\perp} = 0.06$ . It is clear from Figure 10 that  $NO^+$  EIC has lower thresholds than  $O^+$  EIC and that the altitude region between 150 and 200 km and the region above 400 km have lower thresholds. The currents shown near 100–130 km may not be accurate because the theory may not be valid in this region as a result of demagnetization of the ions ( $v_{th}/\Omega_i \sim 1$ ). The critical currents corresponding to curves B of Figures 1, 7, and 9 are of the order of 200–1000  $\mu A/m^2$ . Thus for typical ionospheres such as those given by curve B one requires large currents to support  $O^+$  or  $NO^+$  EIC. Although our calculations are applicable to plasma with single ion species, on the basis of the results presented in Figures 7, 9, and 10 we can draw qualitative conclusions regarding a multispecies plasma, namely, that when  $H^+$ ,  $O^+$ ,  $O_2^+$  and  $NO^+$  species are present, EIC waves of heavier species are more susceptible to

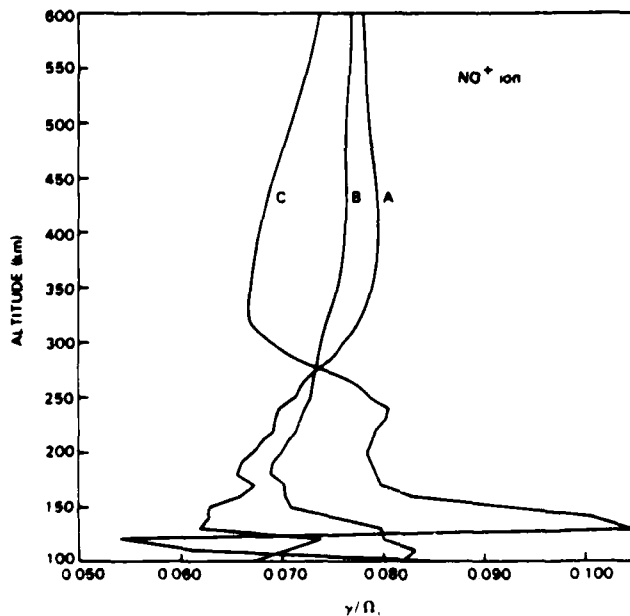


Fig. 8. Growth rate  $\gamma/\Omega_i$  of electrostatic ion cyclotron instability versus altitude for  $NO^+$  ion plasma using curves A–C of Figure 1 with fixed parameters  $k_{\parallel}/k_{\perp} = 0.06$ ,  $k_{\perp} \rho_i = (2)^{1/2}$ , and  $V_c/V_e = 0.3$ .

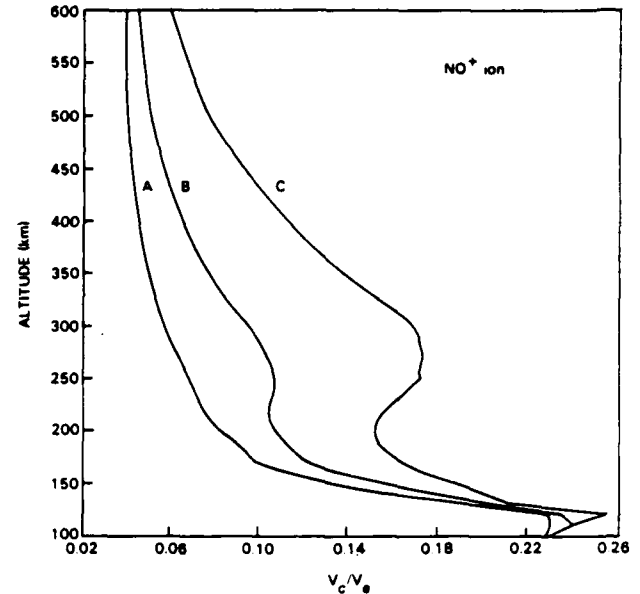


Fig. 9. Critical current drift velocity  $V_c/V_e$  for excitation of electrostatic ion cyclotron instability versus altitude for curves A–C of Figure 1 for  $NO^+$  ion plasma and  $k_{\parallel}/k_{\perp} = 0.06$ ,  $k_{\perp} \rho_i = (2)^{1/2}$ .

destabilization by parallel currents. Thus we conclude that  $NO^+$  or  $O_2^+$  EIC instability can be excited more easily in the bottomside  $F$  region than the  $H^+$  or  $O^+$  EIC instability. This is consistent with the photometric observations of Martelli *et al.* [1977].

#### NONLINEAR SATURATED AMPLITUDES

In the previous section we showed that the collisional electrostatic ion cyclotron instability could be important in the bottomside high-latitude ionosphere. In this section we discuss a possible nonlinear mechanism that might saturate these modes. In the literature several nonlinear saturation mechanisms for the electrostatic ion cyclotron instability have been studied. Davidson [1972] has discussed large-amplitude trapping effects which become important when  $\omega_i \tau_c \gg 1$ , where  $\omega_i = k_{\parallel} (e \phi / m_e)^{1/2}$  is the electron-trapping frequency and  $\tau_c = k_{\parallel} \Delta v$  is the wave correlation time,  $\phi$  is the wave potential,  $k$  is the wave vector, and  $\Delta v$  is the spread in wave phase velocities parallel to the magnetic field. Collisional effects will prevent strong electron trapping. Another mechanism is ion resonance broadening [Dum and Dupree, 1970]. In this work we extend Dum and Dupree's theory to the case of the collisional EIC instability. Physically, the effect of the turbulence generated by the instability may be interpreted as an enhanced ion viscosity. In this section we shall present only estimates of the saturation amplitudes for typical ionospheric parameters and not a comprehensive, full  $F$  region study.

The nonlinear dispersion relation for the electrostatic ion-cyclotron modes, including the effects of resonance broadening, may be obtained by substituting  $\bar{\omega} \equiv \omega + i\Delta\omega^*$  in lieu of  $\omega$  in the ion contribution to (3) [Dum and Dupree, 1970]. Here  $\Delta\omega^*$  is the modification introduced by the effect of a spectrum of finite amplitude modes on the particle orbits (resonance-broadening effect). Thus

$$1 + \epsilon_e^l(k, \omega) + \epsilon_i^nl(k, \omega + i\Delta\omega^*) = 0 \quad (23)$$

is the nonlinear dispersion relation for the EIC modes, where  $\epsilon_e^l$  is the linear dielectric constant and  $\epsilon_i^nl$  is the nonlinear

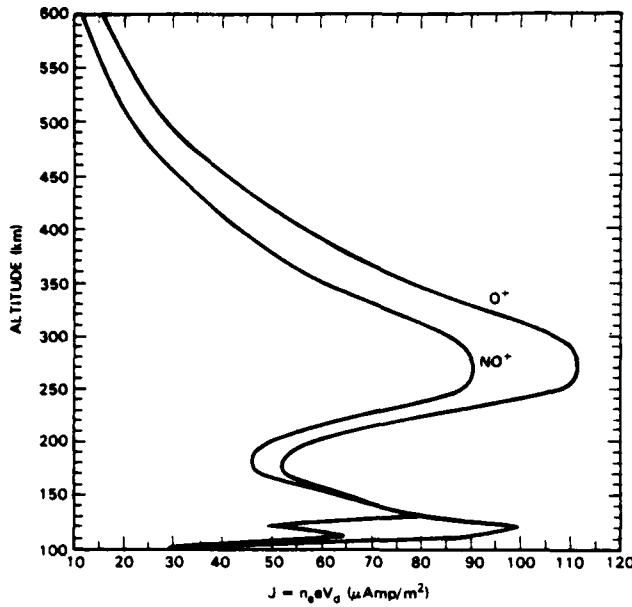


Fig. 10. Threshold currents in  $\mu\text{A}/\text{m}^2$  required to excite  $\text{O}^+$  and  $\text{NO}^+$  EIC waves in  $\text{O}^+$  and  $\text{NO}^+$  plasmas, respectively. The critical currents are calculated for  $J = n_e e V_d$  using  $V_e/V_d$  from curves A of Figures 7 and 9,  $n_e$  from curve A of Figure 1, and  $T_e$  from Figure 2. The parameters used are  $k\rho_i = (2)^{1/2}$  and  $k_\perp/k_\parallel = 0.06$ .

dielectric constant. We note that *Dum and Dupree* [1970] have shown the effect of resonance broadening is important only for ions in the EIC wave case. Hence the contribution coming from the resonance-broadening effect on electrons has been ignored in (23). One may obtain an estimate for the nonlinear saturated amplitudes of EIC modes from (23) by setting the nonlinear growth rate  $\gamma^{\text{nl}}$

$$\gamma^{\text{nl}} = \gamma_k^{\text{l}} - \Delta\omega^{\text{w}} = 0 \quad (24)$$

where  $\gamma_k^{\text{l}}$  is the linear growth rate of the mode with wave number  $k$ . For the EIC instability case,  $\Delta\omega^{\text{w}}$  may be approximated as [*Dum and Dupree*, 1970]

$$\Delta\omega^{\text{w}} \approx (\omega - \Omega_i) \left[ \left( \frac{n_1}{n_1^0} \right)^2 - 1 \right]^{1/2} \quad (25)$$

Here  $n_1$  is the saturated nonlinear amplitude of the wave, and  $n_1^0$  is the threshold level of the nonlinear amplitude at which the resonance-broadening effects assume importance. The expression for  $n_1^0$  is

$$\begin{aligned} \frac{n_1^0}{n} &= \left( \frac{T_i}{ZT_e} \right) \left( \frac{\Omega_i}{k_\perp v_i} \right)^2 \frac{(\omega_k - \Omega_i)}{\Omega_i [F_1(\mu_i)]^{1/2}} \\ &\approx \left( \frac{T_i}{ZT_e} \right) \frac{1}{\mu_i (F_1)^{1/2}} \left( \frac{\omega - \Omega_i}{\Omega_i} \right) \end{aligned} \quad (26)$$

where

$$\begin{aligned} F_1(x) &\approx \frac{1}{4} \left[ 1 - \frac{1}{4} \left( \frac{x}{2} \right)^4 + \frac{1}{9} \left( \frac{x}{2} \right)^6 + \dots \right] \quad x \leq 2 \\ F_1(x) &= \frac{1}{\pi x} \left[ 1 - \frac{1}{4} \left( \frac{x}{2} \right)^4 + \frac{1}{9} \left( \frac{x}{2} \right)^6 + \dots \right] \quad x \geq 3 \end{aligned}$$

It may be noted that the broadening of resonances above corresponds to an enhancement in the group of ions that can

exchange energy with the wave via resonance interaction. Stabilization of the mode results when the resonance is broadened to an extent such that the bulk of the ion distribution interacts with the wave and absorbs energy from it, thereby leading to a steady finite amplitude nonlinear state. We now use (24)–(25), to compute the nonlinear saturated amplitudes for the collisional EIC modes. From (24) and (25) one has

$$(\omega - \Omega_i) \left[ (n_1/n_1^0)^2 - 1 \right]^{1/2} \approx \gamma_k^{\text{l}} \quad (27)$$

which leads to

$$\left( \frac{n_1}{n} \right)^2 \approx \left( \frac{n_1^0}{n} \right)^2 \left[ 1 + \frac{(\gamma_k^{\text{l}})^2}{(\omega - \Omega_i)^2} \right] \quad (28)$$

or

$$\begin{aligned} \left( \frac{n_1}{n} \right)^2 &\approx \frac{(T_i/T_e)^2 (\Omega_i/k_\perp v_i)^4 [(\omega_r - \Omega_i)^2/\Omega_i^2]}{F_1(k_\perp v_i/\Omega_i)} \\ &\cdot \left\{ 1 + \frac{[(T_e/T_i)\Omega_i\Gamma_1(v_e/k_\perp^2 v_e^2)(k_\parallel V_d - \omega_r) - k_\perp^2 \rho_i^2 v_{ii} - v_{in}]^2}{(\omega_r - \Omega_i)^2} \right\} \end{aligned} \quad (29)$$

using (17) and including  $v_{ii}$  collisions.

For the case  $T_e \approx T_i$  one has

$$(\omega - \Omega_i) = \Omega_i \Gamma_1$$

which leads to

$$\begin{aligned} \left( \frac{n_1}{n} \right)^2 &\approx \frac{(\Omega_i/k_\perp v_i)^4 \Gamma_1^2}{F_1(k_\perp v_i/\Omega_i)} \\ &\cdot \left\{ 1 + \left[ \frac{v_e}{k_\parallel^2 v_e^2} (k_\parallel V_d - \omega_r) - \frac{k_\perp^2 \rho_i^2 v_{ii} - v_{in}}{\Omega_i} \right]^2 \right\} \end{aligned} \quad (30)$$

Expression (30) gives the nonlinear saturated amplitudes of density fluctuations associated with the collisional ion-cyclotron modes due to resonance-broadening effects in the presence of both electron  $v_e$ , ion-ion  $v_{ii}$ , and ion-neutral  $v_{in}$  collisions applicable to bottomside ionospheric altitudes. A comparison with the collisionless case, discussed by *Dum and Dupree* [1970], shows that the saturated amplitudes can be higher in the collisional case by an increment of approximately  $\sim \frac{1}{2} [(V_d/V_e)(1/k_\parallel \lambda_e)]^2$ . We note that in the above comparison it is implied that  $\gamma_{ke}/(\omega_k - \Omega_i) \ll 1$ , where  $\gamma_{ke}$  is the collisionless growth rate.

#### 4. SUMMARY AND DISCUSSION

In this study we have presented a comprehensive treatment of the theory of the electrostatic ion cyclotron instability in the collisional bottomside ionosphere. We have derived the linear dispersion relations for the ion cyclotron instability, including both electron and ion collisions, and solved analytically the dispersion relation in three limits: collisionless, weakly collisional, and collisional. In addition, we have solved the linear dispersion relation exactly using numerical methods using parameters typical of the high-latitude bottomside ionosphere. We note that the linear growth rates in the bottomside collisional regime can be of the same order as the corresponding topside collisionless growth rates. We have considered three cases corresponding to three different ionospheric conditions. The normal ionosphere is bracketed by two other ionospheres with minimum density around  $10^4 \text{ cm}^{-3}$  at the lower end and maximum peak density of  $10^6 \text{ cm}^{-3}$  at the high



end. The minimum density profile corresponds to a weakly collisional case ( $v_{te}/\Omega_e < 10^{-4}$ ) and this can be considered as an extension of the previous collisionless EIC instability theories. The maximum density profile corresponds to disturbed conditions, yielding high electron collisions and ion collisions. We have also considered pure  $O^+$  and pure  $NO^+$  plasmas and solved the dispersion relation for single species in both cases. We arrive at the following conclusions based on the linear calculation:

1. Given the realistic ionospheric parameters, we find that the theory of collisionless EIC instability [Kindel and Kennel, 1971] cannot be extended to the bottomside  $F$  region ( $z < 400$  km). Since the critical drift velocities and growth rates are sensitive to  $n_e$  and  $T_e/T_i$ , a theory of collisional EIC using self-consistent collision frequencies and  $T_e/T_i$  should be used for accurate prediction of EIC excitation.

2. Electron collisions destabilize the EIC wave, which results in higher growth rates. However, the ion-ion collisions damp the modes, the damping being equal to  $v_{ti}$  in the  $k_{\perp}\rho_i \gg 1$  limit and  $v_{ti}k_{\perp}^2\rho_i^2/2$  in the  $k_{\perp}\rho_i \ll 1$  limit. The EIC instability growth rate maximizes for  $k_{\perp}\rho_i \gtrsim 1$ .

3. For realistic profiles of the ionosphere the collisional EIC wave growth rates are reduced by ion-neutral collisions in the bottomside  $F$  region and by ion-ion collisions above 300 km, as expected.

4. For profiles given in Figure 1 the collisionless theory (ion collisions dominate electron collisions) prevails for curve A and collisional theory (electron collisions are stronger and dominate ion collisions) prevails for curve C.

5. The growth rate maximizes in the weakly collisional (curve A, Figure 1) regime at an altitude of 400 km and in the strongly collisional (curve C, Figure 1) regime at an altitude of 250 km. In the collisional domain (curve C, Figure 6) the growth rate has a minimum at an altitude of 300 km and achieves a further lower value at  $E$  region altitudes (150 km or less).

6. The critical drift velocity required to excite the EIC waves depends on the electron densities and thus is quite different in the collisionless and collisional domains as shown in Figures 7 and 9.

7. For realistic ionospheric profiles the growth rate is weakly dependent on the mass ratio  $m_e/m_i$ . However, we find that the critical drift velocity is much smaller for EIC waves corresponding to gyrofrequencies of heavier ions than the critical drift corresponding to lighter-ion ( $H^+$ ) EIC wave excitation. Our single species calculation shows that  $NO^+$  or  $O_2^+$  EIC instability is much easier to excite than  $O^+$  or  $H^+$  EIC instability. Thus in a multicomponent plasma, EIC waves at  $NO^+$  will be excited first, before, for example,  $O^+$  EIC waves, and in the bottomside ionosphere EIC instability at  $H^+$  gyrofrequency is unlikely to be excited.

8. The theory is applicable above 130 km altitude, since below 130 km the ions get demagnetized due to strong ion neutral collisions.

In addition, we have discussed a nonlinear saturation mechanism for the electrostatic ion cyclotron instability in the collisional regime based upon Dupree's [1966] ion resonance-broadening theory. Dupree's resonance-broadening theory is valid only for a broad spectrum of waves which are assumed isotropic and incoherent; that is, the wave coherence time (spectral width) is much shorter than an ion cyclotron period. For a narrow (coherent) wave spectrum, resonance-broadening theory must be replaced by an analysis which considers exact ion dynamics in a coherent wave [Davidson, 1972;

Aumodt, 1970]. Recent nonlinear numerical simulations [Pritchett et al., 1981; Okuda and Ashour-Abdalla, 1981] of the collisionless ion cyclotron instability indicate a large-amplitude coherent wave spectrum in the nonlinear regime. However, these simulations also show several modes excited in the saturation phase of the ion cyclotron instability. To our knowledge, there have been no nonlinear simulations of the collisional current-driven ion cyclotron instability. We shall now discuss some particular examples of the auroral ionospheric application of the collisional EIC instability.

In a recent study using sounding rockets, Yau et al. [1983] have recorded  $O^+$  waves and strong perpendicular ion acceleration (ion conics) events at low altitudes (400–600 km) in the high-latitude ionosphere during the expansive phase of an auroral substorm. Large relative density fluctuations ( $\leq 10\%$ ) were also recorded near the ion conic acceleration regions. One major candidate for conic formation is EIC wave heating [Ungstrup et al., 1979; Okuda and Ashour-Abdalla, 1981]. Considering typical high-latitude parameters, i.e.,  $T_e \approx T_i \approx 0.1$  eV, electron density corresponding to curve A of Figure 1 ( $n_e \approx 3 \times 10^4$ ,  $v_{te}/\Omega_e \approx 2 \times 10^{-5}$ ,  $v_{ti}/\Omega_i \approx 7 \times 10^{-3}$ ), the growth rate of  $O^+$  EIC waves, with  $\lambda_{\perp} \sim 11$  m ( $k_{\perp}\rho_i \sim 1.4$ ,  $\rho_i \sim 2.56$  m for  $O^+$  ions), and  $\lambda_{\parallel} \sim 200$  m, is  $0.07 \Omega_i$  or  $21$  s $^{-1}$ , taking  $\Omega_i$  for  $O^+$  in a 0.5 Gauss magnetic field as 300 Hz (Figure 6, curve A). The corresponding growth rate for  $NO^+$  EIC waves ( $\lambda_{\perp} \sim 15$  m) is  $0.08 \Omega_i$  or  $12$  s $^{-1}$ , taking  $\Omega_i$  to be 150 Hz. The critical drift velocities can be read off of Figure 7 for  $O^+$  ions. For the above parameters the critical drift velocity at an altitude of 300 km, for example, is  $0.09 V_e$  (curve A, quiet conditions), which corresponds to  $53 \mu A/m^2$  for  $n_e \sim 3 \times 10^{10}/m^3$ . For  $NO^+$  ions, under the same conditions the critical drift velocity is  $\sim 0.06 V_e$  (Figure 9), which corresponds to  $40 \mu A/m^2$ . For other profiles, (curves B (normal conditions) and C (disturbed conditions) of Figure 1) critical drift velocities are higher and require currents  $> 100 \mu A/m^2$  and  $\sim 1000 \mu A/m^2$ , respectively. In view of these results we find that the ionospheric conditions corresponding to curve A of Figure 1 are most conducive to EIC excitation at  $NO^+$  and  $O_2^+$  gyrofrequencies. From equation (30) the saturated amplitude for typical parameters (i.e.,  $T_e \approx T_i \approx 0.1$  eV,  $\Omega_i \approx 3 \times 10^2$  s $^{-1}$ ,  $v_{te}/\Omega_e \approx 10^{-4}$  s $^{-1}$ ,  $v_{ti}/\Omega_i \approx 10^{-3}$ ,  $v_{ti}/\Omega_i \sim 10^{-2}$ ) is found to be approximately  $n_1/n_0 \approx 0.24$ , according to ion resonance-broadening theory for  $k_{\perp}\rho_i = 1.2$ ,  $k_{\parallel}/k_{\perp} = 0.1$ , and  $V_d \gtrsim 2 \times 10^6$  cm/s. We note that the saturation amplitude  $n_1/n_0$  of EIC waves in the collisionless regime, using (30), is slightly smaller ( $n_1/n_0 \approx 0.22$ ) than the collisional case.

Compelling evidence of the presence of energetic heavy ionospheric ions at high altitudes ( $> 1000$  km) [Hultqvist, 1983; Klumpar et al., 1984; Yau et al., 1984] leads one to suggest that the bottomside ionosphere, which is a source of heavy ions, is indeed acting as an accelerating region for these heavy ions [Hultqvist, 1983]. Furthermore, energetic heavy ions,  $NO^+$  and  $O_2^+$ , have been observed at outer magnetospheric altitudes on days of high geomagnetic activity [Klecker et al., 1985; Craven et al., 1985]. High geomagnetic activity at higher altitudes is usually indicative of a disturbed ionosphere, which could sustain large ionospheric currents that drive collisional EIC waves in the bottomside ionosphere unstable. Thus we conjecture that the ion cyclotron instability at the ion (heavy) cyclotron frequency, driven unstable by parallel, field-aligned currents, may selectively accelerate the  $NO^+$ ,  $O_2^+$ , and  $O^+$  ions in the transverse direction at low altitudes, and these transversely accelerated ions form the heavy-ion conics at the higher altitudes.

**Acknowledgments.** This work was supported by the Defense Nuclear Agency, the National Aeronautics and Space Administration, and the Office of Naval Research. We wish to thank C. L. Rino of SRI International for providing the Sondrestrom data. We thank G. Ganguli and Y. C. Lee for useful discussions.

#### REFERENCES

- Aamodt, R. E., Particle motion in the presence of three dimensional finite amplitude harmonic cyclotron waves, *Phys. Fluids*, **13**, 2341, 1970.
- Banks, P. M., and G. Kockarts, *Aeronomy*, vol. A and B, Academic, Orlando, Fla., 1973.
- Bering, E. A., The plasma wave environment of an auroral arc: Electrostatic ion cyclotron waves in the diffuse aurora, *J. Geophys. Res.*, **89**, 1635, 1984.
- Bythrow, P. F., T. A. Potemra, W. B. Hanson, L. J. Zanetti, C.-I. Meng, R. E. Huffman, F. J. Rich, and D. A. Hardy, Earthwind directed high-density Birkeland currents observed by HILAT, *J. Geophys. Res.*, **89**, 9114, 1984.
- Chaturvedi, P. K., Collisional ion cyclotron waves in the auroral ionosphere, *J. Geophys. Res.*, **81**, 6169, 1976.
- Chaturvedi, P. K., and P. K. Kaw, Current driven ion cyclotron waves in collisional plasma, *Plasma Phys.*, **17**, 447, 1975.
- Chaturvedi, P. K., P. Satyanarayana, G. Ganguli, M. J. Keskinen, and J. D. Huba, Local and nonlocal theories of collisional current driven ion cyclotron instability, *Bull. Am Phys. Soc.*, **29**, 1192, 1984.
- Clemmow, P. C., and J. P. Dougherty, *Electrodynamics of Particles and Plasmas*, Addison-Wesley, Reading, Mass., 1969.
- Craven, P. D., R. C. Olsen, C. R. Chappell, and L. Kakani, Observations of molecular ions in the earth's magnetosphere, *J. Geophys. Res.*, **90**, 7599, 1985.
- D'Angelo, N., Type 3 spectra of the radar aurora, *J. Geophys. Res.*, **78**, 3587, 1973.
- Davidson, R. C., *Methods in Nonlinear Plasma Theory*, Academic, Orlando, Fla., 1972.
- Drummond, W. E., and M. N. Rosenbluth, Anomalous diffusion arising from microinstabilities in a plasma, *Phys. Fluids*, **5**, 1507, 1962.
- Dum, C. T., and T. H. Dupree, Nonlinear stabilization of high frequency instabilities in a magnetic field, *Phys. Fluids*, **13**, 2064, 1970.
- Dupree, T. H., A perturbation theory for strong plasma turbulence, *Phys. Fluids*, **9**, 1773, 1966.
- Fejer, B. G., R. W. Reed, D. T. Farley, W. E. Swartz, and M. C. Kelley, Ion cyclotron waves as a possible source of resonant auroral radar echoes, *J. Geophys. Res.*, **89**, 187, 1984.
- Ganguli, G., P. Palmadesso, and Y. C. Lee, A new mechanism for excitation of electrostatic ion-cyclotron waves and associated perpendicular heating, *Geophys. Res. Lett.*, **13**, in press, 1985.
- Hoffman, J. H., W. H. Dodson, C. R. Lippincott, and H. D. Hammack, Initial ion composition results from the Isis 2 satellite, *J. Geophys. Res.*, **79**, 4246, 1974.
- Hultqvist, B., On the origin of hot ions in the disturbed dayside magnetosphere, *Planet. Space Sci.*, **37**, 173, 1983.
- Kelly, J. D., Sondrestrom radar—initial results, *Geophys. Res. Lett.*, **10**, 1112, 1983.
- Kindel, J. M., and C. F. Kennel, Topside current instabilities, *J. Geophys. Res.*, **76**, 3055, 1971.
- Kintner, P. M., M. C. Kelley, and F. S. Mozer, Electrostatic hydrogen cyclotron waves near one earth radius altitude in the polar magnetosphere, *Geophys. Res. Lett.*, **5**, 139, 1978.
- Kintner, P. M., M. C. Kelley, R. D. Sharp, A. G. Shieltetti, M. Temerin, C. Cattell, P. F. Mizera, and J. F. Fennell, Simultaneous observations of energetic (keV) upstreaming ions and electrostatic hydrogen cyclotron waves, *J. Geophys. Res.*, **84**, 7201, 1979.
- Klecker, B., D. Hovestadt, E. Mobius, M. Scholer, G. Gloecker, and F. M. Ipavich, Observation of energetic molecular ions in the outer magnetosphere, paper presented at the Chapman Conference on Ion Acceleration in the Magnetosphere and Ionosphere, AGU, Wellesley, Mass., June 3-7, 1985.
- Klumpar, D. M., W. K. Peterson, and E. G. Shelly, Direct evidence for two-stage (bimodel) acceleration of ionospheric ions, *J. Geophys. Res.*, **89**, 10779, 1984.
- Levine, A. M., and A. F. Kuckes, Excitation of electrostatic ion cyclotron oscillations, *Phys. Fluids*, **9**, 2263, 1966.
- Martelli, G., P. N. Collis, M. Giles, and P. J. Christiansen, Optical detection of electrostatic ion cyclotron waves in the auroral plasma, *Planet. Space Sci.*, **25**, 643, 1977.
- Milić, B., Spontaneous excitation of long-wave ion-cyclotron and ion-acoustic oscillations in fully ionized plasmas, *Phys. Fluids*, **15**, 1630, 1972.
- Ogawa, T., H. Mori, S. Miyazaki, and H. Yamagishi, Electrostatic plasma instabilities in highly active aurora, *Mem. Natl. Inst. Polar Res. Spec. Issue Jpn.*, **18**, 312, 1981.
- Okuda, H., and M. Ashour-Abdalla, Formation of a conical distribution and intense ion heating in the presence of hydrogen cyclotron waves, *Geophys. Res. Lett.*, **8**, 811, 1981.
- Pritchett, P. L., M. Ashour-Abdalla, and J. M. Dawson, Simulation of the current-driven electrostatic ion cyclotron instability, *Geophys. Res. Lett.*, **8**, 611, 1981.
- Spitzer, L., *Physics of Fully Ionized Gases*, Wiley-Interscience, New York, 1962.
- Ungstrup, E., D. M. Klumpar, and W. J. Heikkilä, Heating of ions to superthermal energies in the topside ionosphere by electrostatic ion cyclotron waves, *J. Geophys. Res.*, **84**, 4289, 1979.
- Varma, R. K., and D. Bhadra, Collisional effects in a hot plasma at ion gyrofrequency, *Phys. Fluids*, **7**, 1082, 1964.
- Yau, A. W., B. A. Whalen, A. G. McNamara, P. J. Kellogg, and W. Bernstein, Particle and wave observations of low-altitude ionospheric acceleration events, *J. Geophys. Res.*, **88**, 341, 1983.
- Yau, A. W., B. A. Whalen, W. K. Peterson, and E. G. Shelly, Distribution of upflowing ionospheric ions in the high-altitude polar cap and auroral ionosphere, *J. Geophys. Res.*, **89**, 5507, 1984.
- P. K. Chaturvedi, J. D. Huba, and M. J. Keskinen, Geophysical and Plasma Dynamics Branch, Naval Research Laboratory, Code 4780, Washington, DC 20375.
- S. L. Ossakow, Plasma Physics Division, Naval Research Laboratory, Washington, DC 20375.
- P. Satyanarayana, Science Applications International Corporation, 1710 Goodrich Drive, P. O. Box 1303, McLean, VA 22102.

(Received November 5, 1984;  
revised June 14, 1985;  
accepted July 11, 1985.)

**APPENDIX G**

**Excitation of Lower-Hybrid Instability  
by Longitudinal Currents**

**P. Satyanarayana and P.K. Chaturvedi  
Science Applications International Corporation**

# Excitation of lower-hybrid instability by longitudinal currents

P. Satyanarayana and P. K. Chaturvedi\*

Science Applications International Corporation, 1710 Goodridge Drive, P. O. Box 1303, McLean, Virginia 22102

PREVIOUS PAGE  
IS BLANK



(Received 30 April 1985; accepted 10 October 1985)

The stability of a homogeneous plasma with currents along the magnetic field is investigated. It is found that electrons streaming along the magnetic field lines in a neutralizing positive ion background could excite lower-hybrid instability. The critical drift velocity should exceed the parallel phase velocity for instability:  $V_d > \omega_r/k_{\parallel}$ , where  $\omega_r$  is the lower-hybrid frequency  $\sqrt{\Omega_e \Omega_i}$ . This condition is found to be easily met in the laboratory and space plasmas and is applicable both in the collisionless and collisional plasmas.

One of the well-known instabilities driven by currents flowing along the magnetic field lines is the ion-cyclotron instability, first suggested by Drummond and Rosenbluth.<sup>1</sup> This instability has been observed in the laboratory Q machines<sup>2</sup> and is widely applied to space plasmas to explain the small-scale density irregularities in the high-latitude F region and magnetosphere.<sup>3</sup> This instability was conjectured to be responsible for the heating and transverse acceleration of the ions in the near-earth space plasmas.<sup>4</sup> For the ion-cyclotron instability the drift velocity should exceed the parallel phase velocity, and at ion-cyclotron frequency this critical drift velocity is such that  $V_d > \omega_r/k_{\parallel}$ , where  $\omega_r \approx \Omega_i$ ,  $\Omega_i$  being the ion-cyclotron frequency. In this brief communication we report that the parallel currents can also excite lower-hybrid waves, if  $V_d > \omega_r/k_{\parallel}$  for  $\omega_r \approx \omega_{lh}$ , where  $\omega_{lh} = \sqrt{\Omega_e \Omega_i}$  is the lower-hybrid frequency. We find this condition to hold good in a collisionless as well as in a collisional plasma. Lower-hybrid drift instability, driven by a source of free energy dependent on the gradients in the equilibrium quantities such as plasma density, plasma temperature, and the confining magnetic field or cross-field currents or both, has been extensively studied in the literature.<sup>5</sup> Here we show that the free energy associated with the field-aligned currents can drive lower-hybrid instability (LHI) in a homogeneous plasma in the absence of any cross-field currents. In our case  $V_d < V_e$ ,  $\omega_r$  is like the lower-hybrid frequency, and  $k_{\parallel}/k_y \ll 1$  (where  $k_{\parallel}$  is the wavenumber along the field and  $k_y$  is the wavenumber along the y direction). We show that the parallel currents can excite LHI both in the collisionless and collisional plasma by treating the ions as demagnetized, and by considering the electrons as kinetic in the collisionless domain and as fluid in the collisional domain. In the following, we present the linear stability analysis of an infinite homogeneous plasma with currents along the field lines under electrostatic approximation and give a short discussion.

We consider an infinite homogeneous plasma confined by a uniform magnetic field along the z direction ( $\mathbf{B} = B\hat{z}$ ). We assume an equilibrium relative drift ( $V_d$ ) between the electrons and the ions, represented by a drifting Maxwellian electron distribution. In this analysis we restrict ourselves to electrostatic perturbations, which is valid for  $\beta = 8\pi n(T_e + T_i)/B^2 < m_e/m_i \ll 1$ , where  $T_e$  and  $T_i$  are the electron and ion temperatures, respectively. The perturbations are of the form  $\exp[i(\mathbf{k} \cdot \mathbf{r} - \omega t)]$ , where

$\omega = \omega_r + i\gamma$  is the complex mode frequency and  $\mathbf{k}$  is the wavenumber. In the following, we show that instability can occur for drift velocity smaller than the electron thermal velocity in a homogeneous plasma. The lower-hybrid instability is characterized by strongly magnetized electrons and unmagnetized ions:

$$|\omega| < \Omega_e, \quad k_y \rho_e < 1, \quad (1)$$

$$|\omega| > \Omega_i, \quad k_y^2 \rho_i^2 > 1, \quad (2)$$

where  $\rho_j = V_j/\Omega_j$  is the Larmor radius,  $V_j = (2T_j/m_j)^{1/2}$  is the thermal velocity,  $\Omega_j = |e_j|B/m_j c$ ,  $e_j$  is the charge, and  $m_j$  is the mass of the  $j$ th species. Since for  $V_d = 0$  the plasma is stable, we would expect instability to occur for  $k_{\parallel} V_d > \omega_r \approx \omega_{lh} \approx \sqrt{\Omega_e \Omega_i}$ , where  $\omega_r$  is the real part of the wave frequency and  $k_{\parallel}$  is the wavenumber parallel to the magnetic field. We use a simple BGK model to represent the electron collisions to investigate the LHI in the collisional domain. The dispersion relation derived by Clemmow and Dougherty<sup>6</sup> is used. For a plasma with Maxwellian electrons drifting through a stationary neutralizing ion background, the electrostatic dispersion relation is given as<sup>3</sup>

$$1 + \chi_e(\mathbf{k}, \omega) + \chi_i(\mathbf{k}, \omega) = 0, \quad (3)$$

where

$$\chi_e = \frac{(1/k_y^2 \lambda_e^2) \sum \Gamma_n(b_e) [1 + \xi_e Z(\xi_e)]}{1 + i(v_e/k_{\parallel} V_e) \sum \Gamma_n(b_e) Z(\xi_e)}, \quad (4)$$

$$\chi_i = \frac{1}{k_y^2 \lambda_i^2} \sum \Gamma_n(b_i) [1 + \xi_i Z(\xi_i)], \quad (5)$$

$\xi_e = (\tilde{\omega} + n\Omega_e)/k_{\parallel} V_e$ ,  $\xi_i = \omega/k_i V_i$ ,  $\tilde{\omega} = (\omega - k_{\parallel} V_d + i\gamma_e)$ ,  $Z$  is the plasma dispersion function,  $\Gamma_n(b_j) = I_n(b_j) \times \exp(-b_j)$ ,  $b_j = k_y^2 \rho_j^2/2$ , and  $\lambda_j^2 = (T_j/4\pi n e^2)$ . Based on the criteria given in Eqs. (1) and (2), we treat the ions as demagnetized and the electrons in the kinetic limit, thus retaining the full  $Z$  function for the electrons. The dispersion relation, in the limit  $|\xi_i| \gg 1$ , then becomes

$$1 + \frac{\omega_{pe}^2}{\Omega_e^2} \frac{1}{k_y^2 \rho_e^2} \left( \frac{1 + \Gamma_0(b_e) \xi_e Z(\xi_e)}{1 + i(v_e/k_{\parallel} V_e) \Gamma_0(b_e) Z(\xi_e)} \right) - \frac{\omega_{pi}^2}{\omega^2} = 0, \quad (6)$$

where

$$\omega_{pj} = \sqrt{4\pi n e^2/m_j}.$$

**Collisionless domain:**  $\nu_e = 0$ . Equation (6) can be solved numerically for  $\omega$ , but first we expand the electron Z function in the  $|\xi_e| \ll 1$  limit and show analytically that for  $V_d > \omega_{th}/k_{\parallel}$  the lower-hybrid wave can become unstable. In this limit, for  $\nu_e = 0$ , Eq. (6) becomes

$$a + \frac{\Gamma_0(b_e)}{b_e} i\sqrt{\pi} \frac{(\omega - k_{\parallel} V_d)}{k_{\parallel} V_e} = \frac{\omega_{th}^2}{\omega^2}, \quad (7)$$

where  $a = 1/k_{\parallel}^2 \rho_e^2 + \Omega_e^2/\omega_{pe}^2 \approx 1$ . For  $\gamma/k_{\parallel} V_e < 1$  it can easily be shown from Eq. (7) that

$$\omega_r \approx \sqrt{\Omega_e \Omega_i} / \sqrt{a} \quad (8)$$

$$1 + \frac{\omega_{pe}^2}{\Omega_e^2} \frac{1}{k_{\parallel}^2 \rho_e^2} \left( \frac{[\Gamma_0(b_e) + \alpha]}{[\Gamma_0(b_e) + \alpha] - 2(\omega - k_{\parallel} V_d + i\nu_e)(\omega - k_{\parallel} V_d)/k_{\parallel}^2 V_e^2} \right) - \frac{\omega_{pe}^2}{\omega^2} = 0, \quad (10)$$

where  $\alpha = 2(1 - \Gamma_0)\nu_e^2/k_{\parallel}^2 V_e^2$ . In order to demonstrate the destabilization of these modes in the collisional domain we consider the limit  $|\omega_{pe}^2/\omega^2| \gg 1$ . Then, Eq. (10) can be written as

$$\omega^2 = \omega_{th}^2 k_{\parallel}^2 \rho_e^2 \left( 1 - \frac{2(\omega - k_{\parallel} V_d)(\omega - k_{\parallel} V_d + i\nu_e)}{k_{\parallel}^2 V_e^2 [\Gamma_0(b_e) + \alpha]} \right) \quad (11)$$

for which

$$\omega_r \approx \omega_{th} k_{\parallel} \rho_e$$

$$\times \left( 1 - \frac{2\nu_e}{k_{\parallel}^2 V_e^2} \frac{(\omega_r^2 - k_{\parallel}^2 V_d^2)}{k_{\parallel}^2 V_e^2} \frac{1}{[\Gamma_0(b_e) + \alpha]} \right)^{1/2}, \quad (12)$$

$$\gamma \approx - \frac{2b_e}{[\Gamma_0(b_e) + \alpha]} \frac{(\omega_r - k_{\parallel} V_d)}{k_{\parallel} V_e} \frac{\nu_e}{k_{\parallel} V_e} \frac{\omega_{th}^2}{\omega_r}. \quad (13)$$

Equations (12) and (13) describe the lower-hybrid instability with real frequency on the order of the lower-hybrid frequency and  $\gamma > 0$  for  $V_d > \omega_{th}/k_{\parallel}$ . The LHI driven by parallel currents [Eqs. (12) and (13)] is quite different from the Buneman type instability or ion-acoustic instability discussed by Liewer and Krall.<sup>5</sup> For Buneman instability,  $V_d > V_e$  and  $\mathbf{k} \cdot \mathbf{B} = 0$ ; for ion-acoustic instability,  $T_e < T_i$  and  $\omega_r \approx k_{\parallel} c_s$ , although  $V_d$  could be less than  $V_e$ . Here  $c_s = \sqrt{T_e/m_i}$ . The LHI driven by field-aligned currents alone was considered in the fluid limit by Lee,<sup>7</sup> which is valid in the limit  $k_{\parallel} \rho_e \ll 1$ .

We solve Eq. (6) numerically in the collisionless and collisional limit for a hydrogen plasma. Excellent agreement is seen between the numerical and analytical roots. In Fig. 1 we present the growth rate normalized to lower-hybrid frequency as a function of collision frequency for  $b_e = 0.01$ . The solid (dotted) curve represents a numerical [analytical, Eq. (13)] result. We set  $\omega_{pe}^2/\Omega_e^2 = 20$ ,  $k_{\parallel}/k_y = 0.1$ , and  $V_d/V_e = 0.6$ . Figure 1 shows the good agreement between analytical and numerical results and the destabilization by the electron dissipation. The growth rate seems to maximize for  $\nu_e/\Omega_e \approx 0.06$  in this domain. In addition, we solve Eq. (6), which does not contain ion Landau damping, and compare with the solutions of Eq. (5), which contains the full ion Z function and thus the ion Landau damping effects. The

and

$$\gamma \approx - \left( \frac{\sqrt{\pi}}{2} \right) \frac{\Gamma_0(b_e)}{b_e} \frac{1}{a^2} \frac{(\omega_r - k_{\parallel} V_d)}{k_{\parallel} V_e} \sqrt{\Omega_e \Omega_i}, \quad (9)$$

which shows that the growth rate  $\gamma > 0$  for  $V_d > \omega_r/k_{\parallel}$  and  $\omega_r \approx \sqrt{\Omega_e \Omega_i}$ , the lower-hybrid frequency.

**Collisional domain:**  $\nu_e/k_{\parallel} V_e \gg 1$ . In this case the electrons can be treated in the fluid limit, allowing us to expand the electron Z function in the  $|\xi_e| \gg 1$  limit. In this limit, for  $\nu_e/k_{\parallel} V_e \gg 1$ , Eq. (6) becomes

results are shown in Fig. 2. We set  $\nu_e = 0$ ,  $\omega_{pe}^2/\Omega_e^2 = 20$ ,  $k_{\parallel}/k_y = 0.1$ , and  $V_d/V_e = 0.8$  and 1.0. The solid lines (no ion Landau damping,  $|\xi_i| \gg 1$ ) show that the growth rate maximizes around  $b_e \approx 0.35$ . The dotted line (with full ion Z function) for  $V_d/V_e = 1$  shows that ion Landau damping significantly damps the mode; for  $V_d/V_e = 0.8$  the mode is unstable for  $0 < b_e < 0.3$  (not shown in the figure). Detailed parametric studies will be presented in a future paper.

It is instructive to compare the growth rate of the current-driven LHI with that of the beam-driven LHI.<sup>8</sup> For example, for  $V_d > \omega_{th}/k_{\parallel}$  and  $k_{\parallel}/k_y \approx \sqrt{m_e/m_i}$ , the growth rate in the collisionless domain is given from Eq. (9) as  $\gamma \approx \sqrt{\pi} (V_d/V_e) \sqrt{\Omega_e \Omega_i}$ . For typical auroral zone parameters,  $V_d/V_e \approx 0.7$ , thus yielding a growth rate of  $\gamma \approx 0.7 \sqrt{\Omega_e \Omega_i}$  for a hydrogen plasma, whereas, for beam-driven LHI the growth rate is given as  $\gamma_b \approx \sqrt{\pi} (n_b/n) (V_b/V_{th})^2 \sqrt{\Omega_e \Omega_i}$ . Here  $n$  is the ambient density and  $V_b$ ,  $V_{th}$ , and  $n_b$  are the velocity, thermal veloc-

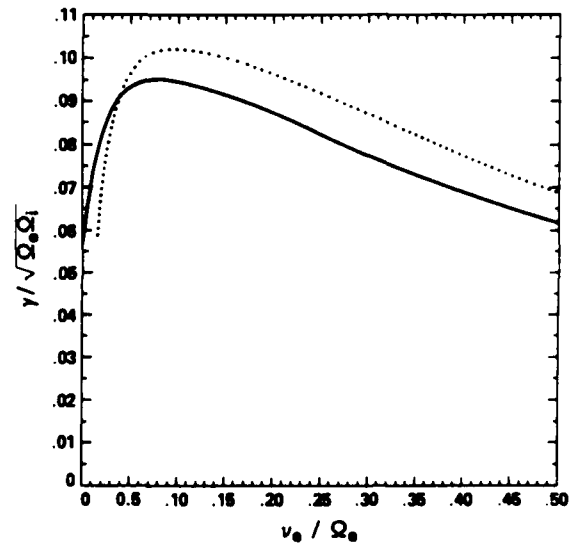


FIG. 1. Growth rate normalized to  $\sqrt{\Omega_e \Omega_i}$  as a function of electron collision frequency normalized to  $\Omega_e$ . The solid lines represent numerical [Eq. (6)] and the dotted lines represent analytical [Eq. (13)] results, respectively. The parameters are given in the text.

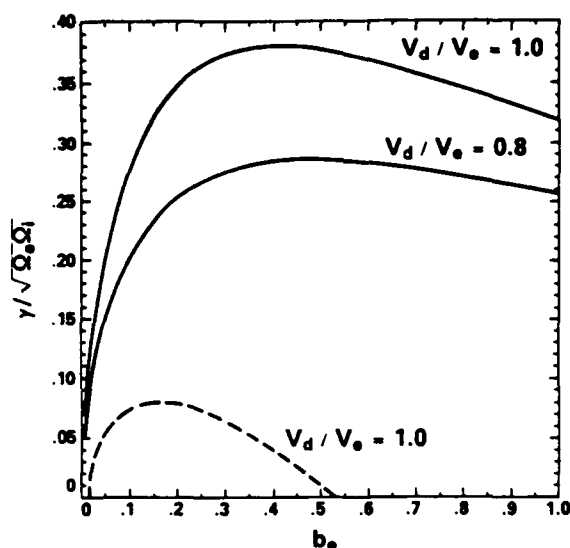


FIG. 2. Normalized growth rate versus  $b_e$ , without ion Landau damping [solid lines, Eq. (6)] and with full  $Z$  function for ions [dotted line, Eq. (5)]. The parameters are given in the text.

ity, and density of the beam, respectively. For  $V_d/V_{e0} \approx 1$  and  $n_b/n \approx 10^{-4}$ , the growth rate is  $\gamma \approx 10^{-4} \sqrt{\Omega_e \Omega_i}$ , which is much less than the growth rate of the current-driven LHI. The major result of this paper is the identification of the current-driven LHI and that it has a higher growth rate than the beam-driven LHI in the region where  $n_b \ll n$ . Also, Eq. (13) shows that the collisional growth rate is much higher than the collisionless growth rate.

In conclusion, we have shown that lower-hybrid instability can be excited by magnetic field-aligned currents. This instability is present in the collisionless and collisional plasmas when the parallel drift velocity exceeds the parallel phase velocity at lower-hybrid frequency. In the collisionless plasma the destabilization is caused by inverse Landau damping, whereas in the collisional case it is caused by electron collisions. In the collisional domain the growth rate is usually higher than the growth rate in the collisionless domain. For sufficiently large  $V_d$  the lower-hybrid instability

driven by parallel currents and the associated ion heating may be observed in a laboratory Q machine. Furthermore, since  $k_y \rho_i \gg 1$  for this instability, it can possibly generate very small scale density irregularities in the F-region ionospheric plasmas. It is also known that magnetic shear can have a stabilizing influence on the lower-hybrid-type instabilities.<sup>9</sup> As an estimate of the magnetic shear required for the stabilization of the LHI (which occurs for  $\omega_r \ll k_y V_i$ ),<sup>10</sup> one finds that  $\rho_i/L_s > (1/k_y \rho_e)$ , where  $L_s$  is the magnetic shear length. In the ionospheric situations, the magnetic shear produced by field-aligned currents for  $V_d/V_e = 0.7$  is such that  $\rho_i/L_s = 10^{-4}$  and thus is somewhat small to have any stabilizing influence, although the effects of magnetic shear on this instability need to be investigated. Detailed analysis including the shear effects and geometrical effects resulting from the finite current channel will be presented in a future publication.

#### ACKNOWLEDGMENTS

We thank the referee for several suggestions.

This work was supported by the U. S. Defense Nuclear Agency and the U. S. Naval Research Laboratory under Contract No. N00014-85-C-2018.

<sup>11</sup> Present address: Geophysical and Plasma Dynamics Branch, Naval Research Laboratory, Washington, D.C. 20375.

<sup>12</sup> W. E. Drummond and M. N. Rosenbluth, *Phys. Fluids* **5**, 1507 (1962).

<sup>13</sup> R. W. Motely and N. D'Angelo, *Phys. Fluids* **6**, 296 (1963).

<sup>14</sup> P. Satyanarayana, P. K. Chaturvedi, M. J. Keekinen, J. D. Huba, and S. L. Ossakow, *J. Geophys. Res.* (in press).

<sup>15</sup> M. Ashour-Abdalla, M. Okuda, and C. Z. Cheng, *Geophys. Res. Lett.* **8**, 795 (1981); A. W. Yau, B. A. Whalen, A. G. McNamara, P. J. Kellogg, and W. Bernstein, *J. Geophys. Res.* **88**, 341 (1983).

<sup>16</sup> N. A. Krall and P. C. Liewer, *Phys. Rev. A* **4**, 2094 (1971); R. C. Davidson and N. T. Gladd, *Phys. Fluids* **18**, 1327 (1975).

<sup>17</sup> P. C. Clemmow and J. P. Dougherty, *Electrodynamics of Particles and Plasmas* (Addison-Wesley, Reading, MA, 1969).

<sup>18</sup> K. F. Lee, *J. Plasma Phys.* **23**, 249 (1980).

<sup>19</sup> K. Papadopoulos and P. Palmadesso, *Phys. Fluids* **19**, 605 (1976).

<sup>20</sup> N. A. Krall, *Phys. Fluids* **20**, 311 (1977).

<sup>21</sup> M. N. Rosenbluth, in *Plasma Physics* (IAEA, Vienna, 1965), p. 485.

## **APPENDIX H**

### **Parallel Current Effects on Auroral E-Region Plasma Instabilities**

**P.K. Chaturvedi, J.D. Huba, and S.L. Ossakow  
Naval Research Laboratory**

**P. Satyanarayana  
Science Applications International Corporation**

PARALLEL CURRENT EFFECTS ON  
AURORAL E-REGION PLASMA INSTABILITIES

P.K. Chaturvedi, J.D. Huba, and S.L. Ossakov  
Plasma Physics Division  
Naval Research Laboratory  
Washington, DC 20375-5000

and

P. Satyanarayana  
Science Applications International Corporation  
McLean, Virginia 22102

May 1986

PREVIOUS PAGE  
IS BLANK



## ABSTRACT

We consider the effect of a field-aligned current on the development of plasma instabilities in the auroral electrojet. It is found that the inclusion of the parallel current modifies the threshold criteria for the onset of the Farley-Buneman instability, and may cause excitation of oblique ion sound waves. We apply these results to the auroral E-region and show that they may explain some observations of auroral irregularities, for example, the presence of type I irregularities for sub-threshold conditions (when the electron Hall drift is less than the ion-sound speed), and the observation of irregularities which are not highly field-aligned.

## I. INTRODUCTION

It is generally agreed that the electrojet current in the auroral E-region is responsible for generation of the plasma density irregularities which have been detected by several experimental techniques [Fejer and Kelley, 1980]. The coherent radar backscatter returns at 50 Mhz (which are caused by the presence of 3-meter size irregularities) have yielded a large amount of data on the features of these irregularities. These irregularities have been classified into three types based upon the doppler spectra of the radar returns. The type I irregularities display a narrow spectral peak around the ion sound velocity and are believed to be caused by the Farley-Buneman instability; this instability can occur when the electron Hall drift velocity exceeds the ion-sound velocity [Balsley and Ecklund, 1972]. The type II irregularities are believed to be a result of a nonlinear cascade by large scale size irregularities that are generated by the gradient-drift instability mechanism (the Hall current acting upon a transverse gradient) and can be excited for electron drift speeds less than the ion sound velocity. The type II spectra are relatively broad around the  $\underline{E} \times \underline{B}$  electron Hall drift velocity [Greenwald, 1974; Greenwald et al., 1975]. Both the type I and II spectra are caused by modes that are excited in the direction transverse to the ambient magnetic field (as the driving electric field is also perpendicular to the magnetic field).

However, there are many instances when the irregularity observations are found to show departures from the above patterns. There have been observations of type I irregularities at a time when the electron Hall drift was subcritical, i.e., less than the ion sound speed,  $C_s$  [Siren et al., 1977]. There is now evidence of a new type of irregularity, termed type III, which displays even a narrower doppler spectra than the type I,

but peaked around velocities less than the ion sound speed and not as highly field-aligned as the types I and II, i.e., has a finite structure along the magnetic field [Haldoupis et al., 1985; Fejer et al., 1984a; Greenvald et al., 1975]. A field-aligned current-driven electrostatic ion-cyclotron instability has been invoked to interpret these irregularities [D'Angelo, 1973; Chaturvedi, 1976; Ogawa et al., 1981; Fejer et al., 1984b; Bering, 1984; Haldoupis et al., 1985; Providakes et al., 1985; Satyanarayana et al., 1985]. However, the theory for the ion-cyclotron instability can only be justified in the upper E-region (altitudes  $\geq 130$  km) where ions are magnetized ( $\nu_{in} < \Omega_i$ , where  $\nu_{in}$  is the ion-neutral collision frequency and  $\Omega_i$  is the ion gyrofrequency), and care must be exercised while using the ion-cyclotron instability mechanism at lower altitudes where the ions are collisional, i.e.,  $\nu_{in} \geq \Omega_i$  (~ 100-120 km altitudes).

In this report, we consider the plasma instability processes occurring at E-region altitudes, where ions are collisional, and include the effects of an equilibrium parallel current. We find that the inclusion of a parallel electron drift makes possible the excitation of the Farley-Buneman (F-B) instability for electron Hall drifts lower than the ion-sound speed, and can result in the excitation of obliquely propagating F-B and ion-sound modes. In this regard, we mention that auroral irregularities have been observed in the regions of downward Birkeland currents (that are carried by the thermal electrons) [Tsunoda et al., 1976; McDiarmid and McNamara, 1978]. In this work, we have not considered any nonlocal effects for these modes [Kav, 1972; Moorcroft, 1984; St.-Maurice, 1985]. In the following, we first present a brief outline of the theoretical approach and then discuss the results for the auroral E-region situation.

## II. THEORY

A general dispersion relation describing the auroral E-region modes has been given in many places; we consider the one derived by Fejer et al. [1984b] using the two-fluid equations. The use of fluid equations is valid for wavelengths greater than the ion-mean-free path ( $\geq$  a meter) [Schmidt and Gary, 1973]. The coordinate system used here has the z-axis aligned with the Earth's magnetic field,  $B_0 \hat{z}$ . An equilibrium transverse electric field,  $E_{0x}$ , results in the electron Hall drift,  $v_{0y}$ , along the y-axis (East-West direction). A density gradient exists along the x-axis (north-south direction) but will be ignored here and an equilibrium parallel current,  $J_{0z}$ , (carried by thermal electrons with a drift velocity,  $v_{0z}$ ) is assumed to be present. The ions are assumed collisional ( $\nu_{in} \geq \Omega_i$ ), and the electrons are magnetized ( $\nu_{en} \ll \Omega_e$ ), where  $\nu_{\alpha n}$  and  $\Omega_{\alpha} (= e_{\alpha} B_0 / m_{\alpha} c)$  are, respectively, the particle collision frequency with neutrals and the gyrofrequency, and  $m_{\alpha}$  is their mass. For obliquely propagating modes [ $\sim \exp(ik_y y + ik_z z - i\omega t)$ ], the dispersion relation is

$$(\omega - \mathbf{k} \cdot \mathbf{v}_0)(\nu_{in} - i\omega) + \{\omega[\Omega_i^2 + (\nu_{in} - i\omega)^2] + ik_z^2 C_s^2 (\nu_{in} - i\omega)\} \frac{\hat{y}}{\nu_{in}} = 0 \quad (1)$$

where

$$\hat{y} = \frac{\nu_e \nu_{in}}{\Omega_e \Omega_i} \left( 1 + \frac{\Omega_e^2}{\nu_e^2} \frac{k_z^2}{k^2} \right); \quad C_s^2 = \frac{(T_e + T_i)}{m_i} \quad (2)$$

In the above, recombination damping is neglected (as it is important only for the long wavelength modes, and, we are interested in the 3 meter irregularities) and electron inertia is ignored. The symbols used have their standard meanings:  $\mathbf{k} = k_y \hat{e}_y + k_z \hat{e}_z$  is the modal wavenumber and  $\omega$  the

complex frequency,  $\underline{v}_0$  is the equilibrium electron drift velocity with a Hall component ( $v_{oy}$ ) and a parallel component ( $v_{oz}$ ), and temperature,  $T_e$ , is expressed in energy units.

For collisional altitudes ( $v_{in} > \Omega_i$ ), we may rewrite eq. (1) as

$$(\omega - \underline{k} \cdot \underline{v}_0) + \left[ \omega v_{in} - i(\omega^2 - k^2 C_s^2) \right] \frac{\dot{\Psi}}{v_{in}} = 0 \quad (3)$$

This dispersion relation can be solved to yield the Farley-Buneman instability and the ion-acoustic instability, respectively, in the approximations  $|\omega| < v_{in}$  and  $|\omega| > v_{in}$ . We now present the analytical expressions for the two cases, and, will present some numerical results appropriate for the auroral electrojet in the next section.

#### A. Modified Farley-Buneman Instability

It is straightforward to obtain the usual result of the Farley-Buneman instability from the above (i.e.,  $k_z = 0$ ). One finds that [Fejer et al. 1984b] the real frequency and the growth rate are given as ( $\omega = \omega_r + \gamma$ ,  $|\gamma| < \omega_r$ )

$$\omega_r = \frac{1}{(1 + \Psi)} k_y v_{oy} \quad (4a)$$

and

$$\gamma = \frac{\Psi}{v_{in}(1 + \Psi)} (\omega_r^2 - k_y^2 C_s^2) \quad (4b)$$

where  $\Psi = v_e v_{in} / \Omega_e \Omega_i$ . Instability occurs when  $v_{oy} > (1 + \Psi) C_s$ .

For  $k_z \neq 0$ , we can write (3) as

$$\omega = \frac{\underline{k} \cdot \underline{v}_0}{(1 + \Psi)} + i \frac{(\omega^2 - k^2 C_s^2) \dot{\Psi}}{v_{in}(1 + \Psi)} \quad (5)$$

where  $\dot{\Psi}$  has been defined in (2). From (5), we can write approximate expressions for real frequency and the growth rate of the modes as follows ( $\omega = \omega_r + i\gamma$ ,  $|\gamma| < \omega_r$ )

$$\omega_r = \frac{1}{(1 + \dot{\Psi})} (k_y v_{oy} + k_z v_{oz}) \quad (6a)$$

$$\gamma = \frac{\dot{\Psi}}{v_{in}(1 + \dot{\Psi})} (\omega_r^2 - k^2 C_S^2) \quad (6b)$$

The new instability condition is given by

$$v_{oy} + \frac{k_z}{k_y} v_{oz} > (1 + \dot{\Psi}) C_S \quad (7)$$

For a parameter domain such that  $(k_z/k)(\Omega_e/v_e) \gg 1$  [and,  $(\Omega_e/v_e)(v_{in}/\Omega_i)(k_z^2/k^2) > 1$ ], it may be readily verified that the growth rate (and the real frequency) in (6) maximize for  $(k_z/k) \sim 2(v_{oy}/v_{oz})$ . Note that this implies that the modes are not too highly field-aligned ( $k_z/k \gg v_e/\Omega_e$ ). In the general case, the criteria determining the optimum growth rate (and the real frequency) are somewhat complex, and we have not attempted to present them here. For  $k_z = 0$ , (7) yields the usual instability criterion ( $v_{oy} > (1 + \dot{\Psi}) C_S$ ) of the Farley-Buneman instability. For  $k_z \neq 0$  and  $v_{oz} = 0$ , we recover the result that the inclusion of parallel wavelengths increases the threshold value of electron drift required for the excitation ( $v_{oy} > (1 + \dot{\Psi}) C_S$ ) [Ossakov et al., 1975]. Since,  $\dot{\Psi} \gg 1$  for the parameter domain of our interest, the requirement,  $v_{oy} > \dot{\Psi} C_S$ , may become prohibitively large in actual situations. However, it is clear from (7) that for sufficiently large values of  $v_{oz}$ , an

obliquely propagating mode may still be excited and, further, the instability criterion may be met for  $v_{oy} < C_s$ .

### B. Ion-Acoustic Instability

The ion-acoustic wave excitation by the Hall current in auroral electrojet has been discussed by Kaw [1973]. Here we include the effects of a parallel current on this mode. For  $v_{in} < |\omega|$ , we find from (3) that the dispersion relation for obliquely propagating ion sound waves is

$$\omega(\omega + i\bar{v}_{in}) - k^2 C_s^2 = -i \frac{m_e}{m_i} \frac{k^2}{k_z^2} v_e (\omega - \underline{k} \cdot \underline{v}_0) / \left(1 + \frac{v_e^2}{\omega_e^2} \frac{k^2}{k_z^2}\right) \quad (8)$$

where  $\bar{v}_{in} = v_{in} + (\pi/2)^{1/2} (\omega^4 / |k| k^2 v_i^3) \exp(-\omega^2 / 2k^2 v_i^2)$ , and we have included the ion-Landau damping effects for completeness. We can write the real frequency and growth rate for these modes from (8) as ( $\omega = \omega_r + i\gamma$ ,  $|\gamma| < \omega_r$ ),

$$\omega_r \approx k C_s \quad (9a)$$

$$\gamma \approx -\frac{1}{2} \bar{v}_{in} - \frac{1}{2} \frac{m_e}{m_i} \frac{k^2}{k_z^2} v_e \left(1 - \frac{\underline{k} \cdot \underline{v}_0}{\omega_r}\right) / \left(1 + \frac{v_e^2}{\omega_e^2} \frac{k^2}{k_z^2}\right) \quad (9b)$$

Physically, the current-driven ion-acoustic instability is related to the parallel dissipative motion of electrons. In the absence of equilibrium currents ( $\underline{v}_0 = 0$ ), the second term in (9b) represents the damping of the mode by the collisional parallel electron motion ( $v_e$ ) that inhibits them from being redistributed in wave potential in Boltzmann-like distribution  $[n_e = n_0 \exp(e\phi/T_e)]$ , thereby making the density-potential relationship

complex. In the presence of equilibrium currents ( $\underline{v}_0$ ), the electrons "see" the waves at a Doppler-shifted frequency ( $\omega - \underline{k} \cdot \underline{v}_0$ ); for equilibrium drift velocity larger than the wave phase velocity in the drift direction ( $\omega < \underline{k} \cdot \underline{v}_0$ ), the wave energy in the drift frame becomes negative. Thus, the dissipation of the negative energy wave leads to a wave growth. The second term in the denominator in the growth term in (9b) results from the transverse collisional motion of electrons, and has an effect of reducing the growth rate. For the case of Hall currents,  $\underline{v}_0 = v_{oy} \underline{e}_y$ , we recover from (9b), the instability discussed by Kaw [1973]. For a parallel current,  $\underline{v}_0 = v_{oz} \underline{e}_z$ , a collisional ion-acoustic instability is obtained. In general, the instability criterion may be written down as,

$$\frac{k_y}{k} \frac{v_{oy}}{C_s} + \frac{k_z}{k} \frac{v_{oz}}{C_s} > 1 + \frac{\bar{v}_{in}}{v_e} \frac{k_z^2}{k^2} \frac{m_i}{m_e} \left( 1 + \frac{v_e^2}{\Omega_e^2} \frac{k_y^2}{k_z^2} \right) \quad (10)$$

where as noted before,  $\bar{v}_{in}$  includes the ion-Landau damping effects. In the upper auroral E-region where  $v_{in}$  is sufficiently small (so that  $v_{in} < \omega_r - kC_s$ ), we find that a parallel current (in possible conjunction with the Hall current) may drive an oblique ion-sound mode unstable. This result may have relevance to the observations of non-field-aligned auroral irregularities [Haldoupis et al., 1985]. We also mention that, as noted by Kaw [1973], the time-dependence of the ion sound wave frequency due to the evolution of electron temperature ( $T_e$ ) in a collisional medium is not a problem here. In the partially ionized auroral E-region,  $T_e$  reaches a steady state value in an energy relaxation time  $(m_e v_e / m_i)^{-1}$  after which it stays constant, the neutrals providing the sink of energy. Further, the experimental observations of enhanced electron temperatures (which make



$T_e/T_i > 1$ ) [Shlegel and St.-Maurice, 1981] suggest a possible excitation of ion-sound waves, as the thresholds for excitation at  $T_e/T_i > 1$  are lower than the case with  $T_e = T_i$  [Kindel and Kennel, 1971].

### III. DISCUSSION

In the above, we have included the effects of a parallel equilibrium current (carried by drifting electrons) on the excitation of the Farley-Buneman and ion acoustic instabilities in the auroral electrojet. The presence of a parallel current modifies the dispersion equation for these modes, and makes possible the excitation of obliquely propagating modified Farley-Buneman and ion acoustic modes instability for sub-critical levels of electron Hall drift ( $v_{oy} \leq C_s$ ). We now present some numerical estimates for the threshold requirements on the parallel currents for the excitation of these modes in the auroral E-region.

We numerically solve (3) for parameters appropriate to the auroral electrojet region. For an altitude of 105 km we consider the following typical parameters:  $v_e = 4 \times 10^4 \text{ sec}^{-1}$ ,  $v_{in} = 2.5 \times 10^3 \text{ sec}^{-1}$ ,  $\Omega_e = 8.8 \times 10^6 \text{ sec}^{-1}$ ,  $\Omega_i = 1.8 \times 10^2 \text{ sec}^{-1}$ , and  $C_s = 350 \text{ m/sec}$ . For 3 m wavelength waves we note that  $v_{in}/kC_s = 3.5$ . In Fig. 1 we plot the real frequency  $\omega_r/kC_s$  vs  $k_z/k_y$  (Fig. 1a) and the growth rate  $\gamma/kC_s$  vs  $k_z/k_y$  (Fig. 1b) for  $v_{oy}/C_s = 1.0$  and  $v_{oz}/C_s = 0$  (A), 25 (B), 50 (C) and 75 (D). We note the following. First in the absence of a parallel current ( $v_{oz} = 0$ ), the turn-on criterion for instability is  $v_{oy} > (1 + \sqrt{2})C_s$ . Since we have taken  $v_{oy}/C_s = 1$  we expect the Farley-Buneman to be stable and this is clearly evident from curve A in Fig. 1b (i.e.,  $\gamma < 0$ ). Second, for finite values of  $v_{oz}$  and  $k_z$  unstable modes can be excited (e.g., see curves C and D of Fig. 1b). The band of unstable modes corresponds to modes with  $\omega_r > kC_s$

(e.g., see curves C and D of Fig. 1a). Third, for sufficiently large values of  $k_z/k_y$  (for our parameters  $k_z/k_y > 0.02$ ), the unstable modes become damped (i.e.,  $\gamma < 0$ ). This is because  $\omega_r \approx (k_z/k_y)^{-1}$  for large  $k_z/k_y$  (i.e.,  $k_z/k_y > v_e/\Omega_e$ ); as  $k_z/k_y$  increases,  $\omega_r$  decreases and eventually  $\omega_r < kC_s$  so that  $\gamma < 0$ . And fourth, increasing values of  $v_{oz}/C_s$  lead to enhanced growth rates and a broader range of instability in  $k_z/k_y$ . In Fig. (1c), we have plotted the critical Hall drift required for the excitation of the instability in presence of  $v_{oz}$  and  $k_z$ . It can be readily seen that for sufficiently large value of  $v_{oz}$ , the instability may occur for  $v_{oy}/C_s < 1$  (for oblique modes).

At somewhat higher altitudes in the E region, the ion-neutral collision frequency decreases so that  $v_{in} < \omega_r$ . For example at  $\sim 115$  km we consider the following parameters:  $v_e = 4.0 \times 10^3 \text{ sec}^{-1}$ ,  $v_{in} = 3.6 \times 10^2 \text{ sec}^{-1}$ ,  $\Omega_e = 6.6 \times 10^6 \text{ sec}^{-1}$ ,  $\Omega_i = 1.8 \times 10^2 \text{ sec}^{-1}$ , and  $C_s = 350 \text{ m/sec}$ . For 3 m wavelength modes, we note that  $v_{in}/kC_s = 0.25 < 1$ , and ion acoustic waves may be excited. In Fig. 2 we plot the real frequency  $\omega_r/kC_s$  vs.  $k_z/k_y$  (Fig. 2a) and the growth rate  $\gamma/kC_s$  vs.  $k_z/k_y$  (Fig. 2b) for the above parameters with  $v_{oy}/C_s = 1.0$  and  $v_{oz}/C_s = 0$  (A), 25 (B), 50 (C), and 75 (D). The important features are the following. First, as in Fig. 1, for  $v_{oz} = 0$  there are no unstable modes (curve A of Fig. 2b). As  $k_z/k_y$  becomes large we note that  $\omega_r \sim kC_s$  and  $\gamma \sim v_{in}/2$  in accordance with (9). Second, for finite values of  $v_{oz}$  and  $k_z$  unstable modes can be excited (as in Fig. 1). In this case we note that the threshold parallel velocity for instability is lower than in the previous case; for example, for  $k_z/k_y = 5.0 \times 10^{-3}$  the threshold velocity is  $v_{oz} = 17 C_s$  for the parameters used in Fig. 2 while it is  $v_{oz} = 29 C_s$  for those used in Fig. 1. Third, the unstable waves have maximum growth rates somewhat larger than those shown

in Fig. 1, and peak at somewhat lower values of  $k_z/k_y$ . And fourth, the most significant difference between Figs. 1 and 2 is the asymptotic behavior of  $\omega_r$  and  $\gamma$  for large  $k_z/k_y$ . In Fig. 1, both  $\omega_r$  and  $\gamma$  monotonically decrease for large values of  $k_z/k_y$ ; however, in Fig. 2 both  $\omega_r$  and  $\gamma$  asymptote to  $k_y C_s$  and  $-v_{in}/2$ , respectively for large  $k_z/k_y$ . This difference may have observable consequences with regard to the nonlinear evolution of these modes. We will discuss this shortly.

We see from the above results that for oblique modes ( $k_z \neq 0$ ), the threshold Hall drift for the excitation of the Farley-Buneman instability is very high. Thus, for the excitation with  $v_{oz} = 0$  and  $k_z/k = .02$ , the criterion is  $v_{oy} > \sim 3.5$  km/sec. Such drift velocities would correspond to transverse electric fields  $\geq 175$  mV/m, a value that is much larger than the reported (though infrequent) measurements of fields up to 150 mV/m. However, there are also measurements, at times, of large scale parallel currents on the order to tens of  $\mu A/m^2$  in the high latitude ionosphere [e.g., Bythrow et al., 1984]. These currents close in the E-region. Thus, obliquely propagating modes in the E-region would be affected by plasma flows both in the transverse as well as in the parallel direction. For a current  $J_{oz} \sim 94 \mu A/m^2$  [Bythrow et al., 1984], with  $n_0 \sim 10^4 \text{ cm}^{-3}$ , the parallel electron drift velocity computed from the expression,  $J_{oz} \sim n_0 e v_{oz}$ , is  $v_{oz} \sim 60$  km/s. One finds from Fig. 1 that, for oblique propagation in the presence of such a parallel drift velocity, the Farley-Buneman instability may still directly generate 3 meter irregularities for the sub-critical electrojet velocities, i.e.,  $v_{oy} < C_s$ , or  $E_{01} < 20$  mV/m. The Doppler returns in this case would be peaked around a velocity different from the electron Hall drift. We note that an excitation for the sub-threshold conditions of type I irregularities has been reported [Siren

et al., 1977]. However, we wish to mention here that the large parallel currents are also accompanied by enhancements in the ambient density. Thus, the computation of parallel electron drift velocity from the observed current for the corresponding density (as has been done above), often leads to values of drift speeds that fail to meet the thresholds required for excitation. A possibility, that needs to be experimentally checked, is that these large structured currents cause a structure in the density also, with the regions of low density experiencing the plasma wave excitation. We further note here that it has been suggested that the field aligned current generated ion-sound turbulence may be taken into account by introducing an effective (anomalous) electron collision frequency ( $\nu^*$ ), and this large  $\nu^*$  then may be used to explain the excitation of oblique Farley-Buneman instability [Volochevich and Liperovski, 1975]. However, the recent observations of non-field aligned radar echoes apparently can not be explained by this theory [Haldoupis et al., 1986].

We have noted earlier that the ion-acoustic instability is likely to occur at upper E-region altitudes, where the ion-neutral collision frequency is smaller than the wave frequency. The electrojet current (the electron Hall drift) is maximum at ~ 105-110 km altitudes, and decreases upwards. Thus, ion sound wave excitation may be primarily caused by the field-aligned currents, with possible contributions from the electrojet. For  $k_z/k_y \sim .01$  and  $v_{in}/v_e \sim 10$ , we find from Fig. 2 that a transverse field of ~ 20 mV/m and  $v_{oz} \sim 25$  km/sec could result in the wave excitation. Larger transverse electric fields and/or larger parallel currents can result into excitation of modes with higher  $k_z/k_y$ .

We find from the above estimates that in general the linear excitation of modes with large  $k_z/k_y \sim .2$  involves threshold requirements which appear

difficult to satisfy, based upon the observed magnitudes of currents. Therefore, we suggest the possibility that the modes that are excited linearly with small  $k_z$  saturate nonlinearly by generating modes with larger  $k_z$  that are frequently observed. A theory suggesting this effect has recently been proposed [Rosenbluth and Sudan, 1986].

In conclusion, we have suggested here that the field-aligned currents may influence the generation of small-scale plasma irregularities in the auroral electrojet, via the Farley-Buneman and ion-acoustic instabilities. This effect could explain the generation of irregularities that are non-field aligned, or, are generated under the subcritical conditions. These irregularities are detected by the VHF radar, and, usually appear to be colocated with the electrojets. We also note that auroral irregularities have been detected in the regions of the downward Birkeland currents [Tsunoda et al., 1976; McDiarmid and McNamara, 1978]. Large field-aligned currents are usually associated with disturbed geomagnetic conditions, and some of these observations have shown such a correlation. Although, we have not considered any nonlocal effects, considering the small scalesizes ( $\lambda_{\perp} \sim 3$  meter,  $\lambda_{\parallel} \sim 30 - 300$  meters) of interest, the basic effect of parallel currents modifying the threshold criteria of electrojet current-driven modes should be good to lowest order.

# ACKNOWLEDGMENT

We thank Dr. J.A. Pedder for helpful discussions. We also acknowledge the correspondence with Prof. G. Sofko on the observations by his group. This work was supported by ONR, NASA, and DNA.

## REFERENCES

- Balsey, B.B., and W.L. Ecklund, VHF power spectra of the radar aurora, J. Geophys. Res., 77, 4746, 1972.
- Bering, E.A., The plasma wave environment of an auroral arc: Electrostatic ion cyclotron waves in the diffuse aurora, J. Geophys. Res., 89, 1635, 1984.
- Bythrow, P.F., T.A. Potemra, W.B. Hanson, L.J. Zanetti, C. -I. Meng, R.E. Huffman, F.J. Rich, and D.A. Hardy, Earthward directed high density Birkeland currents observed by HILAT, J. Geophys. Res., 89, 9114, 1984.
- Chaturvedi, P.K., Collisional ion cyclotron waves in the auroral ionosphere, J. Geophys. Res., 81, 6169, 1976.
- D'Angelo, N., Type 3 Spectra of the radar aurora, J. Geophys. Res., 78, 3587, 1973.
- Fejer, B.G., and M.C. Kelley, Ionospheric Irregularities, Rev. Geophys. Space Phys., 18, 401, 1980.
- Fejer, B.G., R.W. Reed, D.T. Farley, W.E. Swartz, and M.C. Kelley, Ion cyclotron waves as a possible source of resonant auroral radar echoes, J. Geophys. Res. 89, 187, 1984a.
- Fejer, B.G., J. Providakes, and D.T. Farley, Theory of plasma waves in the auroral E region, J. Geophys. Res., 89, 7487, 1984b.
- Greenwald, R.A., Diffuse radar aurora and the gradient drift instability, J. Geophys. Res., 79, 4807, 1974.
- Greenwald, R.A., W.L. Ecklund, and B.B. Balsey, Diffuse radar aurora: Spectral observations of non-two-stream irregularities, J. Geophys. Res., 80, 131, 1975.

- Haldoupis, C., P. Prikryl, G.J. Sofko, and J.A. Koehler, Evidence for 50 - Mhz bistatic radio observations of electrostatic ion cyclotron waves in the auroral plasma, J. Geophys. Res., 90, 10983, 1985.
- Haldoupis, C., G.J. Sofko and J.A. Koehler, On ion-acoustic plasma waves at large magnetic aspect angles in the high-latitude E region of the ionosphere, J. Geophys. Res., 91, 5755, 1986.
- Kav, P.K., Wave propagation effects on observation of irregularities in the equatorial electrojet, J. Geophys. Res., 77, 1323, 1972.
- Kav, P.K., Current driven ion wave instability in a weakly ionized collisional magnetoplasma, Physics Lett., 44A, 427, 1973.
- Kindel, J.M., and C.F. Kennel, Topside current instabilities, J. Geophys. Res., 76, 3055, 1971.
- McDiarmid, D.R., and A.G. McNamara, Radio aurora in the dayside auroral oval spatial relationship with field-aligned currents and energetic particles, J. Geophys. Res., 83, 3226, 1978.
- Moorcroft, D.R., Propagation of plasma wave energy in the auroral E region, J. Geophys. Res., 89, 2963, 1984.
- Ogawa, T., H. Mori, S. Miyazaki, and H. Yamagishi, Electrostatic plasma instabilities in highly active aurora observed by sounding rocket S-310JA-7, Memoirs Natl. Inst. Polar Res. Special Issue Japan, 18, 321, 1981.
- Ossakov, S.L., K. Papadopoulos, J. Orens and T. Coffey, Parallel propagation effects on the type 1 electrojet instability, J. Geophys. Res., 80, 141, 1975.
- Providakes, J., D.T. Farley, W.E. Swartz, and D. Riggis, Plasma irregularities associated with a morning discrete auroral arc: Radar interferometer observations and theory, J. Geophys. Res., 90, 7513, 1985.

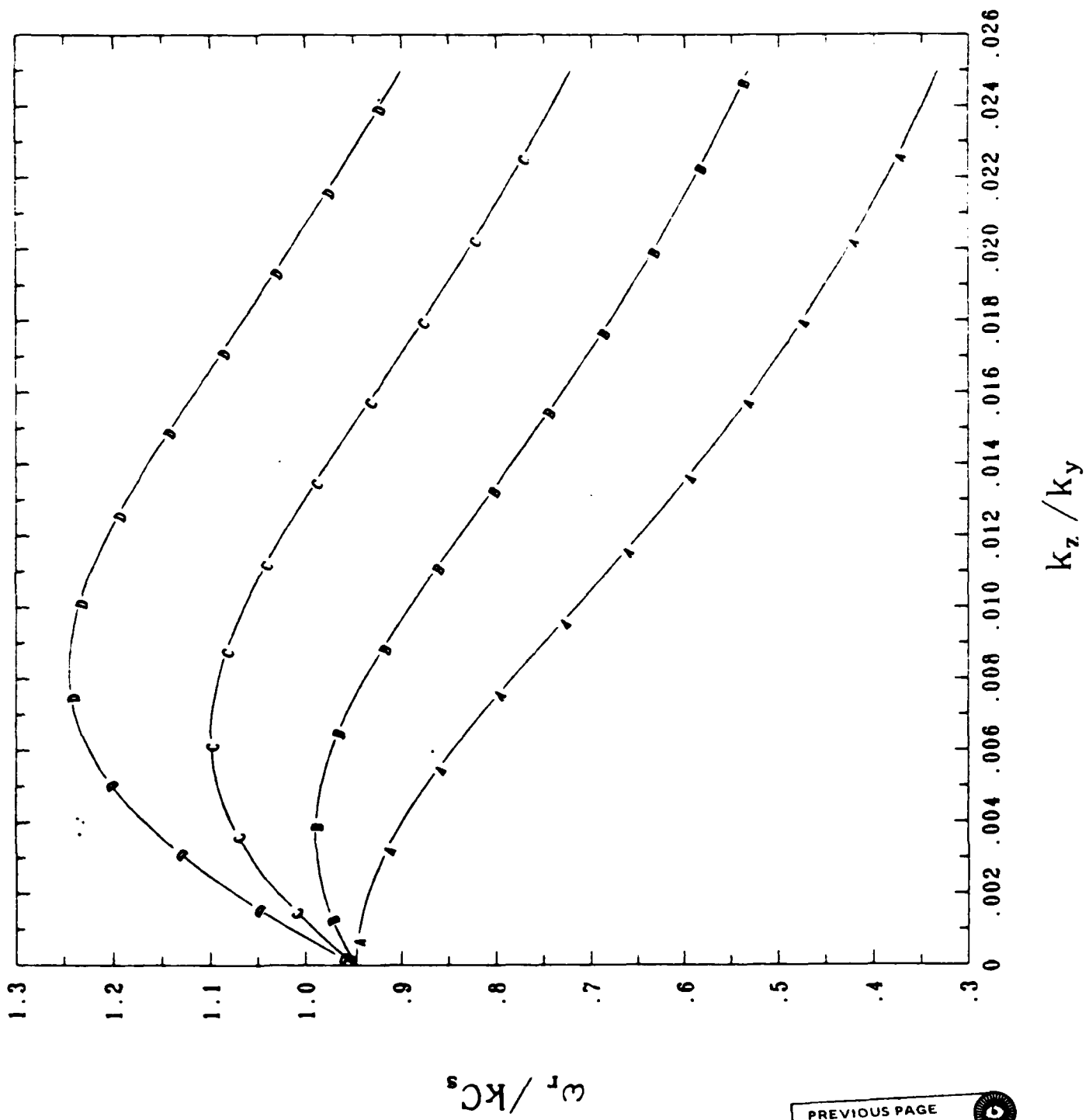


- Rosenbluth, M. and R. Sudan, Almost two-dimensional strong turbulence in a magnetized plasma, to be published in Phys. Fluids, 1986.
- Schmidt, M.J., and S.P. Gary, Density gradients and the Farley-Buneman instability, J. Geophys. Res., 78, 8621, 1973.
- Satyanarayana, P., P.K. Chaturvedi, M.J. Keskinen, J.D. Huba, and S.L. Ossakow, Theory of the current-driven ion cyclotron instability in the bottomside ionosphere, J. Geophys. Res., 90, 12 209, 1985
- Siren, J.C., J.R. Doupnik, and W.L. Ecklund, A comparison of auroral currents measured by the Chatanika radar with 50-Mhz backscatter observed from Anchorage, J. Geophys. Res., 82, 3577, 1977.
- Schlegel, K. and J.P. St.-Maurice, Anamalous heating of the polar E-region by unstable plasma waves, I. Observations, J. Geophys. Res., 86, 1447, 1981.
- St.-Maurice, J.-P., A nonlocal theory of the high-latitude Farley-Buneman instability, J. Geophys. Res., 90, 5211, 1985.
- Tsunoda, R.T., R.I. Presnell, and T.A. Potemra, The spatial relationship between the evening radar aurora and field-aligned currents, J. Geophys. Res., 81, 3791, 1976.
- Volosevich, A.V., and V.A. Liperovskiy, Generation of Small-scale inhomogeneities in a turbulent plasma and radio auroras, Geomagn. Aeronom., 14, 58, 1975.

# FIGURE CAPTIONS

Fig. 1 Plot of  $\omega/k_y C_s$  vs  $k_z/k_y$  for the parameters  $v_{oy}/C_s = 1.0$ ,  $v_{in}/k_y C_s = 3.5$ ,  $v_e/\Omega_e = 4.0 \times 10^{-3}$ ,  $v_i/\Omega_i = 14.0$ , and  $v_{oz}/C_s = 0, 25, 50$ , and 75 (denoted by A,B,C, and D, respectively), and the perpendicular threshold velocity  $v_{oy}/C_s$  vs.  $k_y/k_z$  for the same parameters. (a) The real frequency  $\omega_r/k_y C_s$  vs.  $k_z/k_y$ . (b) The growth rate  $\gamma/k_y C_s$  vs  $k_z/k_y$ . (c) The perpendicular threshold velocity  $v_{oy}/C_s$  vs.  $k_z/k_y$ .

Fig. 2 Plot of  $\omega/k_y C_s$  vs.  $k_z/k_y$  for the parameters  $v_{oy}/C_s = 1.0$ ,  $v_{in}/k_y C_s = 0.25$ ,  $v_e/\Omega_e = 6.0 \times 10^{-4}$ ,  $v_{in}/\Omega_i = 2.0$ , and  $v_{oz}/C_s = 0, 25, 50$ , and 75 (denoted by A,B,C, and D, respectively). (a) The real frequency  $\omega_r/k_y C_s$  vs.  $k_z/k_y$ . (b) The growth rate  $\gamma/k_y C_s$  vs.  $k_z/k_y$ .



PREVIOUS PAGE  
IS BLANK

Figure 1a

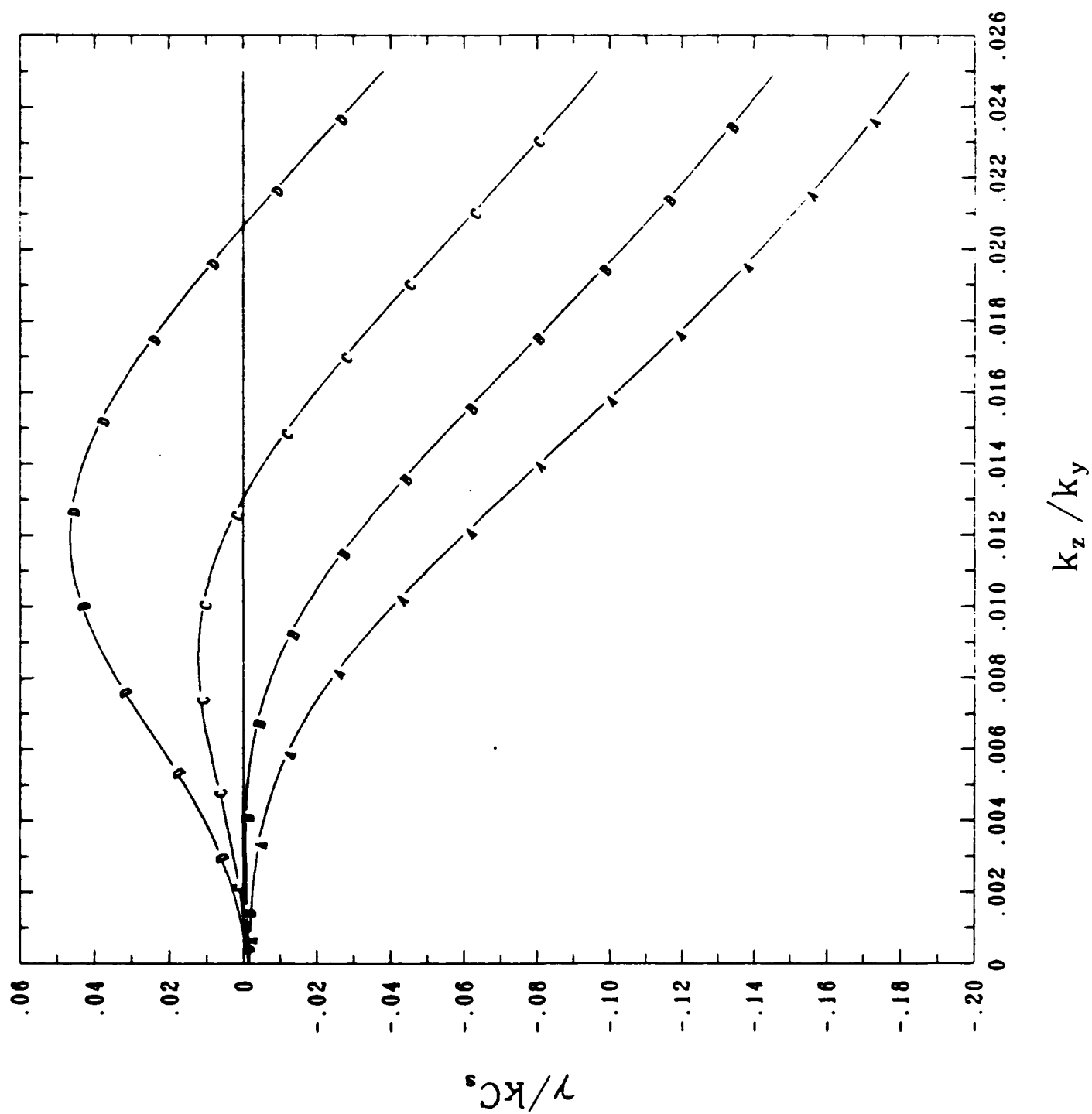


Figure 1b

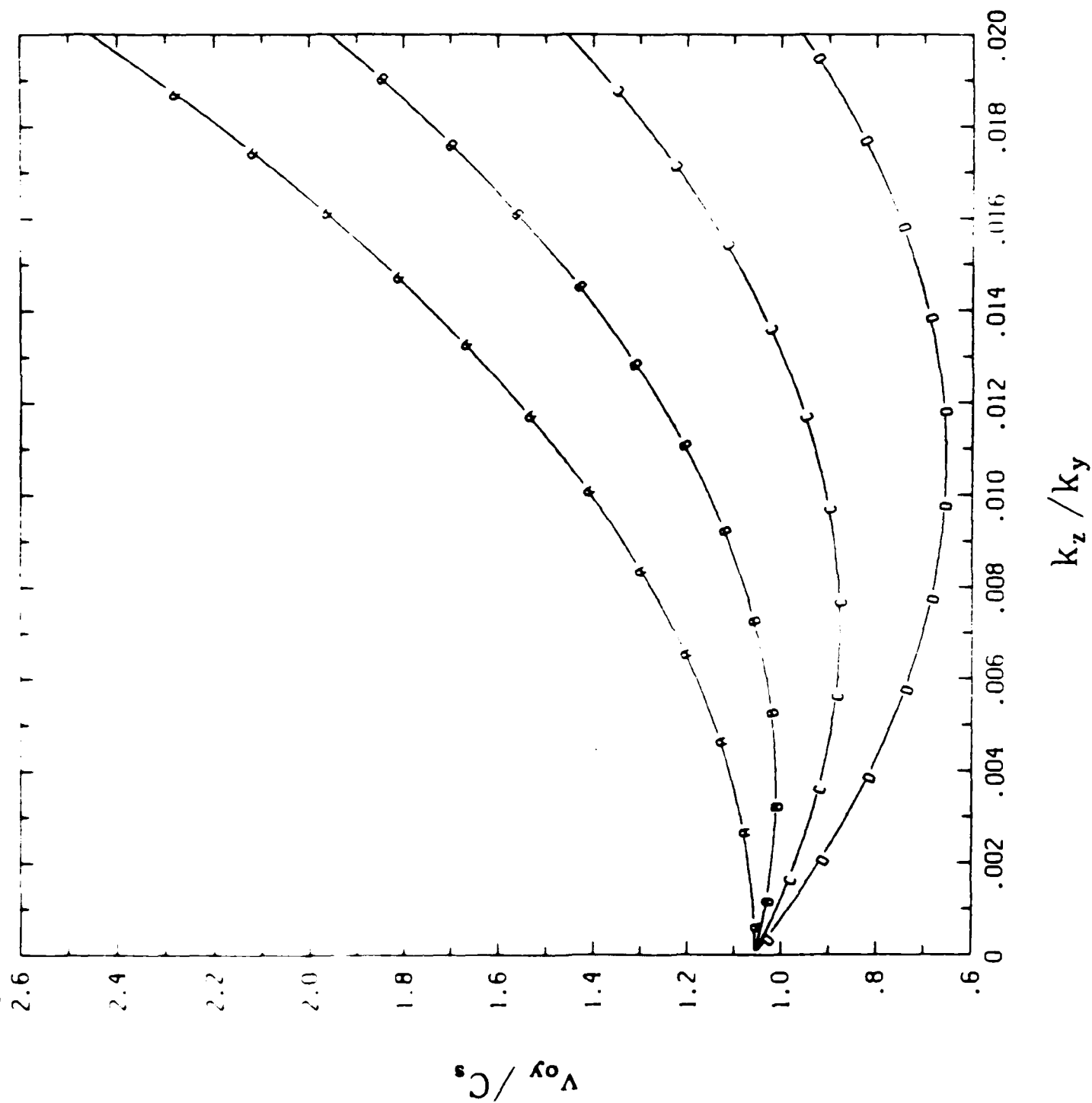


Figure 1c

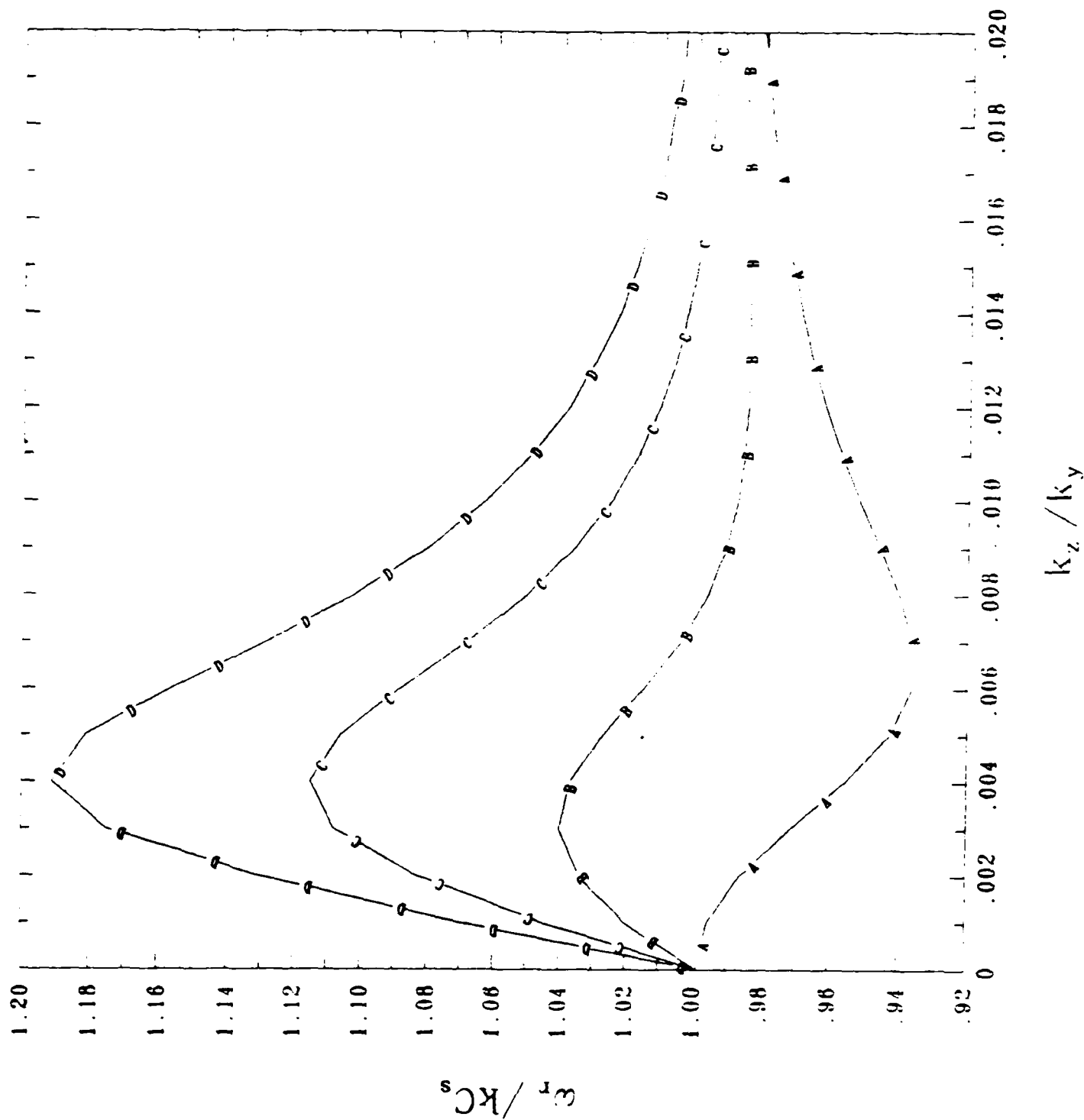


Figure 2a

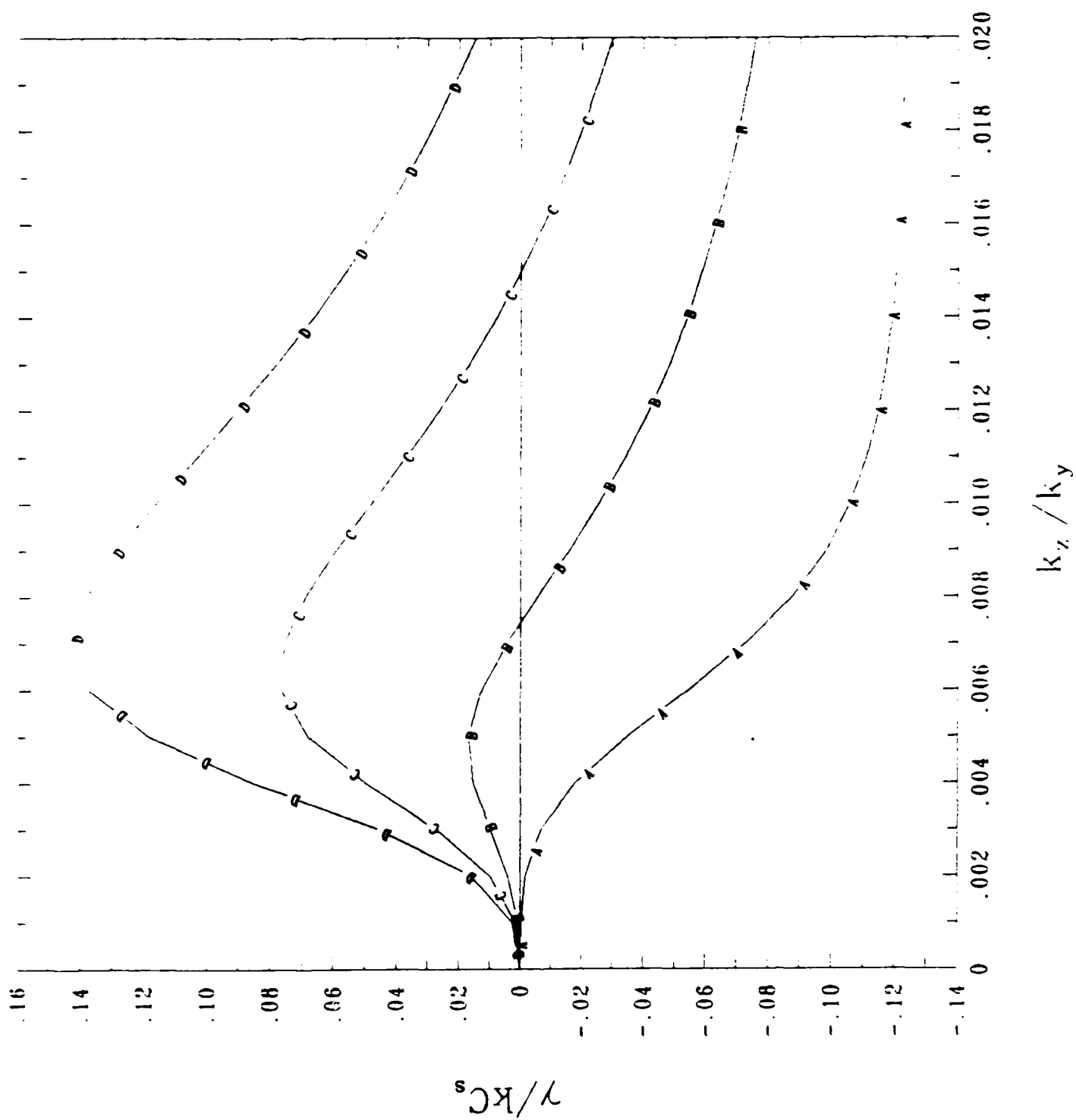


Figure 2b





**APPENDIX I**

**On the Stability of a Stratified Shear Layer**

**P.Satyanarayana and Y.C. Lee**  
**Science Applications International Corporation**

**J.D. Huba**  
**Naval Research Laboratory**



# ON THE STABILITY OF A STRATIFIED SHEAR LAYER

P. Satyanarayana and Y.C. Lee\*  
Science Applications International Corporation  
1710 Goodrich Drive, P.O. Box 1303  
McLean, VA 22102

and

J.D. Huba  
Geophysical and Plasma Dynamics Branch  
Naval Research Laboratory  
Washington, DC 20375-5000

May 1986

## ABSTRACT

The stability of a stratified shear layer is investigated using an exponential density profile and a laminar shear flow with a continuous velocity distribution. It is shown that an exact stability boundary can be obtained for an inhomogeneous inviscid fluid under the action of gravity without the need to impose the Boussinesq approximation. The stability boundary is given by  $J = \hat{k}^2(1 - \beta^2/4 - \hat{k}^2)$  where  $\beta$  is the ratio of the velocity and density gradient scale sizes,  $J$  is the Richardson number and  $\hat{k}$  is the perpendicular wavenumber normalized to the velocity gradient scale size; this reduces to the stability boundary derived by Drazin in the limit  $\beta = 0$ . The solution allows for  $c = 3/2$  where  $c$  is the normalized phase velocity.

\* Permanent address: University of Maryland, College Park, MD 20742



## I. INTRODUCTION

The Kelvin-Helmholtz instability is a widely studied instability driven by velocity shear in neutral fluids as well as in ionized gases<sup>1-6</sup>. In addition to various examples in neutral fluids, the situation of a shear layer under the action of gravity is also encountered in space (e.g., equatorial spread F, the plasmopause) and laboratory (e.g., laser fusion experiments) plasma phenomena. Recent observations show that large velocity shears exist at the equatorward edge of the diffuse auroral boundary<sup>7</sup>. Furthermore, the plasmopause boundary is conjectured to be unstable to a ballooning type shear flow instability<sup>8</sup>. In the case of the equatorial ionosphere, the plasma is confined by a uniform magnetic field and the flow velocity perpendicular to the magnetic field is sheared as a function of the altitude. Gravity is directed opposite to the density gradient so that the system is prone to gravity driven interchange as well as to the shear driven Kelvin-Helmholtz instability. Based on this geometry and physics, linear stability analysis has been performed on a collisional plasma in the equatorial F region of the ionosphere, and a general mode structure equation has been derived<sup>4,5</sup> which reduces to the general Rayleigh equation dealt with in detail by Drazin<sup>2</sup>.

In the neutral fluid literature (for example, Drazin<sup>2</sup>) and by Vinas and Madden<sup>9</sup>, the Boussinesq approximation is generally assumed in performing the analysis of the general Rayleigh equation; this assumption amounts to ignoring all the density gradient terms except the density gradient that contributes to the bouyancy. In this paper, we relax the Boussinesq approximation and show that the neutral stability boundary obtained by Drazin<sup>2</sup> is different: the stability boundary is dependent on the density gradient, leading to more stringent restrictions on the

Richardson number and the stability boundary is determined for modes with phase velocity half that of the peak background flow velocity. The following analysis is based on a smooth velocity profile and an exponential density gradient.

## II. THEORY

The geometry of the plasma and field configuration used in the analysis is as follows: the magnetic field is uniform and in the  $z$  direction ( $\underline{B} = B \hat{z}$ ), the plasma is inhomogeneous along the  $x$  direction,  $n = n_0(x)$ , gravity is acting along the negative  $x$  direction  $\underline{g} = -g \hat{x}$ , and the flow velocity along the  $y$  direction is sheared in the  $x$  direction,  $\underline{V} = -V_0(x) \hat{y}$ .

We consider low frequency fluctuations ( $\omega \ll \omega_{ce}$  where  $\omega_{ce}$  is the electron cyclotron frequency) so that electron inertia is ignored. Two dimensional perturbations are considered. The perturbed quantities vary as  $\phi = \phi(x) \exp[-i(k_y y - \omega t)]$ , where  $\omega = \omega_r + i\gamma$ . The equation that describes the perturbed electrostatic potential is given as<sup>4</sup>

$$\frac{\partial^2 \phi}{\partial x^2} + p(x) \frac{\partial \phi}{\partial x} + q(x) \phi = 0 \quad (1)$$

where  $p(x)$  and  $q(x)$  are given by

$$p(x) = \frac{\partial \ln n_0}{\partial x} \quad (2)$$

$$q(x) = -k^2 + \frac{1}{n} \left[ \frac{1}{V_0} \frac{\partial V_0^2}{\partial x^2} + \frac{\partial \ln n_0}{\partial x} \frac{\partial \ln V_0}{\partial x} + \frac{J}{n} \frac{\partial \ln n_0}{\partial x} \right] \quad (3)$$

where  $V_0 = \bar{V}_y U(X)$ ,  $c = \omega/k_y \bar{V}_y$ ,  $\Omega = c - U(x)$ ,  $X = x/L_v$ ,  $\hat{k} = k_y L_v$ , and  $J = (g/L_n)/(\bar{V}_y^2/L_v^2)$ . Here  $L_v$  and  $L_n$  are the gradient scale lengths of the velocity and density, respectively. Equation (1) is a general equation that describes Rayleigh-Taylor and Kelvin-Helmholtz instabilities for arbitrary density profiles and drift velocities. This equation is identical to that obtained for counterstreaming neutral fluids in a gravitational field<sup>2</sup>.

In this paper we consider an exponential profile for the density such that  $n_0(x) = n_0 \exp(\beta X)$  where  $\beta = L_v/L_n$  and represent the drift velocity by a smooth profile  $U(X) = \tanh(X)$ . We let  $\beta$  be arbitrary and thus generalize the problem analyzed by Drazin<sup>2</sup>. This is the main objective of this paper. The coefficients  $p(X)$  and  $q(X)$  can be rewritten as

$$p(X) = \beta \quad (4)$$

$$q(X) = \hat{k}^2 - \left[ \frac{2 \sec^2 X (\tanh X + \beta)}{(c - U)} \right] + \frac{J}{(c - U)^2 (1 - U^2)} \quad (5)$$

Using the Boussinesq approximation Drazin<sup>2</sup> set  $p = 0$  and ignored  $\beta$  in the second term in  $q$ , which lead to the condition  $c = 0$ . We relax these assumptions in the following analysis.

Using the transformation  $\psi = \phi \exp \left[ \int dX p(X)/2 \right]$  we write (7) as

$$\frac{\partial^2 \phi}{\partial X^2} + Q(X) \phi = 0 \quad (6)$$

where

$$Q(X) = q(X) - p(X)'/2 - p(X)^2/4 \quad (7)$$

Equations (4) and (5) together with (6) and (7) yield

$$\frac{\partial^2 \phi}{\partial X^2} + \left[ -k^2 - \frac{\beta}{4} + \left( \frac{\text{sech}^2 X (2 \tanh X + \beta)}{(c - U)} - 2 + \frac{J}{(c - U)^2 (1 - U^2)} \right) \right] \phi = 0 \quad (8)$$

With  $U$  as the independent variable, (8) can be written as

$$(1 - U^2) \frac{\partial^2 \phi}{\partial U^2} - 2U \frac{\partial \phi}{\partial U} + \left[ \frac{-(k^2 + \beta/4)}{(1 - U^2)} + \frac{2c - \beta}{(c - U)} + \frac{J}{(c - U)^2 (1 - U^2)} \right] \phi = 0 \quad (9)$$

Equation (9) is a second order differential equation with four singular points at  $U = \pm 1$ ,  $c$ , and  $\infty$ . The new terms in this equation are  $-(\beta/4)/(1 - U^2)$  and  $(2c - \beta)/(U - c)$ ; the former, obtained by retaining the first derivative term in (1), introduces a lower cut-off in the stability boundary, and the latter, obtained by retaining the cross term involving the density inhomogeneity and velocity inhomogeneity, allows for  $c$  to take the value  $\beta/2$ .

The solution of (8) can be represented by the Reynold's symbol

$$R = \begin{pmatrix} -1 & c & 1 & \infty \\ \frac{1}{2} \mu_+ & \frac{1}{2} (1 - \lambda) & \frac{1}{2} \mu_- & -1 \\ -\frac{1}{2} \mu_+ & \frac{1}{2} (1 - \lambda) & \frac{1}{2} \mu_- & 2 \end{pmatrix} U$$

where  $\mu_{\pm}$  and  $\lambda$  are the exponents at the singular points  $U = \pm 1$  and  $c$ , respectively.



We assume a solution of the form

$$\phi = (U + 1)^{\mu_+} (U - 1)^{\mu_-} (U - c)^{\lambda} \quad (10)$$

The exponents  $\mu_{\pm}$  and  $\lambda$  can be determined as the coefficients of  $1/(U + 1)$ ,  $1/(U - 1)$ , and  $1/(U - c)$ , respectively:

$$4\mu_{\pm}^2 = \hat{k}^2 - \frac{J}{(1 - c)^2} \quad (11)$$

$$(\lambda^2 - \lambda)(1 - c^2) = - \frac{J}{(1 - c^2)} \quad (12)$$

Note that for  $c = 0$  the exponents (11) and (12) reduce to those given by Drazin<sup>2</sup>. These exponents have to satisfy the condition

$$(\mu_+ + \mu_- + \lambda)(\mu_+ + \mu_- + \lambda - 1) - 2 = 0 \quad (13)$$

as can be seen by matching the coefficients of the constant terms. From (13)  $\mu_+ + \mu_- + \lambda = 1$  or  $-2$ . The latter condition yields a convergent solution with the constraint  $2c - \beta = 0$  or  $c = \beta/2$ .

Using the definitions for  $\mu_{\pm}$  and  $\lambda$  from (11) and (12) in the condition

$$\mu_+ + \mu_- + \lambda = 1 \quad (14)$$

we obtain

$$J = \hat{k}^2(1 - \beta^2/4 - \hat{k}^2) \quad (15)$$

From equation (15) we see that, for  $\beta = 1$ , the critical Richardson number is  $9/64$ , which means that for  $J > 9/64$  the flow is stable; the cut off wavenumber is  $\hat{k} = \sqrt{3}/2$ . These should be compared with that of a Boussinesq fluid: critical  $J$  is  $1/4$  and cut off  $\hat{k}$  is  $1$ . Finally, the stability boundary is not neutral as was the case with a Boussinesq fluid, but the waves have a phase velocity that is half that of the peak background flow velocity, i.e.,  $c = 1/2$  as opposed to  $c = 0$  for a Boussinesq fluid. Finally, for a fluid in a gravity free field ( $J = 0$ ) the Kelvin-Helmholtz unstable domain is given by  $0 < \hat{k} < (1 - \beta^2)^{1/2}$ . These conclusions can be clearly seen in Fig. 1, where we plot  $J$  versus  $\hat{k}$ . The figure shows the stability boundaries for various values of  $\beta$ . It is worth noting that for  $\beta > 2$ , that is if the density gradient scale length is half or less than the velocity gradient scale length, the Kelvin-Helmholtz instability is stable and the system is only unstable to the gravity driven interchange, i.e., only when  $J < 0$ .

We apply the results to the plasmopause boundary based on the observations of velocity shears observed by Kelley<sup>7</sup> and compare our results with those of Vinas and Madden<sup>8</sup>. The velocity shear  $V_0/L_v$  is estimated to be  $0.17$  Hz; when mapped to the plasmopause region<sup>7</sup> this yields a local Richardson number of  $\sim 0.18$  [Ref. 8]. Vinas and Madden<sup>8</sup> show that  $\beta = 1.5$ , which when substituted into (15) yields the critical Richardson number  $J < 0.047$  for instability. Thus, our calculations suggest that such strong shears may not drive shear flow instability if steep density gradients exist at the same time.

### III. SUMMARY

In summary, we have shown that the mode equation for a stratified shear layer under the action of gravity can be solved for stability boundary without the need to impose the Boussinesq approximation. For  $L_y = L_x/8 = 1$ , the critical Richardson number is  $9/64$  as opposed to  $1/4$  and the unstable wavenumber domain is smaller with a cut off for  $J = 0$  at  $\hat{k} = \sqrt{3}/2$  rather than at  $\hat{k} = 1$ . In addition, the waves do not have a zero phase velocity but a phase velocity that is half the peak background flow velocity. These changes are due to the density gradient terms that were ignored in the Boussinesq approximation. In addition, we have shown that plasmopause boundary may not be unstable to shear flow ballooning instability if strong density gradients exist in conjunction with strong shears at the diffuse auroral boundary at ionospheric heights.

### ACKNOWLEDGMENTS

This work was supported by the Defense Nuclear Agency and Office of Naval Research.

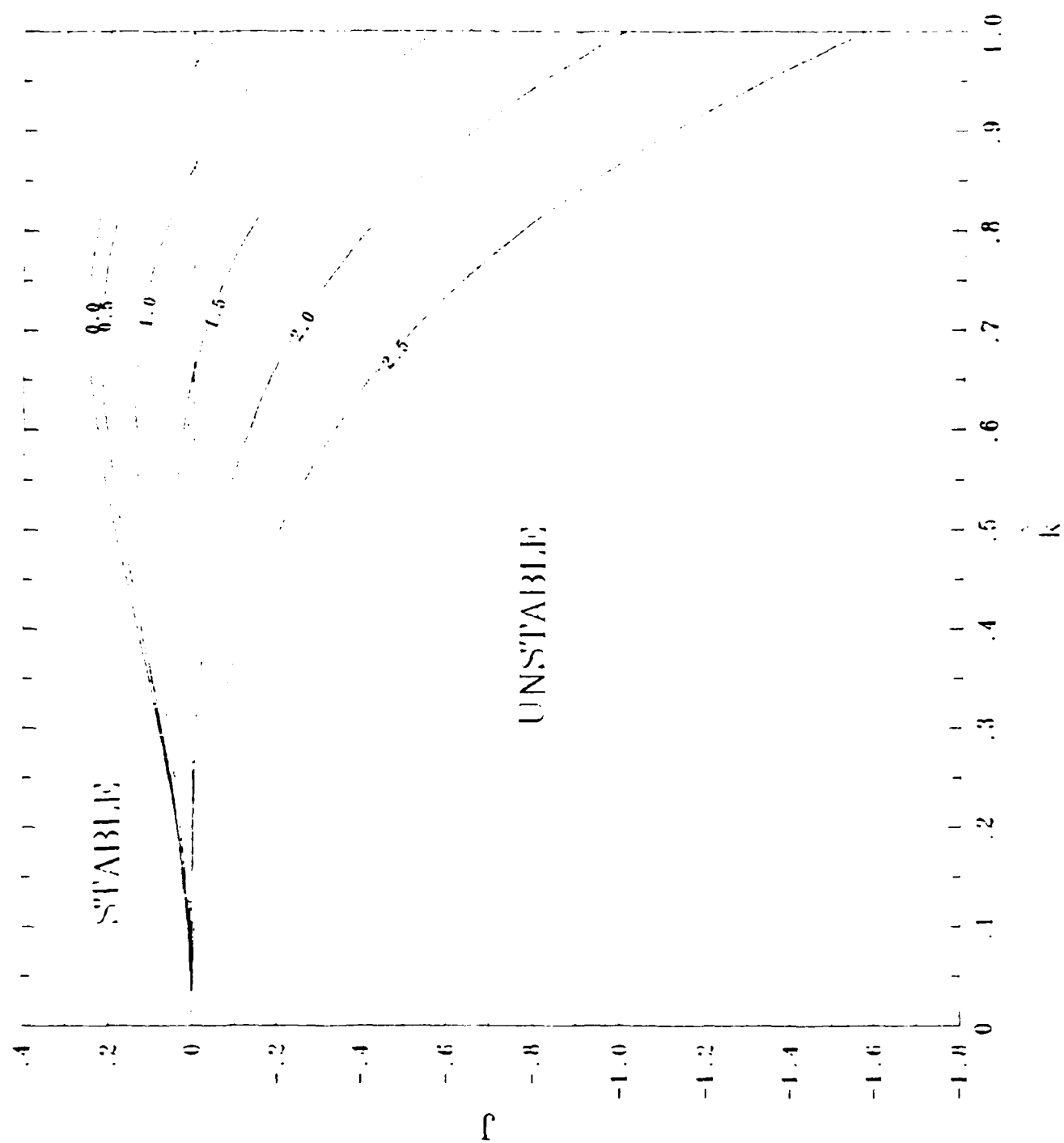
## REFERENCES

1. S. Chandrasekhar, Hydrodynamic and Hydromagnetic Stability, Int. Ser. Monographs on Physics, Clarendon Press (1961).
2. P.G. Drazin, J. Fluid Mech., 1, 214 (1958).
3. P.G. Drazin and W.H. Reid, Hydrodynamic Stability, Cambridge University Press, 124 (1980).
4. P.N. Guzdar, P. Satyanarayana, J.D. Huba, and S.L. Ossakow, Geophys. Res. Lett., 9, 547 (1982).
5. P. Satyanarayana, P.N. Guzdar, J.D. Huba, and S.L. Ossakow, J. Geophys. Res., 89, 2945 (1984).
6. A.B. Mikhailovskii, Theory of Plasma Instabilities, Vol. II, Consultants Bureau (1974).
7. M.C. Kelley, J. Geophys. Res., 91, 3225 (1986).
8. A. Vinas and T.R. Madden, J. Geophys. Res., 91, 1519 (1986).

# FIGURE CAPTION

Figure 1. The stability boundary  $J$  versus  $\hat{k}$  for  $\beta = 0.0, 0.5, 1.0, 1.5, 2.0$ , and  $2.5$ . The plasma is unstable (stable) in regions below (above) each curve. The case  $\beta = 0$  corresponds to the Boussinesq fluid treated by Drazin. Note that for  $\beta \geq 2$ ,  $J < 0$  is required for instability.









**APPENDIX J**

**Dynamics of the Large Scale Return Currents  
on Auroral Field Lines**

**Supriya B. Ganguli and H.G. Mitchell, Jr.  
Science Applications International Corporation**

**P.J. Palmadesso  
Naval Research Laboratory**



# **Dynamics of the Large Scale Return Currents on Auroral Field Lines**

**SUPRIYA B. GANGULI AND H. G. MITCHELL, JR.**

*Science Applications International Corporation  
McLean, VA 22102*

**P. J. PALMADESSO**

*Geophysical and Plasma Dynamics Branch  
Plasma Physics Division*

**November 11, 1985**

**This research was sponsored by the Office of Naval Research  
and the National Aeronautics and Space Administration.**



**NAVAL RESEARCH LABORATORY  
Washington, D.C.**

**Approved for public release; distribution unlimited.**



REPORT DOCUMENTATION PAGE				
1a REPORT SECURITY CLASSIFICATION <b>UNCLASSIFIED</b>			1b RESTRICTIVE MARKINGS	
2a SECURITY CLASSIFICATION AUTHORITY			3 DISTRIBUTION/AVAILABILITY OF REPORT	
2b DECLASSIFICATION/DOWNGRADING SCHEDULE			Approved for public release; distribution unlimited.	
4 PERFORMING ORGANIZATION REPORT NUMBER(S) <b>NRL Memorandum Report 5673</b>			5 MONITORING ORGANIZATION REPORT NUMBER(S)	
6a NAME OF PERFORMING ORGANIZATION <b>Naval Research Laboratory</b>	6b OFFICE SYMBOL (If applicable) <b>Code 4780</b>	7a NAME OF MONITORING ORGANIZATION		
6c ADDRESS (City, State, and ZIP Code) <b>Washington, DC 20375-5000</b>		7b ADDRESS (City, State, and ZIP Code)		
8a NAME OF FUNDING/SPONSORING ORGANIZATION <b>NASA and ONR</b>	8b OFFICE SYMBOL (If applicable)	9. PROCUREMENT INSTRUMENT IDENTIFICATION NUMBER		
8c ADDRESS (City, State, and ZIP Code) <b>Washington, DC 20546 Arlington, VA 22217</b>		10 SOURCE OF FUNDING NUMBERS		
		PROGRAM ELEMENT NO (See page ii)	PROJECT NO.	TASK NO. WORK UNIT ACCESSION NO.
11 TITLE (Include Security Classification) <b>Dynamics of the Large Scale Return Currents on Auroral Field Lines</b>				
12 PERSONAL AUTHOR(S) <b>Ganguli, Supriya B.* Mitchell, H.G., Jr.,* and Palmadesso, P.J.</b>				
13a TYPE OF REPORT <b>Interim</b>	13b TIME COVERED FROM TO	14 DATE OF REPORT (Year, Month, Day) <b>1985 November 11</b>	15 PAGE COUNT <b>43</b>	
16 SUPPLEMENTARY NOTATION <b>*Science Applications International Corporation, McLean, VA 22102</b> (Continues)				
17 COSATI CODES			18 SUBJECT TERMS (Continue on reverse if necessary and identify by block number)	
FIELD	GROUP	SUB-GROUP	13-moment system of transport equations Temperature anisotropy Return currents	
19 ABSTRACT (Continue on reverse if necessary and identify by block number) Multimoment fluid plasma simulations have been performed to study the dynamics of auroral field lines in the presence of large scale field-aligned return currents. The flux tube plasma has a rapid initial response to the onset of current. Electron velocity increases with the application of return current to the system. Electron temperature exhibits adiabatic cooling and temperature anisotropy but the electrons cool much more compared to their polar wind value. We have only considered cold ionospheric electrons in this simulation. The hydrogen ion drift velocity decreases and hydrogen ion temperature increases. The hydrogen ion temperature still exhibits the polar wind characteristics, i.e., the increase in temperature at the lower end of the tube, temperature anisotropy and adiabatic cooling.				
20 DISTRIBUTION/AVAILABILITY OF ABSTRACT <input checked="" type="checkbox"/> UNCLASSIFIED/UNLIMITED <input type="checkbox"/> SAME AS RPT <input type="checkbox"/> DTIC USERS			21 ABSTRACT SECURITY CLASSIFICATION <b>UNCLASSIFIED</b>	
22a NAME OF RESPONSIBLE INDIVIDUAL <b>J. D. Huba</b>			22b TELEPHONE (Include Area Code) <b>(202) 767-3630</b>	22c OFFICE SYMBOL <b>Code 4780</b>

10. SOURCE OF FUNDING NUMBERS

PROGRAM ELEMENT NO.	PROJECT NO.	TASK NO.	WORK UNIT ACCESSION NO.
61153N	RR033-02-44	W-15494	DN430-607 DN380-475

16. SUPPLEMENTARY NOTATION (Continued)

This research was sponsored by the Office of Naval Research and the National Aeronautics and Space Administration.

## CONTENTS

I. INTRODUCTION .....	1
II. THE MODEL .....	2
III. SIMULATIONS AND RESULTS .....	6
i. Polar Wind Simulation .....	6
ii. Return Current Simulation .....	8
IV. DISCUSSIONS AND SUMMARY .....	11
ACKNOWLEDGMENTS .....	11
REFERENCES .....	31
APPENDIX .....	33





## DYNAMICS OF THE LARGE SCALE RETURN CURRENTS ON AURORAL FIELD LINES

### I. INTRODUCTION

The behavior of plasma on the auroral magnetic field lines has been the subject of a number of studies in recent years. Theoretical models of the polar wind (current free cases) have been developed by Banks and Holzer [1968, 1969], Holzer et al. [1971], Lemaire and Scherer [1973], and Schunk and Watkins [1981, 1982]. Using the 13-moment system of transport equations of Shunk [1977], Schunk and Watkins [1981, 1982] have studied the steady state flow of a fully ionized  $H^+ - O^+ -$  electron plasma along geomagnetic field lines.

Using the same 13-moment system of equations, Mitchell and Palmadesso [1983] developed a dynamic numerical model of the plasma along an auroral field line. The plasma consists of the electrons, hydrogen and oxygen ions. The electrons and the hydrogen ions are the dynamic species in the model. They have performed simulations for the case of a current-free polar wind and the case in which an upward field aligned current was applied along the field line.

However, there has been some recent interest concerning the return currents which motivated us to undertake a numerical study using a computer simulation to investigate the dynamics of the large scale return currents on the auroral field lines. The field aligned return currents flow from the magnetosphere to the ionosphere and are carried by cold electrons of ionospheric origin. It is now well established that the field aligned currents play an important role in the magnetosphere-ionosphere coupling process. In terms of region 1/region 2 large scale field aligned current systems [Iijima and Potemra, 1976] large scale return currents are

Manuscript approved August 12, 1985.

identified as region 1 at the morning sector and region 2 at the evening sector. The typical value of this current-system varies usually from  $1.0 \mu\text{A}/\text{m}^2$  to  $2.0 \mu\text{A}/\text{m}^2$ . Within the region 1/region 2 current system, small-scale distributions of both upward and downward currents are observed in association with auroral arcs.

We have performed simulations to study the dynamics of the large scale return currents on auroral field lines, using the dynamic numerical model of Mitchell and Palmadesso [1983]. The model is a multi-moment approximation of plasma consisting of the electrons, hydrogen ions and oxygen ions along a segment of geomagnetic field line extending from an altitude of 800 km to 10 RE. We compared our results to those of Mitchell and Palmadesso [1983] to study the difference in dynamics of return currents versus upward currents and the current free polar wind case.

We are also interested in the dynamics of auroral field lines including the effects of anomalous transport processes such as anomalous resistivity and associated anisotropic heating. The work is in progress and will be the subject of a future report.

## II. THE MODEL

The field line model of Mitchell and Palmadesso [1983] was designed to dynamically simulate the behavior of the plasma in a flux tube encompassing an auroral field line. The electrons and the hydrogen ions are the dynamic species in the model. The oxygen ions are a static background population

at a constant temperature. The model uses the 13-moment system of transport equations of Schunk [1977]. The distribution function is assumed to be gyrotropic about the field line direction, which reduces the 13-moment approximation to five moments. The five moments are number density, temperatures parallel and perpendicular to the field line, and species velocity and heat flow along the line. The resulting transport equations are as follows:

$$\frac{\partial n_s}{\partial t} = -v_s \frac{\partial n_s}{\partial r} - n_s \frac{\partial v_s}{\partial r} - \frac{n_s v_s}{A} \frac{\partial A}{\partial r} + \frac{\delta n_s}{\delta t} \quad (1)$$

$$\begin{aligned} \frac{\partial v_s}{\partial t} = & -v_s \frac{\partial v_s}{\partial r} - \frac{k}{m_s} \frac{\partial T_{s\parallel}}{\partial r} - \frac{k T_{s\parallel}}{m_s n_s} \frac{\partial n_s}{\partial r} - \frac{k(T_{s\parallel} - T_{s\perp})}{m_s A} \frac{\partial A}{\partial r} \\ & + \frac{e_s}{m_s} E - \frac{GM}{r^2} + \frac{\delta v_s}{\delta t} \end{aligned} \quad (2)$$

$$k \frac{\partial T_{s\parallel}}{\partial t} = -v_s k \frac{\partial T_{s\parallel}}{\partial r} - 2kT_{s\parallel} \frac{\partial v_s}{\partial r} - \frac{6}{5n_s} \frac{\partial q_s}{\partial r} - \frac{2}{5} \frac{q_s}{n_s A} \frac{\partial A}{\partial r} + k \frac{\delta T_{s\parallel}}{\delta t} \quad (3)$$

$$k \frac{\partial T_{s\perp}}{\partial t} = -v_s k \frac{\partial T_{s\perp}}{\partial r} - \frac{2}{5n_s} \frac{\partial q_s}{\partial r} - \left( \frac{4}{5} \frac{q_s}{n_s} + v_s k T_{s\perp} \right) \frac{1}{A} \frac{\partial A}{\partial r} + k \frac{\delta T_{s\perp}}{\delta t} \quad (4)$$

$$\begin{aligned}
\frac{\partial q_s}{\partial t} = & -v_s \frac{\partial q_s}{\partial r} - \frac{16}{5} q_s \frac{\partial v_s}{\partial r} - \left( \frac{11}{18} T_{s\parallel} + \frac{8}{9} T_{s\perp} \right) \frac{n_s k^2}{m_s} \frac{\partial T_{s\parallel}}{\partial r} \\
& - \left( \frac{17}{9} T_{s\parallel} - \frac{8}{9} T_{s\perp} \right) \frac{n_s k^2}{m_s} \frac{\partial T_{s\perp}}{\partial r} + \frac{4k^2}{9m_s} (T_{s\parallel} - T_{s\perp})^2 \frac{\partial n_s}{\partial r} \\
& + \left[ \frac{n_s k^2}{m_s} (T_{s\parallel} - T_{s\perp}) \left( \frac{1}{3} T_{s\parallel} - \frac{4}{3} T_{s\perp} \right) - \frac{7}{5} v_s q_s \right] \frac{1}{A} \frac{\partial A}{\partial r} + \frac{\delta q_s}{\delta t}
\end{aligned} \tag{5}$$

where,  $n_s$  is the number density of the species  $s$ ,

$v_s$  is the velocity,

$T_{s\parallel}$  is the parallel temperature,

$T_{s\perp}$  is the perpendicular temperature,

$q_s$  is the heat flow,

$m_s$  is the mass,

$e_s$  is the charge of species  $s$ ,

$A$  is the cross-sectional area of the flux tube,

$E$  is the electric field parallel to the field line,

$k$  is Boltzmann's constant,

$G$  is the gravitational constant and

$M$  is the mass of the earth.

The collision terms used in the present simulation are Burgers' [1979] collision terms for the case of Coulomb collisions with corrections for

finite species' velocity differences, and are given in Appendix I.

The scale of this model is large compared to the electron Debye length, so the transport equation (1) for electron number density may be replaced by an expression for charge neutrality:

$$n_e = n_p + n_o \quad (6)$$

We have assumed that the total flux tube current I remains constant

$$I = eA(n_p v_p - n_e v_e) \quad (7)$$

which implies,

$$v_e = \frac{1}{n_e} (n_p v_p - \frac{I}{eA}) \quad (8)$$

Using equations (2), (7) and (8) the electric field E parallel to the field line is calculated.

$$E = \frac{m_s}{en_e A} \frac{\partial}{\partial r} (n_p v_p^2 A - n_e v_e^2 A) - \frac{k}{e} \left[ \frac{\partial T_{e\parallel}}{\partial r} + \frac{T_{e\parallel}}{n_e} \frac{\partial n_e}{\partial r} \right. \\ \left. + \frac{(T_{e\parallel} - T_{e\perp})}{A} \frac{\partial A}{\partial r} \right] - \frac{n_o m_{GM}}{n_e r^2} + \frac{m_e}{e} \left[ \frac{\delta v_e}{\delta t} - \frac{n_p}{n_e} \frac{\delta v_p}{\delta t} \right], \quad (9)$$

### III. SIMULATIONS AND RESULTS

In order to perform the field aligned current simulation we have to perform the current free polar wind simulation first to be used as the initial steady state of the flux tube. This was also done by Mitchell and Palmadesso and will be described briefly here.

#### 1. Polar Wind Simulation (Zero Current)

The polar wind simulation was carried out for a current-free case. The lower boundary is fixed at 800 km. The simulation was carried up to an altitude of 10 RE on an unequally spaced grid. The cell size is small at the lower end of the field line in order to study the transport effects in the presence of the large density gradients due to the small scale height of oxygen and satisfy stability conditions. The flux tube plasma consisting of the hydrogen ions, oxygen ions and the electrons was initialized at a constant temperature of 2000°K. The initial conditions used are those of Mitchell and Palmadesso [1983].

In the polar wind, the hydrogen ions are accelerated upwards in the flux tube to supersonic velocities due to the flux tube divergence and the small partial pressure of  $H^+$  at the upper end of the field line. In steady state polar wind models the hydrogen ion velocity can be either subsonic or supersonic. To date only the supersonic polar wind has been observed. The oxygen ions are the dominant species up to an altitude of around 3500 km. The ambipolar electric field value produces the sharp increase in the

hydrogen ion velocity at the lower end of the flux tube. In the steady state the electrons and the hydrogen ions reach the same maximum velocity, as it is clear from equation (8). This is shown in figure (1b). The total flux along the flux tube is conserved, i.e.,  $nVA = \text{constant}$ . Therefore, as the velocity and the area increase with altitude the density should decrease. The hydrogen ion density decreases as it flows through the diverging flux tube, shown in figure (1a). The electron density also decreases, due to charge neutrality equation (6) .

The hydrogen ion temperature (shown in figure 1c) exhibits three interesting characteristics:

- (1) The temperature increases at the lower end of the tube.
- (2) Adiabatic cooling - supersonic ion gas cools down as it expands in a diverging magnetic field.
- (3) Temperature anisotropy.

The temperature increase is caused by Joule heating of the hydrogen from collisions with the oxygen ions. This effect becomes weaker with increasing altitude due to small scale height of the oxygen. As a result, the hydrogen ion temperature profiles show an increase in temperature before it exhibits adiabatic cooling. The temperature anisotropy develops around 2500 km and is caused by the mirror effect where the perpendicular energy is transferred to the parallel energy.

The electron temperature profiles (shown in figure 1d) exhibit :

- (1) Adiabatic cooling,
- (2) Temperature anisotropy.

However, the latter effect is more prominent in the hydrogen ion temperature profiles. The electron thermal velocity is much higher than the electron bulk flow velocity, hence thermal conductivity is more

effective at reducing flow related temperature anisotropies and gradients for electrons.

It is also noted that when the drift velocity of the hydrogen ions is equal to that of electrons the hydrogen ions cool much more than the electrons. The hydrogen ion temperature profiles maintain significant gradients at high altitudes and exhibit large temperature anisotropies at the upper end of the flux tube.

Mitchell and Palmadesso [1983] compared the results of their polar wind simulation with the previous studies of the polar wind by Schunk and Watkins [1982] and Banks and Holzer [1971] and the results were found to be in good agreement.

## ii. Return Current Simulation

In this section we discuss our results of the field aligned return current simulation and compare those with the polar wind (zero current) case as described in Section I and with the upward current case studied by Mitchell and Palmadesso [1983].

Using the polar wind simulation as the initial steady state of the flux tube, simulations were performed with return currents with a minimum value of  $-1.0 \mu\text{A}/\text{m}^2$  and a peak value of  $-2.0 \mu\text{A}/\text{m}^2$ .

We will first discuss the case where a current of  $-1.0 \mu\text{A}/\text{m}^2$  was applied. With the onset of the current the electron velocity increases with altitude (figure 2). The electron temperature profile still exhibits adiabatic cooling and temperature anisotropy, but since the electron velocity is much higher in this case as compared to the polar wind value,



the electrons cool much more rapidly with increasing altitude. The electron temperature gradient decreases. Notice that here we have only considered cold electrons of ionospheric origin, like Mitchell and Palmadesso [1983]. The electron temperature profiles are shown at time intervals of ten, thirty, fifty and seventy minutes on figures 3(a), 3(b) 3(c) and 3(d), where the response of electron temperature profiles with time are clearly observed. We compared our results with the upward current case of Mitchell and Palmadesso [1983] and notice that unlike the effects of return currents the application of upward current reduces the electron velocity and increases the total electron temperature. In the latter case the electrons are heated in the lower end of the flux tube and the temperature gradient results in a large upward electron heat flow and electron thermal wave propagating up the field line.

The electric field maintains the same profile as before but decreases in magnitude from the polar wind value thereby decreasing the hydrogen ion velocity. This is unlike the upward current case of Mitchell and Palmadesso [1983], where the ambipolar electric field increases by an order of magnitude accelerating the hydrogen ions upwards. The decrease in  $H^+$  velocity causes a velocity ripple which in turn produces an  $H^+$  density depletion and these propagate upwards through the flux tube as the simulation was carried on at later times. Due to the current conservation requirement, the electron velocity increases at the density depletion, and hence the upward propagating velocity ripple is also noticed in the electrons. This effect is clearly seen for times ten, thirty, fifty and seventy minutes after the onset of the current as shown in figures 2(a), 2(b), 2(c) and 2(d). After the velocity ripples pass through the flux tube, the electron velocity settles down at a lower value than before (but

much higher than the polar wind value) in order to maintain the current  $I$  constant. Also, the velocity of the hydrogen ions decreases at the upper end of the flux tube. As before the anisotropy of cooling is evident in the hydrogen ions but the hydrogen parallel and perpendicular temperatures increase as the  $H^+$  ion velocity decreases. The ripple in velocity produces a ripple in the temperature which, like the velocity ripple, also flows up the flux tube with time. The hydrogen ion temperature profiles are shown on figures 4(a), 4(b), 4(c) and 4(d) at ten, thirty, fifty and seventy minutes after the onset of the current.

Simulations were then performed with higher currents up to a peak current of  $\sim 2.0 \mu A/m^2$ . The electron velocity increases with the increase of current (shown in figure 5a), and the electron temperature still exhibits adiabatic cooling and temperature anisotropy (figure 5b). The ambipolar electric field decreases, further decreasing the  $H^+$  velocity (figure 5a). Velocity ripples are observed as before and these propagate through the flux tube as seen in later runs (that is, ten, thirty, fifty and seventy minutes after the onset of this current). To conserve the current flowing in the system, the electron velocity decreases (after the ripple flows out through the tube) with the decrease in hydrogen ion velocity. However, compared to the previous case, the electron velocity still remains at a higher value, while the  $H^+$  ion velocity decreases. The hydrogen ion temperature profile for this current is shown in figure 5(c).

#### IV. DISCUSSIONS AND SUMMARY

We have used a dynamic numerical model to investigate the plasma dynamics in the presence of large scale field aligned return currents. We have also compared our results with those of the current-free polar wind and upward current simulations.

The flux tube plasma has a rapid initial response to the onset of the current. The electron velocity and temperature have rapid response to sudden change in conditions with a time constant of about few minutes. Also, the behavior of the energy transport in the collisionless region determines the time scales on which the flux tube plasma reaches equilibrium.

In this paper we have only considered cold electrons of ionospheric origin. Similar studies of return currents using hot magnetospheric electrons at the upper boundary are in progress and will be the subject of a future report. Kindel and Kennel [1971] examined several current driven instabilities and showed that electrostatic ion cyclotron instability has the lowest threshold. Our simulations show that the electron drift velocity corresponding to a current of  $-1.0 \mu\text{A}/\text{m}^2$  is above the threshold for electrostatic ion cyclotron waves. The effects of anomalous resistivity and anisotropic ion heating arising due to EIC instability will be discussed in a future article.

#### Acknowledgments

This work was supported by the Office of Naval Research and the National Aeronautics and Space Administration.

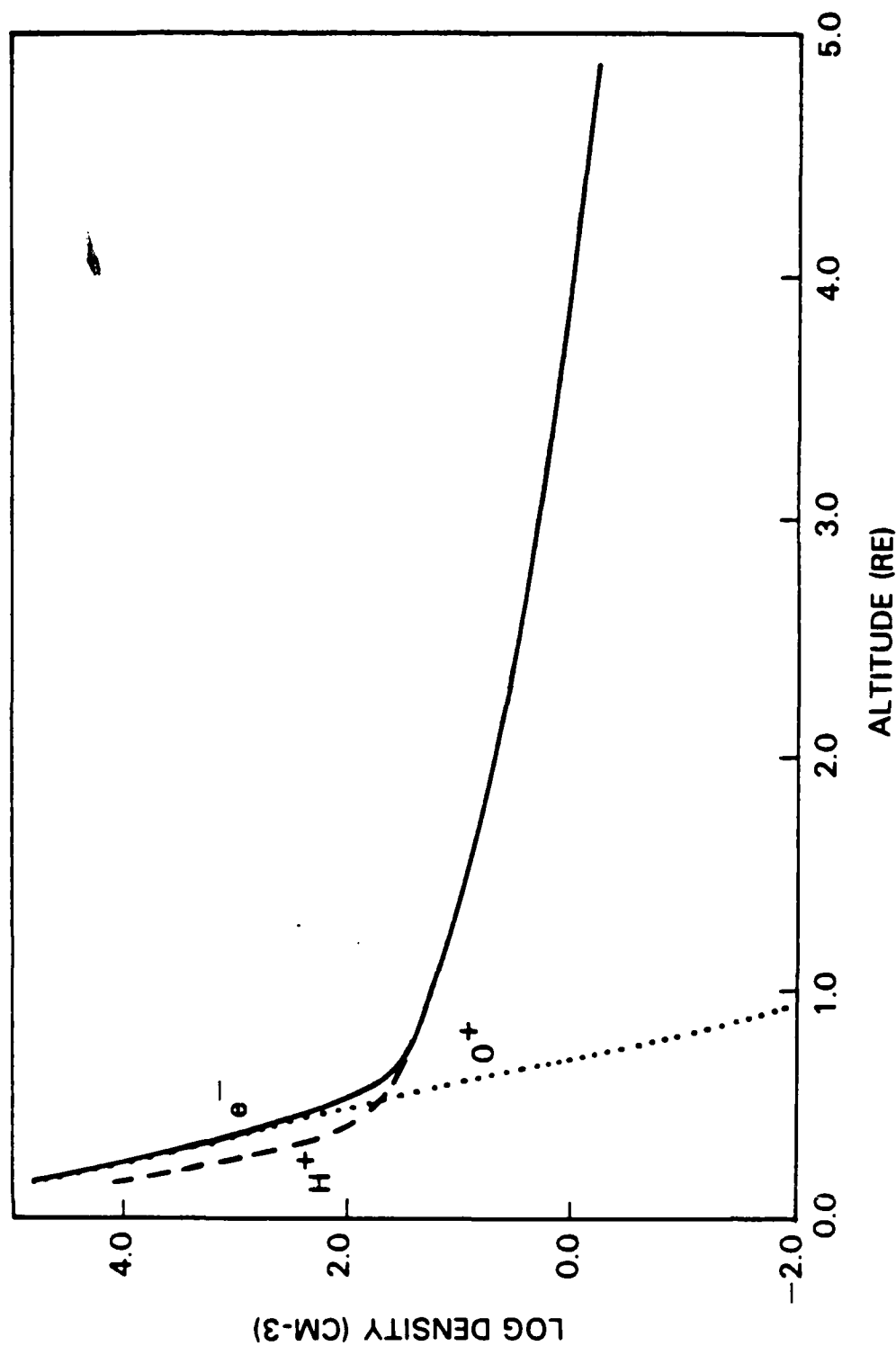


Figure 1. (a) Densities for the steady-state polar wind with no field-aligned current: electrons (solid curve),  $H^+$  (dashed curve),  $O^+$  (dotted curve).

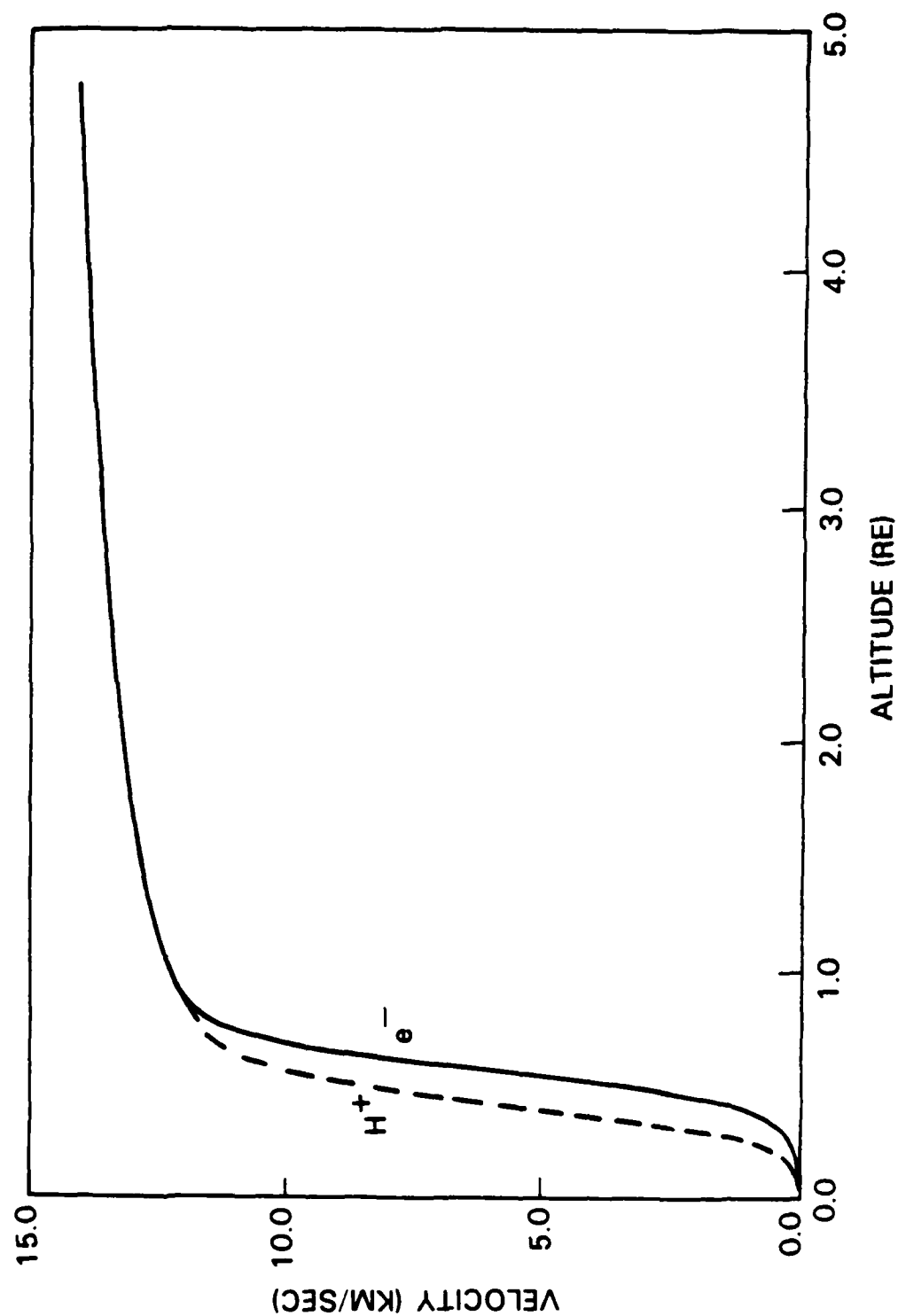


Figure 1. (b) Velocities for the steady-state polar wind with no field-aligned current:  $e^-$  (solid curve),  $H^+$  (dashed curve). The oxygen ion velocity is uniformly zero.

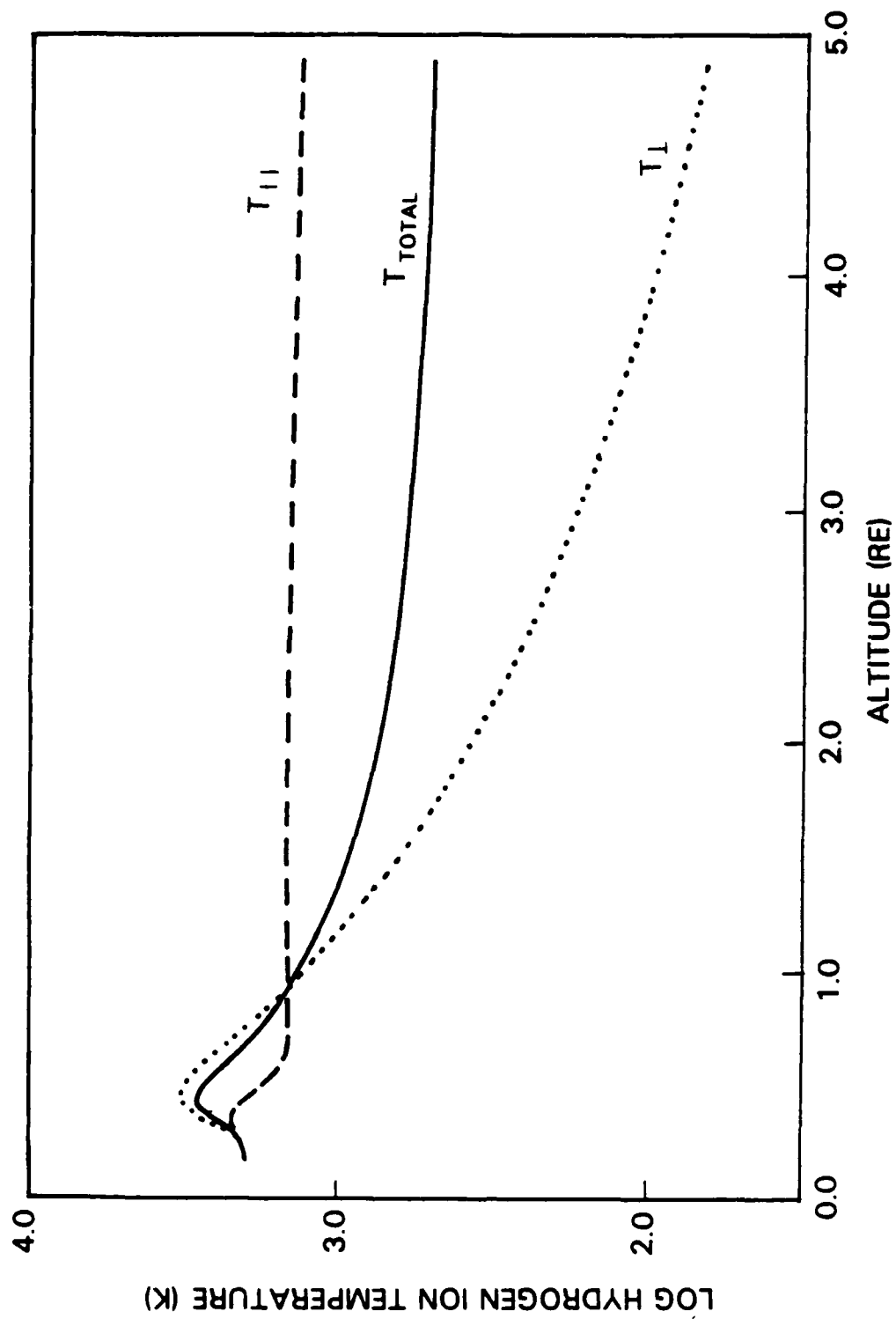


Figure 1. (c) Hydrogen ion temperatures for the steady-state polar wind with no field-aligned current: total temperature (solid curve),  $T_{II}$  (dashed curve),  $T_I$  (dotted curve).

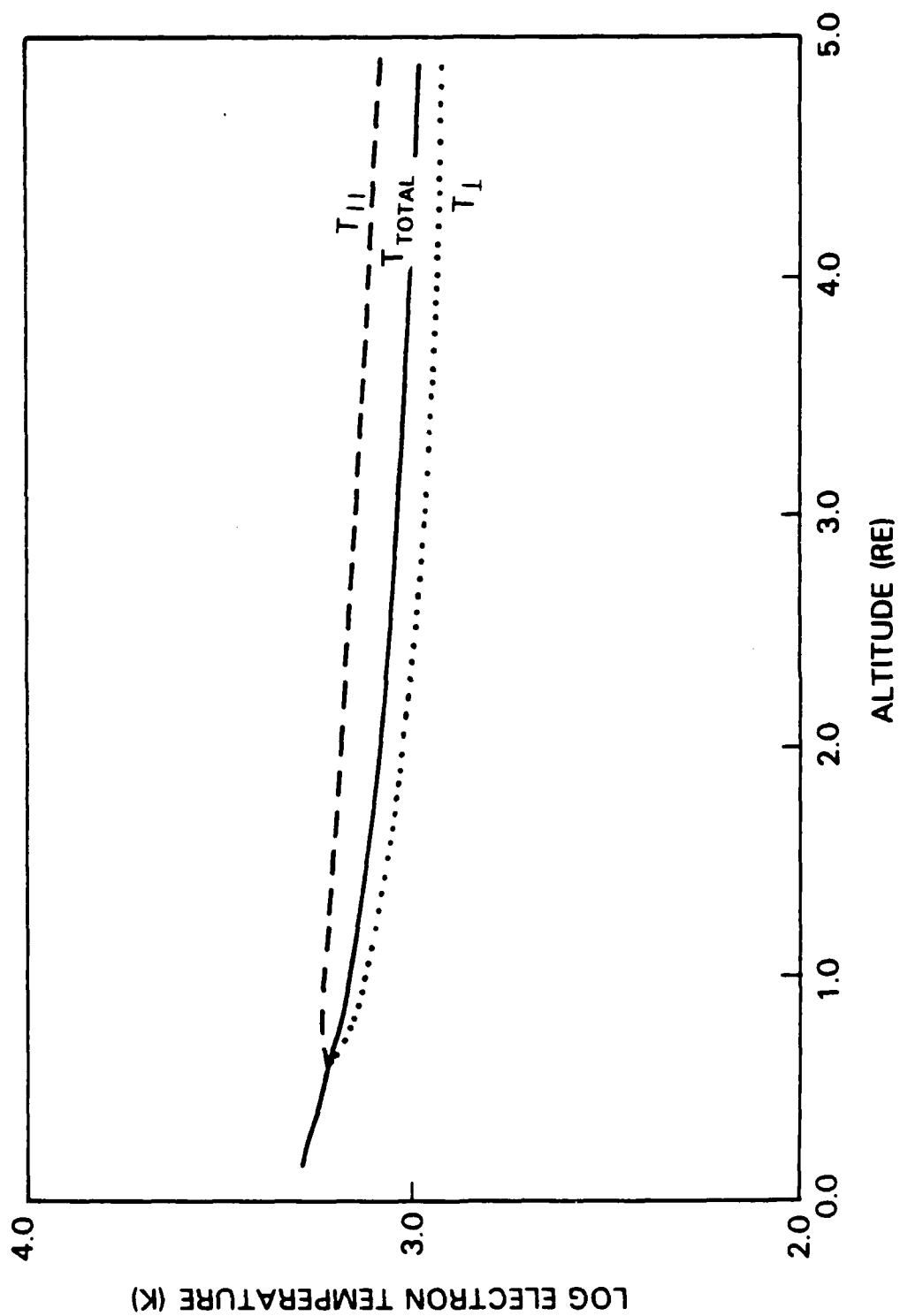


Figure 1. (d) Electron temperatures for the steady-state polar wind with no field-aligned current: total temperature (solid curve),  $T_{II}$  (dashed curve),  $T_I$  (dotted curve).

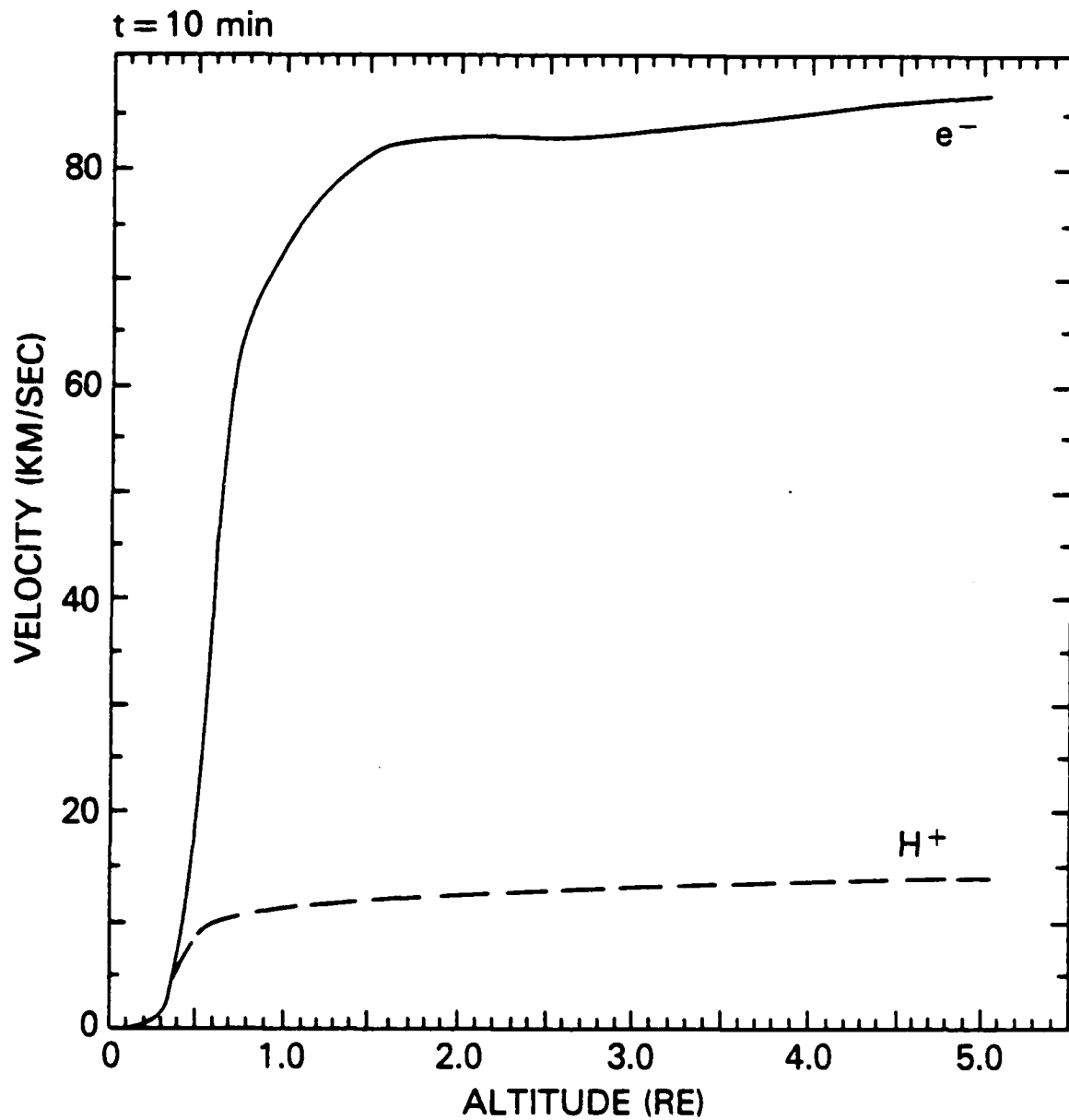


Figure 2. (a). Velocities after 10 minutes after the onset of a current of  $-1.0 \mu\text{A}/\text{m}^2$  at 1500 km:  $e^-$  (solid curve),  $H^+$  (dashed curve).



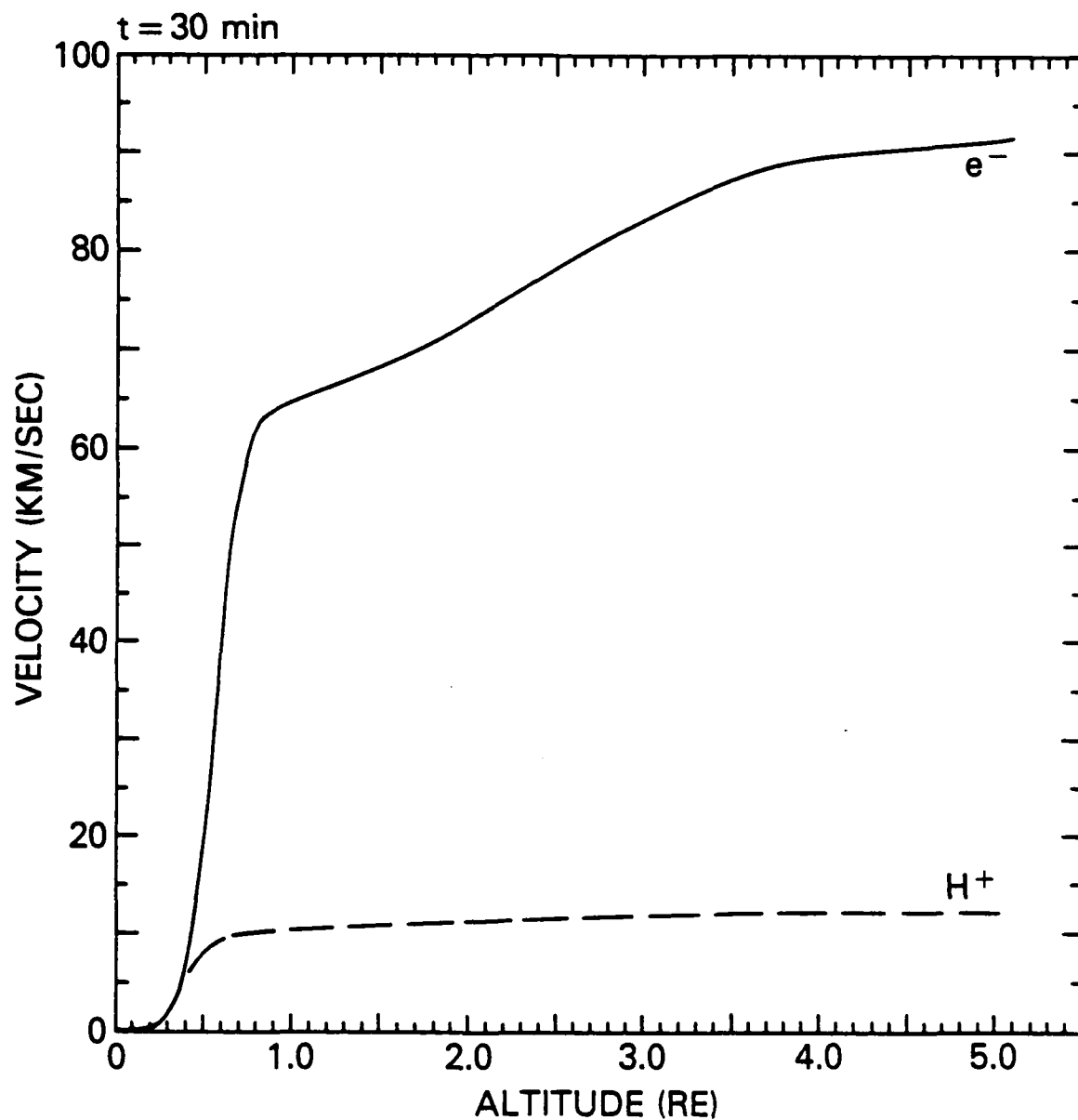


Figure 2. (b) Velocites after 30 minutes after the onset of a current of  $-1.0 \mu\text{A}/\text{m}^2$  at 1500 km:  $e^-$  (solid curve),  $H^+$  (dashed curve).

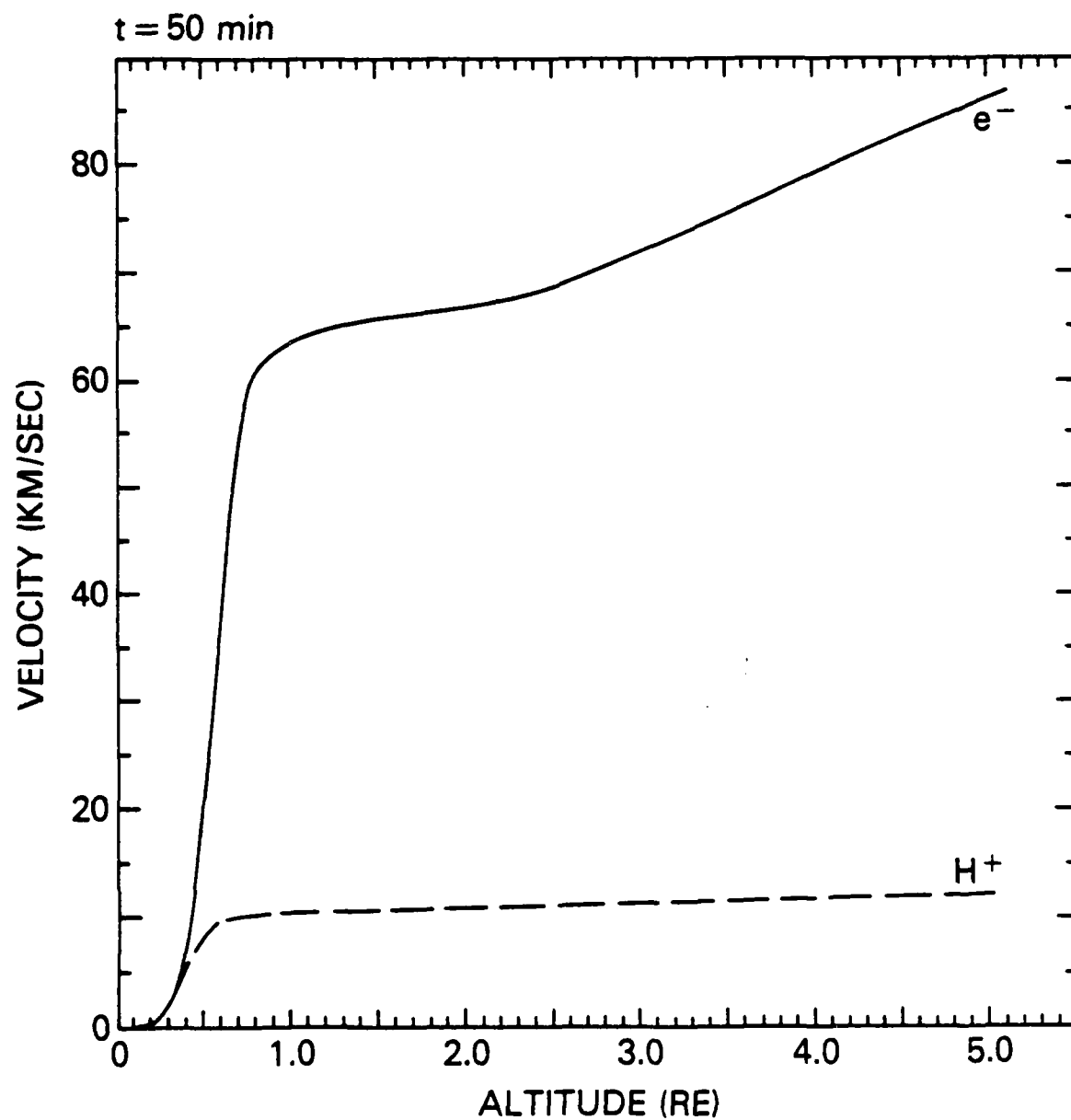


Figure 2. (c) Velocities after 50 minutes after the onset of a current of  $-1.0 \mu\text{A}/\text{m}^2$  at 1500 km:  $e^-$  (solid curve),  $H^+$  (dashed curve).

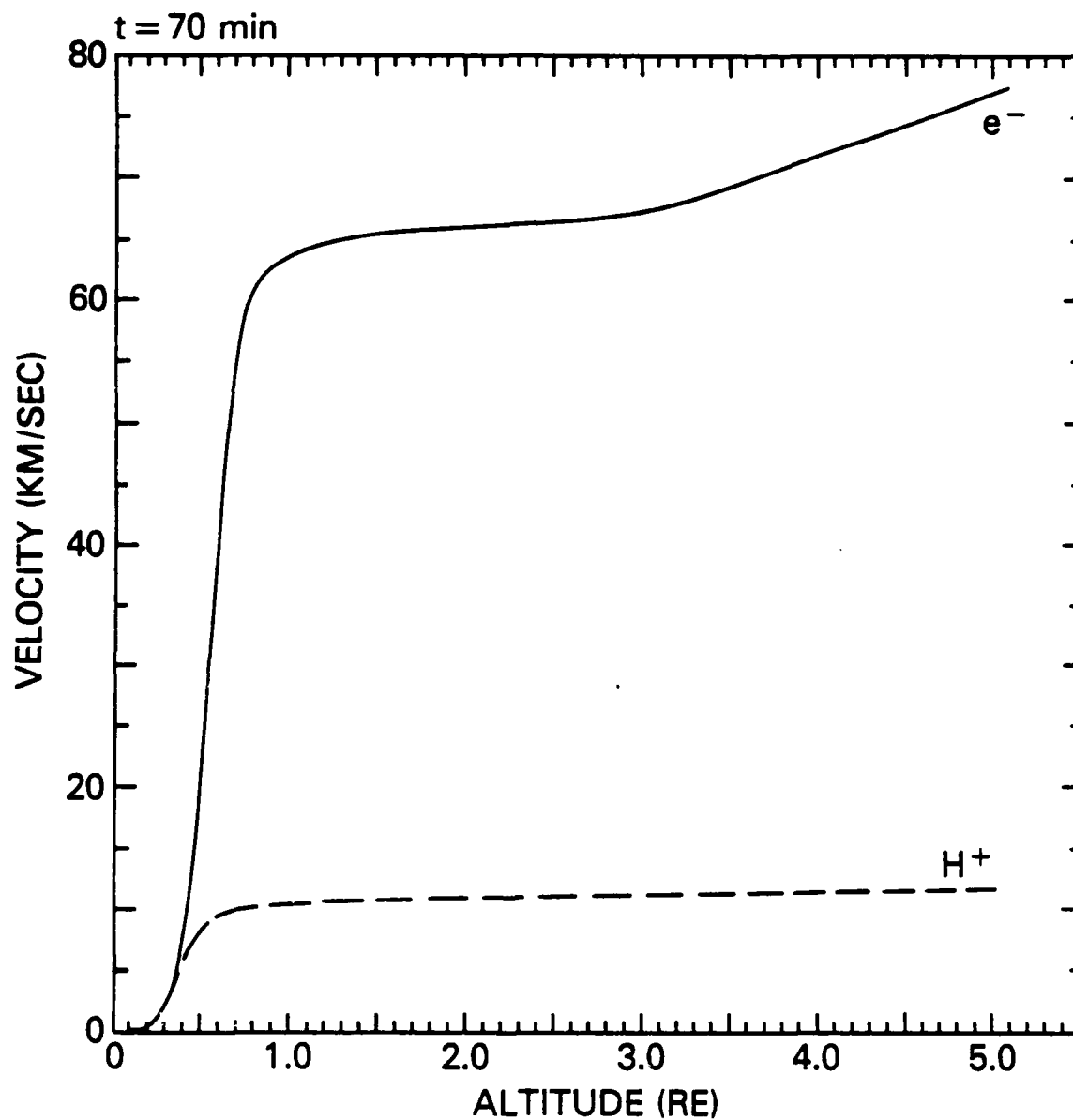


Figure 2. (d) Velocities after 70 minutes after onset of a current of  $-1.0 \mu\text{A}/\text{m}^2$  at 1500 km:  $e^-$  (solid curve),  $H^+$  (dashed curve).

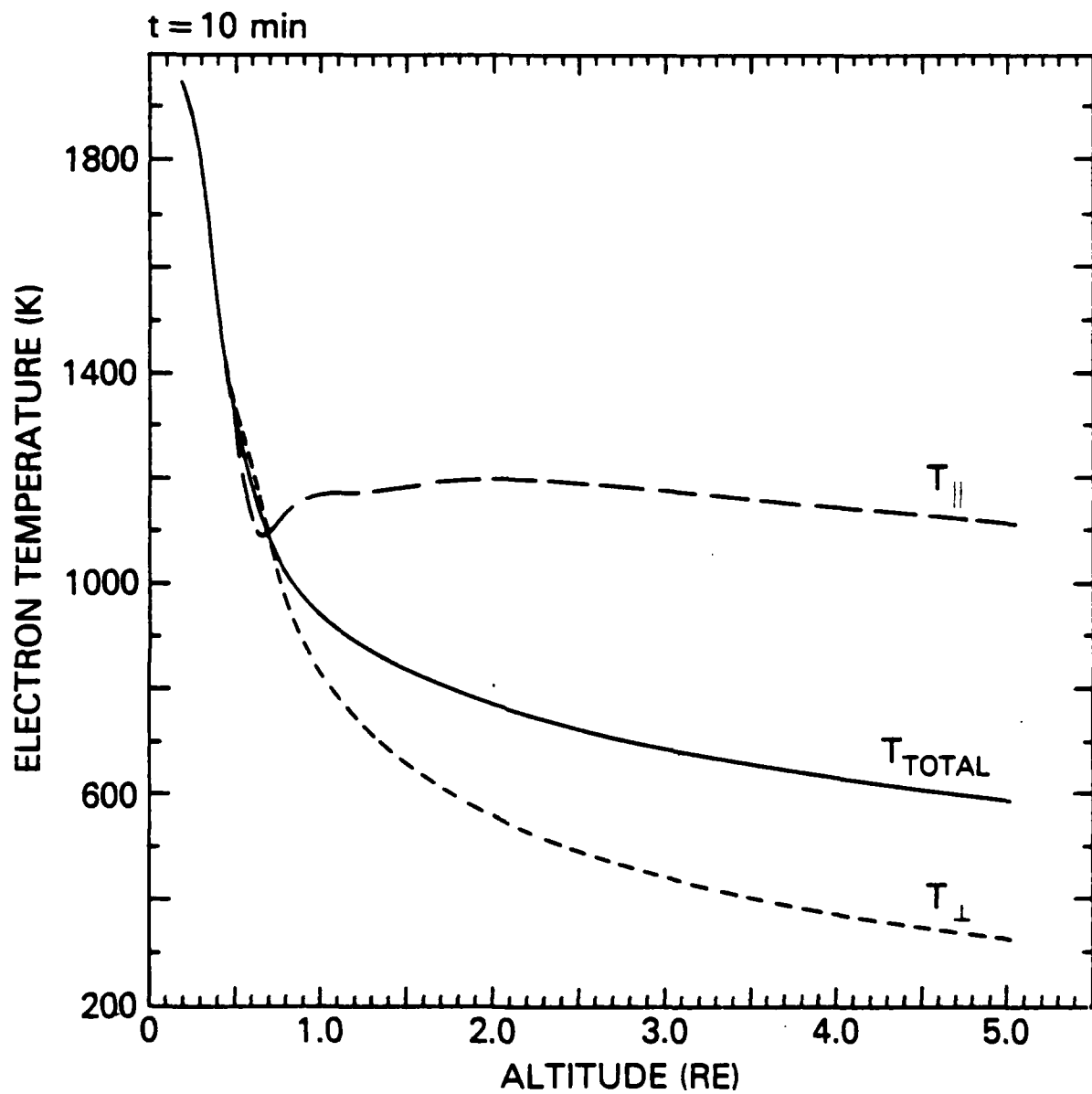


Figure 3. (a) Electron temperatures 10 minutes after the onset of a current of  $-1.0 \mu\text{A}/\text{m}^2$  at 1500 km: total temperature (solid curve),  $T_{\parallel}$  (dashed curve),  $T_{\perp}$  (dotted curve).

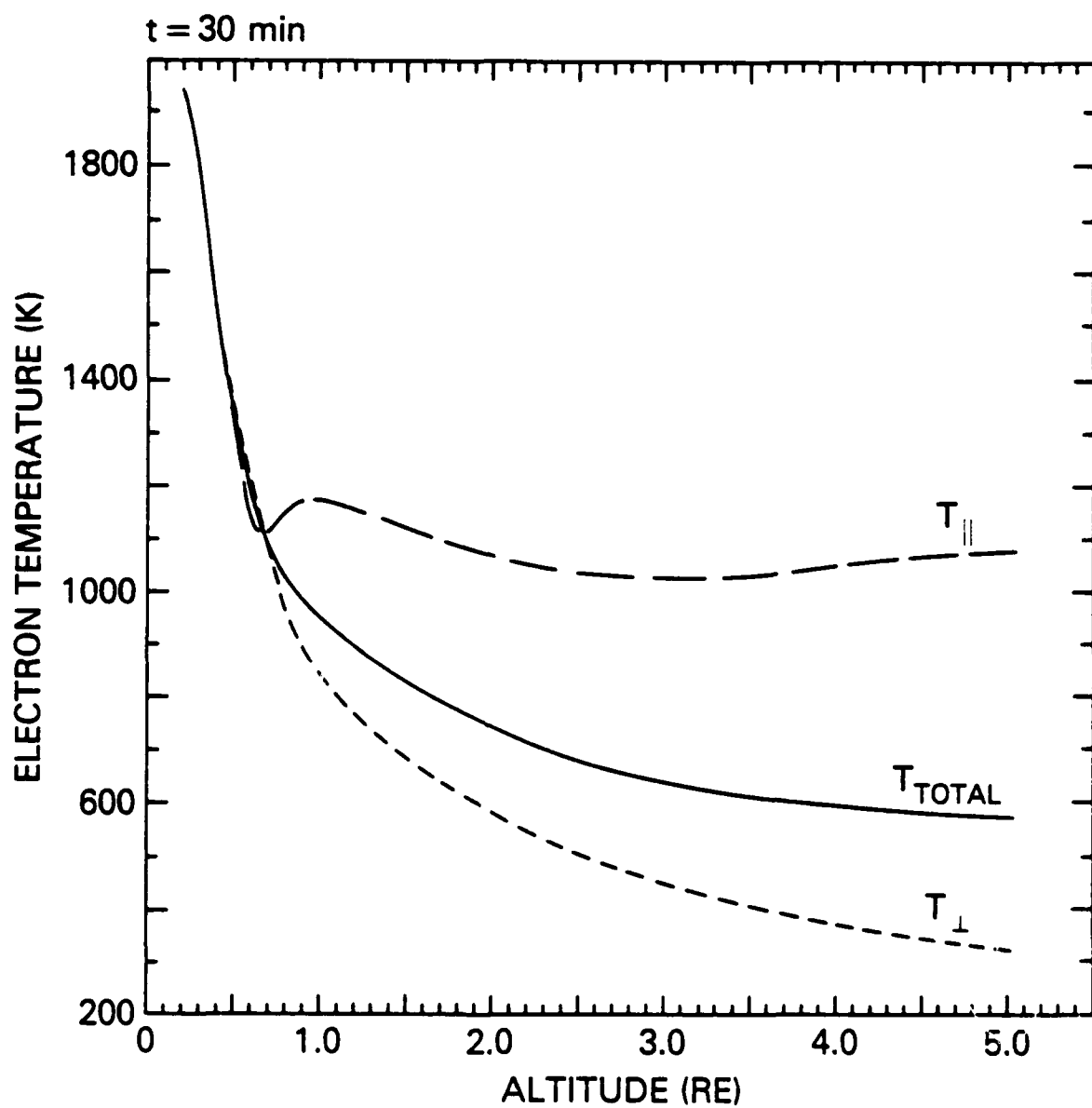


Figure 3. (b) Electron temperatures 30 minutes after onset of a current of  $-1.0 \mu\text{A}/\text{m}^2$ .

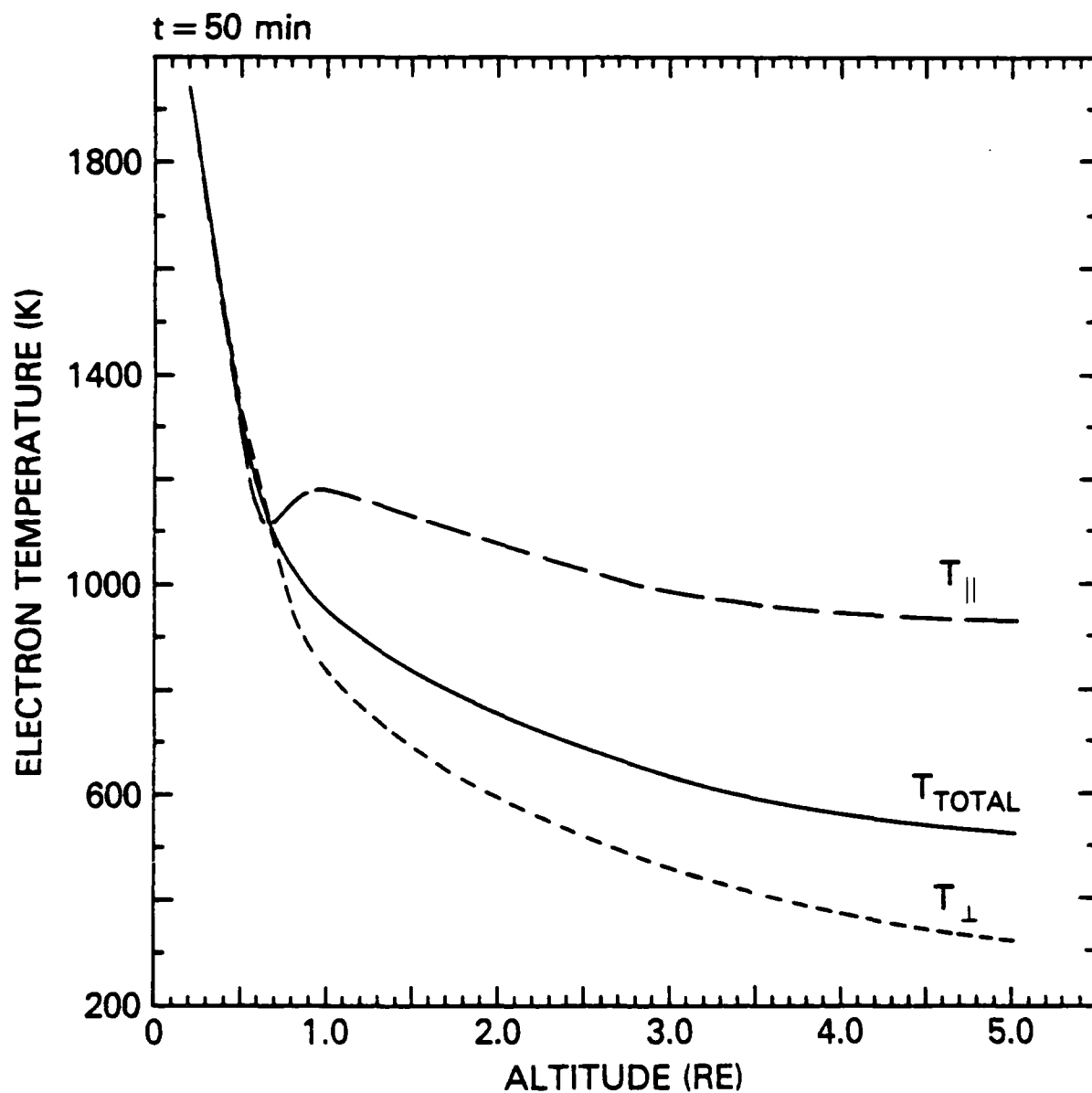


Figure 3. (c) Electron temperatures 50 minutes after onset of a current of  $-1.0 \mu\text{A}/\text{m}^2$ .

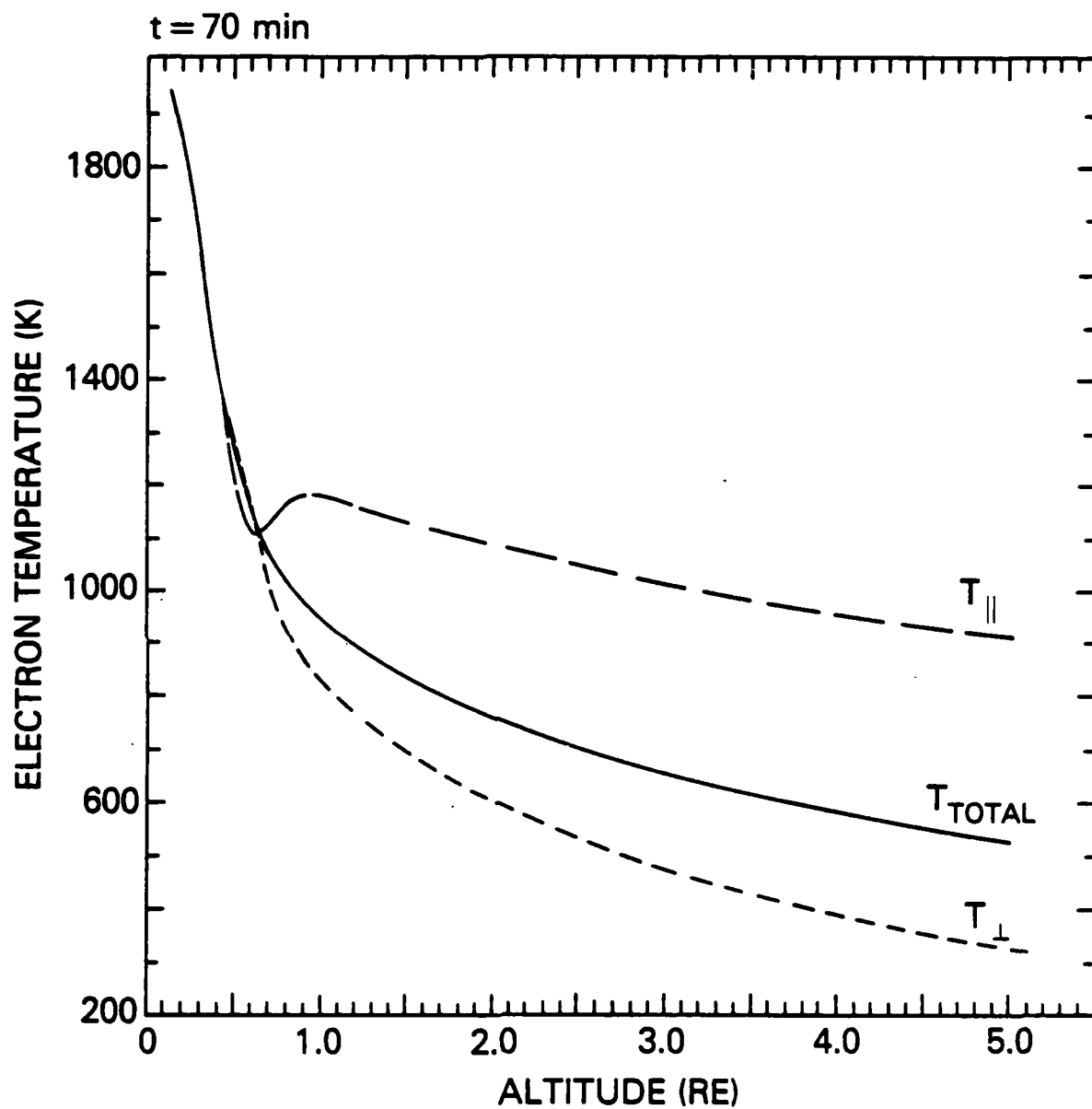


Figure 3. (d) Electron temperatures 70 minutes after onset of a current of  $-1.0 \mu\text{A}/\text{m}^2$ .

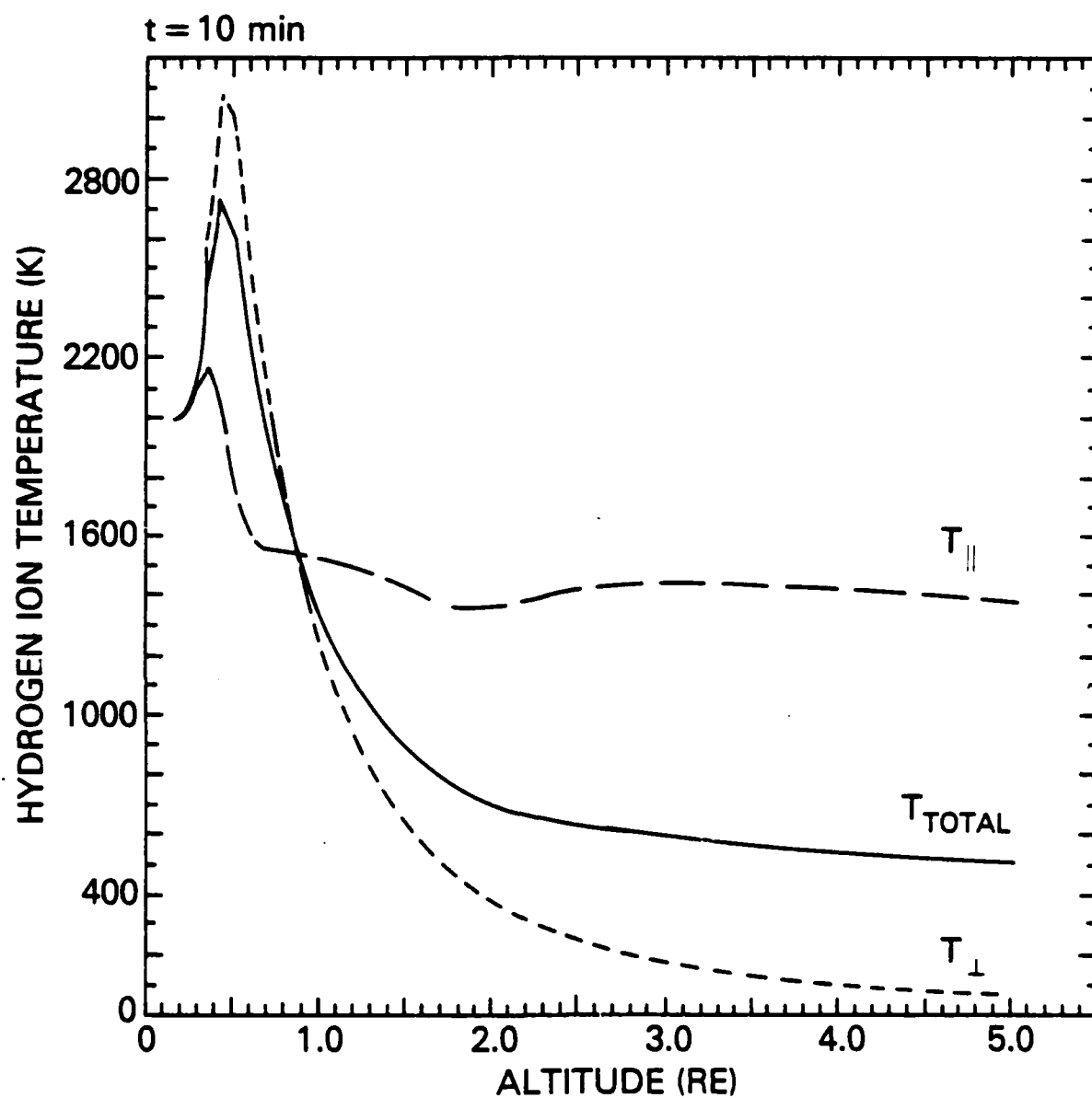


Figure 4. (a) Hydrogen ion temperatures 10 minutes after the onset of a current of  $-1.0 \mu\text{A}/\text{m}^2$ . 1500 km: total temperature (solid curve),  $T_{\parallel}$  (dashed curve),  $T_{\perp}$  (dotted curve).



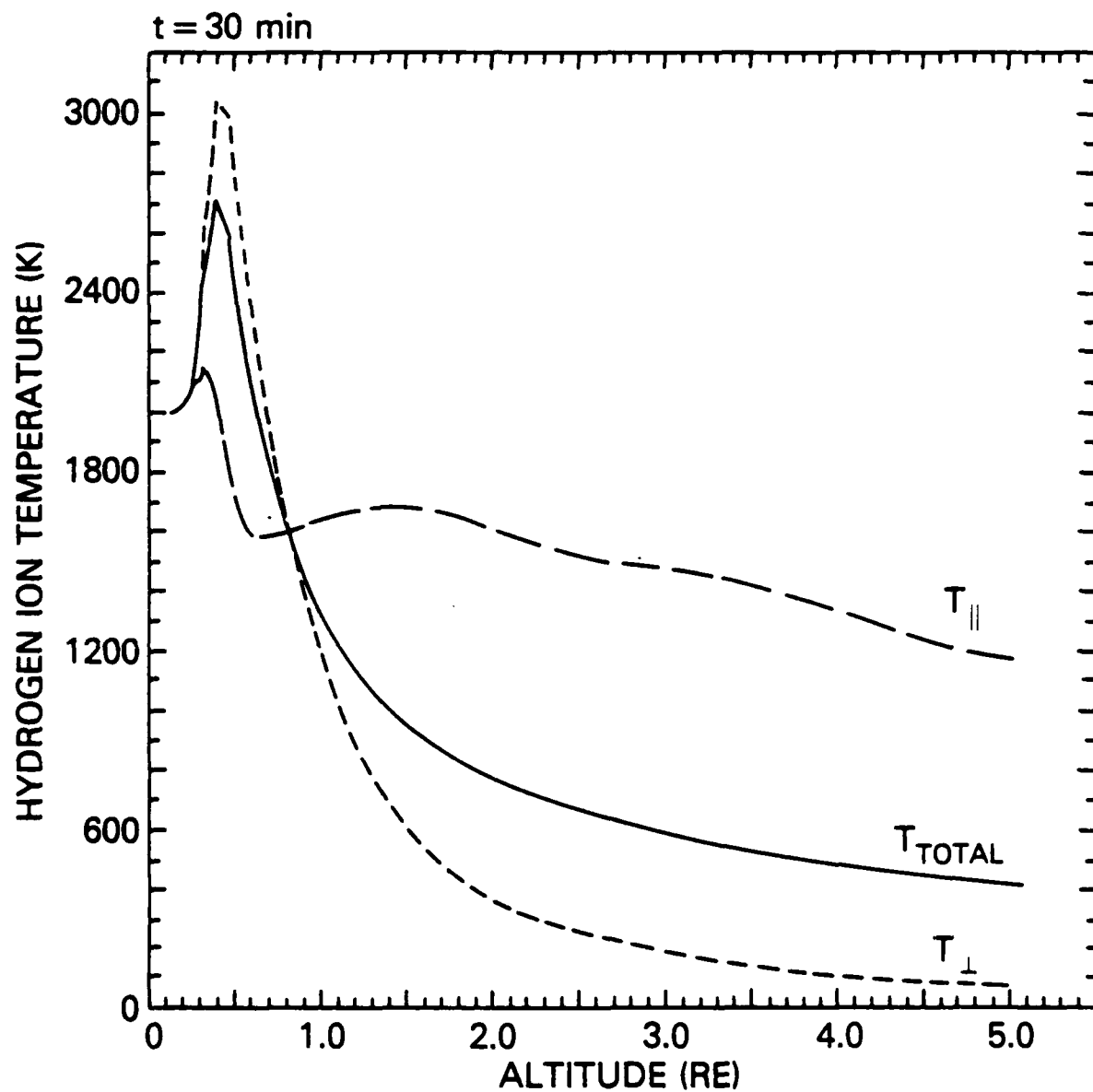


Figure 4. (b) Hydrogen ion temperature 30 minutes after the onset of a current of  $-1.0 \mu\text{A}/\text{m}^2$ .

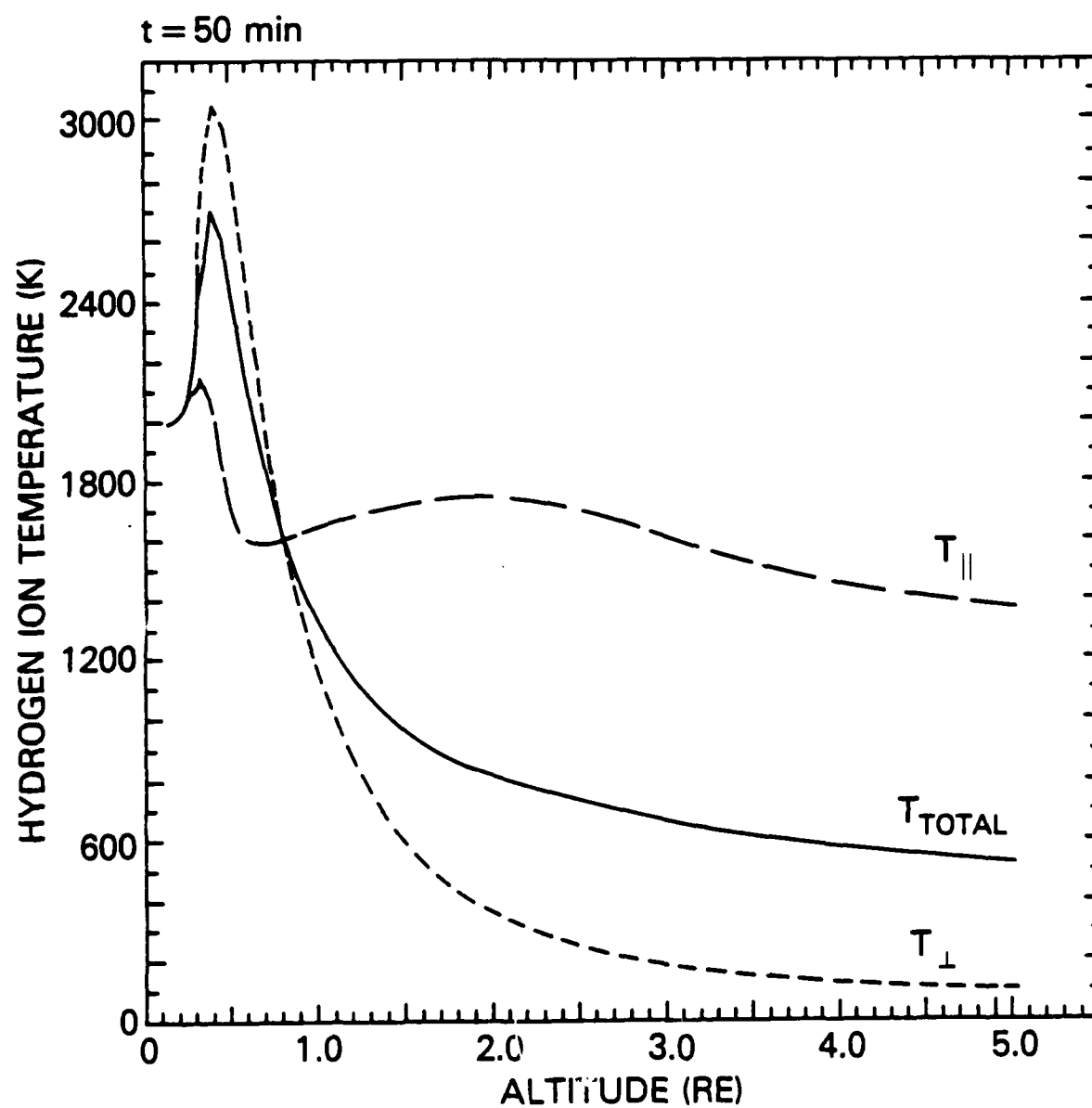


Figure 4. (c) Hydrogen ion temperature 50 minutes after the onset of a current of  $-1.0 \mu\text{A}/\text{m}^2$ .

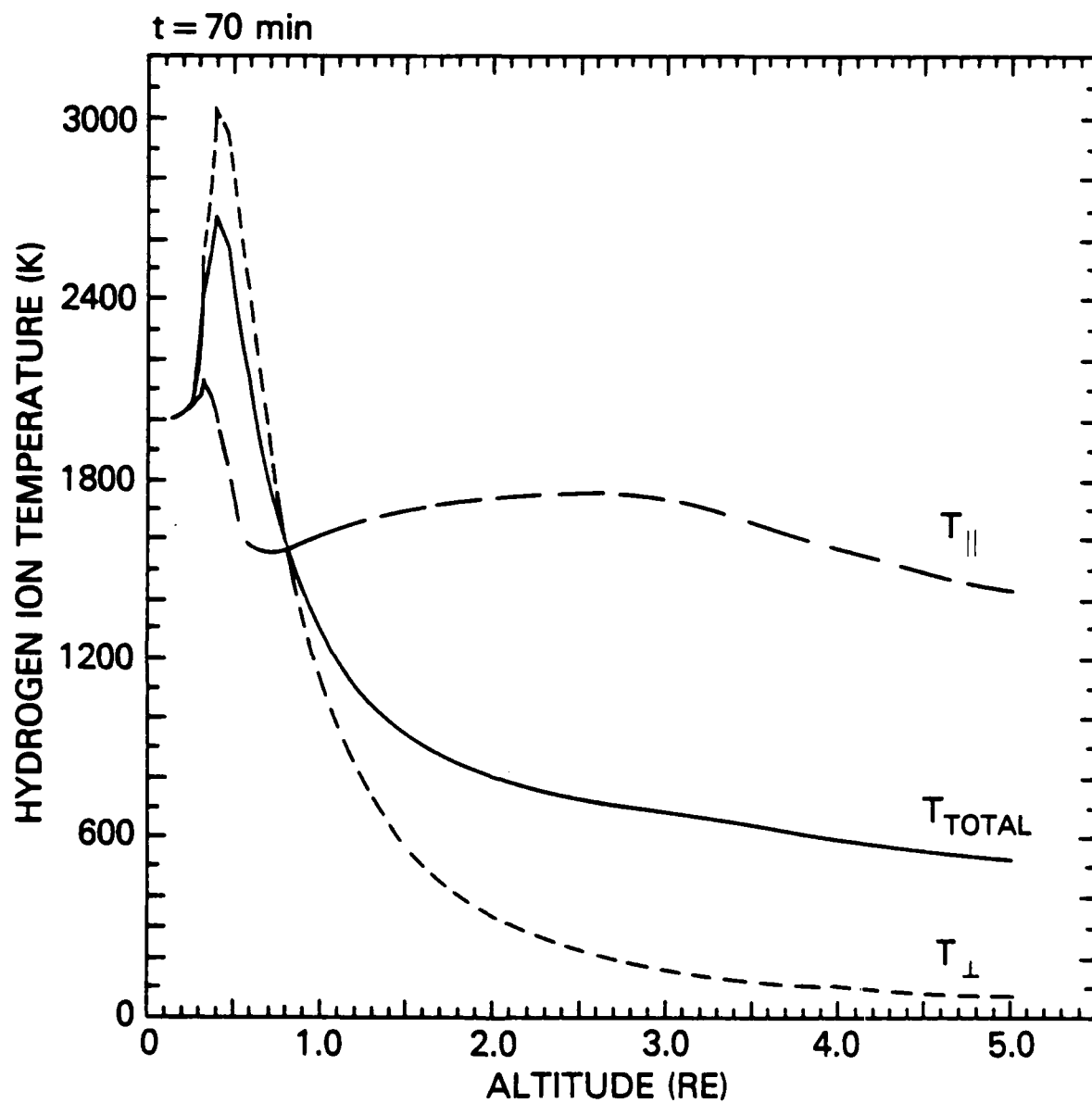


Figure 4. (d) Hydrogen ion temperature 70 minutes after the onset of a current of  $-1.0 \mu\text{A}/\text{m}^2$ .

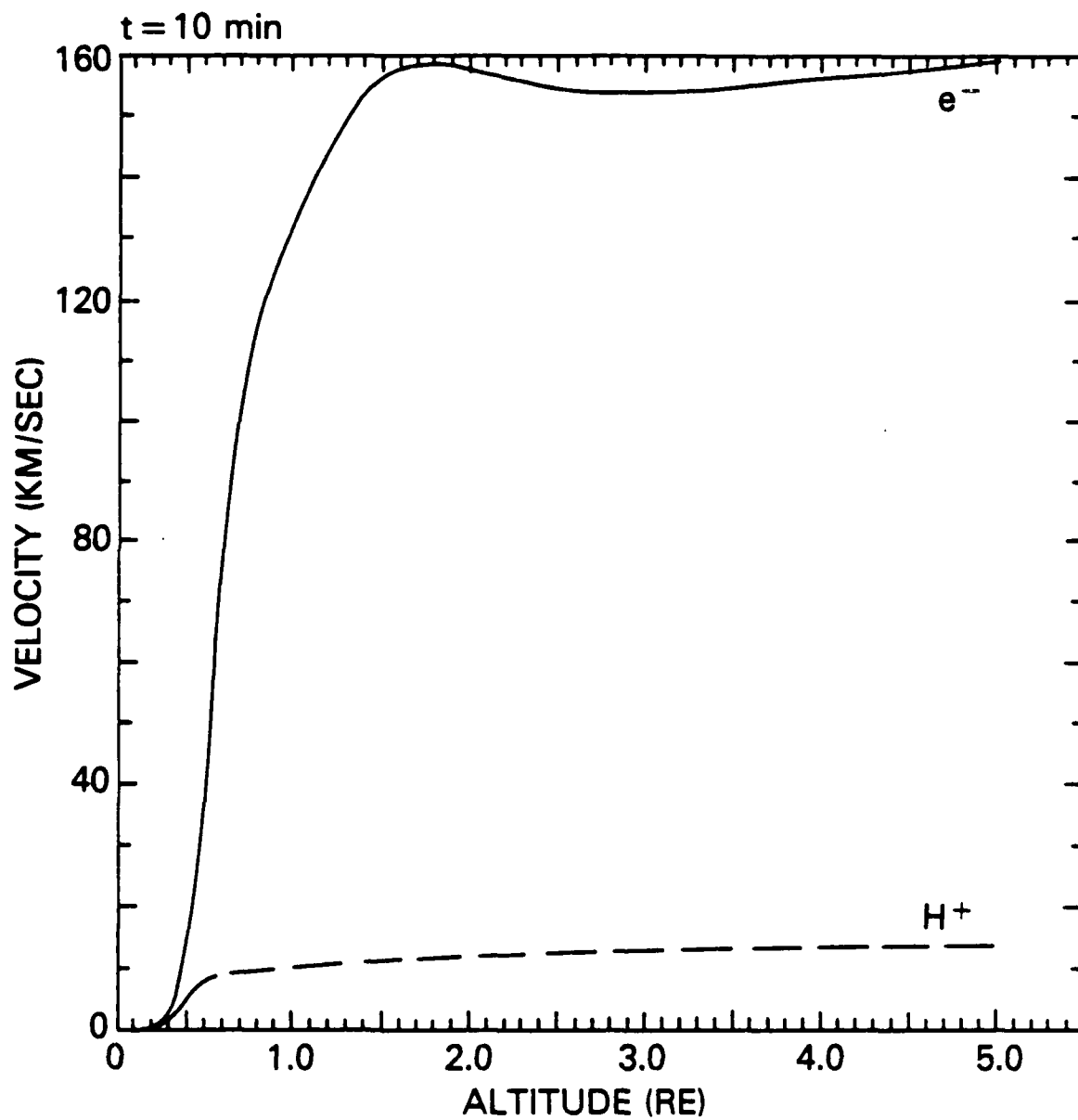


Figure 5. (a) Velocities after 10 minutes after the onset of a current of  $-2.0 \mu\text{A}/\text{m}^2$ .

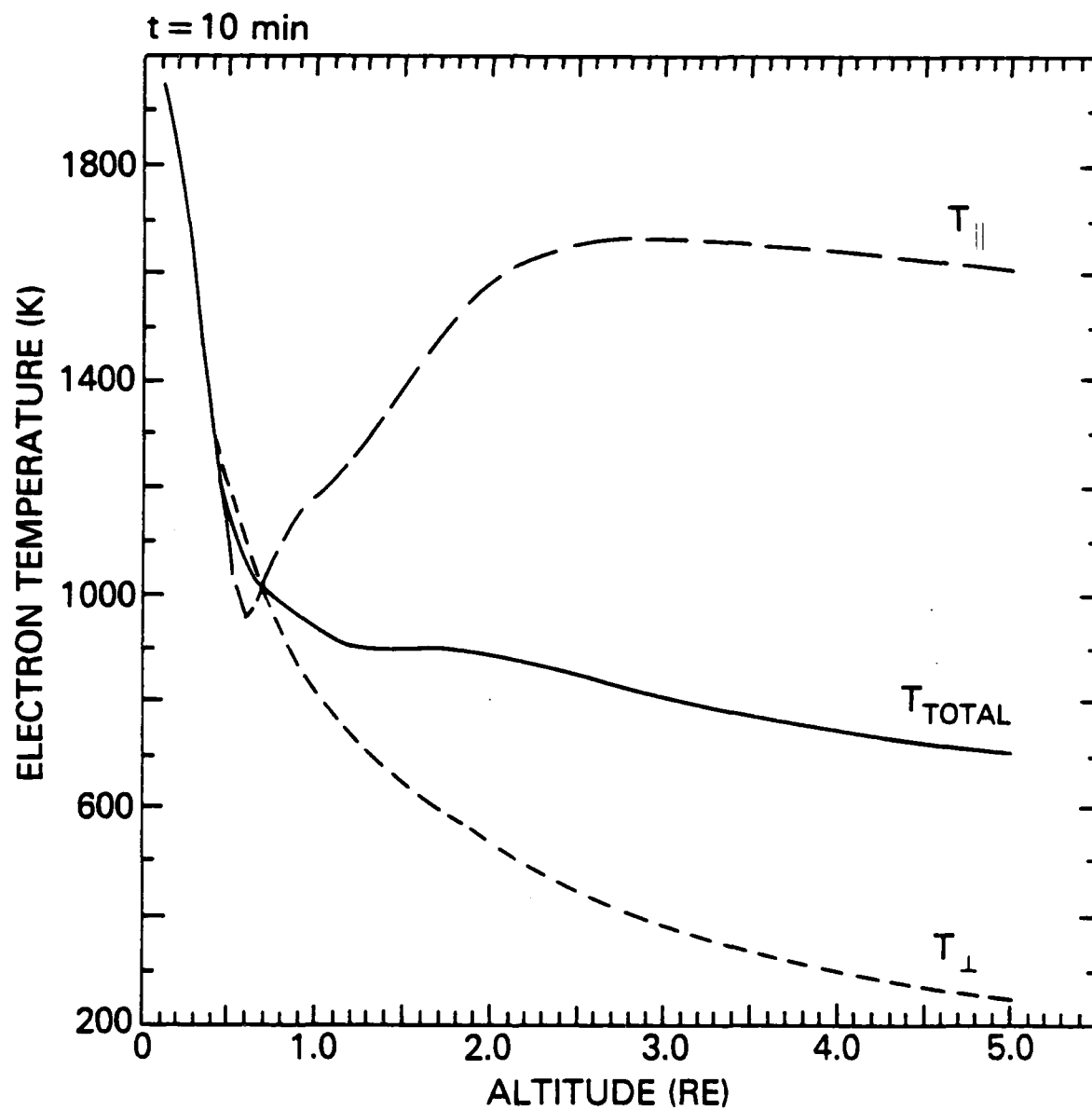


Figure 5. (b) Electron temperature after 10 minutes after the onset of a current of  $-2.0 \mu\text{A}/\text{m}^2$ .

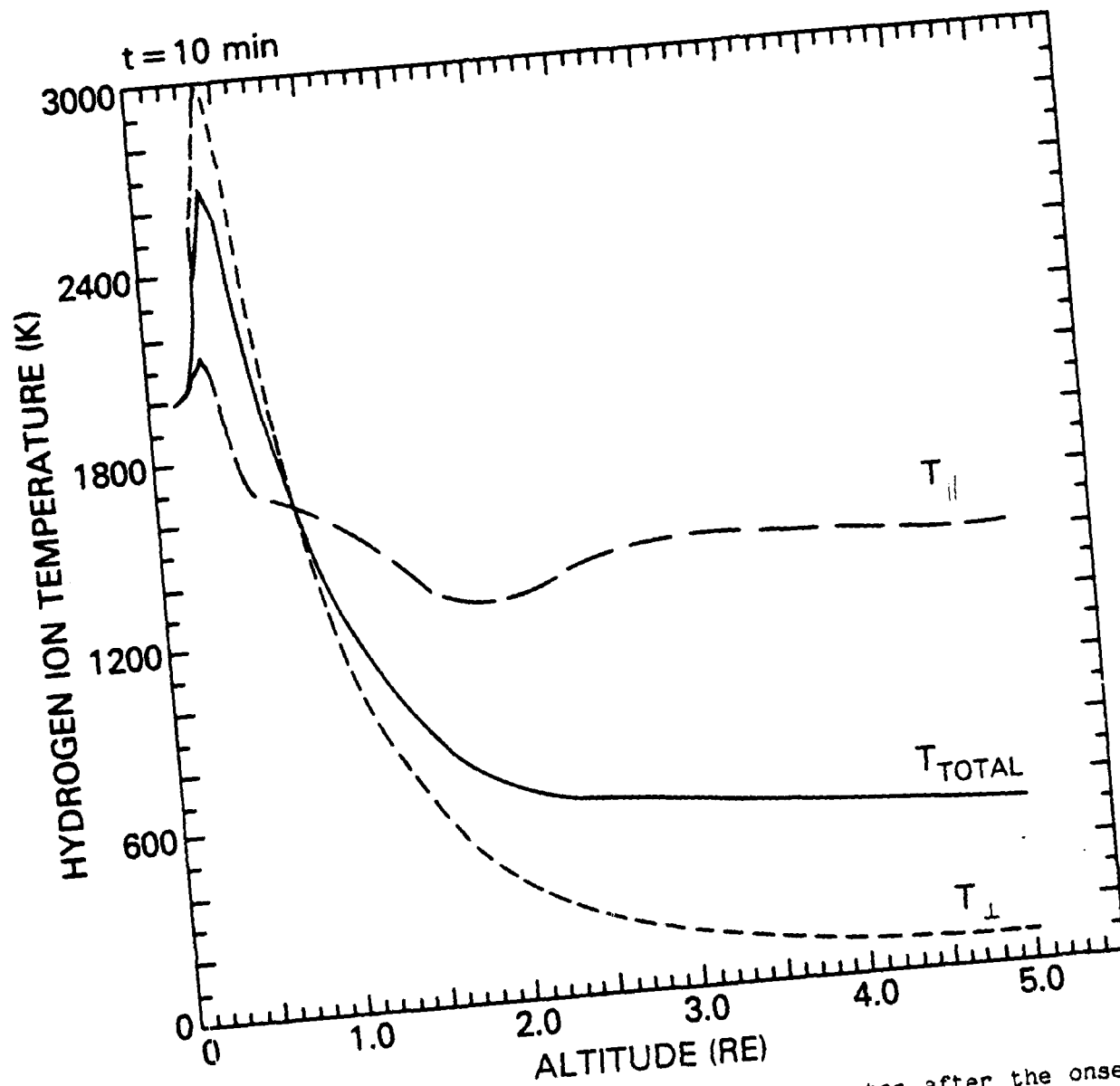


Figure 5. (c) Hydrogen ion temperature after 10 minutes after the onset of a current of  $-2.0 \mu\text{A}/\text{m}^2$ .

## References

- Banks, P.M. and T.E. Holzer, The Polar Wind, J. Geophys. Res., 73, 6846-6854, 1968.
- Banks, P.M. and T.E. Holzer, High-Latitude Plasma Transport: The Polar Wind, J. Geophys. Res., 74 6317-6332, 1969.
- Barakat, A.R., and R.W. Schunk, Transport Equations for Multicomponent Anisotropic Space Plasmas: A Review, Plasma Physics, 24, 389-418, 1982.
- Burgers, J.M., Flow Equations for Composite Gases, Academic Press, New York, 1969
- Holtzer, T.E., J.A. Fedder, and P.M. Banks, A Comparison of Kinetic and Hydrodynamic Models of an Expanding Ion-Exosphere, J. Geophys. Res., 76 2453-2468, 1971.
- Iijima, T, and T.A. Potemra, The Amplitude Distribution of Field-Aligned Currents at Northern High Latitudes Observed by Triad, J. Geophys. Res., 81, 2165, 1976.
- Kindel, J.M., and C.F. Kennel, Topside Current Instabilities, J. Geophys. Res., 76, 3055-3078, 1971.
- Lemaire, J., and M. Scherer, Kinetic Models of the Solar and Polar Winds, Rev. Geophys. Space Phys., 11, 427-468, 1973.
- Mitchell, H.G., Jr., and P.J. Palmadesso, A Dynamic Model for the Auroral Field Line Plasma in the Presence of Field-Aligned Current. J. Geophys. Res., 88, 2131, 1983.
- Schunk, R.W., Mathematical Structure of Transport Equations for Multispecies Flows, Rev. Geophys. Space Phys., 15, 429-445, 1977.

Schunk, R.W. and D.S. Watkins, Electron Temperature Anisotropy in the Polar Wind, J.Geophys. Res., 86, 91-102, 1981.

Schunk, R.W. and D.S. Watkins, Proton Temperature Anisotropy in the Polar Wind, J.Geophys. Res., 87 171-180, 1982.



AD-A171 688

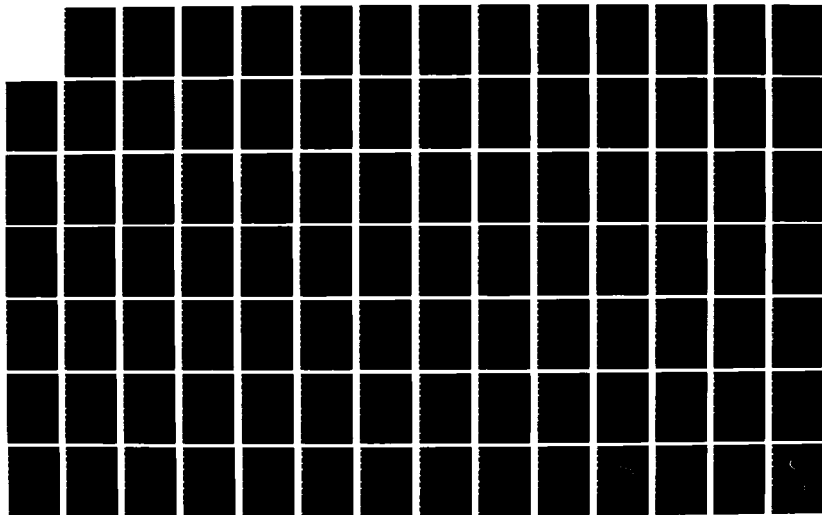
GEOPHYSICAL PLASMAS AND ATMOSPHERIC MODELING(U) SCIENCE  
APPLICATIONS INTERNATIONAL CORP MCLEAN VA  
E HYMAN ET AL JUL 86 SAIC-86/1781 N00014-85-C-2018

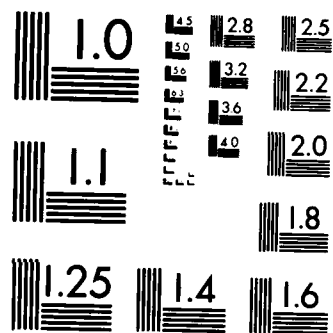
3/8

UNCLASSIFIED

F/G 4/1

ML





MICROCOPY RESOLUTION TEST CHART  
NATIONAL BUREAU OF STANDARDS-1963-A

# APPENDIX

$$\frac{\delta n_b}{\delta t} = 0 \quad (i)$$

$$\frac{\delta v_b}{\delta t} = \sum_a v_b (v_a - v_b) (1 + \phi_{ba}) \quad (ii)$$

$$\begin{aligned} k \frac{\delta T_{b\parallel}}{\delta t} = & \sum_a \frac{m_b v_{ba}}{(m_b + m_a)} \left\{ \frac{6}{5} kT_{a\parallel} - \left[ 2 + \frac{4m_a}{5m_b} \right] kT_{b\parallel} \right. \\ & \left. + \frac{4}{5} kT_{a\perp} + \frac{4m_a}{5m_b} kT_{b\perp} + \left[ 2kT_a + \left( 4 + 6 \frac{m_a}{m_b} \right) kT_b \right] \phi_{ba} \right\} \quad (iii) \end{aligned}$$

$$k \frac{\delta T_{b\perp}}{\delta t} = \sum_a \frac{m_b v_{ba}}{(m_b + m_a)} \left[ 3kT_a - 3kT_b + m_a (v_a - v_b)^2 (1 + \phi_{ba}) \right]$$

$$- \frac{k}{2} \frac{\delta T_{b\parallel}}{\delta t} \quad (iv)$$

$$\begin{aligned} \frac{\delta q_b}{\delta t} = & \sum_a \frac{n_b m_b v_{ba}}{(m_b + m_a)^2} \left[ \frac{27}{10} m_a \frac{q_a}{n_a} - \left( 3m_b + \frac{8}{5} m_a + \frac{13}{10} \frac{m_a^2}{m_b} \right) \frac{q_b}{n_b} \right. \\ & \left. + \frac{3}{2} \frac{m_a}{m_b} (m_a + m_b) kT_b (v_b - v_a) \right] (1 + \phi_{ba}) \quad (v) \end{aligned}$$

Each sum includes all charged particles species in the simulation. the velocity - corrected Coulomb collision frequency  $\nu_{ba}$  is given by

$$\nu_{ba} = \frac{n_a (32\pi)^{\frac{1}{2}} e_b^2 e_a^2 (m_b + m_a) \ln A \exp(-x_{ba}^2)}{3 m_b^2 m_a^3 \alpha_{ba}} \quad (vi)$$

( $\ln A$  is the Coulomb logarithm), and

$$T_b = \frac{1}{3} T_{b\parallel} + \frac{2}{3} T_{b\perp}$$

$$\alpha_{ba}^2 = \frac{2kT_b}{m_b} + \frac{2kT_a}{m_a}$$

$$x_{ba}^2 = \frac{(v_b - v_a)^2}{\alpha_{ba}^2}$$

$$\phi_{ba} = \frac{2}{5} x_{ba}^2 + \frac{4}{35} x_{ba}^4 + \frac{8}{315} x_{ba}^6$$

**APPENDIX K**

**Plasma Transport in the Auroral  
Return Current Region**

**Supriya Banerjee Ganguli  
Science Applications International Corporation**



*PLASMA TRANSPORT IN THE AURORAL  
RETURN CURRENT REGION*

*by*

*Supriya Banerjee Ganguli*





BOSTON COLLEGE  
GRADUATE SCHOOL

The thesis of Supriya Banerjee Ganguli  
entitled PLASMA TRANSPORT IN THE AURORAL RETURN  
CURRENT REGION

submitted to the Department of Physics  
in partial fulfillment of the requirements for the degree of  
Doctor of Philosophy in the Graduate School of  
Boston College has been read and approved by the Committee:

Robert L. Cavillano

Peter J. Schneider

Robert H. Ecker

Rein A. Urtan

2 April 1986  
Date



## TABLE OF CONTENTS

ACKNOWLEDGEMENTS	4
ABSTRACT	5
INTRODUCTION	7
CHAPTER I.	BEHAVIOR OF IONIZED PLASMA IN THE HIGH LATITUDE TOPSIDE IONOSPHERE : THE POLAR WIND
I.1	Introduction 14
I.2	The Model 23
I.3	Polar wind simulation 32
I.4	Discussions 41
I.5	Figures 43
CHAPTER II.	FIELD-ALIGNED CURRENTS IN THE EARTH'S IONOSPHERE AND MAGNETOSPHERE
II.1	Definition 55
II.2	Sources of Field-Aligned Currents (FAC) 57
II.3	Observations
	(a) Early observations of Birkeland currents 59

	(b) Observed densities and their variations with geomagnetic activity	60
	(c) Seasonal variation of FACs	61
	(d) FAC characteristics during substorms	62
	(e) The relationship between FAC and IMF	64
	(f) Discrete and Diffuse Auroras and their relation to FACs	70
II.4	Role of FAC in Magnetosphere-Ionosphere coupling	73
II.5	Figures	82
CHAPTER III. LARGE SCALE RETURN CURRENTS ON AURORAL FIELD LINES, I. 13 MOMENT CALCULATIONS		
III.1	Introduction	89
III.2	The Model	92
III.3	Polar wind simulation	96
III.4	Return current simulation	99
III.5	Discussions	102
III.6	Figures	104
CHAPTER IV. LARGE SCALE RETURN CURRENTS ON AURORAL FIELD LINES, II. 16 MOMENT CALCULATIONS		
IV.1	Introduction	111
IV.2	Return current simulation	112

IV.3	Discussions	122
IV.4	Figures	124
CHAPTER V.	ANISOTROPIC ION HEATING AND ANOMALOUS RESISTIVITY IN THE AURORAL RETURN CURRENT REGION	
V.1	Introduction	144
V.2	The Model	151
V.3	Simulations with ion heating and resistivity	156
V.4	Discussions	166
V.5	Figures	168
CONCLUSIONS AND DIRECTIONS FOR FUTURE WORK		181
APPENDIX 1.I		186
APPENDIX 2.II		189
APPENDIX 3.V		192
REFERENCES		195

## ACKNOWLEDGEMENTS

I wish to thank Dr. P. J. Palmadesso of the Naval Research Laboratory, my thesis advisor, for suggesting this problem and for his advice and guidance.

I would like to thank Dr. R. L. Carovillano of Boston College for his advice throughout graduate school and Dr. W. J. Burke of the Air Force Geophysics Laboratory for his inspiration and teaching in space physics. I am very thankful to Dr. S. J. Marsh of Sachs-Freeman Associates for his helpful advice with regard to numerics. I would like to thank Drs. R. W. Schunk of Utah State University and H. G. Mitchell of Science Applications International Corporation for numerous useful discussions.

Finally I would like to express my deepest appreciation for my parents and my brother whose love, encouragements and inspirations made it all possible.

## ABSTRACT

Multimoment time dependent and steady state multifluid plasma simulations have been performed to study the dynamics of the auroral field line plasma in the presence of large scale field-aligned return currents. This work is intended to contribute to the development of improved fluid models for use in the study of large scale magnetospheric-ionospheric dynamics. Also, a considerable amount of work has been done in the upward current region but the physics of plasma transport in the return current regions has not been thoroughly explored. The theoretical formulations are based on the 13 and 16-moment systems of transport equations. In the polar wind an electron temperature anisotropy develops above 2500 km altitude with  $T_{\perp} > T_{\parallel}$ . The hydrogen ion temperature shows reverse anisotropy, i.e.,  $T_{\parallel} > T_{\perp}$ . Our results are in good agreement with previous theoretical studies of the polar wind and recent experimental observations. The time dependent simulations show the effects of changes on the polar wind plasma dynamics after the sudden application of a current. The electron velocity and temperatures have a rapid response to a sudden change in conditions with a time constant of about a few minutes. The  $H^+$  ion temperatures change on a much longer time scale. The application of return currents to steady state plasma (with a hot electron upper boundary and downward heat flow) reverses the electron temperature anisotropy. Our simulations show that the electron

drift velocity corresponding to a current of  $-0.65 \mu\text{A}/\text{m}^2$  is above the threshold for electrostatic ion cyclotron (EIC) waves. The EIC instability heats the hydrogen ions in the perpendicular direction. The instability also produces anomalous resistivity which heats the electrons. The downward electron heat flow or thermal conduction competes with the upward convection effects to determine the direction of the electron temperature anisotropy. When the resistivity is strong the heating effects dominate. To our knowledge, this is the first successful solution to the 16-moment system of transport equations for the polar wind and first fluid model to investigate simultaneous interaction of ion cyclotron heating, anomalous resistivity and fluid transport processes in the auroral return current region.



## INTRODUCTION

The behavior of plasma on the auroral magnetic field lines has been the subject of a number of studies in recent years. The existence of ionospheric plasma outflow along open magnetic field lines was originally suggested by Axford [1968] and Banks and Holzer [1968]. Theoretical models of the polar wind including hydrodynamic, hydromagnetic, kinetic and generalized transport equation models have been developed by Banks and Holzer [1968, 1969], Holzer et al. [1971], Lemaire and Scherer [1973], Schunk and Watkins [1981, 1982], Mitchell and Palmadesso [1983] and Gombosi et al. [1985]. As explained by Barakat and Schunk [1982] the behavior of both near-equilibrium and non-equilibrium flows is important for understanding of the coupling through mass, momentum and energy transfer between the different regions within the solar terrestrial environment.

We have performed multimoment time dependent and steady state multifluid plasma simulations to study the equilibria and dynamics of the auroral field line plasma in the presence of large scale field-aligned return currents. This work is intended to contribute to the development of improved fluid models for use in the study of large scale magnetospheric-ionospheric dynamics. Also, a considerable amount of work has been done in the upward current region but the physics of plasma transport in the return

current regions has not been thoroughly explored.

It is generally necessary to use fluid theory to construct numerical models of large scale phenomena, even when kinetic effects play an important role in the dynamics. This is due to the fact that the temporal and spatial scales of kinetic theory are tied to plasma frequencies, Debye lengths, gyroradii, etc., which are orders of magnitude smaller than the characteristic scale times and sizes associated with the large scale phenomena. In general, existing computers are not capable of directly handling this broad range of scale sizes. The present fluid theories, e.g., the global models, which represent many of the magnetospheric processes reasonably well, use ideal MHD equations which assume near-Maxwellian distribution functions and until now, do not consider temperature anisotropies and the effects of heat flows. The magnetosphere is nearly collisionless and hence more general fluid models that can handle larger deviations from the Maxwellian are needed. Multimoment models with anomalous transport coefficients may be suitable for this purpose, but much additional work is needed to achieve better understanding of the conceptual issues associated with the physical interpretation of the higher moments and with closure approximations involving higher moments. In the absence of collisions the validity of the approximations cannot be guaranteed in advance, but must be determined by careful study of the problem involved. That is, the model should be thoroughly tested against previous works and

any observations available. Thus, research aimed at the development and study of advanced fluid models should be focussed on problem areas which have been reasonably well studied by other methods and well observed. One such area to consider will be the plasma flow along the auroral field lines where a considerable amount of data is available for comparison with the simulations.

An interest in the dynamics of the large scale field aligned return currents on auroral field lines provides a second motivation for this model. Mitchell and Palmadesso [1983] have performed simulations in which an upward field aligned current of magnitude  $1.0 \mu\text{A}/\text{m}^2$  was applied to the initially steady state polar wind and the time variations of various moments were explained. The physics of plasma transport in the return current regions has not been thoroughly explored; e.g., the cold upflowing ionospheric electrons may excite the EIC instability for very low currents and may thus generate anomalous resistivity.

In order to validate our model (Ganguli et al. [1985 a]) we have studied the solutions to the bi-Maxwellian-based 16-moment system of transport equations in Chapter I. We have analyzed the steady state behavior of the plasma encompassing geomagnetic field lines extending from 1500 km to 10 Re. This, to our knowledge, is the first successful steady state solution to the 16-moment system of transport equations for the polar

wind. Our results have been compared with the previous studies of polar wind and experimental observations of Nagai et al. [1984] and are found to be in good agreement.

In Chapter II we have summarized the observations of field-aligned currents in the earth's magnetosphere. The field aligned return currents flow from the magnetosphere to the ionosphere and are carried by cold electrons of ionospheric origin. It is now well established that the field aligned currents play an important role in the magnetosphere-ionosphere coupling process. In terms of region 1/region 2 large scale field aligned current systems [Iijima and Potemra, 1976] large scale return currents are identified as region 1 in the morning sector and region 2 in the evening sector. Within the region 1/region 2 current system, small-scale distributions of both upward and downward currents are observed in association with auroral arcs.

In Chapter III, we have used our time-dependent model based on the 13-moment system of transport equations to study the dynamics of large scale return currents. However, only cold electrons of ionospheric origin were used. In chapter IV, [Ganguli and Palmadesso, 1985 a] hot electrons are assumed at the upper boundary and the transport equations used are based on 16-moment approximations. The advantage of using the 16-moment

system of transport equations over the 13-moment is explained in Chapter I. In Chapter IV, we have performed two types of simulations. First, we have used the steady state model to investigate the effects of return currents on auroral field line equilibria. Then we have used the time dependent model to explore the effects of changes on plasma dynamics after the sudden onset of a current. The time-dependent model used is explained in Chapter III and Ganguli et al. [1985 b]. For the conditions existing in the topside ionosphere our simulations show that the electron drift velocity corresponding to a current of  $-0.65 \mu\text{A}/\text{m}^2$  is above the threshold for electrostatic ion cyclotron (EIC) waves, because the ionospheric plasma is so cold. Much higher currents are needed to excite instabilities in the case of upward currents. This is an interesting and potentially important result. This was also pointed out by Burke et al. [1983].

In Chapter V, we have shown that the EIC instability heats the hydrogen ions in the perpendicular direction [Ganguli and Palmadesso, 1985c]. The EIC instability can transfer electron momentum to the ions, thereby giving rise to anomalous resistivity. The electrons are heated due to resistivity. It is interesting to note that by increasing the electron temperature the critical velocity for exciting the EIC instability can be modified and the range of the EIC instability can be extended. To our knowledge this is the first fluid model to investigate the

effects of both EIC instability and anomalous resistivity in the auroral return current region [Ganguli and Palmadesso, 1985 b]. The results have been compared with experimental observations.

## **CHAPTER I**

**BEHAVIOR OF IONIZED PLASMA IN THE**

**HIGH LATITUDE TOPSIDE IONOSPHERE :**

**THE POLAR WIND**





## I.1 INTRODUCTION

The behavior of plasma on the auroral magnetic field lines has been the subject of a number of studies in recent years. The existence of ionospheric plasma outflow from polar regions along open magnetic field lines was originally suggested by Axford [1968] and Banks and Holzer [1968]. The term "polar wind" were suggested by Axford [1968] who compared this flow with the solar wind flow. Theoretical models of the polar wind including hydrodynamic, hydromagnetic, kinetic and generalized transport equation models have been developed by Banks and Holzer [1968, 1969], Holzer et al. [1971], Lemaire and Scherer [1973] and Schunk and Watkins [1981, 1982]. Effects of hot electron populations on the polar wind was studied by Lemaire and Scherer [1978, 1983] and Barakat and Schunk [1984]. Examples of other kinds of plasma flow conditions interesting in space physics are pointed out by Demars and Schunk [1979]. The examples are near-equilibrium flows in co-rotating planetary ionospheres and in the solar corona, non-equilibrium flows in planetary magnetospheres and in the terrestrial F-region at high latitudes.

As explained by Barakat and Schunk [1982] the behavior of both near-equilibrium and non-equilibrium flows is important for understanding of the coupling through mass, momentum and energy transfer between the different regions within the solar

terrestrial environment.

Transport equations for aeronomy and space physics were derived by Schunk [1974, 1977]. By taking moments of Boltzmann's equation, a general system of transport equations for a multispecies flow was obtained. The system of equations contained continuity, momentum, energy, pressure tensor and heat flow equations for each species. In general, a finite system of moment equations does not constitute a closed set since the equation governing the velocity moment of order  $r$  contains the velocity moment of order  $r+1$ . It is therefore necessary to adopt a closure approximation, such as an analytic expression for the species velocity distribution function to close the set of equations. Schunk's system of equations was closed by using Grad's 13 parameter approximation of the distribution function to express higher order moments in terms of lower order moments. In Grad's method the distribution function is represented as the product of a Maxwellian and a truncated series of orthogonal polynomials, with a total of 13 (for example) free parameters. The closed system of equations can be applied to both collision-dominated and collisionless regions thus providing a smooth transition between the two regions. In the collision-dominated limit, the pressure tensor and heat flow equations yield Navier-Stokes expressions for the stress tensor and the heat flow vector. In the collisionless limit, the equations can be reduced to the Chew-Goldberger-Low

equations. The other advantage of using the 13-moment system of transport equations is that the stress and heat flow moments are described by transport equations just as density, velocity and temperature moments.

Transport equations based on a bi-Maxwellian species distribution function were first derived by Chew et al [1956] for a collisionless plasma. The heat flows were neglected in that study and the transport equations for species temperatures parallel and perpendicular to the magnetic field were termed 'double-adiabatic' energy equations. This work was extended by several other authors; e.g., Kennel and Green [1966], MacMahon [1965], Friedman et al. [1966], Bowers and Haines [1968], Oraevskii et al. [1968] and Espedal [1969]. Chodura and Pohl [1971] derived a system of transport equations for an anisotropic plasma based on a bi-Maxwellian species distribution and including the transport effects as heat flow and viscosity. The coulomb collisions between the interacting species were taken into account also. The method used to derive this system of equations was an extension of Grad's method and corresponds to a 16-moment approximation for the species distribution function. Demars and Schunk [1979] extended this work by considering anisotropic plasma of arbitrary degree of ionisation. The collision terms for the important charge exchange interaction between an ion and its parent neutral were also calculated. Barakat and Schunk [1982]

in their review paper presented a unified approach to the study of transport phenomena in multicomponent anisotropic space plasmas. A generalized system of equations was presented which can describe subsonic and supersonic flows, collision-dominated and collisionless flows, plasma flows in rapidly changing magnetic field configurations, multicomponent plasma flows with large temperature differences between the interacting species and plasma flows that contain anisotropic temperature distributions.

Comparison studies of transport equations based on Maxwellian and bi-Maxwellian distributions for anisotropic plasmas were performed by Barakat and Schunk [1982]. They have considered the flow of a homogeneous, weakly-ionised plasma subjected to homogeneous electric and magnetic fields. The problem has an analytic solution and the velocity distribution functions obtained from different series expansions were compared with the exact solution. For the Maxwellian expansion, Grad's 5-, 13- and 20-moment approximations were considered and for the bi-Maxwellian expansion 6- and 16-moment approximations were considered. Emphasis was given to modelling the anisotropic character of the distribution function. Their results show that the 20-moment Maxwellian expansion can describe larger non-Maxwellian deviations than the 5- and 13-moments because of the greater number of terms retained at that level of approximation. For the bi-Maxwellian

expansions the 16-moment approximation is better than the 6-moment. As expected an expansion based on a bi-Maxwellian distribution is better suited to describe anisotropic plasmas than the expansion based on a Maxwellian, even if fewer terms are retained in the bi-Maxwellian expansion. Barakat and Schunk [1982] have also performed Monte Carlo simulations of the above mentioned problem (anisotropic plasmas) and compared the simulation results with Maxwellian and bi-Maxwellian expansions. The conclusions remain the same as in their previous study using analytic solutions.

Schunk and Watkins [1981, 1982] have studied the steady state flow of a fully ionized  $H^+ - O^+ -$  electron plasma along geomagnetic field lines extending from 1500 km to 12000 km. They have used the 13-moment system of transport equations of Schunk [1977]. The 13-moment system of transport equations is fairly general and can be used to describe a wide variety of plasma flows. In their first study of the polar wind [1981] they used a 1D gyrotropic version of the 13-moment equations for the electron gas and a simplified set of transport equations for the hydrogen and oxygen ions. Their results show that electron temperature anisotropy develops at altitudes above 2500 km, with  $T_{\perp} > T_{\parallel}$ . Below 2500 km the electron gas is essentially collision dominated. In their next study of the polar wind [1982] they have used the 13-moment system of equations for the hydrogen ions also. The results show that

for supersonic flow at high altitudes the hydrogen ion temperature parallel to the field line ( $T_{p\parallel}$ ) is greater than the temperature perpendicular to the field line ( $T_{p\perp}$ ). The reverse is true for subsonic flow. The results of the 13-moment system of equations were compared to the standard solutions. The difference is small within the plasmasphere where the electron density is high but outside the plasmasphere and in the ionosphere above SAR arcs where the electron density is lower and substantial electron and proton heat flow occurs, the difference between the two sets of solutions is significant.

Mitchell & Palmadesso [1983] used the same 13-moment system of equations and developed a dynamic numerical model of the plasma along an auroral field line extending from 800 km to 10 Re. The plasma consists of the electrons, hydrogen and oxygen ions. The electrons and the hydrogen ions are the dynamic species in the model. They have performed simulations for the case of a current-free polar wind and the case in which an upward field aligned current was applied along the field line. The results of the polar wind simulations have been compared to those of Schunk and Watkins [1981, 1982]. It is seen that for low electron temperature and supersonic hydrogen ion outflow, both exhibit an anisotropic hydrogen ion cooling and both have a region in which the parallel temperature increases with altitude before adiabatic cooling dominates.

The electron temperature profiles, however, cannot be directly compared. The lower boundary of Mitchell and Palmadesso [1983] was held at a constant temperature and the simulation was run until a steady-state was achieved. The outflow condition treats the upper boundary as an electron heat sink and therefore the electron temperature decreases with altitude. Schunk and Watkins [1981] specified the electron temperature and a positive electron temperature gradient at the lower end, as the initial condition to study the electron temperature anisotropy. The upper boundary need not be specified in this case.

The dynamic models must deal with problems implicit in the time dependent moment equations. Some of these simulations have shown instabilities which arise due to the presence of unphysical waves. These waves exist in the numerical model due to the physical approximations made in the theoretical formulation of the problem. Mitchell and Palmadesso [1983] have performed a one-dimensional linear wave analysis of the flux tube model equations. They have shown the existence of two kinds of waves - (i) ion acoustic waves and (ii) thermal waves. The ion acoustic waves are actual physical waves present in the model. These waves are Landau damped in the real system unless the temperature of the electrons is much greater than the temperature of the ions. But Landau damping is absent from the moment equations. The thermal waves, on the other hand, are unphysical. These waves are generated by the

truncation of the moment sequence. By truncating the moment sequence, the amount of velocity dispersion is limited. The waves do not diffuse away in this case, as they would in a real fluid. There are two types of thermal waves: (a) parallel thermal waves in the moment pair  $(T_{s||}, q_{s||})$  and (b) perpendicular thermal waves in the moment pair  $(T_{s\perp}, q_{s\perp})$ . Waves (i) and (ii) can couple and give rise to an unphysical instability when the heat flow is large. Also these waves can influence the time scales upon which the flux tube model dynamically reacts to changes in the field-aligned current. These problems can be solved by adding a thermal diffusion term to the time dependent set of equations. Both the steady state and the time dependent model have limitations and advantages. If we consider the steady state formulation of the problem we can avoid the presence of time dependent instabilities that we have described above. However, the steady state model is more sensitive to the boundary conditions used and does not show any effect of time variation.

Effects of hot electron populations on the polar wind were studied by Lemaire and Scherer [1978, 1983] and Barakat and Schunk [1984]. Barakat and Schunk used a semikinetic model for this purpose and their results show that for higher hot electron temperatures and a greater percentage of hot electrons there is a discontinuity in the kinetic solutions. This transition was interpreted as the presence of a double-layer



existing at the contact surface between the hot and cold electrons.

Gombosi et al. [1985] introduced a hydrodynamic theoretical time-dependent model of the polar wind from 200 km to 12000 km. The plasma consists of  $O^+$ ,  $H^+$  and the electrons similar to the previous studies. Note that the hydrodynamic models do not consider heat flows. The time responses of various ionospheric quantities to sudden changes in conditions were explored. The cases of sudden changes considered are 1) refilling ionosphere - where a heat source and the ionization source were turned on at  $t=0$ , and 2) collapsing ionosphere. It is seen that the electron temperature responds extremely rapidly with a time constant of few minutes, oxygen ions take 20-30 minutes, and hydrogen ions require several hours to change significantly. These calculations also demonstrated that supersonic  $H^+$  ion outflow can develop temporarily as transients, whereas in steady-state models the velocity has to be either subsonic or supersonic.

Chiu et al. [1981] used an adiabatic approach to model the structures of auroral electrostatic potentials. The model was 1-dimensional and steady state. Similar studies, using a 2-dimensional model were reported by Newman et al. [1986]. They have developed the kinetic description of particles and fields above discrete auroral arcs. Details of these works will be

discussed in chapter III, where we discuss the results of our field-aligned return current simulations. Here we note that the adiabatic models are single particle calculations. These models can calculate particle distribution functions fairly accurately in quiet conditions. However, in the presence of collisions or critical currents that excite any instability these calculations break down.

In the remainder of this chapter we shall present our solutions to 16-moment system of transport equations based on the bi-Maxwellian distribution. We have studied the steady state behavior of the plasma encompassing geomagnetic field lines extending from 1500 km to 10 Re. This, to our knowledge, is the first successful steady state solution to the 16-moment system of transport equations for the polar wind. Our results have been compared with previous studies of the polar wind and the experimental observations of Nagai et al. [1984] and are found to be in good agreement.

## 1.2 THE MODEL

The model [Ganguli et al., 1985] simulates the steady state behavior of a fully ionized plasma ( $H^+$ ,  $O^+$  and the electrons) along the geomagnetic field lines in the high

latitude topside ionosphere (extending from 1500 km to 10 Re). The theoretical formulation is based on the 16-moment system of transport equations of Barakat and Schunk [1982]. The 13-moment system of transport equations allow for different species temperature parallel and perpendicular to the field line, but allow only a single heat flow per species. The 16-moment equations allow transverse and parallel thermal energy to be transported separately, which simulates the behavior of a large temperature anisotropy for a collisionless plasma better than the 13-moment equations. This is expected to be an important advantage in studies of auroral field aligned transport which include the effects of return currents and anomalous transport processes, such as anomalous resistivity and associated anisotropic heating.

The electrons and the hydrogen ions are the dynamic species in the model and the oxygen ions form a static background population at a constant temperature. The  $H^+$  and electron temperature anisotropies and heat flows are not sensitive to the oxygen temperature and heat flows, as noticed by Schunk and Watkins [1981, 1982]. Thus maintaining the  $O^+$  ions at a constant temperature did not introduce appreciable errors as far as the  $H^+$  ions and electrons are concerned.

We are interested in the problem of plasma flow along the geomagnetic field lines, which can be reduced to a one-

dimensional problem. We do not expect curvature effects to be important for the relatively cold ionospheric particles. The distribution function is considered to be gyrotropic about the field line direction, which reduces the 16-moments to six moments: number density, velocity of the species parallel to the geomagnetic field line, temperatures parallel and perpendicular to the field line and heat flows parallel and perpendicular along the field line. The resulting transport equations used for the hydrogen ions and the electrons are given as follows:

continuity:

$$\frac{\partial n}{\partial t} + \frac{\partial nv}{\partial r} + \dot{A}nv = \frac{\delta n}{\delta t} \quad (I.1)$$

momentum:

$$\frac{\partial v}{\partial t} + v \frac{\partial v}{\partial r} + \frac{k}{mn} \frac{\partial nT_{||}}{\partial r} + \frac{GM}{r^2} - \frac{eE}{m} + \frac{\dot{A}k}{m}(T_{||} - T_{\perp}) = \frac{\delta v}{\delta t} \quad (I.2)$$

parallel energy:

$$k \frac{\partial T_{||}}{\partial t} + kv \frac{\partial T_{||}}{\partial r} + \frac{2}{n} \frac{\partial nh_{||}}{\partial r} + 2A(h_{||} - h_{\perp}) + 2kT_{||} \frac{\partial v}{\partial r} = k \frac{\delta T_{||}}{\delta t} \quad (I.3)$$

perpendicular energy:

$$k \frac{\partial T_{\perp}}{\partial t} + kv \frac{\partial T_{\perp}}{\partial r} + \frac{1}{n} \frac{\partial nh_{\perp}}{\partial r} + A(2h_{\perp} + kT_{\perp}v) = k \frac{\delta T_{\perp}}{\delta t} \quad (I.4)$$

heat flow equation for parallel energy:

$$\frac{\partial h_{||}}{\partial t} + v \frac{\partial h_{||}}{\partial r} + 3h_{||} \frac{\partial v}{\partial r} + \frac{3}{2} \frac{k^2 T_{||}}{m} \frac{\partial T_{||}}{\partial r} = \frac{\delta h_{||}}{\delta t} \quad (I.5)$$

heat flow equation for perpendicular energy:

$$\begin{aligned} \frac{\partial h_{\perp}}{\partial t} + v \frac{\partial h_{\perp}}{\partial r} + h_{\perp} \frac{\partial v}{\partial r} + \frac{k^2 T_{||}}{m} \frac{\partial T_{\perp}}{\partial r} \\ + A (v h_{\perp} + \frac{T_{\perp} k^2}{m} (T_{||} - T_{\perp})) = \frac{\delta h_{\perp}}{\delta t} \end{aligned} \quad (I.6)$$

charge neutrality:

$$n_e = n_p + n_o \quad (I.7)$$

where,  $n$  = number density

$v$  = species velocity

$A$  = cross-sectional area of a flux tube (proportional to  $1/B$ )

$$A = \frac{1}{A} \frac{\partial A}{\partial r} = - \frac{1}{B} \frac{\partial B}{\partial r} = \frac{3}{r}$$

$B$  = magnetic field of the earth

$E$  = Electric field parallel to the field line

$G$  = gravitational constant

$M$  = mass of the earth

$m$  = mass of the particular species

$T_{||}$  = temperature of the species parallel to the field line

$T_{\perp}$  = temperature of the species perpendicular to the field line

$h_{||}$  = heat flow parallel to the field line

$h_{\perp}$  = heat flow perpendicular to the field line

$k$  = Boltzmann constant

$e$  = electrons

$p$  = hydrogen ions

$o$  = oxygen ions

For a given moment  $F$  of the distribution function,  $\delta F/\delta t$  represents the change in  $F$  due to the effects of collisions and may also include anomalous transport effects associated with plasma turbulence. The collision terms used in this model are Burger's [1979] collision terms for the case of Coulomb collisions with corrections for finite species velocity differences. The collision terms are given in Appendix A.

Using equations (I.1) and (I.2), the oxygen ion density is calculated. We have assumed that the total flux tube current  $I$  remains constant along the tube

$$I = eA (n_p V_p - n_e V_e) \quad (I.8)$$

which implies

$$v_e = \frac{1}{n_e} (n_p v_p - \frac{I}{eA}) \quad (I.9)$$

In this chapter the current  $I$  is assumed to be zero.

Using equations (I.2), (I.7) and (I.8), the electric field  $E$  parallel to the field line is calculated.

$$\begin{aligned} E = & \frac{m_s}{en_e A} \frac{\partial}{\partial r} (n_p v_p^2 A - n_e v_e^2 A) - \frac{k}{e} \left[ \frac{\partial T_{ell}}{\partial r} + \frac{T_{ell}}{n_e} \frac{\partial n_e}{\partial r} \right. \\ & \left. + \frac{(T_{ell} - T_{el})}{A} \frac{\partial A}{\partial r} \right] - \frac{n_o m_e GM}{n_e e r^2} + \frac{m_e}{e} \left[ \frac{\delta v_e}{\delta t} - \frac{n_p}{n_e} \frac{\delta v_p}{\delta t} \right] \end{aligned} \quad (I.10)$$

We will consider the steady state solutions of the equations (1)-(6). This set of ordinary differential equations is solved by first algebraically eliminating all derivatives in a given equation except one and then integrating the resulting quantities numerically along the field line. The new set of equations are:

$$\frac{\partial n_p}{\partial r} = - \frac{n_p}{v_p} \frac{\partial v_p}{\partial r} - \frac{3}{r} n_p$$

(I.11)

$$\begin{aligned} \frac{\partial v_p}{\partial r} = & \frac{1}{\left[ v_p - \frac{k T_{p||}}{v_p m_p} - \frac{T_{e||} k n_p}{m_p v_p (n_o + n_p)} \right]} \\ & \times \left[ \frac{3 k T_{p||}}{r m_p} + \frac{3 k T_{e||} n_p}{r m_p (n_p + n_o)} - \frac{k}{m_p} \frac{\partial T_{p||}}{\partial r} \right. \\ & - \frac{k}{m_p} \frac{\partial T_{e||}}{\partial r} - \frac{k T_{e||}}{m_p (n_o + n_p)} \frac{\partial n_o}{\partial r} - \frac{3 k}{r m_p} (T_{e||} - T_{e\perp}) \\ & - \frac{n_o m_e G M}{m_p r^2 (n_o + n_p)} - \frac{G M}{r^2} + \frac{m_e}{m_p} \frac{\delta v_e}{\delta t} \\ & \left. + \left( 1 - \frac{m_e n_p}{m_p (n_o + n_p)} \right) \frac{\delta v_p}{\delta t} - \frac{3 k (T_{p||} - T_{p\perp})}{r m_p} \right] \end{aligned}$$

(I.12)



The following sets of equations apply both to the  $e^-$  and  $H^+$  ions.

$$\begin{aligned} \frac{\partial T_{||}}{\partial r} = & \frac{1}{\left[ kv - \frac{3k^2 T_{||}}{v} \right]} \left[ -\frac{2}{n} h_{||} \frac{\partial n}{\partial r} + \frac{6}{r} (h_{\perp} - h_{||}) \right. \\ & \left. - \left[ 2T_{||} k - \frac{6h_{||}}{v} \right] \frac{\partial v}{\partial r} + k \frac{\delta T_{||}}{\delta t} - \frac{2}{v} \frac{\delta h_{||}}{\delta t} \right] \end{aligned} \quad (I.13)$$

$$\begin{aligned} \frac{\partial T_{\perp}}{\partial r} = & \frac{1}{\left[ kv - \frac{k^2 T_{||}}{mv} \right]} \left[ \frac{h_{\perp}}{v} \frac{\partial v}{\partial r} - \frac{h_{\perp}}{n} \frac{\partial n}{\partial r} - \frac{3}{r} h_{\perp} - \frac{3kT_{\perp} v}{r} \right. \\ & \left. + \frac{3k^2 T_{\perp}}{mrv} (T_{||} - T_{\perp}) + k \frac{\delta T_{\perp}}{\delta t} - \frac{1}{v} \frac{\delta h_{\perp}}{\delta t} \right] \end{aligned} \quad (I.14)$$

$$\frac{\partial h_{||}}{\partial r} = -\frac{3h_{||}}{v} \frac{\partial v}{\partial r} - \frac{3}{2} \frac{k^2 T_{||}}{v} \frac{\partial T_{||}}{\partial r} + \frac{1}{v} \frac{\delta h_{||}}{\delta t} \quad (I.15)$$

$$\begin{aligned} \frac{\partial h_{\perp}}{\partial r} = & -\frac{h_{\perp}}{v} \frac{\partial v}{\partial r} - \frac{k^2 T_{||}}{vm} \frac{\partial T_{\perp}}{\partial r} \\ & - \frac{3}{r} h_{\perp} - \frac{3k^2 T_{||}}{vrm} (T_{||} - T_{\perp}) + \frac{1}{v} \frac{\delta h_{\perp}}{\delta t} \end{aligned} \quad (I.16)$$

The simulation is carried out on an unequally spaced grid with 100 cells, with smaller cell sizes at the lower end of the flux tube. This enables us to determine the plasma dynamics in the presence of large density gradients due to the small scale height of oxygen.

The equations we solve here represent a system of stiff differential equations. A typical solution of a stiff system has a short initial interval in which it changes rapidly (called an initial transient) after which it settles down to a comparatively slowly varying state. Methods of solving stiff ordinary differential equations have been discussed by Gear et al. [1979]. We have used the general procedure employed by Watkins [1981]. The direction of integration is very important for these equations since the stability of the computation depends on the direction of integration. For example, the velocity equations can be integrated starting from the lower boundary but the electron temperature equations are integrated starting from the upper boundary. First an "initial guess" for each moment profile was obtained, based on observations. The equations are then solved iteratively until a new solution that satisfies all the boundary conditions in steady state is obtained. Unphysical solutions do not satisfy the boundary conditions and are rejected.

### I.3 POLAR WIND SIMULATIONS

Schunk and Watkins [1982] have performed 13-moment polar wind simulations for both supersonic and subsonic hydrogen ion outflow. Until recently it was not clear if the polar wind is supersonic or subsonic. Nagai et al. [1984] first reported the supersonic nature of the polar wind along polar cap field lines. The data for this study were obtained from the DE 1 satellite. These observations clearly show that the hydrogen ion outflow in the polar ionosphere is supersonic in nature. Subsonic polar wind has not yet been observed. The theoretical study of Raitt et al. [1975, 1977] showed that if the  $H^+$  ion outflow changes from subsonic to supersonic the transition is always below 1500 km. We therefore use 1500 km as our lower boundary similar to Schunk and Watkins [1981]. We shall thus consider hydrogen ion outflow as supersonic.

As noted above, solutions have been obtained for the current free case. The boundary conditions selected are similar to those of Schunk and Watkins [1981, 1982]. At the lower boundary (1500 km) we set the  $H^+$  ion velocity at 16 km/s,  $H^+$  ion density at  $80 \text{ cm}^{-3}$ , and oxygen ion density at  $5000 \text{ cm}^{-3}$ . The hydrogen ion temperature at the lower boundary is  $T_{p||} = T_{p\perp} = 3500^\circ\text{K}$  while the electron temperature is  $T_{e||} = T_{e\perp} = 1000^\circ\text{K}$ . The oxygen ion temperature was kept constant at  $1200^\circ\text{K}$  along the entire length of the flux tube. The heat flows are

$q_{e||} = .1396 \times 10^{-7}$  erg-cm/sec,  $q_{e\perp} = .1749 \times 10^{-7}$  erg-cm/sec,  
 $q_{p||} = .6487 \times 10^{-8}$  erg-cm/sec and  $q_{p\perp} = .9794 \times 10^{-7}$  erg-cm/sec.  
 The results of this current free polar wind simulation are shown in figures (I.1.a) - (I.1.g). Figure (I.1.a) shows oxygen ion density, (I.1.b) shows  $H^+$  ion density, (I.1.c) shows electron density, (I.1.d) shows hydrogen ion velocity. Oxygen ions are the dominant species only up to an altitude of 3500 km. The heavier ions  $O^+$  are bound to earth by gravity while the ambipolar electric field tries to hold the hydrogen ions and electrons together, with the result that  $H^+$  ions are accelerated upwards. Supersonic  $H^+$  ions flow along divergent magnetic field lines. The hydrogen ion momentum balance equation shows that the ambipolar electric field value produces the sharp increase in  $H^+$  ion velocity at the lower end of the tube. The electron velocity also increases with altitude as is evident from equation (I.9) and is shown in Figure (I.1.e). The  $H^+$  ion and electron velocities for this chapter in figures (I.1) and (I.2) are plotted on a logarithmic scale to compare with Schunk and Watkins [1981]. For the  $H^+$  ions, the total flux along the flux tube is conserved, i.e.,  $nVA = \text{constant}$ . Therefore, as the velocity and the area increases the density should decrease. The hydrogen ion density decreases as it flows through the diverging flux tube. The electron density also decreases, as is evident from the charge neutrality equation (I.7).

A study of equation (I.12) reveals that at the upper end of the flux tube the velocity variation is driven mainly by the terms containing the hydrogen ion temperature anisotropy, electron temperature anisotropy, hydrogen ion temperature and electron temperature parallel to the field line, i.e., mirror forces and parallel pressure gradients.

Figure (I.1.f) shows the hydrogen ion temperature parallel and perpendicular to the geomagnetic field. The hydrogen ion temperature exhibits two basic characteristics:

- (1) Adiabatic cooling - Supersonic ion gas cools down as it expands in a diverging magnetic field.
- (2) Temperature anisotropy.

These effects were also displayed by the previous studies of the polar wind using the 13 moment system of equations by Schunk and Watkins [1982] and Mitchell and Palmadesso [1982]. Like Schunk and Watkins [1982], we obtained solutions for only positive  $H^+$  heat flow at the lower boundary. This implies that an upward flow of heat from the lower ionosphere is required for a supersonic hydrogen ion outflow [Schunk, 1982]. This upward flow of heat is associated with a negative  $H^+$  temperature gradient.

At the lower end of the flux tube, due to rapid expansion of the supersonic ion gas, both  $T_{\perp}$  and  $T_{\parallel}$  decrease

with altitude. This was also noted by Schunk and Watkins [1982]. The hydrogen ion temperature perpendicular to the field line decreases continuously. Appreciable temperature anisotropy develops around 2500 km. The temperature anisotropy is more prominent in the  $H^+$  ions than in the electrons. This is because of the fact that the hydrogen ions have supersonic velocities and in the collisionless region heat transport is not efficient for  $H^+$  ions, compared to that for electrons. As the particles move up in a decreasing magnetic field,  $v_{\perp}$  decreases in order to keep the adiabatic invariant  $\mu = mv_{\perp}^2/B$  constant. As the total energy of the particle is conserved, the decrease in  $(1/2)mv_{\perp}^2$  results in an increase of  $(1/2)mv_{\parallel}^2$ . That is, perpendicular energy gets converted to parallel energy. A study of equation (I.13) and (I.14) shows that the temperature variation is produced mainly as an interaction between the convection process and the adiabatic effects. The convective terms are the terms that contain the convective part of the time derivative ( $V \partial/\partial r$ ) in the Boltzmann equation and for most of the interesting cases they represent the thermal convection processes. The collisions play an important role below 2500 km. In equations (I.15) and (I.16) the temperature gradient terms are very important.

We compared our solution of the equations based on the 16-moment system with that of Schunk and Watkins' [1982] solution of the 13-moment equations. The general behavior of

the  $H^+$  ion temperature parallel and perpendicular to the field line remains the same.  $H^+$  ion temperature perpendicular to the field line decreases continuously with altitude. Parallel temperature first decreases and then increases and finally tends to remain constant with altitude. We observe an anisotropy with  $T_{\perp} > T_{\parallel}$  below 2500 km. Schunk and Watkins [1982] observed similar anisotropy for the low electron temperature case when they lowered the  $H^+$  ion temperature and heat flow and when the oxygen ion density was increased at the lower end. They have pointed out that the results are sensitive to the boundary conditions used, in the sense that the qualitative picture remains the same but the quantitative behavior changes.

We have also compared our results with those of Mitchell and Palmadesso [1983] and Holzer et al. [1971]. Mitchell and Palmadesso [1983] started their simulation at 800 km at the lower boundary. At this level the  $H^+$  ion temperature increases with altitude due to Joule heating caused by  $H^+$  ion collisions with oxygen ions. This effect rapidly decreases with altitude. The general qualitative picture here is in good agreement with our results.

Holzer et al. [1971] have compared the solutions of hydrodynamic and kinetic equations for supersonic polar wind outflow in a collisionless regime. Both hydrodynamic and

kinetic solutions show that  $T_{\perp}$  decreases continuously.  $T_{\parallel}$  for both cases decreases rapidly with altitude and then tends to become constant. For the hydrodynamic case at all altitudes the hydrogen ion temperature parallel to the field line was greater than that perpendicular to the field line. The kinetic solutions showed a region at the lower end where  $T_{\perp}$  was greater than  $T_{\parallel}$ . The cross-over region was noticed at the lower end. In these cases also we notice that our solutions are in good agreement with Holzer et al. [1971].

Finally, we compared our results with Nagai et al. [1984]. Nagai et al. [1981] have used the data from Dynamics Explorer (DE) to demonstrate the supersonic nature of the polar wind. The observations were obtained from  $65^{\circ}$  to  $81^{\circ}$  invariant latitude and altitude near  $2R_E$ . The results show that for an estimated range of spacecraft potential of +3V to +5V, a temperature range of 0.1 to 0.2 eV was obtained corresponding to flow velocities of 25 to 16 km/s. Calculated Mach numbers are 5.1 for a velocity of 25 km/sec, 3.9 for 21 km/sec and 2.6 for 16 km/sec. There are different ways to define the  $H^+$  ion Mach number. Here, the single ion Mach number definition is used, i.e.,  $M = V_p / (kT_p/m_p)^{1/2}$ . The Mach numbers calculated from our results corresponding to a flow velocity of 16 km per second is 2.7 and 4.1 for a velocity of 21 km/sec.

We have varied slightly the  $H^+$  ion velocity, density and



temperature at the lower end to study the sensitivity of the solutions to these parameters. At the lower end the hydrogen ion density is increased to  $100 \text{ cm}^{-3}$ , velocity is decreased to 10 km/second and the temperature is raised to 3800°K. The results of these changes are presented in figures (I.2.a) - (I.2.f). The qualitative picture and relative importance of the contributing terms remain the same as before. The quantitative change is obvious as the initial conditions are changed. The Mach number calculated in this case of flow velocity of  $16 \text{ km s}^{-1}$  is 2.68. This is in good agreement with the value 2.6 calculated by Nagai et al. [1984].

Electron temperatures parallel and perpendicular to the geomagnetic field lines are shown in Figure (I.1.g). The most important effects exhibited by electron temperature are:

- (1) temperature anisotropy
- (2) below 2500 km the electron gas is collision dominated, as noted by Schunk et al. [1981].

"Collision dominated" implies that the collisional relaxation rate is greater than the rate associated with the driving term that produces the anisotropy. Appreciable temperature anisotropy develops above 2500 km. Both temperature parallel and perpendicular to the field line increases with altitude. Heat flow is downward here (that is, heat flows from the magnetosphere to the ionosphere) as considered by Schunk et al. [1981] with positive temperature gradients. Also, as noticed

by Schunk et al. [1981], the electron temperature ratio at the upper end is  $T_{\perp}/T_{\parallel} \sim 2$ . The contributions from the collision terms are very important below 2500 km in equations (I.13) and (I.14). Since the collision terms are important in this region, the electron temperature anisotropy observed in this region is very small. The anisotropy increases with altitude. The electron temperature variation is produced mainly as a balance between heat flow processes and the mirror force process. In order to preserve the adiabatic invariant in an increasing magnetic field (downward heat flow), the electron perpendicular energy increases with the decrease in parallel energy. The parallel and perpendicular temperature gradients are positive for this case and these terms are important at all altitudes in equations (I.15) and (I.16). The electron species velocity is less than the electron thermal velocity.

Our results here are in good agreement with Schunk and Watkins [1981] low electron temperature case. Schunk and Watkins [1981] varied the boundary electron temperature gradients to see the extent to which their solutions are valid. Their results show that with the increase in boundary electron temperature gradient the electron temperature is increased but the direction of anisotropy remained the same. It is also clearly explained by Schunk and Watkins [1981] that this observed anisotropy is opposite to that predicted by the Chew-Goldberger-Low (double adiabatic) energy equations. The

tendency of the adiabatic terms to produce an anisotropy with  $T_{||} > T_{\perp}$  is also present in our equations, but the heat flow processes dominate over the adiabatic processes and we observe an anisotropy with  $T_{\perp} > T_{||}$ . For very strong heat flows the results of the 13-moment and 16-moment systems of equations are expected to be significantly different.

The electron temperature profiles cannot be directly compared to Mitchell and Palmadesso [1983]. They treated the upper boundary as an electron heat sink, which decreases the electron temperature with altitude.

Now we extend our upper boundary to 10 Re. The electron temperatures parallel and perpendicular to the magnetic field lines are set equal to  $T_{e||} = T_{e\perp} = 6000^{\circ}\text{K}$  at this boundary. The isotropic electron temperature at the magnetosphere helps us to determine the effects of currents and resistivity on electron temperatures in our later studies discussed in chapters IV and V. Actual measurements of the temperature of outflowing ionospheric electrons at the upper end of the flux tube are not available at this time and  $6000^{\circ}\text{K}$  is chosen arbitrarily to suit other measured quantities used as the boundary conditions in this steady state model. The results of these simulations are presented in figures (I.3.a) - (I.3.e). The qualitative picture and the relative importance of the terms remain the same as before. The change in electron

temperature profile is expected as now the upper end is held at a fixed temperature. The ratio  $T_{\perp} / T_{\parallel}$  can vary depending on the upper boundary conditions. The Mach numbers calculated from our results are 4.1, corresponding to a flow velocity of 21 km/sec and 2.7 for a velocity of 16 km/sec.

#### I.4 DISCUSSIONS

We have studied the steady state behavior of the plasma encompassing the geomagnetic field lines using equations based on the 16-moment system of transport equations. This is the first successful steady state solution to the 16-moment set of transport equations for the polar wind [Ganguli et al., 1985a]. Previous theoretical works on the polar wind including hydrodynamic, adiabatic and transport equations have been discussed and compared for advantages and disadvantages of each procedure and in order to validate our model. In a generalised system of transport equations, the advantages of using the 16-moment system with a bi-Maxwellian distribution function, as compared with the 13-moment system with a Maxwellian distribution function have been discussed. The results of this simulation are compared with the above-mentioned previous studies of the polar wind and recent experimental results based on DE-1 satellite observations.

The asymptotic behavior of the solutions of the transport equations at high altitudes is quite sensitive to the boundary conditions applied at the lower end of the flux tube. This, coupled with absence of any standard set of assumptions for specifying those dynamic variables for which upper boundary conditions must be supplied, leads to considerable variation of the results at high altitudes in the studies referenced above. Effectively, one finds similar ionospheres and widely different magnetospheres in this group of calculations (i.e., different characteristics for the upflowing plasma component of ionospheric origin in the magnetosphere). While this makes quantitative comparison of results somewhat difficult, it is clear that qualitative agreement among the various calculations is good. Our results are in good agreement with the observations of Nagai et al. [1984].

We are interested in investigating the effects of return currents and anomalous transport processes on auroral field line equilibria, which we will discuss in the following chapters.



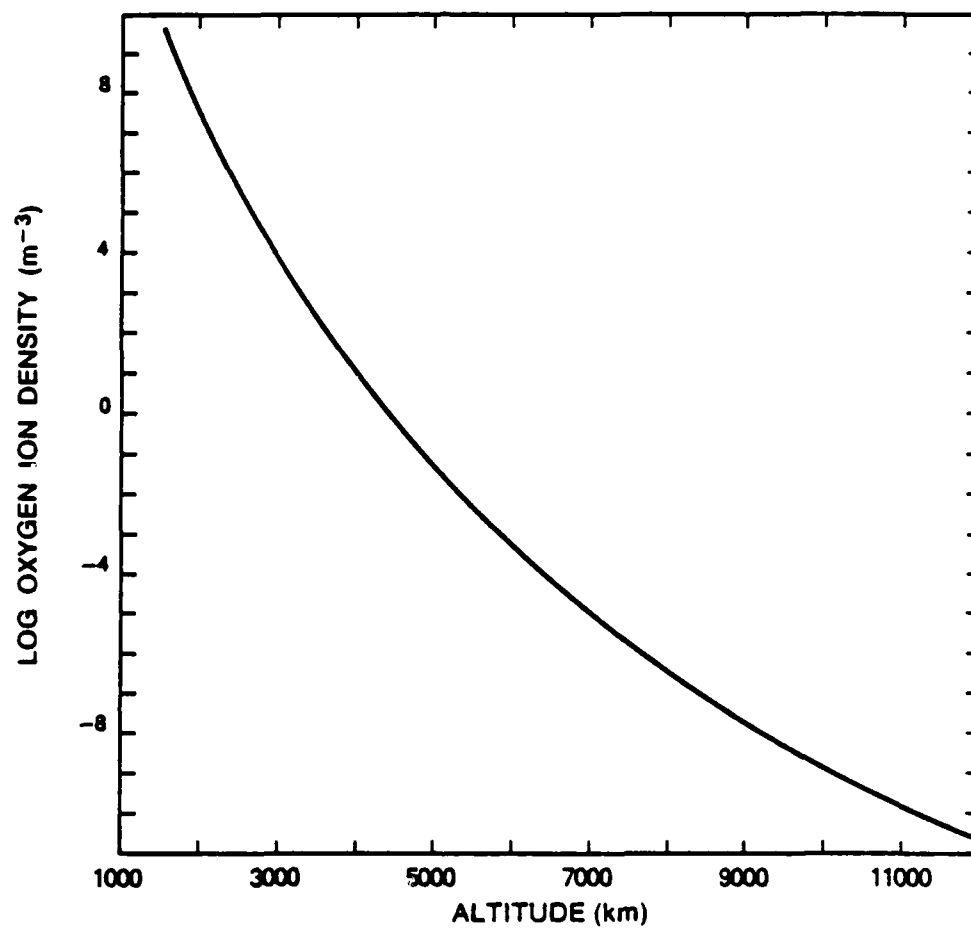


Fig. L1.a — Oxygen ion density profile for steady-state polar wind

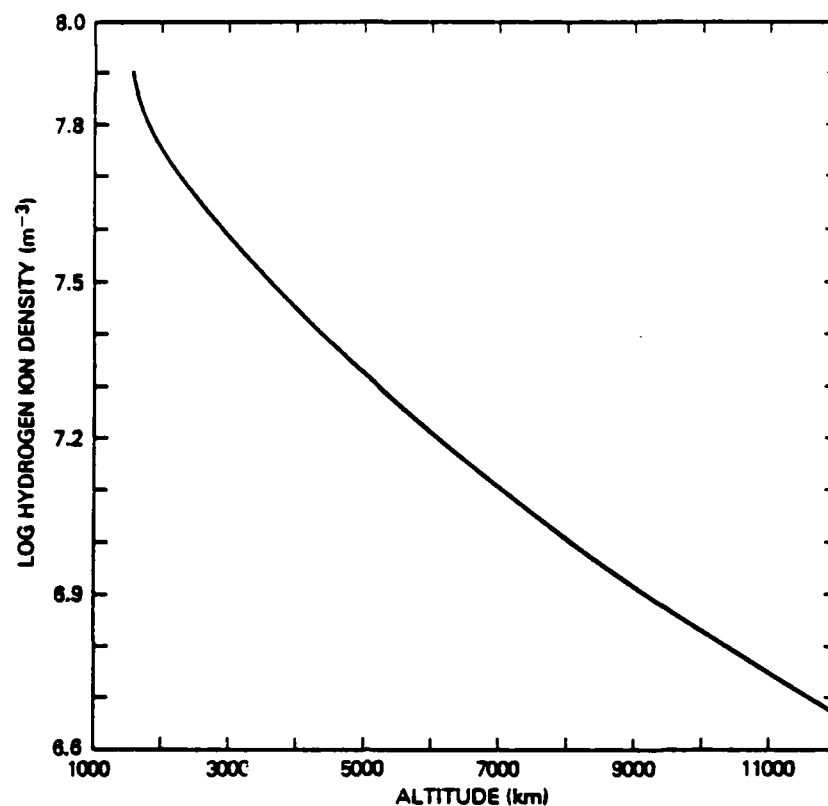


Fig. 1.1.b —  $H^+$  ion density profile vs altitude

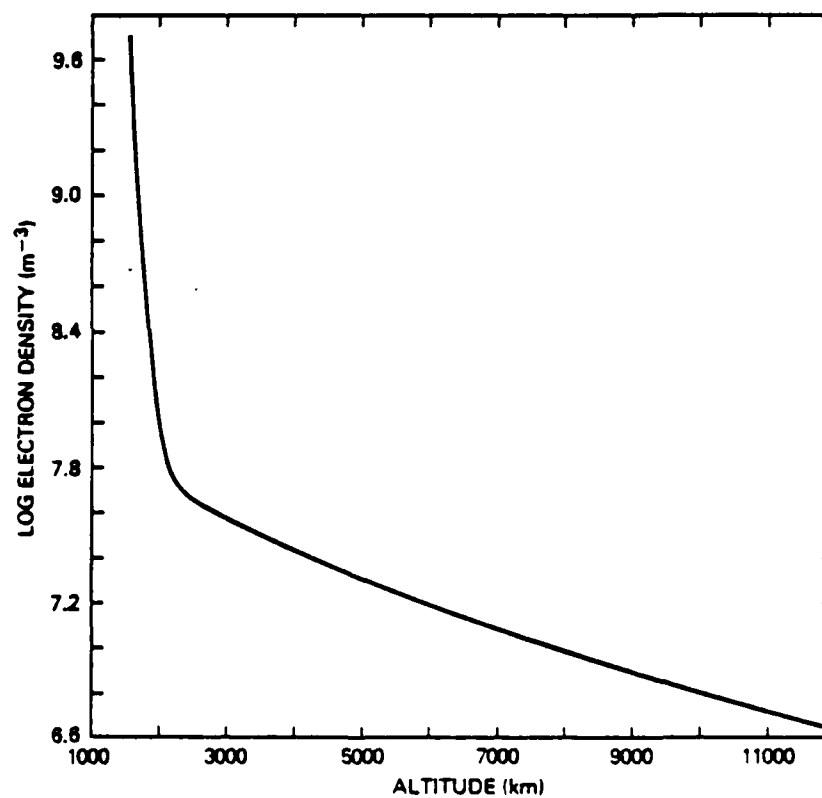


Fig. 1.1.c — Electron density profile vs altitude



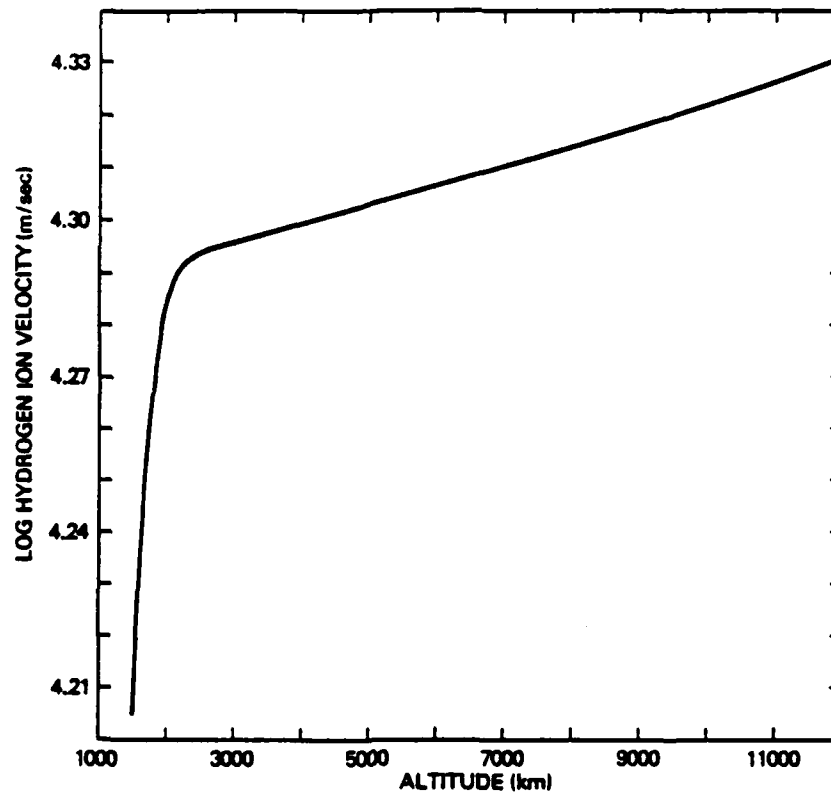


Fig. I.1.d —  $H^+$  ion velocity profile vs altitude

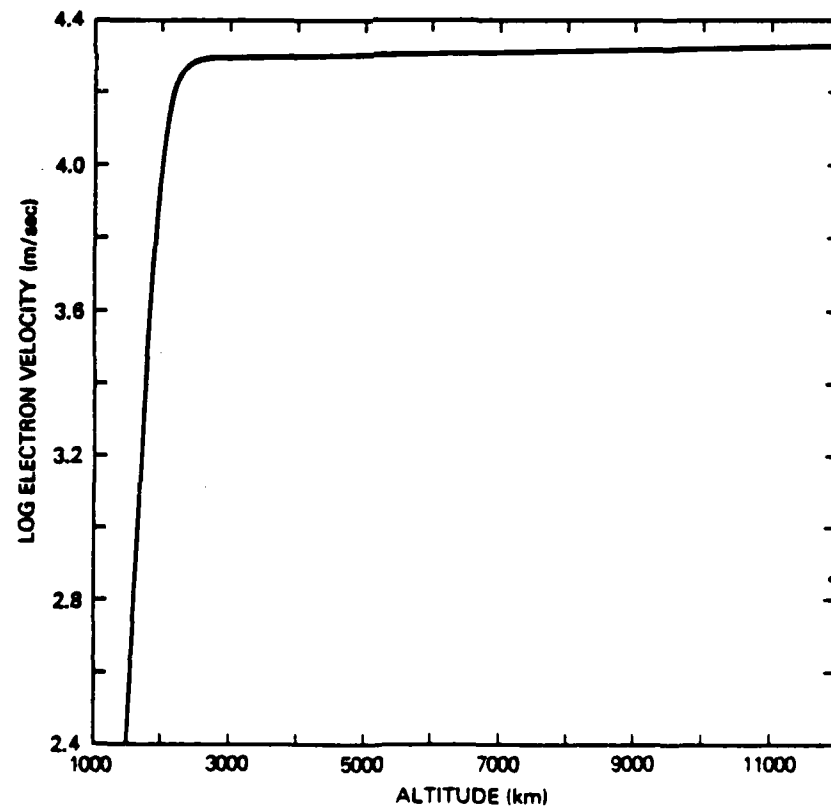


Fig. I.1.e — Electron velocity profile vs altitude

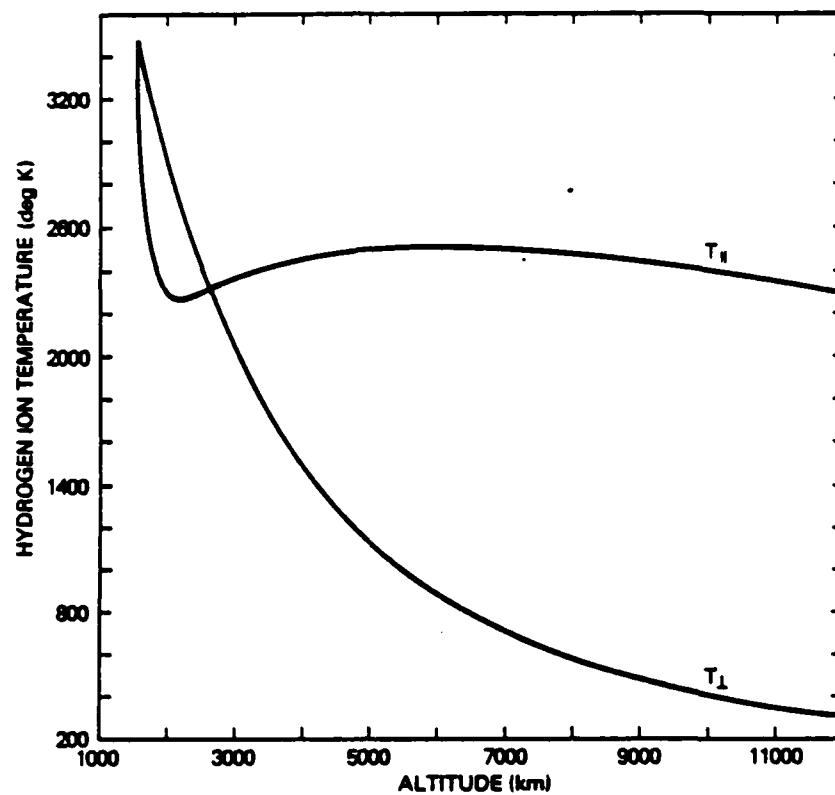


Fig. I.1.f —  $H^+$  ion temperature parallel and perpendicular to the geomagnetic field

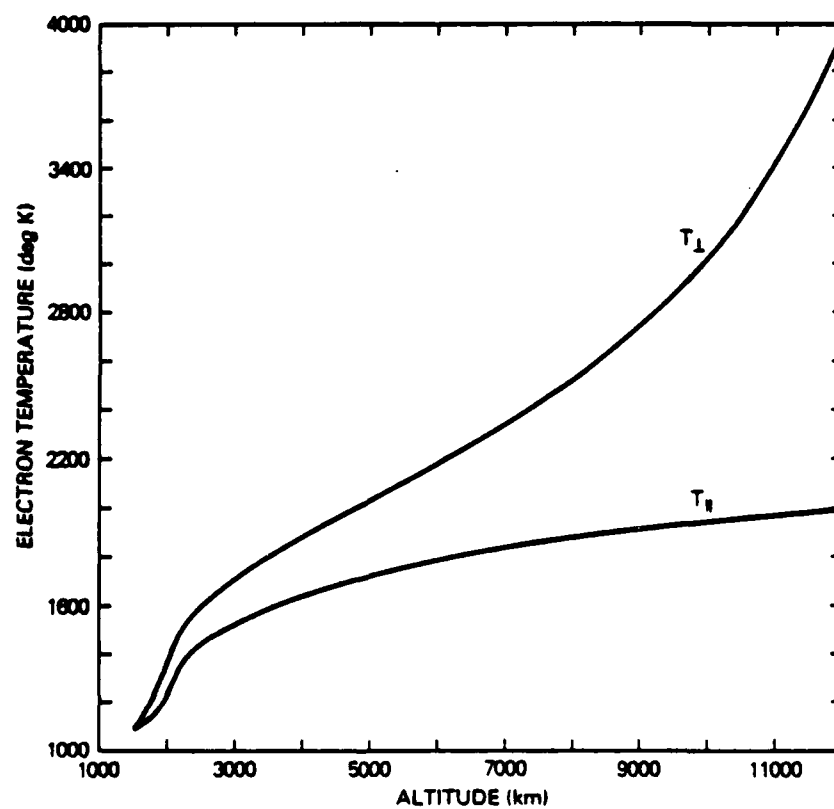


Fig. I.1.g — Electron temperature parallel and perpendicular to the geomagnetic field

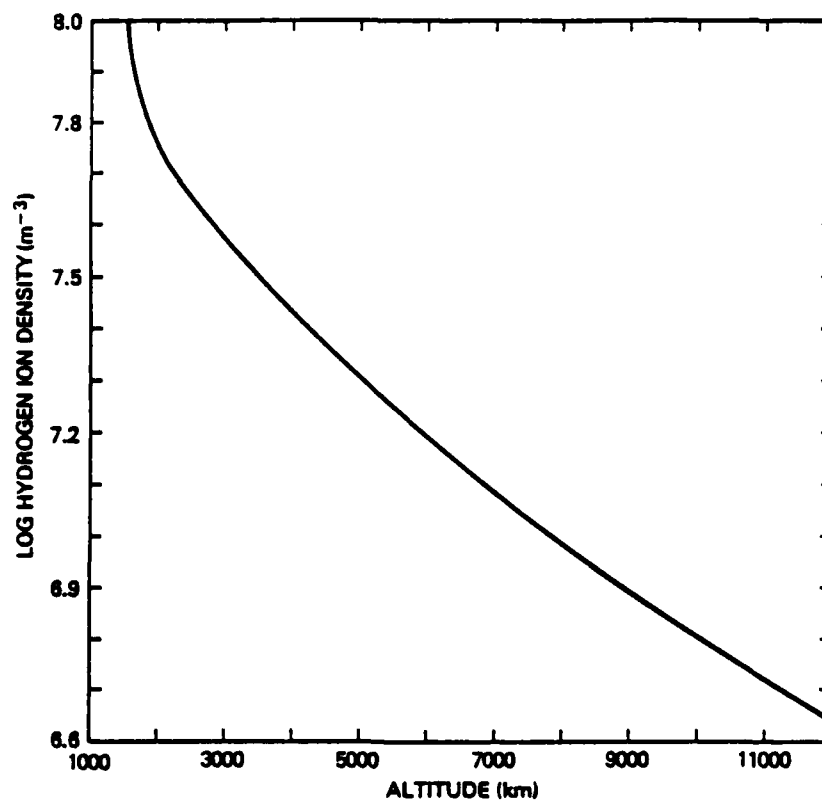


Fig. 1.2.a — H<sup>+</sup> ion density profile vs altitude

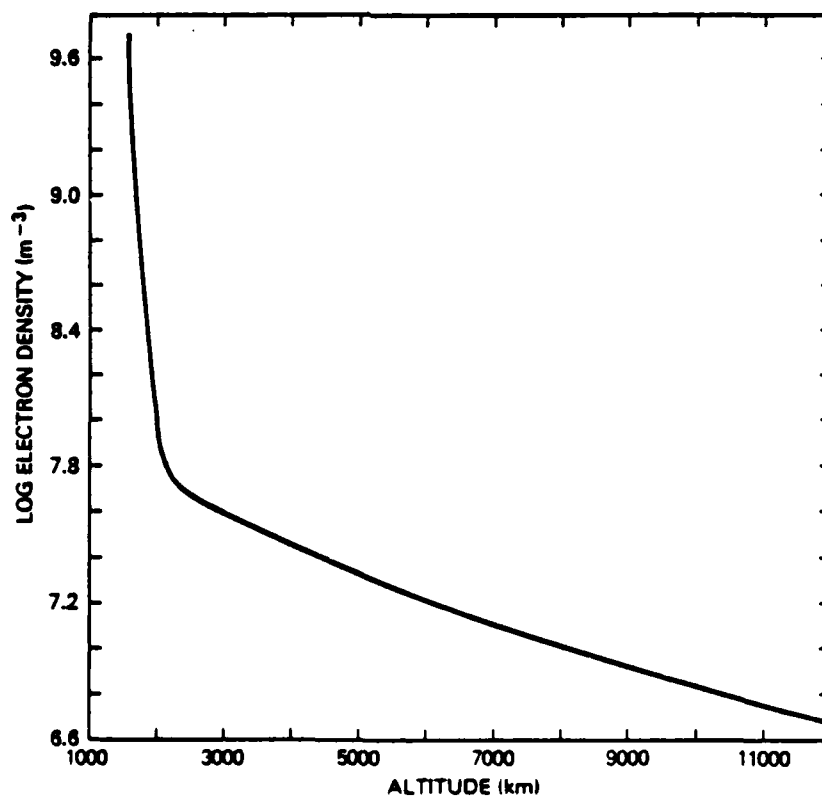


Fig. 1.2.b — Electron density profile vs altitude

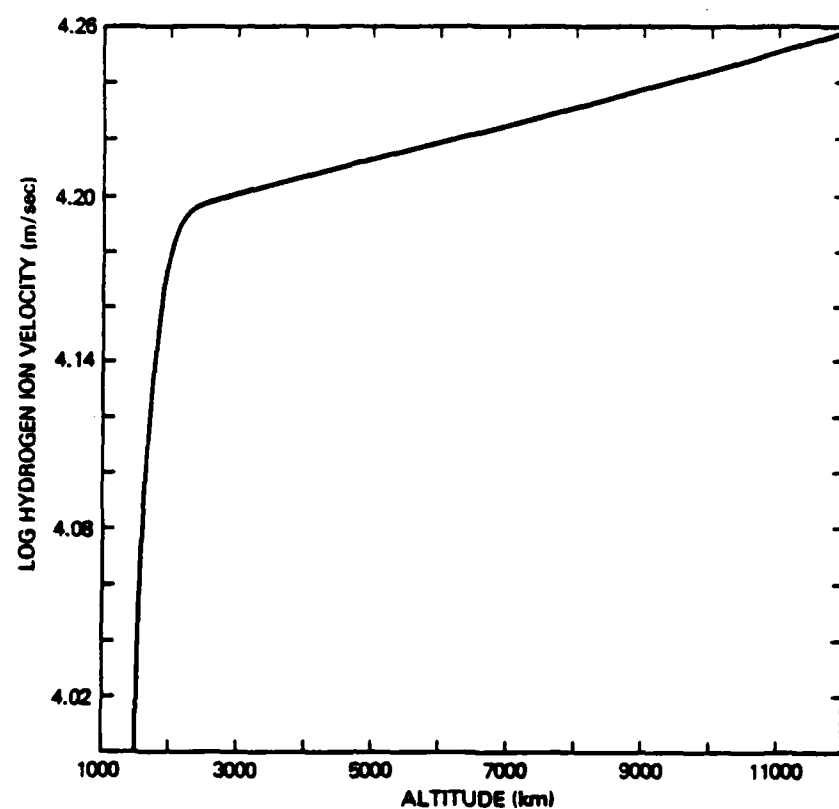


Fig. 1.2.c —  $H^+$  ion velocity profile vs altitude

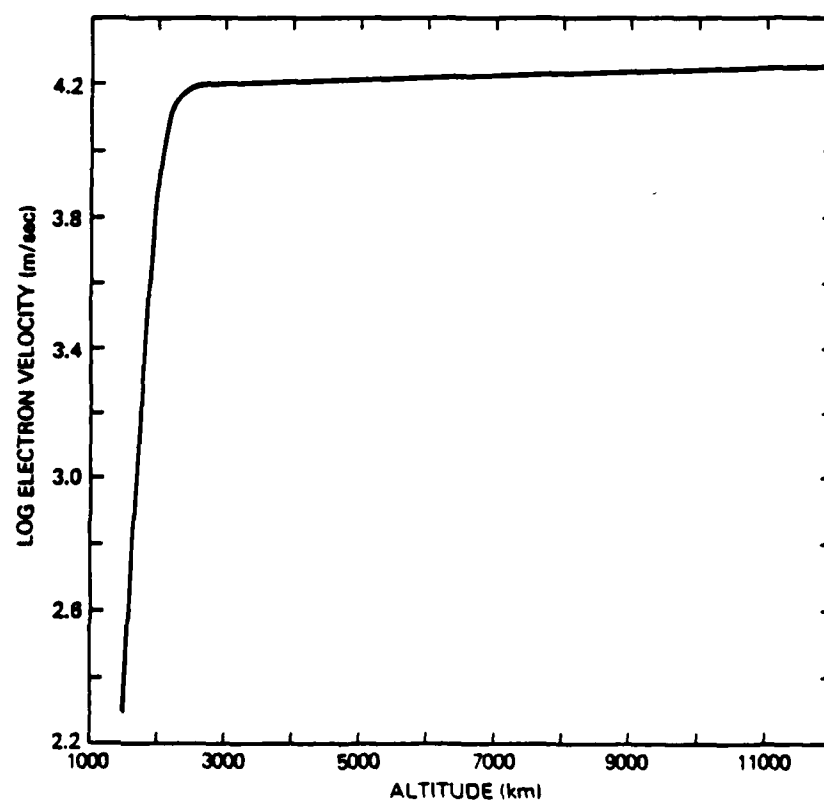


Fig. 1.2.d — Electron velocity profile vs altitude

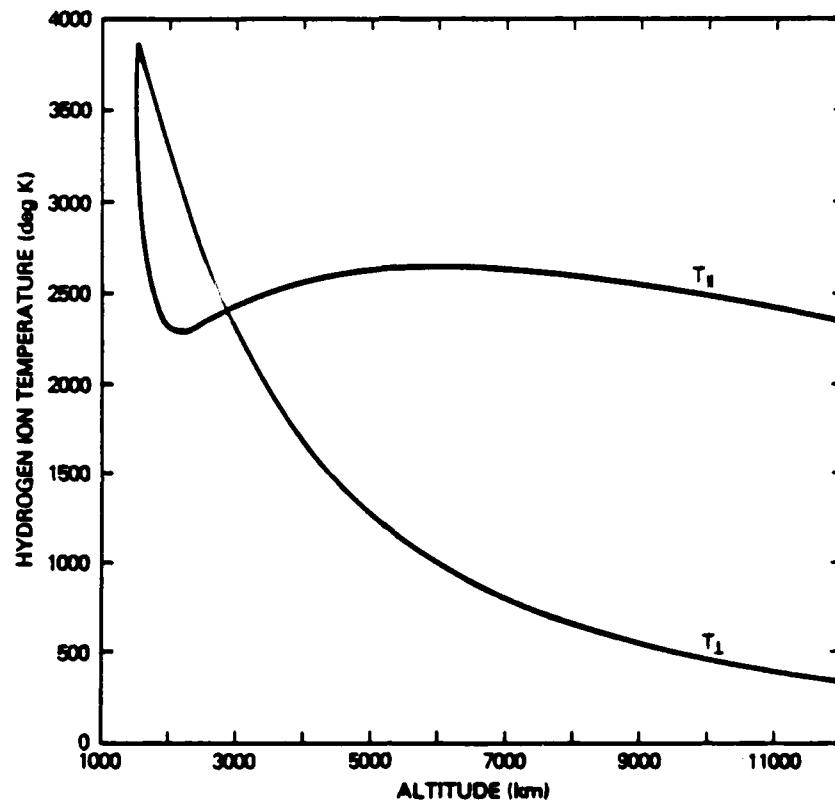


Fig. I.2.e —  $H^+$  ion temperature parallel and perpendicular to the geomagnetic field

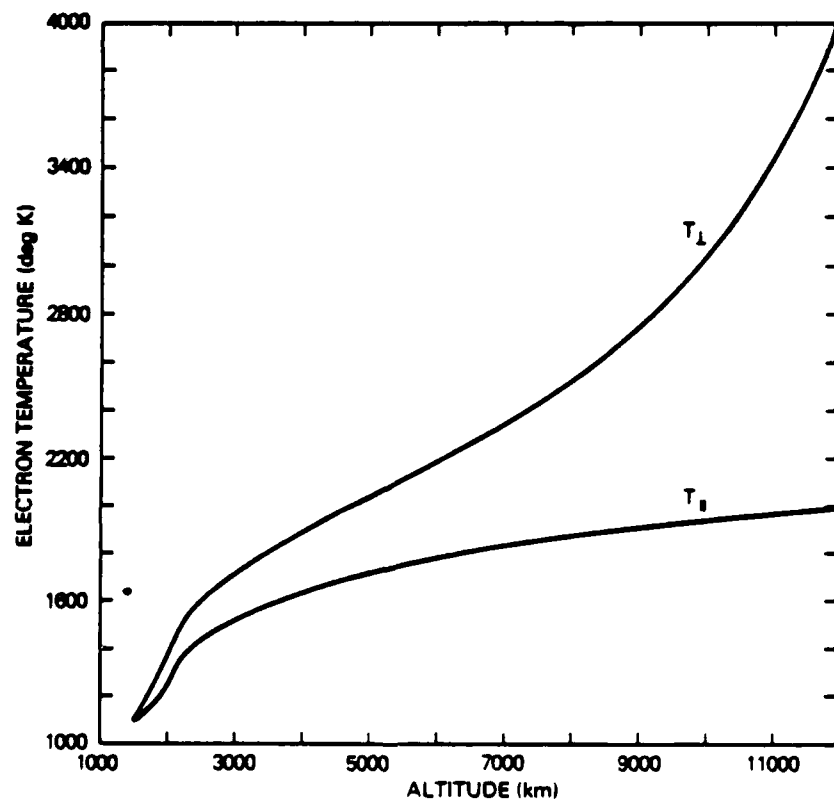


Fig. I.2.f — Electron temperature parallel and perpendicular to the geomagnetic field

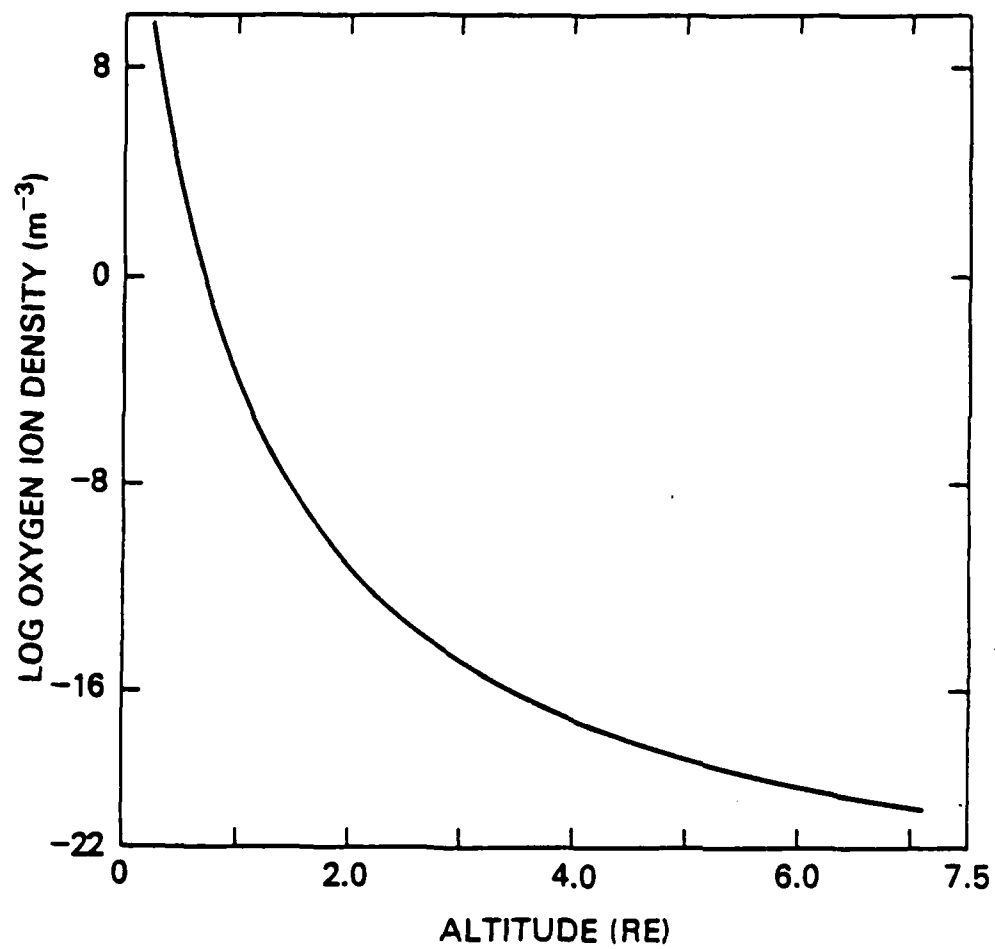


Fig. L3.a — Oxygen ion density profile for steady-state polar wind

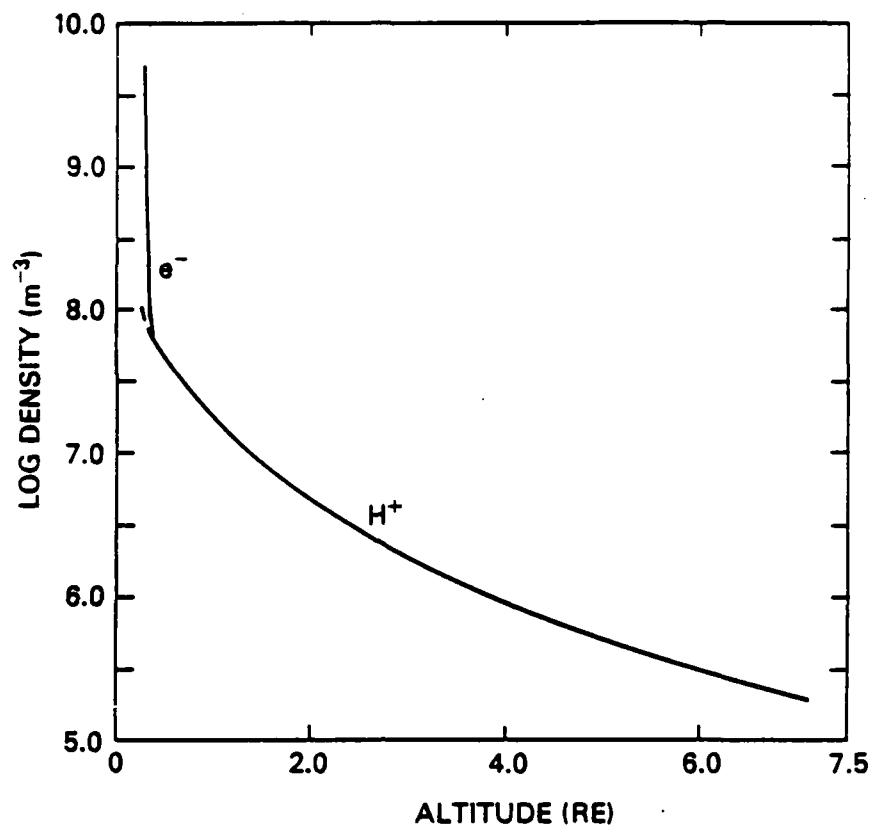


Fig. I.3.b —  $H^+$  and  $e^-$  density variation with altitude

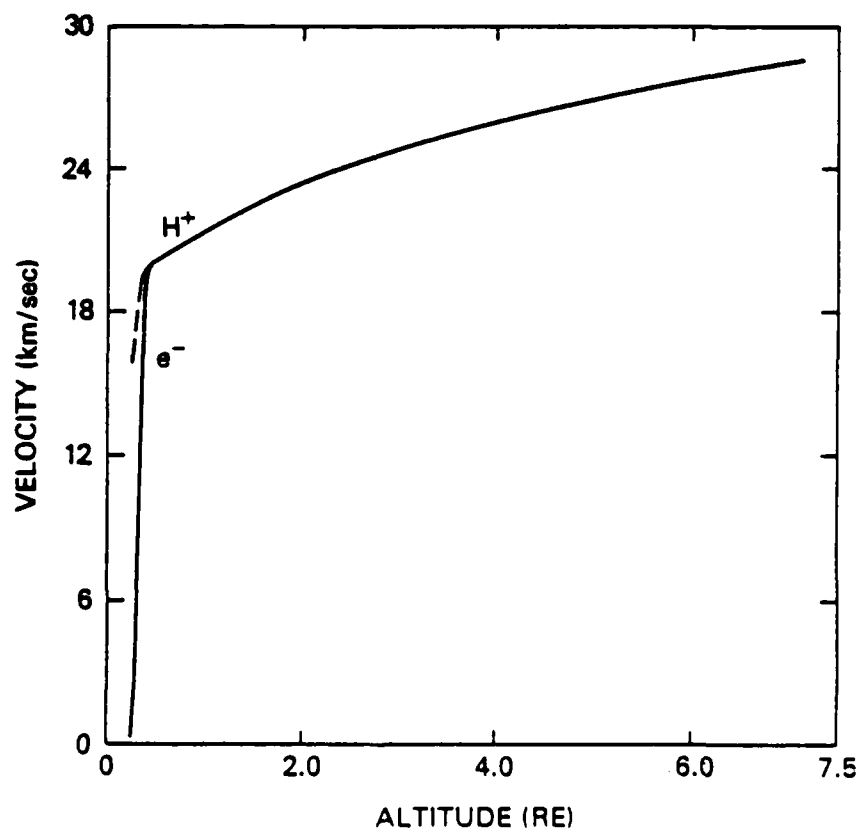


Fig. I.3.c —  $H^+$  and  $e^-$  velocity variation with altitude

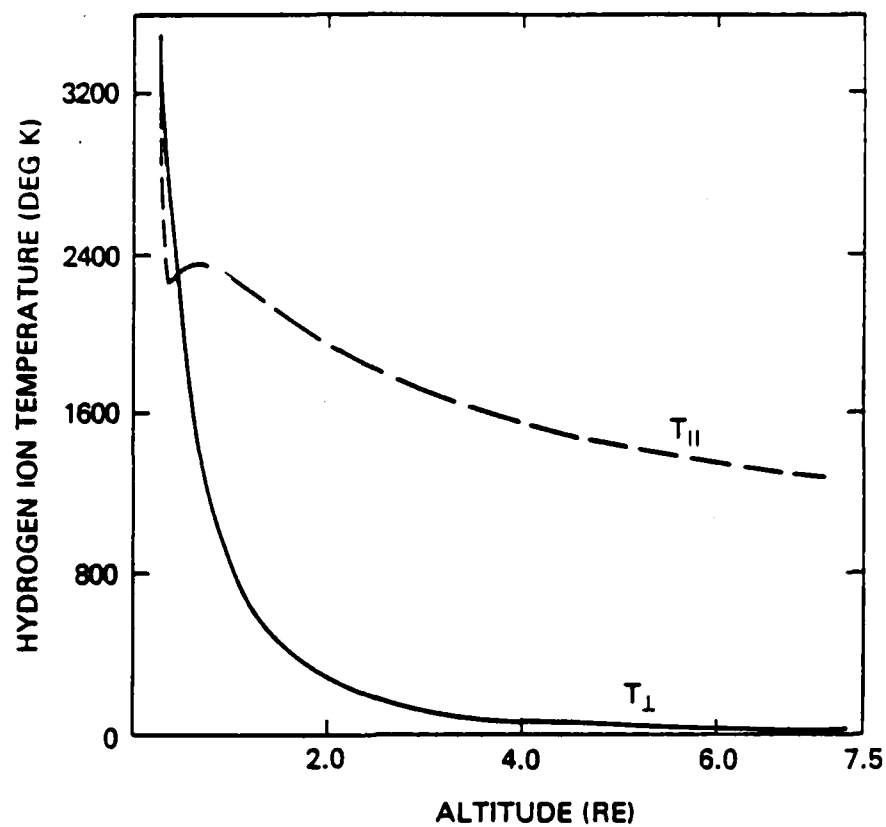


Fig. 1.3.d —  $H^+$  ion temperature parallel and perpendicular to the geomagnetic field

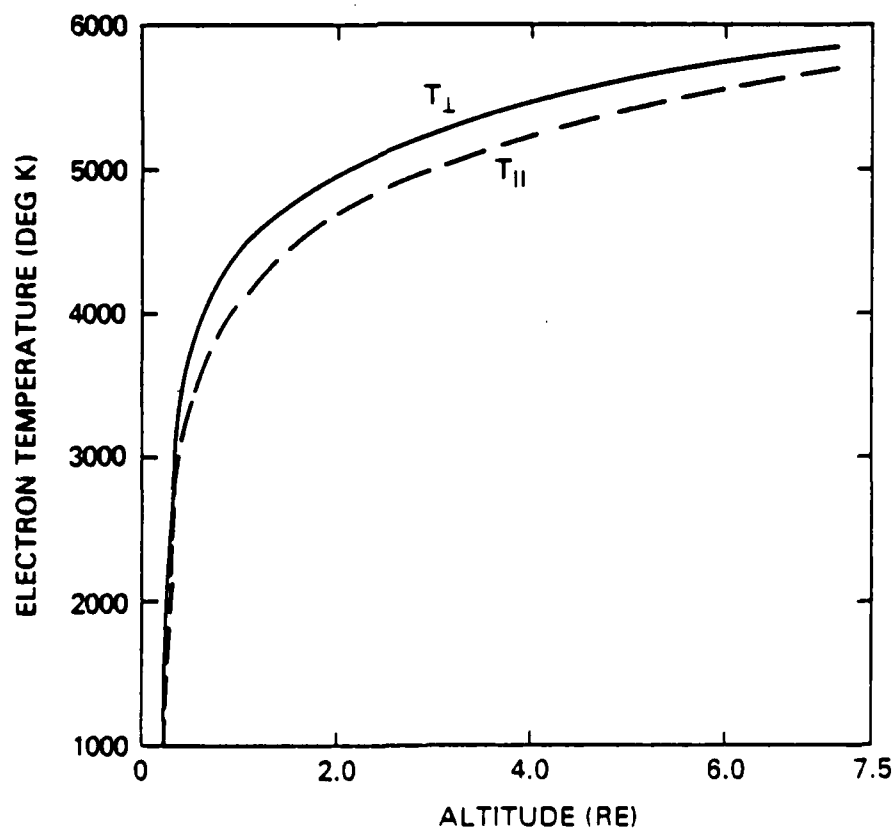


Fig. 1.3.e — Electron temperature parallel and perpendicular to the geomagnetic field



## **CHAPTER II**

### **FIELD-ALIGNED CURRENT SYSTEMS**

#### **IN THE EARTH'S IONOSPHERE AND MAGNETOSPHERE**

In chapter I we have discussed the behavior of current free plasma outflow along geomagnetic field lines in the high latitude topside ionosphere. We are now interested in investigating the effects of field aligned currents on auroral field line equilibria. In this chapter we review the previous works and summarize the observations of field aligned currents in the earth's magnetosphere. The discussion follows the outline below.

- 1 . Definitions
2. Sources of Field-Aligned Currents (FAC)
3. Observations
  - (a) Early observations of Birkeland currents
  - (b) Observed densities and their variations with geomagnetic activity
  - (c) Seasonal variation of FACs
  - (d) FAC characteristics during substorms
  - (e) The relationship between FAC and IMF
  - (f) Discrete and diffuse Auroras and their relation to FACs
4. Role of FAC in magnetosphere-ionosphere coupling.

## FIELD-ALIGNED CURRENTS

### II.1 DEFINITIONS

The currents that flow along geomagnetic field lines of earth's magnetosphere are called the Field Aligned Currents (FAC or  $J_{||}$ ). They were first proposed theoretically by Birkeland in 1908 and hence are also known as Birkeland currents. These currents flow in to the polar and auroral regions and constitute the major link between the ionosphere and the magnetosphere. There are large and small scale FAC's. In both cases, they are closed through the ionospheric Pedersen currents.

Large scale field-aligned currents are concentrated in two principal areas which encircle the geomagnetic pole, as does the so called auroral oval [Iijima and Potemra, 1976a]:

(1) region 1, located near the poleward boundary of the field-aligned current region. The current flows into the ionosphere at dawn and out of it at dusk (figure II.1).

(2) region 2, located near the equatorward boundary. The current flows into the ionosphere at dusk and out of it at dawn.

Three other main types of FAC are:

(3) cusp currents: located poleward of region 1 in the cusp region and are also of opposed polarities. These currents generally flow into the ionosphere in the post noon sector and away from the ionosphere in the prenoon sector, depending on the sign of  $B_y$  [Doyle et al., 1981]. At a given Magnetic Local Time (MLT) the flow of the cusp region FAC is opposite to that of the region 1 FAC [Iijima et al., 1978].

(4) A three-layer overlap of current sheets apparently exists in the Harang discontinuity, near midnight. This layer consists of an upward flowing field-aligned current surrounded to the north and south by the downward flowing currents [Rostoker, 1974].

(5) An altogether different pattern of currents is sometimes observed following extended periods of northward interplanetary  $B_z$ , as noted by Burke et al. [1979]. This was also explained by Iijima et al. [1984].

Within the region 1/region 2 current system, small-scale distributions of both upward and downward currents are observed in association with auroral arcs. Such current systems are associated with local gradients in electric fields and conductivities but do not change the direction of the region 1 or region 2 net currents [Anderson and Vondrak, 1975].

## II.2 SOURCES OF FAC

The sources of different types of FAC were proposed by Stern [1983]. Those are as follows:

(1) Source of region 1 currents : The region 1 current sheets represent the primary circuit between the solar wind and the ionosphere. Near noon  $J_{||}$  is produced by dynamo action of the solar wind on the earth's magnetosphere. Away from noon the source is probably the part of the plasma sheet closest to its outer edge (figure II.2). Dynamo action is the general name given to the process by which an emf is developed around a circuit in a magnetic field, part of which may be in motion [Stern, 1983]. Dynamo action can take place both in open and closed magnetospheres. The region 1 currents draw energy from the solar wind via open field lines. In a closed magnetosphere, the dynamo action is generated due to sunward plasma convection from the plasma sheet. The later process is possible but the energy available from it is very little to contribute as a source of Birkeland currents.

(2) Source of region 2 currents: As plasma flows earthward from the tail of the magnetosphere, magnetic drifts tend to deflect ions toward dusk and electrons toward dawn. This produces a surplus of ions at dusk and of electrons at dawn (fig. II.3). Such a separation was first suggested by Alfven [1939].

It was pointed out by Schield et al. [1969], Helmer [1963] and Karlson [1962, 1963] that unhindered sunward drift of particles of different energy produces different Alfvén layers and each of these layers is accessible only to particles of one sign. This causes charge imbalance in the plasma. This excess charge should either be precipitated or neutralized; in either case a current flows to the ionosphere. These mechanisms are not too rapid and therefore an appreciable build up of space charge is avoided.

(3) Cusp currents: The boundary layer of earth's magnetosphere generates FAC by dynamo action [Eastman et al., 1976; Sonnerup, 1980, Bythrow et al., 1981, Doyle et al. 1981]. These might give rise to cusp currents.

(4) The patterns of polar currents are strongly related to the polar cap electric fields. When the IMF  $B_z$  is southward, the electric field is directed from dawn to dusk across the polar cap. When  $B_z$  has a northward orientation Burke et al. [1979] have detected dusk to dawn electric fields in the central polar cap and this electric field pattern is referred to as type N (figure II.4). The corresponding convection pattern shows sunward convection in the central polar cap and antisunward convection along flanks of the polar cap.

(5) As noted by Stern [1983], the explanation of the current flow near midnight remains unclear. The middle layer of

the three-layer overlap could be the "Harang filament", a continuation of the electric current carried by auroral electrojets. Such a filament has been proposed by Rostoker [1974].

We will now confine ourselves mainly to region 1/region 2 current systems.

### II.3 OBSERVATIONS

#### (a) EARLY OBSERVATIONS OF BIRKELAND CURRENTS

Particle, magnetic field and electric field experiments aboard rockets and satellites have confirmed the presence of Birkeland currents. Reviews of rocket observations of Birkeland currents were presented by Arnoldy [1974], Anderson and Vondrak [1975] and Cloutier and Anderson [1975]. They pointed out that field-aligned currents provide the major link between the magnetosphere and ionosphere. They also suggested that the association of these currents with auroral features on a very small scale implies that auroral acceleration may result from the current flow.

More complete observation of Birkeland currents have come from Satellite experiments. Simultaneous observation of

particles, electric and magnetic field made the measurements complete. Numerous improvements have been made on the measurement techniques and the major findings from these experiments will be discussed in the following sections.

(b) **OBSERVED CURRENT DENSITIES AND THEIR VARIATIONS WITH  
GEOAMAGNETIC ACTIVITY**

Region 1 currents are the strongest and most stable Birkeland currents. Here, the largest current densities occur between 0700 and 0800 MLT, with current flowing into the ionosphere (with an average value  $J_{||} \sim 2.0 \mu\text{A}/\text{m}^2$ , for  $2- \leq K_p \leq 4+$  and between 1500 and 1600 MLT, with current flowing away from the ionosphere ( $J_{||} \sim 1.9 \mu\text{A}/\text{m}^2$  for the same  $K_p$  range) [Iijima and Potemra, 1976a]. The currents in region 1 are statistically larger than the currents in region 2 at all local times except in the pre-midnight to early morning sector. In region 2 the largest current densities occur during the night between 2100 and 2300 MLT, with current flowing into the ionosphere ( $J_{||} \sim 1.0 \mu\text{A}/\text{m}^2$  for  $2- \leq K_p \leq 4+$ ) and between 0100 and 0300 MLT, with current flowing away from the ionosphere ( $J_{||} \sim 1.3 \mu\text{A}/\text{m}^2$ ). The total field-aligned current in region 1 is significantly larger than the total field-aligned currents in region 2 during relatively quiet times while during active periods, the total current flow in both regions become nearly equal.



The field aligned current densities show good correlation with Kp index. The region 1 currents show greater Kp dependence than region 2 currents. The region 1 currents appear to persist during very low geomagnetic activity. Region 2 currents dominate during the local times when auroral electrojets are more active. Figure (II.5) [Iijima and Potemra, 1978] shows distribution and flow directions of large-scale Birkeland currents during active periods.

(c) SEASONAL VARIATIONS OF FACS

Smiddy et al. [1980] have observed in the vicinity of the dawn-dusk meridian that (1) under winter polar cap conditions, the region 1/region 2 current systems are confined to the auroral oval. The polar cap conductivity is too low to support measurable transpolar Pedersen currents. (2) Under summer-like polar cap conditions, the polar cap conductivity is high enough to support transpolar Pedersen currents. In these cases the region 1 currents exceed those of region 2 currents.

In another study by Fujii et al. [1981] it was noted that (1) the single-sheet currents are observed more often in summer than in winter and (2) the intensities of single and double-

sheet field aligned currents on the dayside are larger during the summer than in winter.

(d) FAC CHARACTERISTICS DURING SUBSTORMS

Large scale field-aligned current characteristics during substorm expansion and recovery phases were observed by Iijima and Potemra [1978] using the Triad satellite. The region 1/region 2 current system which exists in quiet condition also persists during active substorm periods ( $|AL| \geq 100\gamma$ ). The average total current flowing into the ionosphere always equals the average total current flowing out of the ionosphere for a wide range of quiet and disturbed conditions. The average total current during quiet conditions is  $\sim 2.7 \cdot 10^6 A$  and during disturbed conditions this quantity is roughly doubled, the latitude widths of region 1 and 2 increase by factors of 1.2-1.3, and the centers of these regions shift equatorward by  $2^\circ$ - $3^\circ$ .

During active substorm periods the densities of region 2 Birkeland currents show their largest enhancement in the local time sector, i.e., the pre-midnight to early morning sector, where the westward auroral electrojet is most active.

In the Harang discontinuity sector (2000-2400 MLT), when the westward auroral electrojet has intruded deeply into the

evening sector, the Triad magnetometer data exhibit complicated and fine-structured variations. These variations indicate the presence of complex field-aligned currents in this sector.

Figure (II.6) illustrates substorm associated changes super-imposed upon the basic distributions of Birkeland currents [Iijima and Potemra, 1978]. The alignment of current sheets is generally along the boundary of the auroral oval but noticeable distortions of this alignment occur during the substorm. The alignment of current sheets in regions 1 and 2 varies throughout the course of substorm activity [Potemra, 1979]. During highly disturbed states of auroral activity, the alignment of current sheets in the evening sector of region 1 varies the most. During the recovery phase, in the morning sector of both region 1 and 2, the alignment of current sheets varies. The intensity distribution along either current sheet system may also undergo changes.

Shuman et al. [1981] using the data from S3-2 satellite have made interesting conclusions. The polar orbiting satellite, S3-2, has provided measurements of the ambient magnetic field, the electric field and the auroral electron flux during the very intense substorm period of March 26, 1976. They have calculated the height-integrated Pedersen conductivity during the active time which was typically  $10-30 \Omega^{-1}$ . The corresponding particle precipitation on the nightside was the major factor in

controlling the magnitude of the ionospheric conductivity, outweighing the influence which sunlight has in quiet times. High particle fluxes corresponded to the region of upward currents.

(e) THE RELATIONSHIP BETWEEN FIELD-ALIGNED CURRENTS AND INTERPLANETARY MAGNETIC FIELD (IMF)

Since the FAC system plays an important role in the coupling processes which connect the interplanetary medium and the auroral ionosphere, the FAC intensities should show a good correlation with various solar wind and IMF parameters.

The effect of IMF on Birkeland currents has been studied by Iijima and Potemra [1982], Iijima et al. [1978], Saflekos and Potemra [1980], Doyle et al. [1981] and McDiarmid et al. [1977, 1978a, 1978b].

The basic spatial distribution of flow direction patterns of the region 1 and region 2 currents is not affected by the IMF, but the current intensity changes. When the interplanetary magnetic field  $B$  is directed toward the sun ( $B_y < 0$ ,  $B_x > 0$ , in solar magnetospheric co-ordinates) larger current intensities occur on the dusk side of the North Pole [McDiarmid et al., 1978] and on the dawn side of the South Pole [Saflekos and Potemra,

1980]. When the IMF is directed away from the sun ( $B_Y > 0$ ,  $B_X < 0$ ) the above current distributions are reversed.

Iijima and Potemra [1982], using the Triad Satellite data, have correlated the densities of region 1 FAC in the morning sector (0800 to 1300 MLT) during IMF  $B_Y > 0$  and in the afternoon sector (1100 to 1600 MLT) during IMF  $B_Y < 0$  with a variety of interplanetary quantities. They have used the least square technique to compute the correlation coefficients. Of the various quantities computed we will consider the following only: IMF  $B_Z$ ,  $B_Y$ , Akasofu's  $\epsilon$  parameter, and  $(B_Z^2 + B_Y^2) \sin^2(\theta/2)$  which closely resembles the Kan and Lee [1979] function  $VB \sin^2(\theta/2)$ .

Perreault and Akasofu [1978] and Akasofu [1979] found an interplanetary quantity  $\epsilon(t)$  which correlates well with magnetic storms and individual magnetospheric substorms.  $\epsilon(t)$  is known as the energy coupling function between the solar wind and the magnetosphere and is given by

$$\epsilon(t) = VB^2 \sin^4(\theta/2) l_0^2$$

where  $V$  is the solar wind speed,  $B$  is the magnitude of the interplanetary magnetic field,  $\theta$  is the angle between the  $z$  direction of geocentric solar-magnetospheric coordinate and IMF in  $Y, Z$  plane and  $l_0$  is a constant length = 7 earth radii.

Kan and Lee [1979], on the basis of a field line reconnection concept, have calculated the power delivered by the solar wind dynamo to the open magnetosphere as

$$P = \phi_{KL}^2 / R = (V/R) \varepsilon(t)$$

where,  $R$  is the equivalent resistance connected to the solar wind-magnetosphere dynamo.  $\phi_{KL}$  is the polar cap potential, given by

$$\phi_{KL} = VB \sin^2(\theta/2)$$

The Kan and Lee formula is similar to that of Sonnerup's [1974] calculation of the reconnection electric field, given by

$$E_R = VB \sin(\theta/2)$$

Figure (II.7) shows region 1 current densities plotted against negative values of  $B_z$  (southward) and positive values of  $B_z$  (northward). The current densities show good correlations with southward directed  $B_z$  but relatively poor correlation with northward directed  $B_z$ . This supports the interpretation of a half-wave rectifier response of the magnetosphere in regard to Birkeland currents and  $B_z$  [Iijima and Potemra, 1982]. The half-wave rectifier response of the magnetosphere was first suggested

by Arnoldy [1977] and shows that the merging occurs only when the IMF has a southward component ( $\theta > 90^\circ$ ) and no merging component exists when the IMF has a northward direction ( $\theta < 90^\circ$ ). A geometrical explanation of this has been offered by Crooker [1980].

As seen in (figure II.7), current densities of 1 to 2  $\mu\text{A}/\text{m}^2$  persists at the origins of the plots indicating that a northward IMF does not completely "shut off" the system of Birkeland currents [Iijima and Potemra, 1982]. These currents may be related to the convective flow (and associated electric fields) which prevail during periods of northward IMF [Iijima and Potemra, 1982]. The electric field and the corresponding convection pattern during periods of Northward IMF [Burke et al., 1979] is discussed in section 2 and is shown in figure (II.4).

The correlation of Birkeland current densities with  $B_y$  and  $(B_z^2 + B_y^2)^{1/2} \sin^2(\theta/2)$  is good. The correlation with the  $\epsilon$  parameter is fair as only the currents are considered and not the total power.

It was pointed out by Iijima and Potemra [1982] that as the various good correlations (noted above) dominantly involve IMF  $B_y$  and  $B_z$  and their orientation with respect to the geomagnetic field, magnetic reconnection may play an important

role in determining the strength of the region 1 FAC.

Reiff et al. [1981] have shown that the magnitude of the cross-polar cap potential drop is dependent on the orientation of the IMF. When  $B_z$  has a southward orientation, the cross polar cap potential drop ranges from about 50 to 150 kv (as noted from S3-2 satellite data) and the electric field drives convection in the anti-sunward direction (dawn to dusk electric field) over the polar cap. The electric field can be uniformly distributed across the summer polar cap, but more frequently it is concentrated along either the dawn or the dusk flank of the cap [Heppner, 1972]. The particular flank along which the convection concentrates is determined by the sign of the Y component of the IMF [Friis-Christensen et al., 1972]. During these periods the closed and the open field line portions of the magnetosphere form a coupled system. Reiff et al. [1981] using AE-C data have shown that during a period of southward  $B_z$  the cross polar cap potential drop is well correlated with various interplanetary quantities and with the several formulae derived theoretically on the basis of magnetic reconnection theory. Such formulae were given by Hill [1975], Kan and Lee [1979] and many other workers. The Kan and Lee function and Akasofu's  $\epsilon$  parameters are seen to be well correlated with  $B_z$  south cases. Similar work has been done by Doyle and Burke [1982].

During the periods of northward  $B_z$ , the cross polar cap



potential drop decreases to about 10 kv (as noted from S 3-2 satellite data). The electric field is either very irregular or is configured to drive antisunward convection along the flanks of the polar cap and sunward convection in the central polar cap [Burke et al., 1979] as shown in figure (II.4). During periods of southward IMF the polar cap potential drop is highly correlated with the theoretically derived merging rates [Reiff et al., 1981]. These same theories are unable to explain polar cap potential  $\phi_{p.c.}$  variations during periods of northward IMF.

Figure (II.8) is a plot of  $\phi_{p.c.}$  (as measured by S 3-2). Akasofu's  $\epsilon = VB^2 \sin^4 (\theta/2)$  and the Kan and Lee function  $\phi_{KL} = VB \sin^2 (\theta/2)$  versus universal time. V and B are taken from King's data Book [1979]. The formulae used to get  $\phi$  from  $\epsilon$  and  $\phi_{KL}$  function are based on Reiff's [1981] regression analysis based on the data from AE-C.

$$\phi_1 = 39 + 0.014 \phi_{KL}$$

$$\phi_2 = 30 + 0.0051 \epsilon$$

Figure (II.8) shows that cases with  $B_z > 0$  is not explained by existing models. Work needs to be done for the cases of northward  $B_z$  and the periods of magnetic quieting. This was suggested by Burke (private communication).

Based on ground magnetometer measurements, Maezawa [1976]

suggested that during periods of northward IMF the open and closed field line portions of the magnetosphere become decoupled. Viscous interactions near the Low Latitude Boundary Layer drive residual magnetospheric convection at these times.

It is interesting to note that the interplanetary quantities which are well correlated with the region 1 current system are also well correlated with the polar cap potential drop derived on the basis of magnetic reconnection theories. This supports the suggestion made by Iijima and Potemra [1982] that magnetic reconnection may play an important role in determining the strength of region 1 Birkeland currents.

(f) DISCRETE AND DIFFUSE AURORAS AND THEIR RELATION TO FACS

At this stage we can roughly classify the aurorae into two types: discrete and diffuse. This distinction is important as it is now believed that during an auroral substorm the first indication is seen as the auroral breakup near an arc located between the discrete and diffuse auroras in the midnight sector [Akasofu, 1964]. A discrete aurora appears as a single, bright strand, well separated from other auroras by a dark luminosity with a latitudinal width of, at least, several tens of km. [Kamide, 1981].

Small scale field-aligned current systems are embedded

within the large-scale current system, as detected by satellites. Rocket experiments [Anderson and Vondrak, 1975] have measured currents into and out of the ionosphere with scale lengths of 10-20 km. Currents out of the ionosphere are carried by energetic electrons precipitating to form discrete arcs. Return currents are found at the equatorward boundaries of the arc. Simultaneous measurements by the Triad satellite and by all-sky cameras indicate that in the evening sector, discrete arcs are found in region 1 and diffuse aurora in the region 2 current system [Armstrong et al., 1975; Kamide and Akasofu, 1976].

There are two broad classes of discrete arcs, depending on the regions of the ionosphere in which they are found : (1) discrete arcs found in the auroral oval which tend to be aligned in the magnetic east-west direction. They are produced by the precipitation of electrons with energies of several keV. (2) Discrete arcs found in the polar cap are usually sun aligned. They appear most frequently during periods of magnetic quieting while the IMF has a northward component. The electrons that produce these arcs typically have average energies of  $\leq 1$  keV. The plasma sheet is not a source of discrete arcs [Burke et al., 1981]. Discrete arcs appear to be associated with inverted-V events. Kamide and Akasofu [1976] using simultaneous satellite and ground-based observations found that in the evening sector, discrete arcs are confined within the latitudinal region of the upward field-aligned current. Evans et al. [1977], Carlson and Kelley [1977] and Kamide and Rostoker [1977] showed that the

precipitating keV electrons constitute the upward field-aligned current within auroral arcs. Using all-sky camera and triad satellite data, Armstrong et al. [1975] noted that the poleward boundary of the discrete arc marks the poleward boundary of the field aligned current regime.

The diffuse aurorae are characterized by electrons whose pitch angle distributions are nearly isotropic [Burke et al., 1980]. These electrons have energy spectra which either decrease monotonically with increase in energy or have thermal, Maxwellian shapes. Proton fluxes in this region are significant. Near the equatorward boundary of this region the energy fluxes of protons and electrons are of comparable magnitude. Kamide et al. [1979] have shown that in the evening sector, the downward field-aligned current was co-located with the diffuse aurora. Kamide and Akasofu [1975] pointed out that the eastward electrojet is observed only in the evening diffuse aurora region. Identification of diffuse aurora in the evening hours is relatively easy, compared to the morning hours. Using the data from Chatanika radar, Horwitz et al. [1978] showed that the electric field in the evening diffuse aurora is directed generally poleward, whereas it is equatorward in the region of discrete aurora. Lui et al. [1977] have established that the evening diffuse aurora is due to electron precipitation from the plasma sheet. Snyder and Akasofu [1974] indicated that the diffuse aurora can also have considerable structure on small (25 - 50 km) scales especially in the morning sector.

## II.4 ROLE OF FIELD-ALIGNED CURRENTS IN MAGNETOSPHERE

### - IONOSPHERE COUPLING

Field-aligned currents constitute the major link between the magnetosphere and the ionosphere. The upward field-aligned currents are carried by electrons which flow down from the magnetosphere to the ionosphere. The return currents are carried by cold electrons of ionospheric origin. The finite Pedersen conductivity of the ionosphere allows the flow of Birkeland currents which couple the convective flows of plasma in the ionosphere and the distant magnetosphere. The power generated by the solar wind magnetosphere dynamo is dissipated partly into the ionosphere by Joule heating ( $\mathbf{E} \cdot \mathbf{J}$ ). The electrodynamic magnetosphere-ionosphere coupling can be described in terms of an electrical circuit in which the magnetosphere generally provides a voltage source ( $\mathbf{J} \cdot \mathbf{E} < 0$ ) and the ionosphere represents the electrical load ( $\mathbf{J} \cdot \mathbf{E} > 0$ ). The Hall currents ( $v_i \gg \alpha_i$ ,  $v_e \ll \alpha_e$ ) do not affect the energetics of the circuit.

The presence of potential drops along the field lines make the coupling imperfect. Under such conditions of imperfect coupling, Kan and Lee [1980] have shown that the equipotential contours are distorted into V-shaped structures near the convection reversal boundary and S-shaped on the equatorward side.

An early and relatively simple theory of magnetosphere-

ionosphere coupling was proposed by Vasyliunas [1970] and is described schematically in the following figure.

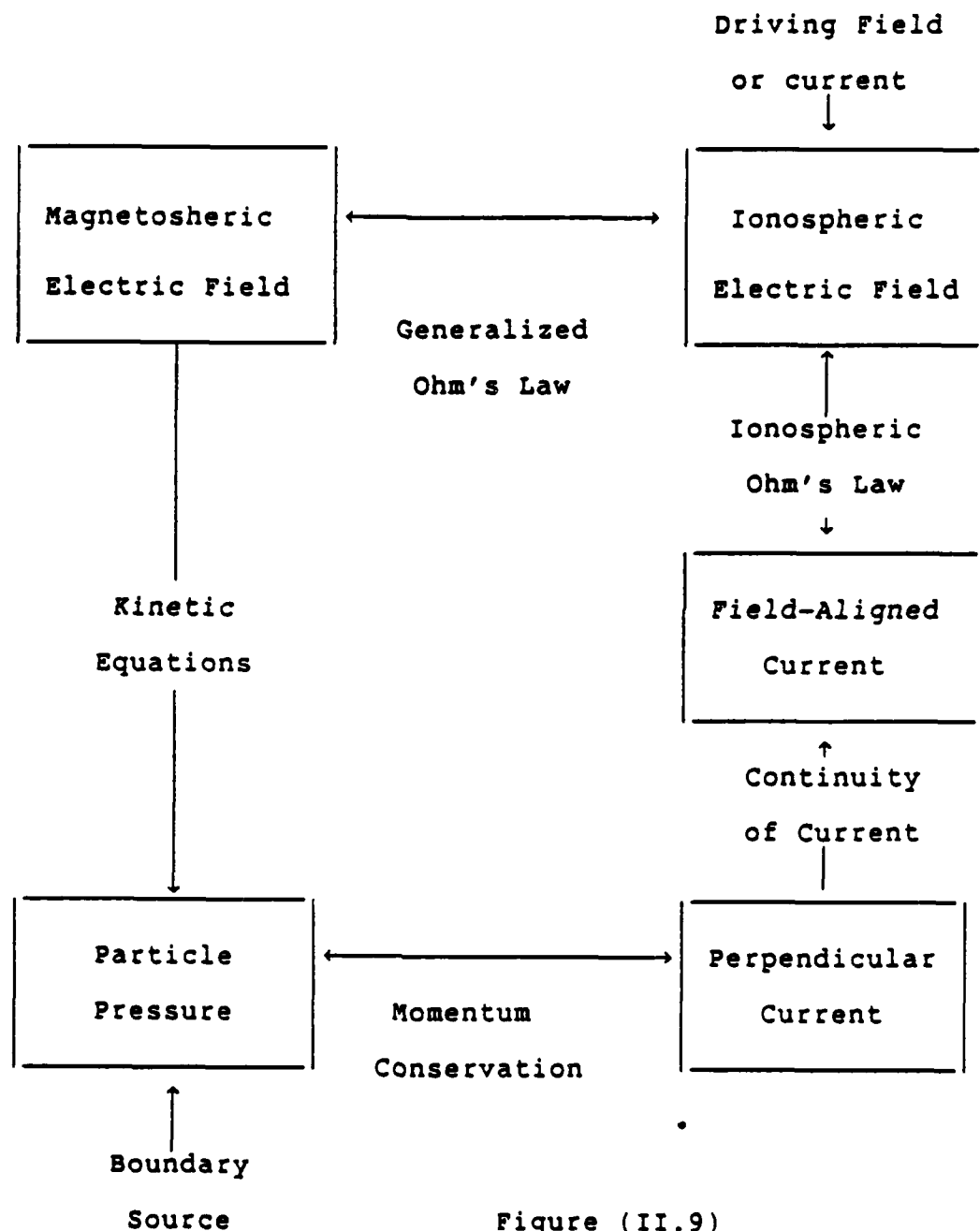


Figure (II.9)

Figure (II.9) shows the outline of the calculation of the self consistent magnetospheric convection process. The principal quantities calculated are kept in boxes, equations or principles which provide the link are shown as a line joining the two boxes.

Since this is a closed system one can start from any point. It is convenient to start from the magnetospheric electric field for convenience.

Link (1): Calculation of charged particle distributions in a given configuration of electric and magnetic fields is a familiar process. When adiabatic processes are considered the simplest method is to calculate the single particle trajectories and apply Liouville's theorem. For nonadiabatic processes it is necessary to develop a transport equation by suitable transformation of the Boltzmann equation. It is also necessary to specify the particle population at the boundary of the region under study as a boundary condition, if the particles can move up to the region. At 10 to 15  $R_e$  on the nightside, the electric field is such that the particles move from magnetotail towards the earth. Then it is necessary to specify the particle population at the near earth end of the magnetotail and the observed plasma sheet population is a reasonable choice. With a knowledge of magnetospheric electric field, the motion and distribution of protons and electrons and

especially the plasma pressure at any point can be calculated.

Link (2): From plasma pressure gradients the electric current perpendicular to the magnetic field can be calculated.

The momentum conservation equation for the plasma with the approximation that the flow speed is small compared to the plasma particle thermal speed (valid throughout the magnetosphere beyond the plasmopause except possibly at the neutral sheet) is

$$\nabla \cdot \mathbf{p} = (1/c) \mathbf{J} \times \mathbf{B} \quad (\text{II.1})$$

in Gaussian units.

If the pressure is isotropic, we can solve for  $J_{\perp}$  and get

$$J_{\perp} = \frac{cB \times \nabla p}{B^2} \quad (\text{II.2})$$

Link (3): The current density given by (i) usually has non-zero divergence, but the total current density should have a zero (approximately) divergence even if the convection is highly nonsteady, as long as quasi-neutrality is maintained. The divergence of  $J_{\perp}$  must be cancelled by divergence of the magnetic field aligned current density  $J_{\parallel}$ .



For isotropic pressure,

$$\frac{\partial}{\partial s} \left( \frac{J_{||}}{B} \right) = \frac{2 (B \times \nabla B) \cdot \nabla p}{B^4} \quad (\text{II.3})$$

As expected from simple pictures of particle drifts, field aligned currents are present whenever the pressure gradient has a component along the direction of  $\nabla B$  drift. The total current density flowing in and out of the ionosphere at any point must be found by integrating the last equation along the field line. For isotropic pressure it must be constant along the field line.

Integrating equation (II.3) we get

$$J_{||} = \frac{B_m C}{2B_e} \left( \nabla p \times \frac{B_e}{B_e} \right) \cdot \nabla \int \frac{dl}{B} \quad (\text{II.4})$$

where,  $B_e$  is the magnetic field at the equator and  $B_m$  is the mirror field.

Link (4): From the requirement that these field aligned currents must be closed by perpendicular ohmic currents in the ionosphere, the configuration of the electric field in the

ionosphere is obtained.

From continuity of current in the ionosphere

$$\nabla \cdot \mathbf{I} = J_{||} \sin \chi \quad (\text{II.5})$$

where  $\mathbf{I}$  is the height integrated horizontal current density, and  $\chi$  is the inclination of the magnetic field.

If  $\mathbf{E}$  at the top of the ionosphere has no horizontal variation except on a sufficiently long scale ( $\geq 10$  km), then

$$\mathbf{I} = \Sigma \cdot ( \mathbf{E} + \mathbf{V}_n / c \times \mathbf{B} ) \quad (\text{II.6})$$

where  $\Sigma$  is the height integrated conductivity tensor and  $\mathbf{V}_n$  the velocity of neutral gas in the ionosphere. Substituting for  $\mathbf{I}$  in the expression for  $\nabla \cdot \mathbf{I}$ ,  $\mathbf{E}$  is uniquely determined from  $J_{||}$  given  $\mathbf{V}_n$  and  $\Sigma$ .

Link (5): The ionospheric electric field can be mapped into the magnetosphere, and the requirement that it agrees with the magnetospheric electric field assumed at the outset determines the magnetospheric electric field and thus closes the system of equations.

The electric field at the top of the ionosphere and within the magnetosphere are related by generalized ohm's laws and can

be calculated from one another. For quasi steady convection where the electric field is derived from a potential it is required to calculate the potential drop along the field line from the ionosphere to the equatorial plane. A good first approximation is that the conductivity along the field lines is high enough so that potential drop can be neglected and potential can be mapped out from ionosphere to magnetosphere. Numerical calculations based on these general concepts of Vasyliunas [1970] were performed by Harel et al. [1981]. Mirror forces, anomalous resistivity and other effects caused by instabilities may produce significant potential drops which can be calculated in principle if  $J_{||}$  is known.

Apart from global coupling there are medium size coupling events. As an example of a medium size coupling event the westward travelling surges can be considered. The associated current sheets stretch out to beyond 10000 km altitude and close through ionospheric currents. The intense field aligned current associated with the surge itself is carried by field aligned electron beams which have been electrostatically accelerated at higher altitudes. The intense current sheet drives the magnetospheric plasma unstable to the waves that heat the ions. The volume of the magnetosphere affected by a westward travelling surge is the volume connected to an area of the earth that is  $6^\circ$  in longitude and  $5^\circ$  to  $10^\circ$  in latitude along the auroral oval. The plasma motion in this large volume give rise to currents in both the magnetosphere and ionosphere that couple these regions

together during substorm events.

A relatively good understanding has now emerged for the global scale modelling of the magnetosphere-ionosphere coupling problem (based upon such descriptions as by Vasyliunas, described above and many recent and more detailed studies). However, the M-I coupling problem for smaller scales involves more complex plasma effects, like the effects associated with parallel potential drops. These effects involve kinetic phenomena such as upflowing ionospheric ions and complex wave particle interactions. These phenomena have forced us to abandon the idea that the topside ionosphere plays a passive role in the MIC processes. A great deal of work has been done on the electrostatic ion cyclotron instability in terms of its effect on particle heating and plasma transport properties. The feedback effects of wave turbulence generated by the auroral electron beam upon the distribution of parallel electric field have not been quantitatively clarified.

The ion conics and ion beams play important roles in the M-I coupling processes. Also, anomalous resistivity can lead to the selective acceleration of one or more ion species in a multi-ion plasma. It is clear that wave-particle interactions and the plasma turbulence often associated with them play a critical role in MIC phenomena over a significant range of scale sizes. The complex interactions between these processes are still being

studied but it is clear that a fully satisfactory understanding of MIC can be achieved only after all the major processes of this type and the major interactions between microscopic and macroscopic processes have been identified.



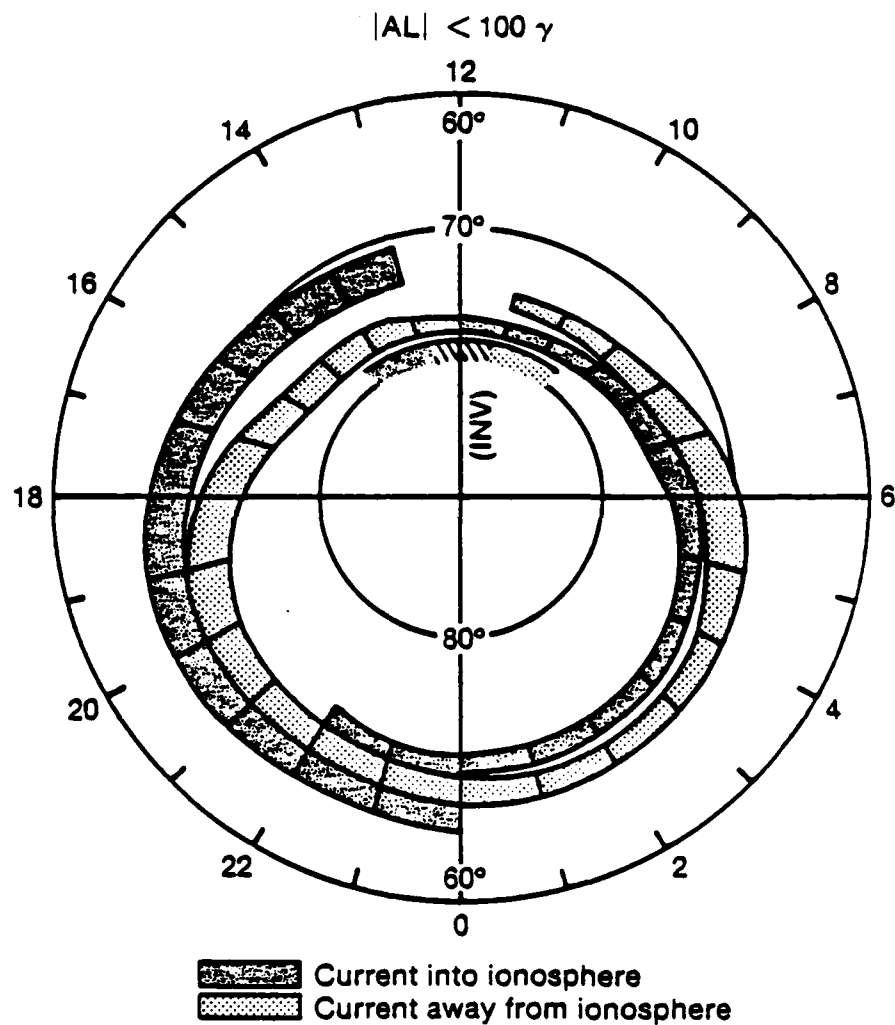


Fig. II.1 — Flow of quiet-time Birkeland currents into and out of the polar ionosphere  
[Iijima and Potemra, 1976b, their figure 6]

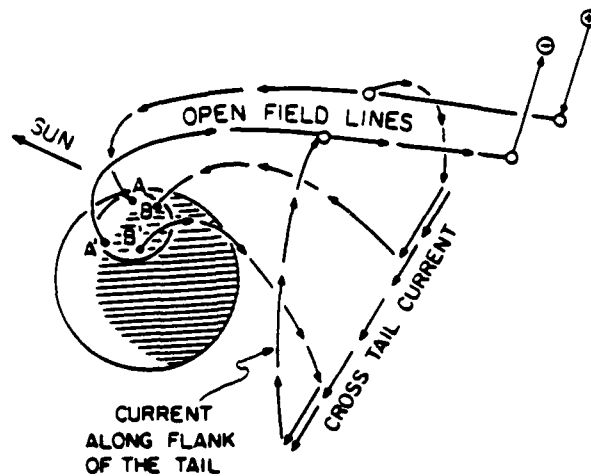


Fig. II.2 — The sources of region 1 currents on open lines and in the plasma sheet [Stern, 1983b, his figure 2]

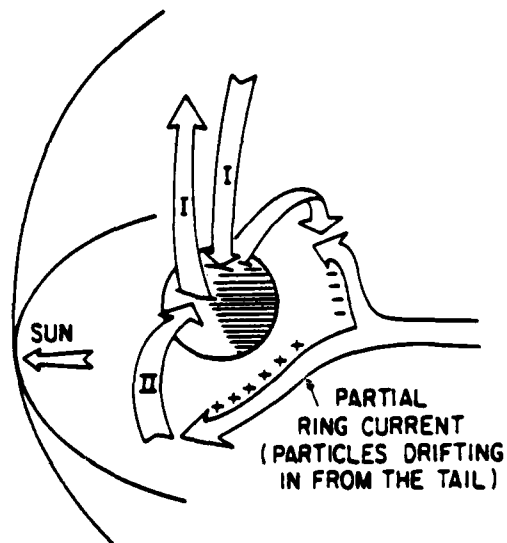


Fig. II.3 — The closure of region 2 currents by partial ring current [Stern, 1983b, his figure 3]



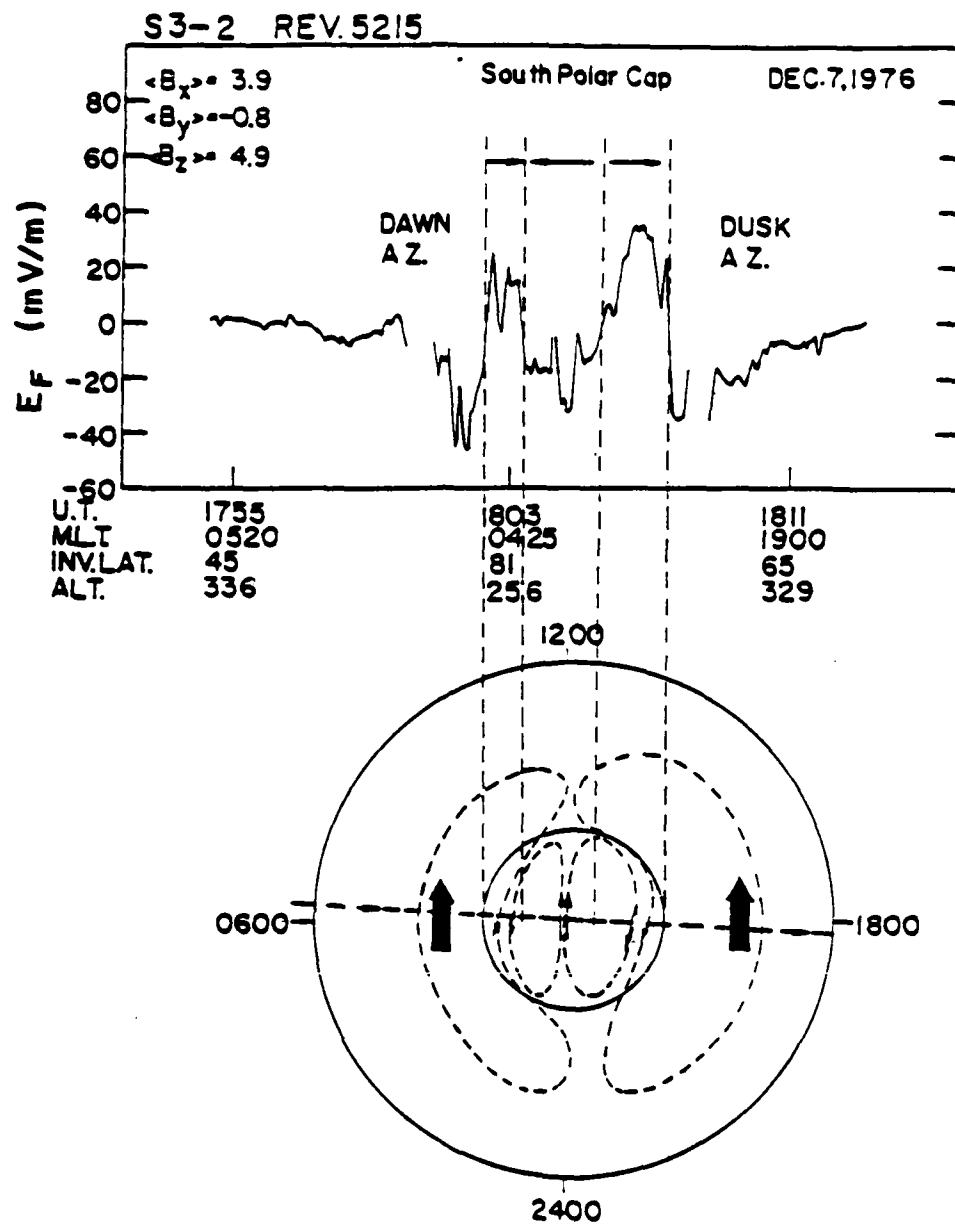


Fig. II.4 — N type electric fields in the central polar cap [Burke et al., 1979b, their figure 2]

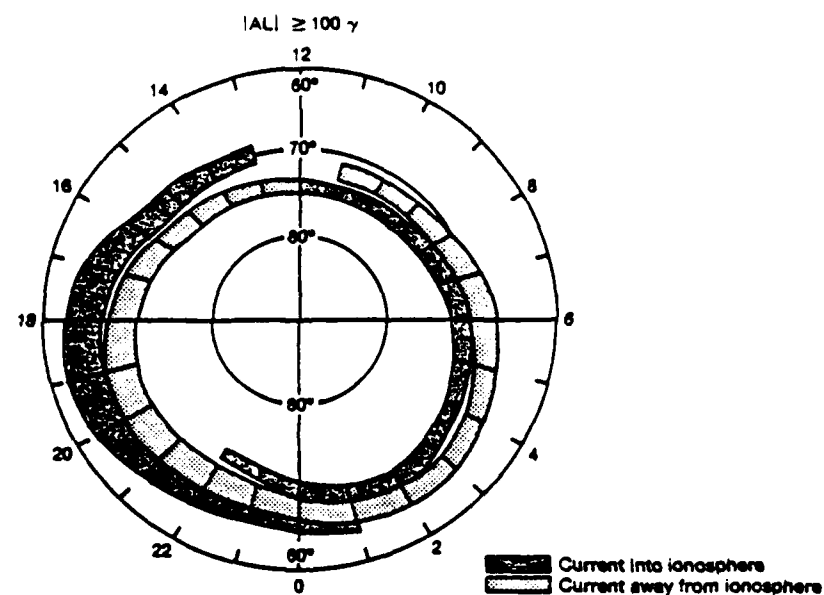


Fig. II.5 — Distribution and flow directions of large-scale Birkeland currents during active periods [Iijima and Potemra, 1978a, their figure 13]

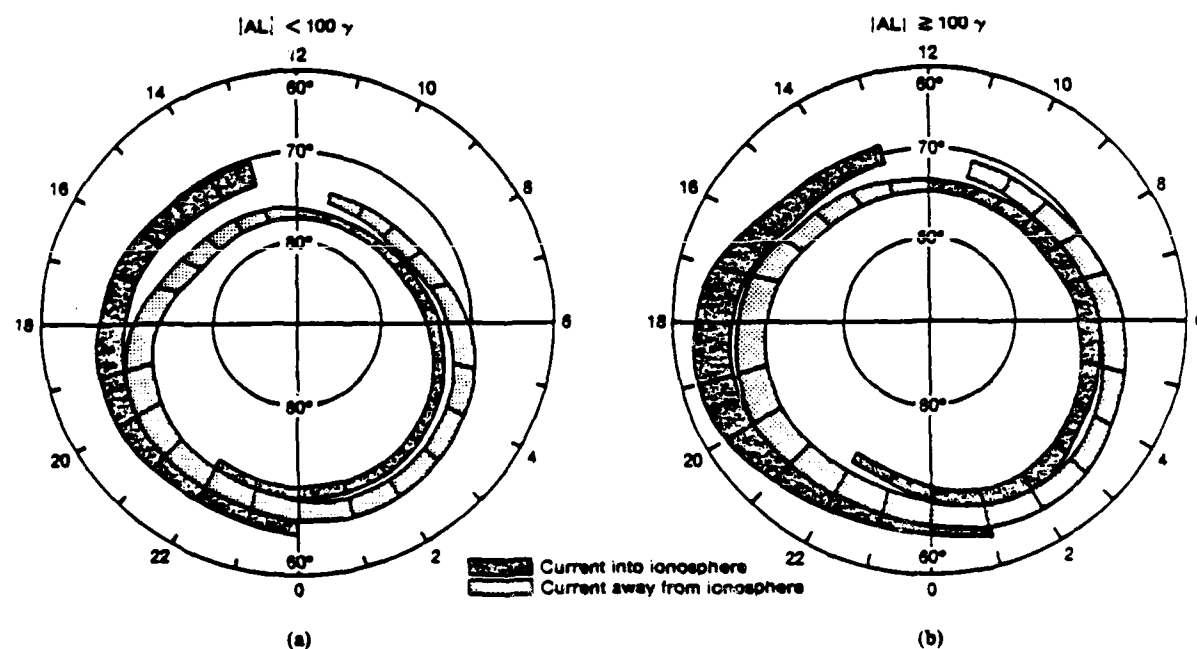


Fig. II.6 — Substorm associated changes superimposed upon the basic distributions of Birkeland currents [Iijima and Potemra, 1978a, their figure 15]

AD-A171 688

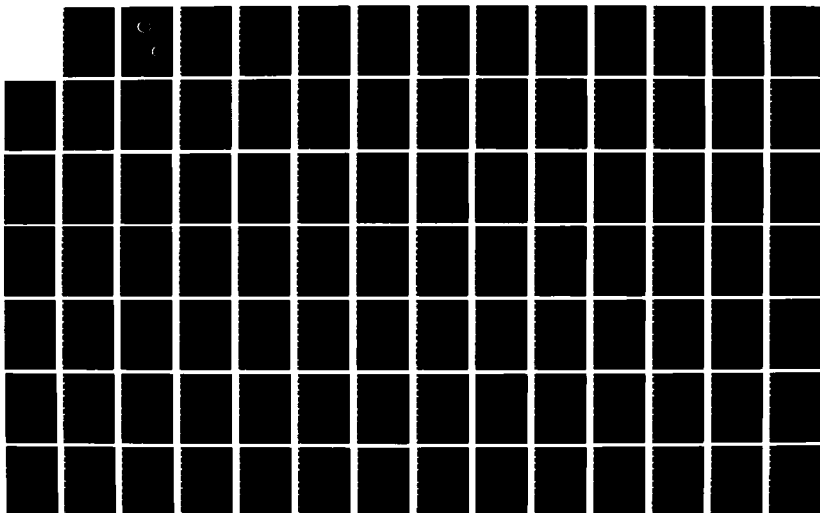
GEOPHYSICAL PLASMAS AND ATMOSPHERIC MOEELING(U) SCIENCE  
APPLICATIONS INTERNATIONAL CORP MCLEAM VA  
E HYMAN ET AL JUL 86 SAIC-86/1781 N88014-85-C-2018

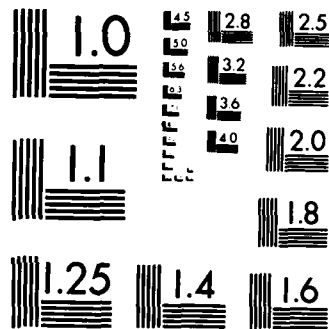
4/8

UNCLASSIFIED

F/G 4/1

NL





MICROCOPY RESOLUTION TEST CHART  
NATIONAL BUREAU OF STANDARDS 1963-A

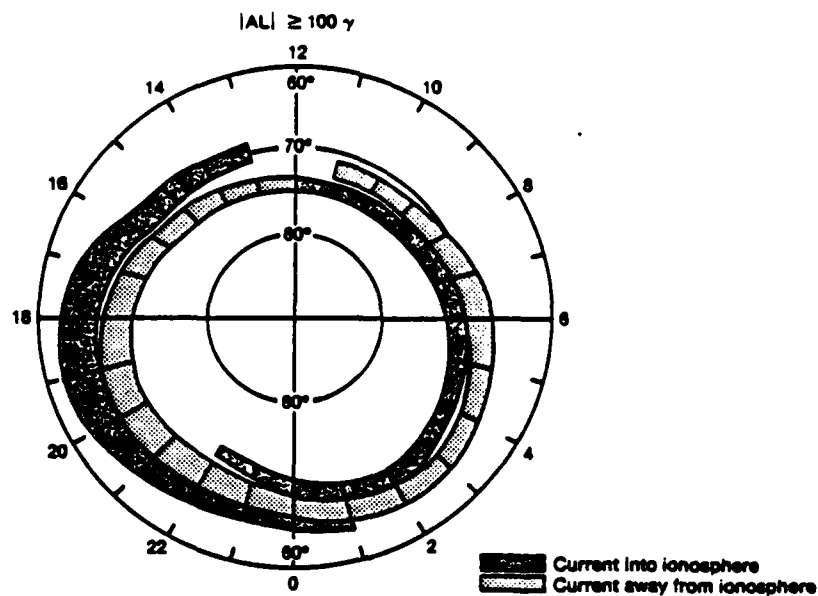


Fig. II.5 — Distribution and flow directions of large-scale Birkeland currents during active periods [Iijima and Potemra, 1978a, their figure 13]

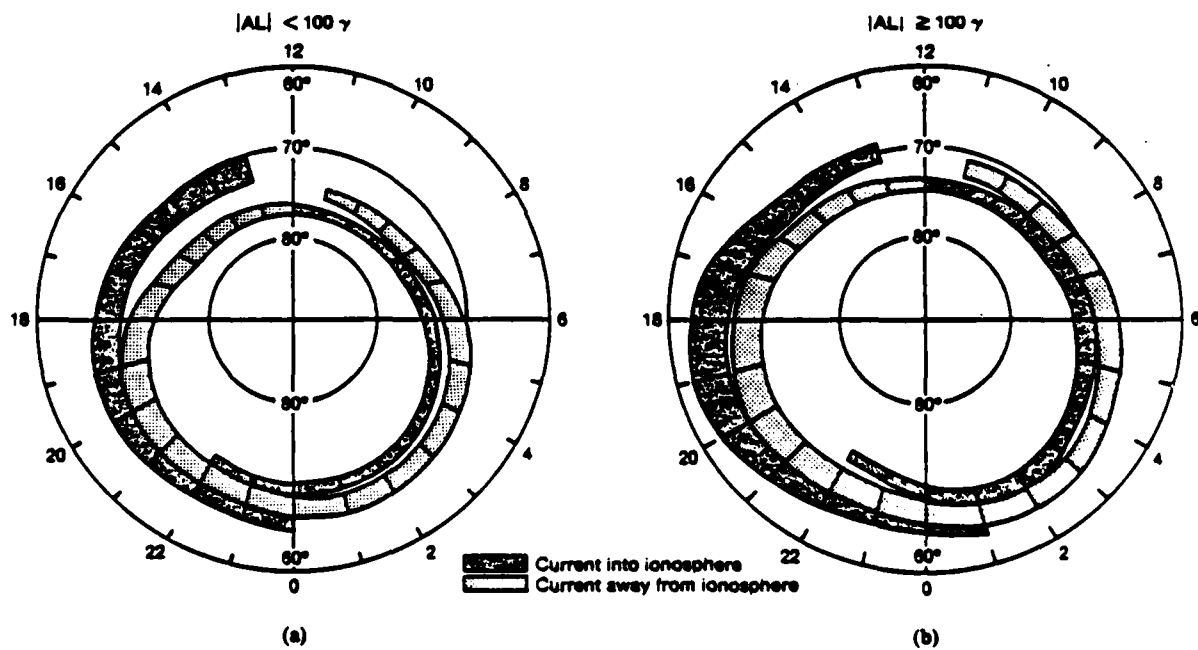


Fig. II.6 — Substorm associated changes superimposed upon the basic distributions of Birkeland currents [Iijima and Potemra, 1978a, their figure 15]

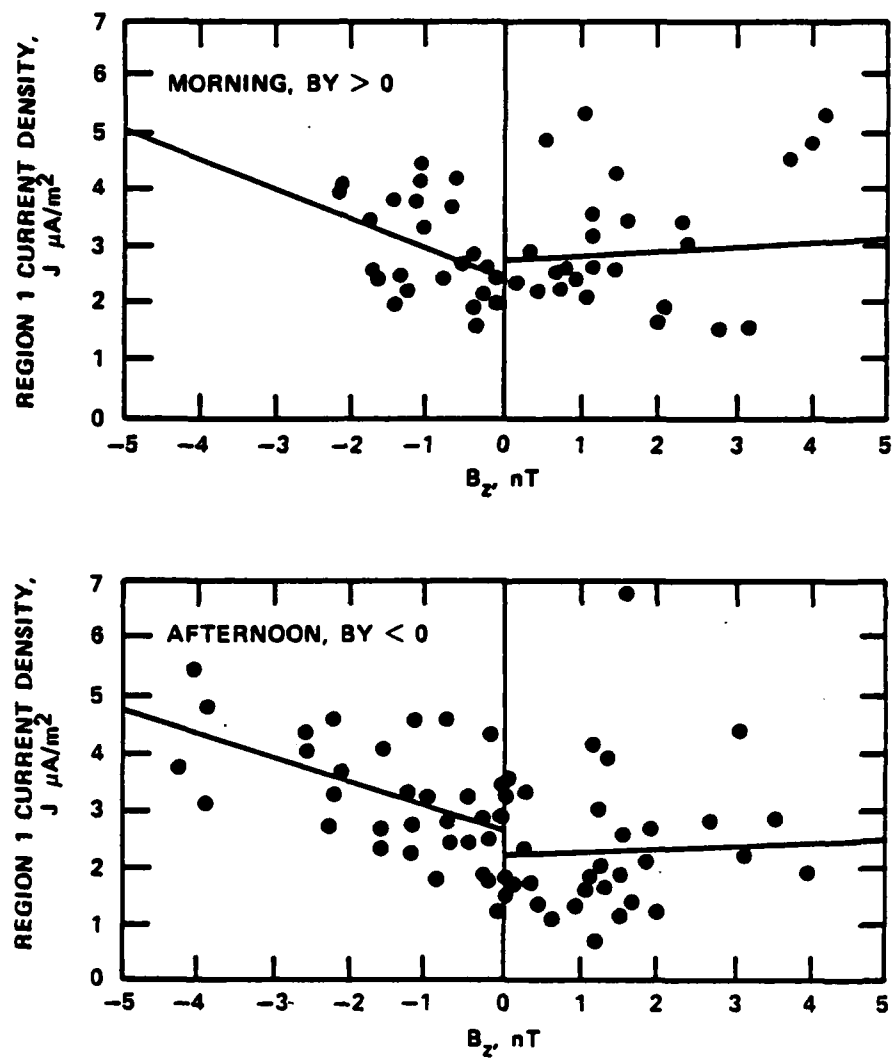


Fig. II.7 — Region I current densities plotted against negative values of  $B_z$  (southward) and positive values of  $B_z$  (northward) [Iijima and Potemra, 1982, their figure 1]

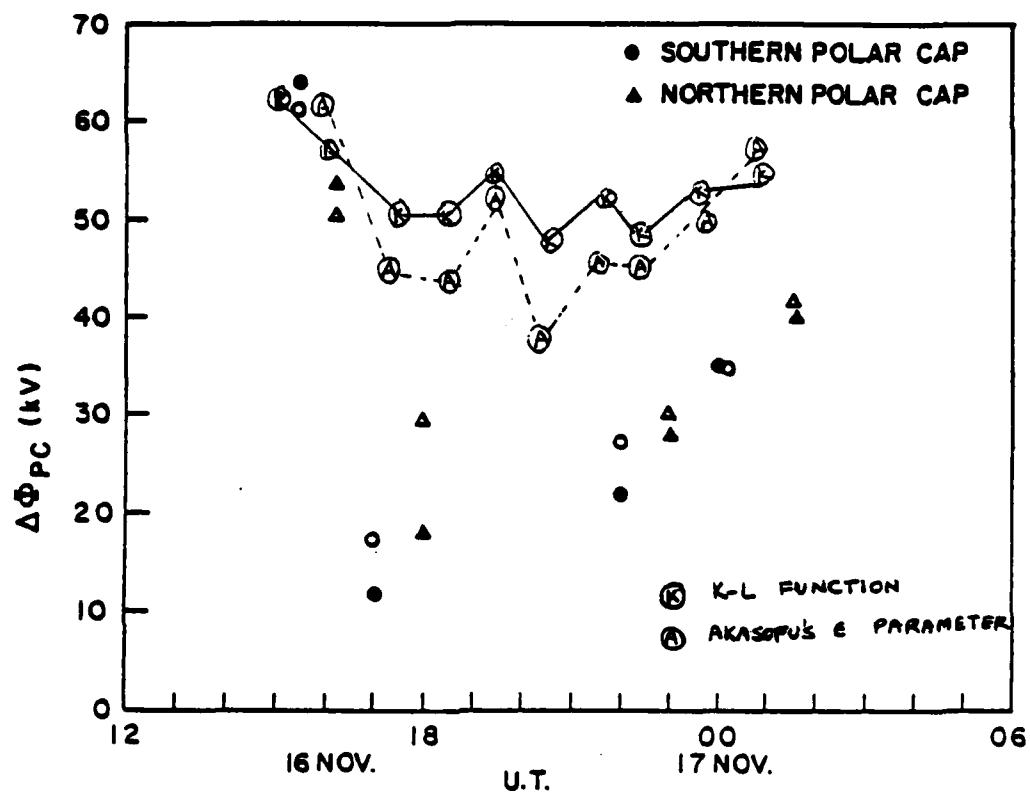


Fig. 11.8 — Plot of  $\Phi_{PC}$  (as measured by S 3-2) vs U.T. (Akasofu's  $\epsilon$  and Kan and Lee function ) are plotted for the given U.T.'s [work done by Burke and Ganguli]





## **CHAPTER III**

### **LARGE SCALE RETURN CURRENTS**

#### **ON AURORAL FIELD LINES**

##### **I. 13 MOMENT CALCULATIONS**



### III.1 INTRODUCTION

Previous works on the polar wind have been discussed in Chapter I and the properties of field-aligned currents have been reviewed in Chapter II. We are interested in investigating the dynamics of the large scale field aligned return currents on auroral field lines. The field aligned return currents flow from the magnetosphere to the ionosphere and are carried by cold electrons of ionospheric origin. It is now well established that the field aligned currents play an important role in the magnetosphere-ionosphere coupling process. In terms of the region 1/region 2 large scale field aligned current systems [Iijima and Potemra, 1976] large scale return currents are identified as region 1 in the morning sector and region 2 in the evening sector. The typical strength of this current-system varies usually from 1.0 to 2.0  $\mu\text{A}/\text{m}^2$ . Within the region 1/region 2 current system, small-scale distributions of both upward and downward currents are observed in association with auroral arcs.

Mitchell and Palmadesso [1983] have performed time dependent simulations of upward currents. The model is 1-dimensional and uses 13-moment system of transport equations of Schunk [1977]. The plasma consists of  $\text{H}^+$ ,  $\text{O}^+$  and the electrons with cold electrons at the upper boundary at 10 Re. The lower boundary is at 800 km. It is shown that the flux tube plasma

responds to the current on several time scales. The current applied was  $1 \mu\text{A}/\text{m}^2$ . The electrons are heated initially due to precipitation in the converging magnetic field. The electric field coupling of the electrons to the ions causes thermal oscillations within the flux tube plasma which persist for about an hour. The electric field and the hydrogen ion temperature profiles returned to their polar wind values after the ions reach equilibrium. Higher currents take longer time to reach equilibrium.

Regions of both upward and downward currents were studied by Newman et al. [1986]. The model is 2-dimensional and steady state and uses adiabatic assumptions of particle motion in the presence of a broad-scale electrostatic potential structure. The particle distribution function is bi-Maxwellian. The magnetic equator, the source region for hot protons and electrons, is considered as the upper boundary. The lower boundary is located at 1000 km to avoid particle collisions. Note that the adiabatic model can not consider collisions. The densities of particles are obtained by integrating the distribution function over adiabatically allowed regions of velocity space. Shooting techniques were then applied to solve for values of the electrostatic potential which satisfies quasineutrality conditions of particle densities. The smoothly-varying large-scale potential structure described by this model is representative of the net charge separation and  $E_{||}$  associated

with inverted-V structures, where the actual net charge density on the auroral field line is very small. Estimates of current density show that the upward current is carried by hot electrons of magnetospheric origin and the return current is carried by the cooler electrons of ionospheric origin, as predicted by theory and observations. The results indicate that broad potential structure extending low along the field lines can only describe a stationary quasineutral solution if the representative ionospheric electron population is assumed to be suprathermal (10-100 eV). The signature of a strong electric field seen to extend down to lower altitudes can be interpreted as a sign that cool electrons have been non-adiabatically heated. The model reproduces some of the general characteristics of the quiet-time magnetosphere. However, only low current densities can be used in this model since any instability arising due to field-aligned currents can not be treated by these adiabatic particle calculations.

Various instabilities can arise due to field-aligned currents which exceed certain threshold values. Kindel and Kennel [1971] concluded that for a wide range of electron-to-ion temperature ratios, the electrostatic ion cyclotron wave is unstable to smaller currents than the ion acoustic instability. A detailed discussion on this is given in chapter V. Burke et al. [1983] pointed out that field-aligned return currents require cold plasma drifts near the Kindel and Kennel [1971] limit of

stability.

We have performed simulations to study the dynamics of the large scale return currents on auroral field lines, using the dynamic numerical model of Mitchell and Palmadesso [1983]. The results were documented in Ganguli et al. [1985 b] and are discussed below. We compared our results to those of Mitchell and Palmadesso [1983] to study the difference in dynamics of return currents versus upward currents and the current free polar wind case.

### III.2 THE MODEL

The field line model of Mitchell and Palmadesso [1983] was designed to dynamically simulate the behavior of the plasma in a flux tube encompassing an auroral field line extending from an altitude of 800 km to 10 Re. The electrons and the hydrogen ions are the dynamic species in the model. The oxygen ions form a static background population at a constant temperature. The model uses the 13-moment system of transport equations of Schunk [1977]. The distribution function is assumed to be gyrotropic about the field line direction, which reduces the 13-moment approximation to five moments. The five moments are number density, temperatures parallel and perpendicular to the

geomagnetic field line, and species velocity and heat flow along the line. The resulting transport equations are as follows:

$$\frac{\partial n}{\partial t} + \frac{\partial nv}{\partial r} + \dot{A}nv = \frac{\delta n}{\delta t}$$

(III.1)

$$\frac{\partial v}{\partial t} = -v \frac{\partial v}{\partial r} - \frac{k}{m} \frac{\partial T_{||}}{\partial r} - \frac{kT_{||}}{m n} \frac{\partial n}{\partial r} - \frac{\dot{A}k(T_{||} - T_{\perp})}{m} + \frac{e}{m} E - \frac{GM}{r^2} + \frac{\delta v}{\delta t}$$

(III.2)

$$k \frac{\partial T_{||}}{\partial t} = -v k \frac{\partial T_{||}}{\partial r} - 2kT_{||} \frac{\partial v}{\partial r} - \frac{6}{5n} \frac{\partial h}{\partial r} - \frac{2}{5} \frac{h}{n} \dot{A} + k \frac{\delta T_{||}}{\delta t}$$

(III.3)

$$k \frac{\partial T_{\perp}}{\partial t} = -v k \frac{\partial T_{\perp}}{\partial r} - \frac{2}{5n} \frac{\partial h}{\partial r} - \left( \frac{4}{5} \frac{h}{n} + v k T_{\perp} \right) \dot{A} + k \frac{\delta T_{\perp}}{\delta t}$$

(III.4)

$$\begin{aligned}
\frac{\partial h}{\partial t} = & -v \frac{\partial h}{\partial r} - \frac{16}{5} h \frac{\partial v}{\partial r} - \left( \frac{11}{18} T_{||} + \frac{8}{9} T_{\perp} \right) \frac{nk^2 \partial T_{||}}{m \partial r} \\
& - \left( \frac{17}{9} T_{||} - \frac{8}{9} T_{\perp} \right) \frac{nk^2 \partial T_{\perp}}{m \partial r} + \frac{4k^2}{9m} (T_{||} - T_{\perp})^2 \frac{\partial n}{\partial r} \\
& + \left[ \frac{nk^2}{m} (T_{||} - T_{\perp}) \left( \frac{1}{3} T_{||} - \frac{4}{3} T_{\perp} \right) - \frac{7}{5} v h \right] \dot{A} + \frac{\delta h}{\delta t}
\end{aligned}
\tag{III.5}$$

where,  $h$  is the total heat flow. Other symbols are same as in chapter I.

The collision terms used in the present simulation are Burgers' [1979] collision terms for the case of Coulomb collisions with corrections for finite species' velocity differences, and are given in Appendix 2.III.

The scale of this model is large compared to the electron Debye length, so the transport equation (III.1) for electron number density may be replaced by an expression for charge neutrality:

$$n_e = n_p + n_o$$

(III.6)



We have assumed that the total flux tube current  $I$  remains constant

$$I = eA (n_p v_p - n_e v_e) \quad (\text{III.7})$$

which implies

$$v_e = \frac{1}{n_e} (n_p v_p - \frac{I}{eA}) \quad (\text{III.8})$$

Using equations (III.2), (III.7) and (III.8) the electric field  $E$  parallel to the field line is calculated.

$$\begin{aligned} E = & \frac{m_s}{en_e A} \frac{\partial}{\partial r} (n_p v_p^2 A - n_e v_e^2 A) - \frac{k}{e} \left[ \frac{\partial T_{e||}}{\partial r} + \frac{T_{e||}}{n_e} \frac{\partial n_e}{\partial r} \right. \\ & \left. + \frac{(T_{e||} - T_{e\perp})}{A} \frac{\partial A}{\partial r} \right] - \frac{n_o m_e GM}{n_e e r^2} + \frac{m_e}{e} \left[ \frac{\delta v_e}{\delta t} - \frac{n_p}{n_e} \frac{\delta v_p}{\delta t} \right] \end{aligned} \quad (\text{III.9})$$

### III. SIMULATIONS AND RESULTS

In order to perform the field aligned current simulations we have to perform the current free polar wind simulation first to be used as the initial steady state of the flux tube. These results will be described briefly here.

#### III.3 Polar Wind Simulation (Zero Current)

The polar wind simulation was carried out for a current-free case. The lower boundary is fixed at 800 km. The simulation was carried up to an altitude of 10 RE on an unequally spaced grid. The cell size is small at the lower end of the field line in order to study the transport effects in the presence of the large density gradients due to the small scale height of oxygen and satisfy stability conditions. The time step selected satisfies the Courant condition. The flux tube plasma consisting of the hydrogen ions, oxygen ions and the electrons was initialized at a constant temperature of 2000°K. The initial conditions used are those of Mitchell and Palmadesso [1983].

In the polar wind, the ambipolar electric field produces the sharp increase in the hydrogen ion velocity at the lower end of the flux tube. The hydrogen ions are further accelerated

upwards in the flux tube by mirror force and pressure gradients. The oxygen ions are the dominant species up to an altitude of around 3500 km. In the steady state the electrons and the hydrogen ions reach the same maximum velocity, as it is clear from equation (III.8). This is shown in figure (III.1.b). The total flux along the flux tube is conserved, i.e.,  $nVA = \text{constant}$ . Therefore, as the velocity and the area increase with altitude the density should decrease. The hydrogen ion density decreases as it flows through the diverging flux tube, shown in figure (III.1.a). The electron density also decreases, due to charge neutrality equation (III.6). Figures (III.1.a) - (III.1.d) are from Mitchell and Palmadesso [1983].

The hydrogen ion temperatures (shown in figure III.1.c) exhibit three interesting characteristics:

- (1) The temperatures increase with altitude at the lower end of the tube.
- (2) Adiabatic cooling - supersonic ion gas cools down as it expands in a diverging magnetic field.
- (3) Temperature anisotropy.

The temperature increase is caused by Joule heating of the hydrogen from collisions with the oxygen ions. This effect becomes weaker with increasing altitude due to small scale height of the oxygen. As a result, the hydrogen ion temperature profiles show an increase in temperature before it exhibits adiabatic cooling. The temperature anisotropy develops around

2500 km and is caused by the mirror effect where the perpendicular energy is transferred to the parallel energy.

The electron temperature profiles (shown in figure III.1.d) exhibit :

- (1) Adiabatic cooling.
- (2) Temperature anisotropy.

However, the latter effect is more prominent in the hydrogen ion temperature profiles. The electron thermal velocity is much higher than the electron bulk flow velocity, hence thermal conductivity is more effective at reducing flow related temperature anisotropies and gradients for electrons.

It is also noted that when the drift velocity of the hydrogen ions is equal to that of electrons the hydrogen ions cool much more than the electrons. The hydrogen ion temperature profiles maintain significant gradients at high altitudes and exhibit large temperature anisotropies at the upper end of the flux tube.

#### III.4 Return Current Simulation

In this section we discuss our results of the field aligned return current simulations and compare those with the polar wind (zero current) case as described in Section I and with

the upward current case studied by Mitchell and Palmadesso [1983].

Using the polar wind simulation as the initial steady state of the flux tube, simulations were performed with return currents with a minimum value of  $-1.0 \mu\text{A}/\text{m}^2$  and a peak value of  $-2.0 \mu\text{A}/\text{m}^2$ .

We will first discuss the case where a current of  $-1.0 \mu\text{A}/\text{m}^2$  was applied. With the onset of the current the electron velocity increases with altitude (figure III.2). The electron temperature profiles still exhibit adiabatic cooling and temperature anisotropy, but since the electron velocity is much higher in this case as compared to the polar wind value, the electrons cool much more rapidly with increasing altitude. The electron temperature gradient decreases. Notice that here we have only considered cold electrons of ionospheric origin, like Mitchell and Palmadesso [1983]. The electron temperature profiles are shown at time intervals of ten, thirty, fifty and seventy minutes on figures (III.3.a), (III.3.b), (III.3.c) and (III.3.d), where the response of the electron temperature profiles with time are clearly observed. We compared our results with the upward current case of Mitchell and Palmadesso [1983] and notice that unlike the effects of return currents the application of upward current reduces the electron velocity and increases the total electron temperature. In the latter case the

electrons are heated in the lower end of the flux tube and the temperature gradient results in a large upward electron heat flow and an electron thermal wave propagating up the field line.

The electric field maintains the same profile as before but decreases in magnitude from the polar wind value, thereby decreasing the hydrogen ion velocity. This is unlike the upward current case of Mitchell and Palmadesso [1983], where the ambipolar electric field increases by an order of magnitude accelerating the hydrogen ions upwards. The decrease in  $H^+$  velocity causes a velocity ripple which in turn produces an  $H^+$  density enhancement and these propagate upwards through the flux tube as the simulation was carried on at later times. Due to the current conservation requirement, the electron velocity increases at the density enhancement, and hence the upward propagating velocity ripple is also noticed in the electrons. This effect is clearly seen for times ten, thirty, fifty and seventy minutes after the onset of the current as shown in figures (III.2.a), (III.2.b), (III.2.c) and (III.2.d). After the velocity ripples pass through the flux tube, the electron velocity settles down at a lower value than before (but much higher than the polar wind value) in order to maintain the current  $I$  constant. Also, the velocity of the hydrogen ions decreases at the upper end of the flux tube. As before the anisotropy of cooling is evident in the hydrogen ions but the hydrogen parallel and perpendicular temperatures increase as the  $H^+$  ion velocity decreases. The

ripple in velocity produces a ripple in the temperature which, like the velocity ripple, also flows up the flux tube with time. The hydrogen ion temperature profiles are shown on figures (III.4.a), (III.4.b), (III.4.c) and (III.4.d) at ten, thirty, fifty and seventy minutes after the onset of the current.

Simulations were then performed with higher currents up to a peak current of  $-2.0 \mu\text{A}/\text{m}^2$ . The electron velocity increases with the increase of current (shown in figure III.5.a), and the electron temperature still exhibits adiabatic cooling and temperature anisotropy (figure III.5.b). The ambipolar electric field decreases, further decreasing the  $\text{H}^+$  velocity (figure III.5.a). Velocity ripples are observed as before and these propagate through the flux tube as seen in later runs (that is, ten, thirty, fifty and seventy minutes after the onset of this current). To conserve the current flowing in the system, the electron velocity decreases (after the ripple flows out through the tube) with the decrease in hydrogen ion velocity. However, compared to the previous case, the electron velocity still remains at a higher value, while the  $\text{H}^+$  ion velocity decreases. The hydrogen ion temperature profile for this current is shown in figure (III.5.c).

Kindel and Kennel [1971] examined several current driven instabilities and showed that the electrostatic ion cyclotron instability has the lowest threshold. Our simulations show that

the electron drift velocity corresponding to a return current of  $-1.0 \mu\text{A}/\text{m}^2$  is already above the threshold for electrostatic ion cyclotron waves, because the ionospheric plasma is so cold. Much higher currents are needed to excite instabilities in the case of upward currents. This is an interesting and potentially important result. This was previously suggested by Burke et al. [1983]. The effects of anomalous resistivity and anisotropic ion heating arising due to EIC instability and a more detailed discussion of instability thresholds is contained in Chapter V.

### III.5 DISCUSSIONS

We have used a dynamic numerical model to investigate the plasma dynamics in the presence of large scale field aligned return currents. We have also compared our results with those of the current-free polar wind and upward current simulations. The flux tube plasma has a rapid initial response to the onset of the current. The electron velocity and temperature exhibit a rapid response to a sudden change in conditions with a time constant of about a few minutes. The electron velocity increases over its polar wind value with the onset of current and the electron temperatures cool rapidly with increasing altitude. The ions respond on a much longer time scale. The  $\text{H}^+$  ion velocity decreases from its polar wind value and temperature increases.



In this chapter we have only considered cold electrons of ionospheric origin. The electron drift velocity corresponding to a return current of  $-1.0 \mu\text{A}/\text{m}^2$  exceeds the critical velocity for exciting the EIC instability. This is an interesting and potentially important result. The effects of the EIC instability and anomalous resistivity arising due to the instability are discussed in Chapter V. Similar studies of return currents using the 16-moment system of transport equations and hot magnetospheric electrons at the upper boundary will be discussed in the next Chapter.



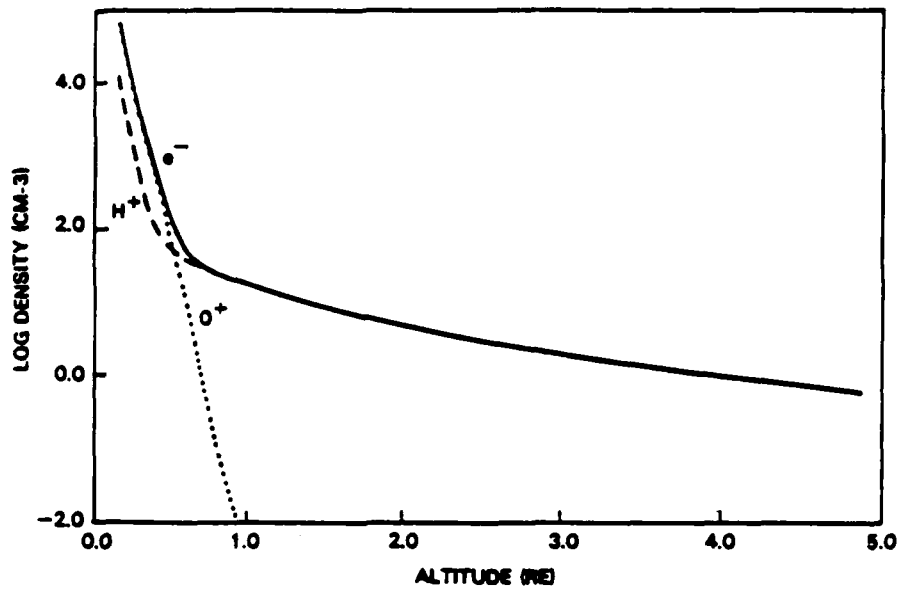


Fig. III.1.a — Densities for the steady-state polar wind with no field-aligned current: electrons (solid curve),  $H^+$  (dashed curve),  $O^+$  (dotted curve)

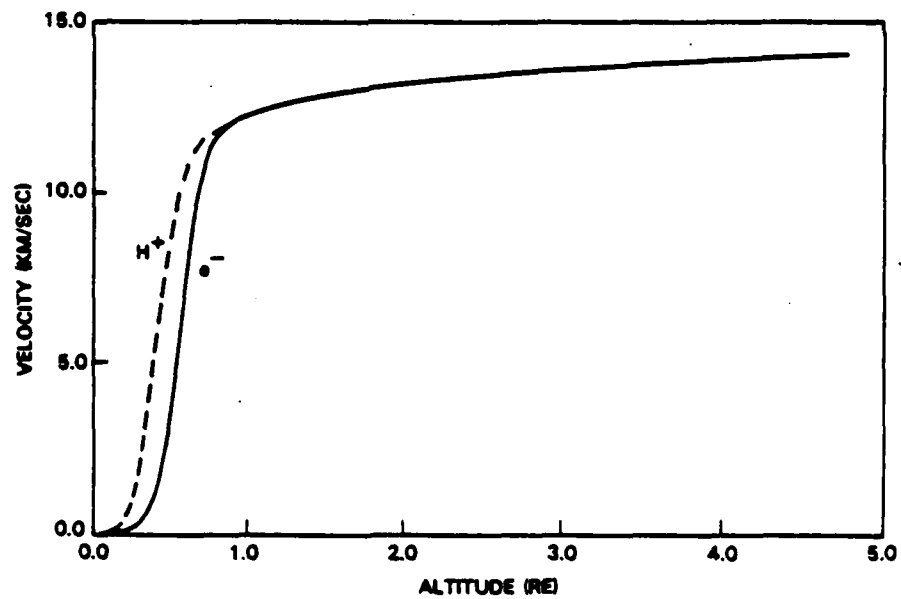


Fig. III.1.b — Velocities for the steady-state polar wind with no field-aligned current:  $e^-$  (solid curve),  $H^+$  (dashed curve). The oxygen ion velocity is uniformly zero.

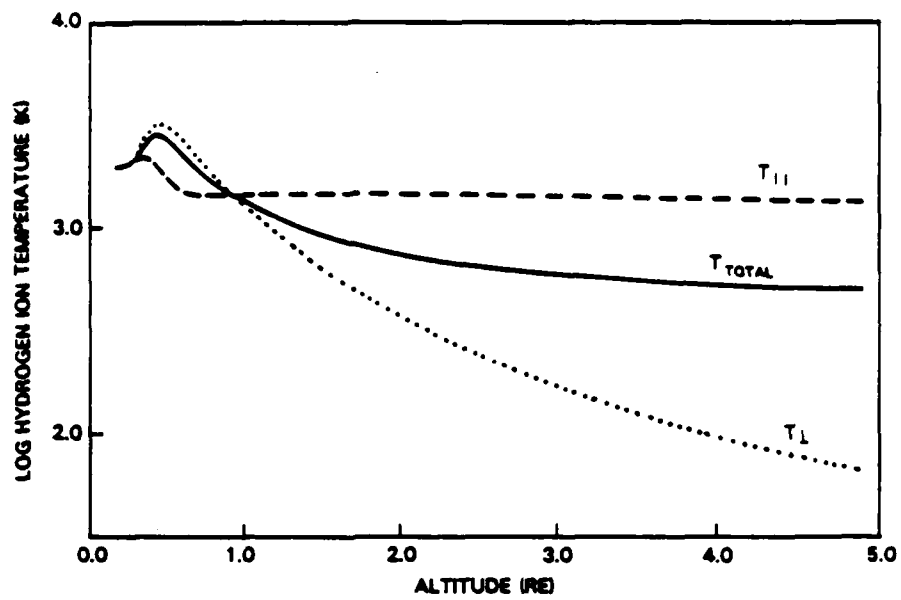


Fig. III.1.c — Hydrogen ion temperatures for the steady-state polar wind with no field-aligned current: total temperature (solid curve),  $T_{||}$  (dashed curve),  $T_{\perp}$  (dotted curve)

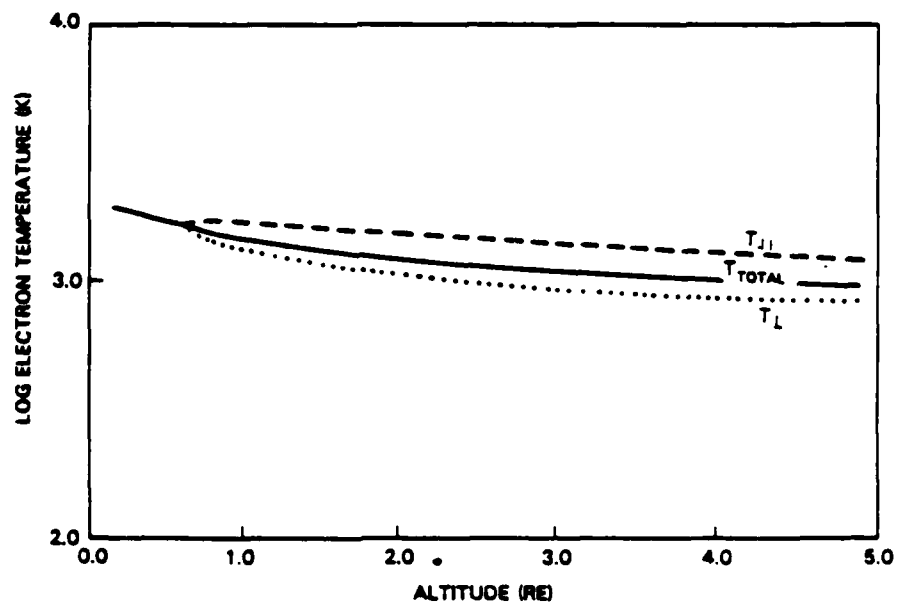
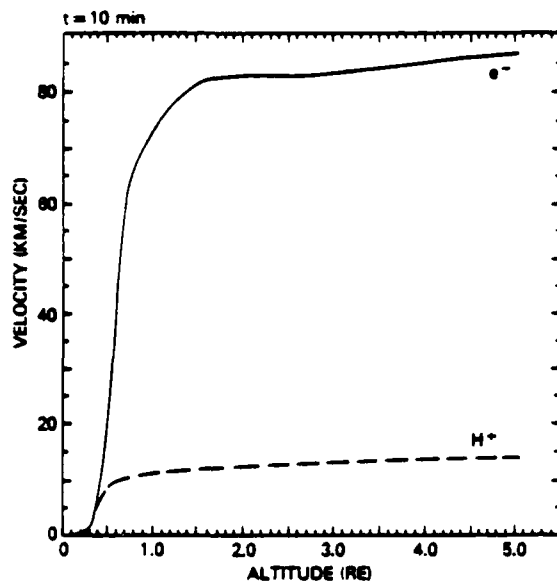
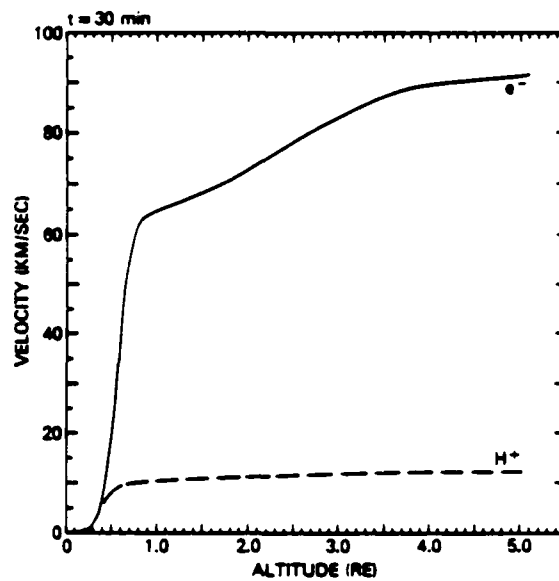


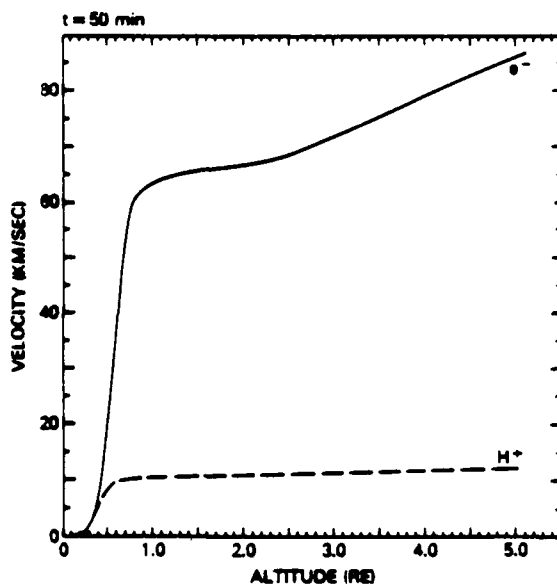
Fig. III.1.d — Electron temperatures for the steady-state polar wind with no field-aligned current: total temperature (solid curve),  $T_{||}$  (dashed curve),  $T_{\perp}$  (dotted curve)



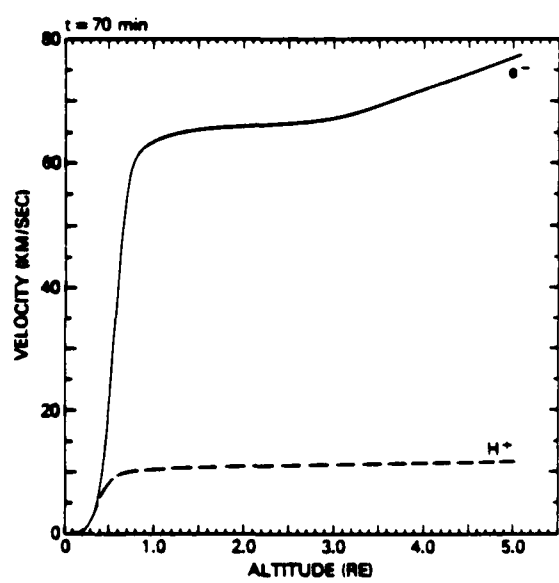
(a)



(b)

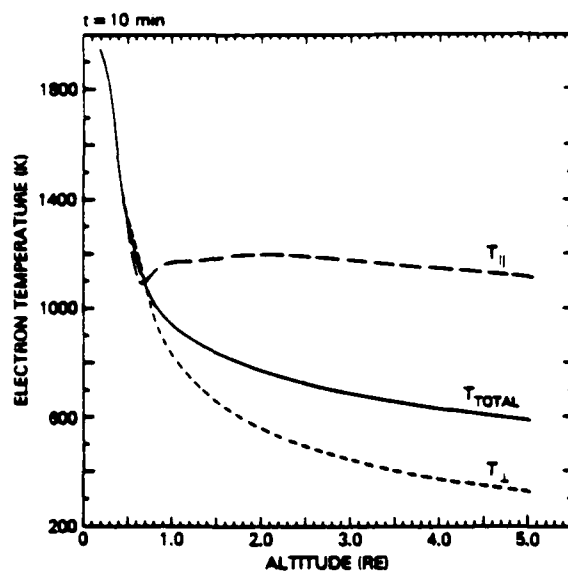


(c)

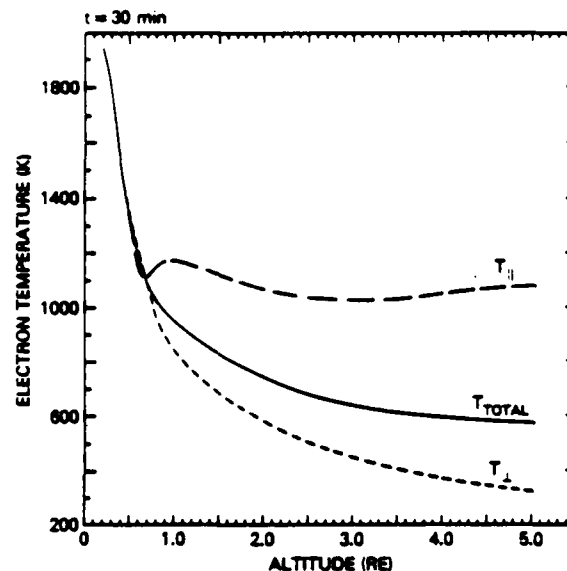


(d)

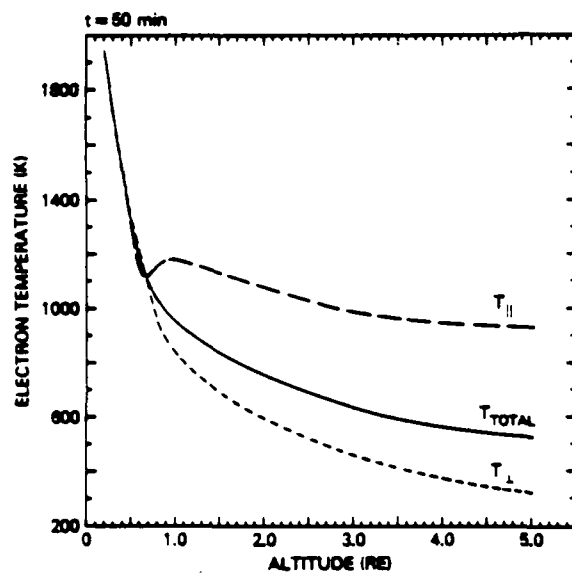
Fig. III.2 — Velocity profiles after the onset of a current of  $-1.0 \mu A/m^2$  at 1500 km:  $e^-$  (solid curve),  $H^+$  (dashed curve)



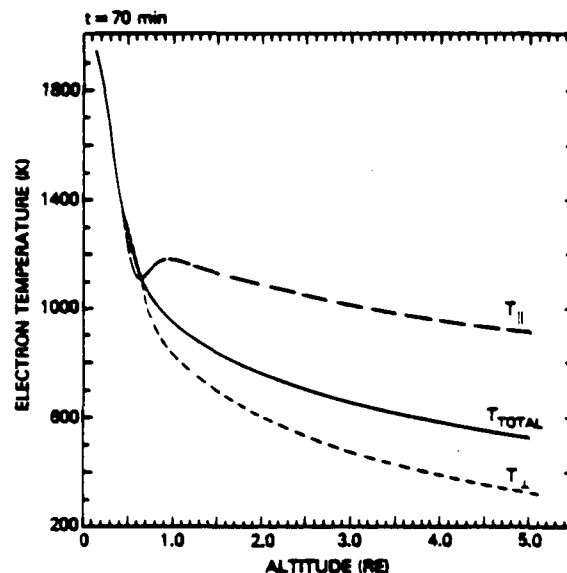
(a)



(b)

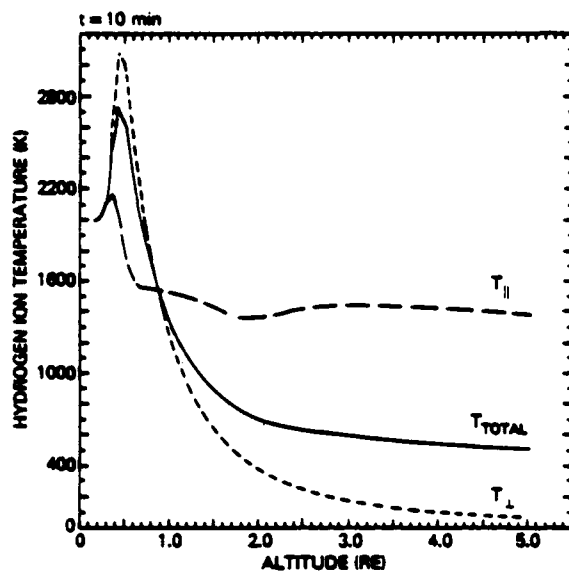


(c)

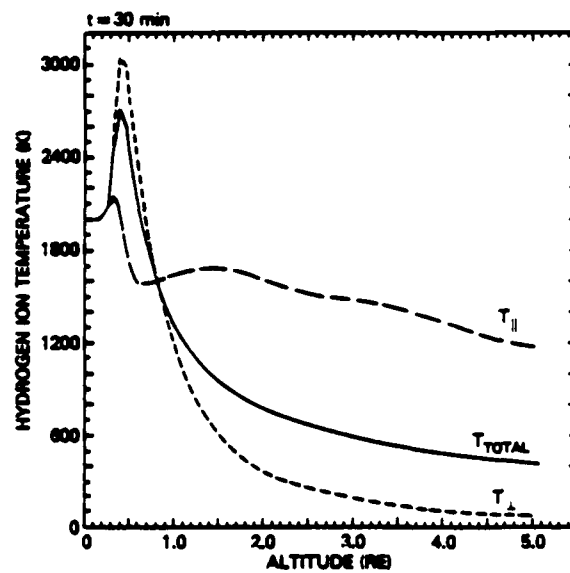


(d)

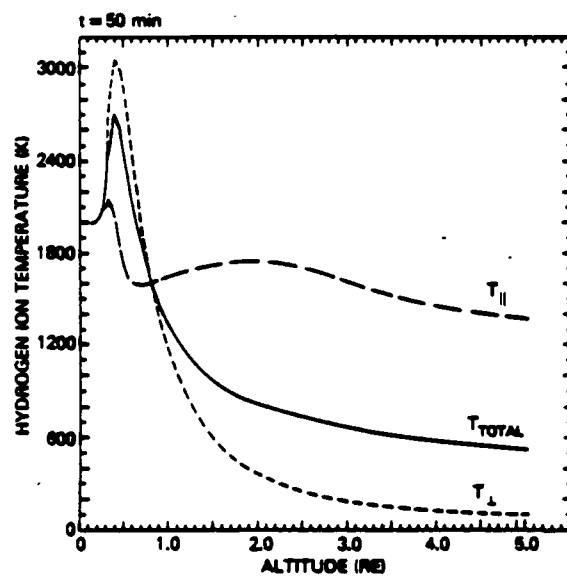
Fig. III.3 — Electron temperatures after the onset of a current of  $-1.0 \mu\text{A}/\text{m}^2$  at 1500 km: total temperature (solid curve),  $T_{\parallel}$  (dashed curve),  $T_{\perp}$  (dotted curve)



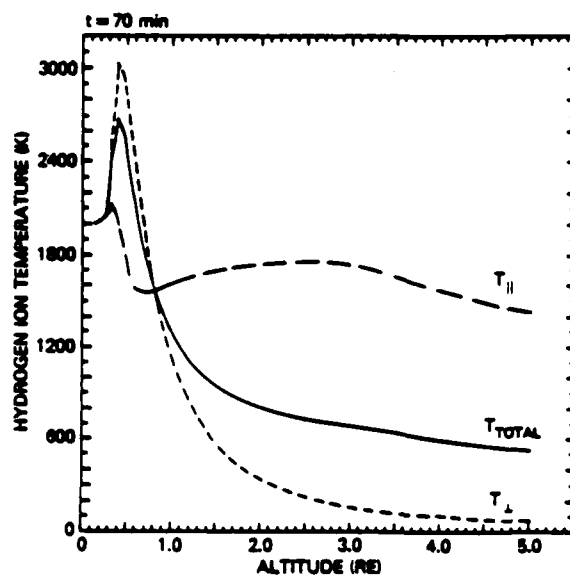
(a)



(b)



(c)



(d)

Fig. III.4 — Hydrogen ion temperatures after the onset of a current of  $-1.0 \mu\text{A}/\text{m}^2$  at 1500 km: total temperature (solid curve),  $T_{\parallel}$  (dashed curve),  $T_{\perp}$  (dotted curve)

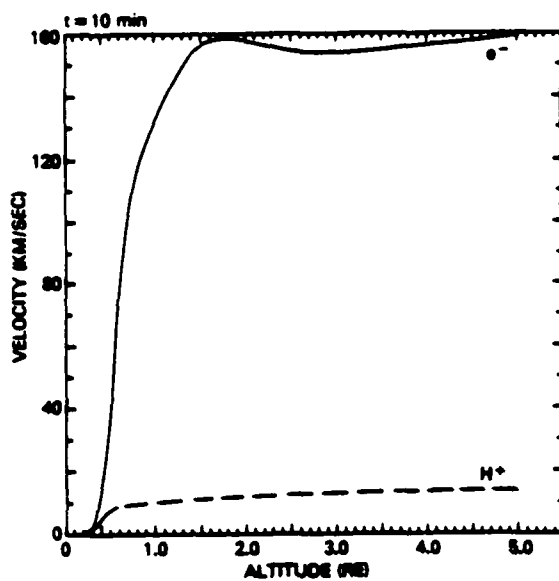


Fig. III.5.a — Velocity profiles after the onset of current of  $-2.0 \mu\text{A}/\text{m}^2$

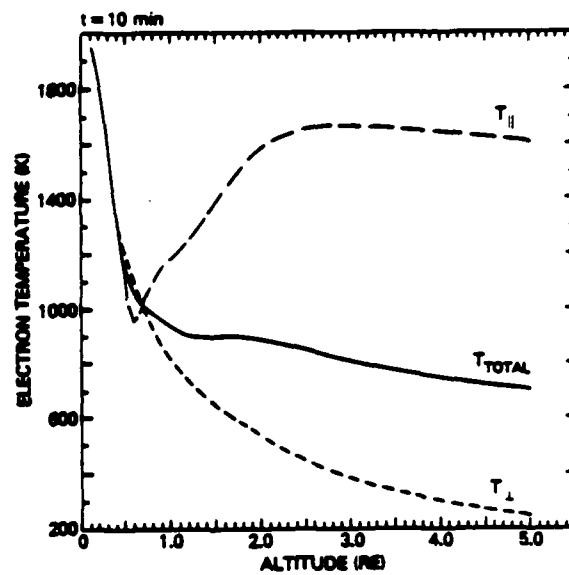


Fig. III.5.b — Electron temperature after the onset of current  $-2.0 \mu\text{A}/\text{m}^2$

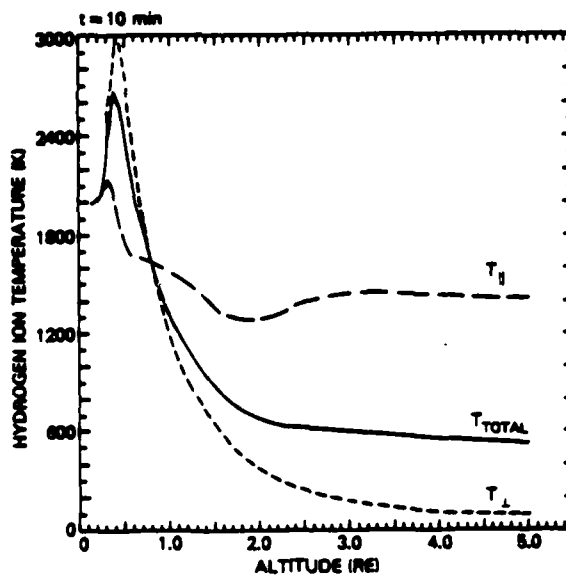


Fig. III.5.c — Hydrogen ion temperature after the onset of current of  $-2.0 \mu\text{A}/\text{m}^2$



## **CHAPTER IV**

### **LARGE SCALE RETURN CURRENTS**

#### **ON AURORAL FIELD LINES**

#### **II. 16 MOMENT CALCULATIONS**



#### IV.1 INTRODUCTION

We are interested in the study of plasma transport on auroral field lines including the effects of return currents as explained in chapter III. In chapter III, we have used our time-dependent model based on the 13-moment system of transport equations. In addition only cold electrons of ionospheric origin were considered.

In this chapter we have performed two types of simulations. First, we have used the steady state model to investigate the effects of return currents on auroral field line equilibria. Then we have used the time dependent model to explore the effects of sudden changes on plasma dynamics after the onset of a current. The steady state model for this simulation has been described in chapter I and Ganguli et al. [1985]. The time-dependent model used is explained in chapter III. The electrons are hot at the upper boundary and the transport equations used are based on 16-moment approximations. The advantage of using the 16-moment system of transport equations over the 13-moment is explained in chapter I. The effects on electron temperatures due to the hot upper boundary conditions and the cold outflow conditions can be seen by comparing the polar wind electron temperature profiles in Chapters I and III. We will also address this issue in section IV.2 of this Chapter.

## IV.2 RETURN CURRENT SIMULATIONS

In this section we discuss the results of our field aligned return current steady state simulations. Using the polar wind solution as the initial steady state of the flux tube, a series of solutions of the 16-moment equations were found with return currents starting with a very small current of  $-0.1 \mu\text{A}/\text{m}^2$ . The current was then increased by small increments and simulations were carried on for a typical range of large scale return currents. In each case the "initial guess" for the profiles was taken to be the solution found for the previous (lower current) case, and the equations were solved iteratively until a new solution was found.

We will first discuss the case where a field aligned return current of magnitude  $-0.1 \mu\text{A}/\text{m}^2$  was applied to the system. With the application of current, the electron velocity increases over its polar wind value (figure IV.1.a). The ambipolar electric field decreases, decreasing the hydrogen ion velocity, also shown in figure (IV.1.a). As the total hydrogen ion flux in the flux tube is constrained to a fixed value, the decrease in hydrogen ion velocity implies an increase in hydrogen ion density. From the charge neutrality condition (equation I.7) it is clear that an increase in hydrogen ion density will increase the electron density also. The increase in density due to onset of current over its polar wind value is shown in figure (IV.5.a),

for all currents. The hydrogen ion temperature increases over its polar wind value, with temperature parallel to the field line being higher than that perpendicular to the field line (shown in figure (IV.1.b)). The hydrogen ion heat flows parallel and perpendicular to the field line increase over their polar wind values. The electron temperature decreases from its polar wind value but the direction of anisotropy remains the same, i.e., the temperature perpendicular to the field line is higher than that parallel to the field line (shown in figure (IV.1.c)). The collisions play an important role up to an altitude of 2500 km. The magnitude of electron heat flows decrease from their polar wind values. Since the current applied is very low the flow characteristics of the electrons remain the same as in the polar wind flow.

The current was increased to  $-0.5 \mu\text{A}/\text{m}^2$ . The electron velocity increases further, the electric field decreases, the  $\text{H}^+$  ion velocity decreases. The hydrogen ion temperature increases and the electron temperature decreases further with altitude with the increase in current. The hydrogen ion temperature variation is produced mainly as an interaction between the convection process and the adiabatic process. With the application of current the contribution from the terms containing the hydrogen ion heat flow anisotropy and the hydrogen ion temperature anisotropy increases. The hydrogen ion temperature gradient

increases. The contribution from the terms containing the mirror force effects increases and this increases the temperature anisotropy of the hydrogen ions. The electron temperature anisotropy decreases. Figures (IV.5) and (IV.6) show all the variables for all the currents.

The next current was  $-.55 \mu\text{A}/\text{m}^2$ . The relative importance of the terms and effects described above remain the same as before and hence are not repeated here.

The current was increased to  $-.65 \mu\text{A}/\text{m}^2$ . The electron velocity and density increase further with the increase of current. The electron density gradient increases. The electron temperature is produced as a balance between the thermal convection and thermal conduction processes. The electron temperatures parallel and perpendicular to the geomagnetic field line, for this current are shown in figure (IV.2a). The contribution from the convection terms are very important at the lower end of the flux tube. It was found by Schunk and Watkins [1981] that the heat flow terms contribute strongly to the temperature anisotropy. The electron temperature anisotropy decreases and temperatures parallel and perpendicular to the field line decrease from the polar wind values. The magnitude of electron heat flow decreases further in the parallel direction. The electron parallel heat flow reverses the direction at the lower end of the field line, which implies that the electrons

require heat flow from the ionosphere at this altitude. The magnitude of perpendicular heat flow decreases at the lower end of the flux tube but increases at the upper end with the increase of current. The electron temperature gradient decreases at the lower end but increases at the upper end of the flux tube. The collisions are important up to 2500 km. The hydrogen ion density and density gradient increases. The  $H^+$  ion velocity decreases, the temperature and temperature anisotropy increases.

We now consider a current of  $-1.0 \mu A/m^2$ . The electron temperature anisotropy is seen reversed at this current from  $T_{\perp} > T_{\parallel}$  to  $T_{\parallel} > T_{\perp}$  and is shown in figure (IV.2b). The actual reversal of anisotropy takes place for a current of  $-.8 \mu A/m^2$  (this current is discussed in chapter V). The electron density enhancement is shown in figure (IV.5.a). The high density flow of the ionospheric electrons and sharp density and velocity gradients at the bottom of the tube actually lowers the electron temperatures before they start to rise again. The flow characteristics are those of ionospheric flow at the lower end of the flux tube, that is, the particles moving in the direction of decreasing magnetic field decrease their velocity in the perpendicular direction in order to preserve their adiabatic invariant. To conserve energy, perpendicular energy is transferred to parallel energy. The temperature parallel to the field line is then higher than that perpendicular to the field line. Comparing these results with those of Chapter III, it is

observed that the application of return currents to upflowing cold ionospheric electrons do not change their anisotropy. This flow is explained in figure (IV.3.a). The arrows in the figure represent the direction of heat flows. Now, let us consider the effects of a hot upper boundary for the electrons. In Chapter I it has been shown that if the upper boundary of the electrons is maintained at a higher temperature than the lower boundary, the tendency of the hot downgoing electrons to conserve their magnetic moment produces an anisotropy with  $T_{\perp} > T_{\parallel}$ . This anisotropy is shown in figure (IV.3.b). The area on the left side of the dotted line shows the part of the flux tube displayed in all the figures while the area on the right side shows the isotropic electron temperature boundary condition actually used in the model. The collisions isotropize the electron temperatures at the lower end. The electron flow is subsonic with cold electrons flowing out of the ionosphere and hot electrons flowing down from the magnetosphere. The downward heat flow or thermal conduction (h) tends to produce an anisotropy with  $T_{\perp} > T_{\parallel}$ , as shown in figure (IV.3.b). However, the thermal convection (nkTV) tends to produce the anisotropy in the reverse direction. In this case the downward conduction wins over the upward convection effect. For the case of current  $-1.0 \mu\text{A}/\text{m}^2$  the effects of thermal convection wins over the heat flow effects and therefore we observe the anisotropy with  $T_{\parallel} > T_{\perp}$ .



For higher currents, that is  $-1.5$  and  $-2.0 \mu\text{A}/\text{m}^2$  the electron density and velocity are further increased. The electron temperature anisotropy increases, with temperature parallel to the field line higher than that perpendicular to the field line. The electrons now show clearly ionospheric flow characteristics. The hydrogen ion velocity decreases and hydrogen temperature and temperature anisotropy increases. Figure (IV.4.a) shows species velocity for this current, (IV.4.b) hydrogen ion temperature anisotropy and (IV.4.c) the electron temperature anisotropy. By comparing figures (IV.1.a) and (IV.4.a) the increase in species velocity difference with the increase in current is clearly seen. Also (IV.1.b) and (IV.4.b) show increase in hydrogen ion temperature anisotropy with increase in current. Figures (IV.1.c) and (IV.4.c) show electron temperature anisotropy reversal with increase of current.

The results of these simulations can be summarized by observing figures (IV.5) and (IV.6). For all currents, figure (IV.5.a) shows the electron density ratio (electron density for any current / polar wind value), (IV.5.b) the hydrogen ion velocities, (IV.5.c) electron velocities, (IV.6.a)  $\text{H}^+$  ion parallel temperature, (IV.6.b)  $\text{H}^+$  ion perpendicular temperature, (IV.6.c) electron parallel temperature, (IV.6.d) electron perpendicular temperature and (IV.6.e) the potential drop along the field line due to each of the currents (as calculated from  $E_{\parallel}$ ). With the increase of current the following events occur

- the electron density ratio (current / polar wind) increases (figure IV.5.a)), the hydrogen ion velocity decreases (figure IV.5.b) and the electron velocity increases (figure IV.5.c). The increase in hydrogen ion parallel temperature is shown in figure (IV.6.a); the perpendicular temperature does not change appreciably (figure IV.6.b). The decrease in electron parallel temperature is shown in figure (IV.6.c) and perpendicular temperature in (IV.6.d). The potential drop along the field line is calculated directly from the parallel electric field. Since  $E_{||}$  is positive, the potential drop is negative and decreases in magnitude with the increase of current.

Our simulations show that the electron drift velocity corresponding to the current of  $-.65 \mu\text{A}/\text{m}^2$  is above the threshold of electrostatic ion cyclotron waves. Plots of the ratio of drift velocity (defined as the relative drift between the electrons and the ions) over critical velocity for excitation of the instability are shown in chapter V. The EIC instability heats the hydrogen ions and can transfer electron momentum to ions, thereby producing anomalous resistivity. These effects have been discussed in detail in chapter V.

We have also performed a similar series of studies of return currents in our time dependent model (16-moment system of transport equations used) to show how the flux tube plasma reacts to sudden changes in conditions, as we apply currents to the

steady state polar wind. The results of application of current in steady state, i.e., the effects on the final equilibrium, have already been discussed. The effects of time variation will now be explained.

We start our simulation with a current of magnitude  $-1.0 \mu\text{A}/\text{m}^2$  applied to the initially steady state polar wind. The electron velocity and temperature have rapid response to sudden changes in conditions with a time constant of about a few minutes. The sudden change in current produces a density enhancement which spreads and grows in time to form a new equilibrium. Electron density variation is shown at 1 1/2 minutes (figure IV.7.a) after the onset of a current of  $-1.0 \mu\text{A}/\text{m}^2$ . The density enhancement is seen in a narrow region at the lower end of the flux tube where the ambipolar electric field is strong. With the increase of time the density enhancement spreads and increases in magnitude as shown at 12 1/2 minutes (figure IV.7.b), 28 minutes (figure IV.7.c) and 4 hours (figure IV.7.d) after the onset of the current. At the steady state the electron density has increased with the application of current. The electric field decreases with the application of current, which decreases the hydrogen ion velocity. Figure (IV.8.a) shows the decrease in hydrogen ion velocity with time from 4 1/2 minutes to 12.3 minutes after the onset of the current. The decrease in  $\text{H}^+$  ion velocity causes a velocity ripple which in turn causes the density ripple and these propagate upwards

through the flux tube in time. The time constant for variation of electron velocity is about a few minutes. The species velocity profiles are shown in figures (IV.8.b) - (IV.8.d) for times 12 1/2 minutes, 28 minutes and 4 hours after the onset of the current. The electron temperature anisotropy of the polar wind ( $T_{\perp} > T_{\parallel}$ ) reverses ( $T_{\parallel} > T_{\perp}$ ) after about 1 1/2 minutes after the onset of the current. The time constant for variation of electron temperature is approximately 1 1/2 minutes. The electron temperature variation with time is shown for parallel and perpendicular temperature separately from 1 1/2 minutes to 4 1/2 minutes in figures (IV.9.a) and (IV.9.b), 4 1/2 minutes to 12.3 minutes in figures (IV.9.c) and (IV.9.d). These figures illustrate the decrease in electron temperature with time. The final configuration after 4 hours is the same as in figure (IV.3). The time changes of electron thermal energy flows parallel and perpendicular to the field line are shown from 1 1/2 to 4 1/2 minutes in figures (IV.10.a) and (IV.10.b). Some noticeable change in the hydrogen ion parallel temperature profile is seen only after 4 1/2 minutes (figure IV.11.a). The  $H^+$  ion temperature after 12 1/2 minutes is shown in Figure (IV.11.b) and after 4 hours in (IV.11.c). The time changes of  $H^+$  ion thermal energy flows parallel to the field line is shown from 4 1/2 to 12 1/2 minutes in figure (IV.12). Note that the  $H^+$  ion perpendicular heat flow does not change much with time. The behavior of the ion mass and energy transport in the collisionless region determines the time scales on which the flux

tube plasma reaches equilibrium.

The current was then increased to  $-1.5 \mu\text{A}/\text{m}^2$ . Since the increment in current was only  $0.5 \mu\text{A}/\text{m}^2$  relative to an already existing steady state of  $-1.0 \mu\text{A}/\text{m}^2$ , the changes in parameters are not as dramatic as in the previous case. The electron density ratio for this current over the polar wind value is shown in figure (IV.13) after 4 hours and 6 minutes after the onset of this current. Appreciable change in the  $\text{H}^+$  ion velocity is noticed after 12 minutes. The electron temperature changes after 22 seconds with  $T_{||} > T_{\perp}$ , shown in figure (IV.14). The variation of  $\text{H}^+$  heat flows and temperatures were very slow with time. The final steady state was reached in 4 hours 6 minutes. The electron velocity increases and the electrons cool down further.

Current of  $-2.0 \mu\text{A}/\text{m}^2$  was then applied to steady state solutions of  $-1.5 \mu\text{A}/\text{m}^2$ . The electron velocity increases further. The density ratio of this current over the polar wind increases and a ripple is observed at 1 1/2 minutes, shown in figure (IV.15.a). At 4 1/2 minutes the velocities and electron temperatures show noticable change but  $\text{H}^+$  ion temperatures do not change much. The density ratio is shown 12 minutes after the onset of the current in figure (IV.15.b), after 30 minutes in (IV.15.c) and after 3 hours 51 second in (IV.15.d). The velocity profiles after 12 minutes are shown in figure (IV.16.a), electron

temperatures in (IV.17.a), hydrogen ion temperatures in (IV.18.a). The species velocity profiles at 3 hours 51 seconds in a converged run is shown in figure (IV.16.b), electron temperatures in (IV.17.b) and  $H^+$  ion temperatures in (IV.18.b).

### IV.3 DISCUSSIONS

We have studied the effects of return currents on auroral field line equilibria. It is seen that electron temperature anisotropy reverses with the increase of return current. The time-dependent calculations show that this reversal takes place in the first few minutes after the onset of current. The time constants for variation of electron temperature and velocity are only a few minutes while that for hydrogen ion temperature is about half an hour. This reversal of anisotropy was not observed in the similar calculations in Chapter III, where we have used only cold electrons of ionospheric origin. These electrons with anisotropy  $T_{||} > T_{\perp}$ , cool down further with the application of return current.

The electron drift velocity corresponding to a current of  $-0.65 \mu A/m^2$  is unstable to the electrostatic ion cyclotron instability. Non-linear effects such as anisotropic ion heating

and anomalous resistivity can arise due to this instability. The effects of these anomalous transport processes on the field line equilibria will be discussed in chapter V.





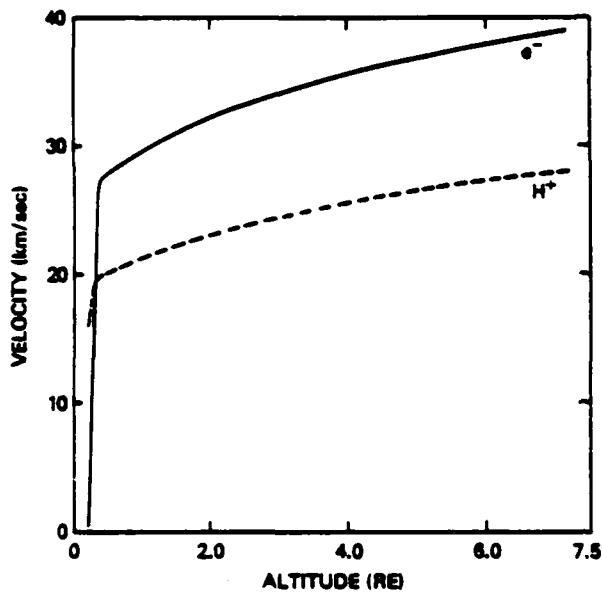


Fig. IV.1.a — Species velocity profiles for a current of  $-1 \mu\text{A}/\text{m}^2$

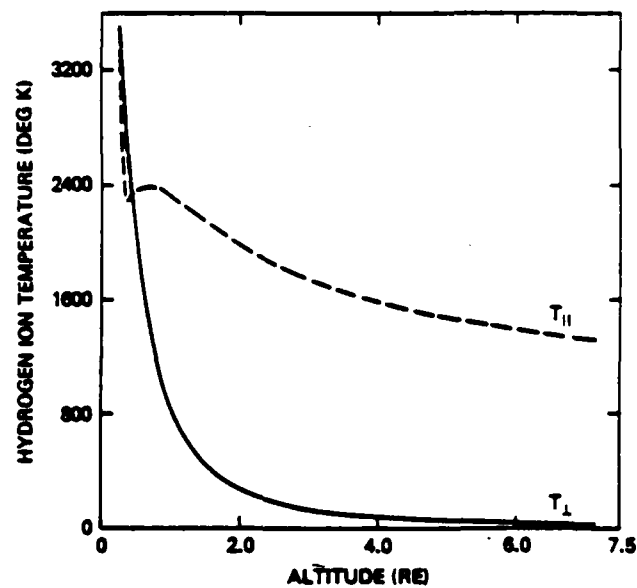


Fig. IV.1.b —  $\text{H}^+$  ion temperatures parallel and perpendicular to the geomagnetic field for a current of  $-1 \mu\text{A}/\text{m}^2$

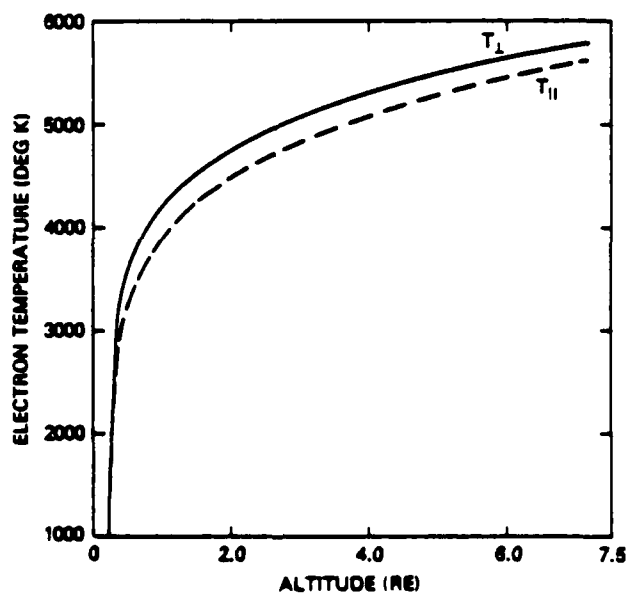


Fig. IV.1.c — Electron temperatures parallel and perpendicular to the geomagnetic field for a current of  $-1 \mu\text{A}/\text{m}^2$

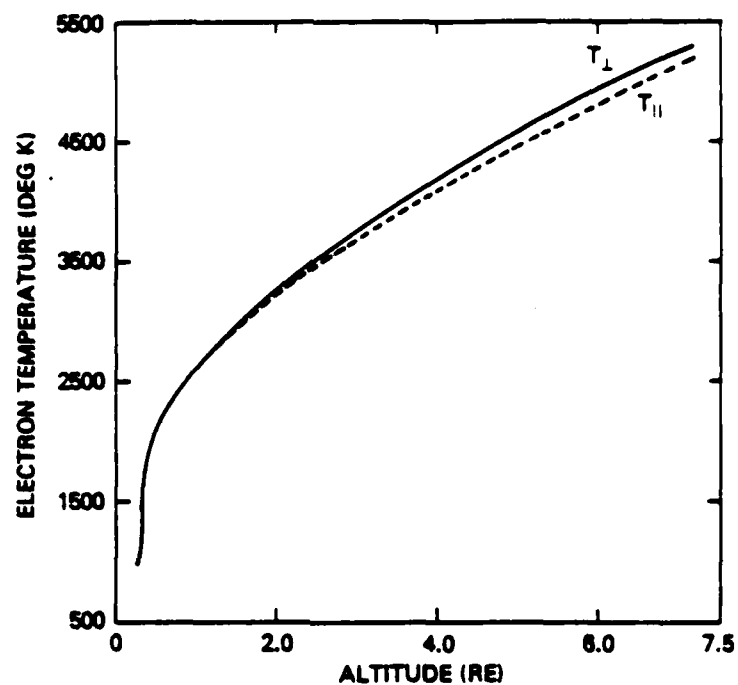


Fig. IV.2.a — Electron temperatures parallel and perpendicular to the geomagnetic field for a current of  $-0.65 \mu\text{A}/\text{m}^2$

Parallel temperature (dashed curve), perpendicular temperature (solid curve)

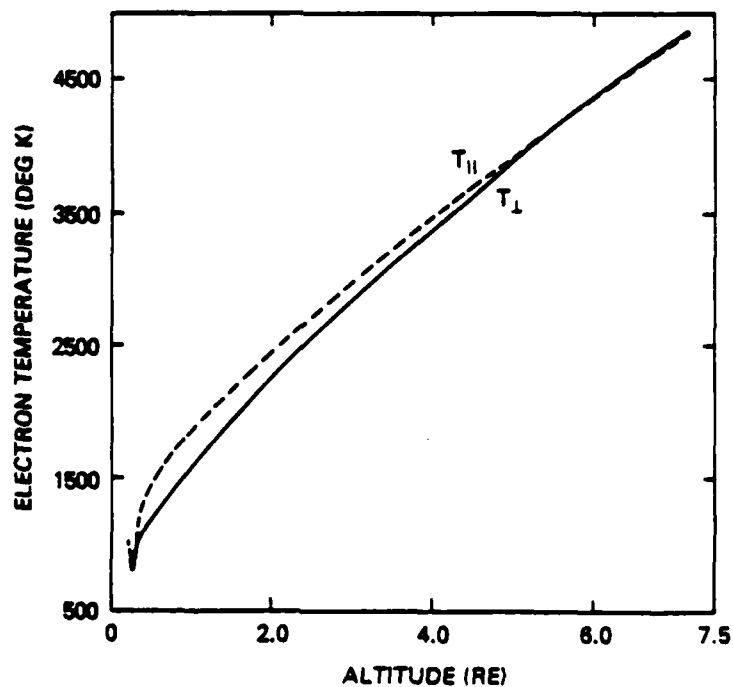
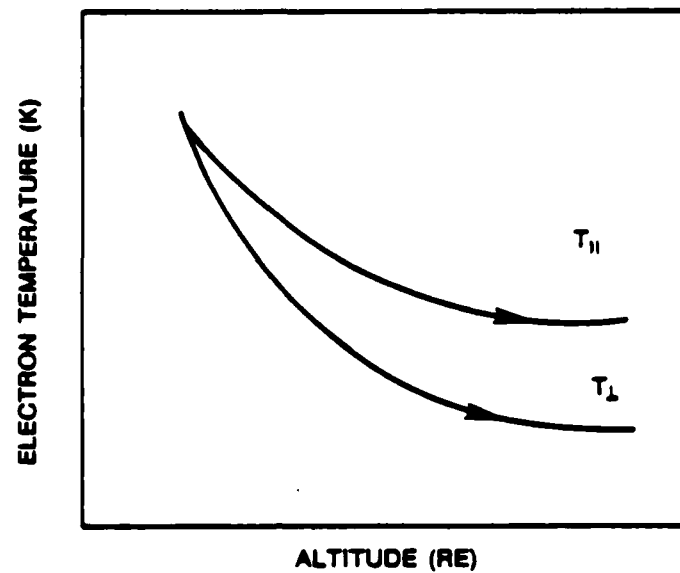
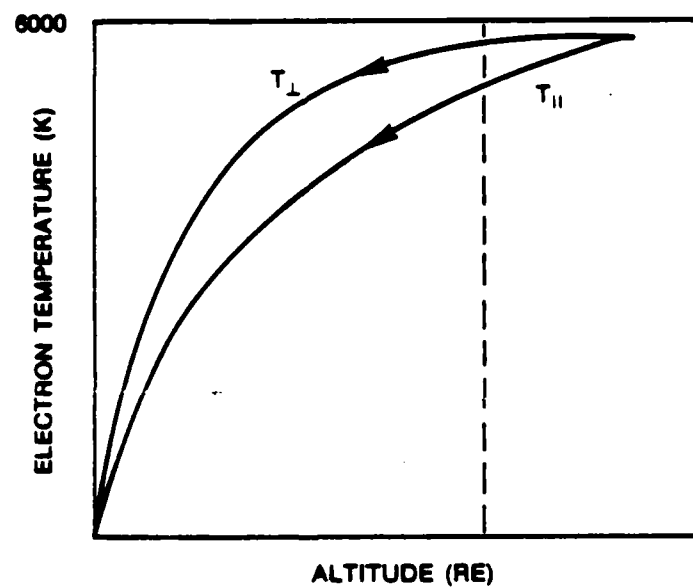


Fig. IV.2.b — Electron temperatures parallel and perpendicular to the geomagnetic field for a current of  $-1.0 \mu\text{A}/\text{m}^2$



(a)



(b)

Fig. IV.3 — Electron temperature anisotropy.  
The arrows indicate the direction of heat flows.

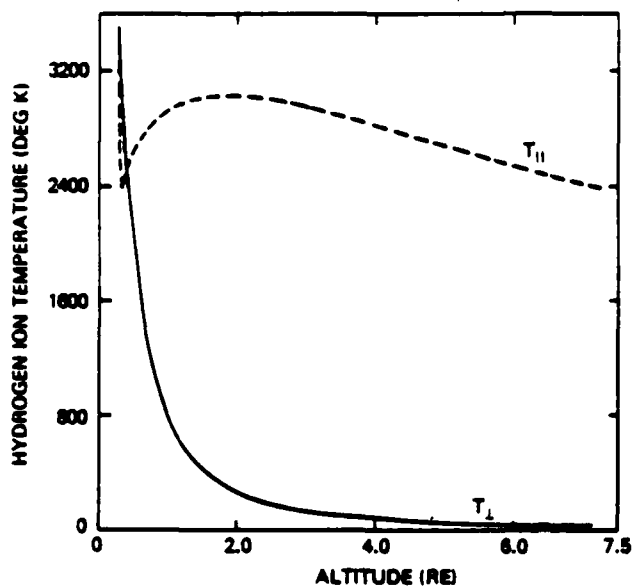


Fig. IV.4.a — Species velocity profiles for a current of  $-1.5 \mu\text{A}/\text{m}^2$

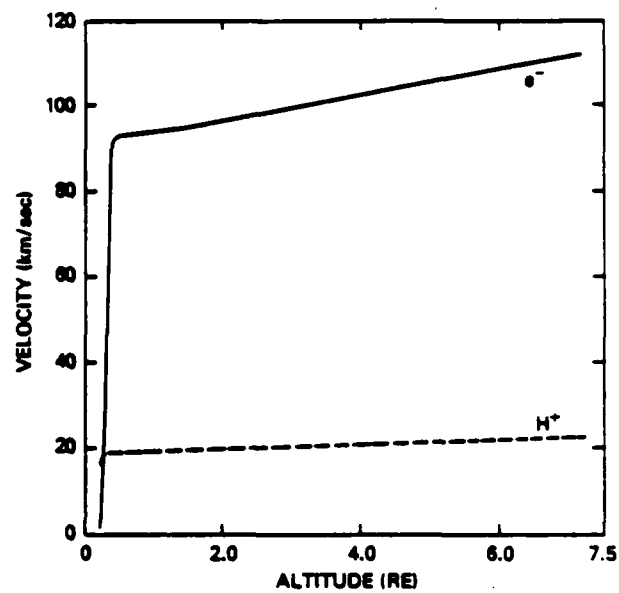


Fig. IV.4.b —  $\text{H}^+$  ion temperatures parallel and perpendicular to the geomagnetic field for a current of  $-1.5 \mu\text{A}/\text{m}^2$

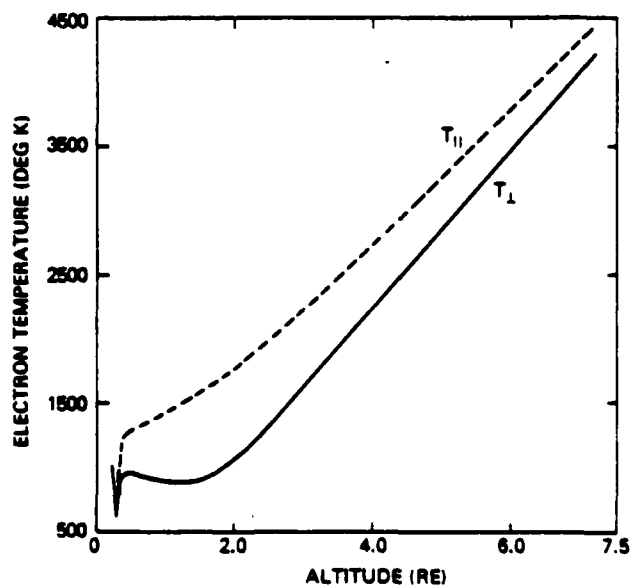


Fig. IV.4.c — Electron temperatures parallel and perpendicular to the geomagnetic field for a current of  $-1.5 \mu\text{A}/\text{m}^2$

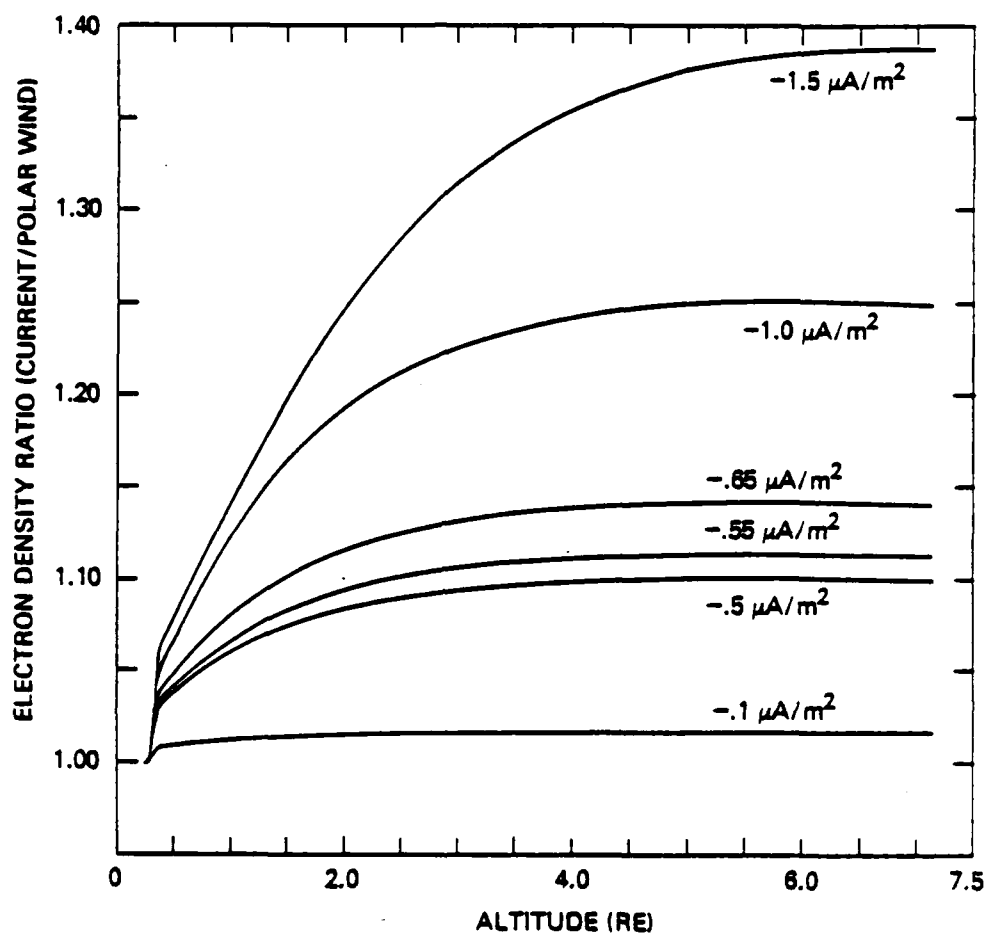


Fig. IV.5.a — Electron density ratio (current/polar wind) for all currents

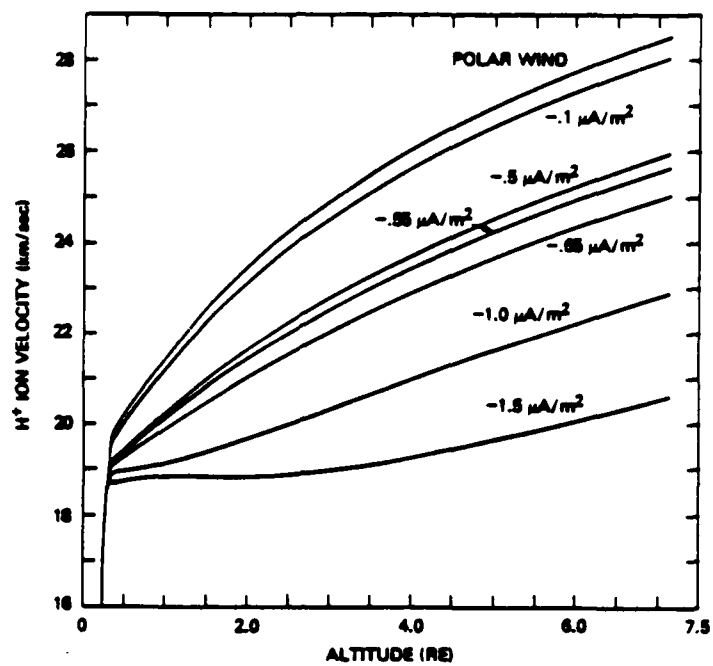


Fig. IV.5.b —  $H^+$  ion velocity profiles for all currents and polar wind

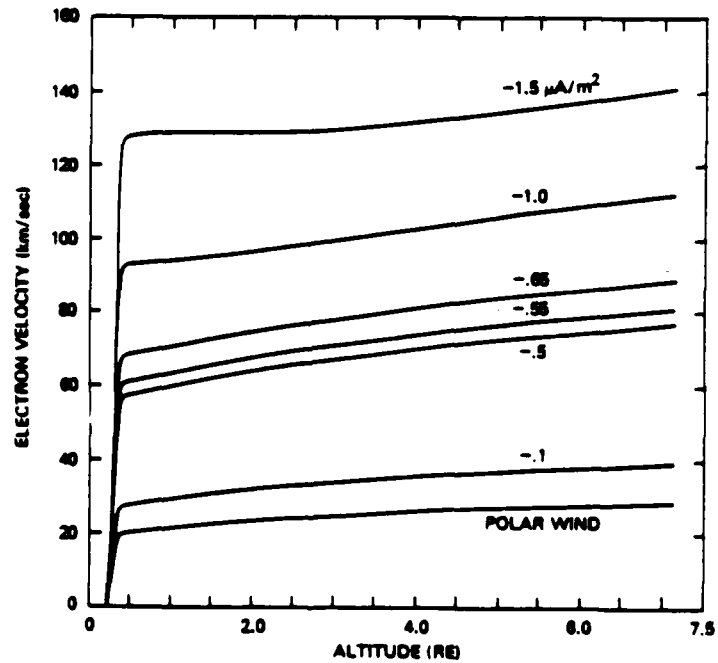


Fig. IV.5.c — Electron velocity profiles for all currents and polar wind

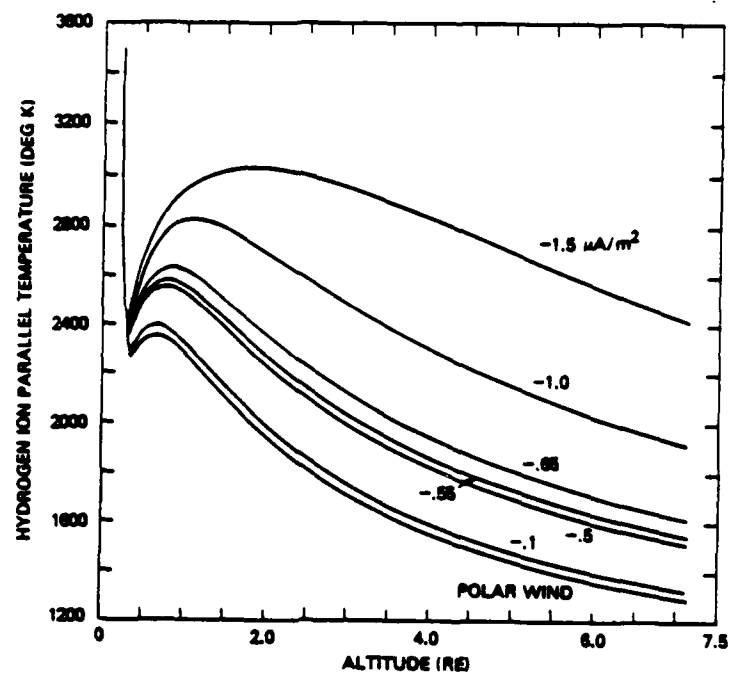


Fig. IV.6.a —  $H^+$  ion parallel temperatures for all currents and polar wind

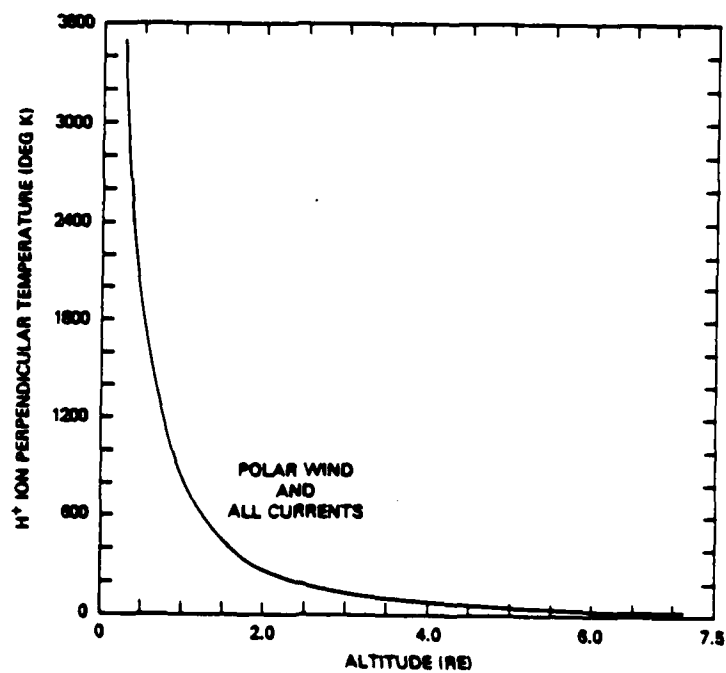


Fig. IV.6.b —  $H^+$  ion perpendicular temperatures for all currents and polar wind

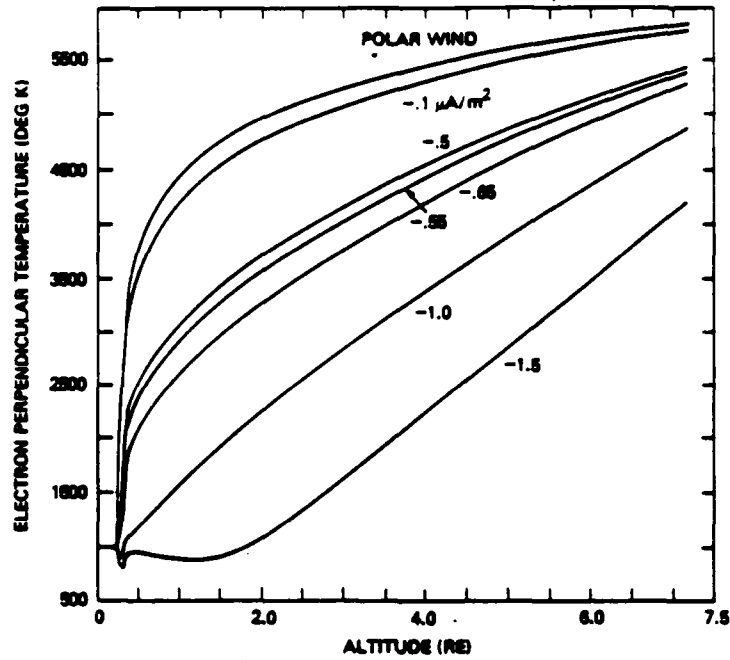


Fig. IV.6.c — Electron parallel temperatures for all currents and polar wind

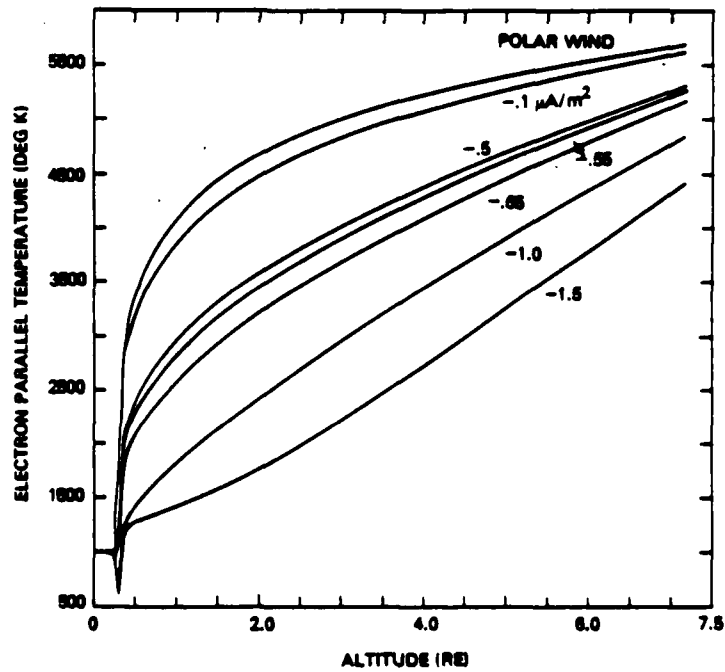


Fig. IV.6.d —  $e^-$  perpendicular temperatures for all currents and polar wind



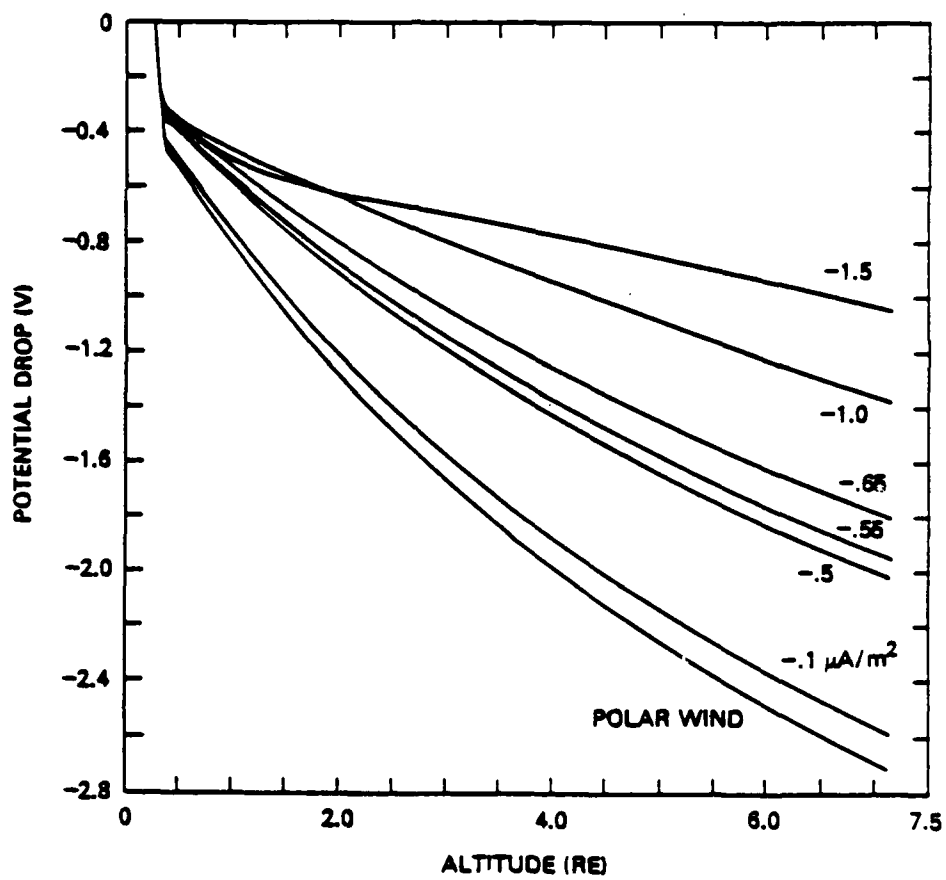
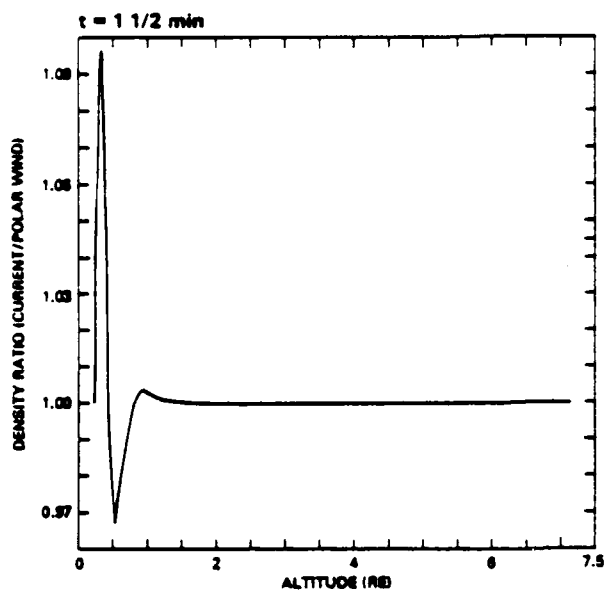
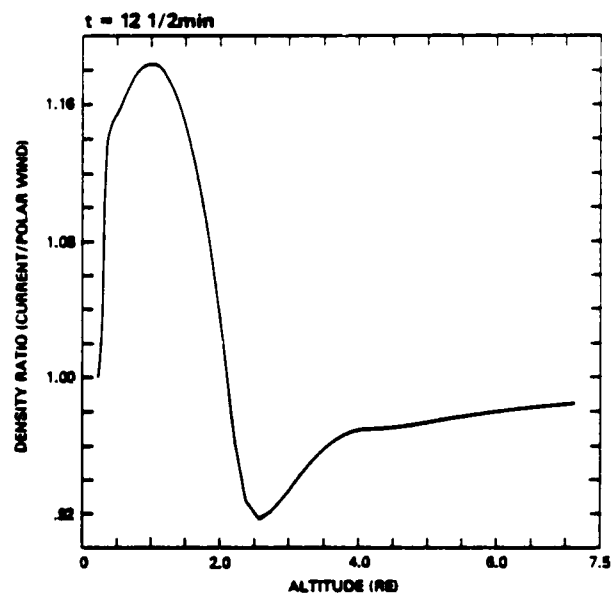


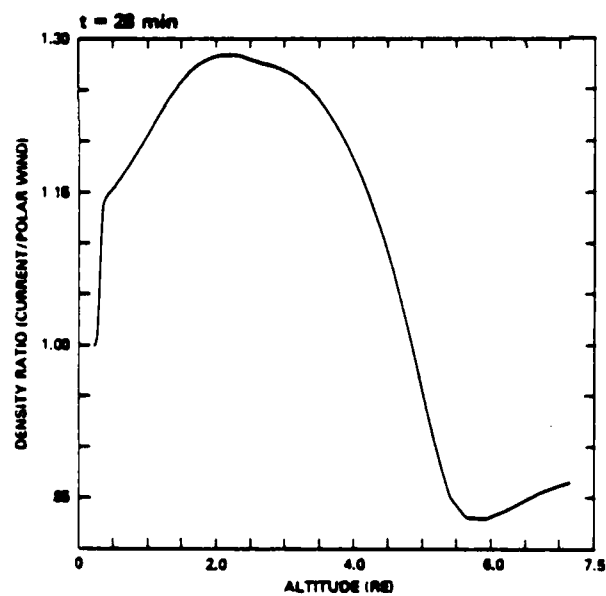
Fig. IV.6.e — Potential drop along the field line for all currents and polar wind



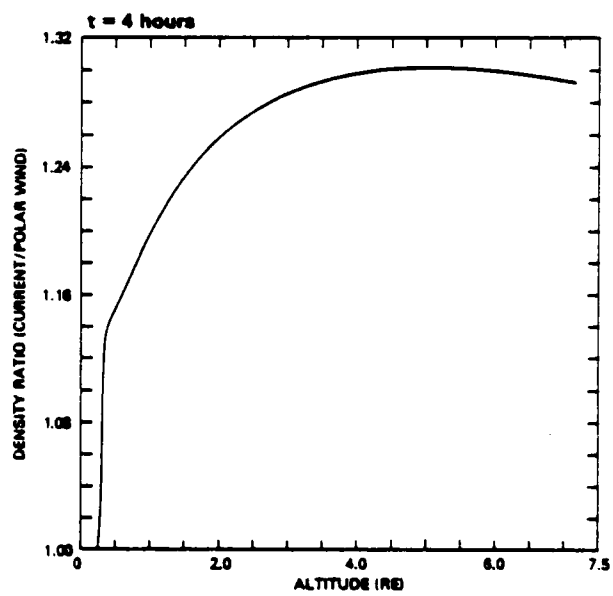
(a)



(b)

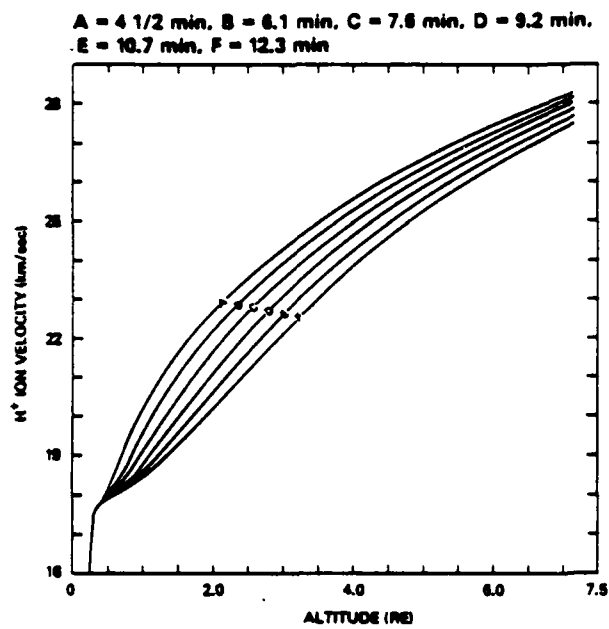


(c)

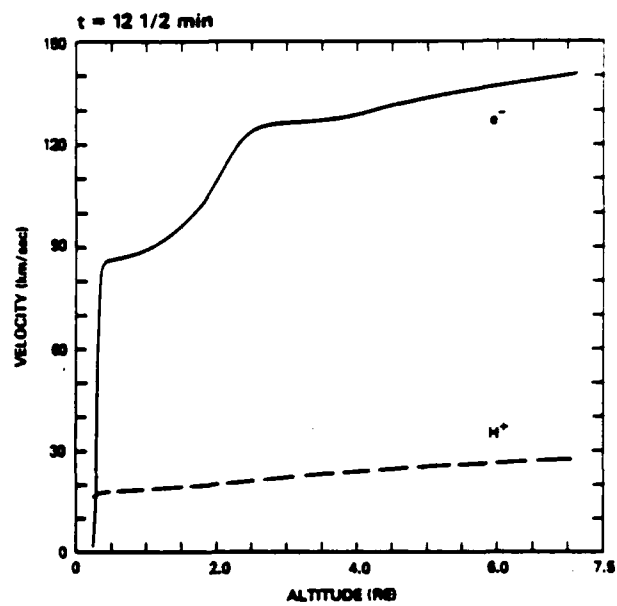


(d)

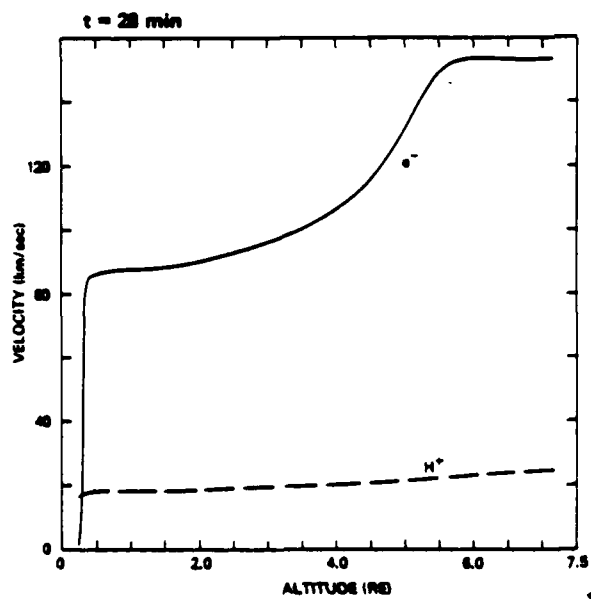
Fig. IV.7 — Electron density ratios after the onset of a current of  $-1.0 \mu\text{A}/\text{m}^2$



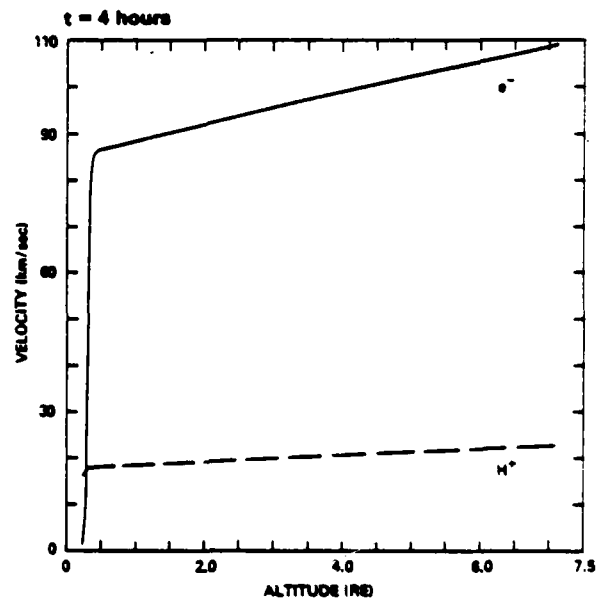
(a)



(b)



(c)



(d)

Fig. IV.8 — Species velocity profiles after the onset of a current of  $-1.0 \mu\text{A}/\text{m}^2$

A = 4 1/2 min, B = 6.1 min, C = 7.6 min, D = 9.2 min, E = 10.7 min, F = 12.3 min

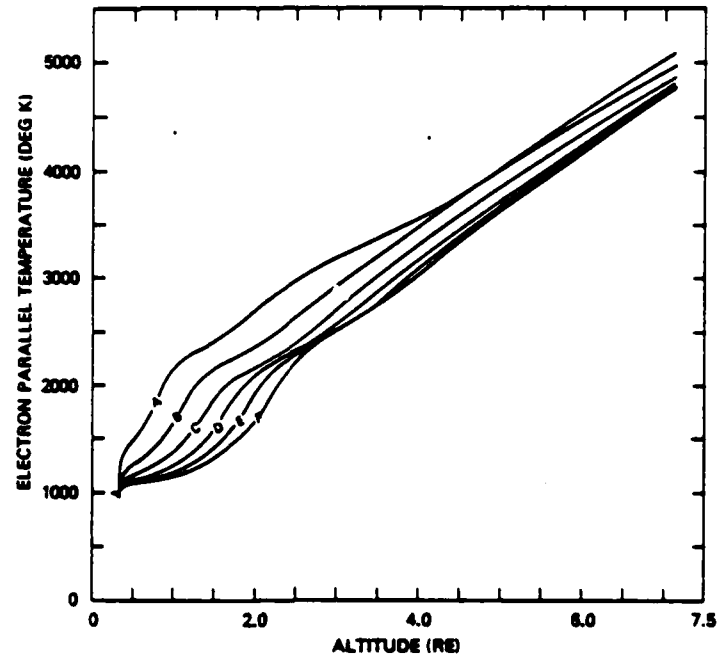


Fig. IV.9.c — Electron parallel temperatures after the onset of a current of  $-1.0 \mu\text{A}/\text{m}^2$

A = 4 1/2 min, B = 6.1 min, C = 7.6 min, D = 9.2 min, E = 10.7 min, F = 12.3 min

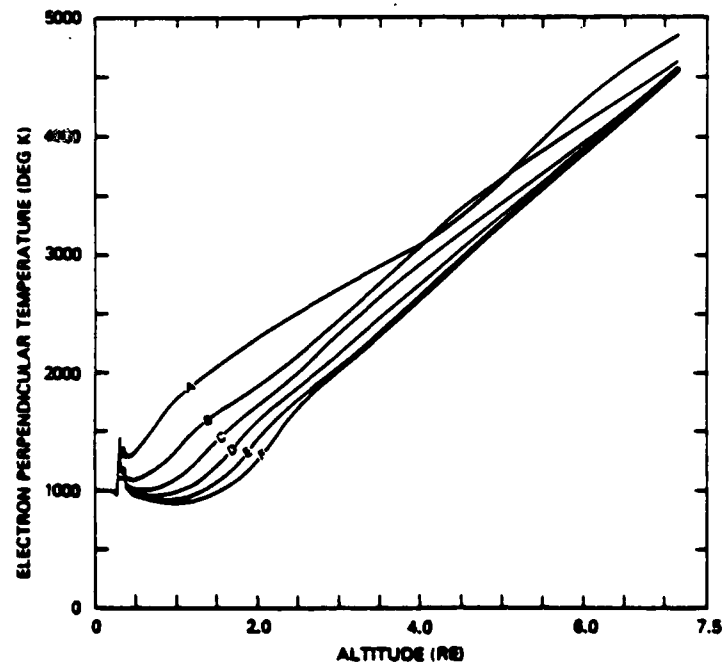


Fig. IV.9.d —  $e^-$  perpendicular temperatures after the onset of a current of  $-1.0 \mu\text{A}/\text{m}^2$

A = 1 1/2 min, B = 2.07 min, C = 2.68 min, D = 3.3 min, E = 3.9 min, F = 4.5 min

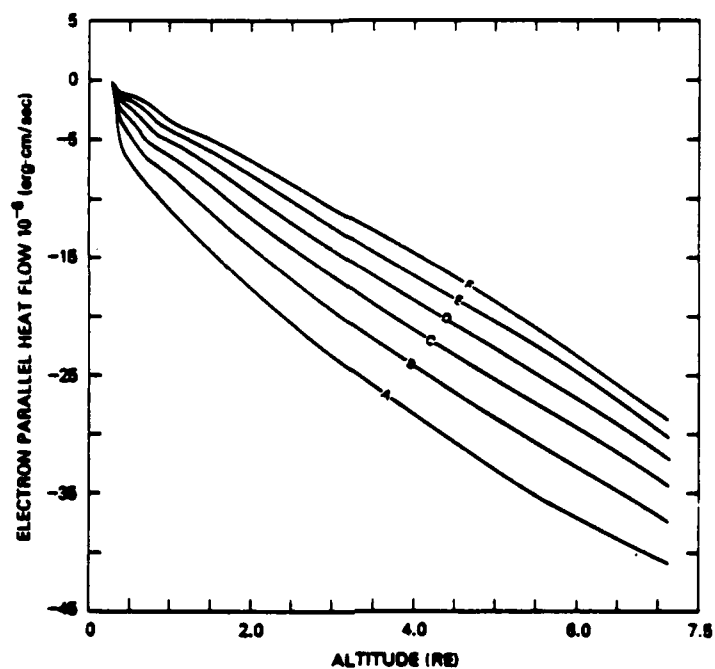


Fig. IV.10.a — Electron parallel heat flows after the onset of a current of  $-1.0 \mu\text{A}/\text{m}^2$

A = 1 1/2 min, B = 2.07 min, C = 2.68 min, D = 3.3 min, E = 3.9 min, F = 4.5 min

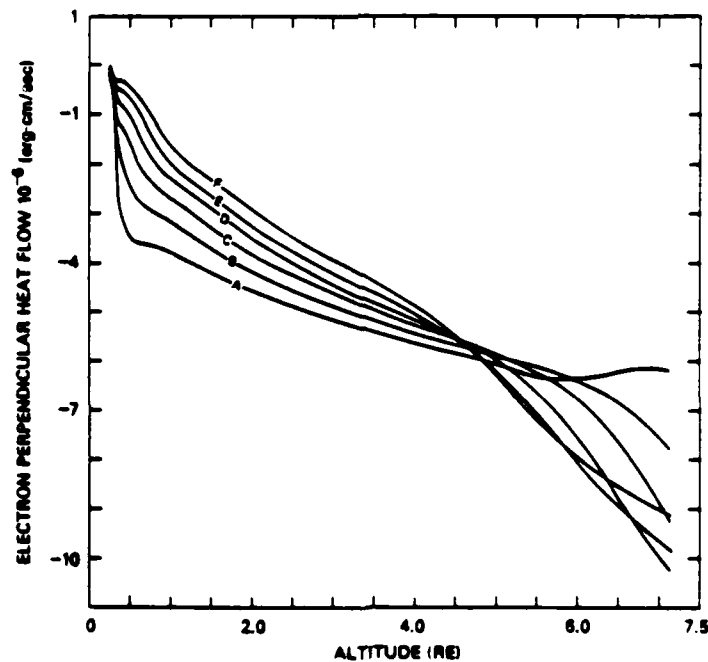


Fig. IV.10.b —  $e^-$  perpendicular heat flows after the onset of a current of  $-1.0 \mu\text{A}/\text{m}^2$

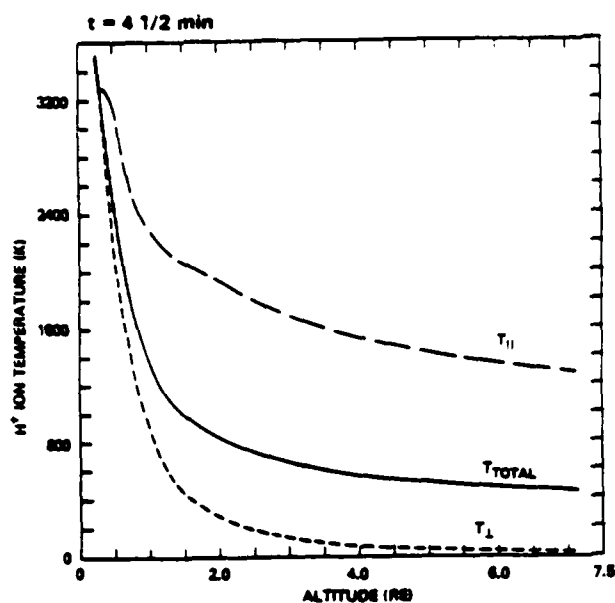


Fig. IV.11.a — Hydrogen ion temperatures and heat flows after the onset of a current of  $-1.0 \mu\text{A}/\text{m}^2$

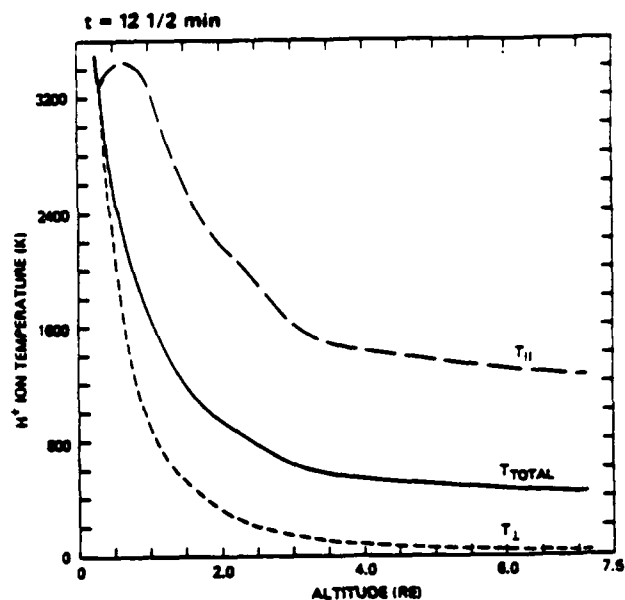


Fig. IV.11.b — Hydrogen ion temperatures and heat flows after the onset of a current of  $-1.0 \mu\text{A}/\text{m}^2$

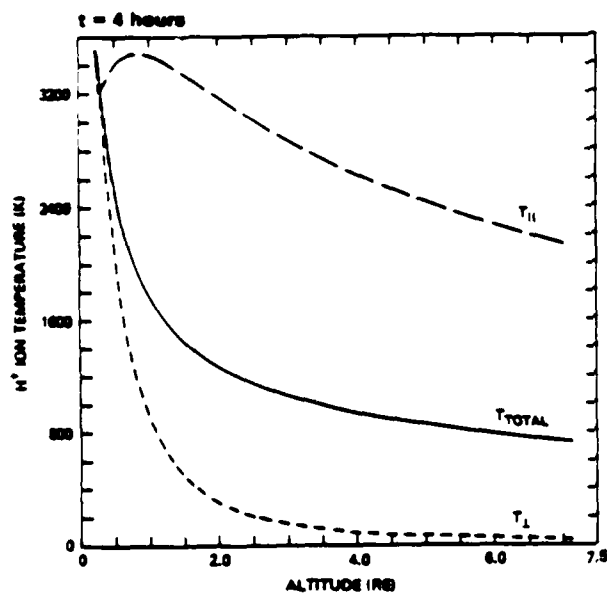


Fig. IV.11.c — Hydrogen ion temperatures and heat flows after the onset of a current of  $-1.0 \mu\text{A}/\text{m}^2$

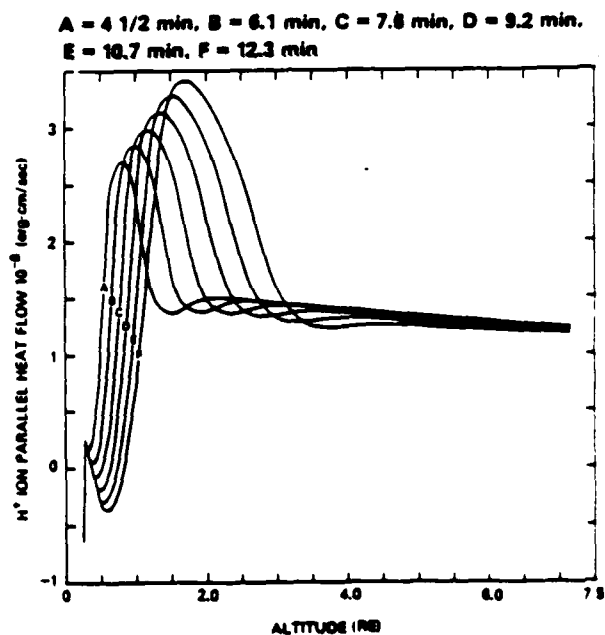
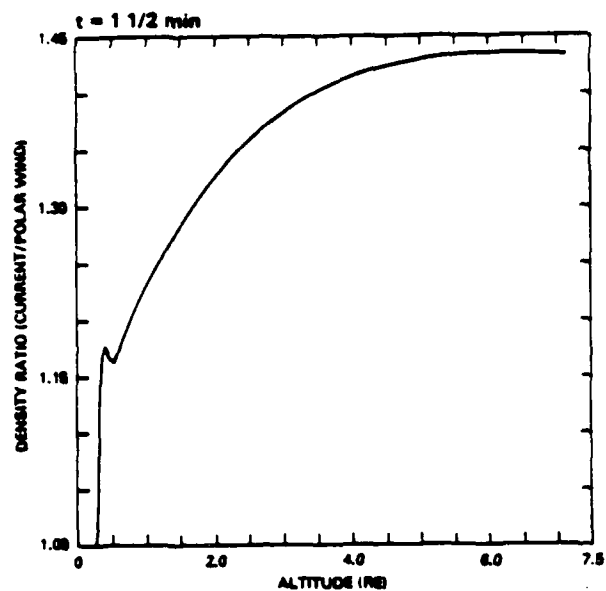
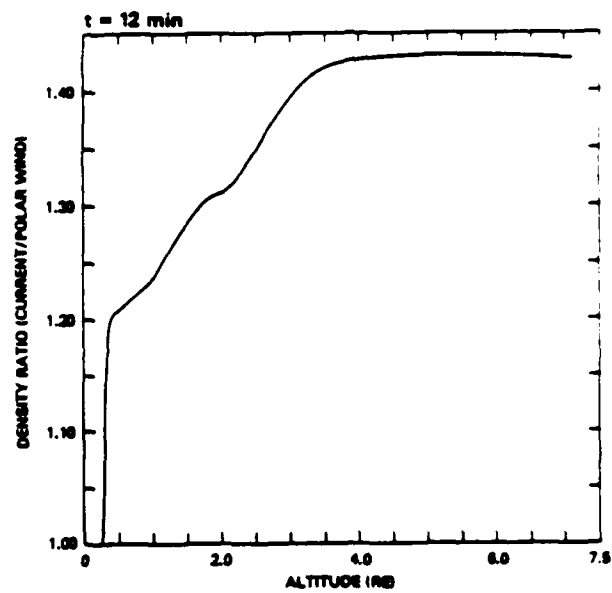


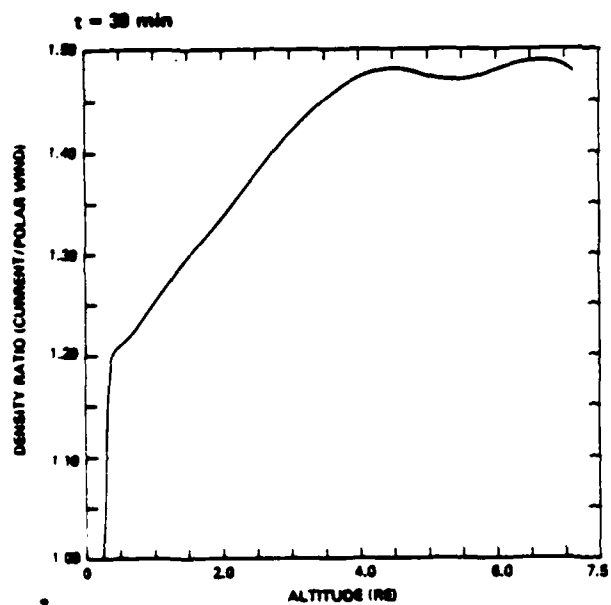
Fig. IV.12 — Hydrogen ion temperatures and heat flows after the onset of a current of  $-1.0 \mu\text{A}/\text{m}^2$



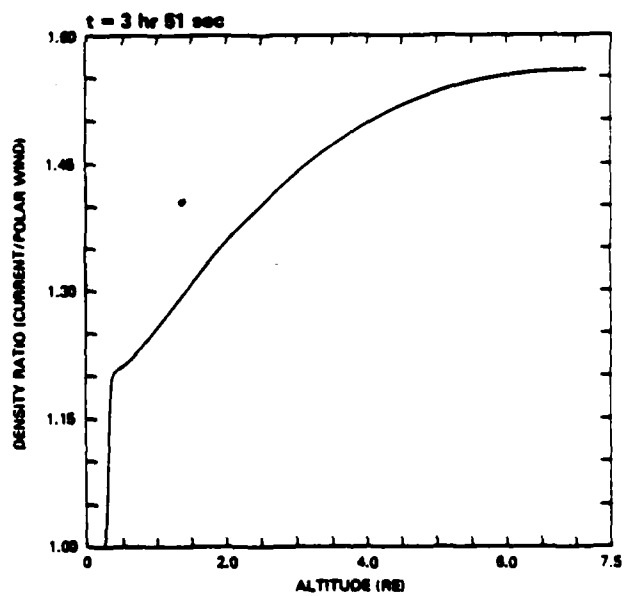
(a)



(b)

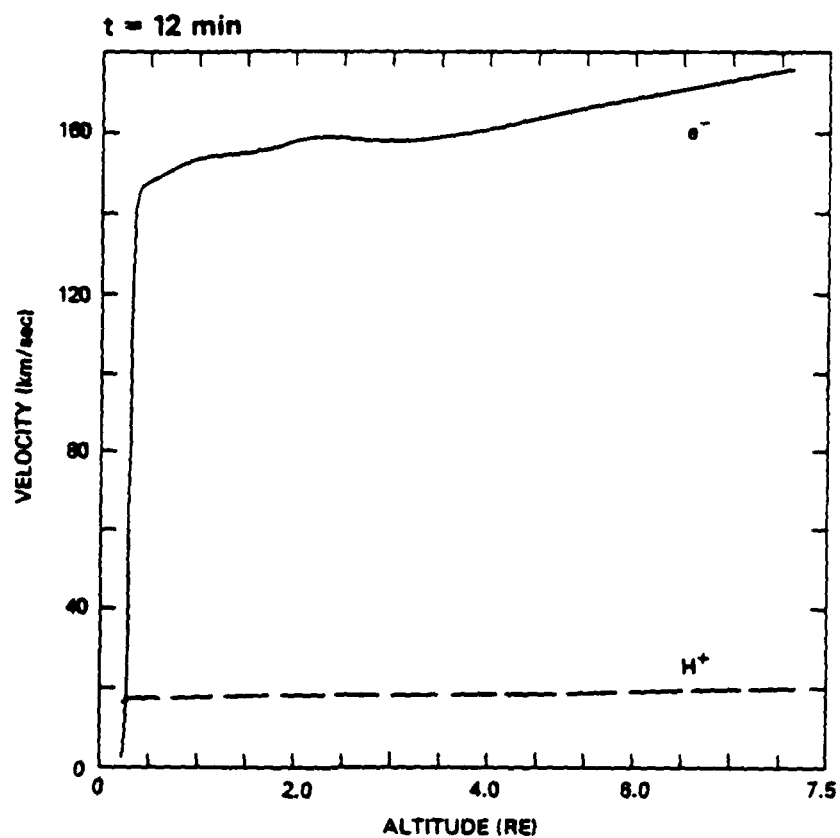


(c)

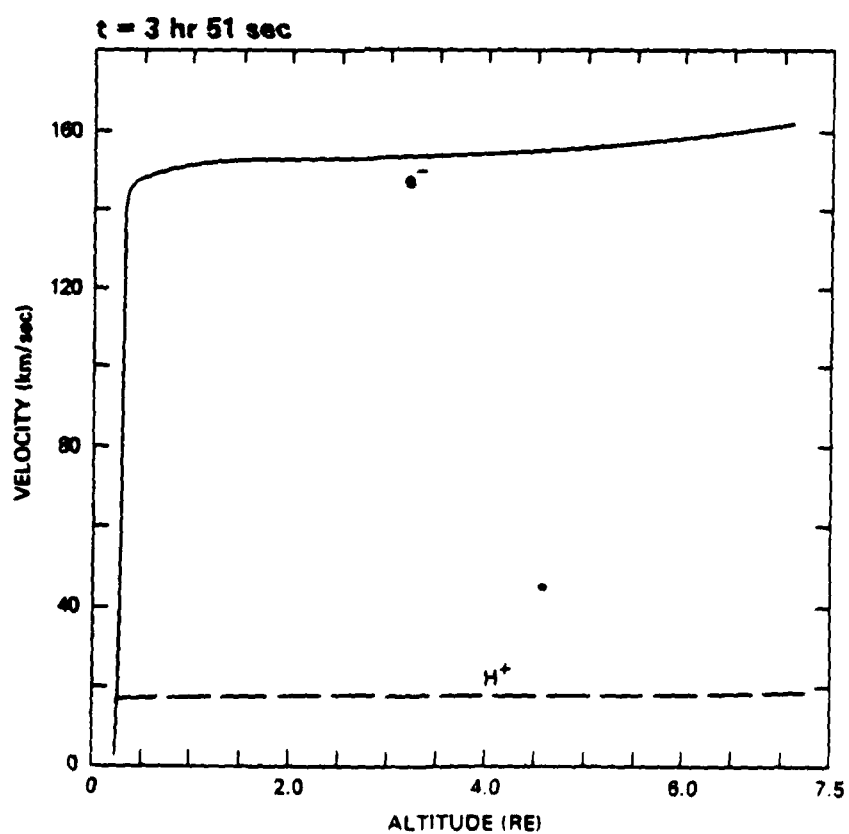


(d)

Fig. IV.15 — Electron density ratios for a current of  $-2.0 \mu\text{A}/\text{m}^2$



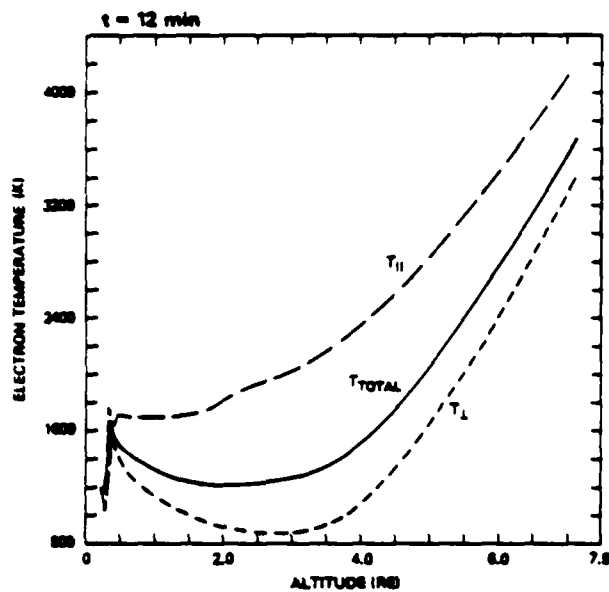
(a)



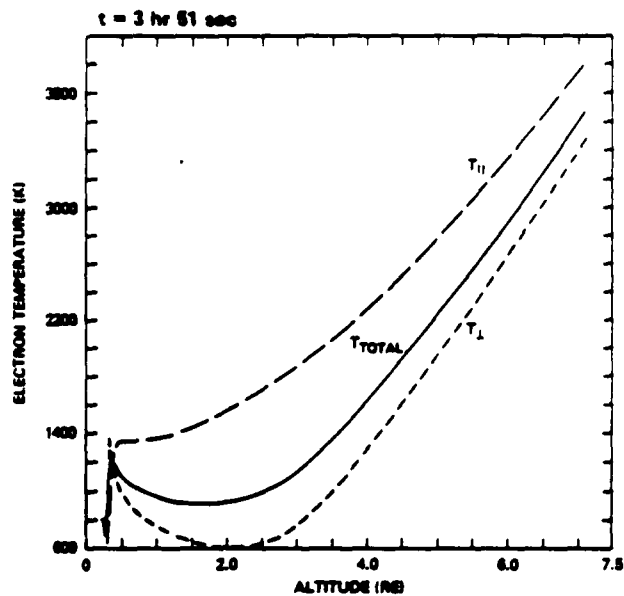
(b)

Fig. IV.16 — Species velocity profiles after the onset of a current of  $-2.0 \mu A/m^2$



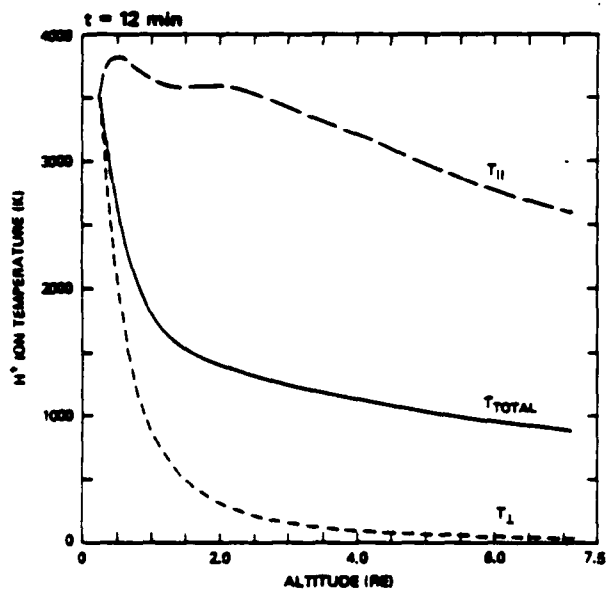


(a)

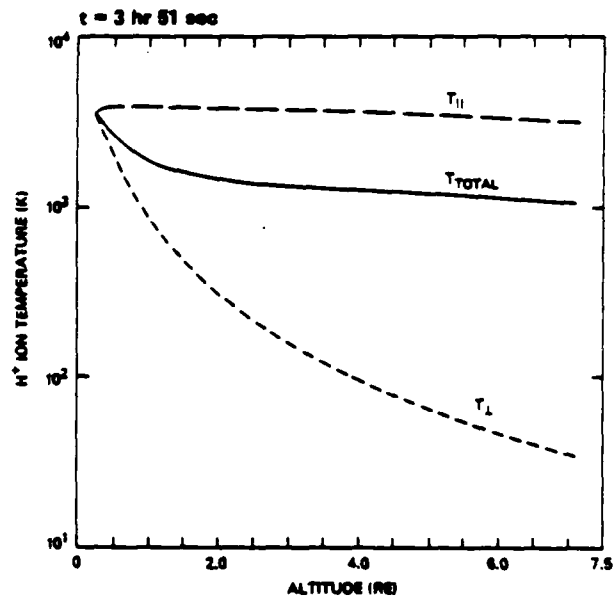


(b)

Fig. IV.17 — Electron temperatures parallel and perpendicular to the geomagnetic field after the onset of a current of  $-2.0 \mu\text{A}/\text{m}^2$



(a)



(b)

Fig. IV.18 —  $\text{H}^+$  ion temperatures parallel and perpendicular to the geomagnetic field after the onset of a current of  $-2.0 \mu\text{A}/\text{m}^2$



CHAPTER V

ANISOTROPIC ION HEATING AND ANOMALOUS RESISTIVITY

IN THE AURORAL RETURN CURRENT REGION



## V.1 INTRODUCTION

The field-aligned currents can give rise to various instabilities. Electromagnetic waves, whose phase velocities tend to be of the order of Alfvén speed or larger, require very strong currents. Electrostatic waves, whose phase velocities are comparable with particle thermal speeds, only require relative drifts of the order of particle thermal speeds in both high and low density plasmas. Therefore, electrostatic waves are more likely to be unstable in the ionosphere. Drummond and Rosenbluth [1962] first showed that when the electron to ion temperature ratio is near unity, oblique electrostatic waves near the ion cyclotron frequency are unstable to smaller currents than is the parallel propagating ion acoustic wave. For the conditions existing in the topside ionosphere Kindel and Kennel [1971] compared the current-driven electrostatic ion acoustic [Fried and Gould, 1961] and ion cyclotron instabilities [Drummond and Rosenbluth, 1962] and concluded that for a wide range of electron-to-ion temperature ratios, the electrostatic ion cyclotron wave is unstable to smaller currents. Therefore, before the conditions for ion acoustic instability are reached, the ion cyclotron waves should already be unstable. The EIC waves were shown to be unstable to cold electron fluxes of the order of  $10^9 - 10^{10}$  el/cm<sup>2</sup>/sec by Kindel and Kennel [1971]. This implies that the magnitude of the critical current for exciting the EIC instability in the auroral ionosphere is  $1.6 \mu\text{A}/\text{m}^2$ . However, our calculations show that the EIC instability is

excited at a much lower current which is  $0.65 \mu\text{A}/\text{m}^2$ . The ions cool down as they flow in a divergent flux tube and are heated as a result of the onset of the instability. Kindel and Kennel [1971] have considered fixed electron temperature and a fixed ion temperature which is higher than our ion temperatures and did not consider the effects of the temperature anisotropy. The higher ion temperature actually increases the threshold for the instability by increasing the critical velocity and thus requiring higher currents, as we will discuss later in this Chapter.

Kindel and Kennel [1971] calculated a critical drift velocity for exciting electrostatic ion cyclotron waves in a hydrogen plasma for arbitrary electron ( $T_e$ ) to ion temperature ( $T_p$ ) ratio. Kai Fong Lee [1972] carried out similar calculations for EIC waves but considered the effects of temperature anisotropy. He found that the properties of the instability depend on the ratio of parallel electron temperature to perpendicular ion temperature ( $T_{e||}/T_{p\perp}$ ). This ratio can be viewed as the product of the ratio of parallel electron to parallel ion temperature ( $T_{e||}/T_{p||}$ ) and the ion temperature ratio ( $T_{p||}/T_{p\perp}$ ). The critical drift velocity is approximately inversely proportional and growth rate is approximately directly proportional to this ratio, but as this temperature ratio increases the dependence on ( $T_{e||}/T_{p\perp}$ ) becomes less sensitive.

In our model we have seen that drift velocity corresponding to a current of  $-0.65 \mu\text{A}/\text{m}^2$  is unstable to electrostatic ion cyclotron waves. Palmadesso et al. [1974] showed that in the absence of plateau formation EIC instability leads to rapid and substantial ion heating. The model assumed the plateau formation was completely inhibited. The instability is excited in the region where the drift velocity is initially greater than the critical velocity. The electrostatic ion cyclotron instability converts the kinetic energy of electron current flow into turbulent fluctuation energy, most of which resides with the ions and ultimately appears as ion thermal energy. The ion temperature and the critical drift ( $V_{\text{CH}}$ ) rise rapidly until  $V_{\text{CH}}$  is nearly equal to the drift velocity of electrons at each altitude, whereupon the instability is almost shut off i.e., the growth rate tends to zero. At this point the turbulence and heating rate are sharply reduced and an equilibrium is established. The residual turbulence pumps heat into the ions at just the rate at which thermal conductivity and other processes can pump it out of the turbulent region. The EIC instability can still be excited provided the correspondingly higher thresholds of the electron drift velocity are exceeded. This calculation made use of idealized semi-empirical profiles of ionospheric parameters, and did not attempt to include plasma transport effects in a self consistent way. Ionson et al. [1976] performed a similar calculation of heating in which they have considered ion temperature anisotropy. Their results show that

the ions are heated primarily perpendicular to the magnetic field. Again, this study emphasized the physics of the instabilities and plasma transport process were not explicitly modelled. Dakin et al. [1976] have investigated ion heating due to electrostatic ion cyclotron turbulence in a Q-machine barium plasma and arrived at the same conclusion, namely, the ions are heated primarily in the direction perpendicular to the background magnetic field.

The EIC waves can transfer electron momentum to ions, thereby giving rise to anomalous resistivity. Anomalous resistivity allows for energy to be taken out of the ordered particle motion such as drifts and put into fluctuating fields and it allows the momentum to be exchanged between the species [Liewer and Krall, 1973]. Resistivity can be classical, where coulomb collisions transfer electron momentum to ions. In a unmagnetized collisionless plasma, interaction with ion waves leads to transfer of electron momentum to ions. In a magnetized collisionless plasma the electron first adiabatic invariant tends to be conserved in low frequency, large (compared to electron larmour radius) scale size ion wave structures. Continuous transfer of electron momentum to ion waves is difficult. When the electron motion is adiabatic, motion is essentially one-dimensional. Parallel velocity space diffusion is required for resistivity. But, strong diffusion rapidly destroys those features of the distribution function which are required to



produce it (positive slopes, multiple streams etc.). Therefore, parallel diffusion in velocity space is invariably a transient phenomenon. Anomalous resistivity produced in the conventional way by the electrostatic ion cyclotron instability, ion acoustic and Buneman instabilities is short lived for these reasons when the electrons are adiabatic.

A new resistivity model based on nonlinear theory was suggested by Palmadesso [1979]. Haber et al. [1978] and Rowland et al. [1981 b] have demonstrated the new resistivity model through their particle simulations. They have shown that under the conditions prevailing in the aurora, the conservation of the first adiabatic invariance is violated for electrons above a certain threshold velocity by the action of a high frequency electron instability which arises when electrons flow in the presence of large amplitude ion waves. The existence of a threshold velocity implies a critical drift velocity,  $V_{CR}$ , which must be exceeded before resistivity is significant. This causes strong dc resistivity and generates electron distributions in good agreement with observations. Large amplitude ion cyclotron waves have been observed by S3-3 [Kintner et al., 1978]. In the presence of an electric field parallel to the ambient strong magnetic field these large amplitude ion waves prevent the acceleration of the bulk of the plasma electrons leading to the formation of a runaway tail. The major portion of the electron distribution function is trapped under these conditions. The

electron distribution function is composed of a central part carrying little or no current and a runaway tail due to untrapped electrons which carry the current. This distribution is unstable [Haber et al., 1978] and gives rise to the high frequency instability ("anomalous Doppler resonance instability") mentioned above. Rowland et al. [1981 a] have shown that by including the quasineutrality effect, most of the electrons can be trapped for  $\delta n/n > 1/4$  independent of the detailed shape or spacing of the cavities of ion waves. The untrapped electron momentum is transferred to the electron waves which in turn transfer their momentum to trapped electrons and finally to the ions. The distribution function obtained by Rowland et al. [1981 b] from their simulation of these parameters was compared to that measured by Kaufmann et al. [1978] and was found to be similar. Rowland and Palmadesso [1983] have shown through a series of 2(1/2)-D particle simulations that the acceleration of runaways is limited not only by an interaction via the anomalous Doppler resonance with electron waves at  $\omega_k = \omega_e \cos \theta$ , but also with the low frequency ion waves. Both interactions act to pitch angle scatter the high velocity electrons and lead to the appearance of anomalous resistivity. Thus, large amplitude ion waves such as the ion cyclotron waves observed on the auroral field lines act to prevent the acceleration of the bulk of the electrons and to limit the acceleration of the high velocity runaways.

Mitchell and Palmadesso [1984] have studied some effects

of anomalous resistivity in the region of upward currents, using a 13 moment model. They have shown how  $O^+$  ions can be accelerated upwards along the auroral field lines due to resistive momentum transfer, if the resistivity is produced as a result of an  $H^+$  ion wave. In this case the  $H^+$  ions experience the resistive electric field as well as an oppositely directed resistive drag force associated with the ion wave, while the  $O^+$  ions react only to the electric field. Ion heating associated with the current driven EIC instability was not modelled in these calculations. The effects of anomalous resistivity are expected to be different in the return current regions. The direction of the resistive electric field is reversed in the return current region, so this effect would tend to exert a downward force on the ions. Also, ion heating due to EIC instabilities is likely to have a substantial effect on the generation of thermal anisotropies, which in turn modify the stability properties of the auroral plasma flow. As noted above, these processes have not been previously studied in the context of the return current regions.

We will add both EIC heating and anomalous resistivity to our simulation. EIC waves will be excited for  $V_D > V_{CH}$  and these waves will heat the ions transversely. Then for  $V_D > V_{CR}$  (provided  $V_{CR} > V_{CH}$ ) anomalous resistivity will be generated. The thermal energy generated by the resistivity is primarily given to the electrons. The modifications to the transport

equations in order to maintain momentum and energy conservation with these processes included are discussed in Appendix (3.V). We shall compare all our results with our previous runs of the same currents to show the effects of electrostatic ion cyclotron instability and anomalous resistivity in the auroral return current region. The results will also be compared with experimental observations.

## V.2 THE MODEL

In order to simulate ion heating and resistivity it is necessary to add an anomalous friction to this model. The anomalous collision frequency for the EIC instability is assumed to have a simple form :

$$\nu_{epH}^* = 0.01 \, \Omega_p \left( \frac{n_p}{n_e} \right) \left( \frac{V_D}{V_{cH}} - 1 \right)^2 \quad V_D \geq V_{cH}$$

$$\nu_{epH}^* = 0 \quad V_D < V_{cH}$$

(V.1)

where,  $V_D$  is the relative drift velocity between the electrons and the ions,

$\Omega_p$  is the hydrogen ion cyclotron frequency.

The numerical coefficient in the expression for  $v_{epH}^*$  in this Chapter is a free parameter which is chosen for numerical stability and to express qualitatively the effects of the anomalous collision processes.

The critical velocity for exciting the EIC instability is given by [Lee, 1972]:

$$\frac{V_{cH}}{V_{ther||p}} = \frac{1 + \Delta(\mu_p^*)}{\Delta(\mu_p^*)} \left( \ln [ 2C\Gamma_1(\mu_p^*) ] \right)^{\frac{1}{2}}$$

(V.2)

where,

$$C = \left( \frac{T_{p||}}{T_{p\perp}} \right) \left( \frac{T_{e||}}{T_{p||}} \right)^{3/2} \left( \frac{m_p}{m_e} \right)^{1/2}$$

$$\Delta = \frac{\Gamma_1(\mu_p)}{1 - G + \left(\frac{T_{pl}}{T_{pll}}\right) \left(\frac{T_{pll}}{T_{ell}}\right)}$$

$$G = \Gamma_1(\mu_p) + \frac{1 - \Gamma_0(\mu_p)}{\mu_p}$$

$$\mu_p = \frac{k_{\perp}^2 v_{th\perp p}^2}{2 \Omega_p^2}$$

$$\Gamma_n(\mu_p) = e^{-\mu_p} I_n(\mu_p)$$

$I_n$  is the modified Bessel function of order  $n$ .

$\mu_p^*$  is the value of  $\mu_i$  which minimizes  $(1 + \Delta)/\Delta$ , namely

$\mu_p^* = 1$ , for this value of  $\mu_p^*$ ,  $(1 - G) = 0.258$ .

$\Gamma_1(1) = 0.21$ .

The perpendicular ion heating rate due to the EIC instability is given in terms of the effective collision frequency by

$$k \frac{\delta T_{p\perp}}{\delta t} = \nu_{peH}^* m_p v_d^2 \quad (V.3)$$

where,

$$n_e m_e \nu_{epH}^* = n_p m_p \nu_{peH}^*$$

The anomalous collision frequency for the resistivity is given by [Mitchell and Palmadesso, 1984] :

$$\nu_{epR}^* = 0.01 \Omega_p \left( \frac{n_p}{n_e} \right) \left( \frac{v_D}{v_{cR}} - 1 \right)^2 \quad v_D \geq v_{cR}$$

$$\nu_{epR}^* = 0 \quad v_D < v_{cR}$$

(V.4)

The critical velocity for anomalous resistivity is assumed to scale as indicated below (based on the work of Rowland et al. 1983):

$$v_{cR} = \frac{1}{4} \left( \frac{\Omega_e}{\omega_{pe}} \right) v_{ther||e}$$

(V.5)

where,  $\omega_{pe}$  is the plasma frequency

$\Omega_e$  is the electron cyclotron frequency

$v_{ther||e}$  is the electron thermal velocity

$$\Omega_e = \frac{eB}{m_e C}$$

The flux is conserved and therefore B is calculated from the total area A of the flux tube, such that AB = constant.

The electron heating rate due to anomalous resistivity is also expressed in terms of an effective collision frequency given in equation (V.4).



$$k \frac{\delta T_e}{\delta t} = v_{epR}^* m_e v_d^2$$

(V.6)

### V.3 SIMULATIONS WITH ION HEATING AND RESISTIVITY

In this section we carry on simulations to study the effects of the ion heating and anomalous resistivity on our previously studied cases of currents discussed in Chapter IV. We have also varied the co-efficients of the anomalous collision frequencies (equations V.1 and V.4) to study their effects on the ion and electron heating rates. In all the figures the changes of the variables due to the EIC instability and the anomalous resistivity are shown in comparison with their previous values with current only. We shall use the expression 'current only' frequently in this chapter. By 'current only' we mean the plasma flow with effects due to currents and where effects of the EIC instability and the resistivity were not included in the model. The solid lines in the figures represent the variable for such current only cases and the dashed lines represent the effects of the changes due to the ion heating and the anomalous resistivity on the variable.

The ratios of relative drift velocity between the electrons and the ions and the critical velocities for exciting the EIC instability are calculated for all the currents and are shown in figure (V.1.a). The theoretical calculations of K. F. Lee [1972] show that the critical velocity for exciting the EIC instability decreases as the ratio of perpendicular ion temperature to parallel electron temperature ( $T_{p\perp}/T_{e\parallel}$ ) decreases. Our calculations show that with increase in altitude the relative drift velocity increases. Also, the  $H^+$  ion thermal velocity decreases (except where the  $H^+$  ion parallel temperature increases) and the ratio of  $T_{p\perp}/T_{e\parallel}$  decreases with altitude, thereby decreasing the critical velocity for the the EIC instability (equation V.2). If the electron temperature is held constant, the critical drift would increase with the increase in ion temperature until  $V_{cH}$  almost equals  $V_D$ , whereby the instability is almost shut off. This case was discussed by Palmadesso et al. [1974]. They have also shown that by increasing the electron temperature (which remained constant throughout the entire length in their calculations) the critical ion temperature can be increased. It is interesting to note that by increasing the electron temperature or the anomalous collision frequency the critical velocity for exciting the EIC instability can be modified and the range of the EIC instability can be extended.

The ratios of  $V_D/V_{cR}$  for all the currents are shown in

figure (V.1.b). The critical velocity for the resistivity decreases with altitude. With increase in altitude, the electron thermal velocity increases, plasma frequency decreases with decreasing density and the electron cyclotron frequency decreases faster than the plasma frequency with decreasing magnetic field, thereby decreasing the critical velocity for the resistivity as shown in equation (V.4).

For a current of  $-0.65 \mu\text{A}/\text{m}^2$  the electrostatic ion cyclotron instability turns on at an altitude of  $1.16 R_e$ , where the relative drift velocity exceeds the critical drift necessary to excite the EIC instability given in equation (V.2). The instability heats the hydrogen ions transversely, as shown in figure (V.2.c). The  $\text{H}^+$  ion heating rate shown in figure (V.9.a) is seen to be relatively constant after an altitude of  $3 R_e$ . The increase in  $\text{H}^+$  ion temperature due to the heating tends to increase the hydrogen ion scale height. The ambipolar electric field, which is inversely related to the scale height of the  $\text{H}^+$  ions, decreases as a result of this increase in scale height, compared to the previous runs with current only. The decrease in ambipolar electric field decreases the hydrogen ion velocity at the lower end of the tube (figure V.2.b). The  $\text{H}^+$  ion density increases for flux conservation. This increases the electron density to maintain charge neutrality. The ratio of the electron density with this instability relative to the current only case is shown in figure (V.2.a). The total current  $I$  remains

constant, which reduces the electron velocity as is evident from equation (I.9) and shown in figure (V.2.b). The electron temperatures decrease at this altitude. The hydrogen ion parallel temperature increases compared to the case of current only where the  $H^+$  velocity decreases. The  $H^+$  ion parallel and perpendicular heat flows are shown in figure (V.2.e).

The anomalous resistivity turns on at an altitude of  $4.4 R_e$ , where the relative drift velocity exceeds the critical drift velocity to excite anomalous resistivity given in equation (V.5). The electrons are heated rapidly because of the resistivity both in the parallel and perpendicular directions. The electron temperature profiles are shown in the figure (V.2.d). The resistivity adds heat isotropically and is strongest at the upper end of the tube. Transport effects on the downward flowing heat then make  $T_{\perp} > T_{\parallel}$ , as explained in Chapter IV. The electric field is due to the ambipolar field,  $E_A$ , and the resistive electric field  $E_R$  (IR drop). The ion heating tends to decrease the ambipolar electric field  $E_A = -\Delta\phi_A / \Delta L$  by increasing the scale height  $\Delta L$ , but the increase in electron temperature tends to increase the ambipolar field by increasing the ambipolar potential  $\Delta\phi_A$ . The ambipolar and resistive electric fields act in opposite directions and therefore compete. At high altitudes the electric field is mainly resistive. The effects of electron thermal energy flow at low altitudes due to electron heating at high altitudes tends to increase the ambipolar electric field at

low altitudes by increasing  $\Delta\phi_A$  but the ion heating effect dominates and the field decreases at low altitude as a result. However, the increase in the ion scale height  $\Delta L$  and electron temperature  $T_e$  means that the ambipolar field becomes stronger at high altitudes. At higher altitudes, the ambipolar electric field and the mirror forces tend to accelerate the  $H^+$  ions, whereas the resistive electric field tends to decelerate the ions. The resistive electric field is balanced by the anomalous friction terms and as a result the  $H^+$  ion velocities increase over their previous values with current only. The hydrogen ion parallel temperature decreases corresponding to this increase in the  $H^+$  ion velocity. The electron velocity also increases to maintain the total current constant.

The collision frequency defined in equation (V.1) is now reduced by half and the above calculations were repeated. It has been shown that the decrease in this frequency decreases the heating rate in the perpendicular ion temperature and the parallel and perpendicular electron temperatures as expected. The final effects and the relative importance of the terms remain the same. Higher electron temperature at the upper end of the field line would allow for higher heat flows in the flux tube. The density ratio between the two frequency runs is shown in figure (V.3.a), species velocity profiles are shown in figure (V.3.b), the hydrogen ion temperature parallel and perpendicular to the field line compared to previous runs with higher frequency

are shown in figure (V.3.c), similar plots of the  $H^+$  ion heat flows in (V.3.e), the electron temperatures in figure (V.3.d) and the electron heat flows in (V.3.f). Dashed lines are not used in the figures since the curves are very close to each other. For the above reasons we would carry on our next set of calculations with this collision frequency.

The current is now increased to  $-0.8 \mu A/m^2$ . The remarkable result seen with this current is that the electron temperature anisotropy changes at the lower end of the flux tube, i.e., from  $T_{e\perp} > T_{e\parallel}$  to  $T_{e\parallel} > T_{e\perp}$ . The change in the anisotropy has been explained in Chapter IV and is shown in figure (V.4). With the increase of current the EIC instability and the resistivity turn on at lower altitude than the previous case. The EIC instability and the perpendicular ion heating turn on at  $0.98 R_e$ . The ion transverse heating rate is higher than that compared to the lower current case. This is due to the increase in drift velocity (occurs in the expression for the heating rate, given in equation (V.3)) with the increase in current. The resistivity is turned on at  $3.5 R_e$ . The strong transverse heating is observed as before. The temperature anisotropy observed is not very high since the temperature at the upper end is held constant at  $6000^\circ K$  and the lower end at  $1000^\circ K$ . The effects described for current  $-0.65 \mu A/m^2$  and the relative importance of the terms remain the same.

The current is now increased to  $-0.9 \mu\text{A}/\text{m}^2$ . The EIC instability turns on at .85 Re and the anomalous resistivity at 3 Re. The effects explained above enhance in magnitude due to the increase in current. The heating rates with currents and altitude are shown in figures (V.10) and (V.9). The electron temperatures are shown in figure (V.5).

The EIC instability turns on at .8 Re for a current of  $-1.0 \mu\text{A}/\text{m}^2$ . The sharp increase in  $\text{H}^+$  ion perpendicular temperature is shown in figure (V.6.a). The resistivity turns on at 2.6 Re. The electron temperature anisotropy for current only case was  $T_{e\parallel} > T_{e\perp}$ . With the onset of resistivity strong transverse electron heating is seen, which reverses the direction of anisotropy. This is shown in figure (V.6.b).

The next current studied was  $-1.1 \mu\text{A}/\text{m}^2$ . The effects observed are similar to  $-1.0 \mu\text{A}/\text{m}^2$  with enhanced magnitude and therefore, will not be repeated.

The current was then increased to  $-1.5 \mu\text{A}/\text{m}^2$ . The multiplication factor of the anomalous collision frequency is changed to 0.001 in order to avoid difficulties in obtaining converged solutions. The EIC instability turns on at .4 Re and the anomalous resistivity at 1.6 Re. The electron density ratio for this case is shown in figure (V.7.a) and the velocity profiles are shown in figure (V.7.b). The  $\text{H}^+$  ion perpendicular

temperature (figure V.7.c) has now increased to  $6100^{\circ}\text{K}$  at the upper boundary. The  $\text{H}^+$  ion heat flows are shown in figure (V.7.e). At the lower boundary the hydrogen ion perpendicular heat flows from the ionosphere to the magnetosphere and then encounters a heat source around  $4 R_e$ , due to the anomalous heating effects. The heat flow has a positive divergence around  $4 R_e$  and a negative divergence located around  $1.5 R_e$  corresponding to the minimum of the  $\text{H}^+$  ion perpendicular temperature curve. Perpendicular ion thermal energy is generated by the EIC instability at high altitudes and conducted downwards and upwards. The downflowing heat is absorbed by cold low altitude ions and convected (nkTV) upwards with the flow. The increase in the perpendicular thermal energy tends to convert this energy to parallel thermal energy and this process tends to increase the  $\text{H}^+$  ion parallel temperature. However, the convective flow velocity increases over the current only case and this tends to decrease the parallel temperature. The latter process dominates and the  $\text{H}^+$  ion parallel temperature decreases at higher altitudes. The electron temperature profiles are shown in figure (V.7.d). The electron temperature anisotropy shows  $T_{\perp} > T_{\parallel}$ . The reasons for the anisotropy reversal are explained in Chapter IV. The electron heat flows are shown in figure (V.7.f). The introduction of effective anomalous collisions tend to decrease the electron heat flows. The anomalous collision frequency is then increased to 0.002 and, as expected, the  $\text{H}^+$  ion perpendicular temperature and the electron temperatures increase



further.

The ratio of the drift velocity over  $H^+$  ion and electron thermal velocities are shown in figures (V.8.a) and (V.8.b). With the increase in current, the relative drift velocity increases and the EIC instability and the hydrogen ion transverse heating turn on at lower altitudes (figure V.1.a and V.9.a). Also, the  $H^+$  ion perpendicular temperature increases with current at all altitudes. The density increases at the lower end of the flux tube but the density ratio for all EIC cases to the corresponding current only cases remained almost the same. The anomalous resistivity turned on at lower altitudes with increase in current (figure V.1.b). According to our preimposed conditions the resistivity turns on only after the EIC instability turns on. The electron transverse and longitudinal heating rates increase with currents and are shown in figures (V.9.b) and (V.9.c). Three kinds of electron temperature profiles were observed for current only cases :

- (1) For lower currents up to  $-0.65 \mu A/m^2$  and  $T_{e\perp} > T_{e\parallel}$ , the resistivity heated the electrons but did not change the direction of anisotropy.
- (2) For currents up to  $-0.9 \mu A/m^2$ , where the anisotropy reversed direction at the middle of the flux tube, the heating caused the reversal at lower altitudes.
- (3) For currents of  $-1.0 \mu A/m^2$  and above where  $T_{e\parallel} > T_{e\perp}$ , the resistivity changed the direction of anisotropy.

The heating rates for all the currents were then plotted for different altitudes, from 3 Re to 7 Re. The  $H^+$  ion heating rates were observed to reach saturation after a certain altitude for each current, shown in figure (V.9.a). Figure (V.10.a) shows that the heating rates do not change much with altitude except to a small degree for higher currents. The electron perpendicular and parallel heating rates increase with altitude and figures (V.10.b) and (V.10.c) exhibit heating rate for different altitudes. The potential drop along the tube for all currents is plotted in figure (V.11.a) and that for a current of  $-1.5 \mu A/m^2$  is plotted in figure (V.11.b). With the increase in current and altitude, the contribution of resistive terms to the electric field increases. The electric field is mainly ambipolar at lower altitudes and resistive at higher altitudes. The electric field changes sign due to this change and this changes the sign of the potential drop along the field line.

If the potential drop along the field line is calculated for a specific current, then from Ohm's law we can calculate the resistivity of the tube. Based on such calculation, a plot of resistance versus current is presented in figure (V.12). The resistance changes approximately linearly with current. The negative sign in resistance is due to the change in sign of the potential drop, which changes from negative to positive. The negative resistance at the lower currents is due to thermoelectric effects associated with ambipolar electric field. The anomalous resistance is positive and increases with the current.

#### V.4 DISCUSSIONS

We have investigated the effects of the EIC instability and anomalous resistivity in the auroral return current region. The hydrogen ions are heated transversely due to the EIC waves and the anomalous resistivity heats the electrons. It is interesting to note that by increasing the electron temperature or the anomalous collision frequency the critical velocity for exciting the EIC instability can be modified and the range of the EIC instability can be extended. Our calculations show that the critical current for exciting the EIC instability in the auroral ionosphere is lower than that calculated by Kindel and Kennel [1971]. It should be noted that the heating and resistivity discussed here may be quite large in the real situation but they are restricted to smaller values in this simulation by the need to maintain numerical stability and stay within the limits of approximations implicit in the fluid equations.

Burch et al. [1983] concluded that the cold ionospheric electrons which carry the downward region-1 Birkeland currents on the morning side are accelerated upwards by potential drops of a few tens of eV at altitudes above 1 Re. Measurements were made by the High Altitude Plasma Instrument (HAPI) on DE-1 satellite. The observations were made primarily near the equatorward edge of the morningside polar cusp and sporadically throughout the cusp region. Upward electron beams of energies from 20 eV to 200 eV

are observed. The resistive electric field is in the right direction to accelerate the electrons upwards. As noted earlier the strength of the anomalous resistivity used in the model is limited by numerical stability considerations but the actual values may be larger. The resistive electric field is balanced by anomalous friction for most electrons but a few may run away and be accelerated by the field. This may explain the observations of Burch et al.

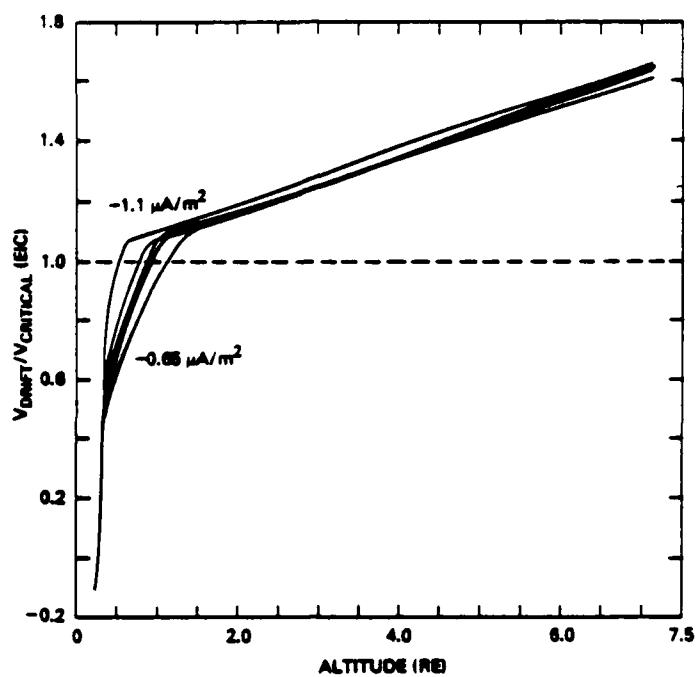


Fig. V.1.a — Ratio of relative drift velocity over critical velocity for exciting EIC instability for all currents

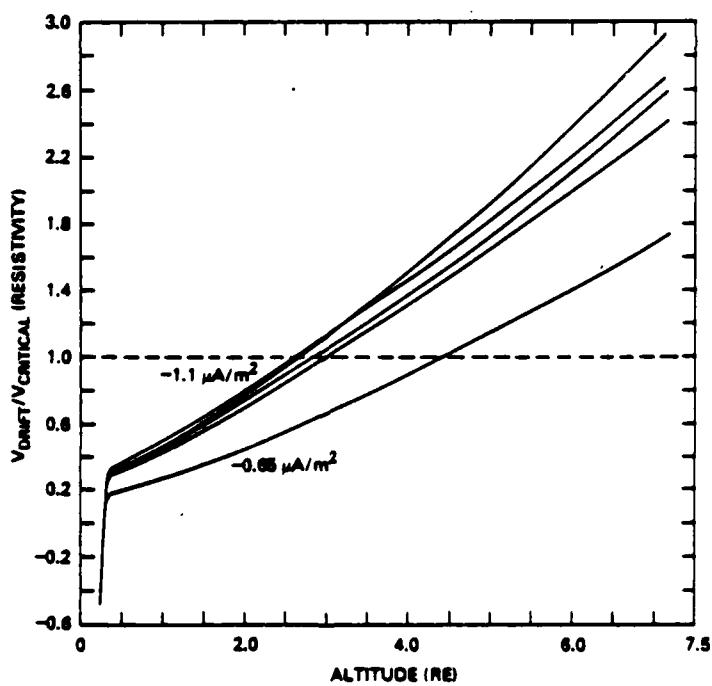


Fig. V.1.b — Ratio of relative drift velocity over critical velocity for exciting anomalous resistivity for all currents

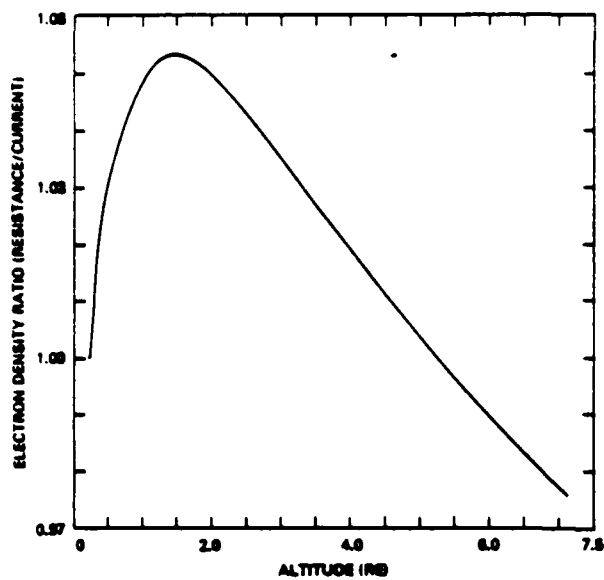


Fig. V.2.a — Electron density ratio for a current of  $-0.65 \mu\text{A}/\text{m}^2$

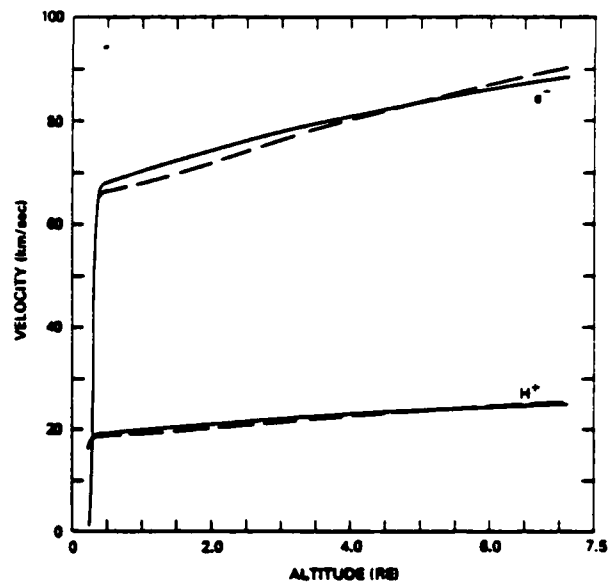


Fig. V.2.b — Species velocity profiles for a current of  $-0.65 \mu\text{A}/\text{m}^2$

Currents with anomalous transport effects included (dashed curves)  
Currents without anomalous transport effects (solid curves)

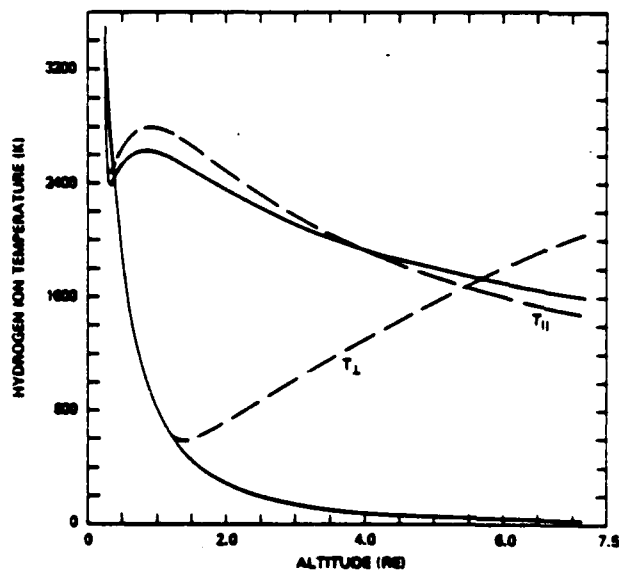


Fig. V.2.c —  $\text{H}^+$  ion temperature parallel and perpendicular to the geomagnetic field for a current of  $-0.65 \mu\text{A}/\text{m}^2$

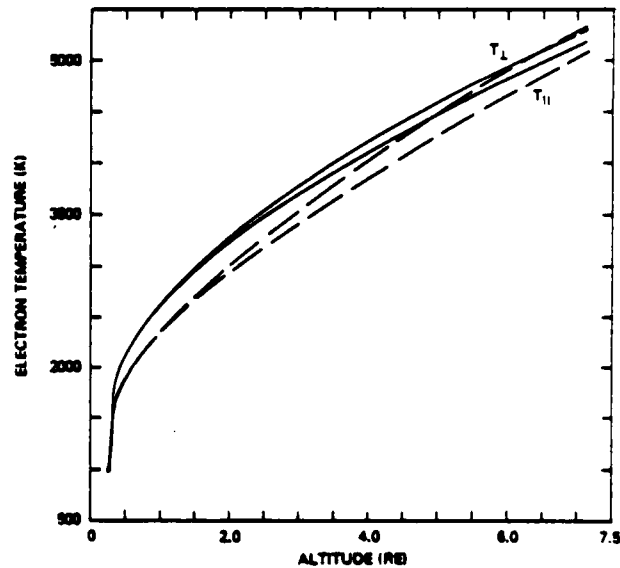


Fig. V.2.d — Electron temperature parallel and perpendicular to the geomagnetic field for a current of  $-0.65 \mu\text{A}/\text{m}^2$

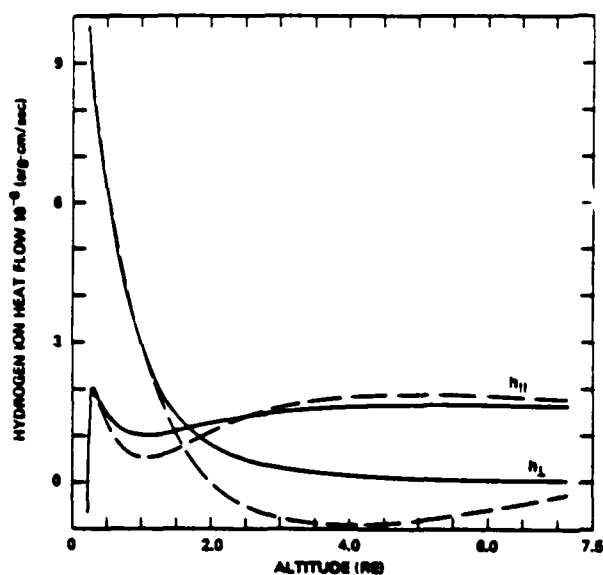


Fig. V.2.e —  $H^+$  ion heat flow parallel and perpendicular to the geomagnetic field for a current of  $-0.65 \mu A/m^2$

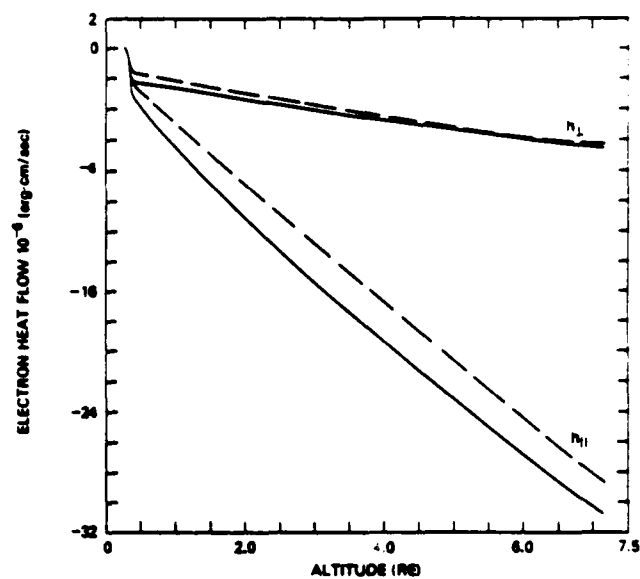


Fig. V.2.f — Electron heat flow parallel and perpendicular to the geomagnetic field for a current of  $-0.65 \mu A/m^2$

Current: with anomalous transport effects included (dashed curves)  
Currents without anomalous transport effects (solid curves)

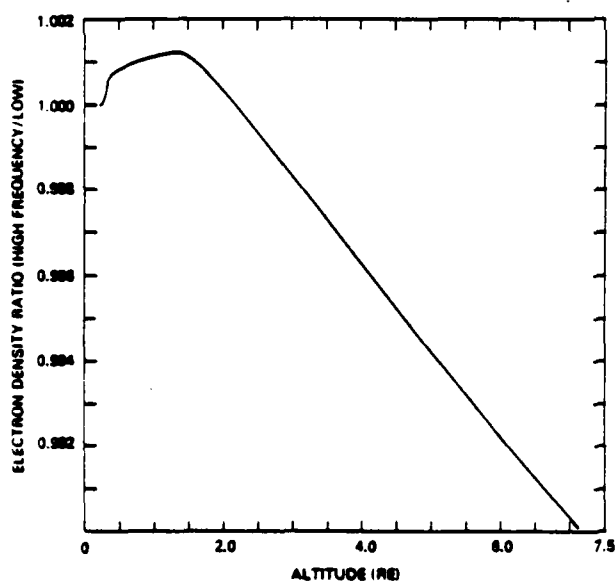


Fig. V.3.a — Electron density ratio (effects of EIC and resistivity for higher frequency/lower frequency) for a current of  $-0.65 \mu A/m^2$

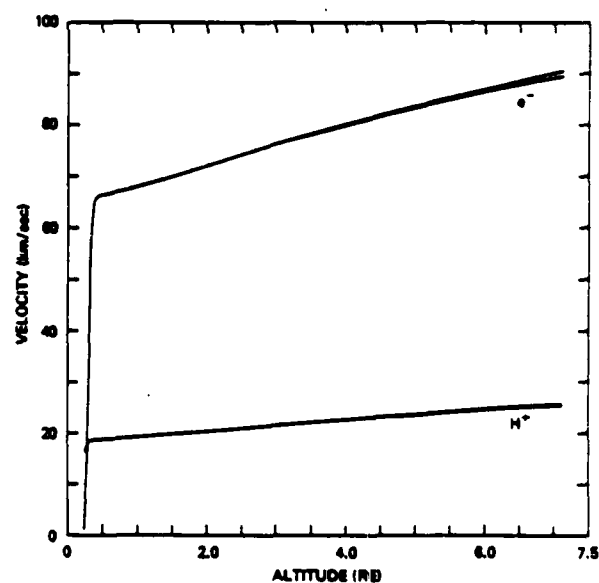


Fig. V.3.b — Species velocity profiles for different collision frequencies for a current of  $-0.65 \mu A/m^2$

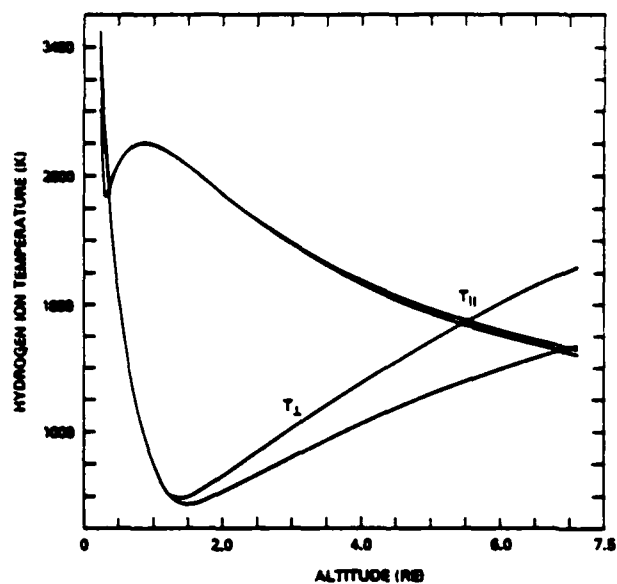


Fig. V.3.c —  $H^+$  ion temperatures for different collision frequencies for a current of  $-0.65 \mu A/m^2$

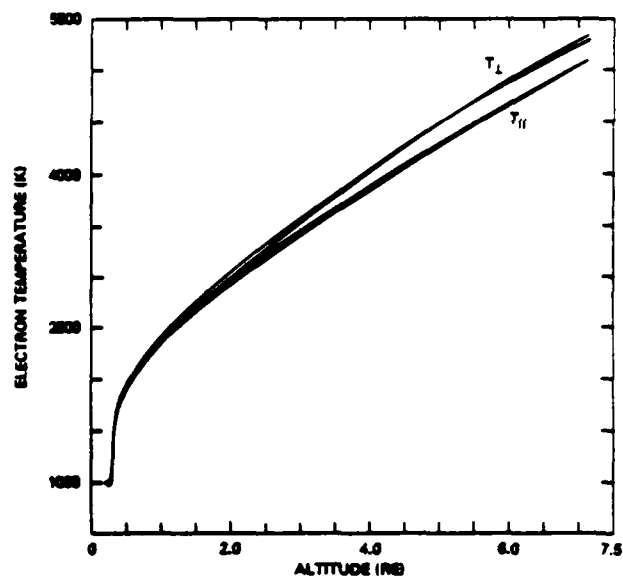


Fig. V.3.d — Electron temperatures for different collision frequencies for a current of  $-0.65 \mu A/m^2$

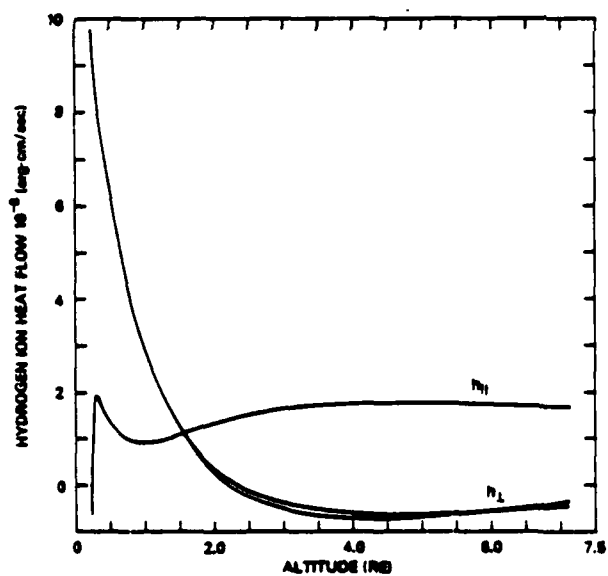


Fig. V.3.e —  $H^+$  ion heat flows for different collision frequencies for a current of  $-0.65 \mu A/m^2$

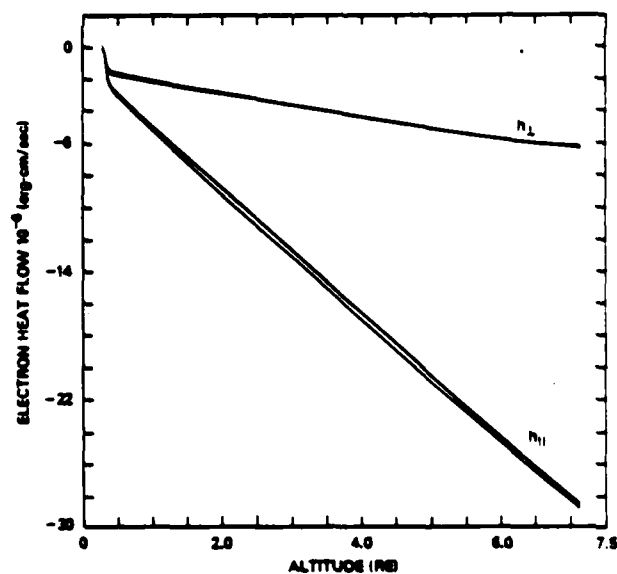


Fig. V.3.f — Electron heat flows for different collision frequencies for a current of  $-0.65 \mu A/m^2$



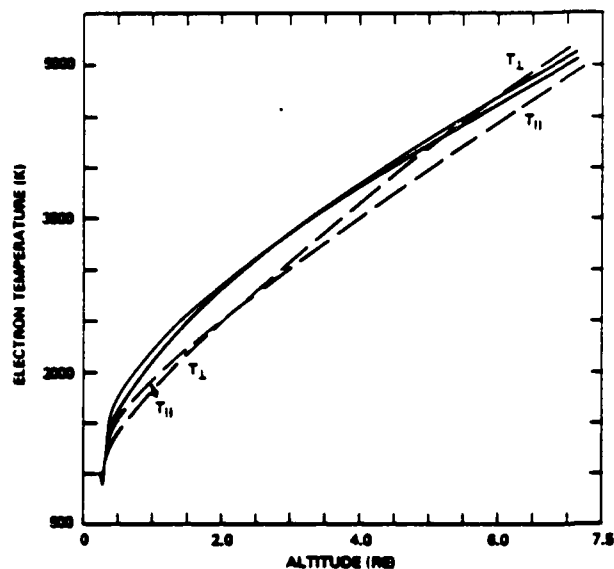


Fig. V.4 — Electron temperatures parallel and perpendicular to the geomagnetic field for a current of  $-0.8 \mu\text{A}/\text{m}^2$

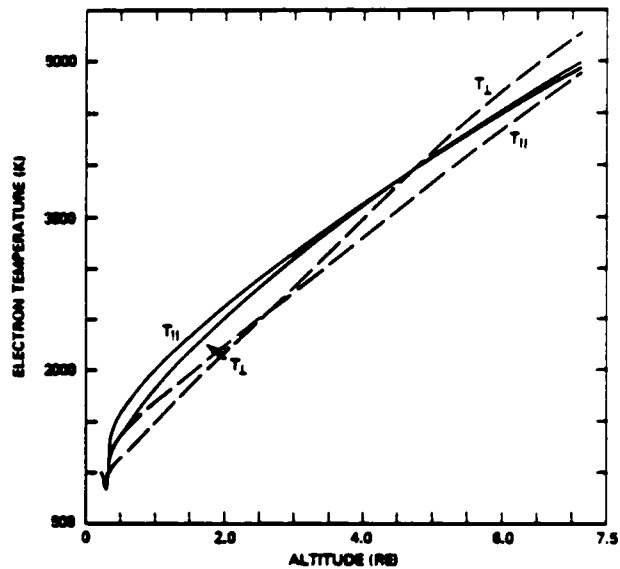


Fig. V.5 — Electron temperatures parallel and perpendicular to the geomagnetic field for a current of  $-0.9 \mu\text{A}/\text{m}^2$

Currents with anomalous transport effects included (dashed curves)  
Currents without anomalous transport effects (solid curves)

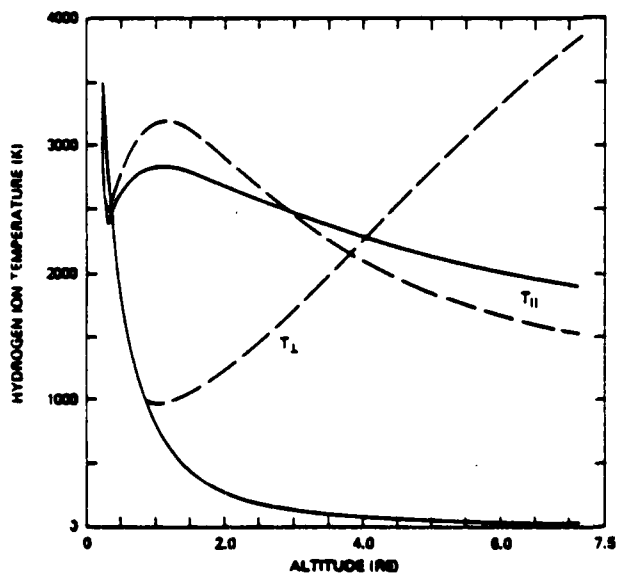


Fig. V.6.a —  $\text{H}^+$  ion temperatures parallel and perpendicular to the geomagnetic field for a current of  $-1.0 \mu\text{A}/\text{m}^2$

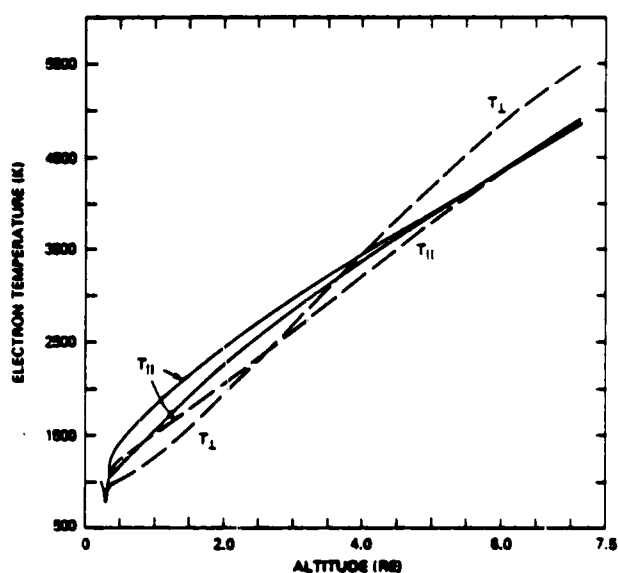


Fig. V.6.b — Electron temperatures parallel and perpendicular to the geomagnetic field for a current of  $-1.0 \mu\text{A}/\text{m}^2$

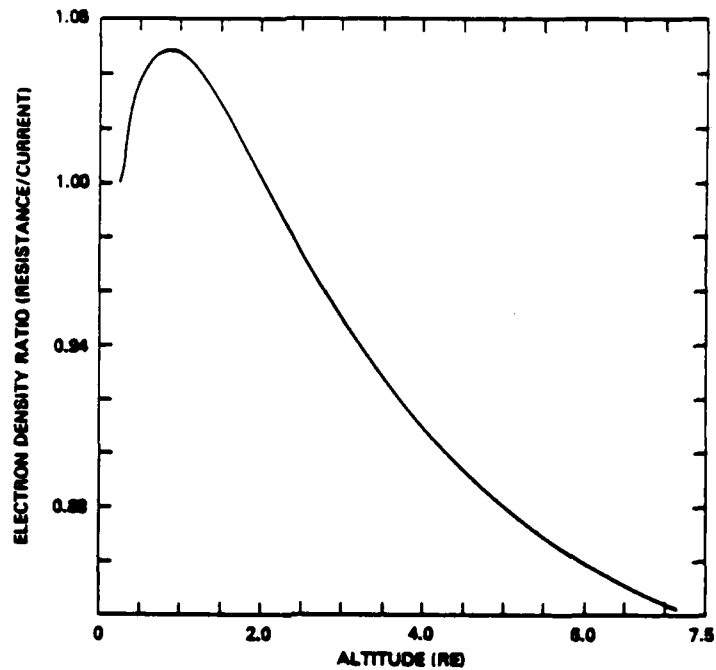


Fig. V.7.a — Electron density ratio for a current of  $-1.5 \mu\text{A}/\text{m}^2$ .  
Dashed curves: Currents with anomalous transport effects included.  
Solid curves: Currents without anomalous transport effects.

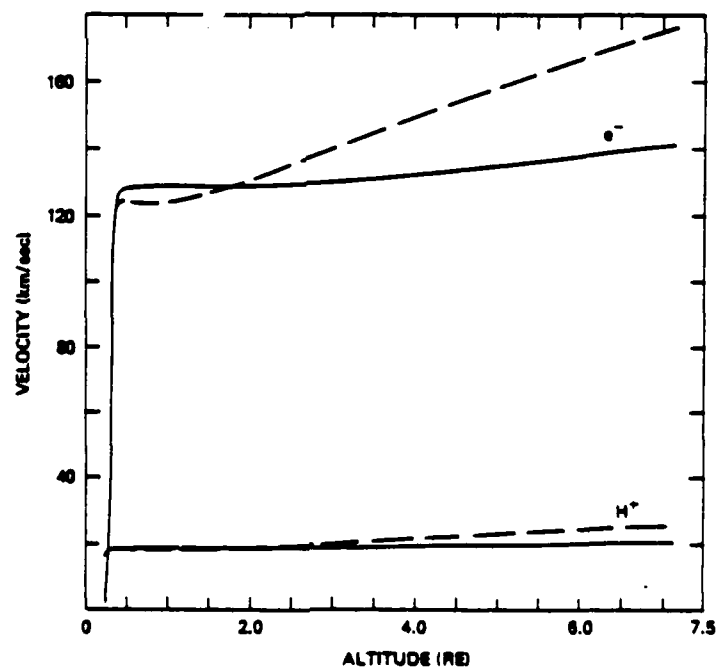


Fig. V.7.b — Species velocity profiles for a current of  $-1.5 \mu\text{A}/\text{m}^2$

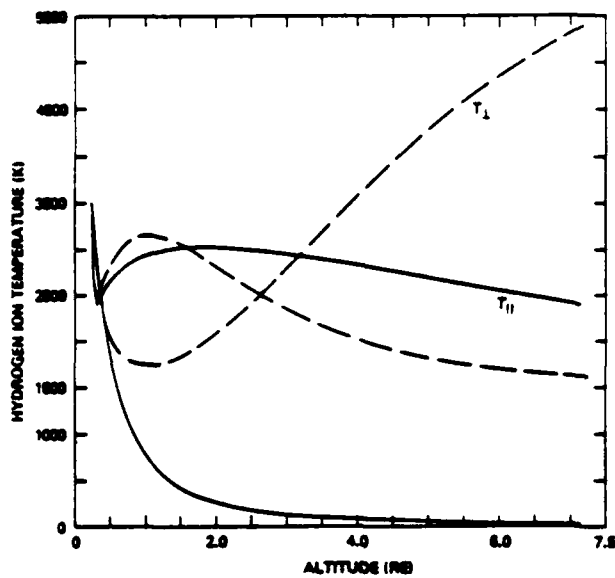


Fig. V.7.c —  $H^+$  ion temperature parallel and perpendicular to the geomagnetic field for a current of  $-1.5 \mu A/m^2$

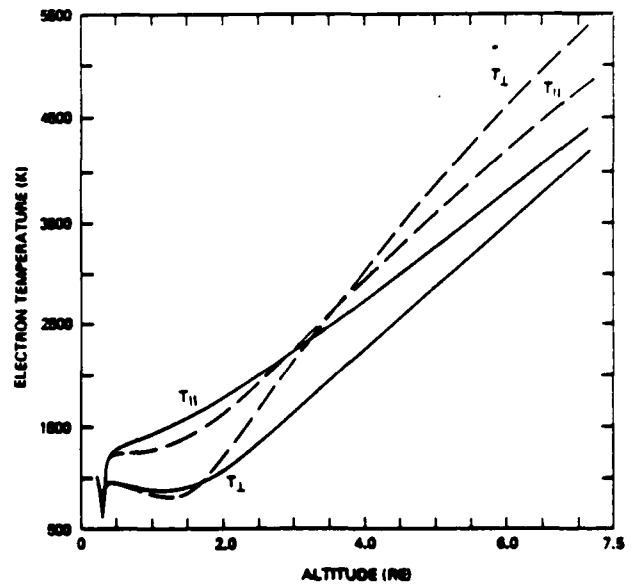


Fig. V.7.d — Electron temperature parallel and perpendicular to the geomagnetic field for a current of  $-1.5 \mu A/m^2$

Currents with anomalous transport effects included (dashed curves)  
Currents without anomalous transport effects (solid curves)

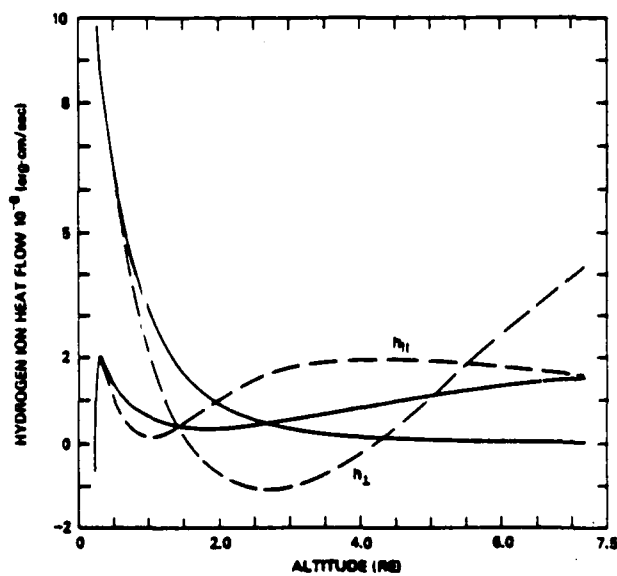


Fig. V.7.e —  $H^+$  ion heat flow parallel and perpendicular to the geomagnetic field for a current of  $-1.5 \mu A/m^2$

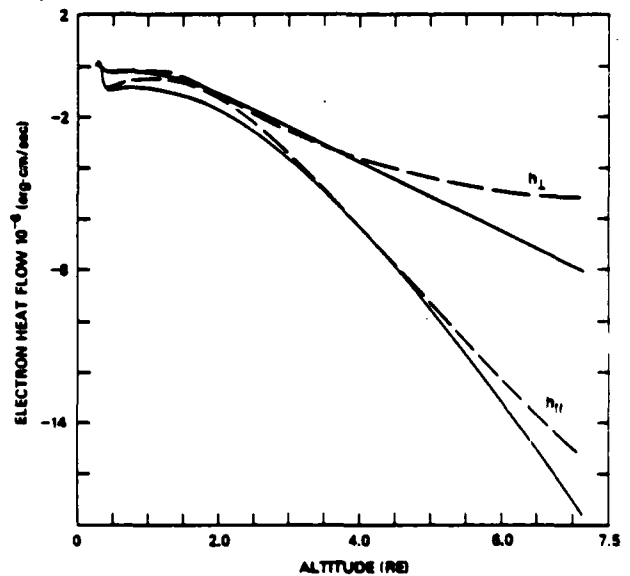


Fig. V.7.f — Electron heat flow parallel and perpendicular to the geomagnetic field for a current of  $-1.5 \mu A/m^2$

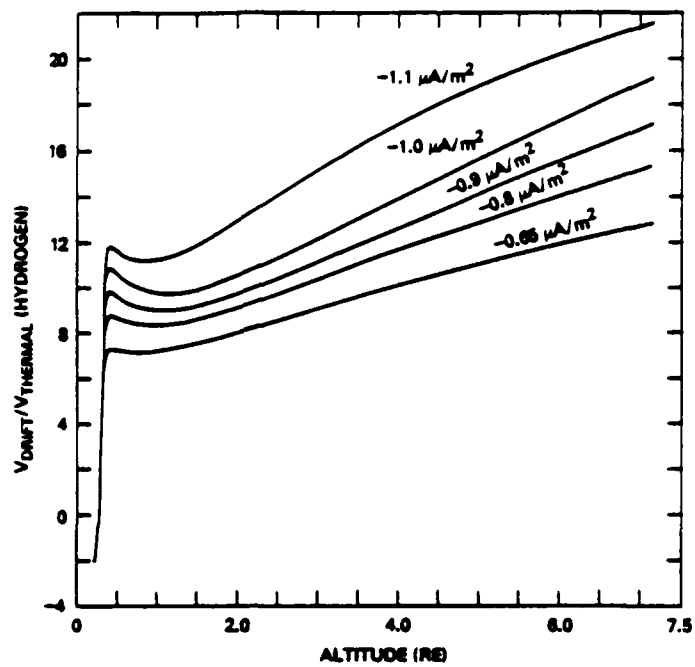


Fig. V.8.a — Ratio of relative drift velocity over thermal velocity of hydrogen ions for all currents

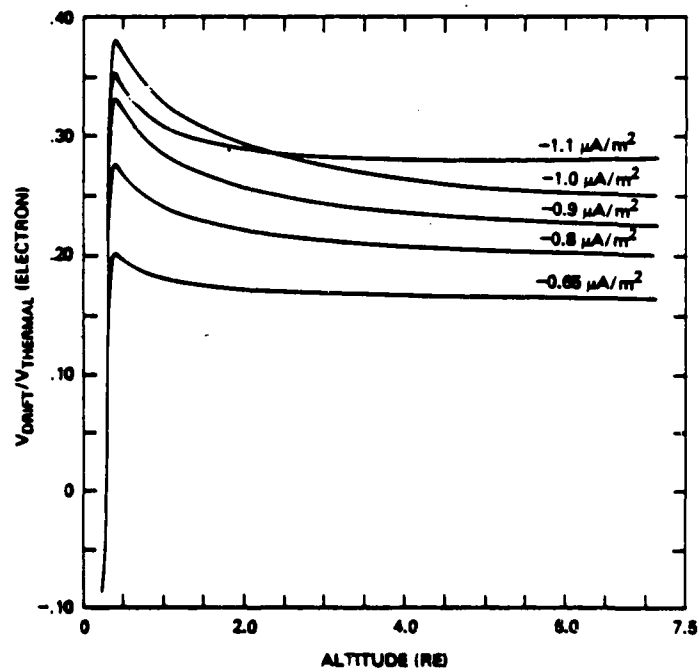


Fig. V.8.b — Ratio of relative drift velocity over thermal velocity of electrons for all currents

AD-A171 688

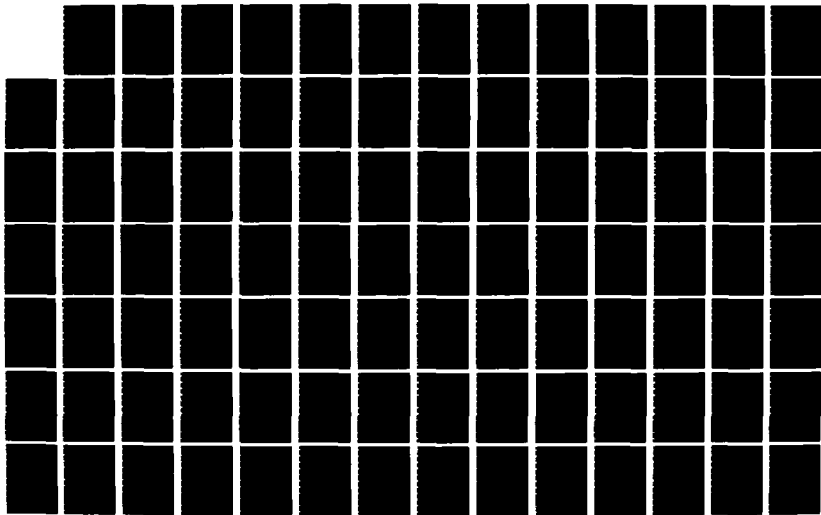
GEOPHYSICAL PLASMAS AND ATMOSPHERIC MODELING(U) SCIENCE 5/8  
APPLICATIONS INTERNATIONAL CORP MCLEAN VA

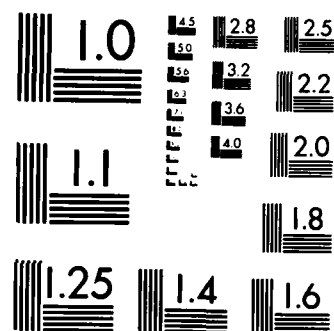
E HYMAN ET AL JUL 86 SAIC-86/1781 N00014-85-C-2018

UNCLASSIFIED

F/G 4/1

NL





MICROCOPY RESOLUTION TEST CHART  
NATIONAL BUREAU OF STANDARDS-1963-A

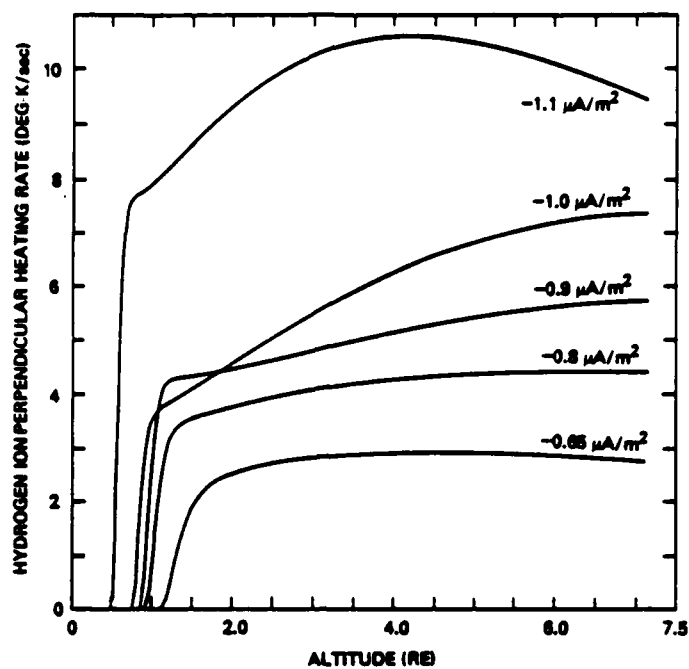


Fig. V.9.a —  $\text{H}^+$  ion perpendicular heating rate vs altitude for all currents

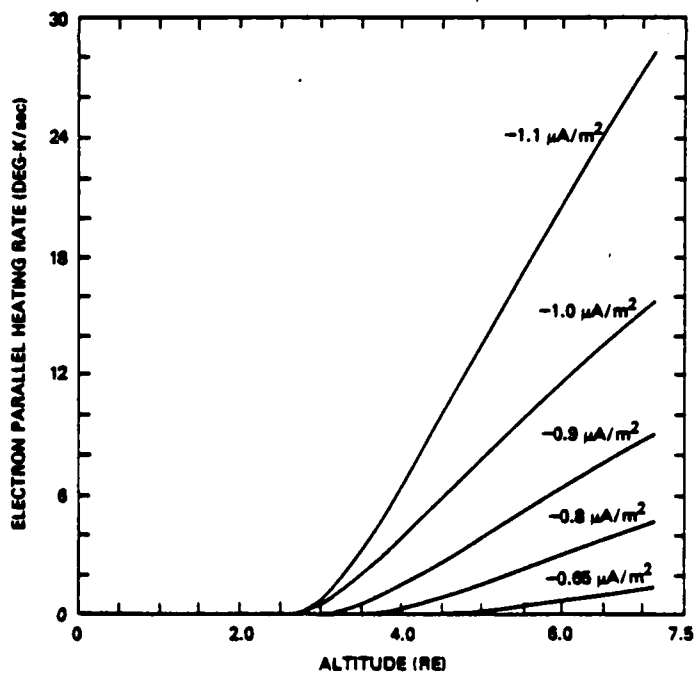


Fig. V.9.b — Electron parallel heating rate vs altitude for all currents

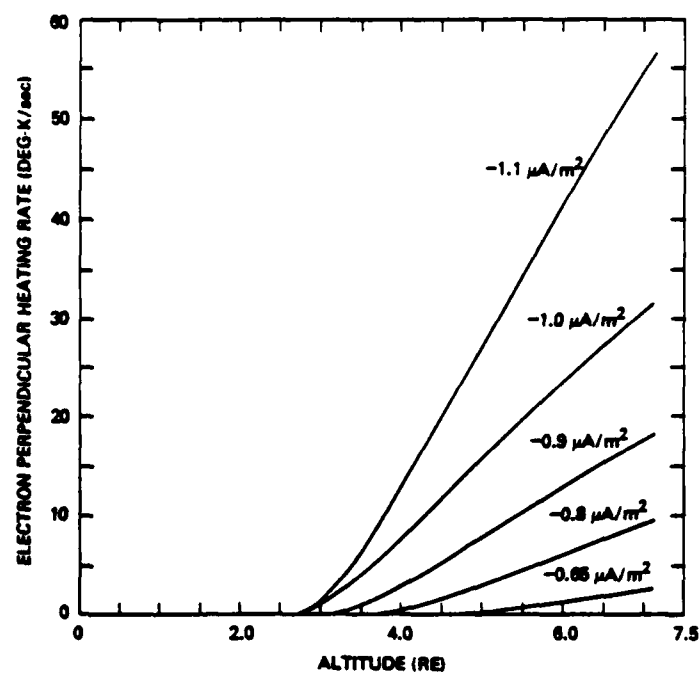


Fig. V.9.c —  $e^-$  perpendicular heating rate vs altitude for all currents

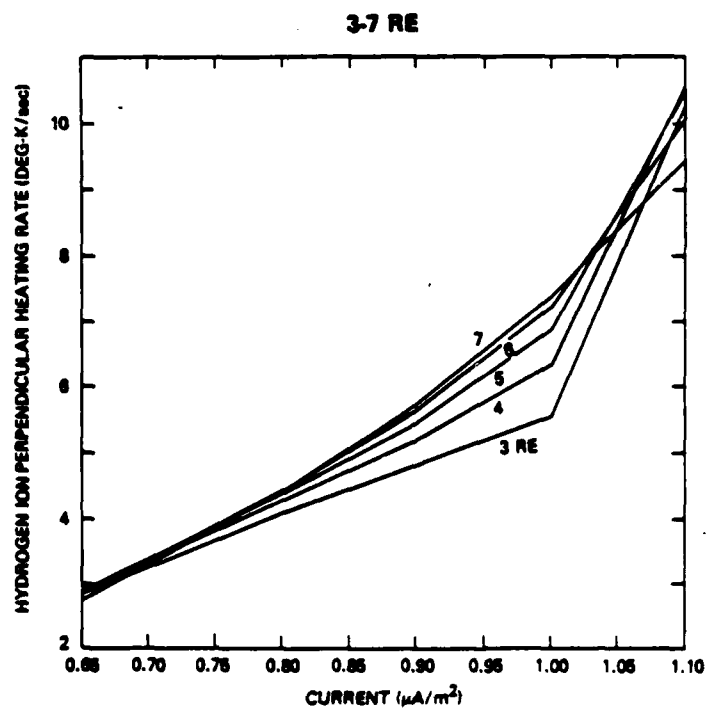


Fig. V.10.a —  $H^+$  ion perpendicular heating rate vs current for different altitudes



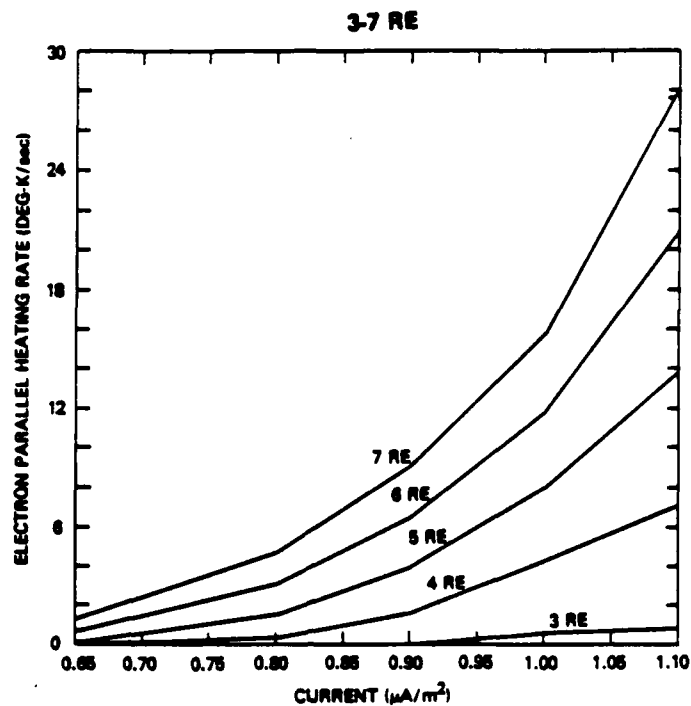


Fig. V.10.b — Electron parallel heating rate vs current for different altitudes

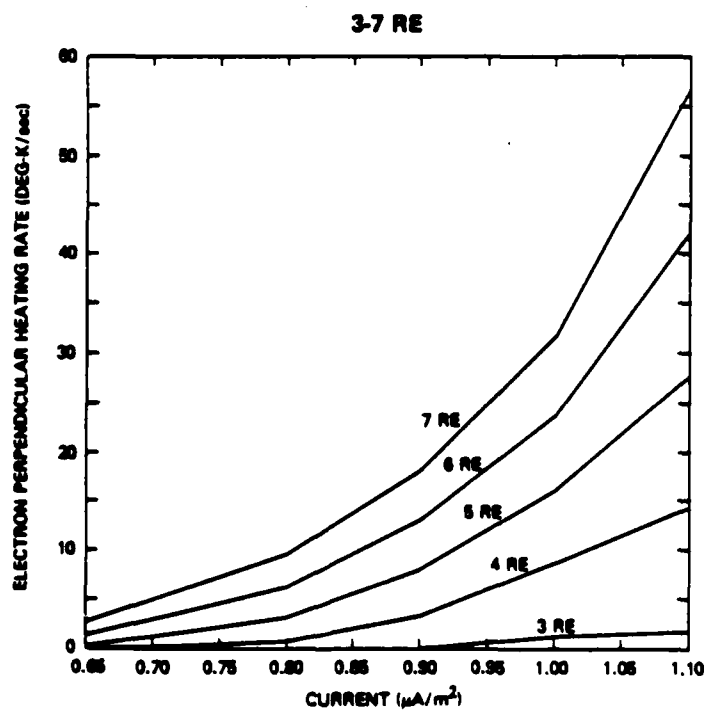


Fig. V.10.c —  $e^-$  perpendicular heating rate vs current for different altitudes

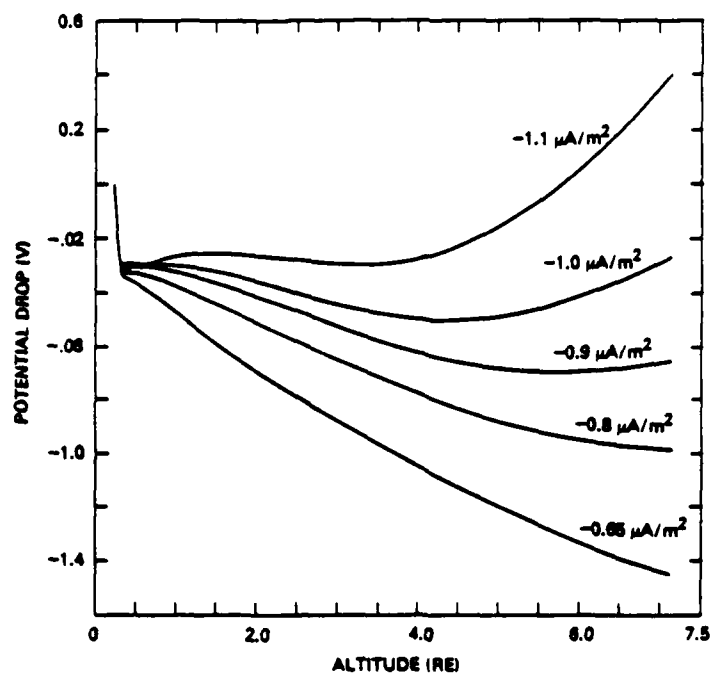


Fig. V.11.a — Potential drop along the tube for all currents

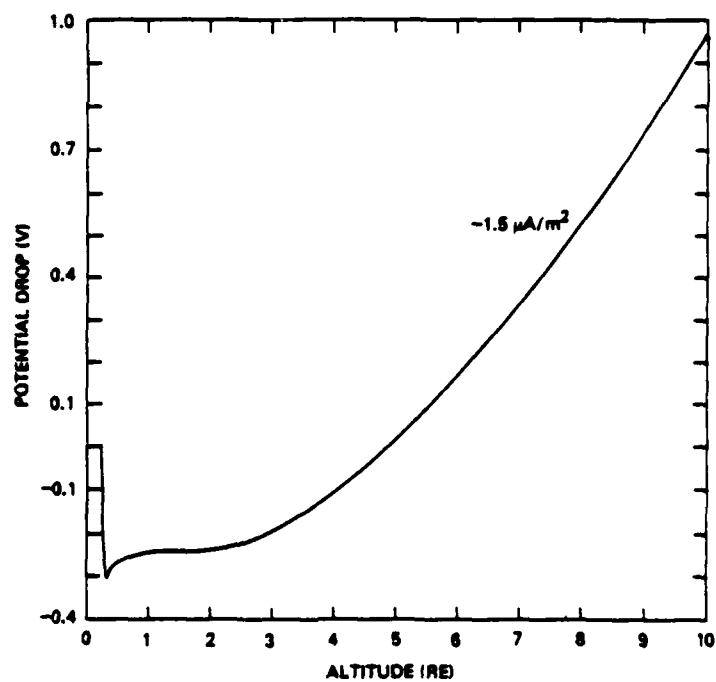


Fig. V.11.b — Potential drop along the tube for a current of  $-1.5 \mu\text{A}/\text{m}^2$

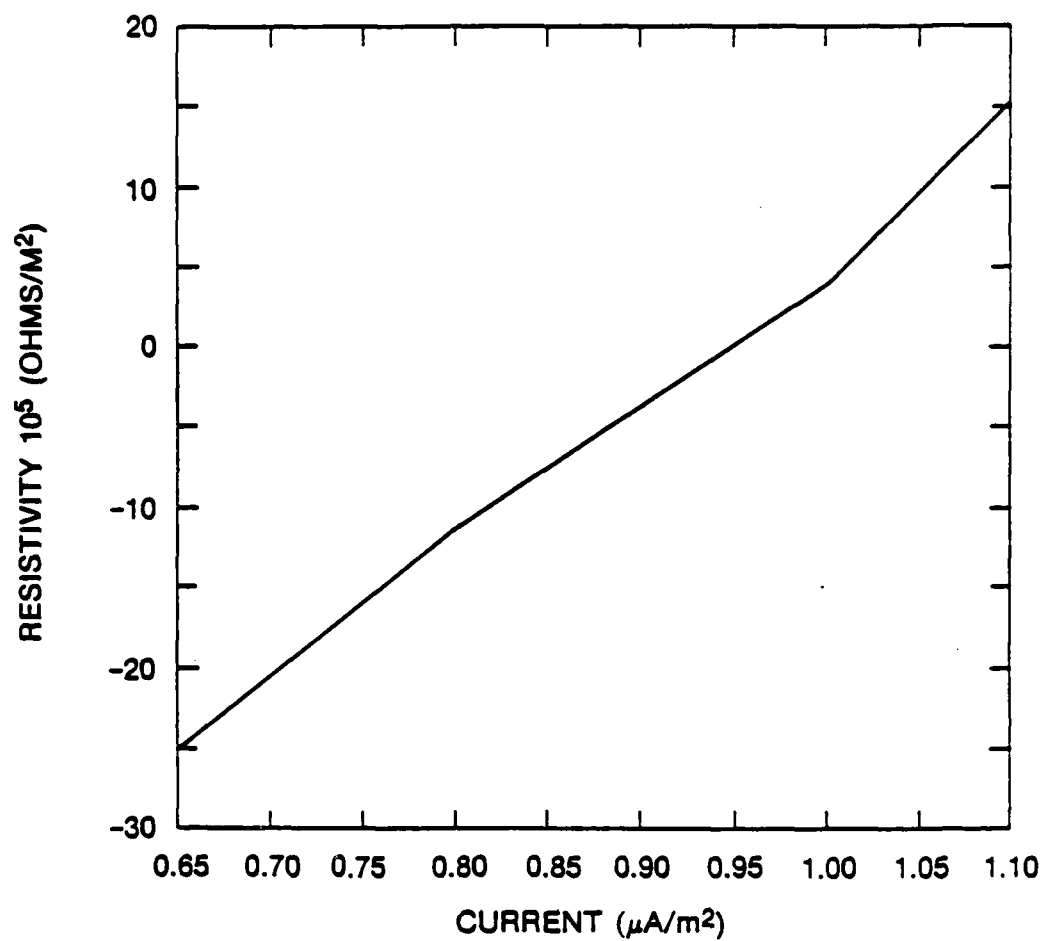


Fig. V.12 — Flux tube resistivity vs current



## CONCLUSIONS

### AND DIRECTIONS FOR FUTURE WORK

Multimoment time dependent and steady state multifluid plasma simulations have been performed to study the dynamics of the auroral field line plasma in the presence of large scale field-aligned return currents. The theoretical formulations are based on the 13- and 16-moment systems of transport equations.

First, in Chapter I, the plasma transport in the high latitude topside ionosphere has been studied in the absence of any field-aligned currents. The electron gas is collision dominated below 2500 km. Above this altitude electron temperature anisotropy develops with  $T_{\perp} > T_{\parallel}$ . The hydrogen ion temperature shows reverse anisotropy, i.e.,  $T_{\parallel} > T_{\perp}$ . The  $H^+$  ion temperature also exhibits adiabatic cooling as the supersonic ion gas expands in a diverging magnetic field. Our results are in good agreement with previous theoretical studies of polar wind and recent experimental observations. These are the first successful solutions to the 16-moment system of transport equations for the polar wind.

In Chapter II, the previous observations of the FAC system in the earth's magnetosphere have been reviewed.

The field-aligned return current simulations have been performed in three stages. The time dependent simulations of Chapter III show that application of a return current to the cold ionospheric upflowing electrons (with cold upper boundary) does not change the electron temperature anisotropy. In Chapter IV, a hot upper boundary has been used for the electrons. The results indicate that the application of return currents to steady state plasma (with a hot electron upper boundary and downward heat flow) reverses the electron temperature anisotropy. In addition, the electron temperature decreases and the electron velocity increases after the application of current. The  $H^+$  ion temperature increases and the  $H^+$  ion velocity decreases. The time dependent simulations show the effects of changes in plasma dynamics due to a sudden application of current. The electron velocity and temperature have a rapid response to a sudden change in conditions with a time constant of about a few minutes. The  $H^+$  ion temperature changes on a much longer time scale. Also, the behavior of the ion transport in the collisionless region determines the time scales on which the flux tube plasma reaches equilibrium.

Our simulations show that the electron drift velocity corresponding to a current of  $-0.65 \mu A/m^2$  is above the threshold for electrostatic ion cyclotron (EIC) waves. This limit is lower than that calculated by Kindel and Kennel [1971], since we have considered temperature anisotropy and have calculated the ion and

electron temperatures in a self consistent way. Kindel and Kennel [1971] have used fixed ion and electron temperatures.

In Chapter V, we have studied the transport effects which occur when the EIC instability heats the hydrogen ions in the perpendicular direction. The heating rate is controlled by the anomalous collision frequency. The EIC instability can transfer electron momentum to the ions, thereby giving rise to anomalous resistivity. The electrons are heated due to resistivity. The downward electron heat flow or thermal conduction competes with the upward convection effects to determine the direction of the electron temperature anisotropy. When the resistivity is strong the heating effects dominate. The increase in the electron temperature caused by anomalous resistivity decreases the critical velocity for exciting the EIC instability and this modifies the way the EIC instability heats the ions. The amplitude of the EIC waves depend on the ion and electron temperatures. From the above calculations we can estimate the electric field associated with the EIC waves.

The potential drop along the field line has been calculated for all currents and from Ohm's law ( $V = IR$ ) the resistivity of the flux tube was calculated. The resistivity is negative for lower currents due to thermo-electric effects associated with the ambipolar electric field and positive for higher currents due to anomalous resistance which is positive and

increases with current. This relationship between field aligned resistivity and field aligned current may be useful in future studies of the transverse distribution of return currents associated with a narrow or discrete region of upward currents. This may lead to an explanation for the observations of Burke et al. [1983] i.e., the transverse spread of the return currents.

These calculations provide interesting insights into the effects of anomalous transport processes in the auroral return current region. However, the heating rates were restricted to lower values due to the numeric stability conditions imposed by the steady state process. In the future, we plan to study higher currents and higher heating rates. Whether higher currents will increase the  $V_{CH}$  so that the marginal stability condition  $V_{CH} = V_D$  will arise is not predictable from this study.

Results show that 16-moment model yields reasonable results which can be understood in physical terms, and this provides some confidence that such models may be useful in the future for large scale magnetospheric modelling.



## APPENDIX 1.I

The collision terms used in Chapter I for the 16-moment system of transport equations are shown here. As explained in Chapter I these are Burger's [1979] collision terms for the case of Coulomb collisions with corrections for finite species velocity differences. The subscripts b and a represents the species, in this case either the electrons or H<sup>+</sup> or O<sup>+</sup>.

$$\frac{\delta n_b}{\delta t} = 0 \quad (1.I.1)$$

$$\frac{\delta v_b}{\delta t} = \sum_a v_{ba} (v_a - v_b) (1 + \phi_{ba}) \quad (1.I.2)$$

$$\begin{aligned} k \frac{\delta T_{b||}}{\delta t} = & \sum_a \frac{m_b v_{ba}}{(m_b + m_a)} \left\{ \frac{6}{5} kT_{a||} - \left[ 2 + \frac{4m_a}{5m_b} \right] kT_{b||} \right. \\ & \left. + \frac{4}{5} kT_{a\perp} + \frac{4m_a}{5m_b} kT_{b\perp} + \left[ 2kT_a + \left( 4 + 6 \frac{m_a}{m_b} \right) kT_b \right] \phi_{ba} \right\} \end{aligned} \quad (1.I.3)$$

$$k \frac{\delta T_{b\perp}}{\delta t} = \sum_a \frac{m_b v_{ba}}{(m_b + m_a)} [3kT_a - 3kT_b + m_a (v_a - v_b)^2 \times (1 + \phi_{ba})] - \frac{k}{2} \frac{\delta T_{b\parallel}}{\delta t} \quad (1.1.4)$$

$$\frac{\delta h_{b\parallel}}{\delta t} = - v_b h_{b\parallel} \quad (1.1.5)$$

$$\frac{\delta h_{b\perp}}{\delta t} = - v_b h_{b\perp} \quad (1.1.6)$$

Each sum includes all charged particles species in the simulation. The velocity - corrected Coulomb collision frequency  $v_{ba}$  is given by :

$$v_{ba} = \frac{n_a (32\pi)^{1/2} e_b^2 e_a^2 (m_b + m_a) \ln A \exp(-x_{ba}^2)}{3m_b^2 m_a \alpha_{ba}^3} \quad (1.1.7)$$

$\ln A$  is the Coulomb logarithm and

$$T_b = \frac{1}{3} T_{b\parallel} + \frac{2}{3} T_{b\perp} \quad (1.1.8)$$

$$\alpha_{ba}^2 = \frac{2kT_b}{m_b} + \frac{2kT_a}{m_a} \quad (1.1.9)$$

$$x_{ba}^2 = \frac{(v_b - v_a)^2}{\alpha_{ba}^2} \quad (1.1.10)$$

$$\phi_{ba} = \frac{2}{5} x_{ba}^2 + \frac{4}{35} x_{ba}^4 + \frac{8}{315} x_{ba}^6 \quad (1.1.11)$$



## APPENDIX 2.III

The collision terms used in Chapter III for the 13-moment system of transport equations are shown here. As explained in Chapter III these are Burger's [1979] collision terms for the case of Coulomb collisions with corrections for finite species velocity differences. The subscripts b and a represent the species, in this case either the electrons or  $H^+$  or  $O^+$ .

$$\frac{\delta n_b}{\delta t} = 0 \quad (2.III.1)$$

$$\frac{\delta v_b}{\delta t} = \sum_a v_{ba} (v_a - v_b) (1 + \phi_{ba}) \quad (2.III.2)$$

$$\begin{aligned} k \frac{\delta T_{b||}}{\delta t} = & \sum_a \frac{m_b v_{ba}}{(m_b + m_a)} \left\{ \frac{6}{5} kT_{a||} - \left[ 2 + \frac{4m_a}{5m_b} \right] kT_{b||} \right. \\ & \left. + \frac{4}{5} kT_{a\perp} + \frac{4m_a}{5m_b} kT_{b\perp} + \left[ 2kT_a + \left( 4 + 6 \frac{m_a}{m_b} \right) kT_b \right] \phi_{ba} \right\} \end{aligned} \quad (2.III.3)$$

$$k \frac{\delta T_{b\perp}}{\delta t} = \sum_a \frac{m_b v_{ba}}{(m_b + m_a)} [3kT_a - 3kT_b + m_a (v_a - v_b)^2 \\ \times (1 + \phi_{ba})] - \frac{k}{2} \frac{\delta T_{b\parallel}}{\delta t}$$

(2.III.4)

$$\frac{\delta h_b}{\delta t} = \sum \frac{n_b m_b v_{ba}}{(m_b + m_a)^2} \left[ \frac{27}{10} m_a \frac{h_a}{n_a} - (3m_b + \frac{8}{5} m_a + \frac{13}{10} \frac{m_a^2}{m_b}) \frac{h_b}{n_b} \right. \\ \left. + \frac{3}{2} \frac{m_a}{m_b} (m_a + m_b) kT_b (v_b - v_a) \right] (1 + \phi_{ba})$$

(2.III.5)

Each sum includes all charged particles species in the simulation. The velocity - corrected Coulomb collision frequency  $\nu_{ba}$  is given by :

$$\nu_{ba} = \frac{n_a (32\pi)^{1/2} e_b^2 e_a^2 (m_b + m_a) \ln A \exp(-x_{ba}^2)}{3m_b^2 m_a \alpha_{ba}^3}$$

(2.III.6)

$\ln A$  is the Coulomb logarithm and

$$T_b = \frac{1}{3} T_{b_{||}} + \frac{2}{3} T_{b_{\perp}}$$

(2.III.7)

$$\alpha_{ba}^2 = \frac{2kT_b}{m_b} + \frac{2kT_a}{m_a}$$

(2.III.8)

$$x_{ba}^2 = \frac{(v_b - v_a)^2}{\alpha_{ba}^2}$$

(2.III.9)

$$\Phi_{ba} = \frac{2}{5} x_{ba}^2 + \frac{4}{35} x_{ba}^4 + \frac{8}{315} x_{ba}^6$$

(2.III.10)





# APPENDIX 3.V

The collision terms used in Chapter V for the 16-moment system of transport equations are shown here. These are similar to those expressed in Appendix 1.I and therefore we have shown only the effects of anomalous transport phenomena denoted by A. The subscripts b and a represent the species, in this case either the electrons or  $H^+$ .

$$\left. \frac{\delta n_b}{\delta t} \right|_A = 0 \quad (3.V.1)$$

$$\left. \frac{\delta v_b}{\delta t} \right|_A = \sum_a v_{baH}^* (v_a - v_b) + \sum_a v_{baR}^* (v_a - v_b) \quad (3.V.2)$$

Critical Frequency:

$$v_{baH}^* = 0.01 \, z_a \left( \frac{n_a}{n_b} \right) \left( \frac{v_D}{v_{cH}} - 1 \right)^2$$

$$v_D > v_{cH}$$

(3.V.3)

$$v_{baR}^* = 0.01 \, z_a \left( \frac{n_a}{n_b} \right) \left( \frac{v_D}{v_{cR}} - 1 \right)^2$$

$$v_D > v_{cR}$$

$$\text{with } v_{cR} > v_{cH}$$

(3.V.4)

$$v_D = v_b - v_a$$

$$k \left. \frac{\delta T_{b||}}{\delta t} \right|_A = B \frac{m_b}{k} v_{baR}^* v_D^2$$

(3.V.5)

For electrons

$$B = \frac{1}{3}$$

(3.V.6)

For Hydrogen ions

$$B = 0$$

(3.V.7)

$$k \left. \frac{\delta T_{bl}}{\delta t} \right|_A = H1 \frac{m_b}{k} v_{baH}^* v_D^2 + R1 \frac{m_b}{k} v_{baR}^* v_D^2$$

(3.V.8)

For electrons

$$H1 = 0$$

(3.V.9)

$$R1 = 2/3$$

For hydrogen ions

$$H1 = 1$$

(3.V.10)

$$R1 = 0$$



## REFERENCES

- Akasofu, S.-I., The development of the auroral substorm, Planet. Space Sci., 12, 273, 1964.
- Akasofu, S.-I., Interplanetary energy flux associated with magnetospheric substorm, Planet. Space Sci., 27, 425, 1979.
- Akasofu, S.-I., Auroral arcs and auroral potential structures, in Physics of Auroral Arc Formation, ed. S.-I Akasofu and J.R. Kan, pp. 1, AGU, Washington, DC., 1981.
- Anderson, H.R. and R.R. Vondrak, Observations of Birkeland currents at auroral latitudes, Rev. Geophys. Space Phys., 13, 243, 1975.
- Armstrong, J.C., S.-I Akasofu, and G. Rostoker, A comparison of satellite observations of Birkeland currents with around observation of visible aurora and ionospheric currents, J. Geophys. Res., 80, 575, 1975.
- Arnoldy, R.L., Signature in the interplanetary medium for substorms, J. Geophys. Res., 76, 5189, 1971.
- Arnoldy, R.L., Auroral particle precipitation and Birkeland currents, Rev. Geophys. Space Phys., 12, 217, 1974.
- Arnoldy, R.L., Review of auroral particle precipitation, in Physics of Auroral Arc Formation, ed., S.-I Akasofu and J.R. Kan, pp 56, AGU Washington, DC 1981.
- Banks, P.M. and T.E. Holtzer, The Polar Wind, J. Geophys. Res., 73, 6846-6854, 1968.

- Banks, P.M. and T.E. Holtzer, High-Latitude Plasma Transport: The Polar Wind, J.Geophys. Res., 74 6317-6332, 1969.
- Barakat, A.R. and R.W. Schunk, Transport Equations for Multicomponent Anisotropic Space Plasmas: A Review, Plasma Phys. 24, 389, 1982.
- Barakat, A.R. and R.W. Schunk, Comparison of Transport Equations Based on Maxwellian and Bi-Maxwellian Distributions for Anisotropic Plasmas, J. Phys. D: Appl. Phys., 15, 1195, 1982.
- Barakat, A.R. and R.W. Schunk, Comparison of Maxwellian and Bi-Maxwellian Expansions with Monte Carlo Simulations for Anisotropic Plasmas, J. Phys. D: Appl. Phys., 15, 2189, 1982.
- Barakat, A.R. and R.W. Schunk, Transport Equations for Multicomponent Anisotropic Space Plasmas: A Review, Plasma Phys., 24, 389, 1982.
- Barakat, A.R. and R.W. Schunk, Effect of Hot Electrons on the Polar Wind, J. Geophys. Res., 89, 9771, 1984.
- Bowers, E. and M.G. Haines, Phys. Fluids, 11, 2695, 1968.
- Burgers, J.M., Flow Equations for Composite Gases, Academic Press, New York, 1969.
- Burch, J., P. H. Reiff, Upward electron beams measured by DE-1: A primary source of dayside region-1 Birkeland currents, Geophys. Res. Lett., 8, 753, 1983.
- Burke, W.J., M.C. Kelley, R.C. Sagalyn, M. Smiddy and S.T. Lai,

- Polar cap electric field structure with northward interplanetary magnetic field, *Geophys. Res. Lett.*, 6, 21, 1979a.
- Burke, W.J., R.C. Sagalyn, M. Smiddy, M.C. Kelley and S.T. Lai., Electric fields at high latitude topside ionosphere near the dawn-dusk meridian (COSPAR) *Space Research*, XIX, 343, 1979b.
- Burke, W.J., D.A Hardy, F.J. Rich, M.C. Kelley, M. Smiddy, B. Shuman, R.C. Sagalyn, R.P. Vancour, P.J.L. Widman, and S.T. Lai, Electrodynamic structure of the late evening sector of the auroral zone. *J. Geophys. Res.*, 85, 1179, 1980.
- Burke, W.J., Electric fields, Birkeland currents and electron precipitation in the vicinity of discrete auroral arcs, in the *Physics of Auroral Arc Formation*, ed. S.-I. Akasofu and J.R. Kan, p 164, AGU, Washington, D.C., 1981.
- Bythrow, P.F., et al., Observational evidence for a boundary layer source of dayside region 1 field-aligned currents. *J. Geophys Res.*, 86. 5577, 1981.
- Carlson, C.W., and M.C. Kelley, Observation and interpretation of particle and electric field measurements inside and adjacent to an active auroral arc, *J. Geophys. Res.*, 82, 2349, 1977.
- Chew, G.F., M.L. Goldberger, and F.E. Low, *Proc. R. Soc., A*, 236, 112-8, 1956.
- Chodura, R. and F. Pohl, *Plasma Phys.* 13, 645, 1971.

- Cloutier, P.A. and H.R. Anderson, Observations of Birkeland currents, Space Sci. Rev., 17, 563, 1975.
- Crooker, N.U., The half-wave rectifier response of the magnetosphere and antiparallel merging. J. Geophys. Res., 85, 575, 1980.
- Daikin, D. R., T. Tajima, G. Benford and N. Rynn, Ion heating by the electrostatic ion cyclotron instability: Theory and experiment, J. Plasma Phys., 15, 175, 1976.
- Demars, H. G. and R. W. Schunk, Transport equations for multispecies plasmas based on individual bi-Maxwellian distributions, J. Appl. Phys., 12, 1051, 1979.
- Doyle, M.A., F.J. Rich, W.J. Burke, and M. Smiddy, Field-aligned currents and electric field observed in the region of dayside cusp, J. Geophys. Res., 86, 5656-5664, 1981.
- Drummond, W. E. and M. N. Rosenbluth, Anomalous diffusion arising from microinstabilities in a plasma, Phys. of Fluids, 5, 1507, 1962.
- Eastman, T.E., E.W. Hones, Jr., S.J. Bame and J.R. Asbridge, The magnetospheric boundary layer. Site of plasma, momentum and energy transfer from the magnetosheath into the magnetosphere, Geophys. Res. Lett., 3, 685, 1976.
- Espedal, M.S., Proc. 9th Int. Conf. on Phenomena in Ionized Gases, Bucharest (Bucharest: Ek. Acad. Rep. Soc. Rom.), 1969.
- Evans, D.S., N.C. Maynard, J. Trpim, T. Jacobsen, and A. Egeland,



- Auroral vector electric field and particle comparisons, 2. Electrodynamics of an arc. J. Geophys. Res., 82 2235, 1977.
- Friedman E., R. Davidson and B. Langdon, Phys. Fluids, 9, 1475, 1966.
- Friis-Christensen, E., et al., Critical component of the interplanetary magnetic field responsible for large geomagnetic events. J. Geophys Res., 77, 3371, 1972.
- Fujii, R., T. Iijima, T.A. Potemra, and M. Sugiura, Seasonal dependence of large-scale Birkeland currents, Geophys. Res. Lett., 8, 1103, 1981.
- Ganguli S. B., P. J. Palmadesso, Studies of Auroral Field Line Equilibria Including the Effects of Return Currents, EOS Trans, AGU, 18, 340, 1985 a.
- Ganguli S. B., H. G. Mitchell, Jr., P. J. Palmadesso, Behavior of Ionized Plasma in the High Latitude Topside Ionosphere, NRL Memorandum Report 5623, Aug 1985 a.
- Ganguli S. B., H. G. Mitchell, Jr., P. J. Palmadesso, Dynamics of the Large Scale Return Currents on Auroral Field Lines, NRL Memorandum Report 5673, Nov 1985 b.
- Ganguli S. B., P. J. Palmadesso, A Simulation of the Auroral Field Line Plasma Including the Effects of Return Currents, Bull. Amer. Phys. Soc., 30, 1466, 1985 b.
- Ganguli S. B., P. J. Palmadesso, Anisotropic Ion Heating in Auroral Return Current Region, EOS Trans., AGU, 66, 1040, 1985 c.

- Goertz, C.K., and Z. W. Boswell, Magnetosphere-ionosphere coupling. J. Geophys. Res., 85, 72, 1980.
- Gombosi, T. I., T. E. Cravens and A. F. Nagi, A time dependent theoretical model of the polar wind: preliminary results, Geophys. Res. Lett., 12, 167, 1985.
- Grad, H., Comm. Pure Appl. Math., 2, 331, 1949.
- Grad, H., Handb. Phys., 12, 205, 1958.
- Haber, I, J. D. Huba, P. J. Palmadesso and K. Papadopoulos, Slope reversal of a monotonically decreasing electron tail in a strong magnetic field, Phys. Fluids, 21(6), 1013, 1978.
- Harel, M., R. A. Wolf, P. H. Reiff, R. W. Spiro, W. J. Burke, F. J. Rich and M. Smiddy, Quantitative simulation of magnetospheric substorm, 86, 2217, 1981.
- Heppner, J.P., Polar cap electric field distributions related to the interplanetary field direction. J. Geophys. Res., 6, 4877, 1972.
- Helmer, J.C., Theory of forbidden zones in the flow of magnetized plasma, Phys. Fluids, 6, 723, 1963. Hill, T.W., Magnetic merging in a collisionless plasma, J. Geophys. Res., 80, 4689, 1975.
- Hill, T.W., and P.H. Reiff, Plasma-sheet dynamics and magnetospheric substorms, Planet. Space Sci, 78, 363, 1980.
- Hill, T.W., Highlights of theoretical progress related to the

- international magnetospheric study, Rev. Geophys. Space Phys., 20, 671, 1982.
- Holtzer, T.E., J.A. Fedder, and P.M. Banks, A Comparison of Kinetic and Hydrodynamic Models of an Expanding Ion-Exosphere, J. Geophys. Res., 76, 2453-2468, 1971.
- Horwitz, J.L., J.R. Dounnik, P.M. Banks, Y. Kamide, and S.-I. Akasofu, The latitudinal distributions of auroral zone electric fields and ground magnetic perturbations, and their response to variations in the interplanetary magnetic field, J. Geophys. Res., 83, 2071, 1978.
- Iijima, T, and T.A. Potemra, The amplitude distribution of field-aligned currents at northern-high latitudes observed by Triad, J. Geophys. Res., 81, 2165, 1976a.
- Iijima, T., and T.A. Potemra, Field-aligned currents in the dayside cusp observed by Triad, J. Geophys. Res., 81, 5971, 1976b.
- Iijima, T. and T.A. Potemra, Large-scale characteristics of field-aligned currents associated with substorms, J. Geophys. Res., 83, 599, 1978a.
- Iijima, T., R. Fujii, T.A. Potemra, and N.A. Suflekos, Field-aligned currents in the south polar cusp and their relationship to the interplanetary magnetic field J. Geophys. Res., 83, 5595, 1978b.
- Iijima, T., and T.A. Potemra, The relationship between interplanetary quantities and Birkeland current densities, Geophys. Res. Lett. 9, 442, 1982.

- Iijima, T. , T. A. Potemra, L. J. Zanetti and P. F. Bythrow, Large-Scale Birkeland currents in the dayside polar region during strongly northward IMF: A new Birkeland current system, J. Geophys. Res., 89, 7441, 1984.
- Ionson, J. A. , R. S. B. Ong and E. G. Fontheim, Anomalous resistivity of the auroral plasma in the topside ionosphere, Geophys. Res. Lett., 3, 549, 1976.
- Kamide, Y., and S.-I. Akasofu, The auroral electrojet and global auroral features, J. Geophys. Res., 80, 3585, 1975.
- Kamide, Y., S.-I. Akasofu, and G. Rostoker, Field aligned currents and the auroral electrojet in the morning sector, J. Geophys. Res., 81, 6141, 1976.
- Kamide, Y., and G. Rostoker, The spatial relationship of field-aligned currents and auroral electrojets to the distribution of nightside auroras. J. Geophys. Res., 82, 5589, 1977.
- Kamide, Y., J.S. Murphree, D.C. Anger, F.T. Berkay, and T.A. Potemra, Simultaneous observations of field-aligned currents and visible auroras by the Triad and Isis 2 satellites, J. Geophys. Res., 84, 4425, 1979.
- Kamide, Y., On the empirical relationship between field-aligned currents and auroras, in Physics of Auroral Arc Formation, ed. S.-I. Akasofu and J.R. Kan, pp. 192, AGU, Washington, D.C., 1981.
- Kan, J.K., and L.C. Lee, Energy coupling function and solar-wind magnetosphere dynamo, Geophys. Res. Lett., 6, 577, 1979.

- Kan, J.R., and L.C. Lee, Theory of Imperfect magnetosphere-ionosphere coupling, Geophys. Res. Lett., 7, 633, 1980.
- Karlson, E.T., Motion of charged particles in an inhomogeneous magnetic field, Phys. Fluids. 5, 476, 1962.
- Karlson, E.T., Streaming of a plasma through a magnetic dipole field, Phys. Fluids, 6, 708, 1963.
- Kaufmann, R. L., P. B. Dusenbery, B. J. Thomas and R. L. Arnoldy, Auroral electron distribution function, J. Geophys. Res., 83, 586, 1978.
- Kennel, C.F. and J.M. Green, Ann. Phys., NY, 38, 63, 1966.
- Kindel, J.M., and C.F. Kennel, Topside Current Instabilities, J. Geophys. Res., 76, 3055-3078, 1971.
- King, J., Data Book, 1979.
- Kintner, P. M., M. C. Kelley, R. D. Sharp, A. G. Ghielmetti, M. Temerin, C. Cattell, P. F. Miegner and J. F. Fennell, Simultaneous observations of energetic (keV) upstreaming and electrostatic hydrogen cyclotron waves, J. Geophys. Res., 84, 7201, 1979.
- Klumpp, D.M., Relationships between auroral particle distributions and magnetic field perturbations associated with field-aligned currents, J. Geophys. Res., 84, 6524, 1979.
- Lee, K. F., Ion cyclotron instability in current-carrying plasmas with anisotropic temperatures, J. Plasma Physics, 8, 379, 1972.

- Lemaire, J., and M. Scherer, Kinetic Models of the Solar and Polar Winds, Rev. Geophys. Space Phys., 11, 427-468, 1973.
- Lemaire, J., and M. Scherer, Field-aligned distribution of plasma mantle and ionospheric plasmas, J. Atmos. Terr. Phys., 40, 337, 1978.
- Lemaire, J., and M. Scherer, Field-aligned current density versus electric potential characteristics for magnetospheric flux tubes, Ann. Geophys., 1, 91, 1983.
- Maezawa, K. Magnetospheric convection induced by the positive and negative Z components of the interplanetary magnetic field; Quantitative analysis using polar cap magnetic records, J. Geophys. Res., 81, 2289, 1976.
- Mallockrode, A.J., and C.W. Carlson, Relations between transverse electric fields and field-aligned currents, J. Geophys. Res., 83, 1426, 1978.
- McDiarmid, L.B., E.E. Budzinski, M.D. Wilson, and J.R. Burrows, Reverse polarity field-aligned currents at high latitudes, J. Geophys. Res., 82, 1513, 1977.
- McDiarmid, L.B., J.R. Burrows, and M.D. Wilson, Comparison of magnetic field perturbations at high latitudes with charged particle and measurements, J. Geophys. Res., 83, 681, 1978a.
- McDiarmid, L.B., J.R. Burrows, and M.D. Wilson, Magnetic field perturbations in the dayside cleft and their relationship to the IMF, J. Geophys. Res., 83, 5753, 1978b.
- MacMahon, A., Phys. Fluids, 8, 1840, 1965.

- Mitchell, H.G., and P.J. Palmadesso, A Dynamic Model for the Auroral Field Line Plasma in the Presence of Field-Aligned Current. J. Geophys. Res., 88, 2131, 1983.
- Mitchell, H. G., and P. J. Palmadesso, Simultaneous energy transport along high-latitude field lines, EOS Trans, 64, 800, 1983.
- Mitchell, H. G. and P. J. Palmadesso,  $O^+$  acceleration due to resistive momentum transfer in the auroral field line plasma, J. Geophys. Res., 89, 7576, 1984.
- Mitchell H. G., S. B. Ganguli, P. J. Palmadesso, Dynamics of Return Currents on Auroral Field Lines, EOS Trans., AGU, 66, 1039, 1985.
- Newman, A. L., Y. T. Chiu and J. M. Cornwall, Two-dimensional quasineutral description of particles and fields above discrete auroral arcs, Aerospace Report No. ATR-85 (7083)-8.
- Oraevskii V., R. Chodura and W. Feneberg, Plasma Phys, 10, 819, 1968.
- Palmadesso, P. J., Plasma instabilities on auroral field lines, EOS Trans., AGU, 60, 351, 1979.
- Palmadesso, P. J., T. P. Coffey, S. L. Ossakow and K. Papadoulos, Topside ionosphere ion heating due to electrostatic ion cyclotron turbulence, Geophys. Res. Lett., 1, 105, 1974.
- Perrault, P., and S.-I. Akasofu, A study of geomagnetic storms, Geophys. J. R. Astron. Soc., 54, 547, 1978.

- Potemra, T.A., Current systems in the earth's magnetosphere, Rev. Geophys. Space Phys., 17, 640, 1979.
- Reiff, P.H., R.W. Spiro, and T.W. Hill, Dependence of polar cap potential drop on interplanetary parameters. J. Geophys. Res., 86, 7639, 1981.
- Rostoker, G., Current flow in the magnetosphere during magnetospheric substorms, J. Geophys. Res., 79, 1994, 1974.
- Russell, C.T. & McPherron, R.L., Semiannual variation of geomagnetic activity, J. Geophys. Res., 78, 92, 1973.
- Rowland, H. L., P. J. Palmadesso and K. Papadopoulos, One-dimensional direct current resistivity due to strong turbulence, Phys. Fluids, 24, 833, 1981a.
- Rowland, H. L., P. J. Palmadesso and K. Papadopoulos, Anomalous resistivity on auroral field lines, Geophys. Res. Lett., 8, 1257, 1981.
- Rowland, H. L. and P. J. Palmadesso, Anomalous resistivity due to low frequency turbulence, J. Geophys. Res., 88, 7997, 1983. Saflekos, N.A. and T.A. Potemra, The orientation of Birkeland current sheets in the dayside polar region and its relationship to the IMF, J. Geophys. Res., 85, 1937, 1980.
- Schunk, R.W., Transport Equations for Aeronomy, Planet Space Sci., 23, 337, 1974.
- Schunk, R.W., Mathematical Structure of Transport Equations for Multispecies Flows, Rev. Geophys. Space Phys., 15, 429-



445, 1977.

Schunk, R.W. and D.S. Watkins, Electron Temperature Anisotropy in the Polar Wind, J.Geophys. Res., 86, 91-102, 1981.

Schunk, R.W. and D.S. Watkins, Proton Temperature Anisotropy in the Polar Wind, J.Geophys. Res., 87 171-180, 1982.

Shield, M.A., J.W. Freeman and A.J. Dessler, A. Source fo field-aligned currents at auroral latitudes. J. Geophys. Res., 74, 247, 1979.

Shuman, B.M., K. P. Vancour, M. Smiddy, . . A. Saflekos, and F.J. Rich, Field-aligned currents, convective electric field, and auroral particle measurements during a mjaor magnetic storm, J. Geophys. Res., 86, 5561, 1981.

Smiddy, M., et al., Effects of high-latitude conductivity on observed convection eleltric fields and Birkeland currents, J. Geophys. Res., 85, 6811, 1980.

Snyder, A.L., Jr., S.-I. Akasofu, and T.N. Davis, Auroral substorms observed from above the north polar region by a satellite, J. Geophys. Res., 79, 1393, 1974.

Sonnerup, B.U.O., Magnetopause reconnection rate, J. Geophys. Res., 79, 1546, 1974.

Sonnerup. B.U.O., Theory of the low-latitude bounbdary layer. J. Geophys. Res., 85, 2017, 1980.

Stern, D.P., The origin of Birkeland currents, Rev. Geophys. Space Phys., 21, 125, 1983a.

Stern, D.P., Electric currents and voltage drops along auroral field lines, Space Sci. Rev., 34, 314, 1983b.

Vasyliunas, V. M., Mathematical models of magnetospheric convection in particles and fields in the magnetosphere, edited by B.H. McCormac, p. 60. D. Reidel, Hingham, Mass., 1970.

**APPENDIX L**

**ICW Turbulence and Auroral E Fields**

**H.L. Rowland  
Science Applications International Corporation**

**and**

**P.J. Palmadesso  
Naval Research Laboratory**



ICW TURBULENCE AND AURORAL E FIELDS

H. L. Rowland

Science Applications, Inc.  
1710 Goodridge Drive  
McLean, VA 22102

and

P. J. Palmadesso

Plasma Physics Division  
Naval Research Laboratory  
Washington, DC 20375

June 1986

# ABSTRACT

Satellite observations have shown highly localized parallel dc electric fields in the aurora embedded in regions of strong electrostatic ion cyclotron turbulence. These dc fields were identified as double layers. We present a series of computer simulations showing that the ICW turbulence will cause the formation of such localized dc fields.

## INTRODUCTION

Temerin et al. (1982) have presented satellite data showing the presence of very localized parallel d.c. electric fields in the aurora. These structures were observed simultaneously with large amplitude electrostatic ion cyclotron waves. Temerin et al. identified these structures as double layers. We will present computer simulations showing that simply the presence of ion cyclotron waves will lead to the appearance of such localized d.c. fields when a parallel potential is applied to a plasma.

A model of anomalous resistivity based upon strong turbulence concepts has been developed to explain the local acceleration of electrons in the aurora [Rowland, et al. (1981a); Rowland, et al. (1981b); Rowland and Palmadesso (1983)]. Several of the predictions of this model have been experimentally confirmed in the laboratory [Lang and Bohmer (1983)]. High time resolution data from AE-D of accelerated auroral electrons also has been shown to be in good agreement with this model [Lin and Rowland (1985)].

In the aurora, electrostatic ion cyclotron waves have been repeatedly observed in the acceleration regions. The waves are large enough that a significant fraction of the electrons can be trapped. When trapping occurs the current can not be carried by the thermal electrons but by a small population of high energy electrons. The trapping also allows the plasma to support parallel dc electric fields to accelerate these electrons. The purpose of this paper is to study in detail how these fields are distributed in the plasma in the presence of ICW turbulence. In an earlier paper we pointed out that the electric field is not uniformly distributed in space [Rowland and Palmadesso (1983)]. Because of the trapping of the bulk of the electrons between the ion cavities, the applied electric field is shielded

from these regions and the applied potential drop only occurs across the cavities. Therefore the field is not uniform in space. This is of course exactly opposite from the spatially uniform fields predicted by weak turbulence theory.

## SIMULATIONS

A series of simulations were performed using a one dimensional Vlasov code. For all the simulations the plasma was initialized as a spatially uniform plasma with a Maxwellian velocity distribution. Between  $t = 0.0$  and  $150 \omega_e$ , the ion density wave is brought up from 0.0 to its maximum value. At  $t = 200 \omega_e$ , the external field is turned on. In all the simulations there is a transitory period of 50 to  $100 \omega_e$  while the plasma redistributes itself in response to the applied field. The field data shown in this paper follows this stage. The field data is time averaged over  $25 \omega_e$ . The simulation is 512 Debye lengths long and is periodic.

The ion turbulence was modelled with modes 2, 4 and 6 with relative amplitudes 0.625, 0.25, and 0.125. This corresponds to a situation where the waves have strong harmonic structure. This is particularly relevant for ion cyclotron waves since the harmonics can appear either due to the linear growth of the current driven instability [Drummond and Rosenbluth (1962)] or simply the non-linear behavior of these waves when they reach large amplitudes [Temerin et al. (1979)]. The ion cyclotron waves in the aurora are observed to have such strong harmonic components [Kintner et al. (1978)]. For this spectrum of ion waves, the distance between the ion density minimums are determined by the first harmonic, mode two. The higher order modes determine how localized the structure is. Figure 1 shows the total electric field before (dashed line) and after (solid line) the external is applied. The



external potential drop is 1.63 Te. Before the external field is turned on one can see the asymmetric electric field associated with the potential barrier of the ion cavity. When the external field is turned on it is localized in this region and acts to bias the local electric field. One first sees a region with a reduced positive electric field followed by a region of larger magnitude negative field. Figure 2 shows the total electric field for the same simulation as Fig. 1 except the external field is now three times larger. The basic shape of the electric field is the same but because the external potential drop is now slightly larger than the internal potential the positive electric field at the left of the potential is greatly reduced.

#### DISCUSSION

The specific purpose of this work is to better understand the microscopic plasma physics that can lead to the acceleration of electrons in the aurora. The electric field profiles shown on Figs. 1 and 2 should be compared to the observations of parallel electric fields in the aurora by Temerin et al. (1982). The basic shape of the observed fields is in excellent agreement with those seen in the simulations. This is especially obvious in the detailed data shown in their Fig. 2. One sees a region of small positive electric field followed by a similar sized region with larger magnitude negative electric field. These parallel field structures were observed embedded in a region of strong ion cyclotron waves as can be seen on their Fig. 1. Current driven ion cyclotron waves will grow at a large angle to the magnetic field so that the ratio of perpendicular to parallel wavelength will be in the range of 10 or 8 to one. From their data one sees that this is the typical ratio between the ICW observed in the perpendicular electric field data and the separation between the localized parallel electric fields.

Spikey electric field structures of the type observed on auroral field lines have often been characterized as "multiple weak ion acoustic double layers". However, the current driven electrostatic ion cyclotron instability is well known to have a lower excitation threshold than the ion acoustic instability [Kindel and Kennel, 1971], and the nonlinear evolution of the mode in the presence of field aligned currents and potential drops distorts the electron distribution function [Rowland et al., 1981] in such a way that subsequent growth of ion acoustic waves is likely to be inhibited. The nonlinear processes described here provide an alternative explanation of the spikey electric field structures which, in our view, is worthy of further consideration.

#### **ACKNOWLEDGEMENTS**

This work was supported by NASA W-14365 and the Office of Naval Research.

## REFERENCES

- Drummond, W., and M. N. Rosenbluth, Anomalous diffusion arising from microinstabilities in a plasma, Phys. Fluids, 5, 1507, 1962.
- Kindel, J. M., and C. F. Kennel, Topside current instabilities, J. Geophys. Res., 76, 3055, 1971.
- Kintner, P. M., M. C. Kelley, and F. S. Lozer, Electrostatic hydrogen waves near one earth radius altitude in the polar magnetosphere, Geophys. Res. Lett., 5, 139, 1978.
- Lang, A., and H. Böhmer, Electron current disruption and parallel electric fields associated with electrostatic ion-cyclotron waves, J. Geophys. Res., 88, 5564, 1983.
- Lin, C. S., and H. L. Rowland, Anomalous resistivity and AE-D observations of auroral electron acceleration, J. Geophys. Res., 90, 4221, 1985.
- Rowland, H. L., and P. J. Palmadesso, Anomalous resistivity due to low frequency turbulence, J. Geophys. Res., 88, 7997, 1983.
- Rowland, H. L., P. J. Palmadesso, and K. Papadopoulos, One-dimensional direct current resistivity due to strong turbulence, Phys. Fluids, 24, 833, 1981a.
- Rowland, H. L., P. J. Palmadesso, and K. Papadopoulos, Anomalous resistivity on auroral field lines, Geophys. Res. Lett., 8, 795, 1981b.
- Temerin, M., K. Cerny, W. Lotko, and F. S. Mozer, Observations of double layers and solitary waves in the auroral plasmas, Phys. Rev. Lett., 48, 1175, 1982.
- Temerin, M., M. Woldroff, and F. S. Mozer, Nonlinear steepening of the electrostatic ion cyclotron wave, Phys. Rev. Lett., 43, 1941, 1979.

## FIGURE CAPTIONS

Figure 1      The low frequency electric field observed with the ion turbulence modeled with modes 2, 4 and 6 with relative amplitudes 0.625, 0.25 and 0.125. The solid (dotted) line shows the field with (without) an applied negative d.c. field. Even though applied uniformly, the electric field appears as localized spikey fields.

Figure 2      The same simulation as in Figure 1 except the applied field is three times longer.

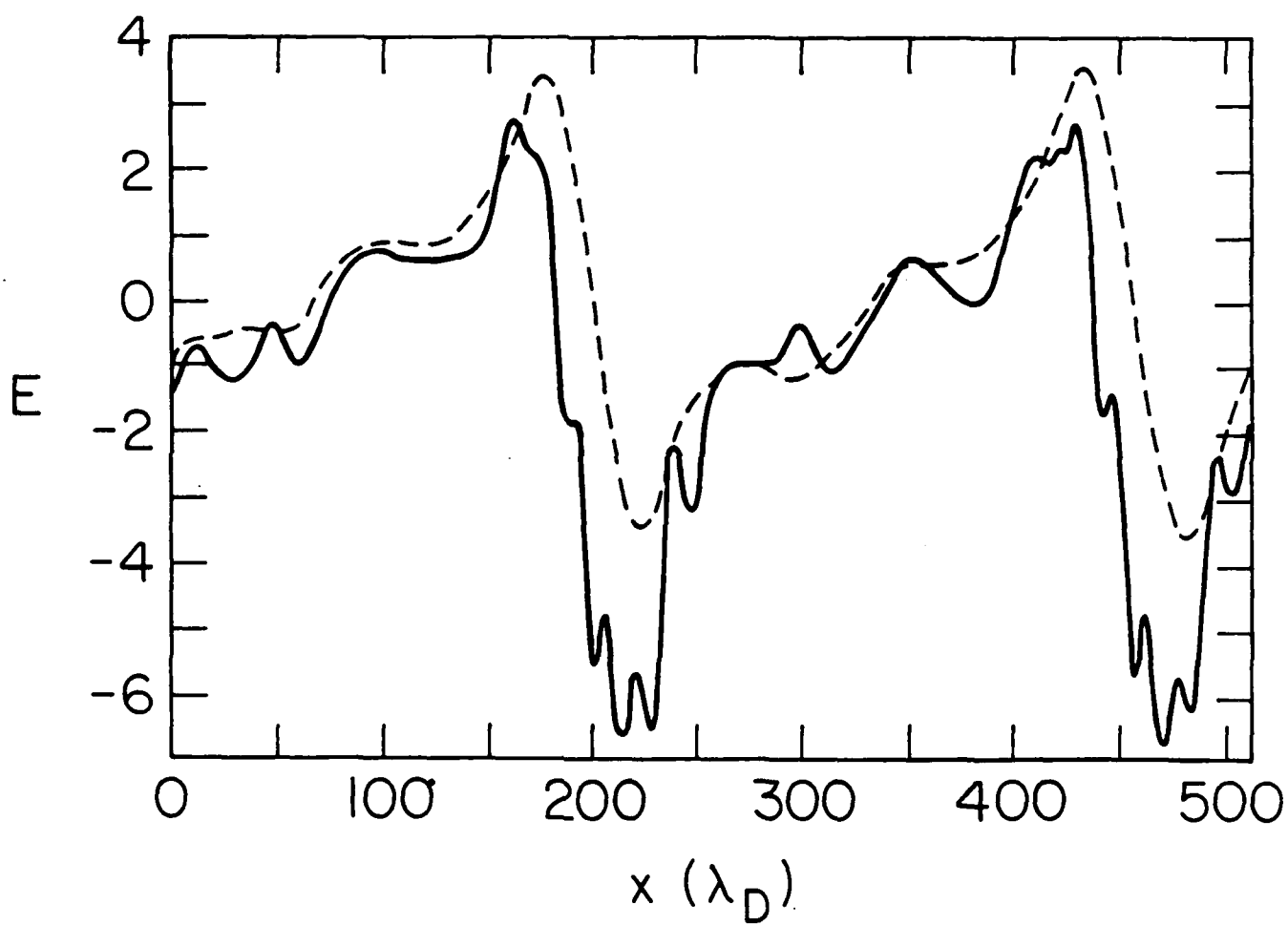


Figure 1

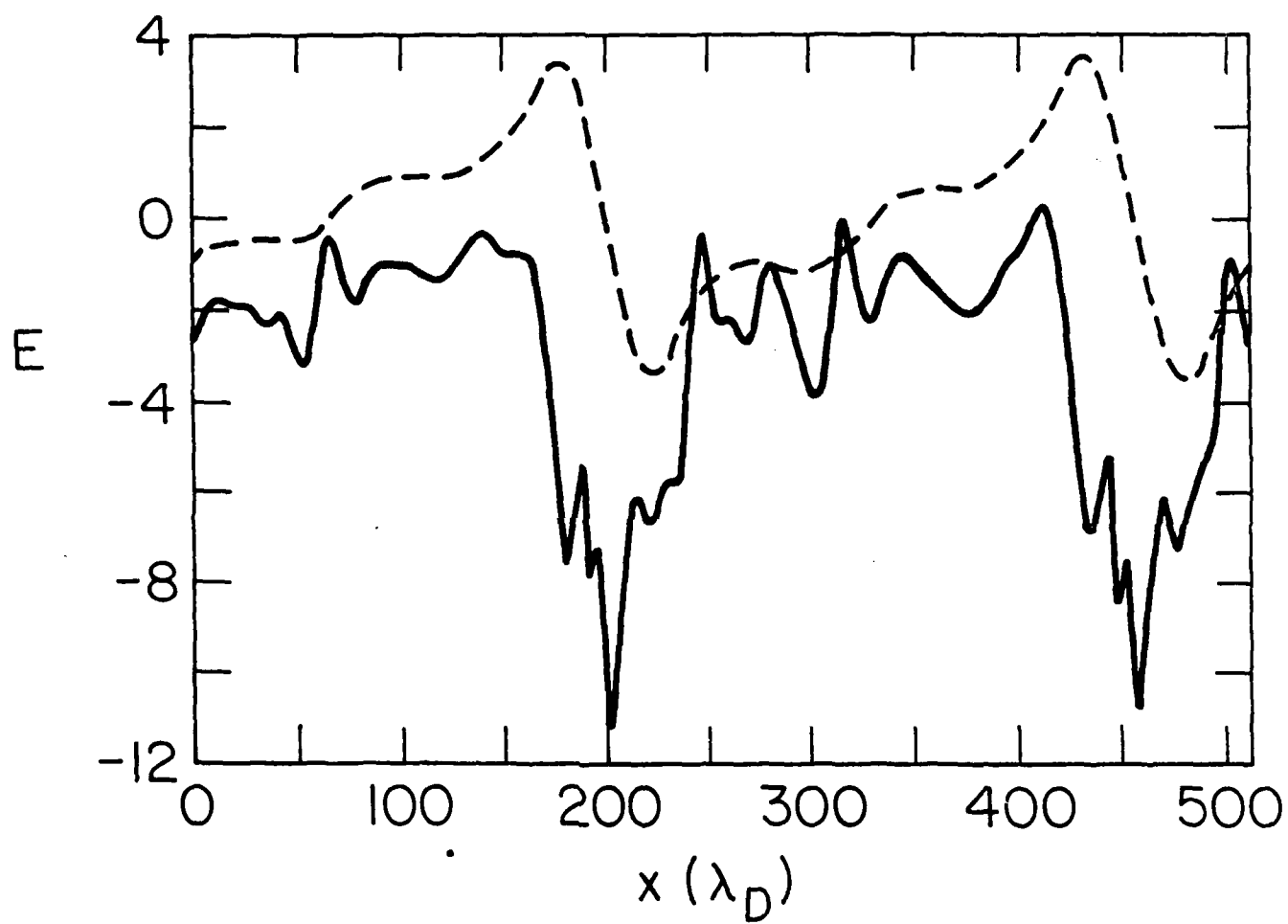


Figure 2

**APPENDIX M**

**Convective Stabilization of Ionospheric Plasma Clouds**

**J.F. Drake**

**Science Applications International Corporation**

**and**

**J.D. Huba**

**Naval Research Laboratory**





CONVECTIVE STABILIZATION OF IONOSPHERIC PLASMA CLOUDS

J.F. Drake\*

Science Applications International Corporation  
McLean, Virginia 22102

and

J.D. Huba

Geophysical and Plasma Dynamics Branch  
Plasma Physics Division  
Naval Research Laboratory  
Washington, DC 20375-5000

October 1985

\* Permanent address: University of Maryland  
College Park, Maryland 20742

# ABSTRACT

We derive a stability criteria for the large-scale structuring of ionospheric plasma clouds due to the  $\mathbf{E} \times \mathbf{B}$  gradient drift instability. For the equilibrium we consider a cylindrical 2D waterbag cloud aligned along a uniform magnetic field that is polarized by a uniform neutral wind. We perform a stability analysis that allows three dimensional perturbations in  $n$ ,  $\theta$ , and  $z$ , and consider both local and global modes. We find that when the parallel wavenumber  $k_z$  exceeds a threshold value, exponentially growing poloidal eigenmodes form which are localized on the "backside" of the cloud. This is in contrast to the  $k_z = 0$  limit in which there are no exponential solutions. As  $k_z$  is increased further, the unstable modes localize at a finite angle away from the backside; at a point where the diamagnetic propagation velocity ( $V_d$ ) balances the convective flow velocity of the background plasma around the cloud ( $V_b$ ). We find that the  $\mathbf{E} \times \mathbf{B}$  gradient drift instability is stable when  $V_d > V_b$  so that the cloud is no longer susceptible to large-scale structuring. We apply these results to ionospheric barium clouds and estimate that they will cease structuring when  $L_{\perp} < (cT/eB)(M+2)/2V_n$  where  $L_{\perp}$  is the transverse size of the cloud,  $T = T_e + T_i$  is the total temperature,  $M = n_c/n_b$ , and  $n_c$  is the cloud density,  $n_b$  is the background density, and  $V_n$  is the neutral wind velocity. For midlatitude barium releases at  $\sim 180$  km we estimate  $L_{\perp} \sim 160 - 480$  m which is consistent with observations.

## I. INTRODUCTION

The evolution of artificial plasma clouds (e.g., barium) in the earth's ionosphere continues to be of interest to space plasma physicists after more than two decades of research. The plasma dynamics associated with ionospheric clouds are of interest since they provide a diagnostic of the ambient ionospheric environment, and also provide experimental data for the study of plasma instabilities. Of particular interest is the onset and evolution of the  $\mathbf{E} \times \mathbf{B}$  gradient drift instability (Simon, 1963; Hon, 1963) which is believed to cause the gross structuring of plasma clouds, i.e., field-aligned striations (Linson and Workman, 1970). This instability is also believed to be responsible for, at times, the structuring of the ambient, high latitude F region ionosphere (Keskinen and Ossakow, 1983). The  $\mathbf{E} \times \mathbf{B}$  gradient drift instability is an interchange mode and is driven by a neutral wind or dc electric field in an inhomogeneous, weakly collisional plasma. A substantial amount of theoretical and computational research has been carried out to understand the  $\mathbf{E} \times \mathbf{B}$  gradient drift instability and its relevance to ionospheric structure (Volk and Haerendel, 1971; Perkins et al., 1973; Zaousky et al., 1973; Shiau and Simon, 1972; Perkins and Doles, 1975; Scannapieco et al., 1976; Chaturvedi and Ossakow, 1979; Keskinen et al., 1980; McDonald et al., 1980, 1981; Huba et al., 1983; Sperling, 1983, 1984; Overman et al., 1983; Sperling and Glassman, 1985; Sperling et al., 1984; Drake et al., 1985).

The bulk of theoretical analyses to date have been based on the local approximation in slab geometry. The local approximation is appropriate for unstable modes which have wavelengths much shorter than the scale length of the density gradient associated with the cloud boundary (i.e.,  $kL \gg 1$  where  $k$  is the wavenumber and  $L$  is the density gradient scale length) (Huba

et al., 1983, Huba and Zalesak, 1983). However, the observed gross structuring of plasma clouds seems to suggest that the dominant modes have  $kL \ll 1$  so that the local approximation may not be valid. The slab or one-dimensional [ $n = n_0(x)$ ] models of plasma clouds do not include a number of important physical effects which appear in more realistic two-dimensional models. The polarization of large plasma clouds in 2D greatly reduces the relative slip velocity of the cloud and the ambient neutral wind thereby weakening the  $\mathbf{E} \times \mathbf{B}$  gradient drift instability (Overman et al., 1983; Zalesak and Huba, 1984). Furthermore, convection and/or propagation of the perturbations from the unstable backside to the stable frontside of the cloud may influence the overall stability of 2D models.

The most detailed linear stability analysis of 2D plasma clouds in the long wavelength regime has been based on the waterbag model (Overman et al., 1983). The purpose of this paper is to extend the analysis of Overman et al. (1983) by including parallel dynamics, i.e., density and potential fluctuations along the ambient magnetic field. Recently it has been shown that the parallel effects can strongly influence the linear stability of ionospheric plasma clouds by stabilizing the short wavelength modes (Sperling, 1983; Sperling et al., 1984; Sperling and Glassman, 1985; Drake et al., 1985). However, these investigations have been based on a 1D cloud model and the need to consider a 2D cloud model is apparent. Thus, in this paper we study the influence of parallel dynamics on the stability of 2D ionospheric plasma clouds. In particular, as in Overman et al. (1983) we consider a simple equilibrium consisting of a 2D cylindrical waterbag, but in contrast to them we consider three dimensional perturbations. We find that the finite parallel dynamics can dramatically alter the  $\mathbf{E} \times \mathbf{B}$  gradient drift instability. Unlike the limit  $k_z = 0$ , exponentially growing poloidal

eigenmodes can exist when  $k_z = 0$ . As  $k_z$  is increased above a threshold value, the unstable modes localize at a finite angle away from the backside; at a point where the diamagnetic propagation velocity ( $V_d$ ) balances the convective flow velocity of the background plasma around the cloud ( $V_b$ ). We find that the  $\mathbf{E} \times \mathbf{B}$  gradient drift instability is stable when  $V_d > V_b$  so that the cloud is no longer susceptible to large-scale structuring. We apply these results to ionospheric barium clouds and estimate that they will cease structuring when  $L_\perp < 0.1 e B (M-2) / 2 V_n$  where  $L_\perp$  is the transverse size of the cloud,  $T = T_e + T_i$  is the total temperature,  $M = n_b/n_0$ , and  $n_0$  is the cloud density,  $n_b$  is the background density, and  $V_n$  is the neutral wind velocity. For midlatitude barium releases at  $\sim 130$  km we estimate  $L_\perp \sim 160 - 480$  m which is consistent with observations.

The organization of the paper is as follows. In the next section we present the assumptions and general equations used in the analysis. In Section III we derive the dispersion equation and in Section IV we present analytical and numerical results. In Section V we investigate the possibility of exponentially growing poloidal eigenmodes. Finally, in Section VI we summarize our findings and discuss the application of our theory to the evolution of ionospheric barium clouds.

## II. GENERAL EQUATIONS AND EQUILIBRIUM

The general three dimensional equations for a warm plasma cloud in a uniform magnetic field  $\mathbf{B} = B \hat{\mathbf{e}}_z$  and a uniform background neutral wind  $\mathbf{V}_n = V_n \hat{\mathbf{e}}_x$  see Fig. 1 are given by (Drake et al., 1985)

$$\frac{\partial n}{\partial t} - \frac{c}{B} \nabla \phi \times \hat{\mathbf{z}} \cdot \nabla n + \frac{\partial}{\partial z} \frac{1}{en_e} \left( \frac{\partial \phi}{\partial z} - \frac{T_e}{ne} \frac{\partial n}{\partial z} \right) = 0 \quad (1)$$

$$\frac{\partial}{\partial t} \frac{v_{in}}{\Omega_i} \nabla_{\perp} \cdot n \hat{\mathbf{e}}_i + D_{\perp i} \nabla_{\perp}^2 n + \frac{v_{in}}{\Omega_i} \hat{\mathbf{z}} \times \nabla_n \cdot \nabla n + \frac{\partial}{\partial z} \frac{1}{en_e} \left( \frac{\partial \phi}{\partial z} - \frac{T_e}{ne} \frac{\partial n}{\partial z} \right) = 0 \quad (2)$$

where  $n_e = e_e v_e / ne^2$  is the parallel resistivity,  $v_e = v_{ei} + v_{en}$ ,  $D_{\perp i} = v_{in} / \Omega_i \cot T_i / eB$  is the perpendicular ion diffusion coefficient,  $v_{ei}$  is the electron-ion collision frequency and  $\Omega_\alpha$  and  $v_{\alpha n}$  are the cyclotron and neutral collision frequencies of the species  $\alpha$ . Equation (1) is the electron continuity equation and (2) arises from charge neutrality ( $\nabla \cdot \mathbf{j} = 0$ ). We have considered the electrostatic limit, have taken  $T_e$  and  $T_i$  to be spatially uniform, have assumed  $v_e / \Omega_e, v_{in} / \Omega_i \ll 1$  so that Hall terms can be discarded, and have neglected the ion parallel diffusion ( $D_{\parallel i}$ ) and perpendicular electron diffusion ( $D_{\perp e}$ ). We therefore assume that

$$\partial / \partial t \gg D_{\parallel i} \partial^2 / \partial z^2, D_{\perp e} \nabla_{\perp}^2.$$

It is convenient to change variables by defining an auxiliary potential

$$\Phi = \phi + \frac{T_i}{e} \ln(n). \quad (3)$$

Equations (1) and (2) then become

$$\frac{\partial n}{\partial t} - \frac{c}{B} \nabla \Phi \times \hat{z} \cdot \nabla n + \frac{\partial}{\partial z} \frac{1}{en_e} \left( \frac{\partial \Phi}{\partial z} - \frac{T}{ne} \frac{\partial n}{\partial z} \right) = 0 \quad (14)$$

$$\frac{c}{B} \frac{v_{in}}{n_i} \nabla_{\perp} \cdot n \nabla_{\perp} \Phi + \frac{v_{in}}{n_i} \hat{z} \times \underline{v}_n \cdot \nabla n + \frac{\partial}{\partial z} \frac{1}{en_e} \left( \frac{\partial \Phi}{\partial z} - \frac{T}{ne} \frac{\partial n}{\partial z} \right) = 0 \quad (15)$$

where  $T = T_e + T_i$ .

We consider a simple equilibrium consisting of a cylindrical waterbag of radius  $r_0$  and density  $n_0$  in a uniform background  $n_b$ :

$$n_0(r) = n_0 H(r_0 - r) + n_b \quad (16)$$

where  $H$  is the Heaviside function. The solution of the equilibrium equations for this configuration is well known. The drag between the cloud and neutral wind polarizes the cloud. The resulting potential  $\Phi_0$  is given by Smythe, '1950'.

$$\frac{c\Phi_0}{B} = \begin{cases} -V_n \frac{M}{M+2} r \sin\theta & r < r_0 \\ -V_n \frac{M}{M+2} \frac{r_0^2}{r} \sin\theta & r > r_0 \end{cases}$$

where  $M = n_0/n_b$ . Note that the quantity  $M$  defined here differs somewhat from earlier definitions where  $M = (n_0 + n_b)/n_b$ . The potential causes the cloud to drift with a uniform velocity

$$\underline{v}_c = V_n \frac{M}{M+2} \hat{e}_x. \quad (7)$$

The linear stability analysis which follows is most easily carried out in the frame of reference of the moving cloud. In this frame the potential  $\Phi_{0c}$  is given by

$$\frac{c\Phi_{0c}}{B} = \begin{cases} 0 & r < r_c \\ v_n \frac{M}{M+2} \left(r - \frac{r_c^2}{r}\right) \sin\theta & r > r_c \end{cases} \quad (8)$$

### III. LINEARIZED EQUATIONS AND DISPERSION EQUATION

We investigate the stability of this equilibrium by considering small perturbations  $\tilde{n}(r, \theta, z, t)$  and  $\tilde{\Phi}(r, \theta, z, t)$  around  $n_0$  and  $\Phi_{0c}$ . Since the equilibrium is independent of  $z$ , we can expand the perturbations in plane waves in the  $z$  direction ( $\tilde{n}, \tilde{\Phi} \sim \exp ik_z z$ ) without loss of generality. In the perpendicular plane such a simple expansion is not generally possible since the equilibrium depends on both  $r$  and  $\theta$ . Equations (4) and (5) yield the linearized equations,

$$\frac{\partial \tilde{n}}{\partial t} - \frac{c}{B} \nabla \Phi_{0c} \times \hat{z} \cdot \nabla \tilde{n} + \frac{c}{B} \frac{n_c}{r_c} \frac{\partial \tilde{\Phi}}{\partial \theta} \delta(r - r_c) - \frac{k_z^2}{en_e} \left( \tilde{\Phi} - \frac{T}{e} \frac{\tilde{n}}{n_0} \right) = 0 \quad (9a)$$

$$\frac{c}{B} \frac{v_{in}}{\Omega_i} (\nabla_{\perp} \cdot n_0 \nabla \tilde{\Phi} + \nabla_{\perp} \cdot \tilde{n} \nabla \Phi_{0c}) + \frac{v_{in}}{\Omega_i} (v_n - v_c) \frac{\partial \tilde{n}}{\partial y} - \frac{k_z^2}{en_e} \left( \tilde{\Phi} - \frac{T}{e} \frac{\tilde{n}}{n_0} \right) = 0. \quad (9b)$$

Equations (9) are solved separately in the region  $r > r_c$  and  $r < r_c$ , and the solutions are then matched using boundary conditions which are obtained from the equations for  $r = r_c$ . In the limit  $k_z = 0$ , this procedure is straightforward since  $\tilde{n} = 0$  and  $\nabla^2 \tilde{\Phi} = 0$  for  $r = r_c$ . In the case  $k_z \neq 0$ , the equations for  $\tilde{n}$  and  $\tilde{\Phi}$  in the region  $r = r_c$  are much more complicated so further simplifications must be made. We limit the calculation to



perturbations for which  $\partial/\partial\theta \gg 1$ . In this limit the  $\theta$  dependence of  $\bar{n}$  and  $\bar{\phi}$  can be represented by the eikonal  $\bar{\phi}, \bar{n} = \exp[iS(\theta)]$  where

$$\nabla S = ik_\theta(\theta) \hat{e}_\theta. \quad (10)$$

In this limit the perturbations are strongly localized around the boundary  $r_0$  and decay exponentially away from this boundary. Thus, for  $r \neq r_0$  we write

$$\bar{\phi}_\pm(r, \theta, t) = \hat{\phi}_\pm \exp[iS(\theta)] \exp[\pm k_{r\pm}(r - r_0) \exp i\gamma t] \quad (11)$$

where  $k_{r\pm} r_0 \gg 1$  and  $+$  and  $-$  refer to the region  $r > r_0$  and  $r < r_0$ , respectively. The specific range of parameters for which the form of  $\bar{\phi}$  given in (11) is valid will be presented later. Similar expressions can be written for  $\bar{n}_\pm(r, \theta, t)$ . Finally, we have assumed  $\bar{n}$  and  $\bar{\phi}$  grow exponentially in time with a growth rate  $\gamma = \gamma_r + i\omega_r$ . For the present,  $\gamma$  must be considered a local growth rate  $\gamma(\theta)$ . Eventually, we will investigate under what circumstances exponentially growing normal modes of the cloud can exist.

With the form of  $\bar{\phi}$  (and  $\bar{n}$ ) given in (11), (9a) and (9b) reduce to algebraic expressions for  $k_{r\pm}$  in the regions  $r \neq r_0$ .

$$\begin{aligned} k_{r+}^2 - k_\theta^2 - \frac{\alpha k_z^2}{\gamma_+} \left\{ \gamma + ik_\theta \frac{2M}{M+2} v_n \sin\theta \right. \\ \left. - \frac{2}{M+2} v_n \frac{v_{in}}{\Omega_i} [ik_\theta \cos\theta - k_{r+}(1+M) \sin\theta] \right\} = 0 \end{aligned} \quad (12a)$$

$$k_{r-}^2 - k_\theta^2 - \frac{\alpha k_z^2}{\gamma_-} \left\{ \gamma - \frac{2}{M+2} v_n \frac{v_{in}}{\Omega_i} [ik_\theta \cos\theta + k_{r-} \sin\theta] \right\} = 0 \quad (12b)$$

$$\gamma_+ = \gamma + k_z^2 D_{\parallel e} + ik_\theta \frac{2M}{M+2} v_n \sin\theta, \quad (12c)$$

$$\gamma_- = \gamma + k_z^2 D_{\parallel e}, \quad (12d)$$

$\alpha = \hat{n}_e a_1 / v_e v_{in} \gg 1$ , and  $D_{\parallel e} = T/m_e v_e$  is the parallel electron diffusion coefficient. In (12) we have assumed for simplicity that  $\alpha$  and  $D_{\parallel e}$  are continuous across the cloud boundary, which requires the density dependence of  $v_e$  to be weak (i.e.,  $v_{en} \gg v_{el}$ ). Finally, from (9a),

$$\gamma_\pm \hat{n}_\pm = k_z^2 \hat{\phi}_\pm / en_{e\pm}. \quad (13)$$

The matching conditions for  $\hat{n}_\pm$ ,  $\hat{\phi}_\pm$  and  $k_{r\pm}$  at  $r = r_0$  can be derived from (9). The radial  $\mathbf{E} \times \mathbf{B}$  convection of the cloud causes the density  $\hat{n}$  to be singular at the cloud boundary (third term in the continuity equation). It is convenient therefore to separate out the singular behavior of  $\hat{n}$  so that in the region  $r = r_0$

$$\hat{n}(r, \theta, t) = [\hat{N} \delta(r-r_0) + \hat{n}_+ H(r-r_0) + \hat{n}_- H(r_0-r)] \exp[iS(\theta)] \exp[i\omega t]. \quad (14)$$

The potential  $\hat{\phi}$  remains finite at the boundary so (9a) can be written as

$$[\gamma + k_z^2 D_{\parallel e} + (c/B) ik_\theta \phi'_{0c}] \hat{N} + (c/B) ik_\theta n_c \hat{\phi} = 0 \quad (15)$$

for  $r = r_0$ . Equation (15) now contains no singularities at  $r = r_0$ . However, the radial electric field  $\phi'_{0c}$  is discontinuous across  $r = r_0$  since it is zero for  $r < r_0$  and finite for  $r > r_0$ . This discontinuity must be

balanced by a corresponding jump in the potential  $\hat{\phi}$  at the boundary. Thus, from (8) and (15), we find

$$\hat{\phi}_+/Y_+ = \hat{\phi}_-/Y_- \quad (16)$$

This condition can also be derived from the requirement that the tangential component of  $\vec{v}_E$  across the boundary of the plasma cloud be continuous (see Appendix A). The continuity equation then reduces to

$$Y_- \hat{N} + (c/B) k_\theta n_0 \hat{\phi}_- = 0. \quad (17)$$

The matching condition for  $k_{r\pm}$  can be derived by integrating (9b) across the boundary,

$$\begin{aligned} -n_b k_{r+} \hat{\phi}_- - (n_b + n_c) k_{r-} \hat{\phi}_- + \frac{B}{c} \frac{2V}{M+2} n_0 [ik_\theta \cos\theta \hat{N} + (1+M) \sin\theta \hat{n}_- \\ - \sin\theta \hat{n}_+] + \frac{1}{2} k_z^2 \frac{T}{e} \hat{N} = 0. \end{aligned} \quad (18)$$

Equations (13) and (16)-(18) can then be combined into a single relation between  $k_{r+}$  and  $k_{r-}$ ,

$$k_{r+} Y_+ + (1+M) k_{r-} Y_- - \frac{2V}{M+2} M k_\theta^2 \cos\theta + i a M k_z^2 k_\theta \frac{cT}{eB} = 0. \quad (19)$$

Equations (12) and (19) constitute a local dispersion equation for the  $\vec{E} \times \vec{B}$  instability with  $k_z = 0$  based on a 2D waterbag equilibrium.

#### IV. EVALUATION OF THE LOCAL DISPERSION EQUATION

We first evaluate the local growth rate  $\gamma(\theta)$  by solving the dispersion equation given by (12) and (19). We consider two limits: the cold plasma limit ( $T = 0$ ) and the warm plasma limit ( $T \neq 0$ ).

##### A. Cold Plasma Limit: $T = 0$

In the cold plasma limit (19) simplifies to

$$k_{r+} \gamma_+ + (1+M)k_{r-} \gamma_- = \frac{2V_n}{M+2} M k_\theta^2 \cos\theta \quad (20a)$$

where

$$\gamma_\pm = \gamma + 2ik_\theta M V_n \sin\theta / (M+2) \quad (20b)$$

$$\gamma_- = \gamma \quad (20c)$$

since  $D_{pe} = T = 0$ . Equations (12a) and (12b) for  $k_{r\pm}$  remain unchanged. In the limit of small  $k_z$ , (12a) and (12b) yield

$$k_{r\pm} \approx k_\theta \quad (21a)$$

and the growth rate  $\gamma$  can then be calculated from (20),

$$\gamma = M \gamma_0 (\cos\theta - 1 \sin\theta) \quad (21b)$$

$$\gamma_0 = \frac{2M}{(M+2)^2} \frac{V_n}{r_c} \quad (21c)$$

where  $m = k_{\theta} r_c$  is the poloidal mode number. The growth rate peaks at  $\theta = 0$  (the backside of the plasma cloud) and is linearly proportional to  $m$ . The growth rate in (21) is consistent with previous rigorous and heuristic investigations of the stability of circular waterbag models of plasma clouds (Overman et al., 1983; Zalesak and Huba, 1984). For  $\theta = 0$ , the second term on the right side of (21b) causes the mode to propagate at a finite frequency. This propagation results as the fluid outside of the cloud convects around the circular boundary and carries the perturbation. The point  $\theta = 0$  corresponds to a stagnation point of the flow so there is no finite frequency there. Finally, from (21a) the assumption that the modes are strongly localized around the cloud boundary requires  $m \gg 1$ .

To obtain analytic expressions for the growth rate of modes with  $k_z = 0$ , we consider only the case  $\theta = 0$  which corresponds to the most unstable mode. Later we will present numerical solutions of the more general dispersion relation in which this restriction is relaxed. For  $\theta = 0$ , we have  $k_{\theta+} = k_{\theta-} = k_{\theta}$  and  $\gamma_+ = \gamma_- = \gamma$  and the dispersion equations are given by,

$$\gamma k_{r_c} = m^2 \gamma_0, \quad (22a)$$

$$k_{r_c}^2 = m^2 + \lambda^2 \left( 1 - i \frac{M+2}{M} \frac{m \gamma_0}{\gamma} \frac{v_{1n}}{\Omega_1} \right) \quad (22b)$$

with the solution

$$\gamma = m \gamma_0 \left\{ \left[ m^2 + \lambda^2 \right] - \lambda^4 \frac{(M+2)^2}{4M^2} \frac{v_{1n}^2}{\Omega_1^2} \right\}^{1/2} + i \lambda^2 \frac{M+2}{2M} \frac{v_{1n}}{\Omega_1} \left( m^2 + \lambda^2 \right)^{-1} \quad (23a)$$

where

$$\lambda = \alpha^{1/2} k_z r_0. \quad (23b)$$

As  $k_z$  is increased from zero, over the interval  $\lambda < m$  the growth rate is roughly given by its  $k_z = 0$  limit. For

$$1 \ll \lambda^2/m^2 \ll m^2/v_{in}^2 \quad (24a)$$

the growth rate decreases with  $k_z$  as

$$\gamma = m^2 \gamma_0 / \lambda. \quad (24b)$$

Over this range  $k_r = \alpha^{1/2} k_z \gg k_9$  so that  $k_z$  causes the mode to become more localized near the cloud boundary. For

$$\lambda^2 = \alpha k_z^2 r_0^2 > \frac{4 M^2}{(M+2)^2} \frac{\Omega_1^2}{v_{in}^2} m^2 \quad (25)$$

the mode is stable. Note that (25) implies that the lowest order poloidal modes are stabilized first as  $k_z$  is increased.

To confirm the analytic results for  $T = 0$  and to generalize the results for  $\theta \neq 0$ , we present Fig. 2 which is obtained by solving (12) and (19) numerically. It is easy to show that in the cold plasma limit the mode number  $m$  enters the dispersion relation only through the functions  $\gamma/m$  and  $\lambda/m$ . Thus, in Fig. 2 we plot (a) the growth rate  $\gamma_r/m\gamma_0$  vs  $\lambda/m$  and (b) the real frequency  $\omega_r/m\gamma_0$  vs.  $\lambda/m$  for  $v_i/\Omega_i = 0.025$ ,  $M = 2$ , and  $D_{ie} = 0$  (i.e.,  $T = 0$ ), and several values of  $\theta$ : (A)  $\theta = 0^\circ$ , (B)  $\theta = 22.5^\circ$ , (C)  $\theta = 45^\circ$ , (D)  $\theta = 67.5^\circ$ , and (E)  $\theta = 90^\circ$ .

We note the following from Fig. 2. First, the growth rate  $\gamma_r$  is a maximum when  $k_z = 0$ , and decreases as  $\theta$  increases. For  $\theta = 90^\circ$  there is no growth. On the other hand, the real frequency  $\omega_r$  increases in magnitude as a function of  $\theta$  for  $\lambda = 0$ , i.e.,  $k_z = 0$ . These points are consistent with (21). Second, for all values of  $\theta$ ,  $\gamma_r$  decreases as  $\lambda$  increases which is consistent with (24b), while  $\omega_r$  remains roughly constant. Finally, the modes become purely propagating for sufficiently large  $\lambda$ , i.e.,  $\gamma_r = 0$  but  $\omega_r \neq 0$ . The value of  $\lambda$  denoted by the arrow in Fig. 2a corresponds to the stabilization point predicted by (25) ( $\lambda/m = 40$ ) which is in excellent agreement with the numerical results ( $\lambda/m = 40.4$ ). We also note that the stabilization point is independent of  $\theta$ .

#### B. Warm Plasma Limit: $T \neq 0$

We only analytically investigate modes at  $\theta = 0$ . Equations (12) and (19) reduce to

$$k_r r_c \gamma_- = m(m\gamma_0 - i \frac{M}{M+2} \frac{\Omega_i}{v_{in}} k_z^2 D_{ie}) \quad (26a)$$

$$k_r^2 r_c^2 = m^2 + \lambda^2 \gamma / \gamma_- \quad (26b)$$

where  $k_{r\pm} = k_r$ ,  $\gamma_+ = \gamma_- = \gamma + k_z^2 D_{ie}$  and we have neglected the terms proportional to  $v_{in}/\Omega_i$  in (26b) for  $k_r$ . This approximation is justified for sufficiently large  $T$  (to be proven later).

For  $k_z \neq 0$ , the finite temperature corrections drop out of (26) and the growth rate reduces to  $\gamma = m\gamma_0$  as in the cold plasma limit. As  $k_z$  increases, the second term on the right side of (26a) becomes comparable to the driving term  $\gamma_0$  when  $k_z^2 D_{ie} = \gamma_0 v_{in}/\Omega_i \ll \gamma_0$ . At this point  $k_z^2 D_{ie}$  can

still be neglected compared with  $\gamma - \gamma_0$  in the definition of  $\gamma_-$ . Thus, the eigenvalue  $\gamma$  is given by

$$\gamma = \frac{(m\gamma_0 - i\omega_0)m}{(m^2 + \lambda^2)^{1/2}}, \quad (27a)$$

where

$$k_{rc}^2 = m^2 + \lambda^2 \quad (27b)$$

$$\omega_0 = \frac{M}{M+2} \frac{cT}{eB} \frac{\lambda^2}{r_c^2} \quad (27c)$$

Thus,  $k_z$  decreases the growth rate as in the  $T = 0$  limit and causes the mode to propagate at a finite frequency which increases with  $k_z$ .

When  $k_{ze}^2 \gg \gamma_0^2 / \Omega_i$ , the modes to lowest order simply propagate at the frequency given in (27a). To calculate the growth rate in this limit,  $k_{ze}^2$  can no longer be neglected compared with  $\gamma$  in  $\gamma_-$ . In (26b) we assume  $k_{ze}^2 \ll \gamma$  so that

$$k_{rc} = (m^2 + \lambda^2)^{1/2} - \frac{\lambda^2}{(m^2 + \lambda^2)^{1/2}} \frac{k_{ze}^2}{2\gamma}$$

and from (26a)

$$\gamma = (-i\omega_0 + m\gamma_0) \frac{m}{(m^2 + \lambda^2)^{1/2}} - k_{ze}^2 \frac{m^2 + \lambda^2/2}{(m^2 + \lambda^2)}. \quad (28a)$$

The  $\underline{E} \times \underline{B}$  gradient drift instability is stable for

$$k_{ze}^2 \frac{m^2 + \lambda^2/2}{(m^2 + \lambda^2)^{1/2}} > m^2 \gamma_0. \quad (28b)$$



Note that this inequality again implies that the lowest poloidal mode numbers are stabilized first. The assumption that  $\gamma \gg \kappa_z^2 \rho_{ie}$  is valid at the stability point for

$$\kappa_z \rho_s \gg (v_n/v_s) v_{in}^2 / \Omega_i^2, \quad (28c)$$

where  $v_s = [T/\pi_1]^{1/2}$  is the sound velocity and  $\rho_s = v_s/\Omega_i$  is the effective ion Larmor radius. Also, the neglect of the terms proportional to  $v_{in}/\Omega_i$  in (28a) and (28b) near the stability point are valid in this same limit. Thus, when (28c) is satisfied, finite temperature effects stabilize the  $\underline{E} \times \underline{B}$  instability, and the stability point is given in (28b). In the opposite limit

$$\kappa_z \rho_s \ll (v_n/v_s) v_{in}^2 / \Omega_i^2, \quad (29)$$

the cold plasma effects stabilize the mode and the stability point is given in (25).

To verify our analytic results for  $T \neq 0$ , and to extend these results to  $\theta \neq 0$ , we present numerical solutions to the complete dispersion equation [(12) and (19)]. In Fig. 3 we plot (a) the growth rate  $\gamma_r$  vs.  $\lambda$ , and (b) the real frequency  $\omega_r$  vs.  $\lambda$  for the parameters  $v_i/\Omega_i = 0.025$ ,  $M = 2$ ,  $m D_{ie} / \alpha r_{c0}^2 \gamma_0 = 5.0 \times 10^{-4}$ , and several values of  $\theta$ : (A)  $\theta = 0^\circ$ , (B)  $\theta = 22.5^\circ$ , (C)  $\theta = 45^\circ$ , (D)  $\theta = 67.5^\circ$ , and (E)  $\theta = 90^\circ$ . Note that in the warm plasma limit the mode number  $m$  enters the dispersion relation as  $\gamma/m$ ,  $\lambda/m$  and  $D_i$  so that Fig. 3 is not valid for all  $m$ .

In Fig. 3 we note several similarities to Fig. 2. The growth rate  $\gamma_r$  decreases as  $\theta$  or  $k_z$  increases and the mode is stable ( $\gamma_r < 0$ ) for sufficiently large  $k_z$ . On the other hand, for  $T = 0$  (or  $D_{ie} = 0$ ) the mode stabilizes at a much smaller value of  $k_z$  (other parameters being equal) and the stability point is sensitive to  $\theta$ . The arrow denotes the value of  $k$  for marginal stability ( $\gamma_r = 0$ ) based on (28b) for  $\theta = 0^\circ$ . This value ( $k/m = 15.8$ ) is in very good agreement with the numerical result  $k/m = 15.5$ .

It is also illuminating to calculate the damping rate of the instability in the limit of very large  $k_z$ . There are two modes of the system. The first damps at the ion diffusion rate,

$$\gamma = - |k_r|^2 D_{\perp} \quad (30a)$$

where

$$k_r = -i k_\theta \frac{\Omega_i}{v_{in}} \frac{M}{M+2} \quad (30b)$$

and  $D_{\perp} = (cT/eB)v_{in}/\Omega_i$  is the ion diffusion coefficient based on the total temperature  $T = T_e + T_i$ . The second damps at the electron parallel diffusion rate

$$\gamma = - k_z^2 D_{ie}. \quad (31)$$

## V. SOLUTION OF THE POLOIDAL EIGENVALUE EQUATION

In Section III we derived a local dispersion equation [(12) and (19)] which was solved to obtain the growth rate  $\gamma(\theta)$  in Section IV. This local growth rate is peaked on the backside of the cloud ( $\theta = 0$ ). Since the equilibrium depends on the angle  $\theta$ , the poloidal mode number  $m$  is not a good quantum number. In general, the equilibrium will couple the various poloidal modes and under some circumstances these modes may couple to form an exponentially growing eigenmode. We now investigate under what conditions the gradient drift instability forms an eigenmode as it grows on the cylindrical waterbag.

Such eigenmodes can exist if solutions  $\tilde{\phi}(\theta)$  can be constructed which are localized around some angle  $\theta_0$ . To obtain these solutions we take the growth rate in (12) and (19) to be independent of  $\theta$  so that the dispersion equation yields  $k_\theta(\theta, \gamma)$ . We then make the identification  $k_\theta = -i r_c^{-1} \partial/\partial\theta$  to obtain a differential equation for  $\tilde{\phi}(\theta)$ .

In the limit  $\lambda^2 = \alpha k_z^2 r_c^2 \ll 1$ , (12) yields  $k_{r\pm} = k_\theta$  and the local dispersion equation in (19) becomes

$$\gamma_0 \partial \tilde{\phi} / \partial \theta - i \gamma \exp(i\theta) \tilde{\phi} + \omega_0 \tilde{\phi} = 0. \quad (32)$$

Since this equation is first order in  $\partial/\partial\theta$ , there are no bounded solutions so that there are no exponentially growing global eigenmodes when  $k_z$  is small. This result is consistent with previous calculations in the limit  $k_z = 0$  where it was shown that the energy always cascades to lower poloidal mode numbers (Overman et al., 1983). The local growth rate [see (21)] is the approximate rate of increase of the amplitude of a broad spectrum of modes centered around  $k_\theta$ .

We now consider the case where  $\lambda^2 \gg 1$  while  $k_z$  is sufficiently small so that the terms proportional to  $v_{in}/\Omega_1$  in (12a) and (12b) can be neglected. We also assume that  $\gamma \gg k_z^2 D_{ie}$ . With these constraints (12a) and (12b) simplify to

$$k_{\perp} = \alpha^{1/2} k_z$$

and (19) yields the equation

$$\gamma_0 \cos\theta \frac{\partial^2}{\partial \theta^2} \tilde{\phi} + [\omega_0 + \gamma_0 \lambda \sin\theta] \frac{\partial}{\partial \theta} \tilde{\phi} + \gamma \lambda \tilde{\phi} = 0. \quad (33)$$

We simplify this equation by defining a new dependent variable

$$\tilde{\phi} = \hat{\phi} \exp[-f(\theta)]$$

with  $\partial f / \partial \theta = [\omega_0 + \gamma_0 \lambda \sin\theta] / 2\gamma_0 \cos\theta$  and find that

$$\partial^2 \hat{\phi} / \partial \theta^2 + V(\theta) \hat{\phi} = 0 \quad (34a)$$

where the potential  $V(\theta)$  is given by

$$V(\theta) = \left\{ \left( \frac{\gamma}{\gamma_0} \cos\theta - \frac{1}{2} \right) \lambda - \frac{\omega_0}{2\gamma_0} \sin\theta - \frac{1}{4\gamma_0^2} [\omega_0 + \gamma_0 \lambda \sin\theta]^2 \right\} \frac{1}{\cos^2\theta}. \quad (34b)$$

We first consider the limit  $T = 0$  and expand  $V(\theta)$  around  $\theta = 0$ .

$$V = \lambda \left( \frac{\gamma}{\gamma_0} - \frac{1}{2} \right) - \frac{1}{4} \lambda^2 \theta^2. \quad (35)$$

The bound state solutions for this potential have eigenvalues

$$\gamma = \gamma_0 (n + \frac{1}{2}), \quad (36)$$

where  $n$  is a nonnegative integer. The mode is localized on the backside of the cloud and has an angular width  $\Delta\theta = \lambda^{-1/2} \ll 1$ , which decreases with increasing  $\kappa_z$  (see Fig. 4a). Thus, the expansion of  $V$  around  $\theta = 0$  is valid for  $\lambda \gg 1$ . Our earlier assumption that the mode is localized near  $r_0$  is also valid since  $k_r r_0 = \lambda \gg 1$ . Note also that higher order modes  $n$ , which have more structure in the poloidal direction, have larger growth rates. This result is consistent with local theory where  $\gamma$  increases with the poloidal mode number  $m$ .

An important point to emphasize is that although the solution with  $n = 0$  has a angular width  $\Delta\theta \ll 1$ , it is nevertheless the lowest order mode which can exist when  $\lambda \gg 1$ . In other words, there is no mode with  $\partial/\partial\theta \sim 1$ .

The potential  $V$  in (34) is modified by finite thermal effects when  $\omega_0 = \gamma_0 \lambda$ . Comparing the magnitude of the various terms in (34), we find that the term proportional to  $(4\gamma_0^2)^{-1}$  is of order  $\lambda \gg 1$  larger than the remaining terms unless the terms within the bracket cancel. We therefore look for a mode localized around the angle  $\theta_0$  defined by

$$\sin\theta_0 = -\omega_0/\gamma_0 \lambda. \quad (37)$$

Near  $\theta_0$  the potential assumes the form

$$V(\theta) = \lambda \frac{\gamma}{\gamma_0} \frac{1}{\cos\theta_0} - \frac{1}{2} \lambda - \frac{1}{4} \lambda^2 (\theta - \theta_0)^2. \quad (38)$$

The bounded solutions have eigenvalues

$$\gamma = \gamma_0(n+1) \left[ 1 - \frac{\omega_0^2}{\gamma_0^2 \lambda^2} \right]^{1/2}, \quad (39)$$

where  $n$  is again a nonnegative integer. When  $\omega_0 \ll \gamma_0 \lambda$ , the growth reduces to the previous zero temperature result in (36). As  $\omega_0$  increases the growth rate decreases until the mode becomes stable at  $\omega_0 = \gamma_0 \lambda$  or

$$\alpha^{1/2} k_z \frac{cT}{eB} > \frac{2}{M+2} v_n. \quad (40)$$

The reduction of the growth rate in (39) is a consequence of the localization of the mode at an angle  $\theta_0 \neq 0$ . The growth rate in (39) can be rewritten as

$$\gamma = \gamma_0(n+1) \cos\theta_0.$$

At the marginal stability point,  $\theta_0 = \pi/2$ , i.e., the mode localizes in a region where there is no driving force. Above the threshold in (40) there are no bounded solutions to (34) since  $\theta_0$  moves into the complex plane. The physics behind the localization of the mode can be readily understood and is presented in the next section.

## VI. SUMMARY AND CONCLUSION

We have investigated the influence of finite parallel wavelength on the stability of a cylindrical plasma cloud. We first derived a dispersion relation for the local growth rate  $\gamma(\theta)$  of the  $\mathbf{E} \times \mathbf{B}$  gradient drift instability, where  $\theta$  is the poloidal angle ( $\theta = 0$  on the "backside" of the cloud as shown in Fig. 1). For sufficiently large values of the parallel wavenumber  $k_z$  the local growth rate is negative for all values of  $\theta$ . In the cold plasma limit,

$$k_z \rho_s < (v_n/v_s) v_{in}^2 / \Omega_i^2, \quad (41)$$

the stability criterion is given in (25) while in the warm plasma limit [the inequality in (41) is reversed], the stability condition is given in (28b). In both cases the lowest poloidal mode numbers are stabilized at the smallest values of  $k_z$ . In (41) we have defined the sound velocity as  $v_s$  and the effective Larmor radius  $\rho_s = v_s / \Omega_i$ .

We have also investigated under what conditions exponentially growing poloidal eigenmodes can exist. In the limit

$$\lambda^2 = \alpha k_z^2 r_c^2 \ll 1, \quad (42)$$

with  $\alpha = \Omega_e \Omega_i / v_e v_{in}$ , there are no exponentially growing solutions. In this limit the energy cascades to lower poloidal mode numbers as the instability grows as found by Overman et al. (1983). When  $\lambda^2 \gg 1$ , the gradient drift instability grows exponentially in time and the lowest order eigenmode becomes localized on the "backside" of the plasma cloud with a width  $\theta \sim \lambda^{-1/2} \ll 1$ . Thus, the cascade of energy to lower mode numbers no longer

takes place when  $k_z$  is sufficiently large. The structure of the mode for this case is illustrated in Fig. 4a. This figure is drawn in the rest frame of the circular cloud. The neutral wind is moving from the left to right with a uniform velocity  $2V_n/(M+2)$  while the background plasma flows to the left with a velocity  $V_b$ . The dashed line illustrates the amplitude of the lowest order mode. Higher order modes with one or more nodes as a function  $\theta$  also exist. There is no mode with  $\theta = 0$ .

At still larger values of  $k_z$  the unstable mode becomes localized at a finite angle  $\theta_0$  given by

$$\sin \theta_0 = -V_d/V_b \quad (43)$$

where

$$V_d = M \frac{cT}{eB} \alpha^{1/2} k_z$$

is the effective diamagnetic velocity and

$$V_b = \frac{2M}{M+2} V_n$$

with  $M = n_c/n_b$ . For a waterbag distribution the density scale length which usually appears in definition of the diamagnetic drift velocity is replaced by the radial scale length of the mode, which in the limit  $\lambda \gg 1$  is  $\alpha^{-1/2} k_z^{-1}$ . For  $V_d > V_b$  or

$$\alpha^{1/2} k_z \frac{cT}{eB} > \frac{2}{M+2} V_n \quad (44)$$



the mode is completely stable. The physical mechanism which causes the localization at  $\theta_0$  as well as the stabilization is illustrated in Fig. 4b. In the local dispersion relation the diamagnetic effects cause the mode to propagate in the poloidal direction with a phase velocity,

$$v_p = V_d / (M+2).$$

The velocity of the background plasma just outside the cloud (in the reference frame of the cloud) is given by

$$\underline{V} = V_b \sin\theta \hat{\theta}.$$

The convection of the background plasma past the cloud causes the mode to propagate with a phase velocity,

$$v_p = V_b \sin\theta / (M+2)$$

These two velocities balance to produce a nonpropagating mode at the angle  $\theta_0$  defined by (43). The dashed line in Fig. 4b illustrates the localization of the mode in this case. When the diamagnetic velocity everywhere exceeds the flow of the background plasma around the cloud the gradient drift instability is convectively stabilized. Convective amplification of perturbations in this finite  $k_z$  limit are also not important. Unlike the limit where  $k_z = 0$ , the rate of propagation of the mode from the unstable backside of the cloud to the stable frontside exceeds the rate of growth of the mode.

Finally, we apply the results of our poloidal eigenfunction analysis to the structuring of barium clouds and discuss their application to the so-called "striation freezing" phenomenon (Linson and Meltz, 1972). Basically, it has been observed that barium clouds released in the ionosphere structure because of the  $\mathbf{E} \times \mathbf{B}$  gradient drift instability and develop field-aligned striations. The first generation of striations can also undergo further structuring, at times, and break up into even smaller striations (i.e., smaller in size transverse to  $\mathbf{B}_0$ ). This process, known as bifurcation, appears to continue until a minimum transverse scale size is reached (which we refer to as the "freezing scale length"). For barium clouds released at altitudes  $\sim 130$  km the freezing scale length is roughly 400 m (Prettie, 1985). A number of studies have been carried out which address this problem (Francis and Perkins, 1975; McDonald et al., 1981; Zalesak et al., 1984; Drake et al., 1985; Sperling and Glassman, 1985). Rather than describe the detailed processes proposed in these papers, it is sufficient to note that there is no generally accepted model of striation freezing at this time; each model has its merits and shortcomings. Although the theory presented in this paper does not explicitly predict a "freezing scale length", we can make an estimate of this size based on (44) and a simple physical argument. The free parameter in (44) is  $k_z$ ; all other parameters are determined by ionospheric conditions. Thus, we need to make a reasonable estimate of  $k_z$ . We do this by noting that transverse perturbations can map parallel to the magnetic field. The relationship between parallel and perpendicular scale lengths is approximately given by

$L_{\parallel} \sim (\sigma_{\parallel} / \sigma_{\perp})^{1/2} L_{\perp} = \alpha^{1/2} L_{\perp}$  where  $L$  and  $\sigma$  refer to the scale size and conductivity, respectively (Farley, 1959; Goldman et al., 1976). Assuming that  $k_z \sim L_{\parallel}^{-1} \sim (\alpha^{1/2} L_{\perp})^{-1}$  we find that (44) can be written as

$$L_{\perp} < \frac{M+2}{2} \frac{cT}{eB} \frac{1}{V_n} . \quad (45)$$

Thus, (45) suggests that barium cloud striations with transverse dimensions smaller than  $L_{\perp}$  would be stable to further structuring by the  $\mathbf{E} \times \mathbf{B}$  gradient drift instability. For typical barium cloud ionospheric parameters at 180 km, i.e.,  $T = T_e + T_i = 0.2$  eV,  $B = 0.5$  G,  $V_n = 50$  m/sec, and  $M = 2 \cdot 10^3$ , we find that  $L_{\perp} = 160-480$  m which is consistent with observations. Of course this result is predicated on the assumption that  $k_z = (\alpha^{1/2} L_{\perp})^{-1}$  which, although plausible, is somewhat ad hoc. In order to remove this assumption it is necessary to consider the finite length of a barium cloud which introduces a physical parameter which will remove the arbitrariness associated with  $k_z$ . We are presently developing such a model.

#### ACKNOWLEDGMENTS

We thank Steve Zalesak and Norm Zabusky for helpful discussions. This research has been supported by the Defense Nuclear Agency.



# APPENDIX: Jump Condition for $\hat{\phi}$

In this appendix we show that the continuity of the tangential  $\nabla\phi$  across the boundary of the plasma cloud also yields (16). The unit vector  $\hat{e}_n$  the outward normal of the surface of the cloud boundary, is given by

$$\hat{e}_n = - \frac{\nabla n}{|\nabla n|} = - \frac{\nabla(n_0 + \bar{n})}{|\nabla(n_0 + \bar{n})|} = \hat{e}_r - \frac{1}{n_c} \nabla N(\theta, z, t). \quad (A1)$$

The two components of the tangential electric field are given by

$$E_1 = \hat{e}_z \times \hat{e}_n \cdot \nabla \phi \quad (A2)$$

$$E_2 = \hat{e}_\theta \times \hat{e}_n \cdot \nabla \phi. \quad (A3)$$

Linearizing E, we find

$$\begin{aligned} \bar{E}_1 &= \hat{e}_z \times \hat{e}_r \cdot \nabla \hat{\phi} - \hat{e}_z \times \nabla N \cdot \nabla \phi_{0c} / n_c \\ &= ik_\theta \hat{\phi} + ik_\theta \hat{N} \hat{\phi}'_{0c} / n_c. \end{aligned} \quad (A4)$$

The continuity of  $\bar{E}_1$  across the boundary therefore requires

$$\hat{\phi}^+ + \hat{N} \hat{\phi}'_{0c} / n_c = \hat{\phi}^-, \quad (A5)$$

which is equivalent to (16). The requirement that  $\bar{E}_2$  be continuous across the boundary yields the same condition.



## REFERENCES

- Chaturvedi, P.K., and S.L. Ossakow, Nonlinear stabilization of the  $E \times B$  gradient drift instability in ionospheric plasma clouds, J. Geophys. Res., 84, 419, 1979.
- Drake, J.F., J.D. Huba, and S.T. Zalesak, Finite temperature stabilization of the gradient drift instability in barium clouds, J. Geophys. Res., 90, 5227, 1985.
- Farley, D.T., Jr., A theory of electrostatic fields in a horizontally stratified ionosphere subject to a vertical magnetic field, J. Geophys. Res., 64, 1225, 1959.
- Francis, S.H., and F.W. Perkins, Determination of striation scale sizes for plasma clouds in the ionosphere, J. Geophys. Res., 80, 3111, 1975.
- Goldman, S.R., L. Baker, S.L. Ossakow, and A.J. Scannapieco, Striation formation associated with barium clouds in an inhomogeneous ionosphere, J. Geophys. Res., 81, 5097, 1976.
- Hoh, F.C., Instability of Penning-type discharges, Phys. Fluids, 6, 1184, 1963.
- Huba, J.D., S.L. Ossakow, P. Satyanarayana, and P.N. Guzdar, Linear theory of the  $E \times B$  instability with an inhomogeneous electric field, J. Geophys. Res., 88, 425, 1983.
- Huba, J.D., and S.T. Zalesak, Long wavelength limit of the  $E \times B$  instability, J. Geophys. Res., 88, 10,263, 1983.
- Keskinen, M.J., S.L. Ossakow, and P.K. Chaturvedi, Preliminary report of numerical simulations of intermediate wavelength  $E \times B$  gradient drift instability in ionospheric plasma clouds, J. Geophys. Res., 85, 3485, 1980.

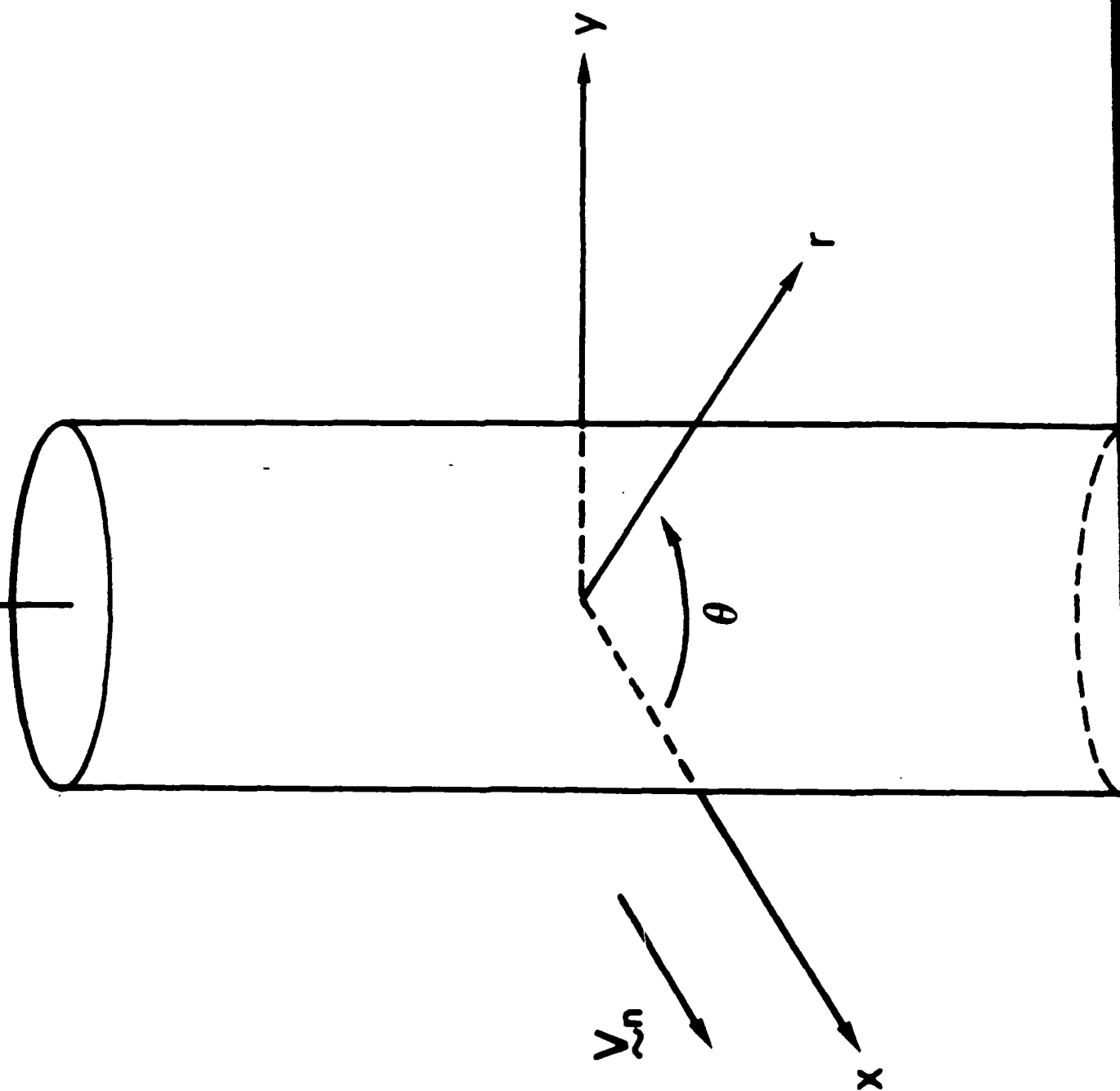
- Keskinen, M.J., and S.L. Ossakow, Theories of high latitude ionospheric irregularities: A review, Radio Sci., 18, 1077, 1983.
- Linson, L.M. and G. Meltz, Theory of ion cloud dynamics and morphology, in Analysis of Barium Clouds, Rep. RADC-TR-72-736, Vol. 1, chap. 5, Avco Everett Res. Lab., Everett, Mass., 1972.
- Linson, L.M., and J.B. Workman, Formation of striations in ionospheric plasma clouds, J. Geophys. Res., 75, 3211, 1970.
- McDonald, B.E., M.J. Keskinen, S.L. Ossakow, and S.T. Zalesak, Computer simulation of gradient drift instability processes in Operation Aefria, J. Geophys. Res., 85, 2143, 1980.
- McDonald, B.E., S.L. Ossakow, S.T. Zalesak, and N.J. Zabusky, Scale sizes and lifetimes of F region plasma cloud striations as determined by the condition of marginal stability, J. Geophys. Res., 86, 5775, 1981.
- Overman, E.A., N.J. Zabusky, and S.L. Ossakow, Ionospheric plasma cloud dynamics via regularized contour dynamics, I, Stability and nonlinear evolution of one-contour models, Phys. Fluids, 26, 1139, 1983.
- Perkins, F.W., N.J. Zabusky, and J.H. Doles III, Deformation and striation of plasma clouds in the ionosphere, 1, J. Geophys. Res., 78, 697, 1973.
- Perkins, F.W., and J.H. Doles III, Velocity shear and the  $E \times B$  instability, J. Geophys. Res., 80, 211, 1975.
- Prettie, C.W., U-Shaped curve constant determined by barium release measurements, Berkeley Research Assoc. Report, PD-BRA-84-320R, 1985.
- Scannapieco, A.J., S.L. Ossakow, S.R. Goldman, and J.M. Pierre, Plasma cloud late time striation spectra, J. Geophys. Res., 81, 6037, 1976.
- Shiau, J.N., and A. Simon, Onset of striations in barium clouds, Phys. Rev. Lett., 29, 1664, 1972.



- Simon, A., Instability of a partially ionized plasma in crossed electric and magnetic fields, Phys. Fluids, 6, 382, 1963.
- Smythe, W.R., Static and Dynamic Electricity, McGraw-Hill, New York, 1950, p. 65.
- Sperling, J.L., Finite parallel wavelengths and ionospheric structuring, J. Geophys. Res., 88, 4075, 1983.
- Sperling, J.L., The evanescence of striation parameters along the geomagnetic field, J. Geophys. Res., 89, 6793, 1984.
- Sperling, J.L., J.F. Drake, S.T. Zalesak, and J.D. Huba, The role of finite parallel length on the stability of barium clouds, J. Geophys. Res., 89, 10,913, 1984.
- Sperling, J.L., and A.J. Glassman, Striation eigenmodes along the geomagnetic field and eigenvalues in the limit of strong ion-neutral collisions, J. Geophys. Res., 90, 2819, 1985.
- Volk, H.J., and G. Haerendel, Striations in ionospheric ion clouds, 1, J. Geophys. Res., 76, 4541, 1971.
- Zabusky, N.J., J.H. Dolis, III, and F.W. Perkins, Deformation and striation of plasma clouds in the ionosphere 2. Numerical simulation of a nonlinear two-dimensional model, J. Geophys. Res., 78, 711, 1973.
- Zalesak, S.T., P.K. Chaturvedi, S.L. Ossakow, and J.A. Fedder, Finite temperature effects on the evolution of ionospheric barium clouds in the presence of a conducting background ionosphere, 1. The simplest case: Incompressible background ionosphere, equipotential magnetic field lines, and an altitude invariant neutral wind, J. Geophys. Res., 90, 4299, 1985.
- Zalesak, S.T., and J.D. Huba, On the linear stability of two-dimensional barium clouds I. The inviscid case, NRL Memo Rept. 5312, 1984.

## FIGURE CAPTIONS

- Fig. 1) Cylindrical geometry and plasma configuration used in the analysis.
- Fig. 2) Plot of  $\gamma/m\gamma_0$  vs.  $\lambda/m$  where  $\lambda = \alpha^{1/2} k_z r_c$ . The parameters used are  $v_i/\Omega_i = 0.025$ ,  $M = 2$ ,  $D_{ie} = 0$  (i.e.,  $T = 0$ ), and several values of  $\theta$ : (A)  $\theta = 0^\circ$ , (B)  $\theta = 22.5^\circ$ , (C)  $\theta = 45^\circ$ , (D)  $\theta = 67.5^\circ$ , and (E)  $\theta = 90^\circ$ . The arrow denotes the value of  $\lambda$  given by (25a) for marginal stability. (a) Plot of the growth rate  $\gamma_r/m\gamma_0$  vs.  $\lambda/m$ . (b) Plot of the real frequency  $\omega_r/m\gamma_0$  vs.  $\lambda/m$ .
- Fig. 3) Plot of  $\gamma/m\gamma_0$  vs.  $\lambda/m$ . The parameters are the same as in Fig. 2 except we assume  $T \neq 0$  and take  $mD_{ie}/\alpha r_c^2 \gamma_0 = 5.0 \times 10^{-4}$ . (a) Plot of the growth rate  $\gamma_r/m\gamma_0$  vs.  $\lambda/m$ . (b) Plot of the real frequency  $\omega_r/m\gamma_0$  vs.  $\lambda/m$ .
- Fig. 4) Schematic of the plasma cloud, flow field, and position of a growing eigenfunction: (a)  $T = 0$ ; (b)  $T \neq 0$ . See text for a detailed description.



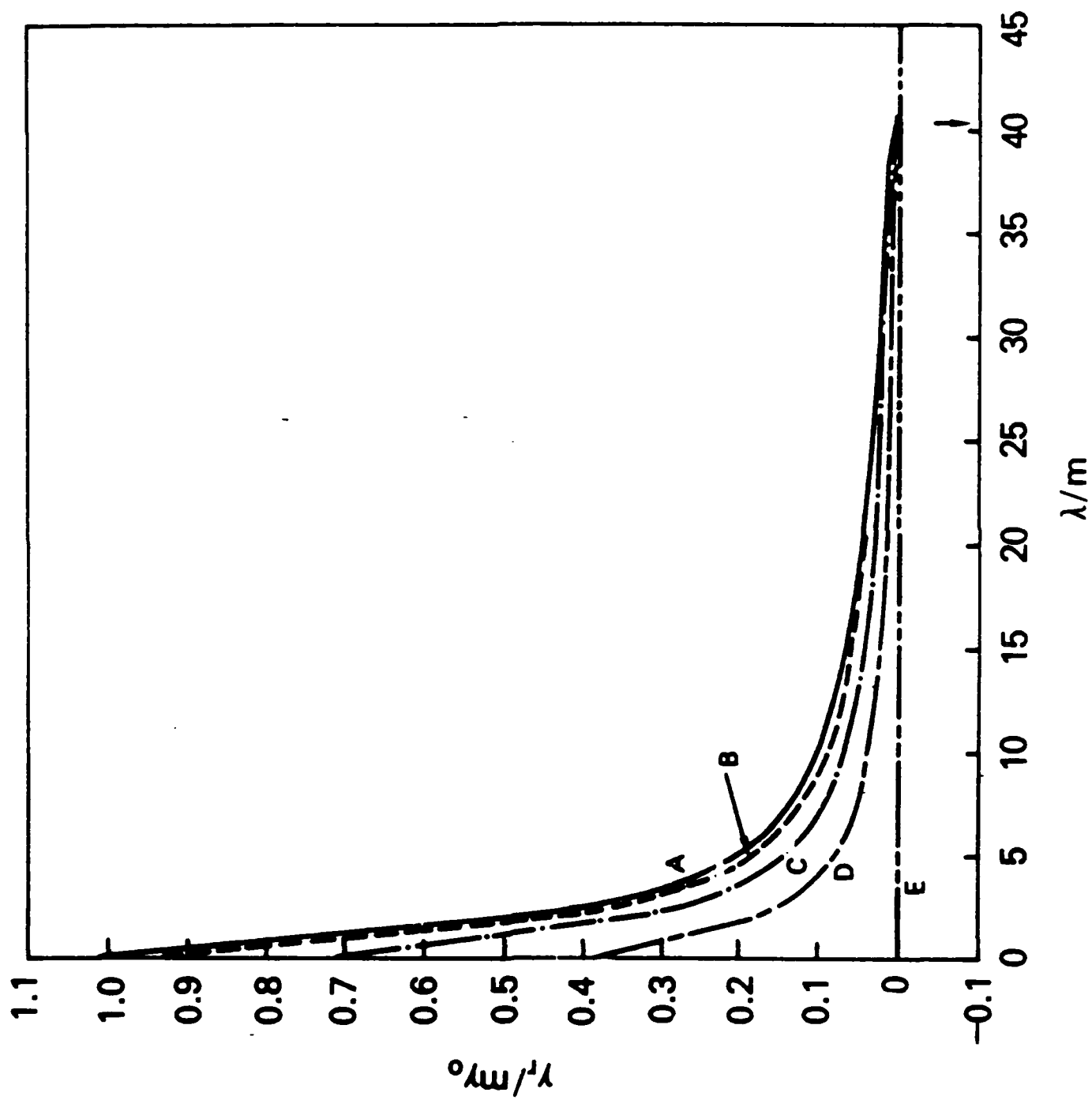


Figure 2a

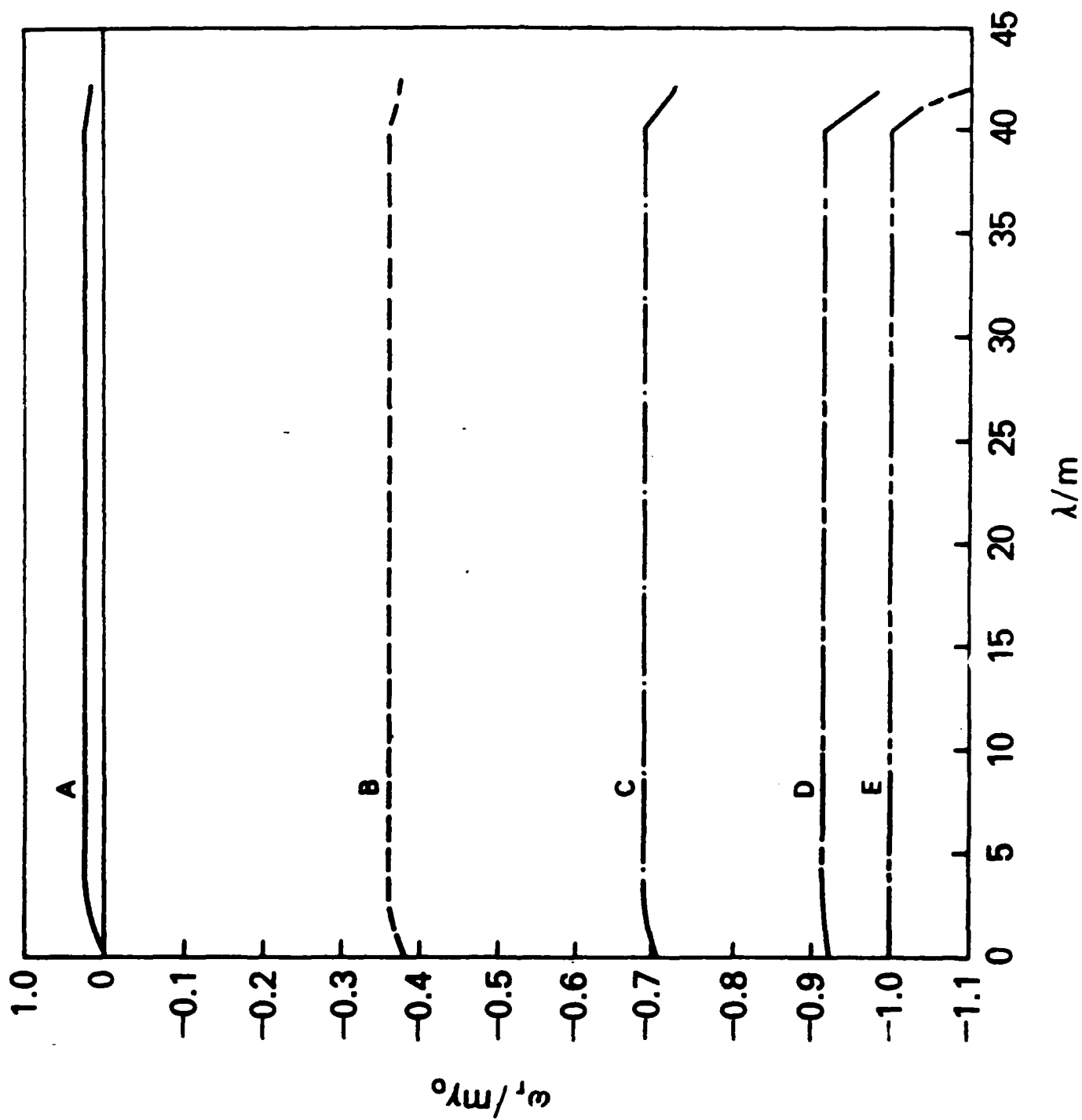


Figure 2b  
M-39

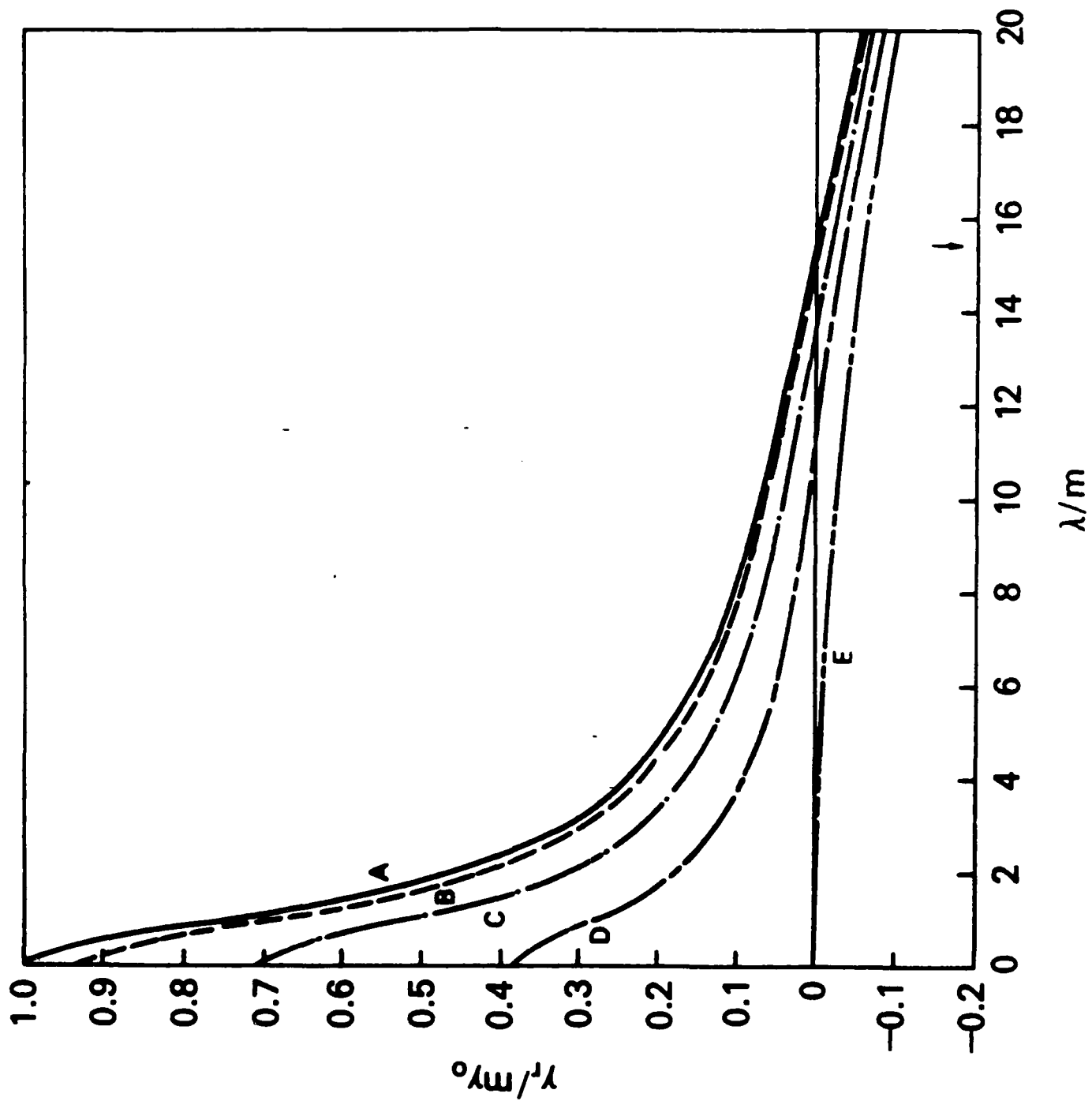


Figure 3a  
M-40

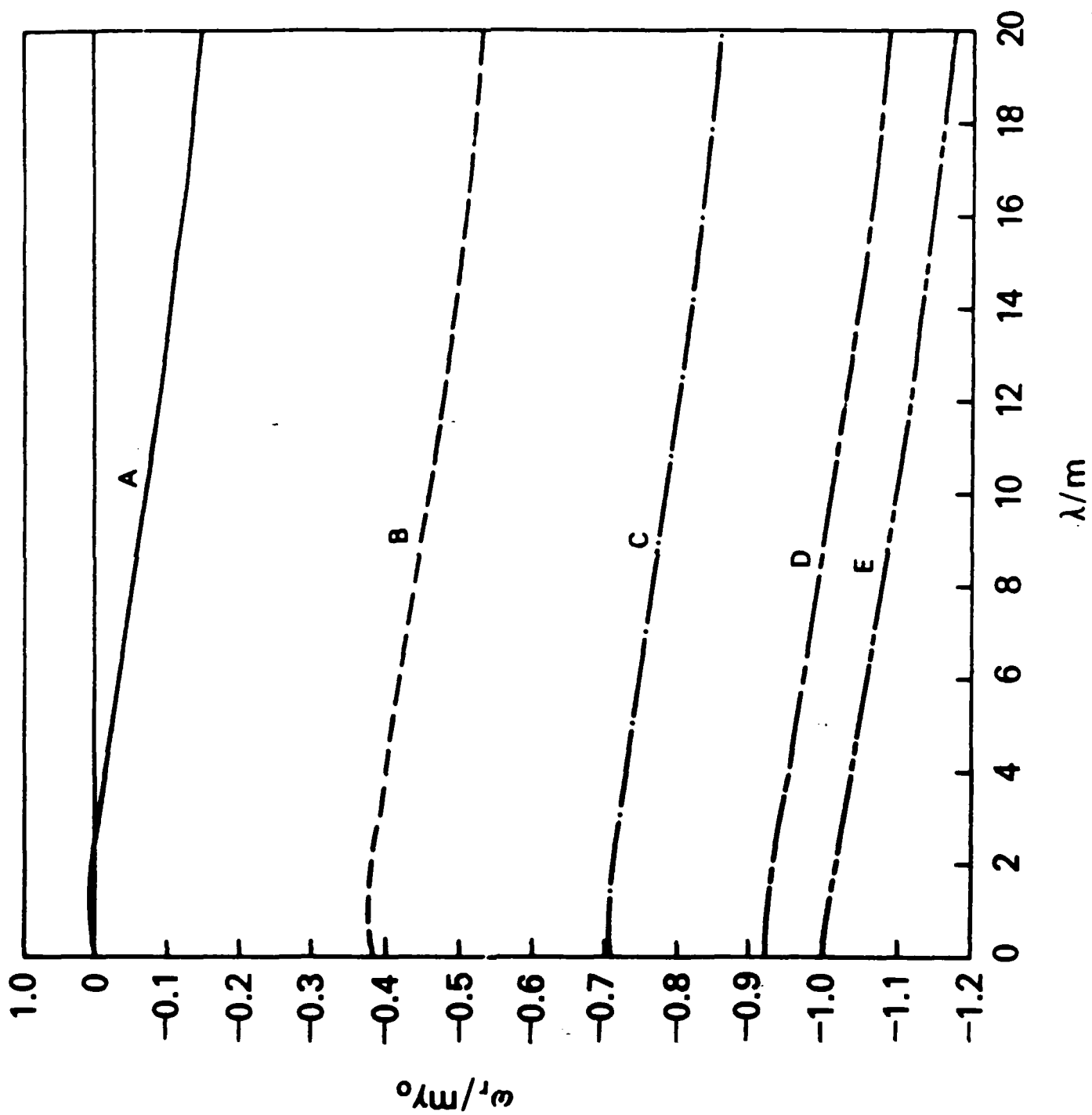


Figure 3b  
M-41

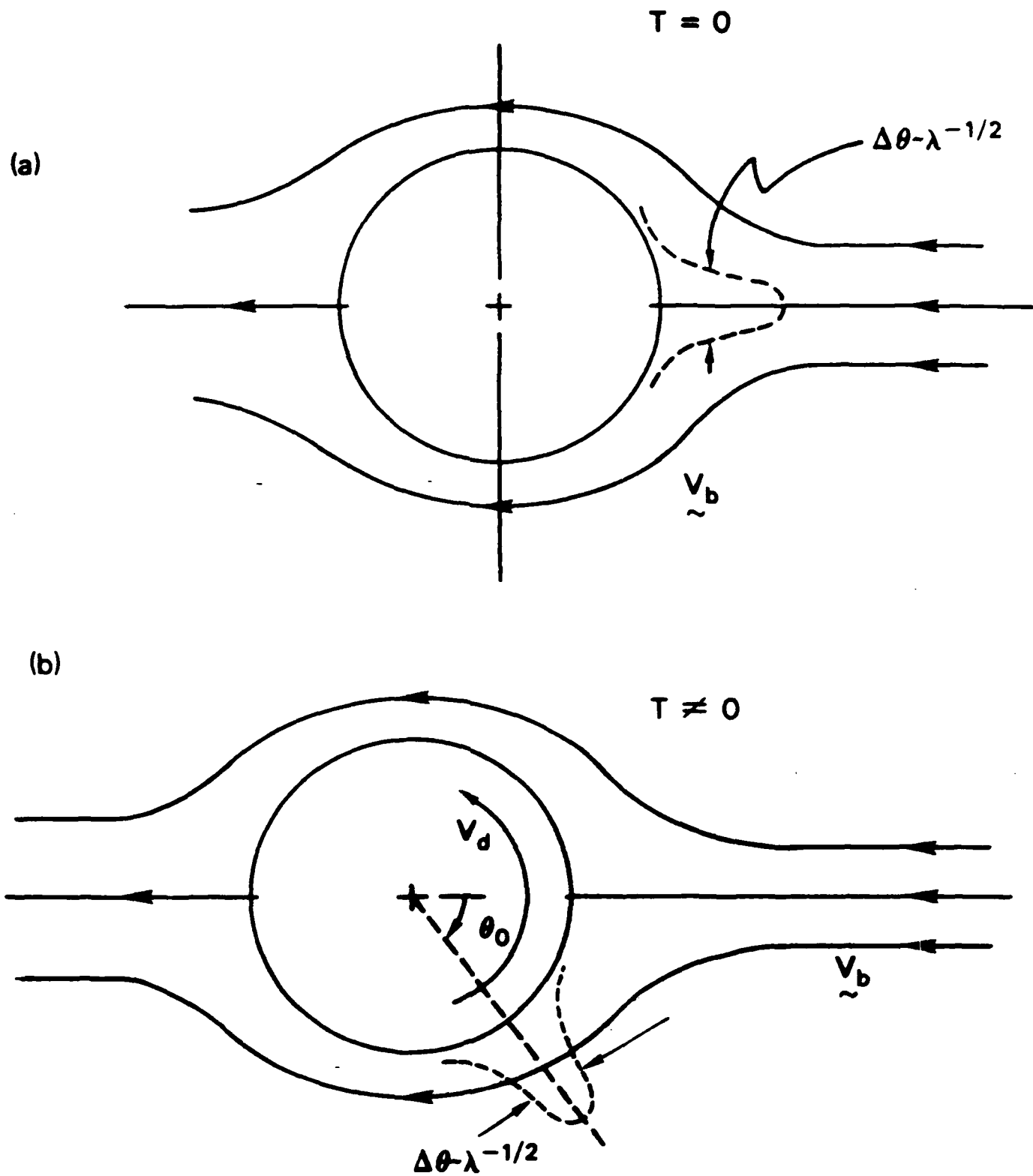


Fig. 4



**APPENDIX N**

**Spectral Characteristics of Interchange Turbulence**

**A.B. Hassam and W. Hall  
Science Applications International Corporation**

**J.D. Huba and M.J. Keskinen  
Naval Research Laboratory**



SPECTRAL CHARACTERISTICS OF INTERCHANGE TURBULENCE

A.B. Hassam<sup>(a)</sup> and W. Hall<sup>(b)</sup>  
Science Applications International Corporation  
McLean, VA 22102

and

J.D. Huba and M.J. Keskinen  
Geophysical and Plasma Dynamics Branch  
Plasma Physics Division  
Naval Research Laboratory  
Washington, DC 20375-5000

March 1986

- (a) Permanent address: Department of Physics and Astronomy, University of Maryland, College Park, MD 20742
- (b) Present address: Department of Physics, Columbia University, New York, NY

# ABSTRACT

The spectral characteristics of turbulence associated with the two-dimensional magnetized Rayleigh-Taylor instability in the presence of a background neutral gas are studied. Particular attention is paid to comparing the electrostatic potential spectra obtained in the ion-neutral collision-dominated case with the spectra from the ion inertia-dominated case. The time-averaged one-dimensional spectra along  $k_x$  and  $k_y$  for the collisional case are found to be  $P_x \propto k_x^{-3.7 \pm 0.3}$  and  $P_y \propto k_y^{-4.6 \pm 0.3}$ , respectively, where  $x$  is the direction of the density gradient and gravity. Correspondingly, the spectra for the inertial case are given by  $P_x \propto k_x^{-3.8 \pm 0.2}$  and  $P_y \propto k_y^{-3.8 \pm 0.2}$ . Thus, the potential spectrum in the collisional case shows a marked anisotropy in contrast to that of the inertial case which is isotropic and exhibits Kolmogorov scaling. The anisotropy in the collisional case is attributed to the frictional nature of the turbulence and the suppression of inertial overshoots. Application of these results to ionospheric turbulence is discussed.

## I. INTRODUCTION

It is well known that ionospheric turbulence can arise from interchange instabilities [Ossakow, 1979; Fejer and Kelley, 1980]. The Rayleigh-Taylor instability is believed to cause the intense nighttime equatorial F region turbulence known as equatorial spread F [Ossakow, 1981; Kelley and McClure, 1981], while the  $\underline{E} \times \underline{B}$  gradient drift instability has been invoked to explain high-latitude ionospheric irregularities [Keskinen and Ossakow, 1983], the rapid structuring of barium clouds [Linson and Workman, 1970], and turbulence in equatorial electrojet [Ossakow, 1979]. These instabilities are similar in character in that they occur in inhomogeneous plasmas and act to interchange high and low plasma density regions. However, they have different driving mechanisms: the Rayleigh-Taylor instability is driven by the gravitational force, while the  $\underline{E} \times \underline{B}$  gradient drift instability is driven by an ambient electric field or a neutral wind. A considerable amount of research has been devoted to the study of these instabilities and their application to ionospheric turbulence. An understanding of saturation amplitudes and power spectral characteristics is essential in order to make comparisons with ionospheric observations.

Interchange instabilities, as they are applied to the ionosphere, can be divided into two categories: collisional and inertial. In the collisional limit the ion-neutral collision frequency is dominant and  $\nu_{in} \gg \omega$ , where  $\nu_{in}$  is the ion-neutral collision frequency and  $\omega$  is the wave frequency; in the inertial limit,  $\omega \gg \nu_{in}$  and neutral collisions may be neglected. In the ionosphere, the transition from the collisional limit to the inertial limit typically occurs in the altitude regime - 500 km [Huba et al., 1985; Kintner and Seyler, 1985]. This altitude may be

somewhat higher for long wavelength modes ( $\lambda \geq 1$  km) if field-aligned integrated quantities are considered [Farley, 1960; Zalesak et al., 1980; Anderson and Mendillo, 1983; Labelle, 1985]. The bulk of the research on nonlinear interchange instabilities in the ionosphere (both theory and simulation) has been restricted to the collisional domain, although it has recently been shown [Mitchell et al., 1985] that inertial effects are important for interchange instabilities in the high latitude ionosphere.

In this paper we investigate the nonlinear evolution of interchange instabilities in the collisional and inertial limits. In particular, for a model system described below, we compare the spectral characteristics of collisional turbulence with that of inertial turbulence. We find that the time-averaged one-dimensional potential spectra along  $k_x$  and  $k_y$  for the collisional case are given by  $P_x \propto k_x^{-3.7 \pm 0.3}$  and  $P_y \propto k_y^{-4.6 \pm 0.3}$ , respectively, where  $x$  is the direction of the density gradient and gravity. Correspondingly, the spectra for the inertial case are given by  $P_x \propto k_x^{-3.3 \pm 0.2}$  and  $P_y \propto k_y^{-3.8 \pm 0.2}$ . Thus, the potential spectrum in the collisional case shows a marked anisotropy in contrast to that of the inertial case which is isotropic and exhibits Kolmogorov scaling. From a physical standpoint, one might expect a fundamental difference between the two limits. This is because in the collisional limit ( $v_{in} \gg \omega$ ), inertial effects, namely, acceleration of the fluid or ram pressure forces, are completely overwhelmed by the ion-neutral friction. That is to say, fluid elements instantaneously move at "terminal velocity" where the gravitational driving force is balanced by the friction. In this strongly collisional limit, as heavy fluid falls, it tends to stretch into finger-like structures with steepening at the leading edge but negligible inertial overshoot. A more structured flow is therefore expected with reduced

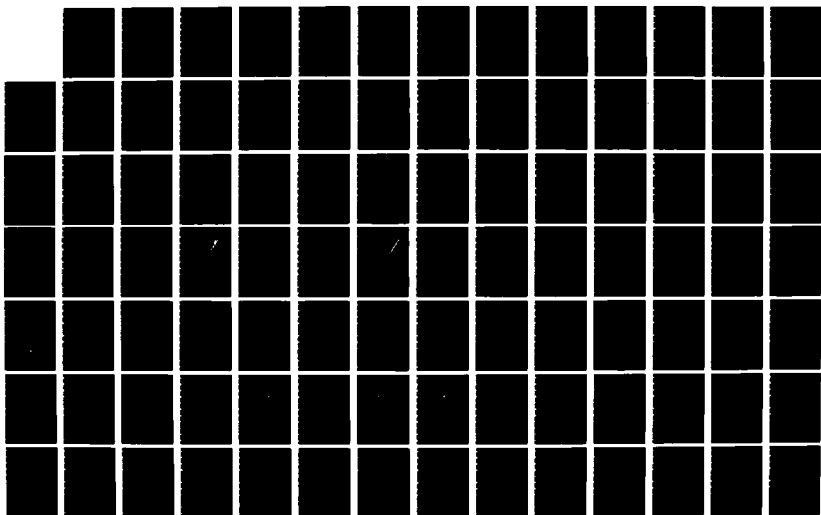
AD-A171 688

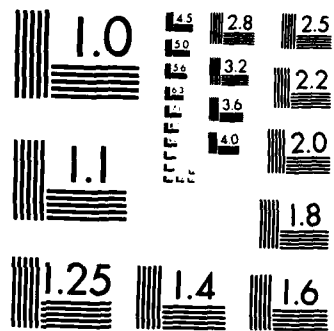
GEOPHYSICAL PLASMAS AND ATMOSPHERIC MOEELING(U) SCIENCE 6/8  
APPLICATIONS INTERNATIONAL CORP MCLEAN VA  
E HYMAN ET AL JUL 86 SAIC-86/1781 N00014-85-C-2018

UNCLASSIFIED

F/G 4/1

NL





MICROCOPY RESOLUTION TEST CHART  
NATIONAL BUREAU OF STANDARDS 1963-A



tendency to isotropize as opposed to the inertial limit ( $v_{in} \ll \omega$ ) where falling fluid elements overshoot, develop swirls, and mix disparate wavelengths. This difference in behavior between the two limits has been observed in numerical simulations of the  $\mathbf{E} \times \mathbf{B}$  gradient drift instability [Mitchell et al., 1985].

The organization of the paper is as follows. In the next section we discuss in some detail the specific model used in our study. In Section III we develop the nonlinear equations. In Section IV we present the results of the numerical solution of the nonlinear equations and examine the power spectral indices for both the collisional and inertial limits. We summarize our findings in Section V.

## II. THE MODEL

The development of a self-consistent and comprehensive theory which describes the spectral characteristics of interchange mode turbulence applied to the ionosphere is, to a large extent, faced with computational difficulties. This is best illustrated by a brief description of the physical system under investigation.

In Fig. 1 we present the plasma configuration and geometry used in the analysis. The ambient magnetic field is in the z-direction ( $\mathbf{B} = B \hat{\mathbf{e}}_z$ ), the gravitational acceleration is in the -x-direction ( $\mathbf{g} = -g \hat{\mathbf{e}}_x$ ), and the density is inhomogeneous in the x-direction ( $n = n_0(x)$  and  $n_0^{-1} \partial n_0 / \partial x > 0$ ). For this situation the plasma is unstable to the Rayleigh-Taylor instability since  $\mathbf{g} \cdot \nabla n_0 < 0$ . For example, in the inertial (i.e., collisionless) limit, the growth rate of the instability is approximately given by

$$\gamma = \begin{cases} (g/L_n)^{1/2} - k_y^2 D, & k_y L_n \gg 1 \\ (k_y g)^{1/2}, & k_y L_n \ll 1 \end{cases}$$

where  $L_n = [n_0^{-1} \partial n_0 / \partial x]^{-1}$  is the scale length of the density gradient,  $k_y$  is the wavenumber in the  $y$  direction, and  $D$  is the diffusion coefficient. For modes  $k_y L_n \gg 1$ , the extent of the mode in the  $x$  direction is small compared to  $L_n$ ; hence, these modes primarily cause small scale turbulence within the density gradient layer. On the other hand, for modes  $k_y L_n \ll 1$  the  $x$ -extent is of order or larger than  $L_n$ ; these modes correspond to gross perturbations of the entire density layer. Note that the growth rate is largest for the  $k_y L_n \gg 1$  modes suggesting that small scale turbulence and associated mixing is rapid while the long scale undulations are slower.

As the instability evolves into the nonlinear regime two points should be noted. First, on a fast time scale, a very broad spectrum of waves can be generated in  $k$  space: the shortest wavelength unstable mode,  $k_{cr}$ , is determined largely by the amount of diffusion,  $D$ , (see Section III), which can be small, thus making  $k_{cr} L_n \gg 1$ . In the ionosphere, interchange turbulence may extend from 10's of m to 10's of km. Second, on a slower time scale, the density gradient scale length itself becomes a complicated function of space and time [i.e.,  $L_n = L_n(x, y, t)$ ]. In order to accurately model this process, a fully two-dimensional fluid simulation with resolution in both the  $x$  and  $y$  directions spanning up to 3 orders of magnitude would be required. At present, such a simulation is prohibitive; less ambitious, but practical, approaches have been taken.

In general, two types of simulations have been performed to understand the nonlinear evolution of interchange instabilities. One type models the macroscopic evolution of the density layer (length scales such that  $0.1 \leq k L_n \leq 10$ ) and are performed in  $x$ - $y$  configuration space. Excellent

examples of this type of simulation are studies of equatorial spread F [Zalesak et al., 1980], barium cloud evolution [Zalesak et al., 1984], and the high latitude  $\mathbf{E} \times \mathbf{B}$  instability [Mitchell et al., 1985]. The other type of simulation has focussed on the small-scale turbulence, i.e., length scales such that  $kL_n \gg 1$ . The purpose of the latter studies is to obtain an understanding of the cascade of wave energy from large to small wavelengths in two dimensions, and to calculate the spectral characteristics of this turbulence. Examples of this type of simulation applied to ionospheric turbulence are Rognlien and Weinstock (1972) and Keskinen et al. (1980).

In the present work, we examine interchange turbulence from the latter vantage point. To be precise, we study the steady state turbulence that develops in a model system which is set up as follows: a magnetized plasma is confined between two horizontal conducting boundaries with plasma density maintained higher at the upper boundary compared to the bottom; gravity points downward. Such a system rapidly develops Rayleigh-Taylor turbulence and a saturated level is reached from the competition between the tendency of the convection to flatten the density gradient between the plates and the tendency of the diffusion to restore the density ramp. This model system, akin to the classic Rayleigh-Benard system, allows us to make a consistent comparison between the collisional and inertial limits.

The model system is clearly not a complete representation of the ionosphere; its chief advantages are that it is a well-posed problem and that it admits steady state solutions (see Rognlien and Weinstock (1974) who used a similar approach). As argued above, however, the short wavelength ( $k_y L_n \geq 1$ ) turbulence of an ionospheric density layer may be expected to equilibrate on time scales faster than the time scale for long-

wavelength layer perturbations. In this sense, the conducting boundary assumption is equivalent to freezing the long-wavelength layer perturbations on the short time scale considered and is therefore not as restrictive as appears at first glance. A study of turbulence in our model can thus be expected to yield suggestive information for the short wavelength spectral characteristics of ionospheric turbulence. In any case, our present study allows an unambiguous comparison of spectral characteristics of collisional and inertial turbulence.

It should be noted that our choice of the conducting boundary model is motivated largely by the fact that it constitutes a well-posed problem that can be investigated using pseudospectral methods. A more attractive choice to study small scale turbulence would, at first sight, be periodic boundary conditions in  $x$  with an imposed ambient density gradient. For the Rayleigh-Taylor instability, however, this choice results in a time-asymptotic state that corresponds to completely vertical flows, periodic in  $y$ , continuing to increase exponentially in magnitude. This reflects the fact that an infinite amount of energy can be tapped from the ambient density gradient if the system is of infinite extent vertically. In a real system, however, periodic vertical flows would have to close at some height, presumably because of density thinning. It is in keeping with this physical fact that we formulate our problem to have an effectively finite vertical extent. Thus, we expect convection cells whose maximum extent in the vertical direction is no more than  $L_n$ . While the imposition of fixed densities at the top and bottom boundaries may not be completely realistic for ionospheric applications, it does allow a quasilinear flattening of the density gradient in the central regions; such a flattening is not possible with periodic boundary conditions in  $x$ .

### III. BASIC EQUATIONS

For the system described in Section II, the Rayleigh-Taylor flute instability is expected to be the fastest growing instability. Assuming that the system is infinitely long in the  $z$ -direction, the ensuing convection will be completely electrostatic and two-dimensional in the plane transverse to  $\underline{B}_0$  (i.e.,  $\underline{k} = k_x \hat{e}_x + k_y \hat{e}_y$  where  $\underline{k}$  is the wavenumber of the perturbation). We assume a background neutral density to exist with  $\nu_{in}$  the ion-neutral collision frequency, and note that the electron neutral collision frequency may be neglected since in the F-region

$\nu_{en}/\Omega_e \ll \nu_{in}/\Omega_i$  ( $\Omega_a$  is the cyclotron frequency of the species  $a$ ; we assume  $\nu_{in} \ll \Omega_i$ ). As long as  $k\rho_i \ll 1$ , where  $\rho_i$  is the mean ion Larmor radius and  $k$  is a typical wavenumber, finite Larmor radius effects may be ignored, while if  $k\lambda_D \ll 1$ ,  $\lambda_D$  being the Debye length, quasi-neutrality may be assumed. We assume isothermal electrons and cold ions for simplicity.

The equations used in the analysis are continuity, momentum transfer, and charge conservation:

$$\frac{\partial n_a}{\partial t} + \nabla \cdot (n \underline{V}_a) = 0 \quad (1)$$

$$0 = -\frac{e}{m_e} \left( \underline{E} + \frac{1}{c} \underline{V}_e \times \underline{B} \right) - \frac{T_e}{m_e} \frac{\nabla n}{n} - \nu_{ei} (\underline{V}_e - \underline{V}_i) \quad (2)$$

$$\frac{d\underline{V}_i}{dt} = \frac{e}{m_i} \left( \underline{E} + \frac{1}{c} \underline{V}_i \times \underline{B} \right) - \nu_{ie} (\underline{V}_i - \underline{V}_e) - \nu_{in} \underline{V}_i + \underline{g} \quad (3)$$

$$\nabla \cdot \underline{J} = \nabla \cdot [n(\underline{V}_i - \underline{V}_e)] = 0 \quad (4)$$

where the various symbols have their usual meaning.

We perturb (1)-(4) about an equilibrium and let  $n = n_0 + \tilde{n}$ ,  $\underline{E} = -\nabla\tilde{\phi}$ , and  $\underline{V}_\alpha = \underline{V}_{\alpha 0} + \tilde{\underline{V}}_\alpha$ . To lowest order in  $v_{\alpha n}/\Omega_\alpha$  the equilibrium drifts are given by  $\underline{V}_{e0} = -(cT_e/eB)(\partial \ln n/\partial x)^{-1} \hat{e}_y$  (the electron diamagnetic drift) and  $\underline{V}_{i0} = g/\Omega_i \hat{e}_y$  (the ion gravitational drift). We solve (2) and (3) for  $\tilde{\underline{V}}_e$  and  $\tilde{\underline{V}}_i$  which are given by

$$\tilde{\underline{V}}_e = -\frac{c}{B} \nabla\tilde{\phi} \times \hat{e}_z$$

$$\tilde{\underline{V}}_i = -\frac{c}{B} \nabla\tilde{\phi} \times \hat{e}_z - \frac{c}{B} \frac{d/dt + v_{in}}{\Omega_i} \nabla\tilde{\phi}$$

where  $d/dt = \partial/\partial t + \underline{V}_i \cdot \nabla$  and we have assumed  $\Omega_i \gg \partial/\partial t$ ,  $v_{in} \gg \underline{V}_{i0} \cdot \nabla$ . Substituting these values into (1) and (4) to arrive at the coupled set of equations for  $\tilde{n}$  and  $\tilde{\phi}$  [Huba et al, 1985]:

$$\frac{\partial}{\partial t} \frac{\tilde{n}}{n_0} - \frac{c}{B} \nabla\tilde{\phi} \times \hat{e}_z \cdot \frac{\nabla n_0}{n_0} - \frac{D_e}{n_0} \nabla^2 \tilde{n} = \frac{c}{B n_0} \nabla\tilde{\phi} \times \hat{e}_z \cdot \nabla \tilde{n} \quad (5)$$

and

$$\frac{g}{\Omega_i} \times \hat{e}_z \cdot \nabla \frac{\tilde{n}}{n_0} - \frac{c}{B} \frac{1}{\Omega_i} \left( \frac{\partial}{\partial t} + \hat{e}_z \times \nabla\tilde{\phi} \cdot \nabla + v_{in} \right) \nabla^2 \tilde{\phi} = 0 \quad (6)$$

where  $D_e = v_{ei} \rho_e^2$  is the electron diffusion coefficient. It may be seen that (5) and (6) are mathematically the same as the Rayleigh-Benard equations [Eqs. (17) and (18) of Lorenz (1963)] provided the substitution  $v_{in} \rightarrow v\nabla^2$  is made in (6).

We normalize the equations in the following manner:  $\hat{x} = x/L$ ,  $\hat{v} = Lv$ ,  $\hat{t} = \gamma_g t$ ,  $\hat{n} = (L/L_n)\bar{n}$ ,  $\hat{\phi} = c\bar{\phi}/(L^2 B \gamma_g)$ ,  $\hat{v} = v_{in}/\gamma_g$ ,  $\hat{D} = D/(L^2 \gamma_g)$ , and  $\gamma_g^2 = g/L_n$ . In this case, the normalized system of equations is given by

$$\frac{\partial \hat{n}}{\partial \hat{t}} + \hat{e}_z \times \hat{\nabla} \hat{\phi} \cdot \hat{\nabla} \hat{n} = \hat{D} \hat{\nabla}^2 \hat{n} + \frac{\partial \hat{\phi}}{\partial \hat{y}} \quad (7)$$

$$\left( \frac{\partial}{\partial \hat{t}} + \hat{e}_z \times \hat{\nabla} \hat{\phi} \cdot \hat{\nabla} + \hat{v} \right) \hat{\nabla}^2 \hat{\phi} = \frac{\partial \hat{n}}{\partial \hat{y}} \quad (8)$$

Hereafter the carets will be suppressed.

The two nonlinearities in (7) and (8) are the  $\underline{E} \times \underline{B}$  drift nonlinearity [ $\underline{v} \cdot \nabla n$  term in (7)] and the polarization drift nonlinearity [ $\underline{v} \cdot \nabla \nabla^2 \phi$  term in (8)] where  $\underline{v} = \hat{e}_z \times \nabla \phi$ . In the collisional case,  $v \gg 1$  and (8) may be approximated as  $v \nabla^2 \phi = \partial n / \partial y$ . This corresponds to flows where the driving gravitational forces are instantaneously balanced by friction. In the opposite limit, the gravitational forces are unbalanced and accelerate the fluid.

The linear dispersion equation of the system is obtained by linearizing (7) and (8) and assuming perturbed quantities vary as  $\sin(k_x x) \exp(ik_y y + \gamma t)$ , where  $k_x$  and  $k_y$  are the positive integers. The dispersion equation is given by

$$(\gamma + v)(\gamma + k^2 D) = (k_y^2 / k^2), \quad (9)$$

where  $k^2 = k_x^2 + k_y^2$ . The boundary between linearly stable and unstable regions of  $k$  space is given by  $k^2 D v = (k_y / k)^2$ . A sketch of this boundary is given in Fig. 2a. The maximum growth rate is obtained for  $k_x = 1$ . In Fig. 2b we give a sketch of  $\gamma$  vs.  $k_y$  for fixed  $k_x$  ( $k_x = 1$ ,  $v = 1$ , and  $D =$

0.1). In general,  $\gamma$  is negative for  $k_y < k_1$ , rises to  $k_y = k_m$  at which point the growth rate is maximum, and then falls off becoming negative for  $k_y > k_2$ . (The other root for  $\gamma$  in (9) is damped for all  $k_y$ .) If we let  $k_x$  and  $v$  be of order unity and assume  $D \ll 1$ , then  $k_1$  and  $k_2$  are given by  $k_1^2 = k_x^4 vD$  and  $k_2^2 = (vD)^{-1}$ . For the collisional limit ( $v \gg 1$ ),  $k_m^2 = k_x / \sqrt{Dv}$ , while for the inertial limit ( $v \ll 1$ ),  $k_m^2 = k_x / \sqrt{D}$ . Note that for very small  $D$ , as is the case for the ionosphere,  $k_m \gg 1$ . Thus the maximum growth rate is obtained for  $k_x = 1$  and  $k_y = k_m \gg 1$ . The maximum growth rate  $\gamma_m$  is approximately  $v^{-1}$  or unity for the collisional or inertial limits, respectively. Also, since we require  $k_2 > k_1$  we find that  $vD < 1$  for  $k_x = 1$ .

The coupled equations for  $\phi$  and  $n$  in (7) and (8) are solved using a pseudospectral method code developed by Fyfe et al. (1977), based on the work of Orszag (1971). The dependent variables  $\phi$  and  $n$  are Fourier-decomposed as follows:

$$\phi(\underline{x}, t) = \sum_{\underline{k}} \phi(\underline{k}, t) \exp(i\underline{k} \cdot \underline{x}) \quad (10a)$$

$$n(\underline{x}, t) = \sum_{\underline{k}} n(\underline{k}, t) \exp(i\underline{k} \cdot \underline{x}), \quad (10b)$$

where  $\underline{k} = k_x \hat{e}_x + k_y \hat{e}_y$ , and  $k_x$  and  $k_y$  are integers. The nonlinear terms are computed by fast Fourier transforming  $\nabla \phi$  and  $\nabla n$  from  $\underline{k}$  space to  $\underline{x}$  space, calculating the nonlinear terms in  $\underline{x}$  space, and then fast Fourier transforming the results back to  $\underline{k}$  space. The equations are then stepped forward in time in  $\underline{k}$  space and the cycle is repeated. Because of the imposition of conducting boundaries at  $x=0$  and  $x=\pi$ , we demand that  $v_x = 0$



at these boundaries. This results in the conditions on  $\phi(\underline{k})$  and  $n(\underline{k})$  given by  $\phi(k_x, k_y) = -\phi^*(k_x, -k_y)$  and  $n(k_x, k_y) = -n^*(k_x, -k_y)$ .

The numerical results presented in this paper are nominally computed on a  $32 \times 32$  mesh. However, to prevent aliasing of the wave energy during the fast Fourier transformation, it is necessary to zero all modes with  $|\underline{k}| > 32/3$ . The linear growth rates of modes obtained from the code were checked with the rates obtained from the solution of (9) and excellent agreement was obtained. The nonlinear couplings of the present code have been tested previously [Drake et al, 1984].

#### IV. SPECTRAL CHARACTERISTICS

In all cases, the system of modes was initialized with small, randomly distributed amplitudes. Two stages were clearly discernible in the time evolution of the system: (1) the linear stage where the  $\underline{k}$  spectrum grew from random noise peaking at small  $k_x$  and large  $k_y$  as predicted from the linear dispersion equation, and (2) the nonlinear stage, where the system reached a turbulent state with the total energy in all the modes, on average, a constant.

The spectrum in the linear stage of the instability is shown in Fig. 3 which is a plot of  $|\phi_{\underline{k}}|$  as a function of  $k_x$  and  $k_y$ . For this case,  $\nu = 1$  and  $D = 8.0 \times 10^{-3}$ . The spectrum peaks at high  $k_y$  as may be expected from the linear dispersion relation. The maximum amplitude also occurs at  $k_x = 1$  and the value of  $|\phi_{\underline{k}}|$  at the peak is consistent with linear theory.

In Fig. 4, we plot the total energy in all the modes ( $E$ ) as a function of time. The energy is defined as

$$E = \frac{1}{2} \sum_{\underline{k}} k^2 |\phi_{\underline{k}}|^2. \quad (11)$$

A collisional case,  $\nu = 4.0$  and  $D = 2.0 \times 10^{-3}$ , is shown in Fig. 4a; an inertial case,  $\nu = 0.1$  and  $D = 8.0 \times 10^{-2}$ , is shown in Fig. 4b. The energy increases from its initial level and asymptotically attains an average saturated level. The collisional case saturates at a value  $E_{\text{col}} \sim 1.9 \times 10^{-3}$  while the inertial case at a value  $E_{\text{in}} \sim 3.1$  (here the subscripts "col" and "in" denote collisional and inertial, respectively). A discussion of the large difference between these two values is presented in Appendix A.

After the total energy saturates, the detailed distribution of energy in  $\underline{k}$  space can still be dynamic as energy is exchanged between different modes in  $\underline{k}$  space as a function of time. The general characteristics of the spectra, however, remain unchanged: most of the energy resides in the long wavelengths and a power law type of falloff to the short wavelengths is found. To examine average features of the spectrum, the spectra were time-averaged after saturation was achieved. The time-averaged spectra are shown in Figs. 5a and 5b. In Fig. 5a the  $|\phi_{\underline{k}}|$  spectrum is shown for a collisional run:  $|\phi_{\underline{k}}|$  vs.  $k_x, k_y$  is plotted for  $\nu = 4.0$ ,  $D = 2.0 \times 10^{-3}$ , and the time averaging was done over approximately 100 linear growth times in the nonlinear regime. Note that the spectrum is quite smooth: the fluctuating peaks have been smoothed out by the time averaging. Most prominent in the collisional spectrum is the anisotropic distribution of

energy for the short wavelengths with relatively little energy in the region around  $k_y = 0$ . This feature is in marked contrast to the corresponding  $|\phi_k|$  spectrum for the inertial case shown in Fig. 5b. The parameters for Fig. 5b were  $\nu = 0.1$ ,  $D = 8.0 \times 10^{-2}$ , with averaging done for approximately 30 linear growth times after saturation. Figure 5b shows that the inertial spectrum is very nearly isotropic in  $k$  space. Similar results have also been obtained using a  $64 \times 64$  grid.

The corresponding averaged  $k$  spectra for the density are shown in Figs. 6a and 6b. Here,  $|n_k|$  vs.  $k_x, k_y$  is plotted. While an anisotropy is evident in Fig. 6a, in both cases the most prominent feature of the spectra is the power in the  $k_y = 0$  modes. This is a reflection of the fact that while on average the turbulence tends to flatten the background ( $k_y = 0$ ) density profile, the fact that we hold the density fixed at  $x = 0$  and  $x = \pi$ , results in sharp structures near the boundaries leading to large power in the  $n(k_x, k_y = 0)$  modes.

The physical reasons for the dissimilarity between the collisional and inertial spectra can be understood quite simply. In the inertial case, it is easy to imagine that a vertically elongated fluid element falling under the influence of gravity could transfer its energy to a horizontally elongated fluid element when it "hits" the bottom boundary. That is to say the vertical flow is diverted horizontally by the bottom plate and the latter expansion, unimpeded by friction (since  $\nu \ll 1$ ), overshoots and creates a fluid element which is equally elongated horizontally. This is not the case in the collisional limit ( $\nu \gg 1$ ). In the collisional case, the overshoot just described is practically eliminated as the friction from the neutrals slows down the  $v_y$  flow almost immediately. Thus, while the

vertical flows are finger-like since the growth rate peaks for large  $k_y$ , they do not drive horizontal finger-like flows. We illustrate this argument by plotting in Fig. 7 snapshots of the flow streamlines in the two cases. Figure 7a is the collisional case, Fig. 7b the inertial. Both figures were obtained from runs evolved with initial random noise; in addition, the figures are to scale with respect to each other. The finger-like character in the collisional limit is clearly evident. It is fairly clear that these flow characteristics should be basic to interchange turbulence in general and not peculiar to our model system. In fact, the same characteristics were observed in the simulations of Mitchell et al. (1985); the latter are 2-D configuration space simulations and allow breakup of the initial density layer.

The foregoing arguments can be further substantiated by examining the Fourier component of (8) appropriate for a mode with finite  $k_x$  but small  $k_y$ . Consider such a mode with  $k_x \sim k$  of order unity. In that case, (8) may be rewritten schematically as

$$\left(\frac{\partial}{\partial t} + \nu\right)\phi_0 \sim k_y n_0 + (\mathbf{v} \cdot \nabla \nabla^2 \phi)_0, \quad (12)$$

where the subscript 0 denotes the Fourier component for which  $k_y \rightarrow 0$ . It is then clear that unless the  $\mathbf{v} \cdot \nabla \mathbf{v}$  nonlinearity plays a role, the power in  $\phi_0$  approaches zero as  $k_y \rightarrow 0$  regardless of collisionality. [We are assuming that  $n_0$  does not diverge as  $k_y \rightarrow 0$ . A divergence is unlikely; at most,  $n_0$  could be isotropic due to the  $\mathbf{v} \cdot \nabla n$  nonlinearity in (7).] Consider now the  $\mathbf{v} \cdot \nabla \mathbf{v}$  term: the maximum contribution from this term is of order  $\phi^2$  where  $|k|$  is taken to be of order unity and  $\phi$  is a typical amplitude in the main part of the spectrum. In the inertial limit,  $\nu \ll$

$\partial/\partial t \sim 1$  and  $\phi \sim 1$  (see Sec. IV). Thus, from (12), we have  $\phi_0/\phi \sim 1$  as  $k_y \rightarrow 0$  which implies that isotropization is possible. In the collisional limit, however,  $\partial/\partial t \ll \nu$  and  $\phi \sim (D/\nu)^{1/2}$  (Sec. IV). Thus the maximum relative value of  $\phi_0$  as  $k_y \rightarrow 0$  is given by  $\phi_0/\phi \sim \nu^{-1}(D/\nu)^{1/2} \ll 1$ . The  $y \cdot \nabla y$  nonlinearity is therefore negligible and, at best,  $\phi_0$  will increase as  $k_y$  if  $n$  is isotropic.

The time-averaged electrostatic potential power spectra shown in Fig. 5 were analyzed further to display the two-dimensional band-averaged spectrum, and the one-dimensional spectra along  $k_x$  and  $k_y$ . The results are shown in Fig. 8 (collisional case) and Fig. 9 (inertial case). Figures 8a and 9a show the band-averaged power spectra  $P(k^2)$  plotted versus  $k^2$ ; the quantity  $P(k^2)$  is defined as

$$P(k^2) = N_k^{-1} \sum_g |\phi_g|^2, \quad (13a)$$

where the summation, for a given  $k^2$ , is over all wave vectors  $g$  such that  $|g|^2 = k^2$  and  $N_k$  is the total number of modes in the band considered. The omnidirectional power spectrum can then be defined by  $2\pi k P(k^2)$ . Figures 8b and 9b are the power spectra  $P_x$  plotted versus  $k_x^2$ , while Figs. 8c and 9c, correspondingly, are plots of  $P_y$  versus  $k_y^2$ . Here,  $P_x$  and  $P_y$  are defined by

$$P_x(k_x) = \sum_{k_y} |\phi_{\underline{k}}|^2, \quad (13a)$$

$$P_y(k_y) = \sum_{k_x} |\phi_{\underline{k}}|^2, \quad (13b)$$

where  $\sum_{k_y}$  indicates a sum over all  $k_y$  for a given  $k_x$ ; likewise for  $\sum_{k_x}$ . The approximate spectral indices, obtained by a least squares fit, are also given in Figs. 8 and 9.

From Fig. 8 (collisional case), and in particular Figs. 8b and 8c, the anisotropy is clearly evidenced by the difference in the slopes of  $P_x$  and  $P_y$ . We find that  $P_x \propto k_x^{-3.7 \pm 0.3}$  while  $P_y \propto k_y^{-4.6 \pm 0.3}$ . In contrast, the corresponding spectra for the inertial case shown in Fig. 9 show a high degree of isotropy [see Figs. 9b and 9c]. Furthermore, the spectral index for the band averaged power (Fig. 9a) is  $-4.4 \pm 0.5$  which is consistent with the Kolmogorov law: the usual two-dimensional Kolmogorov index, stated for  $k^2 |\phi_k|^2$  vs.  $k$ , is expected to be  $-8/3$  [see, for example, Kulsrud and Sudan, 1982]. Thus  $|\phi_k|^2$  would scale as  $k^{-14/3} = k^{-4.66}$  which is within the error bars of our measured spectral index. The Kolmogorov power law may be deduced if one assumes that convective mixing due to the  $\underline{y} \cdot \nabla \underline{y}$  forces is dominant and dissipation is negligible; this is approximately the situation in the inertial limit. We also note that an isotropic power spectrum with  $P(k^2) \propto k^{-4.66}$  would result in a one-dimensional power spectrum  $P_x = P_y \propto k^{-3.66}$ . Our measured slopes for  $P_x$  and  $P_y$  (Figs. 9b and 9c:  $-3.8 \pm 0.2$ ) are therefore, within numerical error, consistent with isotropy and the band-averaged spectrum in Fig. 9a. Results similar to Figs. 8 and 9 were also obtained using a 64 x 64 system.

If (7) and (8) are Fourier analyzed according to (10) but only three coupled field variables are retained, the resulting equations [Huba et al., 1985] are just the well-known Lorenz [1963] equations that were originally applied to the Rayleigh-Benard instability. The three modes in question are, for example, the  $(k_x = 1, k_y = 1)$  mode for  $\phi$  and the  $(1,1)$  and  $(2, 0)$  modes for  $n$ . The Lorenz equations have been intensively studied because

they exhibit chaotic behavior [Lorenz, 1963; Ott, 1981]. In an earlier study [Huba et al., 1985], the possible role of chaotic behavior for ionospheric interchange instability dynamics were discussed. Since the present paper represents a many mode extension of this study, we discuss in Appendix B the role of chaotic dynamics in light of the present work.

## V. SUMMARY

We have investigated the spectral characteristics of plasma turbulence arising from the two-dimensional, magnetized Rayleigh-Taylor instability in the presence of a background neutral gas. By investigating a model system akin to the classic Rayleigh-Benard system, we have shown that a primary difference between collision-dominated and inertial spectra of the electrostatic potential is a marked anisotropy in the former case (Fig. 5a). The one-dimensional power spectra for the collisional case are given by  $P_x \propto k_x^{-3.7 \pm 0.3}$  and  $P_y \propto k_y^{-4.6 \pm 0.3}$ . The inertial spectrum, by contrast, is isotropic and obeys the Kolmogorov law (Figs. 5b and 9a). The two-dimensional band averaged spectrum is found to be  $P \propto k^{-4.4 \pm 0.5}$  which is consistent with the Kolmogorov scaling of  $P \propto k^{-4.67}$ . The one-dimensional spectra are given by  $P_x \propto k_y^{-3.8 \pm 0.2}$  and  $P_y \propto k_y^{-3.8 \pm 0.2}$ . The anisotropy is a reflection of the fact that the turbulent convection in the collision-dominated case represents flow with friction so dominant that fluid elements move at "terminal velocity" and negligible inertial overshoot. Since the linear growth rate peaks for short horizontal scales (Fig. 2a), the strong friction flow is finger-like (Fig. 7a) with more elongated structures vertically rather than horizontally. This corresponds to comparatively reduced power for the  $k_y = 0$  modes.

Although the present simulation is highly idealized in the sense that long wavelength perturbations of the entire density layer are not allowed, it is nevertheless evident that the basic characteristics of flow, finger-like on the one hand and isotropic on the other, should be a fairly general feature of ionospheric turbulence: anisotropic potential power spectra may be expected at low altitudes (i.e., less than 500 km). A similar statement can also be made for  $\underline{E} \times \underline{B}$  drift turbulence as the governing equations for this instability are mathematically identical to the Rayleigh-Taylor equations [Huba et al., 1985]. In fact, fully 2-D simulations, allowing density layer modifications [Mitchell et al., 1985], show strong indications that collisionality governs the level of isotropy of spectra.

Application of these results to measurements of ionospheric turbulence are difficult for several reasons. First, as noted above, our model is somewhat ideal. Second, very little data relating to the spectra of electric field fluctuations in the ionosphere have been reported. And third, the data that has been published are single, one-dimensional spectra. In order to ascertain whether the spectrum is isotropic or anisotropic, it is clear that at least two, one-dimensional spectra should be obtained: orthogonal to one another, and orthogonal to the magnetic field. Nevertheless, it is instructive to point out the data published thus far on ionospheric electric field fluctuations and how it compares with our results.

Cerisier et al. [1985] have recently measured electric field fluctuation spectra at 592 km in the high-latitude topside F region ionosphere. Their measured spectrum of  $|E_k|^2 \propto k^{-1.77}$ , or  $|\phi_k|^2 \propto k^{-3.77}$ , is in close agreement with the one-dimensional Kolmogorov scaling obtained in the inertial regime (Figs. 9b and 9c), but is also consistent with the



results in the collisional regime (Fig. 8b). They hypothesize that the  $\mathbf{E} \times \mathbf{B}$  gradient drift instability is responsible which is an interchange instability very similar to the Rayleigh-Taylor instability (Huba et al., 1985).

Kelley et al. [1982] observed one-dimensional electric field fluctuation power spectra at 502 km, in the vertical direction, during equatorial spread-F to be a power law  $k^{-3}$  in the scale size regime of a few hundred meters to a few tens of meters. This gives a one-dimensional potential power spectrum of approximately  $k^{-5}$  in the vertical direction. Recently, LaBelle et al. [1986] have discussed the spectra of electric field irregularities at 450 km in equatorial spread-F observed in the CONDOR campaign. They showed that the one-dimensional power spectrum of electric field fluctuations in the vertical direction can be represented by a power law  $k^{-2.5}$  for scale sizes between approximately 1 km and a few tens of meters, which gives a one-dimensional potential power spectrum of  $k^{-4.5}$ . These results are more consistent with the collisional regime (Fig. 8c) than the inertial regime (Fig. 9c). It must be noted, however, as Labelle et al. [1986] discuss, that at wavelengths of order 100 m, a knee in the spectrum is observed suggestive of new physical mechanisms at shorter wavelengths (Labelle et al. [1986] suggest drift waves). More to the point, the data from both Kelley et al. [1986] and Labelle et al. [1986] at wavelengths longer than 100 m, above the knee, are not as finely resolved as the short wavelength data. Thus, the comparison cannot be said to be conclusive.

It is difficult to reach any definitive conclusions concerning collision-dominated vs. inertia dominated turbulence based upon a single one-dimensional power spectra. Simultaneous measurements of one-

dimensional power spectra in two directions (transverse to one another and transverse to the magnetic field) are needed to establish whether or not the turbulence is anisotropic (i.e., collisional) or isotropic (i.e., inertial). It is recommended that experimentalists obtain electric field fluctuation data of this type at both low and high ionospheric altitudes to determine if an altitude dependent anisotropy exists in the turbulence.

#### ACKNOWLEDGMENTS

This research has been supported by the Office of Naval Research and the Defense Nuclear Agency.

## APPENDIX A

In Figs. 4a and 4b, we show plots of the total normalized kinetic energy for each of the collisional and ion inertial cases, respectively. The kinetic energy density is normalized to the quantity  $mg(dn_0/dx)L^2$ , i.e., proportional to the gravitational free energy of the system. In the collisional case, Fig. 4a, the normalized saturated energy is  $E = 1.1 \times 10^{-2}$  while, for the inertial case (Fig. 4b), the energy is  $E = 1.5 \times 10^1$ . Note that for the collisional case,  $\nu = 4.0$  and  $D = 2.0 \times 10^{-3}$ , while for the inertial case  $\nu = .1$  and  $D = 8.0 \times 10^{-2}$ . We observe that the turbulent energy in the collisional case is approximately three orders of magnitude smaller than the turbulent energy of the inertial case, and therefore almost quiescent by comparison.

A relatively simple scaling argument that explains the observed difference in saturated energy levels can be deduced from a simple three wave model [Huba et al., 1985]. Noting from Figs. 5a and 5b that the maximum energy resides in the  $k_x = 1$ ,  $k_y = 1$  mode, we consider the following forms for the perturbed potential and density:  $\phi = \phi_{1,1} \sin x \sin y$  and  $n = n_{1,1} \sin x \cos y + n_{2,0} \sin 2x$ . Here  $x$  and  $y$  represent the  $x$  and  $y$  spatial coordinates normalized to  $L$ , and only the coefficients  $\phi_{1,1}$ ,  $n_{1,1}$ , and  $n_{2,0}$  are assumed to be time dependent. Substituting  $\phi$  and  $n$  into (7) and (8) we obtain the following set of coupled ordinary differential equations:

$$\dot{\phi}_{1,1} = -\nu\phi_{1,1} + \frac{1}{2}n_{1,1} \quad (14a)$$

$$\dot{n}_{1,1} = -2Dn_{1,1} + \phi_{1,1} + \phi_{1,1}n_{2,0} \quad (14b)$$

$$\dot{n}_{2,0} = -4Dn_{2,0} - \frac{1}{2} \phi_{1,1} n_{1,1} \quad (14c)$$

where the dot over a variable indicates a time derivative. An estimate of saturation levels can now be obtained by examining the "fixed state" amplitudes of  $\phi$  and  $n$  which are found by setting  $d/dt = 0$  in (14). We find

$$\phi_{1,1}^0 = 4D(1/4vD - 1)^{1/2} \quad (15a)$$

$$n_{1,1}^0 = 8vD(1/4vD - 1)^{1/2} \quad (15b)$$

$$n_{2,0}^0 = 4vD - 1 \quad (15c)$$

where the superscript 0 indicates the "fixed state" value. For our numerical calculations,  $vD \ll 1$  so that  $\phi_{1,1}^0 = 2(D/v)^{1/2}$ . Since the energy of the system is given by  $E = \frac{1}{2} k^2 \phi^2$ , we find that  $E \propto D/v$ . Thus, we expect that the ratio of the saturated energy levels shown in Fig. 4 is given by

$$\frac{E_{in}}{E_{col}} = \frac{D_{in}}{D_{col}} \frac{v_{col}}{v_{in}} \quad (16)$$

where the subscripts "in" and "col" denote inertial and collisional, respectively. Using the appropriate values of  $v$  and  $D$  we find from (16) that  $E_{in}/E_{col} = 1.6 \times 10^3$ ; this is consistent with the numerical value of  $1.4 \times 10^3$ . In addition, the value of  $E_{in}$  based on  $\phi_{1,1}$  alone is  $E_{in} = 3.1$  which is within a factor of 3 of the many mode value in Fig. 5b (i.e.,  $E = 10$ ). The value of  $E_{col}$  based on  $\phi_{1,1}$  is  $E_{col} = 1.9 \times 10^{-3}$  which is within a factor of 5 of the many mode value (i.e.,  $E = 0.01$ ).

Although the simple three wave model explains the large difference in energy levels between the collisional and inertial cases, two comments must be made regarding the limits of applicability of the model. First, as is well known, the fixed states given by (15) do not necessarily correspond to equilibrium states of the system because for certain ranges of  $\nu$  and  $D$  they become unstable. Thus, for purposes of obtaining a scaling for  $\phi$  with  $\nu$  and  $D$ , we would only expect the fixed state scaling to hold provided  $\nu$  and  $D$  are not too far from the stability boundary. For the two cases considered,  $\nu$  and  $D$  were such that the fixed states are stable. Second, we would not expect the three wave scaling to hold for values of  $D$  and  $\nu$  for which  $\phi_{1,1}^0 \gg 1$ , (e.g.,  $\nu \rightarrow 0$ ). This is because (14) does not include any effects of the  $\underline{y} \cdot \nabla \underline{y}$  nonlinearity; for the three modes considered  $\underline{y} \cdot \nabla \underline{y} = 0$ . In contrast, the effects of the  $\underline{y} \cdot \nabla n$  nonlinearity are modeled by the nonlinear terms in (14b) and (14c). Clearly when  $\nu \ll 1$  and  $\underline{y} \cdot \nabla \gg \partial/\partial t$ , or, in normalized units, when  $\phi \gg 1$ , the  $\underline{y} \cdot \nabla \underline{y}$  nonlinearity must be considered in the sense that higher order modes should be allowed in (14). In that case, for  $\nu \ll 1$ , the maximum level of  $\phi_{1,1}$  is expected to be given by  $\underline{y} \cdot \nabla \sim \partial/\partial t$  or  $\phi_{1,1} \sim 1$ . This corresponds to a maximum kinetic energy of the order of the gravitational free energy of the system. For the cases considered by us,  $\phi_{1,1}^0$  is at most of order unity and thus a scaling estimate based on the three wave model is not inconsistent.



## APPENDIX B

We discuss here the relation between our present many mode study of Rayleigh-Taylor turbulence and Lorenz's (1963) three-mode study. We will be concerned mainly with the implications of these two studies to ionospheric turbulence.

To review Lorenz's results, we consider for simplicity the case  $D \ll 1$  which is valid for the ionosphere. We also assume  $v$  to be of order unity; in the ionosphere the transition altitude going from large  $v$  below to small  $v$  above is roughly 500 km. Lorenz's results for  $D \ll 1$  and  $v$  of order unity may be stated as follows: for all  $v > 1$ , the 3 mode equations always asymptote to one of two fixed states ( $\partial/\partial t = 0$ ) in phase space. The fixed states correspond physically to the (1, 1) convective cell turning either in the clockwise or the counterclockwise direction. On the other hand, for  $v < 1$ , no fixed states are obtained; rather, the phase space trajectory revolves about either one or the other of the foregoing fixed points with seemingly random transitions from one to the other. Hence the designation "chaotic". The physical correspondence of this behavior is that the convective cell makes many turns in one of either the clockwise or the counterclockwise directions (with periodic modulations in turnover rate) but, in random fashion, may switch the direction of rotation as time evolves.

The Lorenz results are of interest to ionospheric studies for they suggest a possible dissimilarity in the behavior of convection patterns above and below 500 km [Huba et al., 1985]. If taken at face value, the results imply, that, on average, steady convection would be expected below 500 km and chaotic patterns above this altitude. It is clear however, that

the three mode results would have to be augmented with a many mode study before conclusions can be drawn; in the ionosphere, since  $D \ll 1$ , a wide band of  $k$  vectors is linearly unstable as can be deduced from Fig. 2. To place the three mode results in context with the many mode study, we investigated the following issues:

- (a) In the limit  $\nu \gg 1$ , for which fixed states are predicted from the three-wave Lorenz model, are fixed states possible if many modes are allowed? Clearly for  $D \ll 1$ , this is not so as evidenced by the results shown in Figs. 4a and 5a. A parameter sweep of  $D$  showed that a many mode fixed state ( $\partial/\partial t = 0$  for all modes) was possible only if  $D$  was large enough so that only a few modes (two to four) were unstable linearly [cf. Fig. 2 with  $D$  approaching unity]. In Fig. 10a, we show such a completely time independent nonlinearly saturated  $|n_k|$  spectrum (as evidenced in the  $E$  vs.  $t$  plot in Fig. 10b) for  $\nu = 3.16$  and  $D = 3.16 \times 10^{-2}$ . The linear growth rate for these parameters becomes negative for  $k_y > 3$ . In view of the drastic truncation used to arrive at the Lorenz equations, our result is not surprising. Clearly, however, the case  $D$  of order a few percent is not applicable to the ionosphere.
- (b) The question posed in (a) may be overly restrictive in the sense that the condition  $\partial/\partial t = 0$  for all modes to define "fixed state" is stringent. To come up with a more practical definition of "fixed state", we defined "chaotic convection" to be any motion that consisted in the  $(1, 1)$  convective cell undergoing seemingly random changes in the direction of turnover. Since the  $(1, 1)$



cell typically appears to possess most of the energy (see Figs. 5), a change in direction of this mode would constitute a change in direction of the average convective flow. With this broadened definition, a preliminary search for chaotic convection was made for several values of  $v \ll 1$  (in which regime the Lorenz equations would predict chaos). In apparent paradox, for the several  $v$  values tested, no changes in direction were observed over considerably long time scales (several diffusion times). The convective cell on average keeps turning in the same direction. This result is consistent with the extensive study made by Curry et al. (1985) which found that the level of "chaos" diminishes with increasing number of modes in two dimensions. A possible explanation for the unidirectional vorticity of the large scale is that the smaller scale cells generate sufficient turbulent diffusion to give rise to an effective diffusion coefficient which is of order unity.

In view of (a) and (b), it would seem that the Lorenz physics, insofar as the behavior of large convective cells is concerned, is not directly applicable to the ionosphere in the two dimensional approximation. The most salient features to emerge from our many mode study seem to be the difference between the collisional and inertial spectra, the anisotropy in the former, and the isotropy and the Kolmogorov nature of the latter.



## REFERENCES

- Anderson, D.N., and M. Mendillo, Ionospheric Conditions Affecting the Evolution of Equatorial Plasma Depletions, Geophys. Res. Lett., 10, 541, 1983.
- Braginskii, S.I., Transport Processes in a Plasma, in Reviews of Plasma Physics, ed. M. Leontovich, Vol. 1, Consultants Bureau, New York, 1965.
- Cerisier, J.C., J.J. Berthelier, and C. Beghin, Unstable Density Gradients in the High-Latitude Ionosphere, Radio Sci., 20, 755, 1985.
- Curry, J.H., J.R. Herring, J. Loncaric, and S.A. Orzag, Order and Disorder in Two and Three-dimensional Benard Convection, J. Fluid Mech., 147, 1, 1984.
- Drake, J.F., P.N. Guzdar, A.B. Hassam, and J.D. Huba, Nonlinear Mode Coupling Theory of the Lower-Hybrid-Drift Instability, Phys. Fluids, 27, 1148, 1984.
- Farley, D.T., Jr., A Theory of Electrostatic Fields in the Ionosphere at Nonpolar Geomagnetic Latitudes, J. Geophys. Res., 65, 869, 1960.
- Fejer, B.G. and M.C. Kelley, Ionospheric Irregularities, Rev. Geophys. Space Phys., 18, 401, 1980.
- Fyfe, D., G. Joyce, and D. Montgomery, Magnetic Dynamo Action in Two-dimensional Turbulent Magneto-hydrodynamics, J. Plasma Phys., 17, 317 (1977).
- Huba, J.D., A.B. Hassam, I.B. Schwartz, and M.J. Keskinen, Ionospheric Turbulence: Interchange Instabilities and Chaotic Fluid Behavior, Geophys. Res. Lett., 12, 65, 1985.

- Hudson, M.K., Spread F. Bubbles: Nonlinear Rayleigh-Taylor Mode in Two Dimensions, J. Geophys. Res., 83, 3189, 1978.
- Johnson, F.S., Satellite Environment Handbook, ed. F.S. Johnson, Stanford University Press, Stanford, Calif., 1961.
- Kelley, M.C. and J.P. McClure, Equatorial Spread F: A Review of Recent Experimental Results, J. Atm. Terr. Phys., 43 427, 1981.
- Kelley, M.C., R. Pfaff, K.D. Baker, J.C. Ulwick, R. Livingston, C. Rino, and R. Tsunoda, Simultaneous Rocket Probe and Radar Measurements of Equatorial Spread-F Transitional and Short Wavelength Results, J. Geophys Res., 87, 1575, 1982.
- Keskinen, M.J., S.L. Ossakow, and P.K. Chaturvedi, Preliminary Report of Numerical Simulations of Intermediate Wavelength Collisional Rayleigh-Taylor Instability in Equatorial Spread-F, J. Geophys. Res., 85, 1775, 1980.
- Keskinen, M.J. and S.L. Ossakow, Theories of High-Latitude Ionospheric Irregularities: A Review, Radio Sci., 18, 1077, 1983.
- Kintner, P.M. and C.E. Seyler, The Status of Observations and Theory of the High Latitude Ionospheric and Magnetospheric Plasma Turbulence, Space Sci. Rev., 41, 91, 1985.
- Kolmogorov, A.N., The Local Structure of Turbulence in Incompressible Viscous Fluid for a Very Large Reynolds Number, C.R. Dokl. Acad. Sci. URSS, 30, 20, 1941.
- Kulsrud, R.M. and R.N. Sudan, On Kraichnan's "Direct Interaction Approximation" and Kolmogorov's "Theory in Two-dimensional Plasma Turbulence," Comments Plasma Phys. Controlled Fusion, 7, 47, 1982.
- LaBelle, J., "Mapping of Electric Field Structures from the Equatorial F Region to the Underlying E Region", J. Geophys. Res., 90, 4341, 1985.

- LaBelle, J., M.C. Kelley, and C.E. Seyler, An Analysis of the Role of Drift Waves in Equatorial Spread-F, J. Geophys. Res., 91, 5513, 1986.
- Linson, L.M. and J. B. Workman, Formation Striations in Ionospheric Plasma Clouds, J. Geophys. Res., 75, 3211, 1970.
- Lorenz, E.N., Deterministic Nonperiodic Flow, J. Atmos. Sci., 20, 130, 1963.
- Mitchell, H.G., Jr., J.A. Fedder, M.J. Keskinen, and S.T. Zalesak, A Simulation of High Latitude F-layer Instabilities in the Presence of Magnetosphere-Ionosphere Coupling, Geophys. Res. Lett., 12, 283, 1985.
- Orszag, S.A., Numerical Simulation of Incompressible Flows Within Simple Boundaries. 1. Galerkin (Spectral) Representations, Stud. Appl. Math., 50, 293, (1971).
- Ossakow, S.L., Ionospheric Irregularities, Rev. Geophys. Space Phys., 17, 521, 1979.
- Ossakow, S.L., Spread F Theories - A Review, J. Atm. Terr. Phys., 43 437, 1981.
- Ott, E., Strange Attractors and Chaotic Motions of Dynamical Systems, Rev. Mod. Phys., 53, 655, 1981.
- Rognlien, T.D. and J. Weinstock, Theory of the Nonlinear Spectrum of the Gradient Drift Instability in the Equatorial Electrojet, J. Geophys. Res., 79, 4733, 1974
- Sudan, R.N. and M.J. Keskinen, Unified Theory of the Power Spectrum of Intermediate Wavelength Ionospheric Electron Density Fluctuations, J. Geophys. Res., 89, 9840, 1984.

Zalesak, S.T., and S.L. Ossakow, Nonlinear equatorial spread-F: Spatially large bubbles resulting from large horizontal scale initial perturbations, J. Geophys. Res. 85, 2131, 1980.

Zalesak, S.T., P.K. Chaturvedi, S.L. Ossakow, and J.A. Fedder, Finite temperature effects on the evolution of ionospheric barium clouds in the presence of a conducting background ionosphere I. A high altitude incompressible background ionosphere, J. Geophys. Res., 90, 4299, 1985.

# FIGURE CAPTIONS

- Fig. 1 Geometry and plasma configuration.
- Fig. 2 Linear stability regime of the Rayleigh-Taylor instability.
- (a) The region of instability in  $k$  space; modes are linearly unstable inside the bounded curves. (b) The linear growth rate for fixed  $k_x$  plotted as a function of  $k_y$ . Analytical expressions for the cutoffs,  $k_1$  and  $k_2$ , and the wavenumber for maximum growth,  $k_m$ , are given in the text.
- Fig. 3 A snapshot of the two-dimensional spectrum of  $|\phi_k|$  in the linear stage of the instability showing maximum growth at  $k_y$  large and  $k_x$  of order unity. The parameters are  $\nu = 1$  and  $D = 8.0 \times 10^{-3}$ .
- Fig. 4 Time histories of the total flow kinetic energy shown for (a) the collisional case ( $\nu = 4$  and  $D = 2.0 \times 10^{-3}$ ), and (b) the inertial case ( $\nu = 0.1$  and  $D = 8.0 \times 10^{-2}$ ).
- Fig. 5 Two-dimensional time averaged spectra of  $|\phi_k|$ , plotted on a log scale, shown for (a) the collisional case ( $\nu = 4$  and  $D = 2.0 \times 10^{-3}$ ), and (b) the inertial case ( $\nu = 0.1$  and  $D = 8.0 \times 10^{-2}$ ). Note the anisotropy in the former case. The maximum value of  $|\phi_k|$  in case (a) is  $1.6 \times 10^{-2}$ , and in case (b) is 1.2.
- Fig. 6 Two-dimensional time-averaged spectra of  $|n_k|$ , on log scale, shown for (a) the collisional case ( $\nu = 4$  and  $D = 2.0 \times 10^{-3}$ ), and (b) the inertial case ( $\nu = 0.1$  and  $D = 8.0 \times 10^{-2}$ ). The large amount of power in  $k_y = 0$  modes reflects the fact that the original density ramp has undergone significant quasilinear flattening.

- Fig. 7 A snapshot of the flow streamlines at saturation for (a) the collisional case ( $\nu = 4$  and  $D = 2.0 \times 10^{-3}$ ), and (b) the inertial case ( $\nu = 0.1$  and  $D = 8.0 \times 10^{-2}$ ). The plots are on the same scale. Note the elongated nature of the cells in (a), reflected in the anisotropic spectrum of Fig. 4.
- Fig. 8 Time averaged power spectra at saturation for the collisional case ( $\nu = 4$  and  $D = 2.0 \times 10^{-3}$ ). We note that (a) is the band averaged spectrum while (b) and (c) are line averaged in  $k_y$  and  $k_x$ , respectively. The anisotropy is evident in the difference between (b) and (c).
- Fig. 9 Time averaged power spectra at saturation for the inertial case ( $\nu = 0.1$  and  $D = 8.0 \times 10^{-2}$ ). Cases (a), (b), and (c) are as in Fig. 7. Note the isotropy of the spectrum evident from (b) and (c). The power spectral indices obtained from these plots are consistent with the Kolmogorov scaling.
- Fig. 10 A case of a nonlinear fixed state with  $32 \times 32$  modes ( $\nu = 3.16$  and  $D = 3.16 \times 10^{-2}$ ). The two-dimensional power spectrum of  $|n_k|$  is shown in (a) and the total energy versus time is given in (b). Note that the energy is in complete steady state.



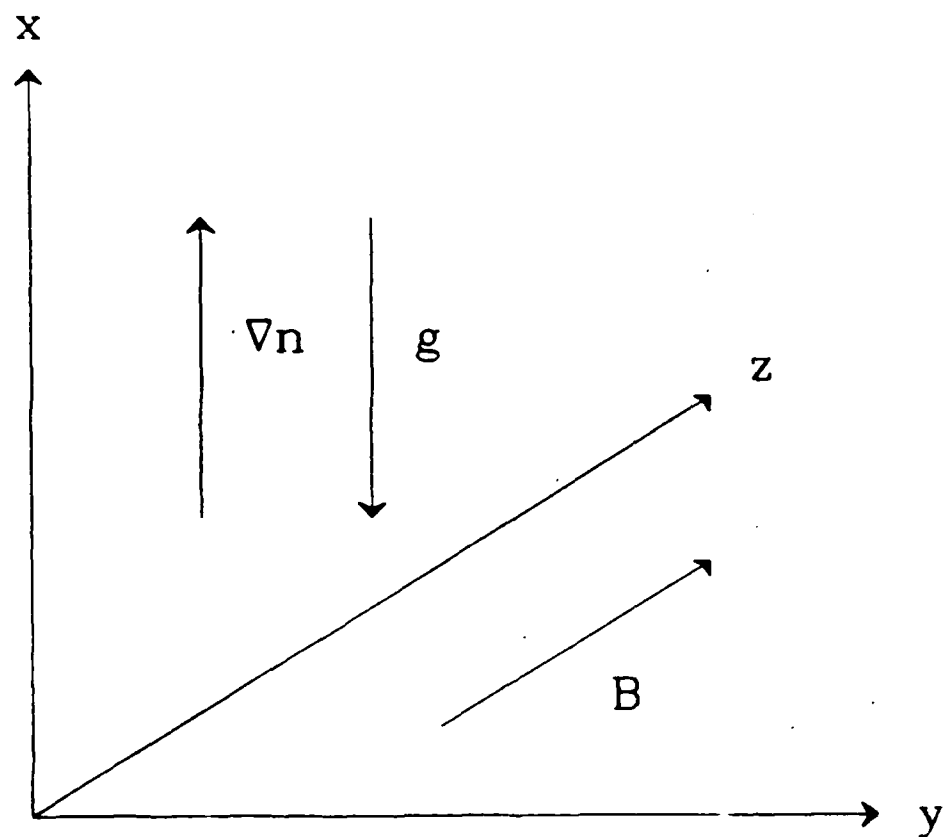


Figure 1  
N-39

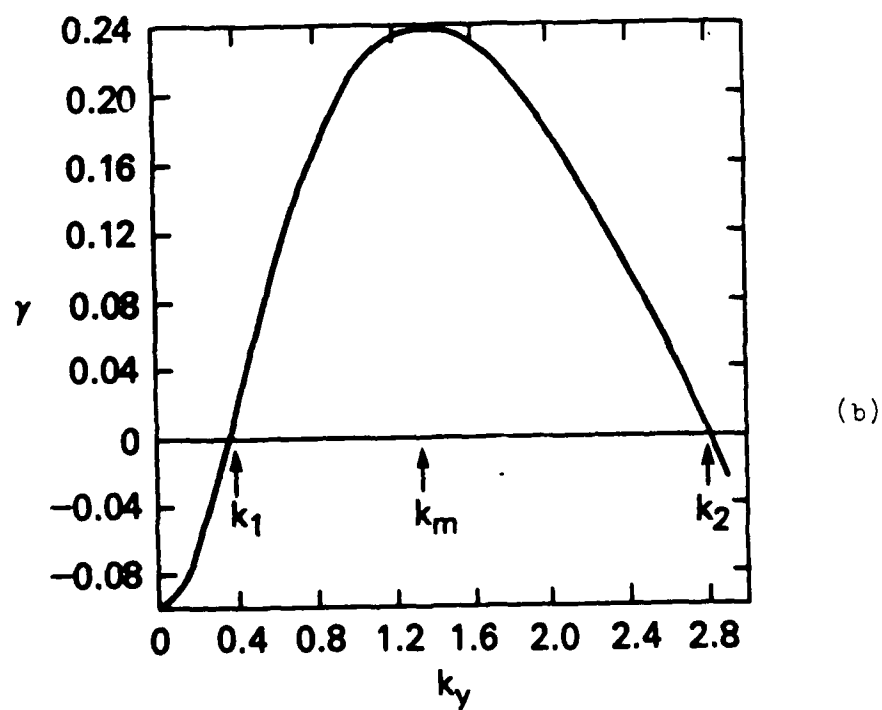
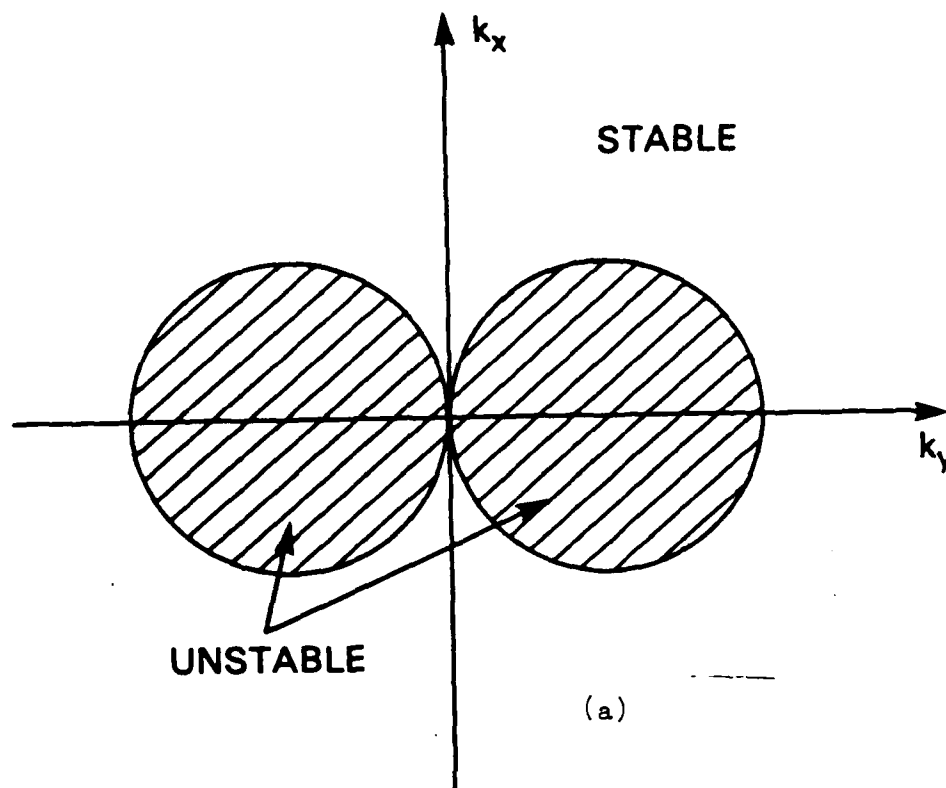


Figure 2  
N-40

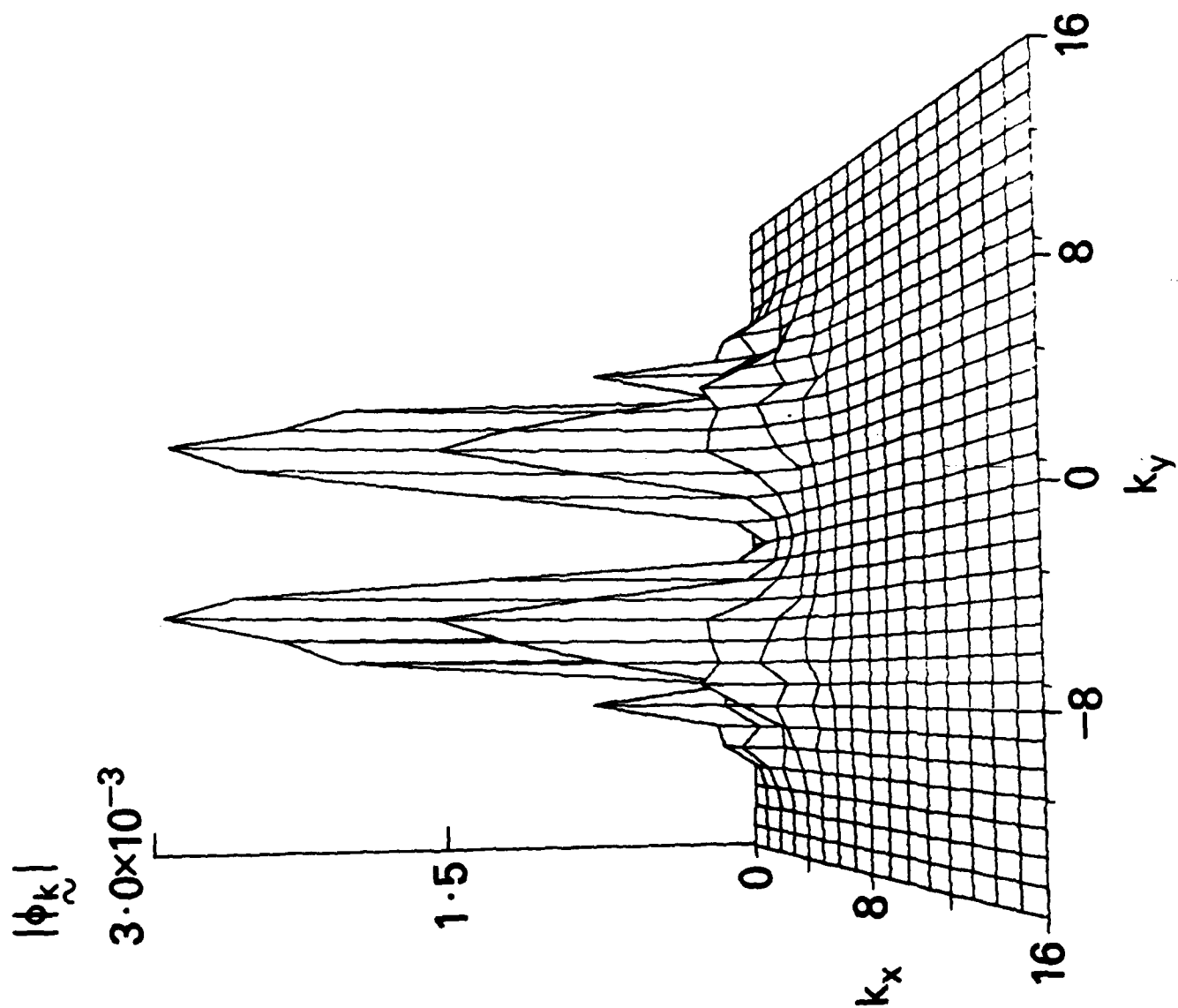


Figure 3

(a)

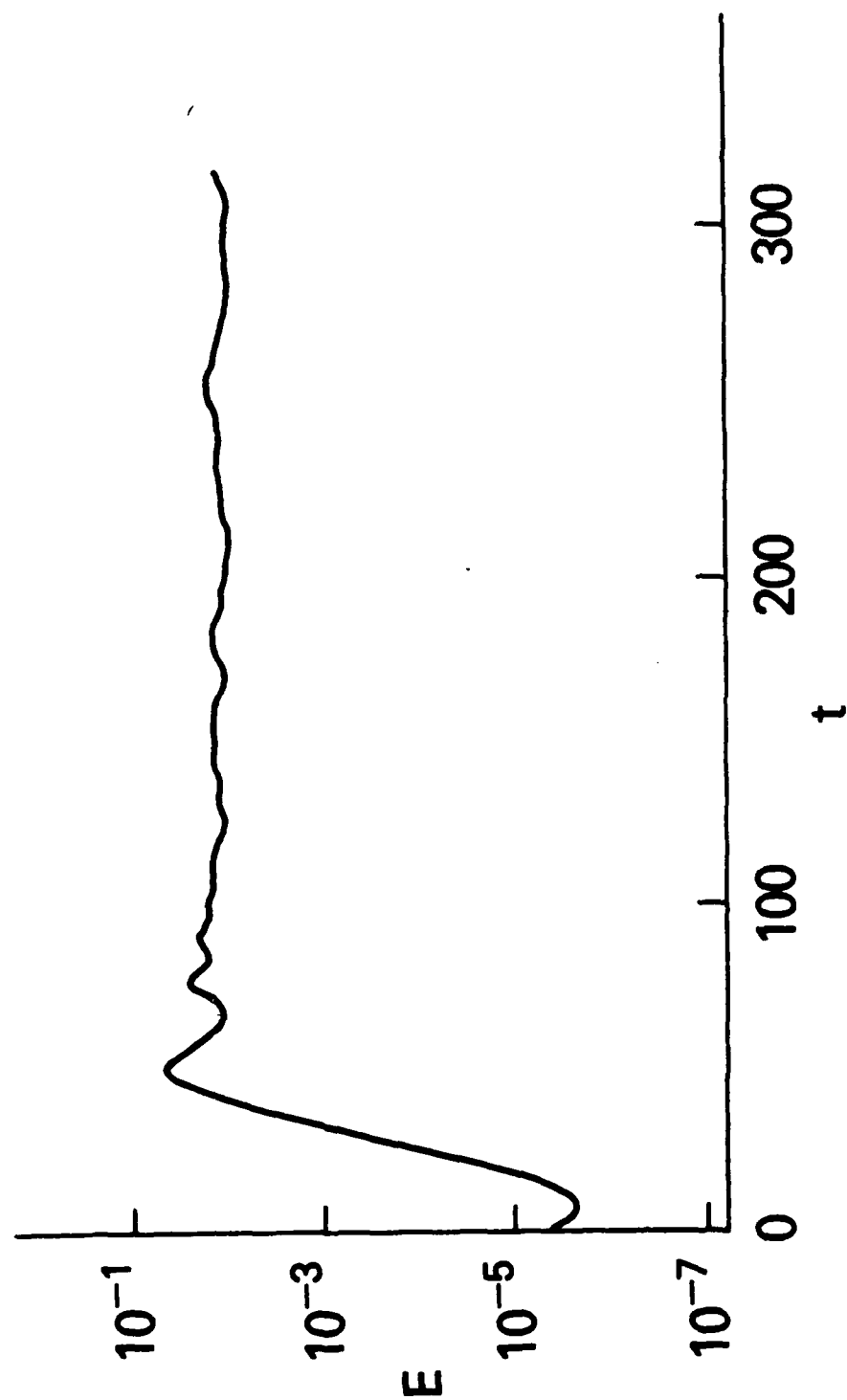


Figure 4a  
N-42

(b)

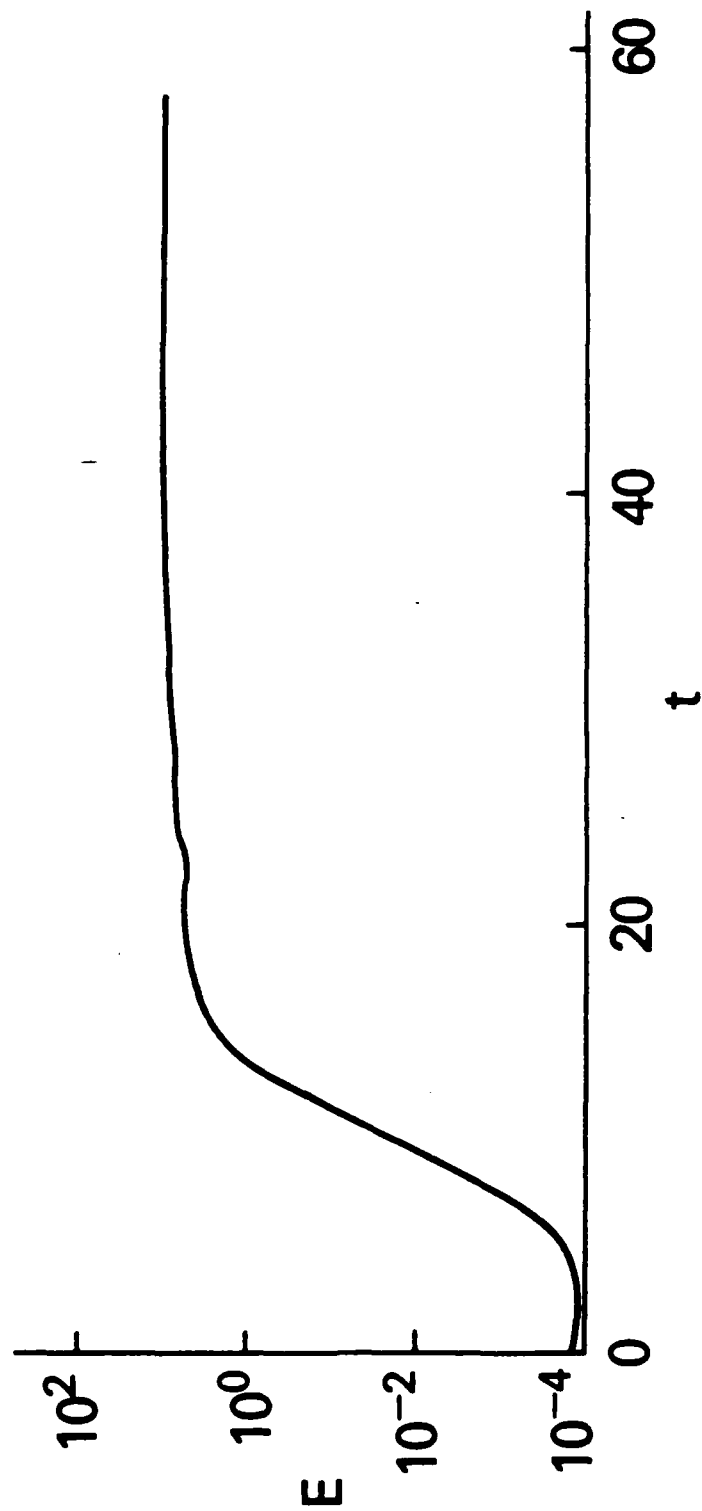


Figure 4b  
N-43

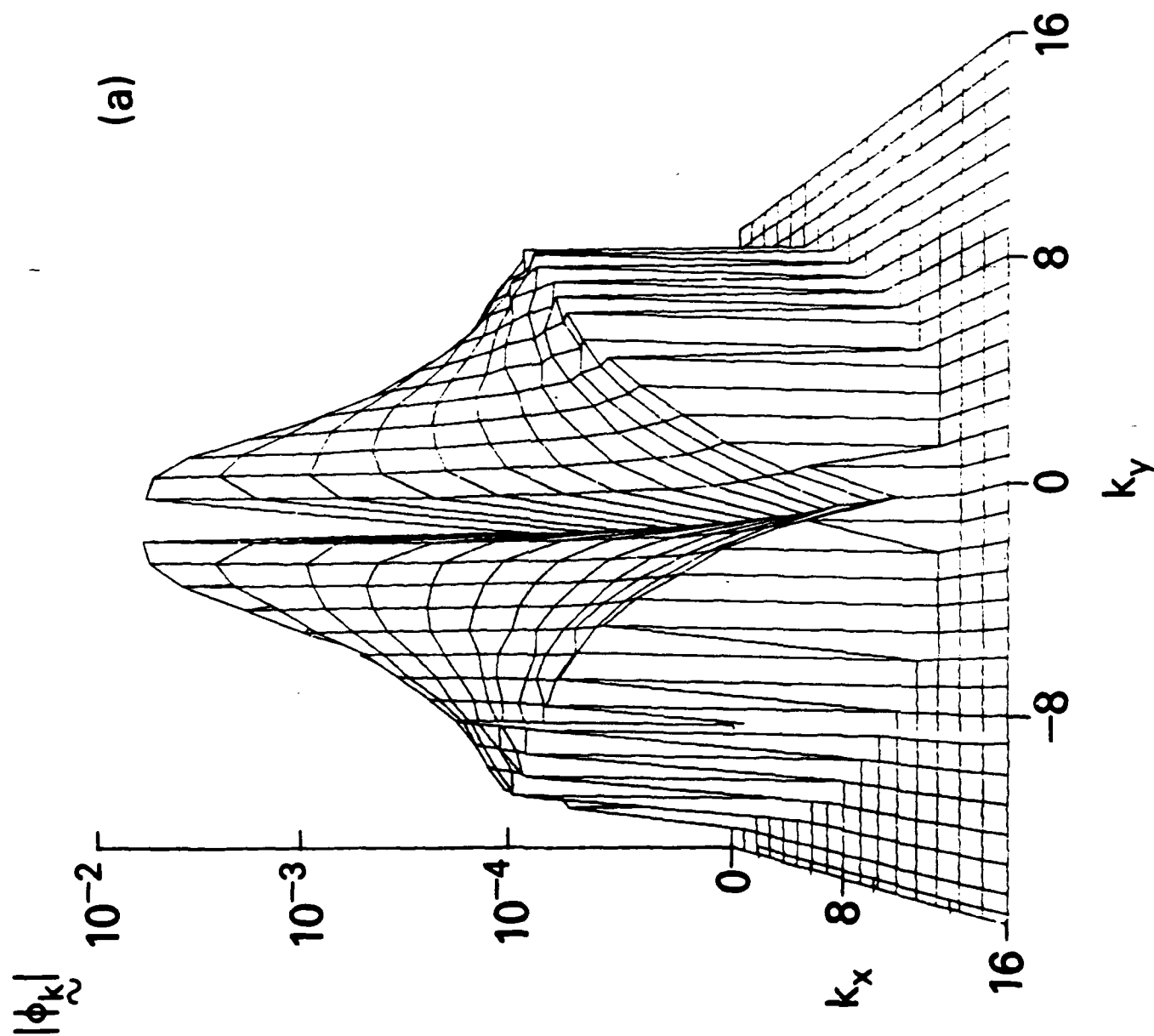


Figure 5a  
N-44

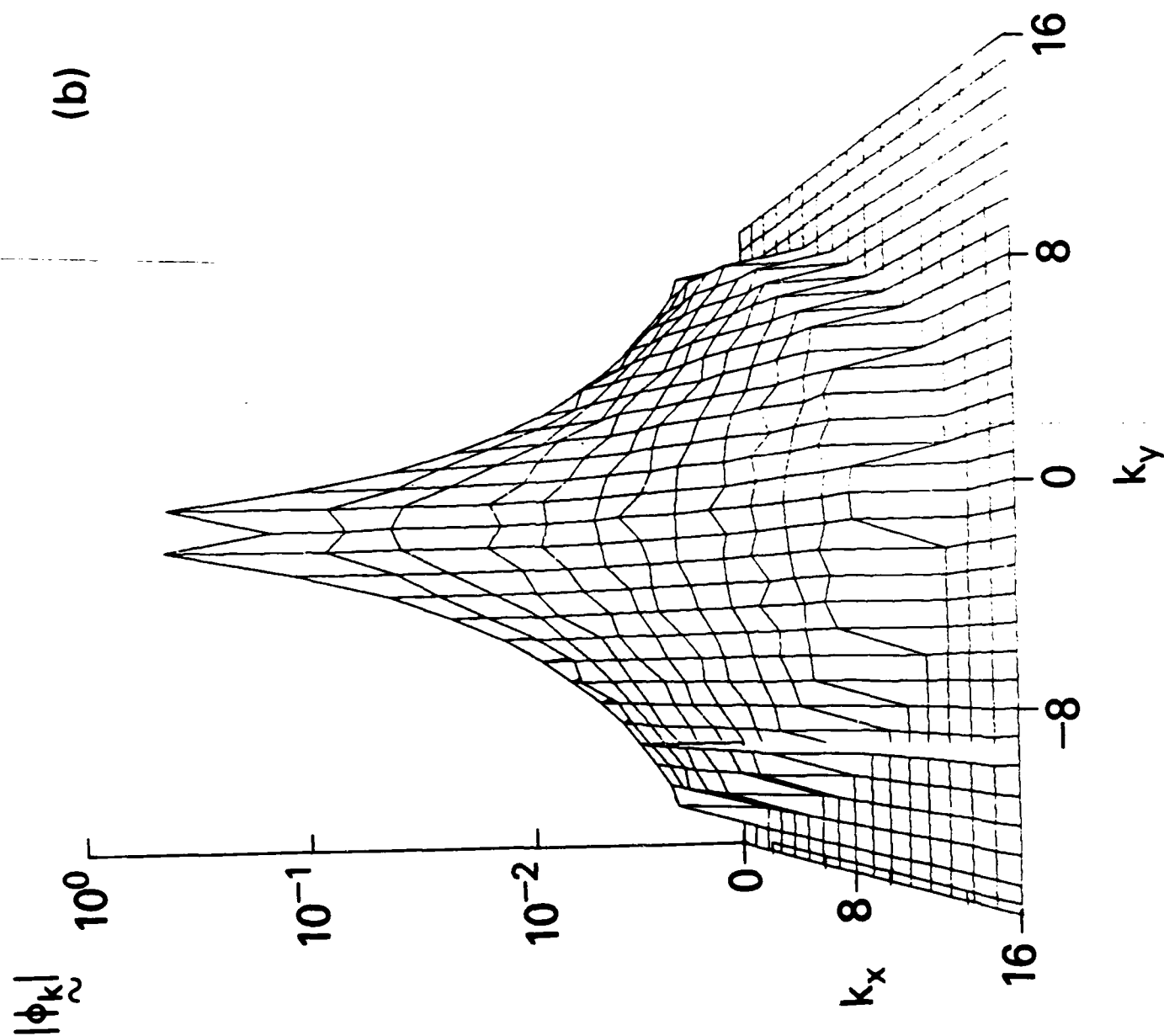


Figure 5b  
N-45

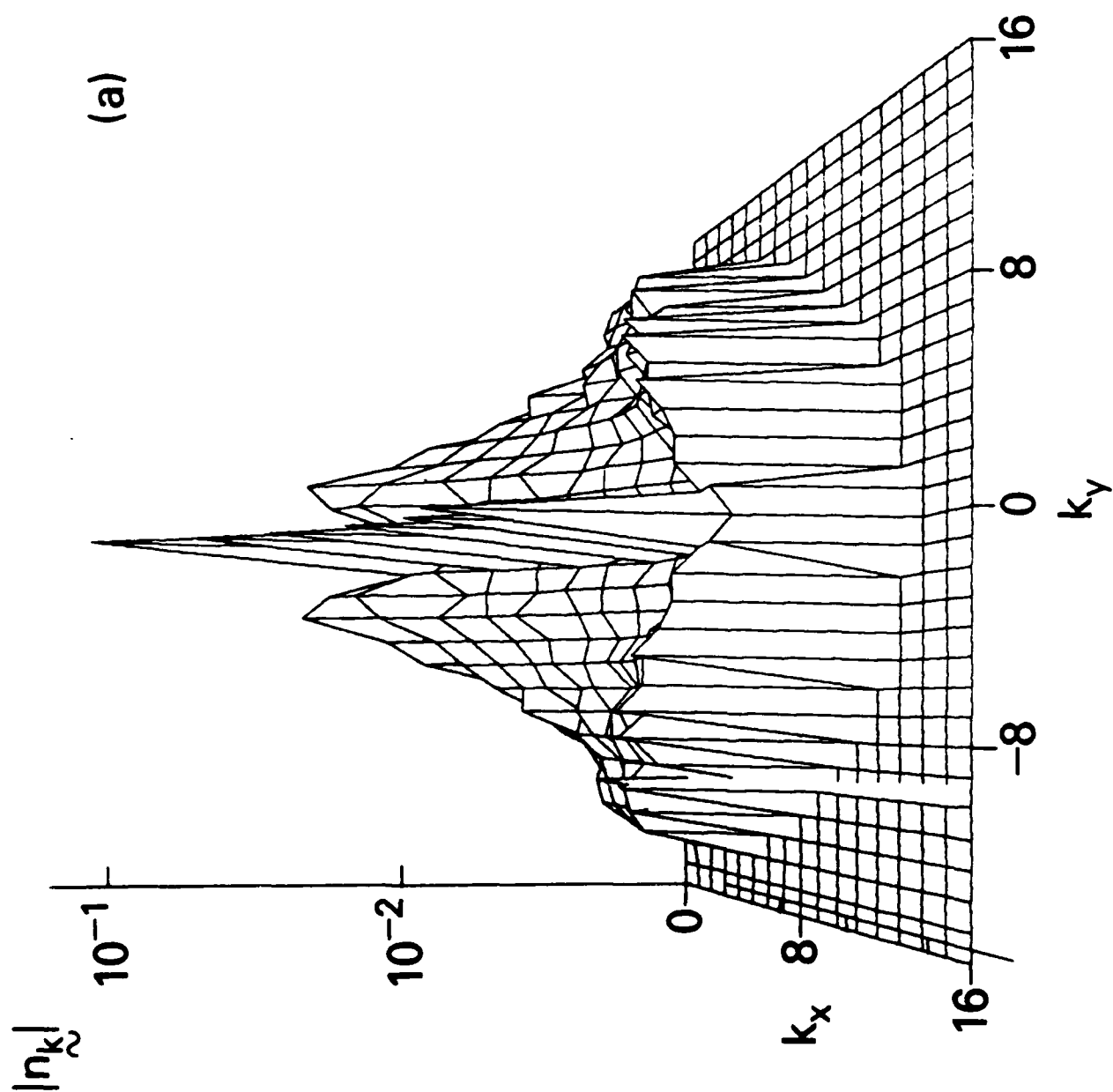


Figure 6a  
N-46



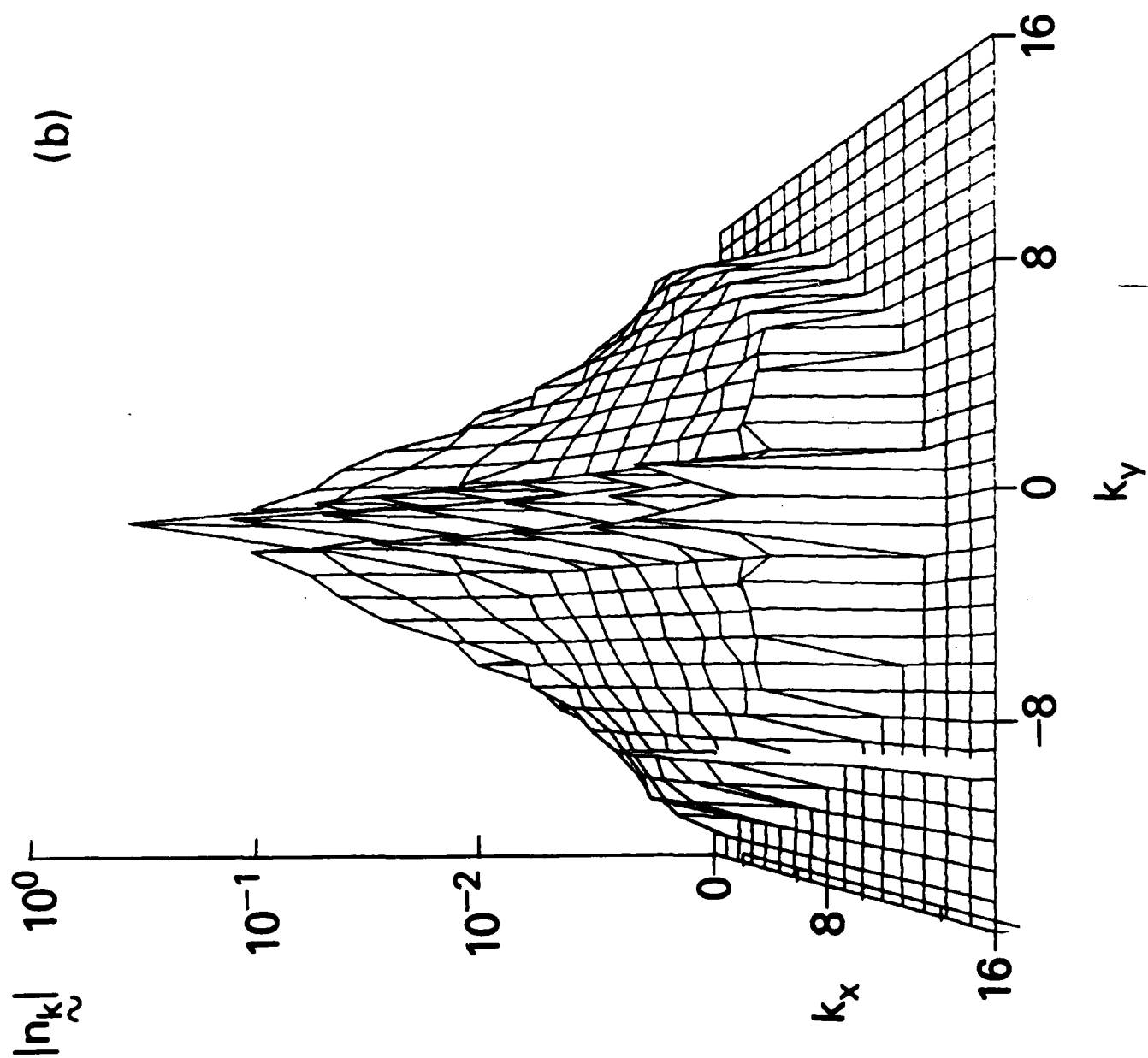


Figure 6b  
N-47

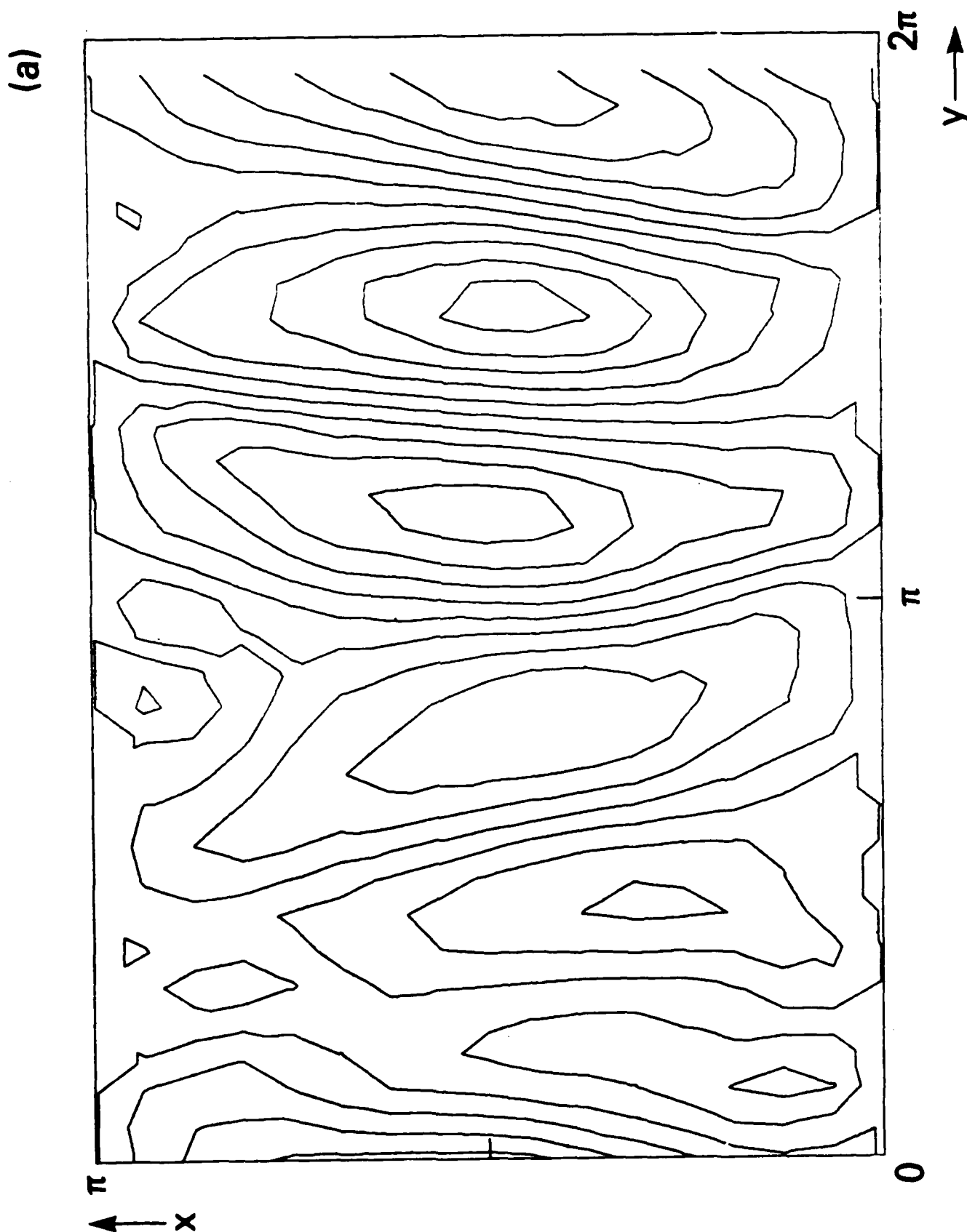


Figure 7a

N-12

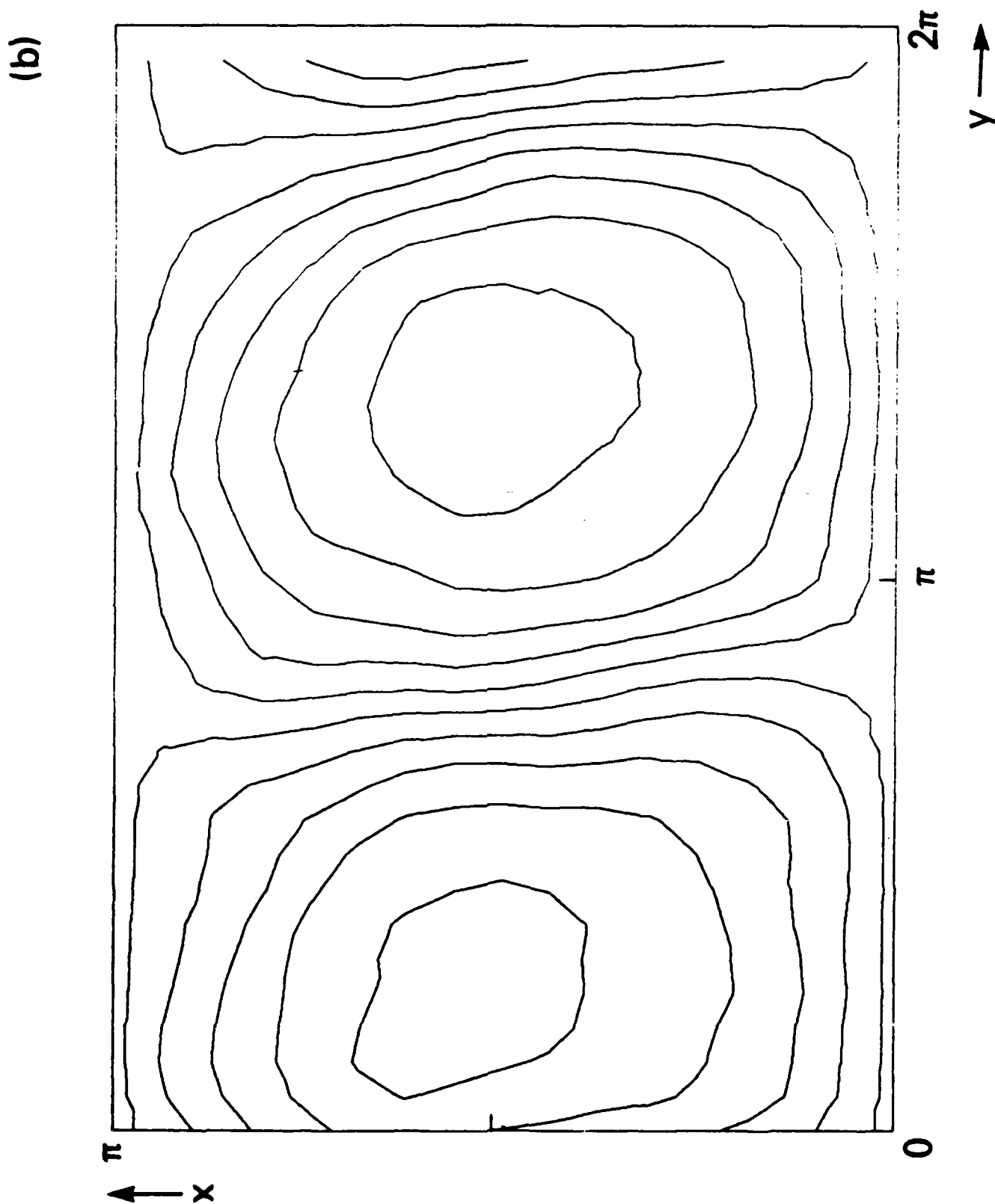


Figure 7b  
N-49

(a)

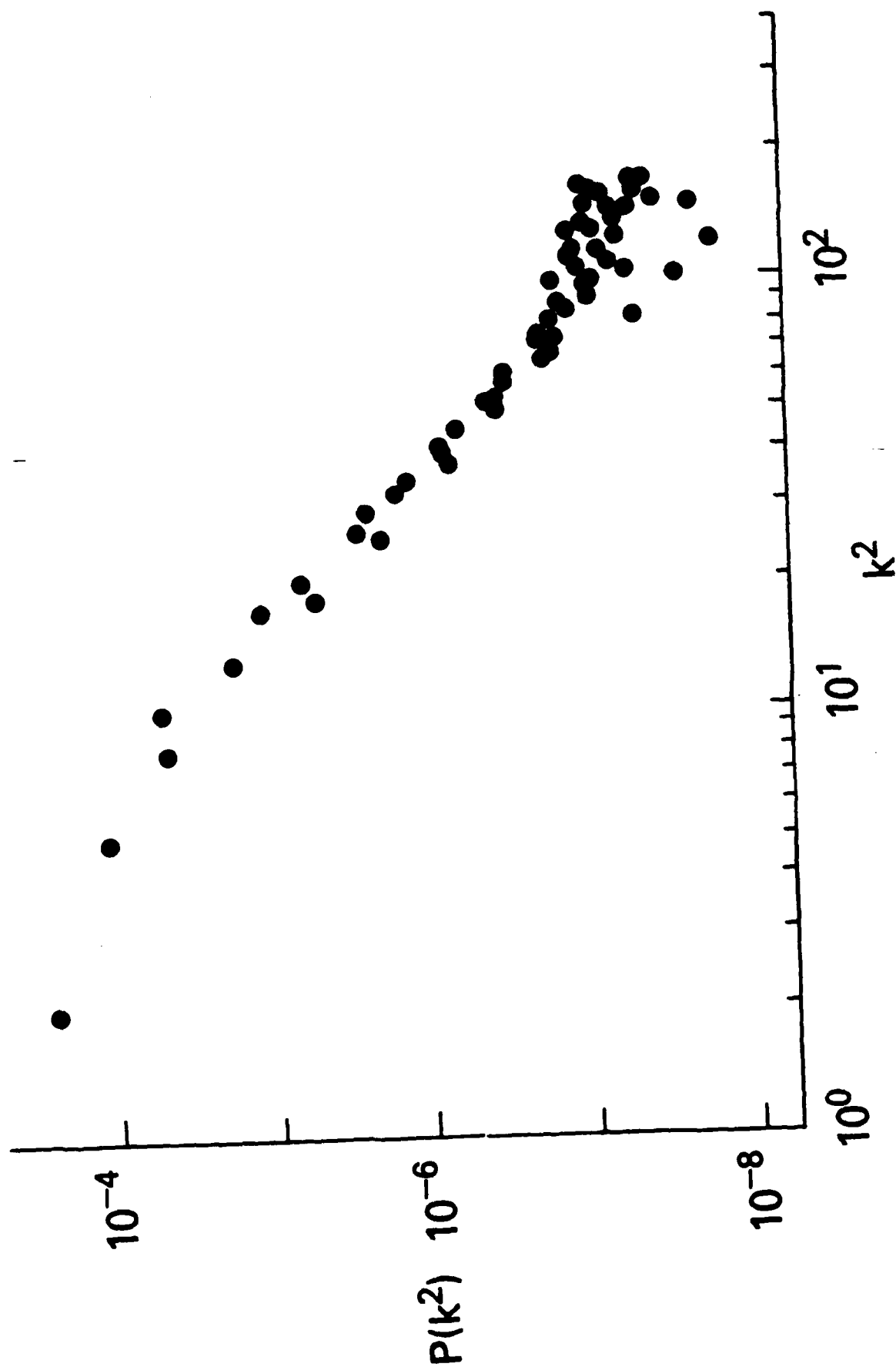


Figure 8a  
N=50

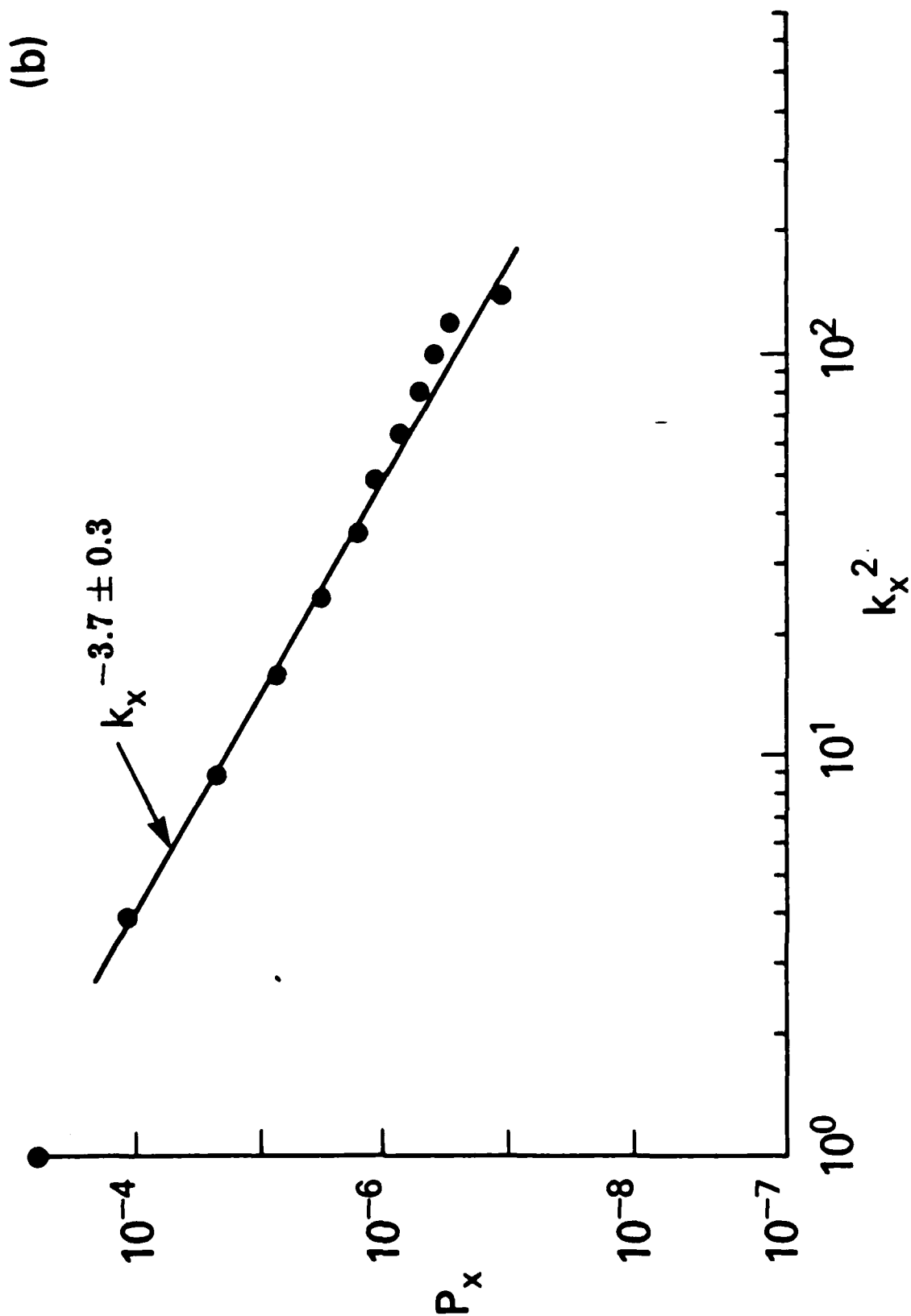


Figure 8b  
N-51

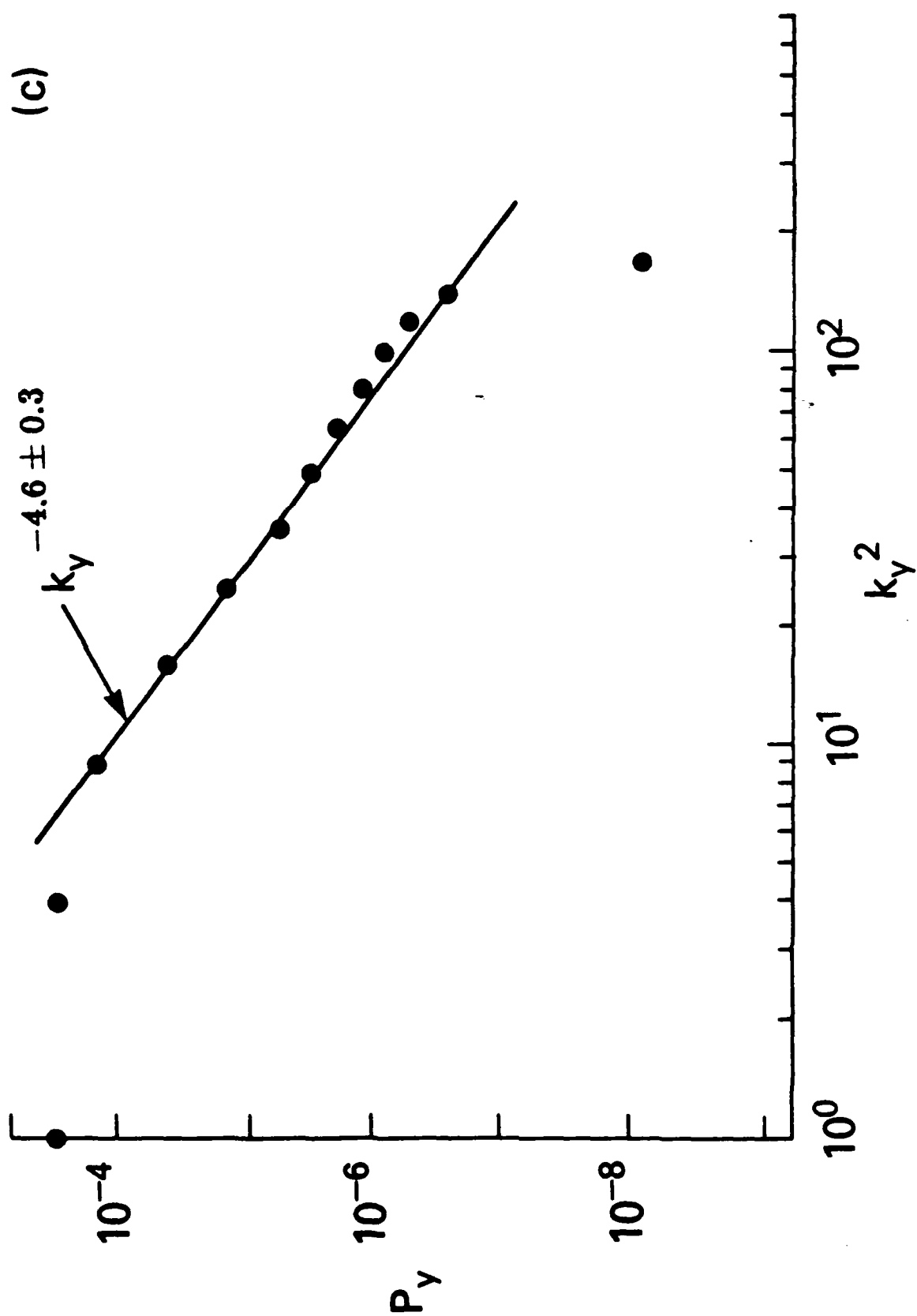


Figure 8c  
N-52

(a)

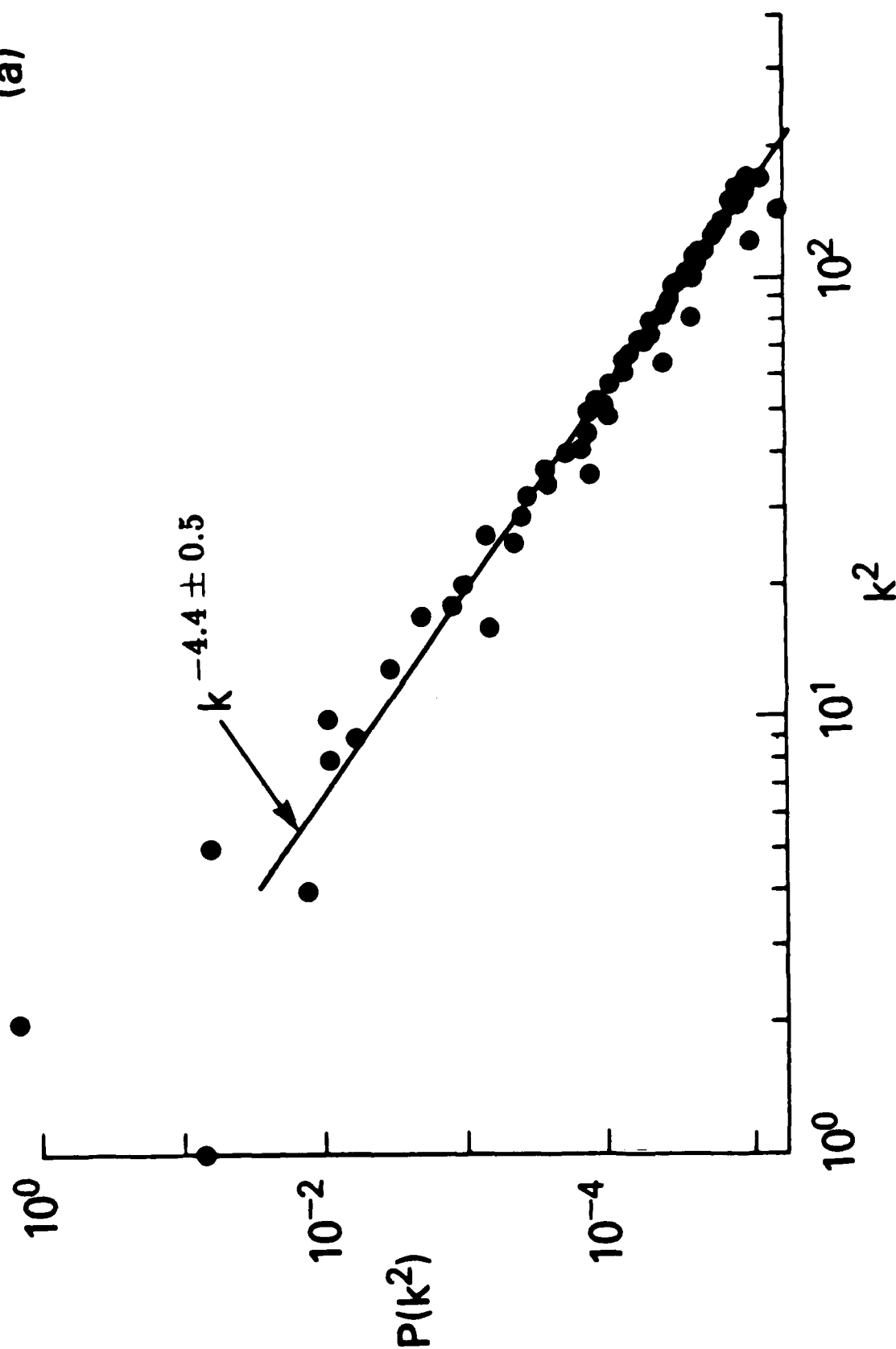


Figure 9a  
N-53

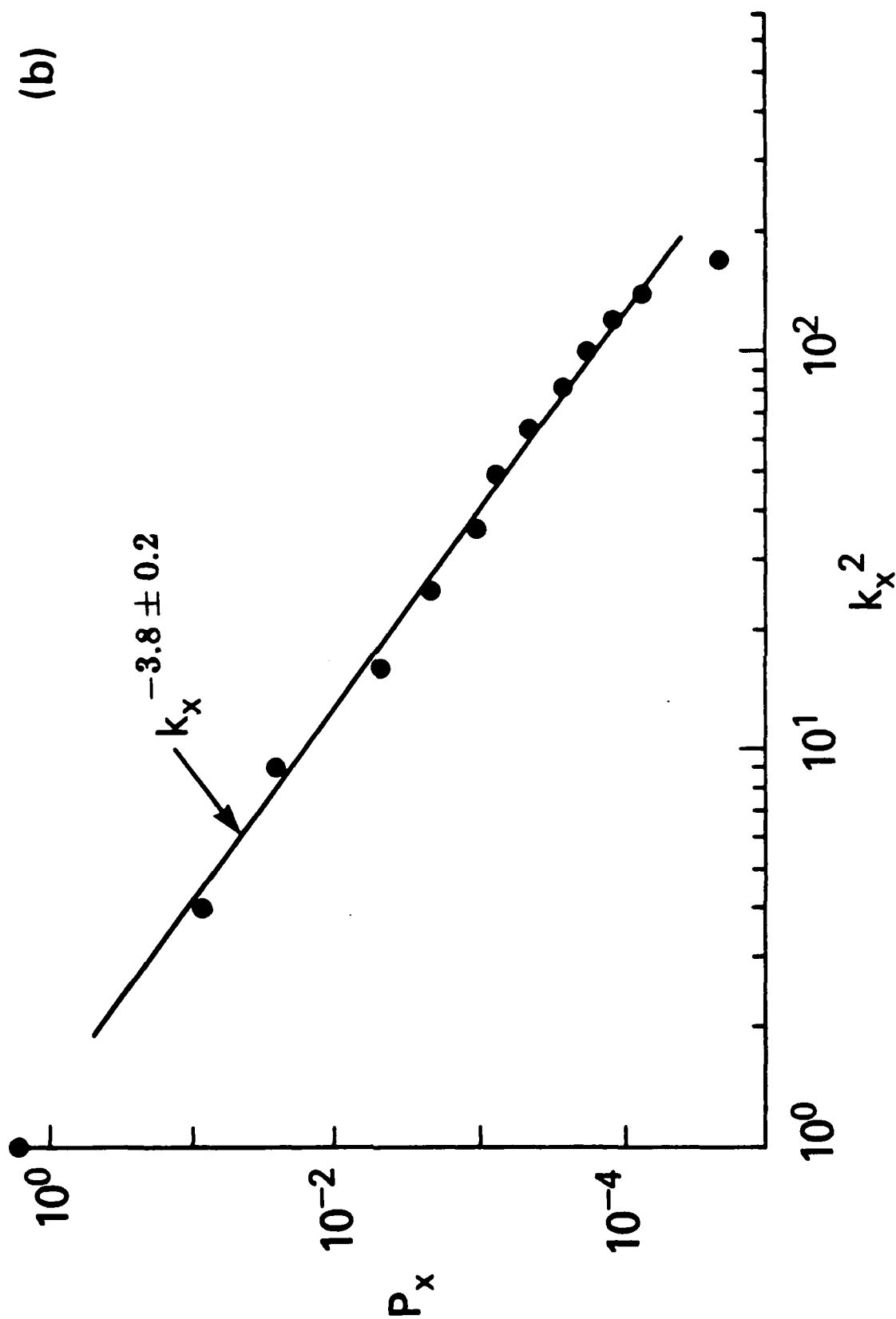


Figure 9b  
N-54



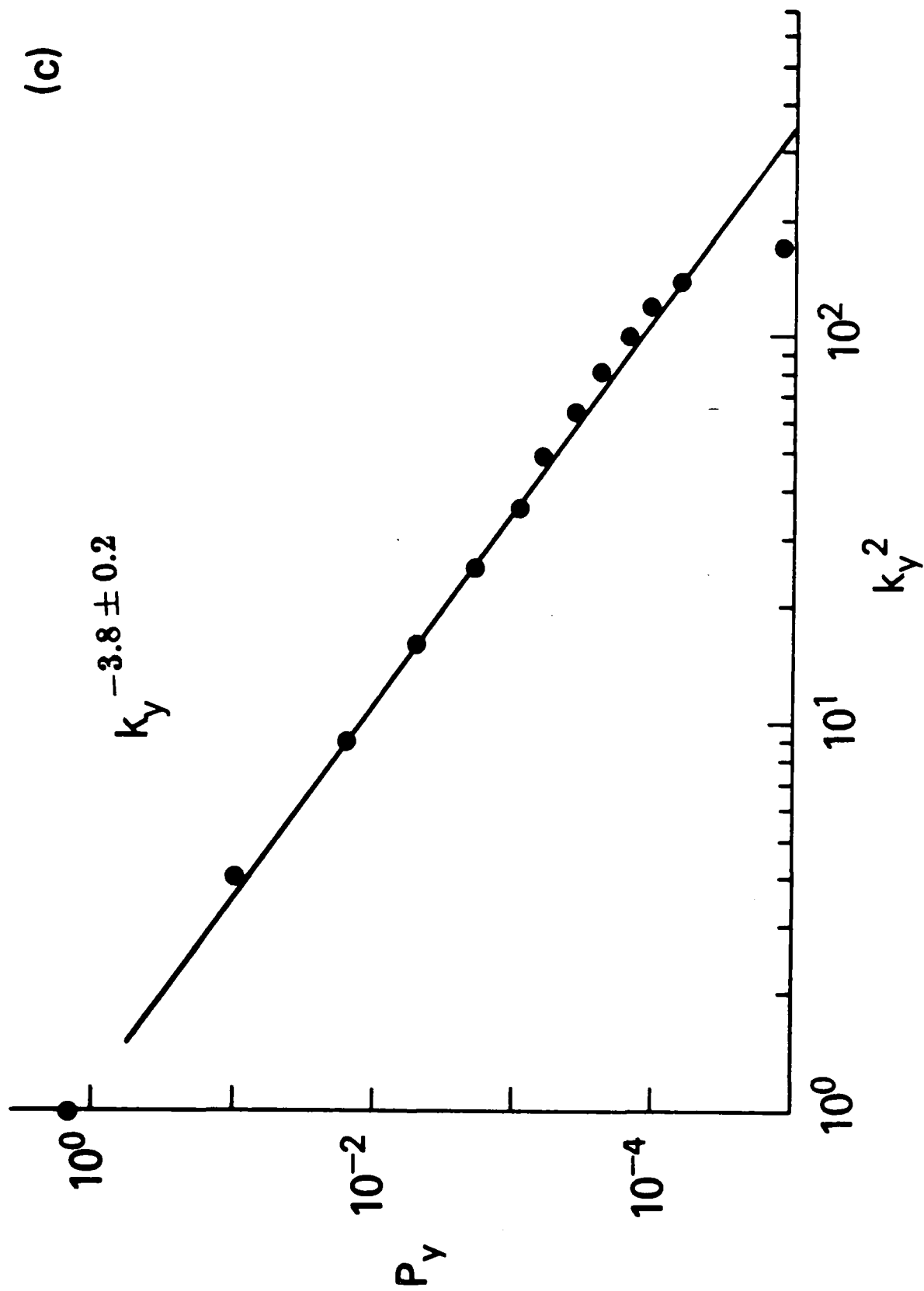


Figure 9c  
N-55

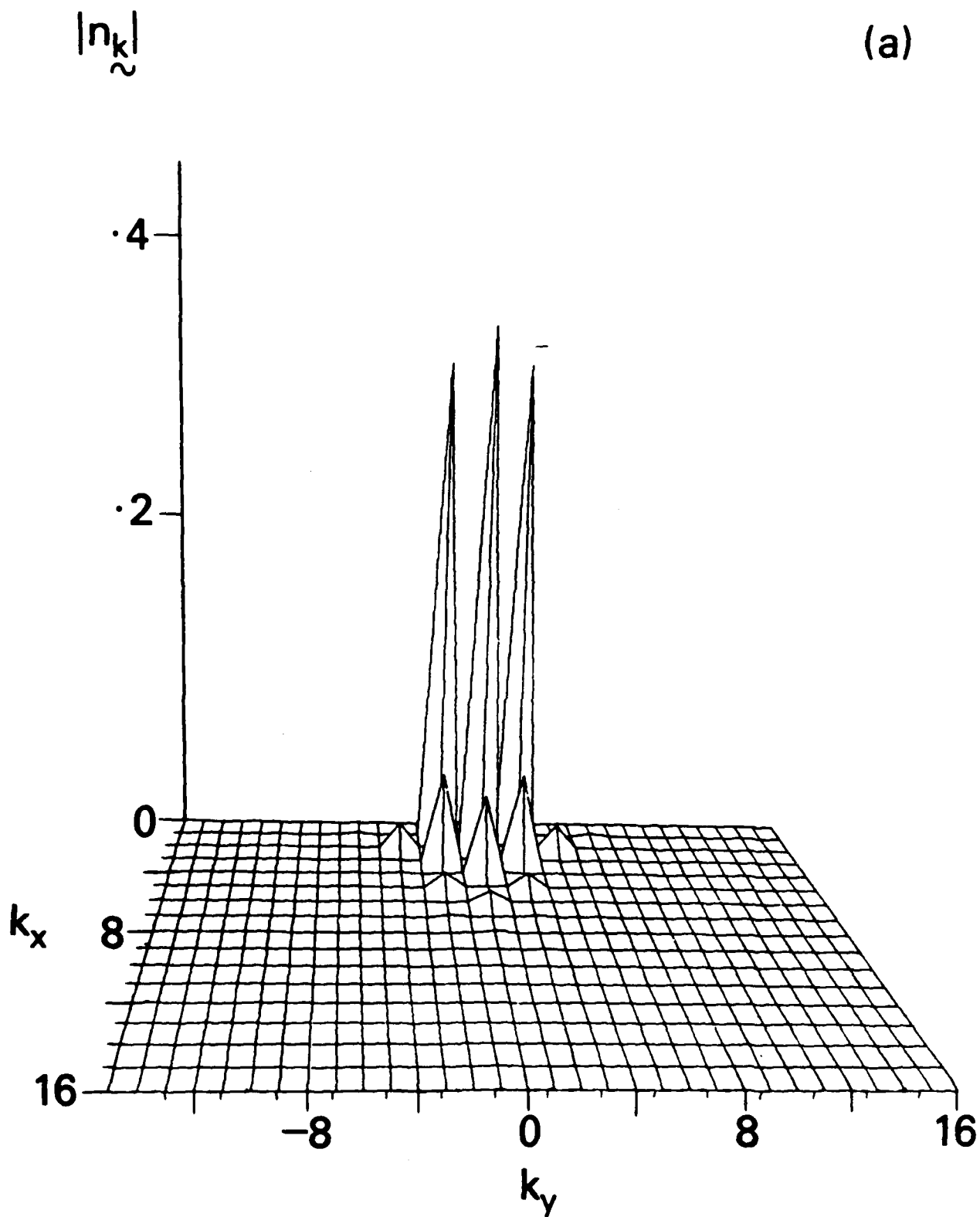


Figure 10a  
N-56

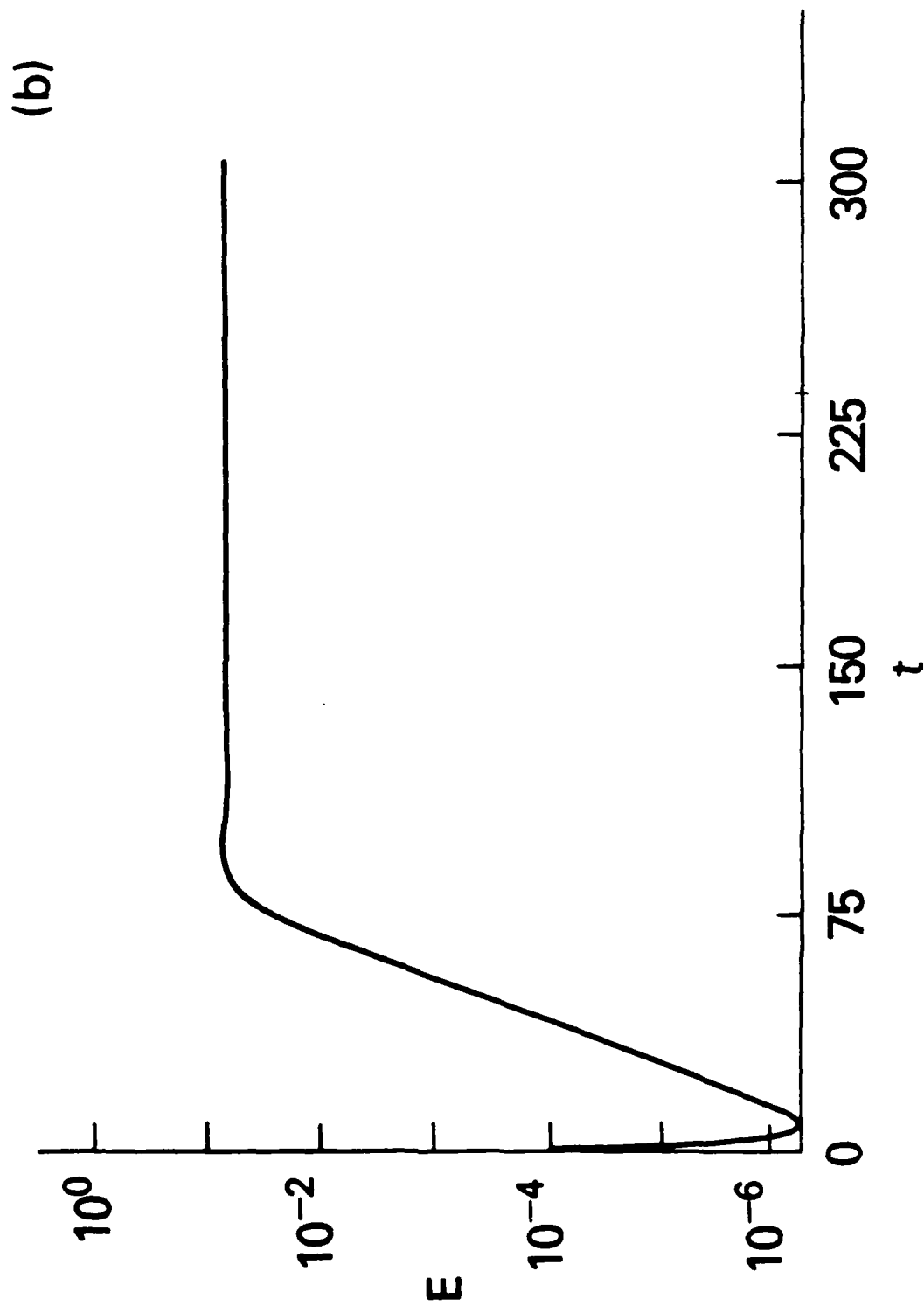


Figure 10b

N-57



**APPENDIX O**

**Early Time Coupling Studies Using a 1D Hybrid Code**

**C. Goodrich and K. Papadopoulos  
Science Applications International Corporation**

**J.D. Huba  
Naval Research Laboratory**



# Early Time Coupling Studies Using a 1D Hybrid Code

C. GOODRICH AND K. PAPADOPOULOS

*Science Applications International Corporation  
McLean, VA 22102*

J. D. HUBA

*Geophysical and Plasma Dynamics Branch  
Plasma Physics Division*

May 29, 1985

This work was sponsored by the Defense Nuclear Agency under Subtask S99QMXBC,  
work unit 00129 and work unit title "Early Time Dynamics."



NAVAL RESEARCH LABORATORY  
Washington, D.C.

Approved for public release; distribution unlimited.





REPORT DOCUMENTATION PAGE				
1a REPORT SECURITY CLASSIFICATION <b>UNCLASSIFIED</b>		1b RESTRICTIVE MARKINGS		
2a SECURITY CLASSIFICATION AUTHORITY		3 DISTRIBUTION/AVAILABILITY OF REPORT  Approved for public release; distribution unlimited.		
2b DECLASSIFICATION/DOWNGRADING SCHEDULE				
4 PERFORMING ORGANIZATION REPORT NUMBER(S) <b>NRL Memorandum Report 5553</b>		5 MONITORING ORGANIZATION REPORT NUMBER(S)		
6a NAME OF PERFORMING ORGANIZATION <b>Naval Research Laboratory</b>	6b OFFICE SYMBOL (If applicable) <b>Code 4780</b>	7a NAME OF MONITORING ORGANIZATION		
6c ADDRESS (City, State, and ZIP Code) <b>Washington, DC 20375-5000</b>		7b ADDRESS (City, State, and ZIP Code)		
8a NAME OF FUNDING SPONSORING ORGANIZATION <b>Defense Nuclear Agency</b>	8b OFFICE SYMBOL (If applicable) <b>RAAE</b>	9 PROCUREMENT INSTRUMENT IDENTIFICATION NUMBER		
9c ADDRESS (City, State, and ZIP Code) <b>Washington, DC 20305</b>		10 SOURCE OF FUNDING NUMBERS		
		PROGRAM ELEMENT NO <b>62715H</b>	PROJECT NO	TASK NO WORK UNIT ACCESSION NO <b>DN380-296</b>
11 TITLE (Include Security Classification) <b>Early Time Coupling Studies Using a 1D Hybrid Code</b>				
12 PERSONAL AUTHOR(S) <b>Goodrich, C.,* Papadopoulos, K.,* and Huba, J.</b>				
13a TYPE OF REPORT <b>Interim</b>	13b TIME COVERED FROM <b>10/84</b> TO <b>10/85</b>	14 DATE OF REPORT (Year, Month, Day) <b>1985 May 29</b>	15 PAGE COUNT <b>42</b>	
16 SUPPLEMENTARY NOTATION <b>*Science Applications International Corporation, McLean, VA 22102</b> (Continues)				
17 COSATI CODES		18 SUBJECT TERMS (Continue on reverse if necessary and identify by block number)		
FIELD	GROUP	SUB-GROUP		
			<b>Early time coupling Ion-ion interactions</b>	
			<b>1D Hybrid simulations Ion energization</b>	
19 ABSTRACT (Continue on reverse if necessary and identify by block number) <p>The results of simulations of very early time HANE processes (i.e., <math>t &lt; \Omega_i^{-1}</math>) using a 1D hybrid code are presented. The purpose of this work is to elucidate important physical phenomena which occur rather than to perform actual early time simulations of a HANE. The focus of this study is primarily on coupling mechanisms. We find that there is no "single" coupling mechanism but that several mechanisms can be effective at various times throughout the debris expansion phase: turbulent coupling, laminar pick-up, and Larmor coupling. Another important result of this study is the generation of very energetic ions. This is caused by the laminar electric field at the leading edge of the magnetic pulse. A fraction of the debris ions can be accelerated up to roughly three times the initial debris expansion velocity (i.e., <math>V_M \sim 3V_d</math>). It is well-known that the initial formation of ion debris patches occurs on a time scale faster than that calculated from the initial expansion velocity. Thus, the observation of accelerated debris ions in the simulations is consistent with HANE data.</p>				
20 DISTRIBUTION STATEMENT OF ABSTRACT <input checked="" type="checkbox"/> UNCLASSIFIED UNLIMITED <input type="checkbox"/> SAME AS RPT <input type="checkbox"/> DTIC USERS		21 ABSTRACT SECURITY CLASSIFICATION <b>UNCLASSIFIED</b>		
22a NAME OF RESPONSIBLE INDIVIDUAL <b>J. D. Huba</b>		22b TELEPHONE (Include Area Code) <b>(202) 767-3630</b>	22c OFFICE SYMBOL <b>Code 4780</b>	

16. SUPPLEMENTARY NOTATION (Continued)

This work was sponsored by the Defense Nuclear Agency under Subtask S99QMXBC, work unit 00129 and work unit title "Early Time Dynamics."

## CONTENTS

I. INTRODUCTION .....	1
II. OVERVIEW OF PHYSICAL PROCESSES .....	2
III. SIMULATIONS AND RESULTS .....	3
IV. DISCUSSION .....	8
ACKNOWLEDGMENT .....	9
APPENDIX - HYBRID CODE DESCRIPTION .....	18
REFERENCES .....	28



## EARLY TIME COUPLING STUDIES USING A 1D HYBRID CODE

### 1. INTRODUCTION

The understanding of atmospheric effects generated by a HANE is of vital importance to DNA. It is well known that HANE's cause severe disturbances in the atmosphere and ionosphere which impact C<sup>3</sup>I systems. In particular, long lasting, large scale ionization irregularities degrade radar and communications signals. To develop predictive capability for such HANE effects, DNA sponsored a major research effort at NRL leading to theoretical and computational models of HANE. Significant progress was made in this area during the past decade leading to the development of sophisticated multifluid codes which incorporate in a self consistent manner anomalous transport due to instabilities. Recent advances in both plasma theory and numerical techniques allow us today to produce substantially more refined and accurate models of the early time HANE phenomenology. These advances indicate the need for a better incorporation of kinetic effects due to strong deviations of the particle distributions from Maxwellian. The new codes allow us to compute the laminar and turbulent dynamic ion response over long time and space scales and for a mixture of ionized species. In this way laminar, electrostatic, Larmor and turbulent coupling processes can be followed dynamically and their relative strength and dynamic interplay can be assessed. This paper is the first to describe this series of investigations, focuses on a particular process, early time debris-air coupling, and stresses quantitative understanding of the underlying physics.

Early time coupling had been a controversial subject in the DNA HANE community in the 1970's. Two "opposing" views were maintained: NRL, LASL and ARA advocated short-range coupling associated with plasma turbulence, while MRC argued for "Larmor coupling" associated with the ion gyration in the ambient magnetic field. To a certain extent, the issue was not whether or not these coupling mechanisms worked, but which mechanism was dominant. The turbulent coupling process developed at NRL was studied by incorporating theoretical estimates of anomalous transport coefficients in a 1D multi-fluid code. Although this procedure yielded results consistent

Manuscript approved February 14, 1985.

with HANE data and provided strong support for turbulent coupling, it was not a self-consistent technique. Moreover, it was not capable of handling kinetic effects such as caused by reflected ions; such reflected ions are known to occur in high Mach number shocks. The present study, using a 1D hybrid code, overcomes these deficiencies. Namely, it allows instabilities to be excited which affect the plasma evolution in a self-consistent manner, i.e., no model anomalous transport coefficients are used, and reflected ions are permitted. Furthermore, the 1D hybrid code inherently includes "Larmor coupling" so that a direct comparison of the relevant importance and interplay of the coupling mechanisms can be made.

The organization of the paper is as follows. In the next section we present an overview of the basic physical processes occurring as debris streams through the air. In Section III we present results of two simulations which demonstrate the various aspects of coupling. Finally, in the last section we summarize our results and discuss their implications to HANE phenomenology.

## II. OVERVIEW OF PHYSICAL PROCESSES

The evolution of the debris-air plasma is characterized by three temporal stages: (1) magnetic field compression; (2) piston formation; and (3) shock formation and evolution. The bulk of this paper describes in detail piston dynamics; for completeness we briefly discuss the other two stages.

In the initial stage, the debris streams outward from the burst point and picks up air electrons which merge with the debris electrons to form a single electron distribution. The compression of the air electrons leads to a compression of the magnetic field since the air electrons are "tied" to the field lines due to the low value of resistivity. This is the first stage of the debris-air interaction and has been well-documented theoretically (Longmire, 1963; Sloan, 1970; Lampe and Hernandez, 1972), numerically (Clark et al., 1974), and experimentally (Ripin et al., 1984).

The next stage involves the dynamics of piston formation and will be discussed in detail in the following section. Briefly, this stage is dominated by the interaction of the two ion streams, i.e., the debris ions and the air ions. It is this phase where various coupling mechanisms

become apparent. The debris ions slow down, while the air ions are picked up; there is momentum exchange between the ion species. There is also a conversion of the directed kinetic energy of the debris to thermal energy of both ions and electrons, i.e., heating and acceleration occurs. And finally, an electrostatic potential forms at the leading edge of the magnetic field compression which causes some debris ions to be accelerated ahead of the magnetic piston and some air ions to be reflected. This final point, although well-known, can be very important to the formation of debris patches in the conjugate regions since it results in very high velocity ions.

Lastly, the final stage involves the formation of a shock wave which "runs" ahead of the piston. We do not describe this phase in detail in this paper, but do show that a minimum time is required for high Mach number shock formation. This minimum time is basically the time needed for the shock to "run" ahead of the accelerated debris or reflected air ions.

### III. SIMULATIONS AND RESULTS

Prior to discussing the details of the simulations, we present a simple model equation that elucidates the various coupling mechanisms to be studied. Moreover, it highlights the distinction between previous models (e.g., KLYSMA) and the present work. We consider the following momentum equation in the x direction for an air ion (i.e., radial direction perpendicular to the ambient magnetic field  $\underline{B} = B\hat{e}_z$ ).

$$\frac{dv_{ax}}{dt} = \frac{eE_x}{m_a} + \Omega_a v_{ay} - v^*(v_{ax} - v_d) \quad (1)$$

where the subscript a refers to air,  $\Omega_a = Z_a eB/m_a c$ ,  $v^*$  is an anomalous ion-ion collision frequency,  $\underline{v}_d = v_d \hat{e}_x$  is the streaming debris velocity,  $e$  is the charge,  $m$  is the mass, and  $Z$  is the charge state. The first term on the RHS of (1) arises from a laminar electric field usually associated with the leading edge of the magnetic compression. It acts to accelerate debris ions and to reflect air ions. The second term in (1) is the magnetic force which is associated with Larmor coupling. The final term in (1) corresponds to turbulent "pick up" of the air and arises because of plasma instabilities. For plasma turbulence such that  $v^* > \Omega_i$  it is clear that turbulent coupling can dominate over Larmor coupling.

Notice that the force  $\Omega_a V_{ay}$  associated with Larmor coupling is proportional to the value of  $V_{ay}$  which, before any form of coupling occurs, is  $V_{ax} = V_{ay} = 0$ . Therefore the laminar force  $eE_x/m_a$  and the turbulent force  $v^*|V_{ax} - V_d| \sim v^*V_d$  will dominate initially even for  $v^* \ll \Omega_a$  (i.e., as long as  $v^* > \Omega_a(V_{ay}/V_d)$ ). The time evolution of  $V_{ay}$  will be given by

$$\frac{dV_{ay}}{dt} = \frac{eE_y}{m_a} = \frac{eV_d B}{m_a c} = \Omega_a V_d \quad (2)$$

In deriving eq. (1a) we assumed an infinitely conducting ( $\eta \rightarrow 0$ ), low  $\beta$  ( $\beta \ll 1$ ) situation so that  $E_y = V_d B/c$ . From eqs. (1) and (2) it is obvious that the time scale for significant Larmor coupling is  $\Omega_a t > 1$ , i.e., the value of  $V_{ay}$  should approach  $V_d$ . At earlier times the laminar and turbulent forces will dominate. The turbulent forces will also dominate even at  $t \gg \Omega_a^{-1}$  as long as  $v^* > \Omega_a |V_{ax} - V_d|/V_d$ . Another important point follows from (1) and (2) if we neglect the laminar and turbulent forces. If  $L$  is the size of magnetic field compression then as long as  $V_{ax} < V_d$  the maximum value of  $V_{ay}$  will be  $V_{ay} = \Omega_a L$ . As mentioned previously the Larmor momentum coupling force in the  $x$  direction becomes significant if  $V_{ay} = \Omega_a L$ . Therefore for effective Larmor coupling  $L > V_d/\Omega_a$ . Namely, an extremely broad magnetic field profile will be required. We will further comment on this point later on.

In previous work, theoretical estimates of  $v^*$  were incorporated in a multi-fluid code (KLYSMA) which solved momentum equations similar to (1) and (2) (Clark et al., 1974). However, the turbulent interaction involves ions interacting with fluctuating electric fields, i.e.,  $v^* = v^*(\delta E)$ . The present simulations incorporate such effects self-consistently. The air momentum equation solved, analogous to (1), is

$$\frac{dV_{ax}}{dt} = \frac{e}{m_a} (E_x + \delta E_x) + \Omega_a V_{ay} \quad (3)$$

where  $\delta E_x$  is self consistently generated because of plasma instabilities (e.g., ion-ion streaming instability (Papadopoulos et al., 1971) and is allowed to act directly on the ion motion, rather than through a model equation such as (1). Given this background, we now present the simulation results.



The simulations were performed using a one dimensional quasi-neutral hybrid code (Chodura, 1975; Winske and Leroy, 1984) whose description is given in Appendix I. The code incorporates ion kinetic effects by following the trajectories of "superparticles", numerically representing many actual ions, in 3 dimensions in velocity space and one dimension in configuration space. The electrons are approximated as a massless fluid described by momentum and energy transport equations; the electron pressure is assumed to be isotropic. These equations, with Maxwell's equations, are solved on a one dimensional spatial grid using moments calculated from the ion distributions. Anomalous resistivity, resulting in magnetic field diffusion and electron ohmic heating, is included as a parameter in the equations with a value consistent with that expected from current driven cross-field instabilities.

The boundary conditions in the code correspond to the conditions we expect at early times. A dense ion beam is injected continuously into the simulation box which is initially filled with a tenuous stationary plasma. In our present results both ion populations are  $H^+$ , but other ion species can be easily considered and will be presented elsewhere. We set up a finite width magnetic field compression within the leading edge of the ion beam. This represents the field compression expected from the cross-field beam motion which, because of finite resistivity, will diffuse into the beam. The width of the compression has been varied to study various physical phenomena. The magnetic field is held fixed at the edges of the simulation box.

We present below the results of two simulations selected to illustrate the underlying physical coupling processes. The initial state is typical of the piston formation stage. It is shown in Fig. 1a, for the case of  $M_A = V_d/V_a = 4$ , where  $V_A$  is defined on the basis of the ambient (i.e., upstream) parameters. A magnetic pulse consistent with  $B/n = \text{constant}$  is introduced at the left hand boundary. In this paper we do not study the formation of the pulse but assume its nature in accordance with previous work mentioned in Section II, and its width  $L$  to illustrate the important physics. In the figures the velocity is in terms of the upstream value of  $V_A$  and of time in terms of the upstream value of  $\Omega_a^{-1}$ . The units of length are in terms of the ion cyclotron value computed for air with velocity  $V_d$

but with the value of the downstream (i.e., compressed) magnetic field. This representation has been selected for clarity of the underlying physics. We consider (1) a "broad"  $L_B = 2R_1$  ( $R_1$  in upstream values) pulse with  $M_A = 4$  and  $n_d/n_a = 16$  and (2) a "narrow"  $L_B =$  pulse with  $M_A = 8$  and  $n_d/n_a = 64$ . Here  $V_d$ ,  $n_d$  are the debris velocity and density,  $n_a$  the air density and  $V_A$  is defined on the basis of the upstream conditions.

#### A. Broad Pulse ( $L_B \approx 2r_{Li}$ )

This simulation is initialized with a magnetic pulse width  $L_B \sim 2r_{Li}$ ,  $V_d/V_A = 4$  and  $n_d/n_a = 16$ . We show a series of results for this run in Fig. 1. Figure 1 displays four important quantities versus distance. The bottom curve represents the magnetic field magnitude, the middle curve (or "dots") represent particle velocities of the debris and air ions (the debris ions have  $V_d \sim 4V_A$  while the air ions have  $V_d \sim 0$ ), and the top curve represents the electric field in the x direction. Figure 1a is at  $t = 0.0019 \Omega_i^{-1}$  where  $\Omega_i$  is based on the upstream value of  $B$ . Note the broad pulse in  $B$  with sharp gradients at the leading and trailing edges. Associated with these gradients are strong laminar electric fields at these edges as shown in the top portion of Fig. 1a. These fields strongly affect the ions. Note in the middle panel that some debris ions are being accelerated ahead of the  $B$  pulse, and air ions are being picked up in a reflection process.

Figure 1b depicts the system at  $t = 0.0386 \Omega_i^{-1}$  and several interesting features are developing. First, the  $B$  field pulse has broadened considerably. The leading edge of the pulse has been "dragged" out to  $x \sim 4r_{Li}$ , and the gradients are not as sharp. Second, the laminar electric field has fallen in intensity and is accompanied by a considerable amount of turbulence in the region  $0 \lesssim r/r_{Li} \lesssim 2.4$  caused by of the ion-ion streaming. This turbulence causes some momentum exchange between debris and air ions, and thermalization of the particles in this region. Finally, also at this time, a fraction of debris ions have been accelerated to a velocity greater than twice the initial velocity.

Figure 1c shows the system at  $t = 0.0874 \Omega_i^{-1}$ . The magnetic pulse continues to broaden and now extends to  $x \sim 6r_{Li}$ . A laminar electric field still exists at  $x \sim 3.6 r_{Li}$ . However, the turbulence in the region  $0 <$

$x/r_{Li} \lesssim 3.6$  has subsided since the relative velocity between debris and air ions is small. The ion motion in this region is dominated by the magnetic field and, in effect, is where "Larmor coupling" is taking place. Perhaps the most interesting region is  $3.6 < x/r_{Li} < 6.0$ . It is clear that debris acceleration and air reflection are continuing. Furthermore, turbulence is developing at the debris-air interface ( $x \sim 4.0 r_{Li}$ ).

Finally, Fig. 1d shows the system at  $t = 0.1542 \Omega_i^{-1}$ . The magnetic pulse is quite broad now, extending out to  $x \sim 8.0 r_{Li}$ . Very intense electrostatic turbulence is occurring at the debris-air mix in the region  $4.2 \lesssim x/r_{Li} \lesssim 8.2$  which is producing coupling between the ion species and thermalizing the particles. Debris particles have been accelerated up to  $V \sim 3V_d$ . In the region  $2.0 \lesssim x/r_{Li} \lesssim 4.0$  the air ions have a velocity  $V \sim 5.0 V_A$  while the debris ions have a velocity  $V \sim 3.0 V_A$ . In this region the momentum coupling is through the magnetic field (Larmor coupling) and the debris and air ions perform gyrations about the magnetic field. Very little turbulence is evident in the electric field, confirming the fact that  $v^* < \Omega_a$ .

Thus, in this simulation it is found that three important processes are affecting coupling, energization, and thermalization: (1) laminar electric fields; (2) turbulent electric fields; and (3) magnetic field pick-up. The laminar fields are most prominent early in the run (Fig. 1a) and cause debris acceleration and air reflection. This is crucial to early time HANE processes since debris ions can be accelerated up to  $\sim 3$  times their initial expansion velocity, and air ions are "picked-up". Turbulent electric fields cause coupling and thermalization of the ion species. In this run they are most effective at the debris-air interface, and ahead of the interface (Figs. 1c and 1d). Finally, "Larmor coupling" is observed within a section of the broad magnetic pulse in Figs. 1c and 1d, i.e., the debris and air ions have rotated about the  $B$  field so that the air ions have a larger  $x$  velocity than that of the debris ( $V_{ax} > V_{dx}$ ). This process supplements any incomplete part of the turbulent coupling and operates on a long time scale.

### B. Narrow pulse ( $L_B = 0.1 r_{Li}$ )

This simulation is initialized with a magnetic pulse width  $L_B = 0.1 r_{Li}$  and  $V_d/V_A = 8$  and  $n_d/n_a = 64$ . The results are shown in Fig. 2. In Fig. 2a we show the plasma system at  $t = 0.0206 \Omega_i^{-1}$ . Already by this time a substantial number of air ions are being reflected from the laminar electric field at  $x \sim 1.5 r_{Li}$ . Furthermore, debris ions have been accelerated up to  $V \sim 2.5 V_d$  and extend out to  $x \sim 4 r_{Li}$ . In this region there is a considerable amount of electrostatic turbulence as seen in the electric field plot. Figure 2b is at  $t = 0.0411 \Omega_i^{-1}$ . The magnitude of the turbulence electric fields have increased from the previous time shown and are quite intense at the debris-air interface ( $x \sim 3.0 r_{Li}$ ). The air ions are being "picked up" because of their turbulence and thermalized. The magnetic field has been dragged out to  $x \sim 7.0 r_{Li}$  by accelerated debris ions. Finally, Figs. 2c and 2d show the ions and fields at  $t = 0.0617 \Omega_i^{-1}$  and  $t = 0.0771 \Omega_i^{-1}$ , respectively. The general features are similar to  $t = 0.0411$  (Fig. 2b). There are intense turbulent fields at the debris-air interface which transfer momentum from the debris to air ions, and also thermalize the particles. Debris ions extend out to  $x \gtrsim 10.0 r_{Li}$  by  $t = 0.0617 \Omega_i^{-1}$ , as well as the  $B_z$  field and low level turbulence. In this run there is no indication of Larmor coupling. One interesting feature seen in Fig. 2d is the "structuring" of the magnetic pulse. In particular, there is a sharp gradient that has developed at  $x \sim 4.8 r_{Li}$  which produces a laminar electric field. This field acts to energize air ions to such that  $V \sim 1.8 V_d$  at  $x \sim 5.0 r_{Li}$ .

### IV. DISCUSSION

We have presented the results of simulations of very early time processes (i.e.,  $t < \Omega_i^{-1}$ ) using a 1D hybrid code. The purpose of this work has been to elucidate important physical phenomena rather than to perform an actual early time simulation of a HANE. The focus of this study has been primarily on coupling mechanisms; an area that has been somewhat controversial within the DNA community. We have found that there is no "single" coupling mechanism but that several mechanisms can be effective at various times throughout the debris expansion phase. In the first simulation, initialized with a "broad" magnetic pulse, the initial coupling

occurs through laminar electric field at the leading edge of the pulse. Subsequent to this, turbulent coupling occurs at the initial debris-air interface while Larmor coupling occurs within the main body of the magnetic pulse. In the second simulation, initialized with a "narrow" magnetic pulse, the only coupling observed was because of the electric field (laminar and turbulent).

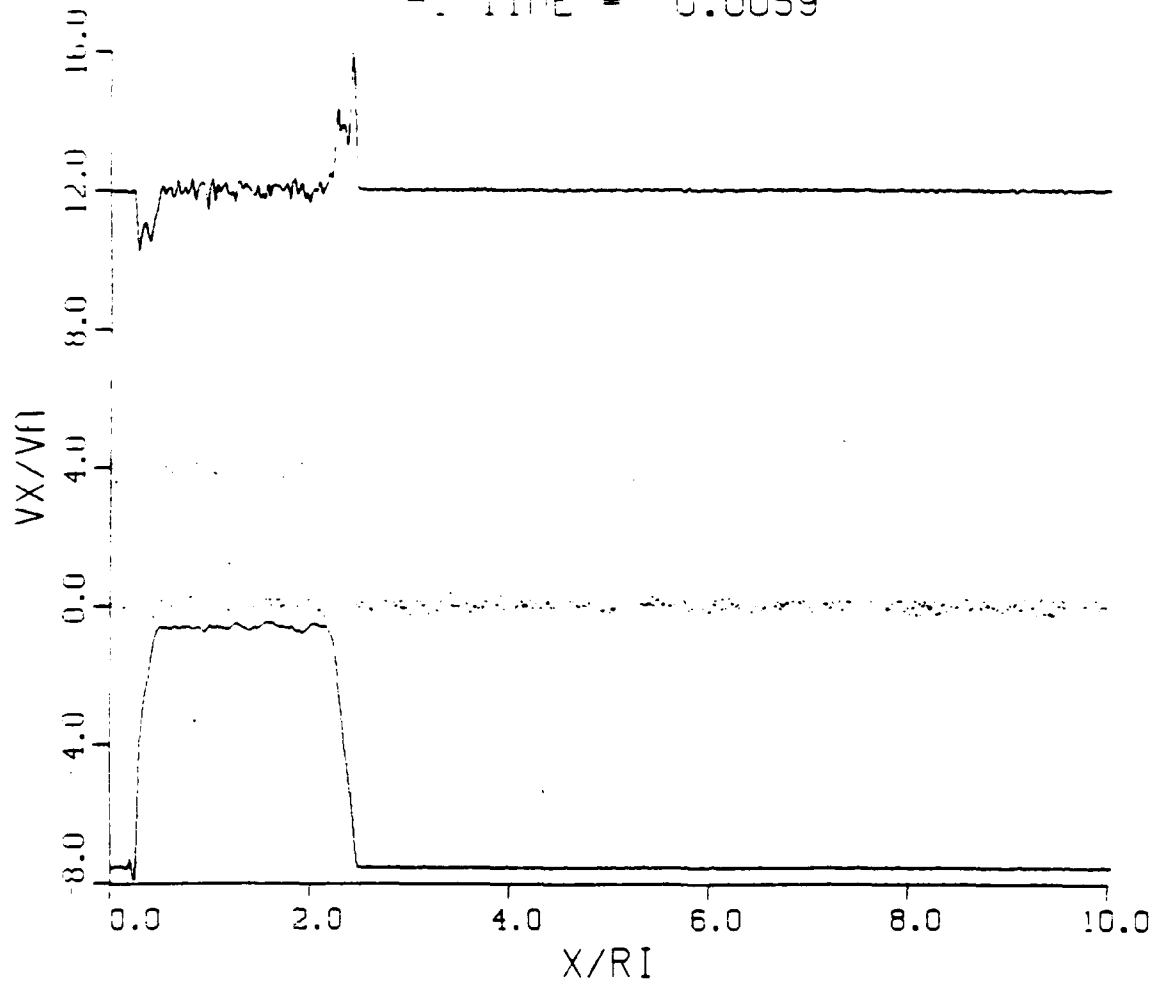
A very important result of this study is the generation of very energetic debris ions. This is caused by the laminar electric field at the leading edge of the magnetic pulse. A fraction of the debris ions can be accelerated up to roughly three times the initial debris expansion velocity (i.e.,  $V_M \sim 3V_d$ ). It is well-known that the initial formation of ion debris patches occurs on a time scale faster than that calculated from the initial expansion velocity. Thus, the accelerated debris ions observed in the simulations is consistent with HANE observations.

Finally, this study dramatically highlights the importance of kinetic phenomena for the understanding of early time processes. Kinetic effects such as plasma turbulence, reflected and accelerated ions, and thermalization of the ions are not fluid processes, and cannot be recovered using only MHD codes. Detailed studies are necessary using codes such as the one described in this paper to properly understand the dynamics of early time HANE expansions.

#### Acknowledgment

This research has been supported by the Defense Nuclear Agency.

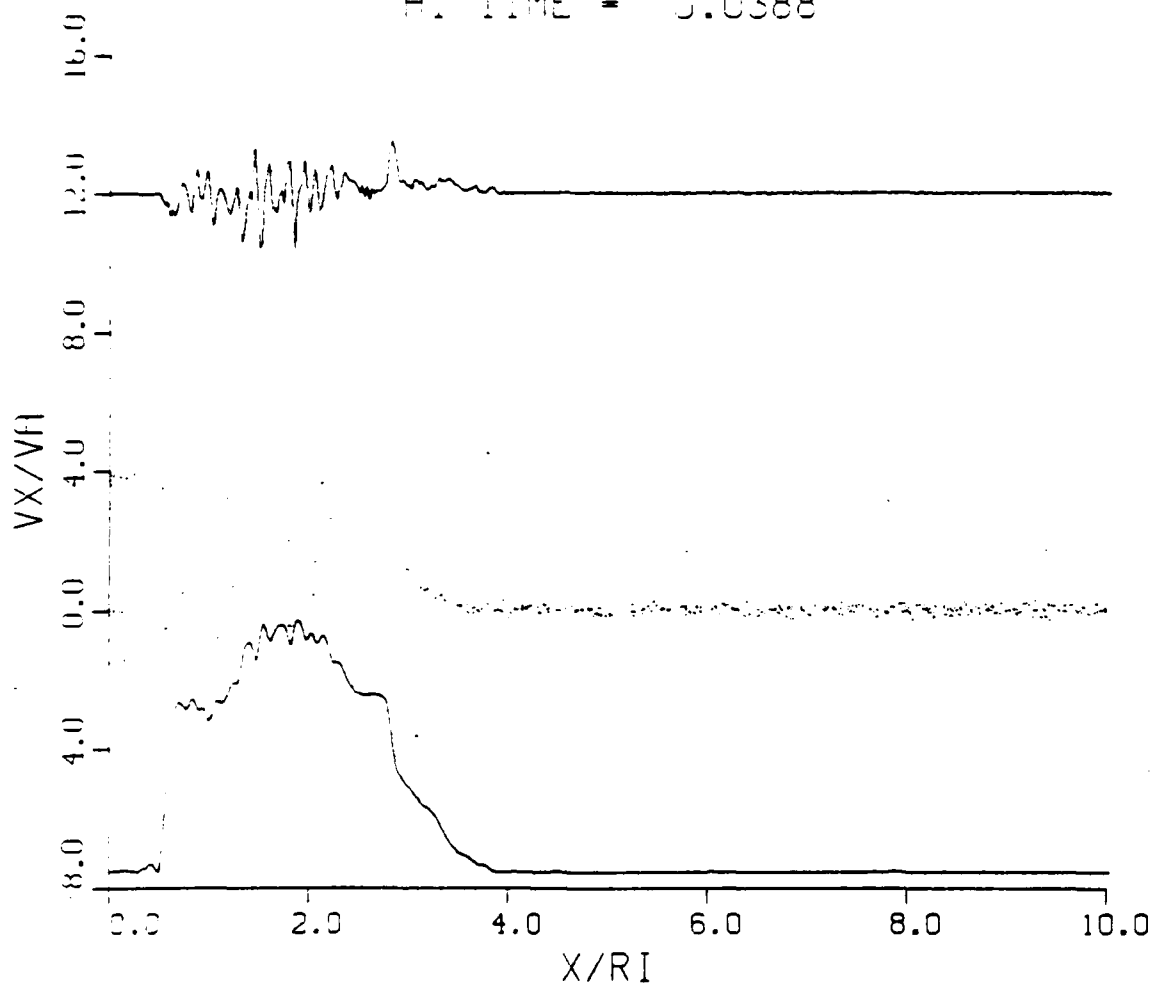
MACH 4 DEBRIS  
 DEBRIS DEN/AMBIENT DEN = 16  
 AT TIME = 0.0059



(a)

Fig. 1 — Evolution of the ambient magnetic field (bottom curve), debris and air ions (middle curves/dots), and electric field in x-direction (top curve) as a function of time. The parameters are  $M_d = V_d/V_A = 4$ ,  $L_B \sim 2r_{Li}$ , and  $n_d/n_a = 16$ . (a)  $t = 0.0059 \Omega_i^{-1}$ ; (b)  $t = 0.0386 \Omega_i^{-1}$ ; (c)  $t = 0.0874 \Omega_i^{-1}$ ; and (d)  $t = 0.1342 \Omega_i^{-1}$ .

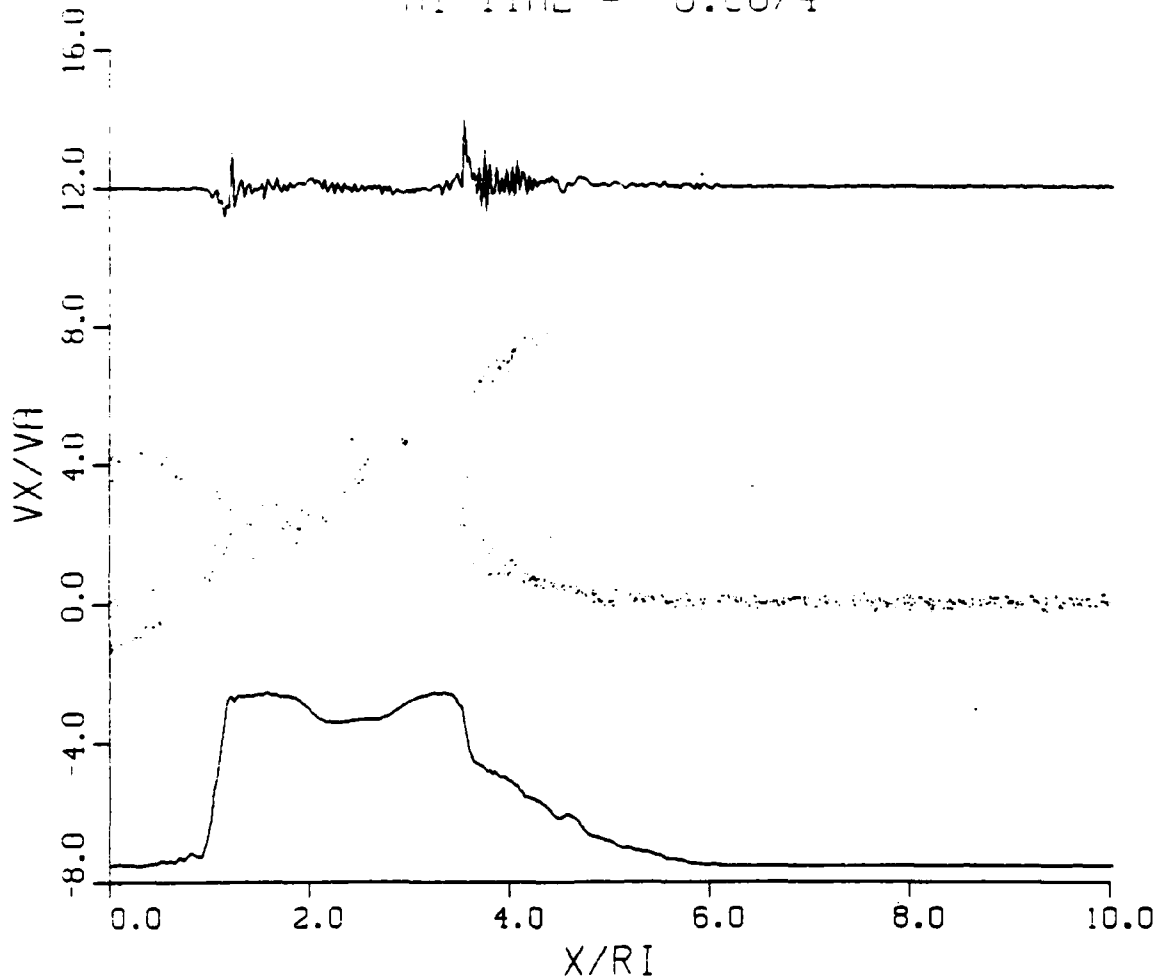
MACH 4 DEBRIS  
 DEBRIS DEN/AMBIENT DEN = 16  
 AT TIME = 0.0388



(b)

Fig. 1 (Cont'd) — Evolution of the ambient magnetic field (bottom curve), debris and air ions (middle curves/dots), and electric field in x-direction (top curve) as a function of time. The parameters are  $M_1 = V_d/V_A = 4$ ,  $L_B \sim 2r_{Li}$ , and  $n_d/n_a = 16$ . (a)  $t = 0.0059 \Omega_i^{-1}$ ; (b)  $t = 0.0386 \Omega_i^{-1}$ ; (c)  $t = 0.0874 \Omega_i^{-1}$ ; and (d)  $t = 0.1342 \Omega_i^{-1}$ .

MACH 4 DEBRIS  
 DEBRIS DEN/AMBIENT DEN = 16  
 AT TIME = 0.0874

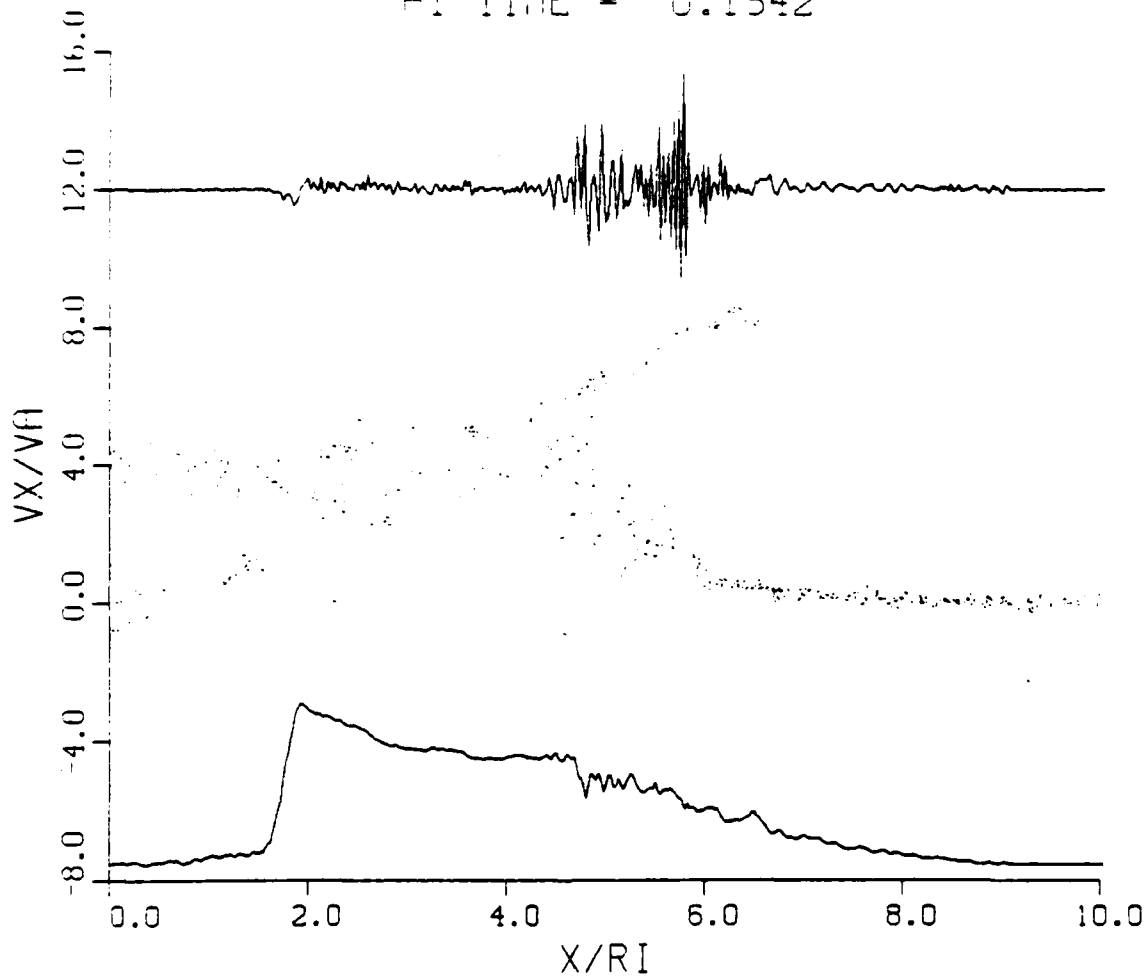


(c)

Fig. 1 (Cont'd) — Evolution of the ambient magnetic field (bottom curve), debris and air ions (middle curves/dots), and electric field in x-direction (top curve) as a function of time. The parameters are  $M_A = V_d/V_A = 4$ ,  $L_B \sim 2r_{Li}$ , and  $n_d/n_a = 16$ . (a)  $t = 0.0059 \Omega_i^{-1}$ ; (b)  $t = 0.0386 \Omega_i^{-1}$ ; (c)  $t = 0.0874 \Omega_i^{-1}$ ; and (d)  $t = 0.1342 \Omega_i^{-1}$ .



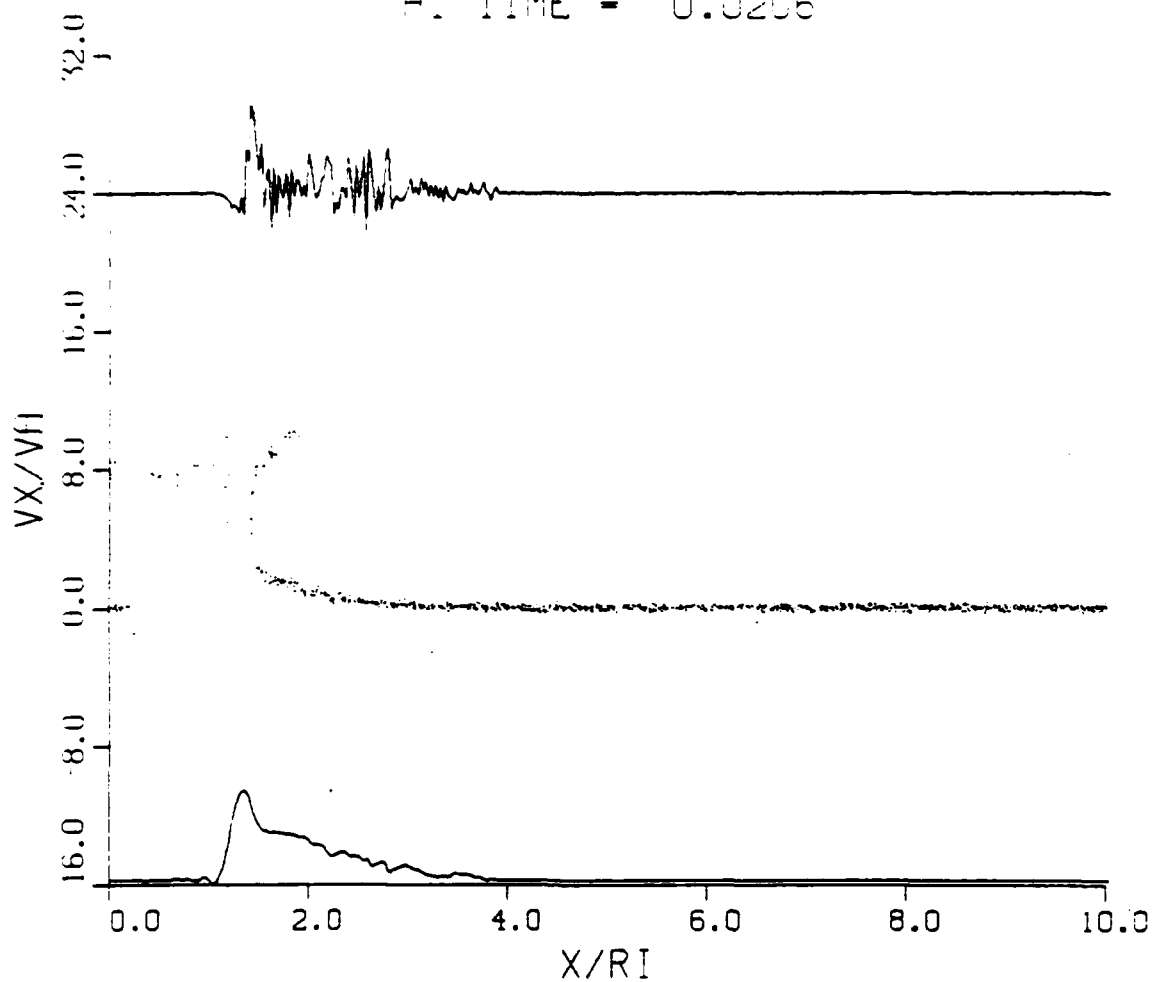
MACH 4 DEBRIS  
 DEBRIS DEN/AMBIENT DEN = 16  
 AT TIME = 0.1542



(d)

Fig. 1 (Cont'd) — Evolution of the ambient magnetic field (bottom curve), debris and air ions (middle curves/dots), and electric field in x-direction (top curve) as a function of time. The parameters are  $M_1 = V_d/V_A = 4$ ,  $L_B \sim 2r_{Li}$ , and  $n_d/n_a = 16$ . (a)  $t = 0.0059 \Omega_i^{-1}$ ; (b)  $t = 0.0386 \Omega_i^{-1}$ ; (c)  $t = 0.0874 \Omega_i^{-1}$ ; and (d)  $t = 0.1342 \Omega_i^{-1}$ .

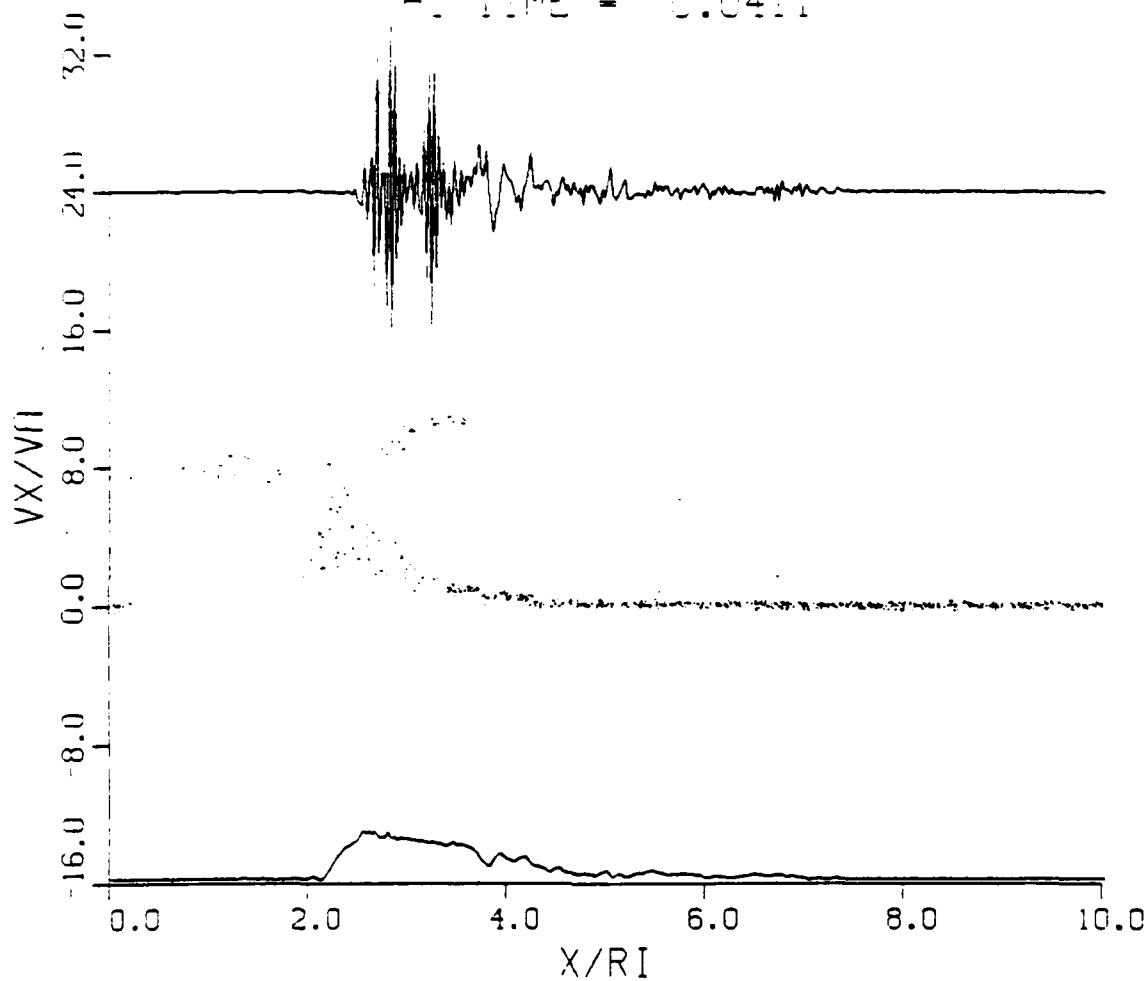
MACH 8 DEBRIS  
 DEBRIS DEN/AMBIENT DEN = 64  
 AT TIME = 0.0206



(a)

Fig. 2 — Evolution of quantities described in Figure 1 but with  $M_A = V_d/V_A = 8$ ,  $L_B \sim 0.5 r_{Li}$ , and  $n_d/n_a = 64$ . (a)  $t = 0.0206 \Omega_i^{-1}$ ; (b)  $t = 0.0411 \Omega_i^{-1}$ ; (c)  $t = 0.0617 \Omega_i^{-1}$ ; and (d)  $t = 0.0771 \Omega_i^{-1}$ .

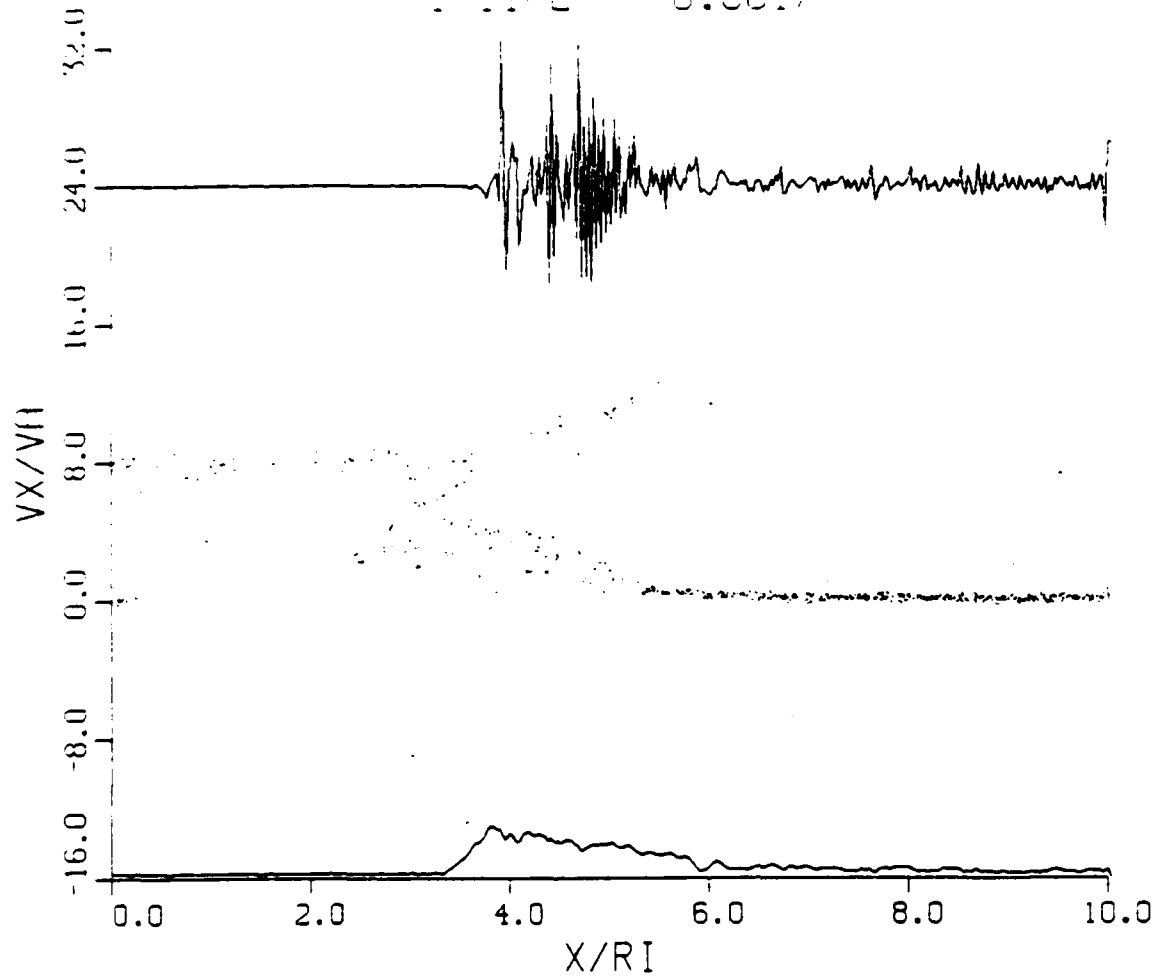
MACH 8 DEBRIS  
 DEBRIS DEN/AMBIENT DEN = 64  
 AT TIME = 0.0411



(b)

Fig. 2 (Cont'd) — Evolution of quantities described in Figure 1 but with  $M_d = V_d/V_A = 8$ ,  $L_B \sim 0.5 r_L$ , and  $n_d/n_a = 64$ . (a)  $t = 0.0206 \Omega_i^{-1}$ ; (b)  $t = 0.0411 \Omega_i^{-1}$ ; (c)  $t = 0.0617 \Omega_i^{-1}$ ; and (d)  $t = 0.0771 \Omega_i^{-1}$ .

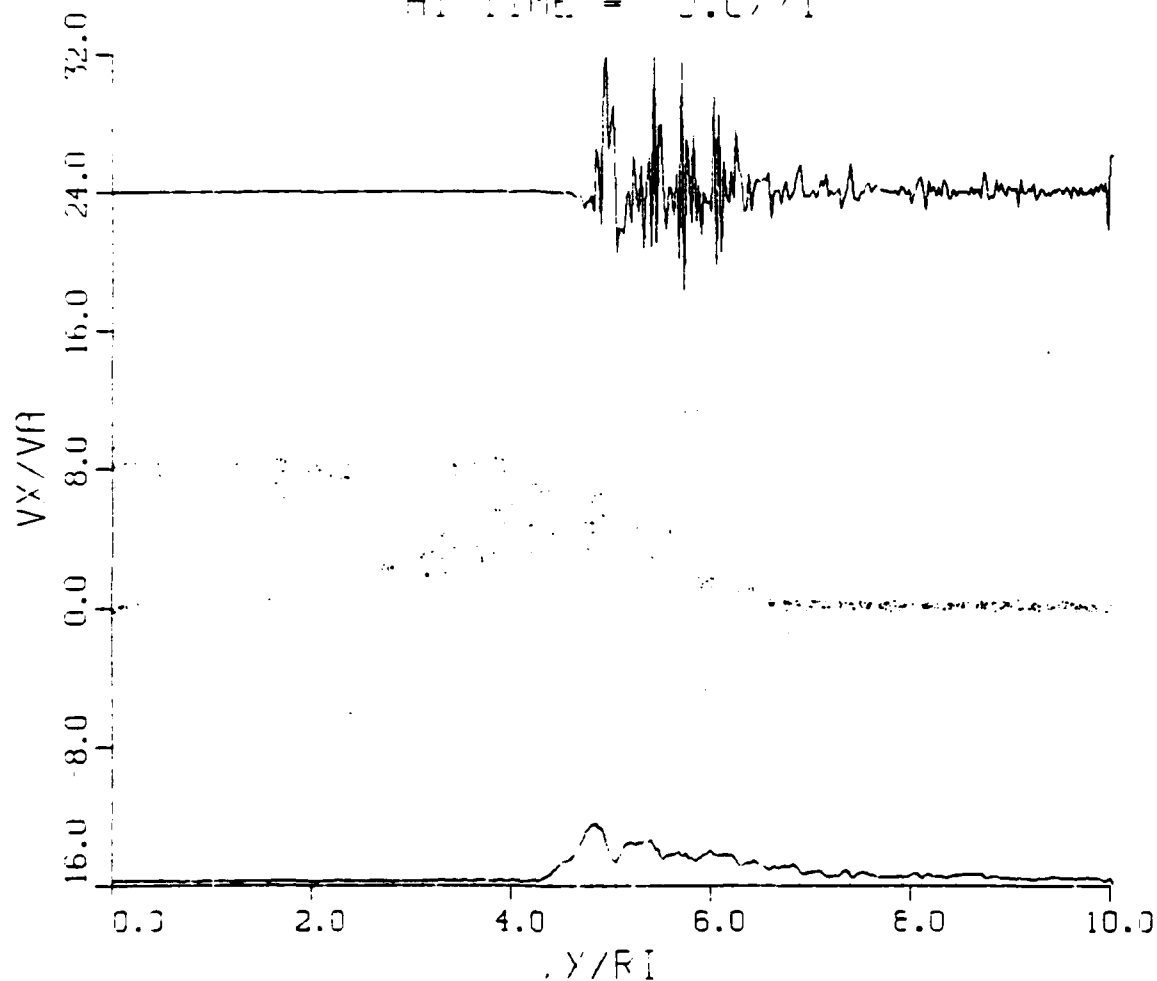
MACH 8 DEBRIS  
 DEBRIS DEN/AMBIENT DEN = 64  
 AT TIME = 0.0617



(c)

Fig. 2 (Cont'd) — Evolution of quantities described in Figure 1 but with  $M_A = V_d/V_A = 8$ ,  $L_B \sim 0.5 r_{Li}$ , and  $n_d/n_a = 64$ . (a)  $t = 0.0206 \Omega_i^{-1}$ ; (b)  $t = 0.0411 \Omega_i^{-1}$ ; (c)  $t = 0.0617 \Omega_i^{-1}$ ; and (d)  $t = 0.0771 \Omega_i^{-1}$ .

MACH 3 DEBRIS  
 DEBRIS DENSITY/AMBIENT DEN = 64  
 AT TIME = 0.0771



(d)

Fig. 2 (Cont'd) — Evolution of quantities described in Figure 1 but with  $M_4 = V_d/V_4 = 8$ ,  $L_B \sim 0.5 r_{Li}$ , and  $n_d/n_a = 64$ . (a)  $t = 0.0206 \Omega_i^{-1}$ ; (b)  $t = 0.0411 \Omega_i^{-1}$ ; (c)  $t = 0.0617 \Omega_i^{-1}$ ; and (d)  $t = 0.0771 \Omega_i^{-1}$ .

## APPENDIX

### HYBRID CODE DESCRIPTION

We describe here the numerical details of the hybrid code used in this paper. This description is taken from Winske and Leroy (1983) with minor changes necessary due to the HANE application. Some of the techniques (e.g., particle-in-cell method) are standard and well known, while others (e.g., solution of the field equations) have been applied primarily to fusion-related problems and hence are generally not familiar to the space science community. The discussion is divided into five parts: (A) an overall description of the simulation methods, (B) treatment of the ions, (C) solutions of the field and electron fluid equations, (D) refinements to the basic model, and (E) discussion of the initial and boundary conditions. The methods pertaining to the first four parts are rather general and could thus be applied to any problem where a 'hybrid' (kinetic ion, fluid electron) description is appropriate. Specific adaptation of the method to the HANE study enters primarily through the last topic, the initial and boundary conditions.

#### A. Overall Description

The simulation method is particle-in-cell (Morse, 1970) with the electrons treated as a fluid (i.e., cell) quantity rather than as discrete particles. The assumption of a massless, charge neutral electron fluid thus eliminates the restriction of time and spatial lengths to be inverse electron plasma frequency and electron Debye length, usually associated with full particle codes. The hybrid models discussed here were originally developed for and extensively applied to dynamical studies of high density pinch experiments by Chodura (1975), Sgro and Nielson (1976) and Hamasaki et al. (1977). These models apply strictly to the case of only one spatial dimension; extension to two dimensions is possible, although nontrivial, as discussed later. Even with only one spatial dimension (which is along the x-axis and thus implies  $\partial/\partial y = \partial/\partial z = 0$ ), all three velocity, magnetic field and electric field components are included. The simulation region has length  $L$ , divided into  $N$  cells, each of length  $\Delta x = L/N$ . There is an additional ('ghost') cell at each end of the system, which helps in keeping track of the particles entering and exiting the system and in setting up

the boundary conditions. The cell quantities (i.e., fields, electron fluid properties, ion velocity moments) are specified at the cell centers. Because the restriction to electron spatial and temporal scales has been eliminated, much larger time steps can be used. Typically, the time step ( $\Delta t$ ) is limited by the condition that ion gyromotion is well defined and the cell size is constrained by the condition that the fastest ions do not traverse one cell in one time step. The cell size and system length are also chosen to resolve length scales of interest to the problem.

### B. Dynamics

The ion component is modeled by a discrete set of particles. The ion distribution is advanced in time by stepping forward each particle in time under the influence of the local, self-consistent Lorentz force. The motion of the ions in a four-dimensional phase space ( $v_x, v_y, v_z, x$ ) is solved by the particle-in-cell technique, using a second-order-accurate but non-reversible scheme (Nielson and Lewis, 1976). The equations for the ion advance (with superscripts denoting the time level) are:

$$\begin{aligned}\vec{v}^0 &= \vec{v}^{-1/2} + (h/2) \vec{E}^0 \\ \vec{v}^{1/2} &= f\vec{v}^{-1/2} + h(\vec{E}^0 + g\vec{B}^0 + \frac{\vec{v}^0 \times \vec{B}}{c} + \vec{P}^0) \\ \vec{x}^1 &= \vec{x}^0 + \Delta t \vec{v}^{1/2}\end{aligned}\tag{A1}$$

where  $h = \Delta t e/m_i$ ,  $f = 1 - (h^2/2)\vec{B}^0 \cdot \vec{B}^0$ ,  $g = (h/2)(\vec{v}^{-1/2} \cdot \vec{B}^0)$ ,  $e$  is the charge and  $m_i$  is the mass of the ions. The electric ( $\vec{E}$ ) and magnetic fields ( $\vec{B}$ ) are evaluated at the particle position  $\vec{x}^0$ .  $\vec{P}$  is a mean friction force,  $\vec{P} = -e\vec{\eta} \cdot \vec{J}$ , exerted by the electrons as a macroscopic force only,  $\vec{J}$  is the current and  $\vec{\eta}$  represents a phenomenological anomalous resistivity which gives rise to Ohmic heating, as will be explained later. After all of the ions have been advanced, the ion density ( $n_i$ ) is updated, by averaging over the positions of all the particles in each cell. The ion mean velocities ( $\vec{v}_i$ ) are also needed at time level 1. The velocities are pushed ahead one half time step,

$$\vec{v}^1 = \vec{v}^{1/2} + (h/2)(\vec{E}^1 + \frac{\vec{v}^{1/2} \times \vec{B}^1}{c} + \vec{P}^1),\tag{A2}$$

using the fields at the new particle positions  $\underline{x}^1$ , in order to accumulate the velocity moments  $\underline{V}_1$ .

The assumption of charge neutrality then implies

$$n_e = n_i \equiv n, \quad (A3)$$

and the continuity equation gives

$$\frac{\partial}{\partial t} (n_e + n_i) = 0 = -\frac{\partial}{\partial x} J_x = -\frac{\partial}{\partial x} en(v_{ix} - v_{ex}) \quad (A4)$$

or

$$v_{ex} = v_{ix}. \quad (A5)$$

Thus, the electron density and one component of the electron fluid velocity are determined.

### C. Field-Fluid Equations

With the assumption of zero electron mass the electron momentum equation reduces to

$$n_e m_e \frac{d\tilde{v}_e}{dt} = 0 = -en_e \left( \tilde{E} + \frac{\tilde{v}_e \times \tilde{B}}{c} \right) - \frac{\partial}{\partial x} p_e \tilde{x} - n_e \tilde{p} \quad (A6)$$

where  $p_e$  is the scalar pressure and  $\tilde{v}_e$  is the velocity of the electron fluid. The transverse (y and z) components of (A6) can be written as Ohm's law

$$\tilde{J} = \eta^{-1} \cdot \left( \tilde{E} + \frac{\tilde{v}_e \times \tilde{B}}{c} \right). \quad (A7)$$

In general, the magnetic field is inclined at some angle with respect to the x axis:  $\tilde{B} = |B| (b_x, b_y, b_z)$  with  $b_x^2 + b_y^2 + b_z^2 = 1$ , and if  $\sigma_{\parallel} (\sigma_{\perp})$  represents the conductivity parallel (perpendicular) to the magnetic field, the conductivity tensor is (Krall and Trivelpiece, 1973):



$$\underline{\sigma} \equiv \underline{\eta}^{-1} = \begin{pmatrix} \sigma_1 & \sigma_y & \sigma_z \\ \sigma_y & \sigma_2 & \sigma_x \\ \sigma_z & \sigma_x & \sigma_3 \end{pmatrix}, \quad (\text{A8})$$

where

$$\sigma_1 = \sigma_{\perp} + (\sigma_{\parallel} - \sigma_{\perp})b_x b_x$$

$$\sigma_2 = \sigma_{\perp} + (\sigma_{\parallel} - \sigma_{\perp})b_y b_y$$

$$\sigma_3 = \sigma_{\perp} + (\sigma_{\parallel} - \sigma_{\perp})b_z b_z$$

$$\sigma_x = (\sigma_{\parallel} - \sigma_{\perp})b_y b_z$$

$$\sigma_y = (\sigma_{\parallel} - \sigma_{\perp})b_x b_z$$

$$\sigma_z = (\sigma_{\parallel} - \sigma_{\perp})b_x b_y.$$

The transverse fields can be expressed in terms of the vector potentials in the usual manner [ $\underline{B} = \underline{\nabla} \times \underline{A}$ ;  $\underline{E} = - (1/c)(\partial \underline{A}/\partial t)$ ]:

$$\begin{aligned} B_y &= \frac{\partial A_z}{\partial x} \\ B_z &= \frac{\partial A_y}{\partial x} \\ E_y &= -\frac{1}{c} \frac{\partial A_y}{\partial t} \\ E_z &= -\frac{1}{c} \frac{\partial A_z}{\partial t} \end{aligned} \quad (\text{A9})$$

and  $\underline{\nabla} \cdot \underline{B} = 0$  implies

$$B_x = \text{constant}. \quad (\text{A10})$$

(The last field component,  $E_x$ , is derived from the x-component of (A6) as will be shown later.)

Neglecting the displacement current, Ampere's law can be expressed

$$\begin{aligned}\frac{\partial^2 A_y}{\partial x^2} &= -\frac{4\pi}{c} J_y \\ \frac{\partial^2 A_z}{\partial x^2} &= -\frac{4\pi}{c} J_z.\end{aligned}\tag{A11}$$

Substituting in Ohm's law (A7) and the definitions of the field components, Eq. (11) becomes a coupled system of equations:

$$\begin{aligned}\frac{\partial^2 A_y}{\partial x^2} &= f_1 \left( \frac{\partial A_y}{\partial t}, \frac{\partial A_z}{\partial t}, \frac{\partial A_y}{\partial x}, \frac{\partial A_z}{\partial x} \right) \\ \frac{\partial^2 A_z}{\partial x^2} &= f_2 \left( \frac{\partial A_y}{\partial t}, \frac{\partial A_z}{\partial t}, \frac{\partial A_y}{\partial x}, \frac{\partial A_z}{\partial x} \right).\end{aligned}\tag{A12}$$

In order to solve this system a fully implicit, space centered difference scheme is used (Richtmyer and Morton, 1967). If we let  $u_j^n = A_y$  at the  $j$ th cell position and  $n$ -th time level (and  $w_j^n = A_z$  in the same way), the left hand side of (A12) is differenced as follows:

$$\frac{\partial^2 A_y}{\partial x^2} = \frac{u_{j+1}^{n+1} + u_{j-1}^{n+1} - 2u_j^{n+1}}{\Delta x^2},\tag{A13}$$

while on the right hand side

$$\frac{\partial A_y}{\partial t} = \frac{u_j^{n+1} - u_j^n}{\Delta t}$$

and

$$\frac{\partial A_y}{\partial x} = \frac{u_{j+1}^{n+1} - u_{j-1}^{n+1}}{2\Delta x}.$$

When this is substituted into (A12), the resulting system of equations can be written symbolically as

$$A_j \cdot \tilde{x}_{j+1} + B_j \cdot \tilde{x}_j + C_j \cdot \tilde{x}_{j-1} = D_j\tag{A15}$$

where

$$\tilde{X}_j = \begin{matrix} u_j^{n+1} \\ w_j^{n+1} \end{matrix} \quad (A16)$$

and  $A_j$ ,  $B_j$ , and  $C_j$  are 2x2 matrices that depend only on components of  $\vec{g}$  and  $V_e$  (evaluated at cell  $j$  at time level  $n$ ) and constants, while  $D_j$  also depends on  $u_j^n$ ,  $w_j^n$ . Thus, all the coefficients  $A$ ,  $B$ ,  $C$  and  $D$  are explicitly known. Note that there are  $N$  cells in the computation mesh  $j=1, 2, \dots, N$  with ghost cells ( $j=0$  and  $j=N+1$ ) at each end.

The set of equations (A15) is easily solved. Assuming a solution of the form

$$\tilde{X}_j = E_j \cdot \tilde{X}_{j+1} + F_j \quad j = 0, 1, \dots, N \quad (A17)$$

and substituting it into (A15), it then follows that

$$\begin{aligned} E_j &= - [B_j + C_j \cdot E_{j-1}]^{-1} A_j \\ F_j &= [B_j + C_j \cdot E_{j-1}]^{-1} \cdot [D_j - C_j \cdot F_{j-1}] \end{aligned} \quad (A18)$$

Because all the  $A_j$ ,  $B_j$ ,  $C_j$  and  $D_j$  are known, if  $E_0$  and  $F_0$  are known (from boundary conditions, as explained later), (A18) can be solved in ascending order to obtain  $E_1, F_1; E_2, F_2, \dots, E_N, F_N$ . Then if  $\tilde{X}_{N+1}$  can be determined (again from boundary conditions), (A17) can be solved in descending order to obtain  $\tilde{X}_N, \tilde{X}_{N-1}, \dots, \tilde{X}_0$ .

Once the components of the vector potential are known, the new values of the electric and magnetic field follow from (A9) and the components of the current from (A11), again using the differencing in (A13) and (A14). The transverse components of  $V_e$  are then easily found from the current and the ion velocity moments:

$$V_{ej} = V_{ij} - J_j / en \quad j = y \text{ or } z. \quad (A19)$$

The last electron fluid quantity to be calculated is the temperature. The electron energy equation can be written as

$$\frac{2}{2} \frac{\partial}{\partial t} (n_e T_e) + \frac{\partial}{\partial x} \left( \frac{3}{2} n_e T_e v_{ex} \right) + n_e T_e \frac{\partial v_{ex}}{\partial x} = Q. \quad (A20)$$

The source term  $Q$  includes resistive heating ( $nJ^2$ ) and loss mechanisms, such as thermal conduction or radiation, depending on the application. Letting

$$p_e = n_e T_e, \quad (A21)$$

(A20) can be rewritten in the form (with  $\gamma = 5/3$ )

$$\left( \frac{\partial}{\partial t} + v_{ex} \frac{\partial}{\partial x} \right) p_e = - \gamma p_e \frac{\partial v_{ex}}{\partial x} + (\gamma - 1) Q \quad (A22)$$

The differencing for  $\partial p_e / \partial t$  and  $\partial v_{ex} / \partial x$  is identical to (A14): for stability reasons "donor cell" differencing is used for the convective term (Richtmyer and Morton, 1967):

$$v_{ex} \frac{\partial p_e}{\partial x} = \frac{v_{exj}^n}{\Delta x} \times \begin{cases} (p_{ej}^{n+1} - p_{ej-2}^{n+1}) & v_{exj} > 0 \\ (p_{ej+1}^{n+1} - p_{ej}^{n+1}) & v_{exj} < 0 \end{cases} \quad (A23)$$

Again, a tridiagonal system is obtained,

$$A_j X_{j+1} + B_j X_j + C_j X_{j-1} = D_j, \quad (A24)$$

except that now all quantities are simple scalars. As before, an assumed solution of the form

$$X_j = E_j X_{j+1} + F_j \quad (A25)$$

leads to

$$E_j = - [B_j + C_j E_{j-1}]^{-1} A_j$$

$$F_j = [B_j + C_j E_{j-1}]^{-1} [D_j - C_j F_{j-1}]. \quad (A26)$$

Appropriate boundary conditions lead to a determination of  $E_0$ ,  $F_0$  (and then to all  $E_j$ ,  $F_j$  in ascending order, using (A26)) and  $X_{N+1}$  (and thus to all  $X_j$  in descending order through (A25)). Since  $n_e (= n_i)$  is known,  $T_e$  is then obtained from (A21). An alternative to (A22) which is sometimes useful (Sgro, 1978) is to write the energy equation (A20) in terms of the entropy  $[S = \ln(p_e n_e^{-\gamma})]$  instead of the pressure.

Finally, the x component of the electron momentum equation (A6) can be solved for  $E_x$ :

$$E_x = -\frac{1}{c} (\vec{v}_e \times \vec{B}_x) - \frac{1}{ne} \frac{\partial p_e}{\partial x}. \quad (A27)$$

This electric field is needed to maintain charge neutrality.

The computation loop through one time step can thus be summarized as follows:

1. Advance the ions one time step and then calculate the ion velocity moments ( $n_i = n_e$ ,  $V_{ix} = V_{ex}$ ,  $V_{iy}$ ,  $V_{iz}$ ).
2. Compute the plasma conductivity  $g$ , according to some prescription. (The resistivity  $\eta$  is  $g^{-1}$ ).
3. Solve the coupled equations for  $A_y$ ,  $A_z$ ; we can then easily calculate  $E_y$ ,  $E_z$ ,  $B_y$ ,  $B_z$  ( $B_x = \text{constant}$ ). From the currents (Ampere's law) and the ion moments calculate the other two electron velocity components,  $V_{ey}$  and  $V_{ez}$ .
4. The electron temperature is obtained next from the solution of the differenced energy equation.
5.  $E_x$  is then calculated from the x-component of the electron momentum equation.
6. Thus, all field and electron fluid components are known and we are ready to move the ions again.

#### D. Refinements

The simulation scheme described thus far is rather general, the only assumptions being quasineutrality, zero electron mass and one spatial dimension. All of these conditions can be replaced by more appropriate ones, as the physical situation dictates. For example, for the study of low frequency ion waves an adiabatic electron model is more appropriate; such a model has been successfully used by Okuda et al. (1978). In some situations phenomena in the lower hybrid frequency range are of interest. In this case electron inertia effects are non-negligible; they have been included in the one-dimensional model of Liewer (Al976) and the two-dimensional model of Hewett and Nielson (Al978). Two-dimensional simulation models with  $m_e = 0$  have been successfully employed by Byers et al. (1978), Hewett (1980) and Harned (1982).

The HANE simulations described in this paper take the conductivity to be constant. A further level of sophistication is to include anomalous processes due to the microphysics, which is occurring on time and distance scales snorter than those resolved in the hybrid model, by means of more complicated transport coefficients. This is done by expressing the conductivity (or resistivity) as a sum of two terms, one representing classical (Spitzer) effects and the other due to anomalous effects arising from microinstabilities due to cross-field currents. Two types of anomalous transport coefficients have been used successfully to model the behavior of laboratory plasmas: one type uses a semi-empirical expression (Chodura, 1975; Sgro and Nielson, 1976), the other is based on a quasilinear analysis of known instabilities (Davidson and Krall, 1977). The transport processes can be further refined to include electron thermal conductivity (Sgro, 1980) and anomalous ion heating (Hamasaki et al., 1977). Multispecies ions can also be included in a straightforward manner (Sgro, 1980; Sgro and Winske, 1981).

### E. Initial and Boundary Conditions

In order to simulate the piston formation stage of the HANE problem, appropriate initial and boundary conditions have been implemented in the hybrid code. We assume initially that a dense cool debris plasma flows across the magnetic field into a tenuous stationary air plasma. In this paper, we assume the debris and air to consist of the same ion species. This assumption is not necessary and we are presently investigating the effects of different debris composition. We assume further that there is a magnetic compression of finite width imbedded in the leading edge of the debris stream, formed as a result of the preceding magnetic compression stage of the coupling is simply maintained at the right boundary. Ions of all species are effectively absorbed at the boundaries. The final boundary condition is on the magnetic field which is held constant at the ambient (air) value at both boundaries. The magnetic compression is taken to be proportional to the electron compression. The width of the magnetic compression is an input parameter in the code. Thus initially in the simulation space we establish a debris ion stream extending a finite distance from the left boundary into the uniformly distributed air ions. A step function compression in the magnetic field, narrower than the debris stream, is initialized at the leading edge of the debris. The magnetic field is initially uniform on both sides of the compression. During the simulation runs, debris ions are continuously injected from the left boundary. This is accomplished by re-initializing the debris ion distribution in the left ghost cell each time step.

## REFERENCES

- Byers, J.A., B.I. Cohen, W.C. Condit, and J.D. Hanson, "Hybrid Simulations of Quasineutral Phenomena in Magnetized Plasma," J. Comp. Phys., 27, 363, 1978.
- Chodura, R., "Hybrid Fluid-Particle Model of Ion Heating in High-Mach-Number Shock Waves," Nucl. Fusion, 15, 55, 1975.
- Davidson, R.C., and N.A. Krall, "Anomalous Transport in High-Temperature Plasmas with Applications to Solenoidal Fusion Systems," Nucl. Fusion, 17, 1313, 1977.
- Hamasaki, S., N.A. Krall, C.E. Wagner, and R.N. Byrne, "Effect of Turbulence on Theta Pinch Modeling by Hybrid Numerical Models," Phys. Fluids, 20, 65, 1977.
- Harned, D.S., "Quasineutral Hybrid Simulation of Macroscopic Plasma Phenomena," J. Comp. Phys., 47, 452, 1982.
- Hewett, D.W., "A global method for Solving the Electron-field Equations in a Zero-inertia-electron-hybrid Plasma Simulation Code," J. Comp. Phys., 38, 378, 1980.
- Hewett, D.W. and C.W. Nielson, "A Multidimensional Quasineutral Plasma Simulation Model," J. Comp. Phys., 29, 219, 1978.
- Krall, N.A. and A.W. Trivelpiece, Principles of Plasma Physics, p. 119, McGraw-Hill, New York 1973.
- Liewer, P.C., "Numerical Studies of Ion Reflection in Collisionless Theta-Pinch Implosions Using a Hybrid Vlasov-Fluid Model," Nucl. Fusion, 16, 817, 1976.
- Longmire, C.L., "Notes on Debris-Air-Magnetic Interaction," The Rand Corporation Report RM-3386-PR, 1963. AD296597.
- Morse, R.L., "Multidimensional Plasma Simulation by the Particle-in-Cell Method," Methods in Computational Physics, Vol. 9, Ed. by B. Alder, S. Fernbach and M. Rotenberg, p. 213, Academic Press, NY, 1970.
- Nielson, C.W. and H.R. Lewis, "Particle-code Models in the Nonradiative Limit," in Methods in Computational Physics, Vol. 16, edited by J. Killeen, B. Alder, S. Fernbach and M. Rotenberg, p. 367, Academic Press, New York, 1976.



- Okuda, H., J.M. Dawson, A.T. Lin and C.C. Lin, "Quasi-neutral Particle Simulation with Application to Ion Wave Propagation," Phys. Fluids, 21, 476, 1978.
- Papadopoulos, K., R.C. Davidson, J.M. Dawson, I. Haber, D.A. Hammer, N.A. Krall, and R. Shanny, "Heating of Counterstreaming Ion Beams in an External Magnetic Field," Phys. Fluids, 14, 849, 1971.
- Ripin, B.H., J. Grun, S. Kacenjar, E.A. McLean, and J.A. Stamper, "Introduction to the Laser-HANE Experiment and Summary of Low-Pressure Interaction Results," NRL Memo Report 5268, 1984. AD138945.
- Sgro, A.G. and C.W. Nielson, "Hybrid Model Studies of Ion Dynamics and Magnetic Field Diffusion During Pinch Implosions," Phys. Fluids, 19, 126, 1976.
- Sgro, A.G., "Calculation of the Effects of Incomplete Preionization in High Voltage Theta Pinches," Phys. Fluids, 21, 1410, 1978.
- Sgro, A.G., "Simulation of the ZT-S reversed Field Pinch," Phys. Fluids, 23, 1055, 1980.
- Sgro, A.G. and D. Winski, "Simulation of the Formation of the PS-1 Spheromak," Phys. Fluids, 24, 1156, 1981.
- Winske, D. and M.M. Leroy, "Hybrid Simulation Tech Applied to Earth's Bow Shock," Comp. Simulations of Space Plasmas - Selected Lectures at 1st ISS, D. Reidel, Holland, 1984.



**APPENDIX P**

**Collisionless Coupling in the AMPTE Artificial Comet**

**K. Papadopoulos**  
**Science Applications International Corporation**

**J.D. Huba**  
**Naval Research Laboratory**

**A.T.Y. Lui**  
**Applied Physics Laboratory**



# COLLISIONLESS COUPLING IN THE AMPTE ARTIFICIAL COMET

K. Papadopoulos  
Science Applications International Corporation  
McLean, Virginia 22102

J.D. Huba  
Geophysical and Plasma Dynamics Branch  
Plasma Physics Division  
Naval Research Laboratory  
Washington, DC 20375-5000

and

A.T.Y. Lui  
Applied Physics Laboratory  
Johns Hopkins University  
Laurel, Maryland 20707

May 1986

## ABSTRACT

Observations of the solar wind-barium interaction associated with the AMPTE artificial comet release of Dec. 27, 1984 are presented. Based on these observations we argue that the solar wind couples momentum (and energy) to the barium ions through both laminar and turbulent processes. The laminar forces acting on the particles are the laminar electric and magnetic fields; the turbulent forces are associated with the intense electrostatic wave activity. This wave activity is shown to be caused by a cross-field solar wind proton-barium ion streaming instability. The observed wave frequencies and saturated amplitudes are consistent with our theoretical analysis.



## I. INTRODUCTION

The in situ measurements of the plasma parameters from the AMPTE (Active Magnetospheric Particle Tracer Explorers) artificial comet releases (Valenzuela et al., 1986; Haerendel et al., 1986) in the solar wind provide us with a unique set of data to test the available theories on the subject of collisionless coupling of magnetized plasma streams under high Mach number conditions ( $M_1 \gg 1$ ) (Haerendel, 1986). The subject is very opportune since it is the controlling factor that determines the momentum coupling process occurring in the interaction of the solar wind with the cometary plasma generated by the ionization of the neutral coma. The overall comet structure, the applicability of MHD or kinetic models; the presence or absence of a cometary shock and the type of the resulting ionopause (Mendis and Houpis, 1982; Ip and Axford, 1982; Fedder et al., 1986; Sagdeev et al., 1986) depends critically on the wave-particle processes producing the momentum coupling, the thermalization, and the isotropization in the interaction. It is the purpose of the present note to compare the AMPTE in situ observations of the plasma parameters and wave signatures (Gurnett et al., 1985; Haerendel et al., 1986) with the theoretical concepts currently applied to the high Mach number interaction problem. In the next section we present a brief description of the experiment as well as the relevant data. Section III reviews the theoretical models for coupling. Section IV compares the AMPTE data with the observations.

## 11. OBSERVATIONAL RESULTS

During the artificial comet experiment on Dec 27, 1984 two canisters of barium were released from the IRM (Ion Release Module) spacecraft. The release was on the morning side of the earth at a geometric radial distance of roughly 17 earth radii. The canisters were exploded simultaneously at a distance  $\sim 1$  km from the spacecraft at 1232 UT. The explosion produced an expanding barium cloud which was rapidly ionized by solar UV ( $\tau_i \approx 28$  sec where  $\tau_i$  is the photoionization time). The interaction of the solar wind, which was flowing at  $\sim 550$  km/sec, with the ionized barium cloud was recorded by the IRM instruments inside the cloud and the magnetic cavity that was created. The UKS spacecraft, located  $\sim 170$  km away, was outside the magnetic cavity and measured magnetic disturbances and particle fluxes generated by the interaction. A schematic of the spacecraft positions and the magnetic field structure is shown in Fig. 1.

We present a set of plasma and field measurements which highlight the dynamic interaction of the solar wind and the barium cloud in Figs. 2-4. In Fig. 2 we show measurements of the electron density from 15 eV to 30 eV ( $n_e$  (Fig. 2a)), the flow velocity of the solar wind protons measured in the range 20 eV to 40 keV in GSE coordinates [ $V_{px}$  (Fig. 2b) and  $V_{pz}$  (Fig. 2e)], and the magnitude of the interplanetary magnetic field [ $B$  (Fig. 2d)] (Haerendel et al., 1986). We note that the magnetic field is in the y-direction and that the electron density does not include the cold electrons associated with the barium ions. The diamagnetic cavity generated by the barium ions is clearly seen during the time UT 12:32:02 and UT 12:33:15. Figure 3 shows the low frequency electric field measurements as a function of time and frequency (Gurnett et al., 1985), the magnitude of the magnetic field, and the barium ion density. Figure 4 displays the electric field



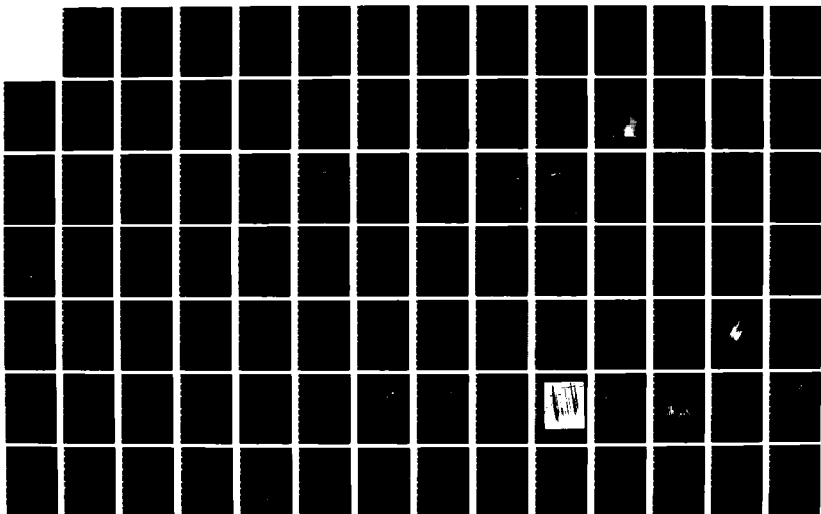
AD-A171 688

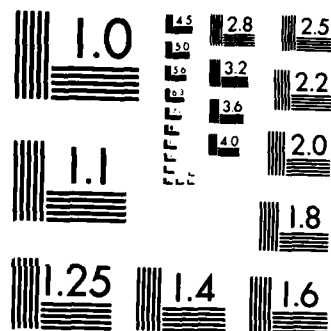
GEOPHYSICAL PLASMAS AND ATMOSPHERIC MOEELING(U) SCIENCE 7/8  
APPLICATIONS INTERNATIONAL CORP MCLEAN VA  
E HYMAN ET AL JUL 86 SAIC-86/1781 N00014-85-C-2018

UNCLASSIFIED

F/G 4/1

NL





MICROCOPY RESOLUTION TEST CHART  
NATIONAL BUREAU OF STANDARDS-1963-A

spectrum upstream of the ion cloud at the time of maximum intensity (UT 12:34:27) (Gurnett et al., 1985). The electrostatic waves reached amplitudes in excess of 140 mV/m. Since the electron density in Fig. 2 does not include the cold electrons, for times prior to 12:34:30 UT we will use the number density from Fig. 3, which is based upon wave emissions at the plasma frequency. For the time period 12:34:30 UT - 12:35:30 UT the values of the electron, proton, and barium densities are not well-known. Finally, for times later than 12:35:30 UT we use the data presented in Fig. 2.

On the basis of these measurements the following picture describing the spatial evolution of the coupling between the solar wind protons and the barium coupling emerges. For times later than UT 12:36:20 the solar wind parameters correspond to the ambient conditions ( $n_e = 2 \text{ cm}^{-3}$ ,  $V_{px} = 550 \text{ km/sec}$ ,  $T_e = 2 \times 10^5 \text{ °K}$  and  $B = 10 \text{ Y}$ ). The interaction between the solar wind protons and the barium cloud starts at the point marked 1, which corresponds to UT 12:36:20, as seen from the initiation of the slowing down of the solar wind (Fig. 2b). During the time period UT 12:36:20 - UT 12:35:25 the initial slowing down rate is relatively weak and is accompanied by moderate wave activity (Fig. 3); density and magnetic field compression (Fig. 2a,d). There is no plasma flow in the z-direction (Fig. 2c). This time coincides with the time that the UK spacecraft records fluxes of hot electrons ( $> 100 \text{ eV}$ ). A much stronger slowing down rate is observed between UT 12:35:25 and UT 12:34:15, accompanied by strong electrostatic wave activity near the local proton lower hybrid frequency. For  $B = 30 - 90 \text{ Y}$ ,  $n_p = 2 - 10 \text{ cm}^{-3}$ , and  $n_e = 2 - 120 \text{ cm}^{-3}$  we note that the proton lower hybrid frequency is  $f_{Hp} = 10 - 30 \text{ Hz}$ . The magnetic field, density, and the temperature continue to increase, while the value of  $V_{pz}$  remains relatively unchanged. This continues until UT 12:34:15 which is

marked as 3. At this point the magnetic field has a value  $B = 85 \gamma$ , the solar wind stream has slowed down to  $V_{px} = 270 \text{ km/sec}$ , corresponding to 0.4 keV flow energy, while a broad ion distribution is observed with an equivalent temperature of  $4 \times 10^6 \text{ }^\circ\text{K}$  (i.e., 0.4 KeV). Notice that at this point the solar wind has lost more than 80% of its flow energy and its thermal spread is comparable to its flow speed. This corresponds to the peak of the electrostatic wave activity (see Fig. 3). The slowing down of the solar wind continues until UT 12:33:20. The magnetic field exceeds 120  $\gamma$  and approaches its maximum value of 145  $\gamma$ . Finally, at UT 12:33:15 we note the beginning of the diamagnetic cavity, the suppression of the wave activity, and the appearance of sunward flowing 0.5 KeV ions. A summary of the key parameters observed during the above times is given in Table I.

We note that there is a marked difference in the nature of the slowing down of the solar wind between the time periods UT 12:36:20 - UT 12:35:27 and UT 12:35:27 - UT 12:34:17. In the former case we point out that the low frequency electrostatic wave activity is intense and that there is little change in the z-component of the solar wind velocity. In the latter time period, the electrostatic noise has weakened considerably and there is a substantial increase in  $V_{pz}$ . These issues will be discussed in more detail in Section IV.

### III. COLLISIONLESS MOMENTUM COUPLING: THEORETICAL CONCEPTS

Prior to discussing the interpretation of the above data with respect to the physics of momentum coupling, we present a brief review of the various coupling processes. We consider the following momentum equation in the  $x$  direction for a solar wind proton (i.e., radial direction perpendicular to the ambient magnetic field  $\underline{B} = B \hat{e}_y$ ).

$$\frac{dV_{px}}{dt} = \frac{eE_x}{m_p} + \Omega_p V_{pz} - v^* (V_{px} - V_b) \quad (1)$$

where the subscript  $p$  refers to solar wind protons,  $\Omega_p = eB/m_p c$ ,  $v^*$  is an anomalous ion-ion collision frequency,  $V_b = V_b \hat{e}_x$  is the streaming barium velocity,  $e$  is the charge, and  $m$  is the mass. The first term on the RHS of (1) arises from a laminar electric field usually associated with the leading edge of the magnetic compression; it acts to accelerate barium ions and to reflect solar wind protons. The second term is the magnetic force which is associated with Larmor coupling. The final term corresponds to turbulent "pick up" of the solar wind and arises because of plasma instabilities. For plasma turbulence such that  $v^* > \Omega_p$ , it is clear that turbulent coupling can dominate over Larmor coupling. Also, notice that the force  $\Omega_p V_{pz}$  associated with Larmor coupling is proportional to the value of  $V_{pz}$  and will be very weak as long as  $V_{pz} = 0$ . The time evolution of  $V_{pz}$  is given by

$$\frac{dV_{pz}}{dt} = \frac{eE_z}{m_p} = \frac{eV_{px} B}{m_p c} = \Omega_p V_{px} \quad (2)$$

In deriving (2) we assume  $E_z = V_{px} B/c$  is the motional electric field of the solar wind.

The subject of the appropriate value of  $v^*$  and the dominant instability that drives it has been extensively studied. We refer the interested reader to Lampe et al. (1975) and summarize only the key conclusions. The counterstreaming between the barium ions and solar wind protons generates a local velocity distribution function such as shown in Fig. 5. Figure 5 is drawn for convenience in the solar wind reference frame. For singly ionized barium the electrons have a relative velocity  $\underline{V} = V_e \hat{e}_x$  with respect to the solar wind protons given by  $V_e = V_{px}(n_b/n_e)$  where  $n_b$  is the density of the barium and  $n_e = n_b + n_p$ .

The dispersion equation for this situation is given by (Papadopoulos et al., 1971)

$$D(\omega, k) = \frac{\omega_b^2}{k^2 v_b^2} Z'\left(\frac{\omega - kV_{px} \cos \theta}{kv_b}\right) + \frac{\omega_p^2}{k^2 v_p^2} Z'\left(\frac{\omega}{kv_p}\right) + 1 + \frac{\omega_e^2}{\Omega_e^2} \left[1 + \frac{\omega_e^2}{\Omega_e^2 k^2} (1 + \beta_e)^{-1}\right] = 0 \quad (3)$$

where  $\omega_\alpha = (4\pi n_\alpha e^2/m_\alpha)^{1/2}$  is the plasma frequency and  $v_\alpha = (T_\alpha/m_\alpha)^{1/2}$  is the thermal speed of species  $\alpha$  (e: electron, b: barium; p: proton),  $\underline{k} = k_x \hat{e}_x + k_z \hat{e}_z$ ,  $\theta = \tan^{-1}(k_z/k_x)$ ,  $\underline{V}_p = V_{px} \hat{e}_x$ ,  $\Omega_e = eB/m_e c$  is the electron cyclotron frequency,  $\beta_e = 8\pi n_e T_e/B^2$  and  $Z'(\zeta) = -2(1 + \zeta Z(\zeta))$  with  $Z$  the plasma dispersion function. In writing (3) we have assumed  $\underline{k} \cdot \underline{B} = 0$  (i.e.,  $k_y = 0$ ) so that we are only considering flute modes, and have assumed that the ions are unmagnetized (valid for  $\omega > \Omega_{p,b}$  and  $k\rho_{p,b} \gg 1$  where  $\rho_{p,b}$  is the near ion Larmor radius of the protons and barium ions, respectively) and the electrons are magnetized. We comment that retaining a finite  $k_y$  can generate the modified two stream instability via  $V_e$

(McBride et al., 1972). However, this instability produces little momentum coupling between the counterstreaming ions; it primarily heats electrons and generates electron tails parallel to  $B$ .

We can simplify (3) by assuming cold ions, i.e.,  $v_b \ll \omega/k - v_{px} \cos \theta$  and  $v_p \ll \omega/k$ . In this limit  $Z(\zeta) = -1/\zeta - 1/2\zeta^3$  and (3) can be written as

$$\frac{\omega_{Hp}^2}{(\omega - k \cdot v_p)^2} + \frac{\omega_{Hp}^2}{\omega^2} = 1 + \frac{c^2}{k^2 c^2} \quad (4)$$

where the proton lower hybrid frequency is

$$\omega_{Hp}^2 = \omega_p^2 (1 + \omega_e^2 / \Omega_e^2)^{-1} \quad (5a)$$

$$\alpha = \frac{n_b}{n_p} \frac{m_p}{m_b} \quad (5b)$$

and

$$\omega_0^2 = \frac{\omega_e^2}{\Omega_e^2} \frac{\omega_e^2}{(1 + \omega_e^2 / \Omega_e^2) (1 + \beta_e)} \quad (5c)$$

Notice that as long as  $n_b/n_p < m_b/m_p = 128$  then  $\alpha < 1$  and the small term in the dispersion relation is due to barium ions. This implies that when  $n_b/n_p < 128$  the excited waves will be proton, rather than barium, lower hybrid waves.

For  $\alpha < 1$  and  $\omega_0^2 \ll c^2 k^2$ , the most unstable waves have the following approximate frequency and wavenumber

$$\omega_r = \omega_{Hp} \quad (6a)$$

$$\gamma = 0.69 \alpha^{1/3} \omega_{Hp} \quad (6b)$$

$$k \cos \theta = \omega_{Hp} / V_{px} \quad (6c)$$

On the other hand, for values of  $\omega_p^2/c^2 k^2$  sufficiently large, the modes can be stabilized because of electromagnetic effects (Papadopoulos et al., 1971; Lampe et al., 1975). The criterion for instability is given by

$$\cos \theta < \frac{c \omega_{Hp}}{V_{px} \omega_e} (1 + \alpha^{1/3})^{3/2} (1 + \beta_e)^{1/2} = \cos \theta_0. \quad (7)$$

For the parameters of interest, we note that  $\alpha \ll 1$  and  $\beta_e \ll 1$  and (7) can be rewritten as

$$\cos \theta < \frac{V_{Ap}}{V_{px}} \left(1 + \frac{n_b}{n_p}\right)^{-1} \quad (8)$$

where  $V_{Ap} = B/(4\pi n_p m_p)^{1/2}$  is the local Alfvén velocity associated with the protons. Notice that the angle  $\theta_0$  separates the angular region of unstable modes from stable modes in the plane perpendicular to the magnetic field (Fig. 6). For values of the RHS of (8) which are comparable to or larger than unity, the entire  $k$ -space plane is unstable, and as shown in Lampe et al. (1975), complete ion-ion momentum coupling accompanies the interaction. The instability weakens substantially when the stable region around  $V_p$  increases (i.e.,  $\theta_0$  increases) leaving only weak off angle modes unstable.



To better illustrate the linear properties of the counterstreaming ion-ion instability, we present numerical solutions of (3) for parameters relevant to the AMPTE release of Dec. 27, 1984. In Figs. 7 and 8 we take  $m_b/m_p = 128$ ,  $v_p/v_{px} = 0.3$ ,  $v_b/v_{px} = 0.01$ , and  $\beta_e = 0.0$ . The most significant variations are for  $n_b/n_p$  and  $V_{Ap}/V_{px}$  so we present results for a range of values for these parameters. In Figs. 7 and 8 we plot  $\gamma_M/\omega_{Hp}$  vs  $V_{Ap}/V_{px}$  for  $n_b/n_p = 0.5, 2.0, 5.0$  and  $10.0$  (for  $\alpha = 3.9 \times 10^{-3}, 1.6 \times 10^{-2}, 3.9 \times 10^{-2}$ , and  $7.6 \times 10^{-2}$ , respectively). In Fig. 7 we consider  $\theta = 0^\circ$ , while in Fig. 8 we consider  $\theta = 60^\circ$ . Here  $\gamma_M$  is the maximum growth rate as a function of  $k$ . We have not plotted  $\omega_r$  or  $k$  but note that (6a) and (6c) are in reasonable agreement with the numerical values. In Fig. 7 we note the following. First, in the limit  $V_{Ap}/V_{px} \gg 1$ , the growth rate asymptotes to its maximum value which is approximately given by (6b) [e.g., for  $n_b/n_p = 0.5$  ( $\alpha = 3.9 \times 10^{-3}$ ) we obtain  $\gamma_M/\omega_{Hp} = 0.108$ ]. Also, in this limit we note that the maximum growth rate increases as  $n_b/n_p$  increases. Second, as  $V_{Ap}/V_{px}$  decreases the growth rate decreases; for sufficiently small values of  $V_{Ap}/V_{px}$  the modes are stabilized because of electromagnetic effects. However, note that the critical value of  $V_{Ap}/V_{px}$  which stabilizes the modes decreases with decreasing  $n_b/n_p$  (e.g., for  $V_{Ap}/V_{px} = 2$  the mode is stable for  $n_b/n_p = 10.0$  but unstable for  $n_b/n_p = 0.5$ ). This is consistent with (8) which, for  $\theta = 0$ , can be written as  $V_{Ap}/V_{px} > (1 + n_b/n_p)$ . We also note that the critical value of  $V_{Ap}/V_{px}$  predicted by (8) is somewhat greater than is found from Fig. 7. That is, for  $n_b/n_p = 0.5, 2.0, 5.0$ , and  $10.0$ , (8) predicts  $\gamma = 0$  for  $V_{Ap}/V_{px} = 1.5, 3.0, 6.0$ , and  $11.0$ , respectively; however, Fig. 7 shows that  $\gamma = 0.01 \omega_{Hp}$  ( $\approx 0$ ) for  $V_{Ap}/V_{px} = 1.2, 2.0, 3.6$ , and  $5.5$ . The reason for this is that (8) is based upon the

assumption of cold protons ( $\omega \gg kv_p$ ) but for the parameters used in Fig. 7 (i.e.,  $v_p/v_{px} = 0.3$ ) this assumption breaks down as  $V_{Ap}/V_{px}$  decreases and thermal effects allow the modes to grow in the stable "cold" plasma regime.

In Fig. 8 we plot  $\gamma_M/\omega_{Hp}$  vs.  $V_{Ap}/V_{px}$  for the same parameters as in Fig. 7 but we consider  $\theta = 60^\circ$ . The basic features of Fig. 8 are the same as Fig. 7. However, two points are worth mentioning. First, and most important, unstable modes exist for values of  $V_{Ap}/V_{px}$  that lead to stable modes in the case of  $\theta = 0$ . In fact, for all values of  $n_b/n_p$  considered, strong growth (i.e.,  $\gamma > 0.01 \omega_{Hp}$ ) exists for  $V_{Ap}/V_{px} > 2$ , and in the case of  $n_b/n_p = 0.5$  exists for  $V_{Ap}/V_{px} > 0.5$ . Again, this behavior is consistent with (8). Second, we note that for the same values of  $n_b/n_p$ , the maximum growth rates are smaller for  $\theta = 60^\circ$  than  $\theta = 0^\circ$ . This appears to be inconsistent with (6b) which indicates the maximum growth rate does not depend upon angle. The reason for the discrepancy is the effect of thermal protons which have a stabilizing influence because of ion Landau damping. Finally, we note that we have chosen  $\theta = 60^\circ$  because nonlinear studies have demonstrated that if the angular region of unstable waves initially satisfied the condition  $\cos \theta < \cos \theta_0 = 0.5$  (i.e.,  $\theta_0 = 60^\circ$ ) then the entire  $k$ -plane subsequently becomes unstable resulting in complete momentum coupling between the ion streams. If  $\cos \theta > 0.5$  then the situation, although mildly unstable, is quickly stabilized by finite temperature effects with little momentum coupling.

#### IV. COMPARISON BETWEEN THEORY AND OBSERVATIONS

We now proceed to analyze the observations with the theoretical models described in Section III. Our approach is to examine in detail the key times marked as 1-4 in Figs. 2 and 3. Table 1 gives the values of the important plasma parameters. We note that all of the data are not well known and we have made estimates of some values. Also, in comparing the theoretical conditions for instability with experimentally observed parameters, one does not expect to find "grossly" unstable conditions since the turbulence observed is generally in the nonlinear regime (i.e., near marginal stability).

The slowing down of the solar wind begins at the point marked 1 in Figs. 2 and 3. From Table 1 we see that  $n_b/n_p = 0.2$  and  $V_{Ap}/U_p = 0.4$ ; from Fig. 8 note that these conditions are marginally stable for the ion-ion instability. Therefore the beginning of the interaction is consistent with the minimum condition for a momentum coupling cross field, counterstreaming proton-barium instability. The theoretically expected electrostatic waves cover the range between  $f_{Hp} = 10$  Hz and  $f_{ce} = 560$  Hz, with most of the energy confined in the 15-40 Hz region. At the time marked 2 (UT 12:35:19) the magnetic field compression starts and there is an attendant increase in  $V_{Ap}/V_{px}$ . Thus, this leads to conditions more favorable to instability and we expect the entire k-plane to become unstable leading to strong momentum coupling. Figure 2 and 3 seem to confirm this. The range of the unstable waves corresponds to 22 Hz - 1.6 kHz with the most of the energy in the 22 - 60 Hz region. Notice that between times marked 1 - 3, the value of  $V_{pz}$  is relatively unchanged and remains close to zero, while  $V_{px}$  is reduced sharply. The ion-ion driven interaction seems to terminate at the time

marked 3 (UT 12:34:27). At this time the solar wind speed is  $|V_{px}| = 250$  km/sec; the protons have lost more than 80% of their initial energy. We comment that the proton temperature is of the order  $5 \times 10^6$  °K so that the proton thermal speed is  $v_p = 200$  km/sec and the wave modes are subsequently suppressed because of proton Landau damping. This is consistent with the wave measurements shown in Fig. 4. Following the time marked 3 (UT 12:34:27) till ~ UT 12:35:50, the value of  $V_{px}$  continues to decrease to almost zero. However, the data are indicative of a different interaction. The slowing down is characterized by very weak electrostatic activity and most important, by an increase in the value of  $V_{pz}$  which reaches 250 km/sec when  $V_{px}$  approaches zero. This is the type of interaction expected from Larmor coupling described by (1) and (2) for  $v^* < n_p$ . It is basically a gyration of the protons about the magnetic field which is piled up in the front of the barium cloud. This stage is followed by entry into the diamagnetic cavity. We can associate the observed sunward flux of 0.5 keV protons with the thermal expansion of the protons when  $V_{px}$  became small.

The detailed spectrum presented in Fig. 4 allows a further comparison with theoretical concepts. As noted before, the instability saturates by trapping. For the proton-barium situation and with  $\alpha \ll 1$  the phase velocity  $V_{ph}$  of the unstable waves lies near the barium flow velocity (see Fig. 6). In the solar wind reference frame we note that (Lampe et al., 1975)

$$V_{ph} = V_{px} (1 - 2^{-4/3} \alpha^{1/3}) \quad (12)$$

Waves growing with this phase velocity will trap protons when their potential is of the order of

$$e\phi = \frac{1}{2} m_p v_{ph}^2 = \frac{1}{2} m_p v_{px}^2 \quad (13a)$$

and barium when

$$e\phi = \frac{1}{2} m_b \left(\frac{v_{ph}}{2}\right)^{2/3} v_{px}^2 \quad (13b)$$

By comparing (13a) and (13b) we find that as long as

$$\frac{n_b}{n_p} > 2 \left(\frac{m_p}{m_b}\right)^{1/2} = 0.18 \quad (14)$$

the condition for proton trapping (13a) will be reached first and will saturate the instability. Since in our case (14) is satisfied, we expect that the instability will saturate by trapping the protons. This is similar to the saturation of the Buneman instability studied by Davidson et al. (1970) which saturates by trapping electrons rather than protons, despite the fact that  $v_{ph}$  is near the proton beam. The amplitude of the electric field required to trap the protons is

$$\bar{E} = \frac{1}{4} \frac{m_p v_{px}}{e} \omega_{Hp} \quad (15)$$

For the parameters given in Table I (i.e.,  $v_{px} = 250 - 400$  km/sec and  $\omega_{Hp} = 107 - 145$  sec<sup>-1</sup>) we find that (15) predicts  $\bar{E} = 67 - 145$  mV/m. Gurnett et al. (1985) report values of  $\bar{E} = 140$  mV/m while noting that the 10 Hz channel was saturated. Thus, these field values are consistent with

the saturation by trapping. Note that the peak spectral density in Fig. 5 is  $\leq 20$  Hz which is consistent with theoretical values. The value of  $v^*$  can be estimated on the basis of the wave spectral energy density  $S(\omega)$  in the lower hybrid region, as given in Fig. 4. It is approximately given by (Papadopoulos, 1977)

$$v^* = \frac{D}{(v_{px} - v_{pn})^2} = \frac{e^2}{\pi_p^2} \frac{S(\omega = \omega_{Hp})}{v_{px}^2} =$$

$$= 100 \left( \frac{100 \text{ km/sec}}{v_{px}} \right)^2 \left( \frac{S(\omega = \omega_{Hp})}{10^{-4} v^2 / \pi^2 \text{ Hz}} \right)$$

where  $D$  is the diffusion coefficient in velocity space. For the measured values at 12:34:27 and  $S(\omega = \omega_{Hp})$  given by Fig. 4 we find  $v^* = 12 - 20$  so that  $v^* \gg \Omega_p, \Omega_b$ .

#### V. SUMMARY AND CONCLUSIONS

We have presented observations of the solar wind-barium interaction associated with the AMPTE artificial comet release of Dec. 27, 1984. Based on these observations we have argued that the solar wind couples momentum (and energy) to the barium ions through both laminar and turbulent processes [see (11)]. The laminar forces acting on the particles are the laminar electric and magnetic fields; the turbulent forces are associated with the intense electrostatic wave activity. This wave activity has been shown to be caused by a cross-field proton-barium ion streaming instability. The observed wave frequencies and saturated amplitudes are consistent with our theoretical analysis.

The following picture emerges. After the barium is released from the canisters, it expands outward and is photoionized. The expanding barium cloud forms a compressed density and magnetic field region on the sunward side of the expansion. As the solar wind protons stream into this region they first interact with the barium ions to generate relatively weak off-angle electrostatic turbulence. This occurs when  $n_b/n_p \leq 1$  and  $V_{ap}/V_{px} \gg 1$ . This turbulence acts to couple the solar wind protons and barium ions, and the protons slow down (see in Fig. 1 between marks 1 and 2). As the protons move deeper into barium ion shells they encounter the compressed magnetic field region (which increases the local proton Alfvén speed) and a more dense barium ion region (which increases  $n_b/n_p$ ). These two factors allow stronger wave growth to occur; this corresponds to the intense wave activity observed between the times marked 2 and 3 on Fig. 3. This turbulence causes the solar wind protons to slow down even more, and also produces proton and barium ion heating. Finally, the protons undergo a gyration about the compressed magnetic field which is indicated by a decrease in  $V_{px}$  and an increase in  $V_{pz}$ . We expect a similar type of interaction to occur in the solar wind-comet interaction. This topic is currently under study and will be reported elsewhere.

There are two more points that we would like to address. First, is the electron heating and electron acceleration. The observed electron heating seems consistent with adiabatic heating. However, in addition to the local heating, the UK spacecraft observed electron fluxes with energy larger than 100 eV, i.e., the period between our marks 1-3. This is the period during which the lower hybrid instability was operating. For the flute mode ( $k_y = 0$ ) instability discussed above, the electrons are adiabatic. However, field aligned suprathermal electron tails can be

produced by the non-flute modes ( $k_y \neq 0$ ), corresponding to the electron-ion modes mentioned in Section III. These modes have frequencies typically 5-6  $f_{Hp}$  and saturate at a lower level. The details of this interaction will be discussed elsewhere. It is sufficient here to note that the existence of wave frequencies in the 200 Hz to 1 kHz range is consistent with the model and with the electron fluxes observed by the UK spacecraft. Second, although the solar wind barium interaction results in complete momentum coupling, the barium has not been picked up by the solar wind during the 3-4 min of the measurements. This is due to the large barium mass and density which would require times of the order of 8-10 min to be picked up. This should be contrasted with the lithium releases for which pick up occurred at much shorter times.

#### Acknowledgment

This research has been supported by NASA (K.P. and A.T.Y.L.), and ONR and DNA (J.D.H.).



TABLE I

UT	$V_{px}$ (km/sec)	$V_{pz}$ (km/sec)	$B$ ( $\gamma$ )	$n_e$ ( $\text{cm}^{-3}$ )	$n_p$ ( $\text{cm}^{-3}$ )	$n_{Ba}$ ( $\text{cm}^{-3}$ )	$f_{Hp}$ (hz)	$V_{Ap}$ (km/sec)
12:36:20	-550	0	20	6*	5	1*	12	195
12:35:15	-400	0	50	20*	10*	10*	23	345*
12:34:27	-250	- 50	85	110	10*	100	17	586*
12:33:50	- 75	-250	130	3010	10*	3000	5	896*

\*Estimate

## REFERENCES

- Davidson, R.C., N.A. Krall, K. Papadopoulos, and R. Shanny, "Electron heating by electron-ion beam instabilities," Phys. Rev. Lett., 24, 579, 1970.
- Feiden, G.A., J.B. Lyon, and J.L. Giuliani, Jr., "Numerical simulations of comets: Predictions for comet Giacobini-Zinner," EOS, 67, 17, 1986.
- Burnett, D.A., R.R. Anderson, B. Häusler, G. Haerendel, G.H. Bauer, R.A. Treumann, H.C. Koons, R.H. Holzworth, and H. Lühr, "Plasma waves associated with the AMPTE artificial comet," Geophys. Res. Lett., 12, 851, 1985.
- Haerendel, G., G. Paschmann, W. Baumjohann, and C.W. Carlson, "Dynamics of the AMPTE artificial comet," Nature, 320, 720, 1986.
- Ip, W.-H. and W.I. Axford, "Theories of physical processes in the cometary coma and ion tails," in Comets, edited by L.L. Wilkening, University of Arizona Press, Tucson, 1982.
- Lampe, M., W.M. Manheimer, and K. Papadopoulos, "Anomalous transport coefficients for HANE applications due to plasma microinstabilities," NRL Memo. Rept. 3076, 1975.
- Mendis, D.A. and H.L.F. Houpis, "The cometary atmosphere and its interaction with the solar wind," Rev. Geophys., 20, 885, 1982.
- McBride, J.B., E. Ott, J.P. Boris, and J.H. Orens, "Theory and simulation of turbulent heating by the modified two-stream instability," Phys. Fluids, 15, 2367, 1972.

- Papadopoulos, K., Review of anomalous resistivity for the ionosphere, *Rev. of Geophys. and Space Phys.*, 15, 113, 1977.
- Papadopoulos, K., R. Davidson, J.M. Dawson, I. Haber, D.A. Hammer, N.A. Krall, and R. Shanny, "Heating of counterstreaming ion beams in an external magnetic field," *Phys. Fluids*, 14, 849, 1971.
- Sagdeev, R.Z., V.D. Shapiro, and V.I. Schevchenko, "MHD turbulence in the solar wind-comet interaction region," *Geophys. Res. Lett.*, 13, 85, 1986.
- Valenzuela, A., G. Haerendel, H. Foppl, F. Melzner, H. Neuss, E. Kieger, J. Stocker, O. Bauer, H. Hofner, and J. Leidel, "The AMPTE artificial comet experiments," *Nature*, 320, 700, 1986.

## FIGURE CAPTIONS

- Fig. 1) Schematic of the spacecraft positions and magnetic field structure for the Dec. 27, 1984 AMPTE release.
- Fig. 2) Particle and field data (from Haerndel et al., 1986).  
 (a) Electron density ( $\text{cm}^{-3}$ ). (b) Solar wind proton velocity (km/sec) in the x-direction (GSE coordinates). (c) Solar wind proton velocity (km/sec) in the y-direction (GSE coordinates). (d) Magnetic field (nT).
- Fig. 3) Particle, field, and electric field wave data (from Gurnett et al., 1985). The barium ion density is based upon emissions at the plasma frequency. Note the intense, low frequency ( $f \sim 30 \text{ Hz} - 1 \text{ kHz}$ ) electrostatic waves during between the times marked 2 and 3.
- Fig. 4) Electric field spectral density as a function of frequency for times UT 12:34:27 and UT 12:33:16 (from Gurnett et al., 1985). Note that the most intense waves for UT 12:34:27 (marked 3 on Figs. 2 and 3) are low frequency (i.e.,  $f \sim 30 \text{ Hz}$ ).
- Fig. 5) Local velocity distributions of the solar wind protons, barium ions, and electrons in the solar wind frame of reference.

Fig. 6) Schematic of unstable waves driven by the magnetized ion-ion instability in the  $k_x - k_z$  plane. The relative drift between ions is in the x-direction.

Fig. 7) Plot of  $\gamma_M/\omega_{Hp}$  vs  $V_{Ap}/V_{px}$  for  $\theta = 0^\circ$  and  $n_b/n_p = 0.5, 2.0, 5.0, 10.0$ . Here  $\gamma_m$  is the maximum growth rate with respect to the wavenumber  $k$ .

Fig. 8) Plot of  $\gamma_M/\omega_{Hp}$  vs.  $V_{Ap}/V_{px}$  for  $\theta = 60^\circ$  and  $n_b/n_p = 0.5, 2.0, 5.0, 10.0$ . Note that for these parameters ( $\theta = 60^\circ$ ), the modes are excited for lower values of  $V_{Ap}/V_{px}$  than in the previous case ( $\theta = 0^\circ$ ), consistent with (8).



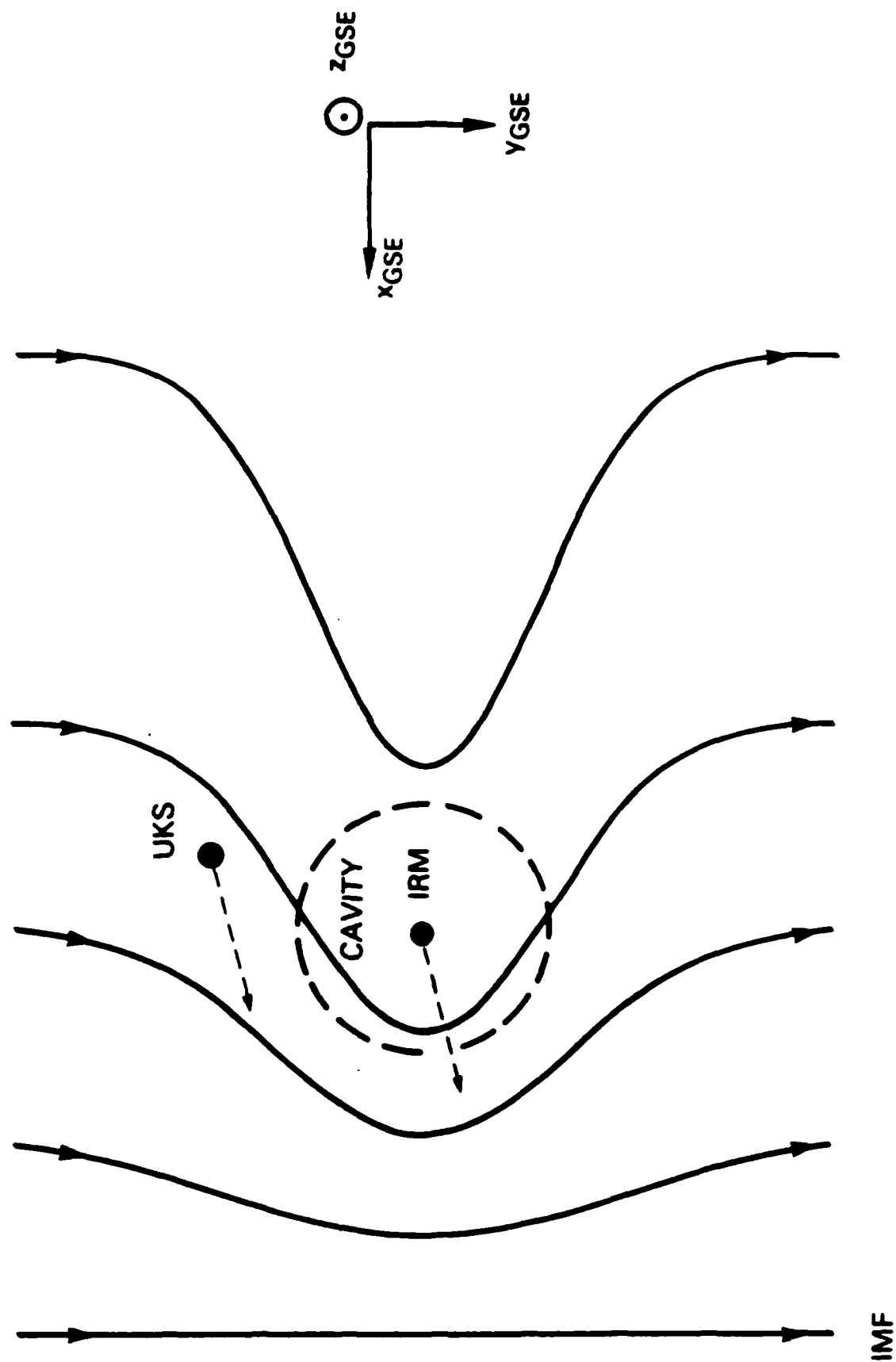


Figure 1

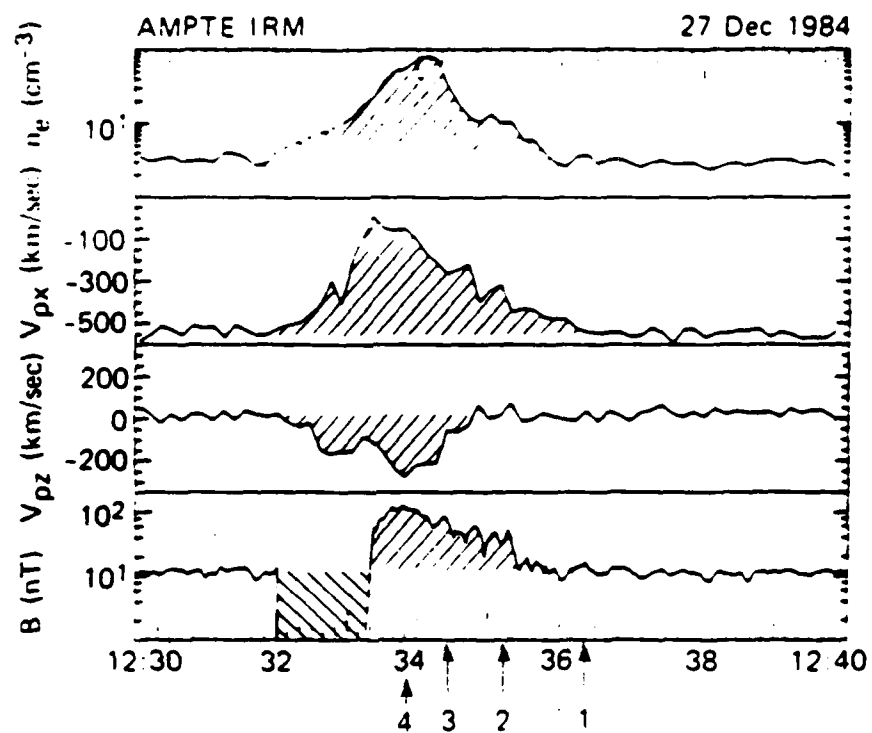


Figure 2



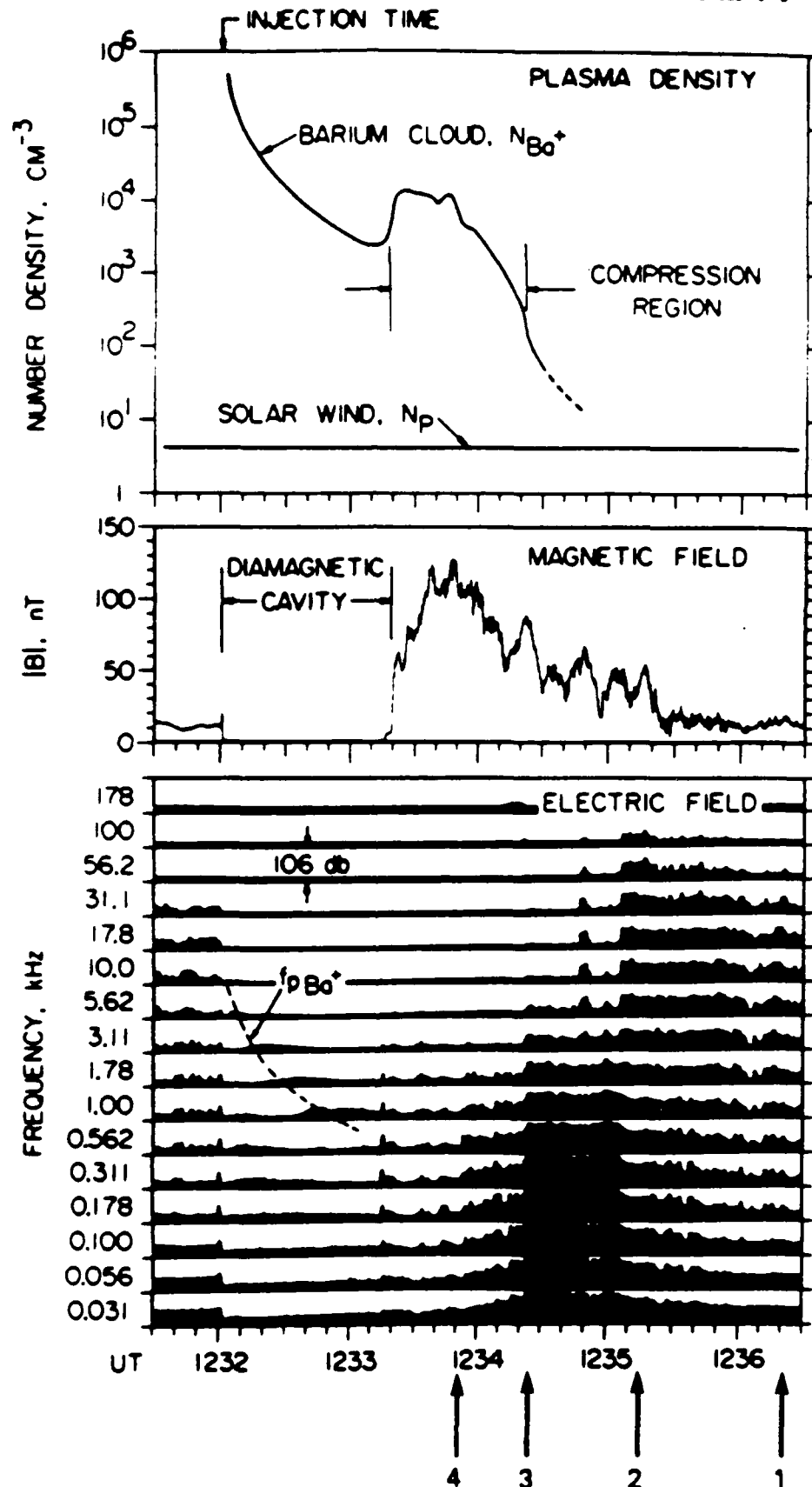


Figure 3  
P-29

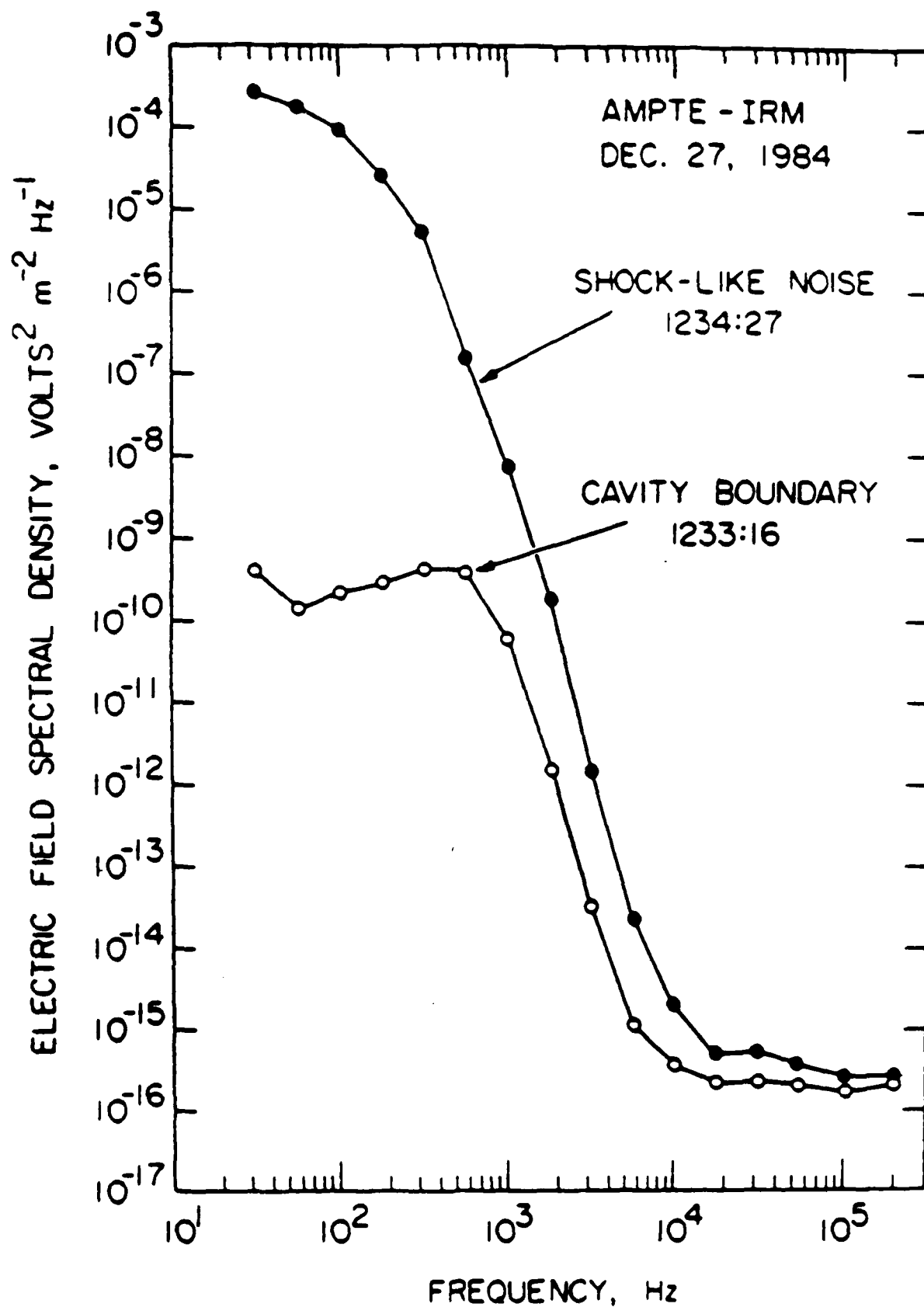


Figure 4  
P-30

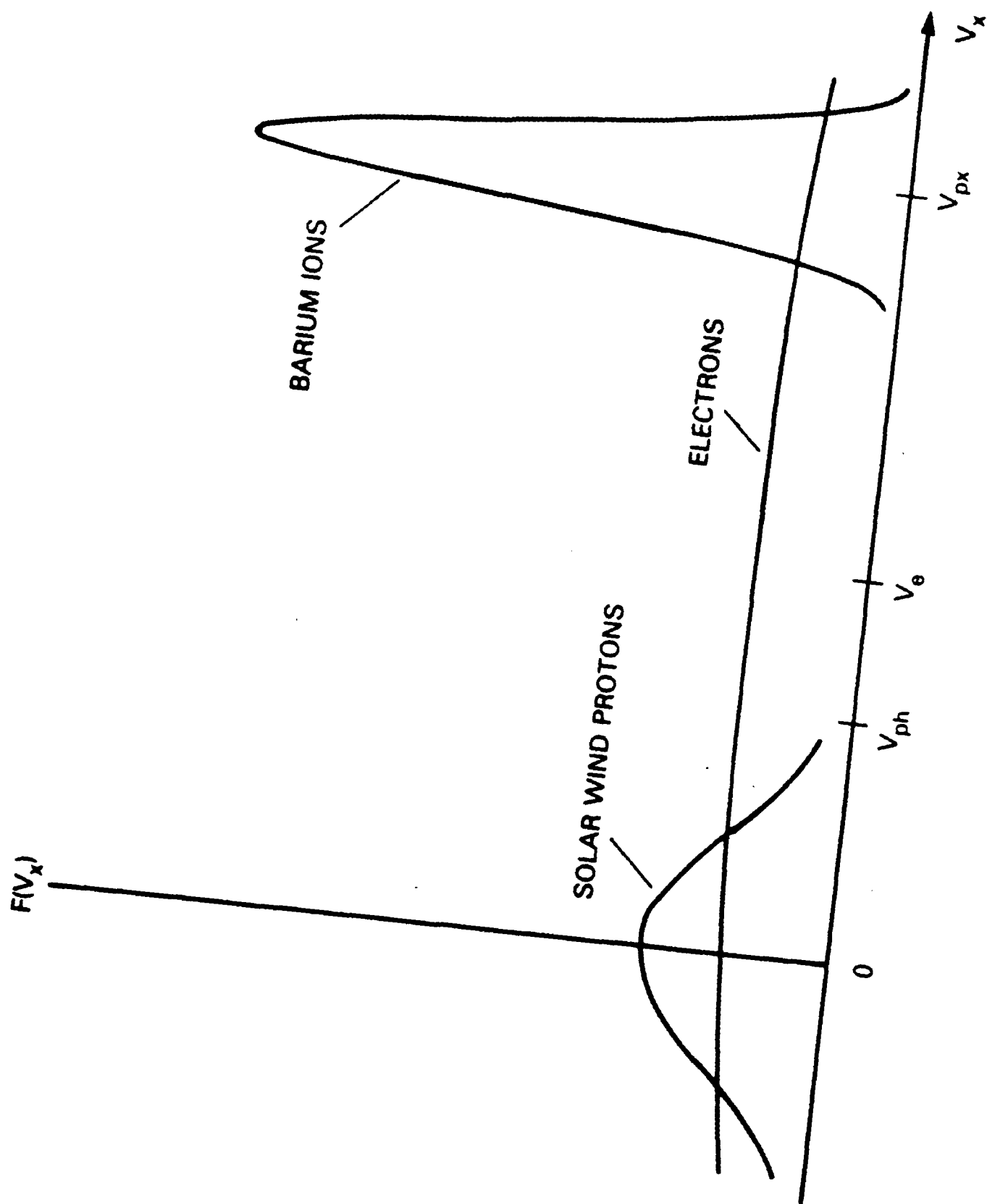


Figure 5

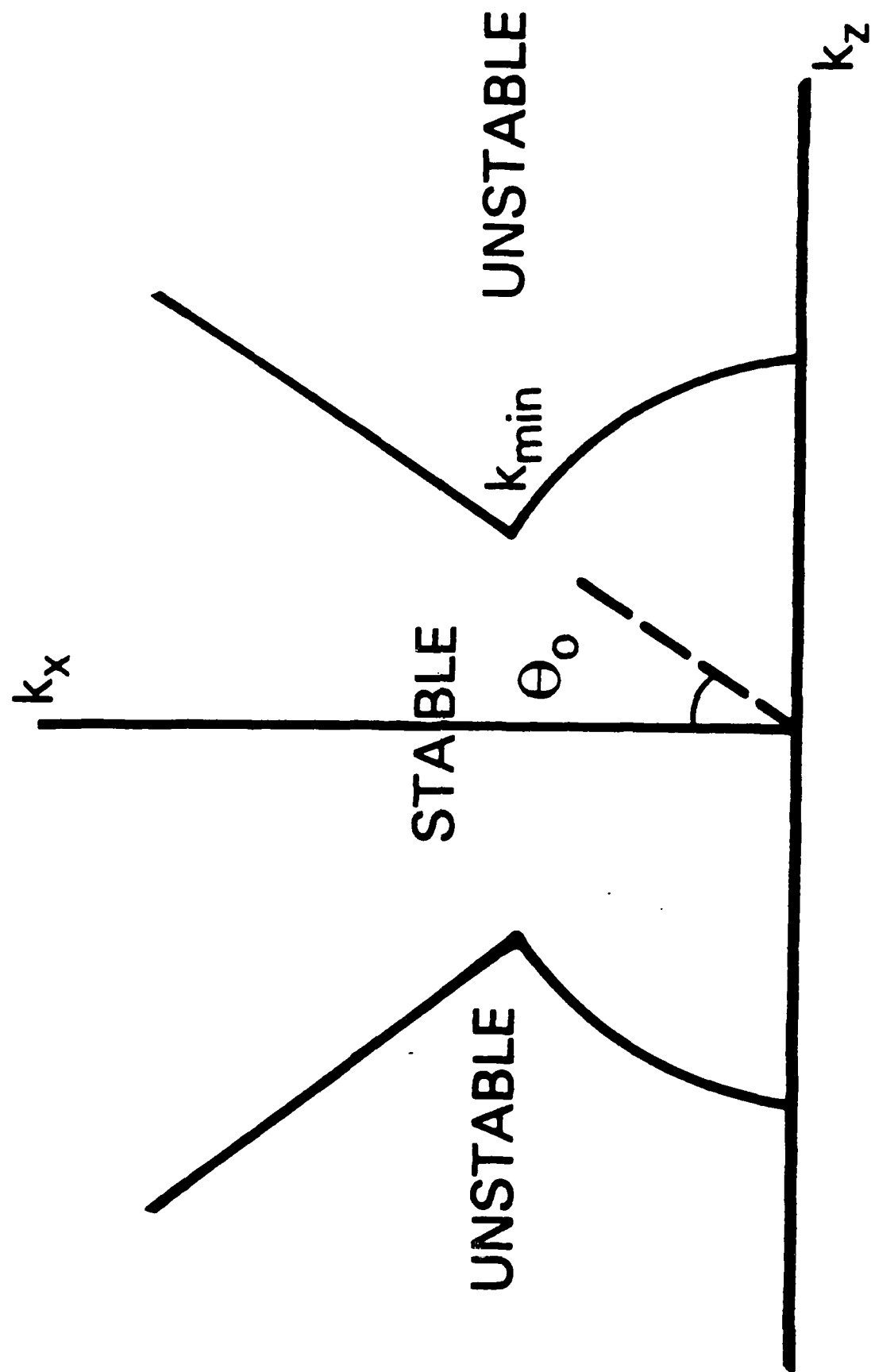


Figure 6

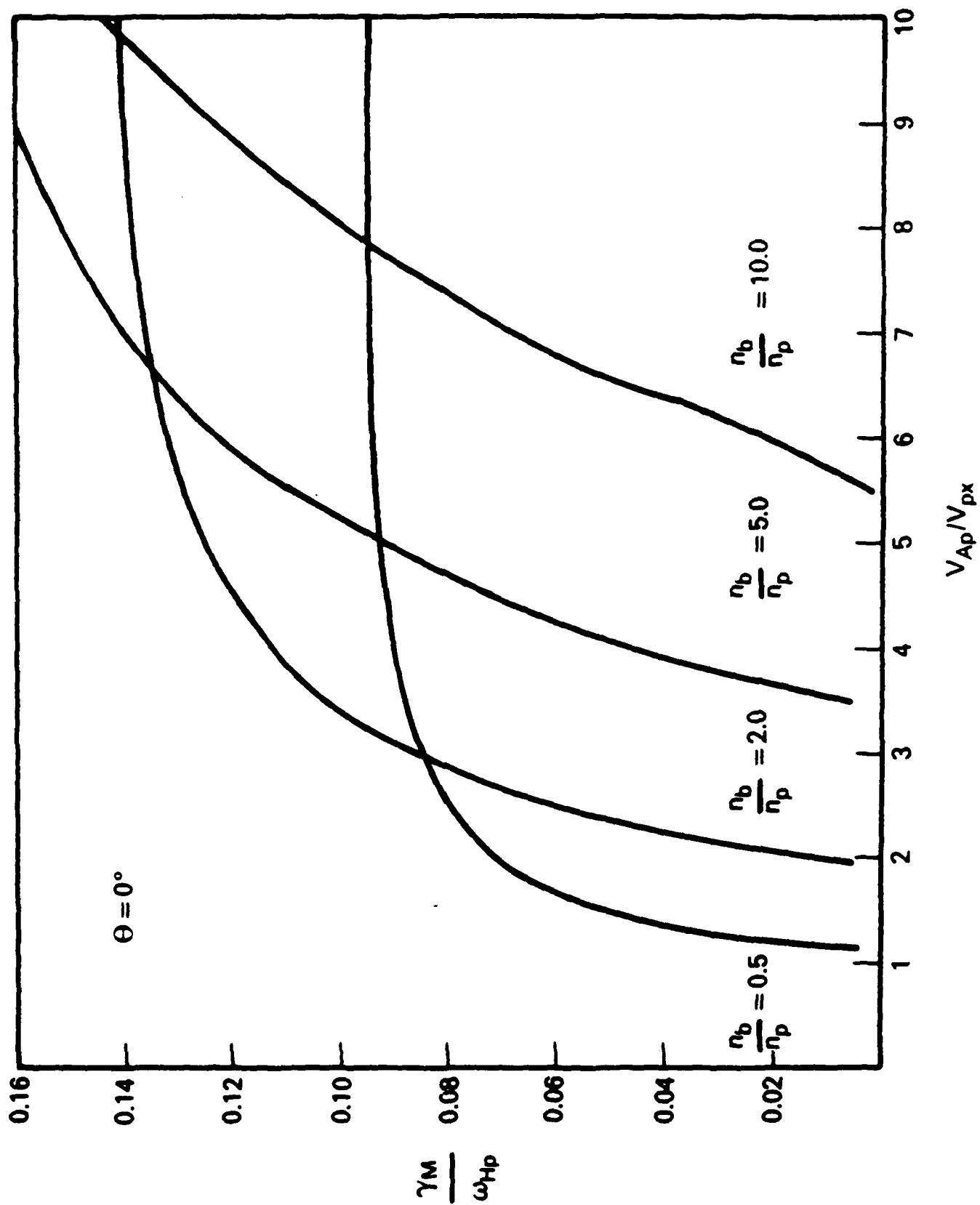


Figure 7

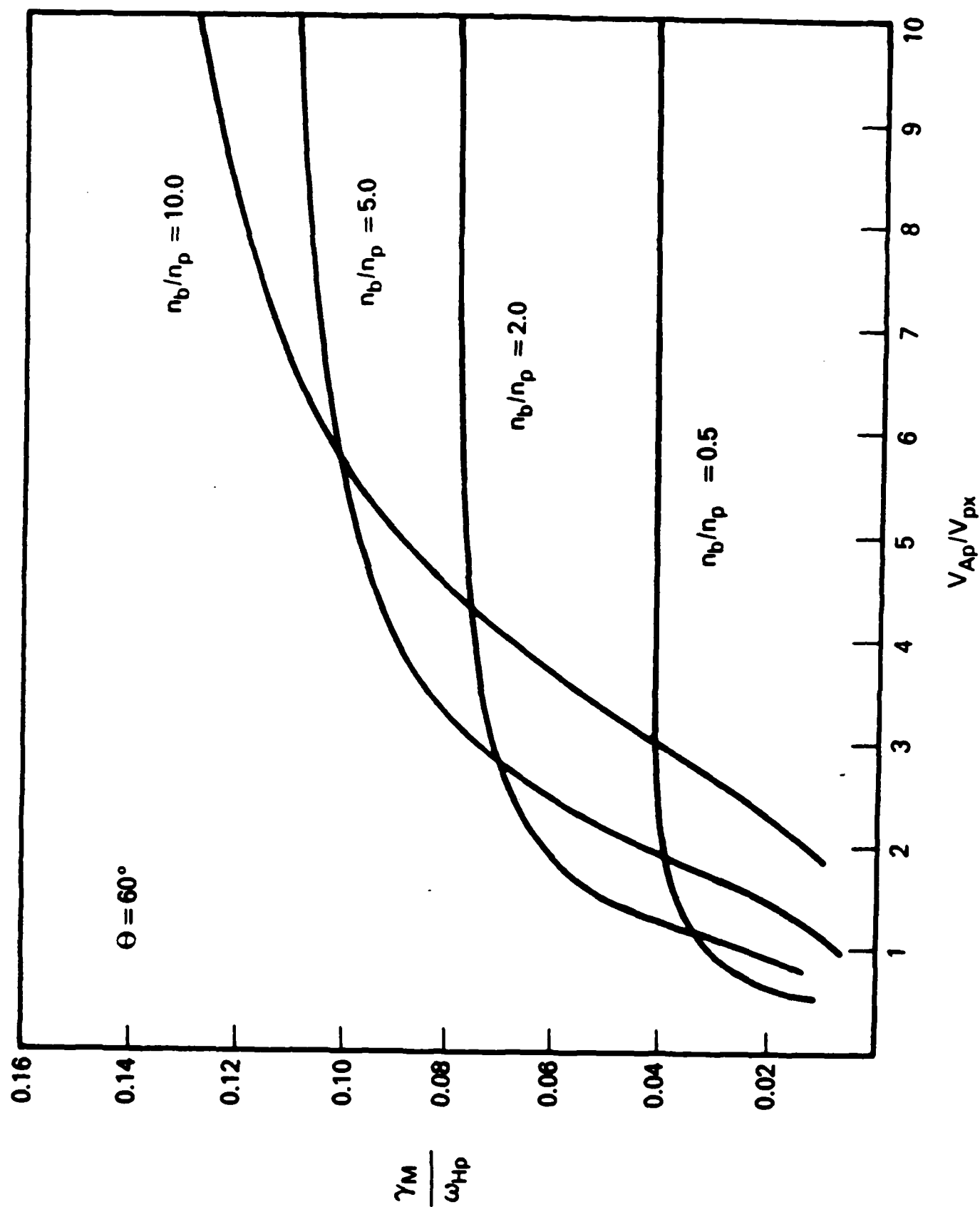


Figure 8

**APPENDIX Q**

**Projections of Plasma Cloud Structures and Their Spectra**

**Norman J. Zabusky  
Fluid Sciences, Inc.**

**Ellis Hyman  
Science Applications International Corporation**

**Margaret Mulbrandon  
Naval Research Laboratory**





# Projections of Plasma Cloud Structures and Their Spectra

NORMAN J. ZABUSKY

*Fluid Sciences, Inc., Pittsburgh, Pennsylvania*

ELLIS HYMAN

*Science Applications, Inc., McLean, Virginia*

MARGARET MULBRANDON

*Geophysical and Plasma Dynamics Branch, Plasma Physics Division, Naval Research Laboratory  
Washington, D. C.*

We have established a relationship between the asymptotic ( $k \rightarrow \infty$ ) spectral index of idealized optically thin localized radiating sources,  $n(x, t)$ , and their scans,  $f$ . For piecewise-constant (pc) clouds, if the envelope of the one-dimensional asymptotic spectrum of the power of  $n$  is proportional to  $k^{-2}$ , then the asymptotic spectrum of the scan depends upon the character of the contour at point  $x_0 = (x_0, y_0)$  where it is tangent at an extremal ray. If the contour at  $(x_0)$  behaves like  $y - y_0 = \gamma(x - x_0)^2$ , then the asymptotic spectral envelope of the power spectral density (PSD) of the scan varies as  $k^{-2(1+\gamma)}$ . For a convex curve with finite curvature at  $x_0$ , we have  $\gamma = 1/2$  and obtain the well-known result,  $k^{-3}$ . In addition, if the radiating density varies spatially in a cloud flank with a power law  $\mu$ , then the asymptotic spectral envelope of the scan's PSD varies as  $k^{-2(1+\mu)}$ . Thus by examining projections of radiating clouds, one cannot distinguish between local gradients of density and the local shape of the boundary curve of the cloud. We also apply the result to the interpretation of optical scans from two PLACES events. These show the onset of steepening and striations. However, the accurately resolved wave number range is insufficient for determining the spectrum associated with the nonlinear dynamics of striation evolution.

## 1. INTRODUCTION

Observation of unstable and turbulent geophysical fluid dynamical processes is often indirect and made from remote sensors. Many processes are observed optically from several vantage points, and the spatial radiance distribution is recorded photographically or electronically. From successive frames, one hopes to deduce the location and morphology of evolving hierarchies of structures. Unfortunately, a detailed reconstruction is impossible because of the lack of precise control of the processes that govern the radiation, the paucity of recording locations, and the lack of detailed in situ (rocket-borne) diagnostics. That is, compared with the progress in laboratory tomography, our problem is highly underdetermined [Shepp and Kruskal, 1978; Deans, 1983].

A long-range goal of the present investigation is to construct simple models of radiating ionospheric plasma clouds that are useful to communication and tracking systems engineers. We are interested in the intercloud distances, scale sizes, gradients and asymmetries with respect to the earth's magnetic field, and ambient winds and the evolution of these structural features. We will distill the bits of information available from field experiments and large-scale nonlinear dynamical computer simulations into cogent models. Conventionally, one discretizes field data and uses the computed power spectral densities (PSD) to compare with realistic turbulent or wave-steepening numerical simulations. However, PSDs and their spectral exponents are subject to errors because of the inadequacy of resolution and dynamical range in experimental and numerical simulation data. Some considerations of the latter were given in the first report of this series [Mulbrandon *et al.*, 1984] and are applied here.

In section 2 we discuss the relation between radiation from

an idealized (piecewise-constant (pc)) cloud,  $n(x)$ , and its projection functions,  $f(x)$ . These are intensity scans through a "slice" of the cloud. For simplicity, the cloud is taken to be sufficiently remote that parallax effects are negligible. That is, all rays emitted by the cloud are perpendicular to the projection plane. We will show that essential properties of  $f(x)$  are related to a combination of two effects: the curvature of the cloud's boundary curve at points where projection rays are tangent to the boundary curve and the density gradient at these points. In section 3 we relate PSDs of clouds to the PSDs of their projection functions. In section 4 we analyze measured scans from two PLACES experiments in light of the above results, and section 5 presents our conclusions.

## 2. PROJECTIONS OF THREE-DIMENSIONAL CLOUDS

### 2.1. Introduction

Ionospheric plasma cloud densities may be approximated by the separable function

$$n(x', t) = n_z(x', y', t) g_{||}(z', t) \quad (1)$$

where  $z'$  is along the earth's magnetic field. Thus  $n_z$  exhibits a steep "backside" and  $g_{||}$  may be approximated by  $\exp -[(z' - z_0)/l]^2$ , where  $l^2 = l_0^2 + (vt)$  approximates a diffusive spreading along  $z'$  with diffusivity  $v$  and  $z_0(t)$  decreases in time as the cloud settles from its high-altitude release point. There is evidence that the symmetry in  $z' - z_0$  may be broken in time, that is, the higher-altitude regions may be more diffuse [Lebeda *et al.*, 1984]. However, to illustrate the nature of projections and the essential issues involved in computing PSDs we suppress the time variable and consider an idealized cloud with piecewise-constant density in a bounded domain  $D$ , namely,

$$\begin{aligned} n &= F_0 & x \in D \\ n &= 0 & x \notin D \end{aligned} \quad (2)$$

Copyright 1986 by the American Geophysical Union.

Paper number 5A8635.  
0148-0227/86/005A-8635\$05.00

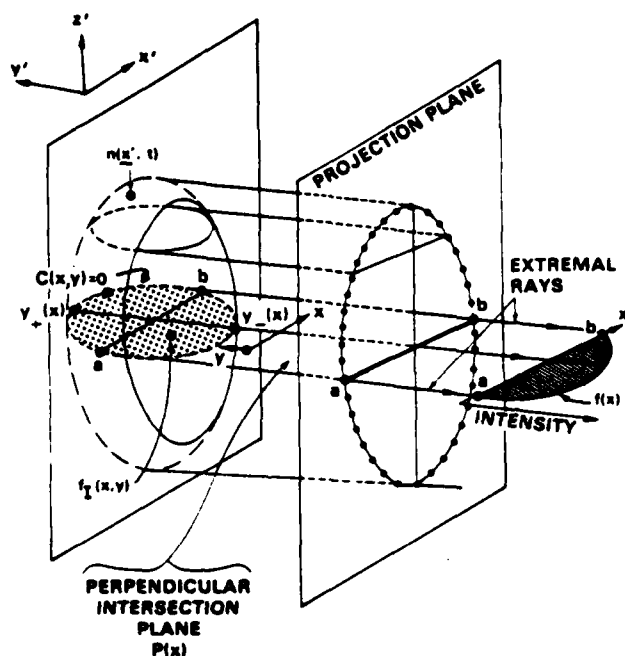


Fig. 1. Schematic of a remote radiating cloud,  $n(x', t)$ , and the projection function,  $f(x)$ , through a slice of the cloud.

Note that a realistic smooth cloud may be approximated by several nested pc clouds, depending upon the accuracy required.

## 2.2. pc Clouds and Scans

Figure 1 shows a pc cloud,  $n(x', t)$ , the curve  $C(x, y) = 0$  (which is the intersection of domain  $D$  and  $P(x)$ , the perpendicular intersection plane), and the projection plane on which the radiance image is recorded. The sketch to the right of the plane is an intensity plot,  $f(x)$ , associated with a "slice," the line  $a-b$  on the projection plane. For an optically thin cloud,  $f(x)$  is obtained by integrating the intersection intensity,  $f_i(x, y)$ , along the  $y$  direction (perpendicular to the projection plane). The limits of integration  $y_+(x)$  and  $y_-(x)$  are the intersections of a line perpendicular to the projection plane with the curve  $C(x, y) = 0$ . That is,

$$f(x) = \int_{y_-(x)}^{y_+(x)} dy f_i(x, y) = F_0(y_+(x) - y_-(x)) \equiv F_0 y(x) \quad (3)$$

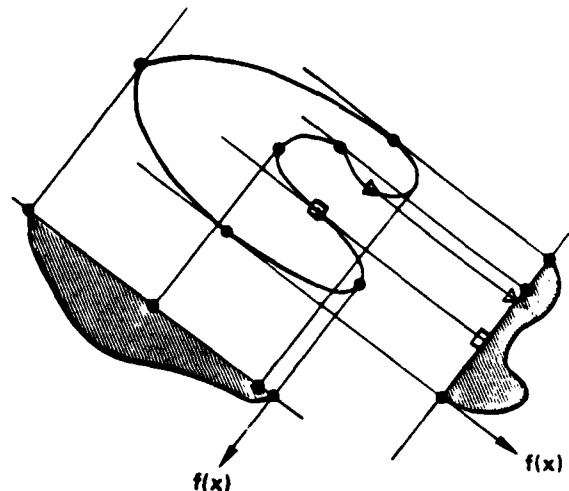


Fig. 2. Two projections of a realistic two-finger cloud showing the effects of tangency points (rectangles and triangles) where  $\kappa = 0$ .

Generally, for non-pc clouds  $f_i(x, y)$  will not be constant and will depend on the orientation angle of the viewer with respect to the magnetic field and ambient wind. Scans resulting from such clouds are discussed in section 2.3.

Consider  $f(x)$  near  $x = x_0$ , where a projection ray is tangent on the left to  $C(x, y) = 0$  (e.g., point  $a$  in Figure 1). Thus for  $x > x_0$  we represent the curve locally for  $y > y_0$  by

$$x - x_0 = s \quad (4a)$$

$$y - y_0 = \gamma s^\tau \quad (4b)$$

where  $s \rightarrow (0+)$ . That is, the right side of (4a) and (4b) may be considered the leading terms in a series in  $s$ , which represents an arbitrary curve. Thus the  $x$  derivative

$$\frac{dy}{dx} \equiv y_x = \frac{dy/ds}{dx/ds} \equiv \frac{y_s}{x_s} = \tau \gamma s^{\tau-1} \quad (5)$$

is singular, constant, or zero as  $s \rightarrow 0$  if  $\tau < 1.0$ ,  $\tau = 1.0$ , or  $\tau > 1.0$ , respectively. Similarly, the curvature

$$\kappa \equiv \frac{y_{xx}x_s - x_{xx}y_s}{(x_s^2 + y_s^2)^{3/2}} = \frac{\gamma \tau (\tau - 1) s^{\tau-2}}{[s^2 + \tau^2 \gamma^2 s^{2\tau}]^{3/2}} \quad \tau < 1 \quad (6)$$

is singular, constant or zero as  $s \rightarrow 0$  if  $\tau > 1/2$ ,  $\tau = 1/2$ , or  $\tau < 1/2$ , respectively. Table 1 summarizes some cases in the vicinity of  $x = x_0$ . The next to last column refers to illustrations given in Figure 2. The last column gives the asymptotic

TABLE 1. Various Curves (Equation (4)) Near an Extremal Ray and the Asymptotic Behavior of the Envelope of the PSD of a Scan for Piecewise-Constant Regions

$\tau$	Functional Form	Local		Figure 2	Asymptotic Behavior of PSD Envelope for pc Regions
		$y_+(x_0)$	$\lambda(x_0)$		
2.0	$y - y_0 = \pm \lambda(x - x_0)^2$	0	$\infty$	(not shown)	$k^{-6}$
4/3	$y - y_0 = \pm \lambda(x - x_0)^{4/3}$	0	$\infty$	cusp	$k^{-14/3}$
1.0	$y - y_0 = \pm \lambda(x - x_0)$	$\gamma$	$\infty$	corner	(not shown)
2/3	$y - y_0 = \pm \lambda(x - x_0)^{2/3}$	$\infty$	$\infty$	(not shown)	$k^{-10/3}$
1/2	$y - y_0 = \pm \lambda(x - x_0)^{1/2}$	$\infty$	$-2/\gamma^2$	circles	$k^{-3}$
1/3*	$y - y_0 = \pm \lambda(x - x_0)^{1/3}$	$\infty$	0	triangles	$k^{-8/3}$
1/4	$y - y_0 = \pm \lambda(x - x_0)^{1/4}$	$\infty$	0	rectangles	$k^{-5/2}$
$\epsilon \ll 1$	$y - y_0 = \pm \lambda(x - x_0)^\epsilon$	$\infty$	0	(not shown)	$k^{-(2+\epsilon)}$

\*All cases are for  $x > x_0$  except  $\tau = 1/3$  which applies for  $-\infty < x < \infty$

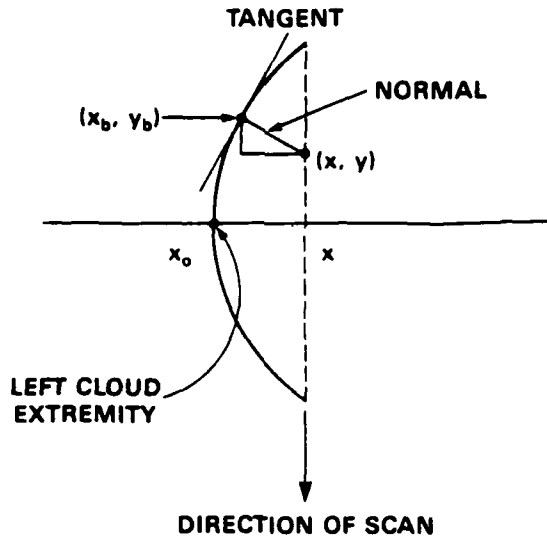


Fig. 3. Sketch and parameters illustrating the intersection density,  $f_I$ , for a cloud with a polynomial density variation in a small layer near its extremity. (Note that  $x_b = x_0 + s$  and  $y_b = y_0 + s'$ .)

behavior of the PSD for pc densities (i.e.,  $\mu = 0$ , as discussed in section 3.2).

For example, the elliptical limaçon

$$(x, y) = (1 - \mu \cos \theta)(\alpha \cos \theta, \beta \sin \theta) \quad (7)$$

has a curvature

$$\kappa = \alpha\beta(1 + 2\mu^2 - 3\mu \cos \theta)/D^{3/2} \quad (8)$$

where

$$D = \alpha^2(\sin \theta - \mu \sin 2\theta)^2 + \beta^2(\cos \theta - \mu \cos 2\theta)^2 \quad (9)$$

From (8) one obtains  $\kappa = 0$  at  $\theta = 0$  if  $\mu = 1/2$  and

$$\left(\frac{y}{\beta}\right) = (2)^{-1/4} \left(\frac{x}{\alpha} - x\right)^{1/4} + \dots \quad (10)$$

which corresponds to the  $\tau = 1/4$  entry in Table 1.

### 2.3. Finite-Gradient Clouds

We now consider more realistic  $n(x)$  with finite gradients near the edge of the boundary of the domain. Hence  $f_I(x, y)$  is no longer constant within the contour of intersection  $C(x, y)$ , and we have two competing space scales at the tangency points, namely, the local radius of curvature and the local gradient scale,  $l = f_I/|\nabla f_I|$ .

To elucidate this competition, we perform a local analysis for a structure with a polynomial flank of degree  $\mu$  in the vicinity of its extremal point. Thus in this boundary layer (with  $y_0 = 0$ )

$$f_I = x_0^{-\mu} [(x_b - x)^2 + (y_b - y)^2]^{\mu/2} F_0 \quad (11)$$

As previously,  $(x_b, y_b) = (x_0 + s, y_0 + s')$  are on the boundary and  $x_0$  is a left cloud extremity. For a given  $(x, y)$  within the cloud,  $(x_b, y_b)$  or  $s$  is chosen such that a normal to the boundary passes through  $(x, y)$  or, as indicated in Figure 3,

$$\frac{y_b - y}{x_b - x} = -(\gamma\tau)^{-1} s^{1-\tau} \quad (12)$$

which follows because the normal to the boundary curve has a slope  $-(\gamma\tau)^{-1} s^{1-\tau}$ . This representation provides a boundary layer in which there is a power law variation. Although this is

one of many possible choices for a compact cloud (one which vanishes outside the boundary), we believe the essential behavior of the asymptotic PSD is unchanged.

The scan intensity is obtained from (3) or

$$f = 2 \int_0^{\Delta} f_I(x, y) dy = 2 \int_0^{\Delta} f_I(x, y(s)) \left(\frac{dy}{ds}\right) ds \quad (13)$$

where  $\Delta = x - x_0 > 0$  and we have replaced the integration over  $y$  by an equivalent one over the contour parameter  $s$ . Thus if we replace  $(x_b, y_b)$  by  $(x_0 + s, y_0 + s')$  and differentiate with respect to  $s$ , keeping  $x$  fixed, we obtain

$$(dy/ds) = \gamma\tau s^{\tau-1} + (\gamma\tau)^{-1} [-\Delta(1-\tau)s^{-\tau} + (2-\tau)s^{1-\tau}] \quad (14)$$

If we substitute (11) and (14) into (13), it becomes

$$f = 2x_0^{-\mu} F_0 \gamma\tau (\Delta^{\mu+\tau}) \int_0^1 (1-\tilde{s})^{\mu} [1 + (\gamma\tau)^{-2} \Delta^{2-2\tau} \tilde{s}^{2-2\tau}]^{\mu/2} \cdot \{\tilde{s}^{\tau-1} + (\gamma\tau)^{-2} \Delta^{1-\tau} [-(1-\tau)\tilde{s}^{-\tau} + (2-\tau)\tilde{s}^{1-\tau}]\} d\tilde{s} \quad (15)$$

where  $\tilde{s} = s/\Delta$ . Thus if one expands all terms in a power series and integrates, the leading term is

$$f \approx 2x_0^{-\mu} F_0 (\gamma\tau) \Delta^{\mu+\tau} + O(\Delta^{\mu+1}) \quad (16)$$

where we have assumed that  $0 < \tau < 1$ . Note the term  $O(\Delta^{\mu+1})$  follows from the second term within the brace of (15).

Thus to leading order, the exponent increases from  $\tau$  to  $(\mu + \tau)$  if a pc cloud is replaced by one whose intersection intensity,  $f_I$ , has a  $\mu$ th degree polynomial flank. Note this indicates that by examining a single projection, one cannot distinguish between local gradients of density and the local shape of the boundary curve of the cloud.

### 3. RELATIONS BETWEEN POWER SPECTRAL DENSITIES OF PC CLOUDS AND THEIR PROJECTIONS

#### 3.1. Clouds

We define the direct and inverse Fourier transforms of an  $m$ -dimensional cloud as

$$\tilde{n}(\mathbf{k}) \equiv \tilde{n}(k_1, k_2, \dots, k_m) = \int_{(m)} n(\mathbf{x}) e^{-i\mathbf{k} \cdot \mathbf{x}} d\mathbf{x} \quad (17)$$

$$\mathbf{x} \in \mathbb{R}^m$$

$$n(\mathbf{x}) \equiv n(x_1, x_2, \dots, x_m) = (2\pi)^{-m} \int_{(m)} \tilde{n}(\mathbf{k}) e^{+i\mathbf{k} \cdot \mathbf{x}} d\mathbf{k} \quad (18)$$

$$\mathbf{k} \in \mathbb{R}^m$$

where  $\int_{(m)}$  symbolizes  $m$  integrations that cover the entire domain and  $d\mathbf{x} \equiv dx_1 dx_2 \dots dx_m$  and  $d\mathbf{k} \equiv dk_1 dk_2 \dots dk_m$ . The last can be written as  $d\mathbf{k} = k^{m-1} dk d\sigma_m$ , where  $k = |\mathbf{k}|$  and  $d\sigma_m$  is the surface measure such that  $\int_{(m-1)} d\sigma_m = 2\pi^{m/2} \Gamma(m/2)$ . The functions  $n$  and  $\tilde{n}$  satisfy Parseval's formula

$$E_T \equiv \int_{(m)} |\tilde{n}|^2 d\mathbf{k} = (2\pi)^m \int_{(m)} |n(\mathbf{x})|^2 d\mathbf{x} \quad (19)$$

where  $|\tilde{n}|^2$  is the PSD. The variation of  $|\tilde{n}|^2$  with  $k$  as  $k \rightarrow \infty$  is called the asymptotic spectral function.

Gelfand et al. [1966] show that if the boundary  $\partial D$  of a pc cloud of density  $F_0$  is a convex surface (i.e., at each point on  $\partial D$  the product of the principal radii of curvature is not equal to 0) and if  $\partial D$  is centrally symmetric about the origin (e.g., like an ellipsoid), then the asymptotic spectrum is

$$\tilde{n}(\mathbf{k}) = 2F_0(2\pi)^{(m-1)/2} (\rho_1 \rho_2 \dots \rho_{m-1})^{1/2} k^{-(m-1)/2} \cos[k\tilde{a} - \frac{1}{2}(m+1)\pi] \{1 + O(k^{-1/2})\} \quad (20)$$

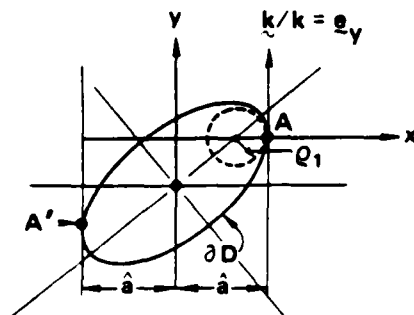


Fig. 4. Parameters used to define the asymptotic spectrum of a convex centrally symmetric piecewise-constant two-dimensional cloud.

where  $k = |k|$ ,  $2a$  is the "diameter" of  $D$  perpendicular to the direction  $k/k$  (which is associated with the index  $m$ ) and  $\rho_1, \rho_2, \dots, \rho_{m-1}$  are the principal radii of curvature at points  $A$  and  $A'$  on  $\partial D$ , namely, the extremal points. Figure 4 illustrates these quantities for an ellipse ( $m = 2$ ) where  $k/k = e_y$ , and the curvatures  $\kappa = 1/\rho_1$  at  $A$  and  $A'$  are the same, since the ellipse is centrally symmetric. The two-dimensional PSD obtained from (20) is

$$E(k) \equiv |\tilde{n}(k)|^2 = 8\pi F_0^2 \rho_1 k^{-3} \cos^2 \left[ k\tilde{a} - \frac{3\pi}{4} \right] \{1 + O(k^{-1/2})\} \quad (21)$$

We define the one-dimensional PSD as

$$E_1(k) \equiv k^{m-1} \int_{(m-1)} d\sigma_m E(k) = k^{m-1} \int_{(m-1)} d\sigma_m |\tilde{n}|^2 \quad (22)$$

and thus  $E_T = \int_{-\infty}^{\infty} dk E_1(k)$ . From (22) with (20) the dominant term in  $E_1(k)$  is

$$E_1(k) = \left[ 2^{m+2} \pi^{(3m/2)-1} / \Gamma\left(\frac{m}{2}\right) \right] F_0^2 k^{-2} (\rho_1 \rho_2 \dots \rho_{m-1}) \cos^2 \left[ k\tilde{a} - \frac{1}{2}(m+1)\pi \right] + \dots \quad (23)$$

That is, the asymptotic dependence of the envelope of the one-dimensional PSD of an  $m$ -dimensional pc cloud with convex boundaries is proportional to  $k^{-2}$  and the quantity in brackets is  $(4\pi)^2$  or  $(4\pi)^3$  for  $m = 2$  or  $3$ , respectively. The amplitude of the asymptotic spectrum is inversely proportional to the product of the curvatures ( $1/\rho_i$ ) at the extremal points.

### 3.2. Projections and Scans

In realistic nonlinear dynamical processes the PSD of the scan,  $|f|^2$ , may often be represented by a power law function  $k^{-p}$  in the region  $k_{j-1} < k < k_j$ , where  $p_j$  is called the spectral index in region  $j$ . (This excludes the dissipative range where some exponential variation with  $k$  usually occurs.) These representations are often obtained by least squares fitting procedures which suppress oscillatory effects. For example, the envelope of maxima of piecewise polynomials can be fitted by  $|f_0|^2 \propto k^{-p}$  when length scales are sufficiently "separated," as discussed by Mul Brandon *et al.* [1984].

In section 2 we have shown that in a small region near the tangent ray (e.g., the origin  $x = x_0$ ), we can represent the projection function as  $f(x) \propto (x - x_0)^r$ . The simplest projection function for a pc convex cloud whose extremal rays lie between  $x_0$  and  $x_1$  can be represented by

$$f(x) = (x - x_0)^r (x_1 - x)^{\tau_1} h(x)$$

where  $h(x)$  is analytic and  $>0$  in  $x_0 < x < x_1$ , and  $r$  and  $\tau_1$  are  $>0$ . The asymptotic spectrum will depend on which exponent is most singular, that is, smaller. For simplicity, we consider one such point and examine the Fourier transform

$$\hat{f}(k) = \int_0^\infty e^{-ikx} x^r h(x) dx = k^{-(r+1)} \int_0^\infty e^{-i\xi \tilde{x}} h(\xi/k) d\xi \quad (24)$$

where  $kx = \xi$ . If one applies the method of stationary phase [Olver, 1974] for  $k \gg 1$ , we can show that the integral is  $O(1)$  and, thus, the asymptotic spectral index of the envelope of  $\hat{f}$  is  $-(r+1)$ , and of  $|\hat{f}|^2$  is  $-2(r+1)$ . (The method of stationary phase is discussed in section 11 of Olver [1974], and theorems for finite-range Fourier transforms are given in section 13. The Riemann-Lebesgue lemma, discussed in section 4.2, plays an important role in obtaining these asymptotic results.)

For example, the symmetric trapezoid of base  $2a$ , upper horizontal  $2b$ , and altitude  $1$  (or area  $= b + a$ ) has the asymptotic envelope spectrum  $|\hat{f}_0|^2 = [4/(b-a)]^2 k^{-4}$  or  $p = 4$  and  $\tau = 1$ . Furthermore, the figure with rounded edges

$$\begin{aligned} f(x) &= 1 & |x| \leq a \\ f(x) &= [1 - (|x| - a)^2/\Delta^2]^\tau & a < |x| \leq b \\ f(x) &= 0 & |x| > b \end{aligned} \quad (25)$$

where  $\Delta = (b-a)$ ,  $\tau > -1$ , has an envelope function with  $p = 2(\tau+1)$ , as discussed by Mul Brandon *et al.* [1984]. For the elliptical arc,  $\tau = 1/2$ ,  $p = 3$  which is intermediate between 2 and 4, the values for the top hat and the trapezoid, respectively. For  $-1 < \tau < 0$ ,  $f(x)$  is singular at  $x = b$  and  $0 < p < 2$  (that is, shallower than a top hat). For  $0 < \tau < 1$ ,  $f(x)$  is singular at  $x = b$ , and for  $\tau \geq 1$ ,  $f(x)$  is continuous and vanishes at  $x = b$ . From these results, we see the known result for piecewise polynomials and powers of piecewise polynomials: the asymptotic spectral index is determined by the nature of the singularities of  $\partial^q f / \partial x^q$ , where these piecewise polynomials intersect. For example, if the first derivative has a singular slope somewhere, then

$$2 < p < 4$$

if  $\partial f / \partial x$  does not have a singular slope but  $\partial^2 f / \partial x^2$  does have a singularity, then

$$4 < p < 6$$

etc.

We conclude with the results: For clouds contained in a finite domain and having an intersection intensity with a polynomial flank of degree  $\mu$  (see equation (11)), the magnitude of the asymptotic spectral index of the envelope of  $|f|^2$  (the PSD of the projection function  $f(x)$ ) is

$$p = 2(1 + \tau + \mu)$$

For pc densities ( $\mu = 0$ ) the asymptotic spectral behavior is given in the last column of Table 1. Note the well-known result: a  $k^{-3}$  dependence occurs when the curvature at the extremal ray is finite ( $\tau = 1/2$ ). Furthermore, the asymptotic spectral index varies continuously from slightly greater than 2 ( $\tau = 0$ ) to indefinitely large values depending upon the nature of the cusp. Note, a linear flank on a convex curve gives an asymptotic PSD  $\propto k^{-5}$ .

### 4. APPLICATION OF RESULTS

We apply the results of the present and previous [Mul Brandon *et al.*, 1984] papers to data from the recent "PLACES"

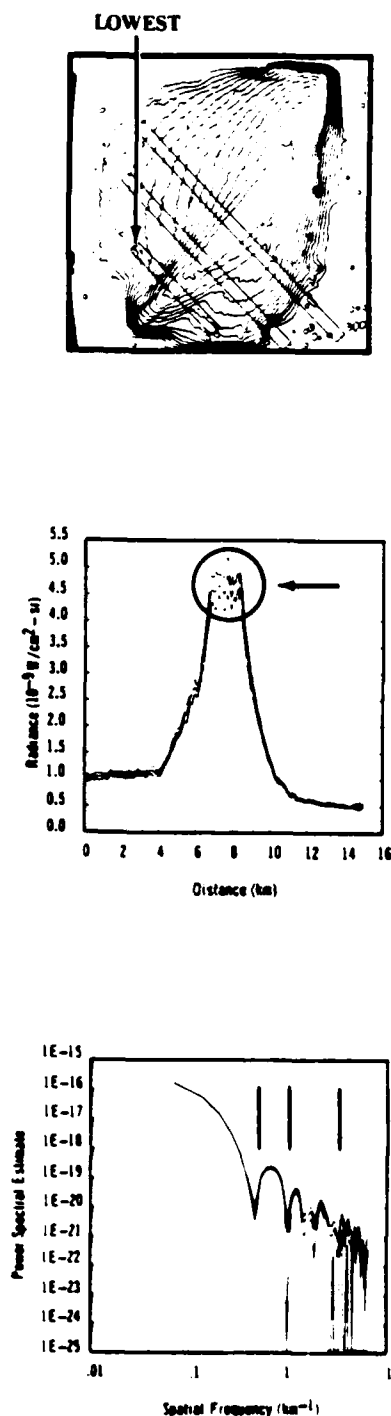


Fig. 5. Event IRIS. PSD contains 100 modes. [Simons *et al.*, 1984, Figures 65 and 66] (a) Smoothed radiance contours and three rectangular regions in which scans are made. (b) Fitted radiance profiles with upper and lower standard deviation corresponding to the lowest scanning rectangle. Small-scale oscillations in arrowed circle indicate striations. (These are resolved with about 10 points per period.) (c) PSD of information in Figure 5b after using a Kaiser-Bessel window.

high-altitude barium cloud releases. Simons *et al.* [1984] present a comprehensive and thoroughly scrutinized collection of optical emission data for events GAIL and IRIS. It represents the state of technology in the early 1980s and will provide guidance for future studies and recommendations. We will

present heuristic arguments to show that the PSD results for these events (release altitude  $\sim 185$  km) are valid for the lowest one quarter of the total available modes. Thus the interesting data are in the transitional  $k$  region and therefore difficult to interpret, as discussed below. Furthermore, the spectra given do not yield any information about the asymptotic spectral index. Such exponents arise in a Rufenach fit to a nonlinear dynamical process, namely,

$$\text{PSD}(K) = [1 + (KL_0)^2]^{-p/2}$$

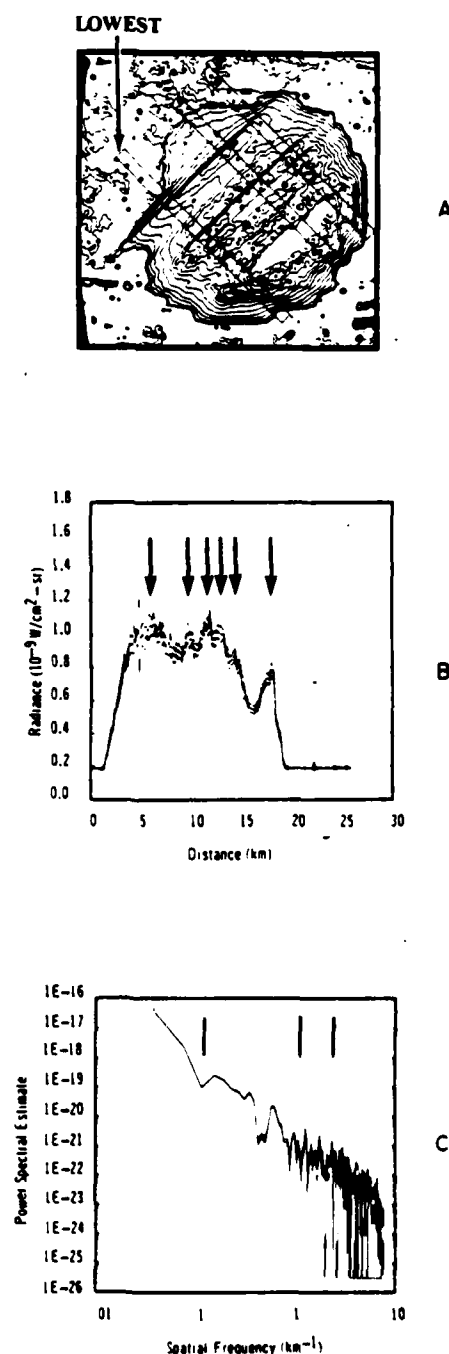


Fig. 6. Event GAIL. PSD contains 200 modes [Simons *et al.*, 1984, Figures 50 and 51]. Caption for Figures 6a, 6b, and 6c is the same as in Figure 5

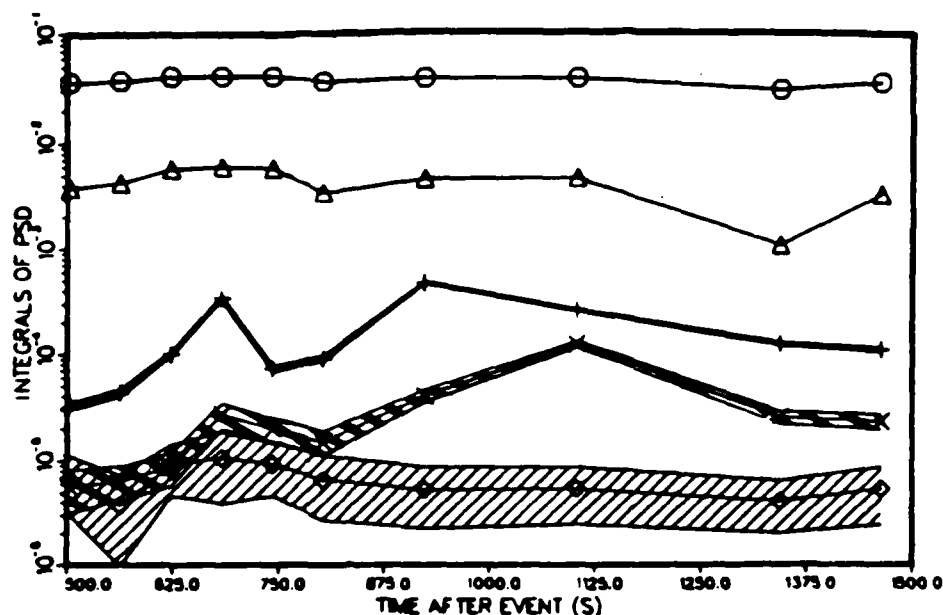


Fig. 7. Evolution of spectral power sums for event GAIL from site D-3 [Simons *et al.*, 1984, Figure 112]. Circles, total power (dc to noise). Triangles,  $0.055 < K < 0.17 \text{ km}^{-1}$ . Plus signs,  $0.17 < K < 0.55 \text{ km}^{-1}$ . Crosses,  $0.55 < K < 1.7 \text{ km}^{-1}$ . Diamonds,  $1.7 < K < 5.5 \text{ km}^{-1}$ .

where  $(KL_0) \gg 1$ . In this section,  $K = \text{radians/kilometer} = (\text{length})^{-1}$  (i.e., not the conventional  $2\pi/(\text{length})$ ) and  $L_0$  is the outer scale length.

Optical emission data for events GAIL and IRIS are given in several forms: non-field-aligned photographs of optical emission; smoothed optical radiance contours (e.g., Figures 5a and 6a); several scans of the contours in a direction transverse to the local magnetic field (e.g., Figures 5b and 6b); and a PSD of a "windowed" scan (e.g., Figures 5c and 6c). In addition, the spectral data are summarized by presenting evolutions of spectral power sums as shown in Figure 7 for event GAIL [Simons *et al.*, 1984, Figure 112]. The figure caption describes the bands of  $K$  in which the power is summed.

Details of the data reduction process have been given by Lebeda [1983] and were amplified by L. Testerman (EG&G, personal communication, 1984). For example, the smoothed radiance contours were obtained from a  $256 \times 256$  digitization of a selected portion of a 35-mm frame. To obtain a fitted

radiance profile with upper and lower standard deviations (three curves), 21 scans were made in each rectangular region and averaged. Each profile was then digitized with 250–500 points (125–250 modes) depending on the resolution of the small-scale oscillations which are attributed to striations. (See the balloon in Figure 5c.) Usually 7 to 10 points per oscillation were considered reasonable. Also, the scan data were "windowed," or made periodic, by multiplying the original data by a prescribed function (a Kaiser-Bessel window). This avoids discontinuities and large contributions to the high-wave-number spectrum at the expense of introducing a frequency domain "smoothing" by convolution [Harris, 1978]. However, this plays a negligible role in the transitional  $K$  region because the half-power width of the window is 0.02 km and the filter power function falls off deeply (to  $10^{-5}$  at 0.1 km). Because of film grain noise and other reasons, the authors generally recommend rejecting data for  $K > 1.7 \text{ km}^{-1}$ , which corresponds to including 1/4 of the available modes

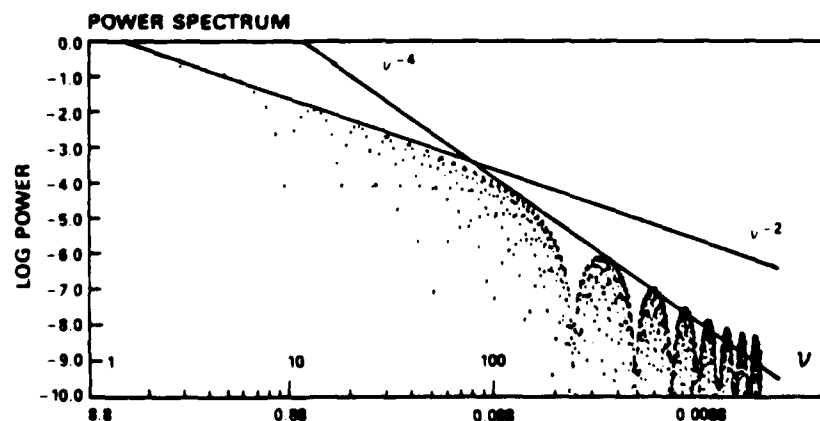


Fig. 8. Plot of  $\log_{10} 1/f^2$  versus  $\log_{10} v$  ( $v$  is mode number from 1 to 2048) for a trapezoid of unit area,  $a = 224$ , and  $b = 240$ . The lower scale of the abscissa is defined so that the first null occurs at 1, the second at 1.2, the third at 1.3, etc. The number at the origin is the ratio of the mesh size to the mean size of the figure ( $8.8 = 2048/232$ ). Straight lines with slopes of  $-2$  and  $-4$  have been drawn through the relevant second maxima.

TABLE 2. Parameters Associated With Spectral Data From Events IRIS and GAIL [Simons *et al.*, 1984]

Event	Figure (This Paper)	Figure [Simons <i>et al.</i> , 1984]	Lowest Mode, km <sup>-1</sup> <i>L</i>	First Null, km <sup>-1</sup> <i>I</i>	Second Null, km <sup>-1</sup> <i>2</i>	Highest Mode, km <sup>-1</sup> <i>H</i>	<i>H</i> / <i>4</i>	Highest Lowest	Estimated Spectral Index
IRIS	5c	66	0.066	0.48	1.0	6.6	1.65	100	...
GAIL	6c	51	0.038	0.12	0.46	7.6	1.9	200	2.5

(*H/4* in Table 2). Table 2 presents pertinent information obtained from the PSD figures of Simons *et al.* [1984].

Before we discuss the information in the PSD, we comment on the morphology of the scans. In Figures 5b and 6b we see a localized region of high radiance with steep flanks, usually of different slope. The steepest gradient is an indication of the steepest gradient within a striation. Three curves are present, a mean of the averages of the 21 scans and a ( $\pm 1$ ) standard deviation. The curves show high-frequency irregular oscillations which are attributed to striations. In addition, Figure 6b shows a set of clumps or irregular peaks of intensity. The "period" in Figures 5b and 6b is about 0.4 km or  $K \approx 2.5$  km<sup>-1</sup>, which is beyond the region *H/4* where the data are considered of good quality.

An approximation consistent with at least the first null of the data is obtained by fitting a symmetrical trapezoid to these scans. We use this only for its convenience and because we have studied the inverse problem of determining spectral indices of numerical data obtained from such figures. For example, the symmetric trapezoid with altitude *A*, upper and lower parallel sides 2*a* and 2*b*, respectively, has a PSD

$$|f|^2 = [A(b + a)(\sin z_+ \sin z_-)/(z_+ z_-)]^2$$

where

$$z_{\pm} = \pi K(b \pm a)$$

Thus if the scales are well separated,  $(b + a)/(b - a) \gg 1$ , then we have a  $K^{-2}$  envelope for  $K_{11} \equiv 2/(b + a) < K < K_{21} \equiv 2/(b - a)$  and a  $K^{-4}$  envelope for  $K > K_{21}$ . Figure 8 shows  $|f|^2$  for  $a = 224$ ,  $b = 240$ ,  $A = 1$  which has well-separated scales. Note that if the scales are not well separated, or

$$1 < (b + a)/(b - a) < 5$$

then the transitional region  $(b + a)^{-1} < 2K < (b - a)^{-1}$  may be complicated, but the index of the envelope changes from 2 to 4. If the flanks were not linear but were replaced by the functions in (25), then the appropriate spectral envelope index would go to  $2(\tau + 1)$  instead of 4.

The first two nulls in Figure 5c are consistent with fitting the scan in Figure 5b with a symmetrical trapezoid whose upper and lower parallel sides are 2*a* = 1.8 km and 2*b* = 6.2 km. The first null of the discrete Fourier transform,  $K_{11} = 2/(b + a) = 0.5/\text{km}$  is associated with the first transition. The first null of the second transition is at  $K_{21} = 2/(b - a) = 1.1/\text{km}$  and is consistent with the second null in Figure 5c. Hence we conclude that the scales are not well separated. The only information available concerning the asymptotic spectrum lies in the range  $K > 1.5/\text{km}$ . This region represents a composite of effects resulting from the  $K^{-4}$  trapezoidal spectrum, the small-scale structures on the trapezoid (their widths and separations), film grain noise, and aliasing. One cannot see the spectral index of individual striations.

Event GAIL had steeper gradients as shown in Figure 6b. One could approximate this scan function by an unsymmetric

trapezoid with an upper parallel side 2*a* = 14.5 km and a base composed of a right segment  $b_1 = 8.45$  km and a left segment  $b_2 = 9.45$  km. The lack of symmetry causes an interference of the nulls and they are not as clean as in the discussion of Figure 5b. However, it is reasonable to approximate the unsymmetric trapezoid with a symmetric one with 2*b* = 17.9 km. Then  $K_{11} = 0.123/\text{km}$  and  $K_{21} = 1.18/\text{km}$ , a good separation of scales. Thus between 0.123 km and 1.18 km the spectral index is changing from 2 to 4. For  $K > 1.2/\text{km}$  a comment similar to that given in the above paragraph applies.

A global gestalt is obtained by examining the evolution of spectral power sums as shown in Figure 7 for GAIL [Simons *et al.*, 1984, Figure 112]. The highest curve is the total power and the lowest curve the power in the region  $1.7 < K < 5.5$  km<sup>-1</sup>. The latter is too noisy and is omitted. The interesting nonlinear effects are the initial rise of curves  $(+ - + - +)$  ( $0.17 < K < 0.55$  km<sup>-1</sup>) and  $(x - x - x)$  ( $0.55 < K < 1.7$  km<sup>-1</sup>) and the subsequent decrease. The decreases around  $t = 700$  s are difficult to interpret and could possibly result from bifurcations or splittings, a process which would be manifest as a growth of some higher-wave-number band that is not resolved by the present data. These two *K* regions are in the transitional region of the trapezoid, and therefore the precise meaning of the variations is difficult to interpret.

As discussed by Mul Brandon *et al.* [1984], to make a good estimate of the asymptotic spectral index from a scan with no noise, one needs at least: 256 modes for a scan function with two *k* space regions and 10,000 modes for a scan function with three well-separated *k* space regions.

Thus we conclude the data presented by Simons *et al.* [1984] do not allow one to deduce the spectral index of striations. There exists a need for better instruments to obtain data on the growth, evolution, and decay of striations. Also, it is obvious that a single unqualified spectral index can be misleading.

## 5. CONCLUSIONS

In this report we have considered the relationship between a radiating cloud and the power spectral density of a scan of its photographic image. To allow us to focus on the uncertainties associated with geometrical aspects, we have assumed idealized conditions, namely, optically thin clouds, no parallax effects, and no distortion due to camera, lenses, and film grain. We have considered clouds with pc and power law radiating intensities. We have not attempted to correlate this radiant intensity with the ion density.

For pc clouds, where the one-dimensional asymptotic spectrum of the power is proportional to  $k^{-2}$ , we have shown that the asymptotic spectrum of the scan depends upon the character of the contour at the point where it is tangent to the extremal ray. If the contour at  $(x_0, y_0)$  behaves like  $y - y_0 = (x - x_0)^t$ , then the asymptotic spectral envelope of the PSD of the scan varies as  $k^{-2(t+1)}$ . In addition, if the radiating intensity in a cloud flank varies with a power law  $\mu$ , then the asymptotic spectral envelope of the scan's PSD varies as  $k^{-2(1+t+\mu)}$ .

We have applied these considerations to data from PLACES events IRIS and GAIL. We have shown that the good data of highest  $K$  are associated with a transitional region and are not associated with the asymptotic spectral index that arises in nonlinear turbulent or wave-steepening dynamical processes.

*Acknowledgments.* We are grateful to L. Testerman and C. Lebeda of EG&G for help in interpreting the data analysis procedures of Simons et al. [1984] and Lebeda [1983]. We also acknowledge constructive remarks by W. Chesnut and C. Rino of SRI and one of the referees. This work was supported by the Defense Nuclear Agency.

#### REFERENCES

- Deans, S. R., *The Radon Transform and Some of Its Applications*, John Wiley, New York, 1983.
- Gelfand, I. M., M. I. Graev, and N. Ya. Vilenkin, *Generalized Functions*, vol. 5, *Integral Geometry and Representation Theory*, Academic, New York, 1966.
- Harris, F. J., On the use of windows for harmonic analysis with the discrete Fourier transform, *Proc. IEEE*, 66, 51-83, 1978.
- Lebeda, C., Procedures for analysis of photographic records of striated clouds, *Rep. EGG 10282-5008*, EG&G, Los Alamos, N. M., June 1983.
- Lebeda, C., S. P. Gary, and M. B. Pongratz, Density spectra as a function of altitude in an ionospheric barium release, *Geophys. Res. Lett.*, 11, 591-594, 1984.
- Mulbrandon, M., N. J. Zabusky, and E. Hyman, Estimating spectral indices from transforms of discrete representations of density functions, *NRL Memo. Rep. 5298*, Nav. Res. Lab., Washington, D. C., 1984.
- Olver, F. W. J., *Asymptotics and Special Functions*, Academic, New York, 1974.
- Shepp, L. A., and J. B. Kruskal, Computerized tomography: The new medical x-ray technology, *Am. Math. Mon.*, 85, 420-439, June-July 1978.
- Simons, D. J., C. F. Lebeda, M. B. Pongratz, T. J. Fitzgerald, and R. R. Dupre, Evolution of structure in the PLACES barium clouds, *Rep. LA 9648-MS*, Los Alamos Natl. Lab., Los Alamos, N. M., Feb. 1984.
- E. Hyman, Science Applications, Inc., 1710 Goodridge Drive, McLean, VA 22102.
- M. Mulbrandon, Geophysical and Plasma Dynamics Branch, Plasma Physics Division, Naval Research Laboratory, Washington, DC 20375-5000.
- N. J. Zabusky, Fluid Sciences, Inc., 5871 Aylesboro Avenue, Pittsburgh, PA 15217.

(Received April 26, 1985;  
revised December 2, 1985;  
accepted January 8, 1986.)



**APPENDIX R**

**A Striation Model and Spectral Characteristics of  
Optical-IR Emission from HANE**

**E. Hyman  
Science Applications International Corporation**

**M. Mulbrandon  
Naval Research Laboratory**

**N.J. Zabusky  
Fluid Sciences, Inc.**



# **A Striation Model and Spectral Characteristics of Optical-IR Emission from HANE**

**E. HYMAN,\* M. MULBRANDON AND N. J. ZABUSKY†**

*Geophysical and Plasma Dynamics Branch  
Plasma Physics Division*

*\*Science Applications International Corp.  
McLean, VA 22102*

*†Fluid Sciences, Inc.  
Pittsburgh, PA 15261*

April 30, 1985

This research was sponsored by the Defense Nuclear Agency under Subtask S99QMSRI,  
work unit 00018 and work unit title "Infrared Structure."



**NAVAL RESEARCH LABORATORY  
Washington, D.C.**

Approved for public release; distribution unlimited.



SECURITY CLASSIFICATION OF THIS PAGE

REPORT DOCUMENTATION PAGE				
1a REPORT SECURITY CLASSIFICATION <b>UNCLASSIFIED</b>			1b RESTRICTIVE MARKINGS	
2a SECURITY CLASSIFICATION AUTHORITY			3 DISTRIBUTION AVAILABILITY OF REPORT  Approved for public release; distribution unlimited.	
2b DECLASSIFICATION/DOWNGRADING SCHEDULE				
4 PERFORMING ORGANIZATION REPORT NUMBER(S)  NRL Memorandum Report 5568			5 MONITORING ORGANIZATION REPORT NUMBER(S)	
6a NAME OF PERFORMING ORGANIZATION  Naval Research Laboratory	6b OFFICE SYMBOL (If applicable)  Code 4780	7a NAME OF MONITORING ORGANIZATION		
6c ADDRESS (City, State, and ZIP Code)  Washington, DC 20375-5000		7b ADDRESS (City, State, and ZIP Code)		
8a NAME OF FUNDING/SPONSORING ORGANIZATION  Defense Nuclear Agency	8b OFFICE SYMBOL (If applicable)  RAAE	9 PROCUREMENT INSTRUMENT IDENTIFICATION NUMBER		
8c ADDRESS (City, State, and ZIP Code)  Washington, DC 20305		10 SOURCE OF FUNDING NUMBERS		
		PROGRAM ELEMENT NO  62715H	PROJECT NO	TASK NO  DN080-323
11 TITLE (Include Security Classification)  A Striation Model and Spectral Characteristics of Optical-IR Emission from HANE				
12 PERSONAL AUTHOR(S) Hyman, E.* Mulbrandon, M. and Zabusky, N.J.†				
13a TYPE OF REPORT Interim	13b TIME COVERED FROM 10/84 TO 10/85	14 DATE OF REPORT (Year, Month, Day) 1985 April 30	15 PAGE COUNT 51	
16 SUPPLEMENTARY NOTATION *Science Applications International Corp., McLean, VA 22102 †Fluid Sciences, Inc., Pittsburgh, PA 15261 (Continues)				
17 COSATI CODES			18 SUBJECT TERMS (Continue on reverse if necessary and identify by block number)	
FIELD	GROUP	SUB-GROUP	Striation model HANE Checkmate	
			Power spectral density IR emission Ionospheric plasma striation	
19 ABSTRACT (Continue on reverse if necessary and identify by block number)  An analytical model of a late-time high-altitude ionospheric striation is presented which incorporates characteristic shapes from recent NRL simulations. The model striation is nonaxisymmetric with a long diffuse tail (frontside), a compact core, and a steep backside. It contains six adjustable parameters to vary the shape and edge properties for sensitivity studies. We vary model parameters and investigate the power spectral density (PSD) as observed from different view angles. We compare results of the model with Chesnut's PSD obtained from photographs of Checkmate. A good fit is obtained with our model without any size distribution of striations.				
20 DISTRIBUTION AVAILABILITY OF ABSTRACT <input checked="" type="checkbox"/> UNCLASSIFIED/UNLIMITED <input type="checkbox"/> SAME AS RPT <input type="checkbox"/> DTIC USERS			21 ABSTRACT SECURITY CLASSIFICATION <b>UNCLASSIFIED</b>	
22a NAME OF RESPONSIBLE INDIVIDUAL J. D. Huba			22b TELEPHONE (Include Area Code) (202) 767-3630	22c OFFICE SYMBOL Code 4780

DD FORM 1473, 94 MAR

93 APR edition may be used until exhausted  
All other editions are obsolete

SECURITY CLASSIFICATION OF THIS PAGE

**16. SUPPLEMENTARY NOTATION (Continued)**

This research was sponsored by the Defense Nuclear Agency under Subtask S99QMSRI, work unit 00018 and work unit title "Infrared Structure."

## CONTENTS

1. INTRODUCTION .....	1
2. A STRIATION MODEL .....	3
3. SCANS .....	6
4. SPECTRAL PROPERTIES .....	8
5. COMPARISON WITH CHECKMATE DATA .....	15
6. SUMMARY .....	19
ACKNOWLEDGMENTS .....	20
REFERENCES .....	37





# A STRIATION MODEL AND SPECTRAL CHARACTERISTICS OF OPTICAL-IR EMISSION FROM HANE

## I. INTRODUCTION

This is the third in a series of papers which use a deterministic approach to estimate spatial spectral indices of optical data from sensors which view structured plasma clouds in the high altitude disturbed atmosphere. In the first paper<sup>(1)</sup> we considered idealized functions of one variable which could represent scans. We established the relationship between continuity properties of these "profile" or "scan" functions, or their derivatives, and the spectral index of their Fourier transforms. We provided numerical examples using simple symmetric geometric figures to illustrate the errors that arise in estimating spectral indices. We estimated the minimum number of modes required to provide a specified accuracy in the asymptotic spectral index. For example to recover the -4 index of the power spectral density of a trapezoid (a profile with three possible space regions) requires about 10,000 modes.

In a second paper<sup>(2)</sup> we related the asymptotic spectral index of a radiating cloud to that of a scan of the cloud. The theory is applicable to convex piecewise constant clouds

Manuscript approved March 5, 1985.

and to more realistic clouds which have polynomial flanks. We used the results of these papers to analyze optical scans from the PLACES experiment. We found that the data has insufficient resolution to determine an asymptotic spectral index associated with nonlinear dynamical (steepening) processes.

In this paper we describe an asymmetrical 6-parameter analytical model suggested by recent computer simulations to represent an isolated late-time high altitude striation from a high altitude nuclear event (HANE). Our early spectral studies<sup>(3)</sup> made direct use of numerical simulation results of barium releases<sup>(4)</sup>. However, the inadequate resolution of sharp gradients and the uncertainties concerning the small-scale physical processes led us to develop an analytical model. The model is easy to use in a sensitivity study and is consistent with available HANE and barium cloud data.

In Section 2 we describe a striation model and in Section 3 we introduce scans. In Section 4 we discuss its spectral properties as we vary parameters of the model and as we change the direction of observation. In Section 5 we examine Checkmate optical data and analyze it in terms of our analytical model. In Section 6 we summarize the results of this paper.

## 2. A STRIATION MODEL

The growth of striations in the late-time high altitude ionosphere is believed to be mediated by a gradient drift instability. When there is relative motion between a plasma and the background gas in a direction perpendicular to the earth's magnetic field, a steepening of plasma density occurs on the backside of the cloud (that is, the side opposite the direction in which the cloud is moving). In the plane perpendicular to the magnetic field, the cloud becomes elongated in the direction along the relative velocity vectors and narrows somewhat in the transverse direction (see Figure 1). The instability induces the formation of striations at the backside which can lead to one or more bifurcations of the cloud.

Recent theoretical and numerical investigations of Zalesak, et al, (5), (6) at NRL employ a new diffusivity model. They show that high conductivity clouds form a long lasting compact core even while the edges diffuse rapidly and, thus, bifurcations are suppressed and the result is a stable 'frozen' striation over extended times. In addition, new features are observed including a more extended diffuse frontside (tadpole tail) and a more rounded steep backside than with previous diffusivity models.

We cannot be certain that the striations that form in the nuclear environment will have the above characteristic shape. The simulations performed for the barium case are a result of the specific ionospheric parameters in that situation. In the nuclear case cloud conductivity is typically much higher, for example. Also, the ratio of plasma to neutral density could be much different. Until simulations with parameters more relevant to specific nuclear events are performed the validity of the model we are proposing will be open to question. Nevertheless, we believe it is instructive to study the properties of a non-axisymmetric striation to identify the observational consequences.

We have constructed a simple 6 parameter analytical model which incorporates these essential new properties. Figure 2 illustrates the model in a plane perpendicular to the magnetic field. Although our model is two dimensional, one could easily introduce a gradual Gaussian dependence along the magnetic field with a scale length large compared to dimensions in the plane.<sup>(3)</sup> Transverse to the field the equation representing the model is

$$\begin{aligned}
 P(r, \theta) &= P_{MAX} (1. - \exp(-A)); & r &\leq R_1(\theta) \\
 &= P_{MAX} \left[ \exp \left[ -A \left[ \frac{r - R_1(\theta)}{R_2(\theta) - R_1(\theta)} \right]^2 \right] - \exp(-A) \right]; & R_1(\theta) < r < R_2(\theta) \\
 &= 0.0 & ; & \quad r \geq R_2(\theta) \quad (1)
 \end{aligned}$$

where

$$R_i(\theta) = \rho_{Bi}\rho_{Ci}/[\rho_{Bi}^2\cos^2\theta + \rho_{Ci}^2\sin^2\theta]^{1/2}, \quad -\frac{\pi}{2} < \theta \leq \frac{\pi}{2}$$

$$R_i(\theta) = \rho_{Fi}\rho_{Ci}/[\rho_{Fi}^2\cos^2\theta + \rho_{Ci}^2\sin^2\theta]^{1/2}, \quad \frac{\pi}{2} < \theta \leq 3\frac{\pi}{2}$$

where  $\theta$  is measured from the backside direction and  $i = 1$  or  $2$ . Here  $R_1(\theta)$  bounds the constant density core and  $R_2(\theta)$  bounds the cloud. These boundaries are each parameterized by three constants:  $\rho_{Bi}$  and  $\rho_{Fi}$  are semiaxes of the ellipses in the backside and frontside directions, respectively, and  $\rho_{Ci}$  are the common semiaxes at  $\theta = \pm \pi/2$ . Where the two ellipses meet, their slopes, are identical. Between  $R_1(\theta)$  and  $R_2(\theta)$  the density falls off radially with a Gaussian dependence which is a function of angle and vanishes at  $R_2(\theta)$ . Note the slope of  $F$  is discontinuous at  $R_2(\theta)$ .

In the discussions below and in Section 3 we have chosen the following values to define the striation: tail length  $\rho_{F2} = 5.0$  km, transverse core radius  $\rho_{C1} = 0.5$  km, longitudinal core radii  $\rho_{B1} = 0.6$  km and  $\rho_{F1} = 0.3$  km. The edge sides  $\rho_{B2}-\rho_{B1}$  and  $\rho_{C2}-\rho_{C1}$  are varied for the different cases discussed. The parameter  $A$  was set equal to 3.

The spectral properties we will discuss are weakly dependent on the specific functional form chosen but are sensitive to the non-axisymmetric properties. The

particular functional form for the striation model given by Equation (1) has no fundamental significance.

We use it because with as few as 6 parameters it correctly reproduces the known properties of striations established in current simulation studies.

### 3. SCANS

Suppose we imagine a detector sufficiently distant from the striation that the rays emitted from the cloud can be assumed to be parallel. We will assume that the radiation is optically thin so that we just add the contributions of the emission from all points in the striation along a line perpendicular to the scan. We can scan across the striation from a variety of observational locations. If we define the observation angle as the angle the detector makes with the long axis of the striation, then a scan in the direction from the backside edge through the tail is  $0^\circ$  (Figure 2).

To perform numerically a scan on the model striation and obtain the profile from a given observational direction a rectangular  $256 \times 256$  grid is imposed. In Figure 2, imagine a grid coordinate system parallel and perpendicular to the long axis of the striation. For example, to do a  $0^\circ$  scan, the vertical spacing will be much smaller than the horizontal spacing so as to just enclose the striation, with little grid spacing outside. To do a  $45^\circ$  scan the striation is rotated (not the grid) so that interpolation to the grid

points is never necessary. To obtain a maximum resolution and assure that the grid just encloses the striation, only the grid spacings are changed as we change scan angle. We then simply sum grid values along an observational direction for each perpendicular grid point.

A scan at  $0^\circ$  results in a symmetric radiance profile, Figure 3, in which we have assumed that the radiative emission from each point of the striation is proportional to the electron density at that point. The units for the ordinate are arbitrary. The abscissa is in km. The ellipse parameters for this profile were chosen so that back and side Gaussian edges are 0.1 km.

If we scan from a location transverse,  $90^\circ$ , (see Figure 2) the resulting radiance profile, given in Figure 4, is highly skewed with the steep region corresponding to the steep gradients at the backside edge. The other side of this profile has a very gradual falloff due to the long diffuse tail. Note, that Figure 4 has a different abscissa scale than in Figure 3. In general, we wish to investigate the spectral properties of this model as a function of viewing angle, as we vary the size of the edges. This will be described in the following section.

#### 4. SPECTRAL PROPERTIES

As we have shown in reference 1, the spectral properties of the profile of an optical scan (for example, the spectral index of the asymptotic envelope) are influenced by the nature of the discontinuities in the profile function or its derivatives. The scale size of any characteristic segment of the profile is manifest in a corresponding region of the power spectral density (PSD) in an inverse sense, i.e. large sizes affect low mode numbers and small sizes affect high mode number regions of the PSD. Within each scale-size regime the most severe discontinuities lead to the slowest falloff with mode number and, hence, dominate the PSD if they represent a source strength comparable to other portions of the profile. In the following paragraphs we present typical PSD's obtained from our model showing the effect of angle variation with thin edges and with thicker edges and we show the differences obtained when the emission is proportional to the square of the electron density.

##### 4.1 Thin Edge Results

Figure 5 is a log-log plot of the PSD for scans of the model of Figure 2 at  $0^\circ$  (unconnected dots) and at  $90^\circ$  (solid line), in which we have taken the back and side edges to be 0.05 km. We have drawn in  $k^{-3}$  and  $k^{-4}$  lines to facilitate



analysis. The ordinate is normalized so that the area under the curve is unity. There are two scales on the abscissa. The lower scale is the wavelength ( $2\pi/k$ ) in km, where  $k = \pi\nu/L$ ,  $\nu$  is the mode number, and the region ranges from  $-L$  to  $L$ . (As stated previously, the scan consists of 256 non-zero values, and these are on a grid of 4096 points.) The upper scale gives the mode number,  $\nu$ , which ranges from 1 to 2048. The mode number in this figure is appropriate only for the  $0^\circ$  case which is for a scan over 1 km (whereas the  $90^\circ$  view consists of a scan over  $\sim 6$  km, and they both have the same number of grid points). Note, also the well defined maxima and minima in the  $0^\circ$  PSD, characteristic of a symmetric profile such as Figure 3 and absent in the  $90^\circ$  case.

The  $90^\circ$  PSD has a spectral index  $\sim -3$ . To understand this consider the profile of Figure 4. On a scale size  $\geq 1$  km the profile consists of two segments: first, the profile of the constant density, elliptically bounded core region and second, the profile of the tail region. The contribution of the first segment to the PSD falls off like  $k^{-3}$ , where  $k$  is proportional to the mode number,<sup>(1)</sup> and that of the second segment has a Gaussian falloff (the PSD of a Gaussian is a Gaussian). Since the radiative emission from the tail is comparable to that from the core region and the power in this region falls off much faster with  $k$ , the spectral character will be dominated by that of the core

region and there will be a  $k^{-3}$  falloff in the PSD. If we consider scale sizes 0.1 km we need to focus on the profile of the backside edge, which is Gaussian. Since this is the only profile segment on this scale size or smaller, the PSD will change from a  $k^{-3}$  to a Gaussian falloff at sufficiently large mode number. Because of insufficient resolution, the 90° curve never exhibits the anticipated large- $k$  Gaussian falloff.

For the 0° scan there appears to be an intermediate region with a  $k^{-3}$  envelope that matches the 90° PSD. This is a reflection of the constant density, elliptically bounded core region, as in the 90° profile. At higher  $k$ , corresponding to scale sizes  $\lesssim$  0.1 km, the PSD is determined by the steep flank edges of the striation. Here we have sufficient resolution to see the Gaussian falloff at these  $k$  values.

Note the profile of Figure 3 can be approximately fit alternatively with a single semicircle of radius 0.5 km or a trapezoid of parallel sides 0.2 and 1.06 km, respectively. The former gives a  $k^{-3}$  PSD in agreement with Figure 5 whereas the latter, in which the scales are not well-separated, gives a  $k^{-4}$  PSD. However, the latter gives nulls at 0.62 km, 0.43 km, 0.315 km, etc. in agreement with Figure 3 whereas the nulls of the former are not in good

agreement with Figure 3. Furthermore, the PSD obtained from the trapezoidal fit to Figure 3 is a very good fit to the model PSD up to the third minimum. This shows the difficulty of assessing a PSD from qualitative considerations.

#### 4.2 Thicker Edge Results

The example we have just used has one simplifying property, that we chose an edge size small compared to the core region. This provided a good separation of scales between the Gaussian edge region and the core region. Let us consider another example in which now the backside edge is 0.1 km and the flanks are 0.3 km. This is a realistic case, since simulations show that flanks have thicker edges than backsides.

To have a well-defined falloff before the Gaussian edge intrudes, the effective width of the profile must be substantially larger than the edge size. Now, if we scan from 0° the profile size is ~ 1. km and the Gaussian edge is 0.3 km which provides insufficient range in k space. Thus, we would expect the Gaussian falloff to intrude well into even the low modes of the spectrum and that there will not be any clearly defined  $k^{-4}$  or  $k^{-3}$  region. On the other hand, at 90° the effective profile size is > 1 km which

compares with an edge size of 0.1 km so that there is a reasonable separation of scales. We expect a well-defined  $k^{-3}$  region.

Figure 6 shows the PSD of this model, observed from an angle of  $10^\circ$ . The line drawn in is  $k^{-3}$  and clearly shows there is no  $k^{-3}$  (nor is there a  $k^{-4}$ ) region. Figure 7 shows the PSD as viewed from an angle of  $80^\circ$ . Again, the  $k^{-3}$  line is drawn in and shows a good fit down to -0.2 km, where the Gaussian falloff begins to dominate. In TABLE I we show the "apparent" spectral index for this model as a function of angle. (The apparent index was obtained by a least squares fit to the data for angles  $\geq 40^\circ$  from the first maximum to the wavelength of Gaussian onset (last column). At smaller angles this breaks down and the index is estimated.) At angles less than  $-40^\circ$  there is no  $k^{-3}$  region at all.

#### 4.3 Emission Proportional to the Square of the Electron Density

Consider, now, a striation with Gaussian edges of 0.1 km. We want to compare the profile for this striation at  $0^\circ$  with a striation of the same size and shape but in which the radiative emission is proportional to the square of the electron density ( $N^2$ ) rather than proportional to the electron density ( $N$ ) itself. This is what will be observed if the striations consist of a recombining plasma rather

than debris ions being excited by solar uv or earthshine ir. Figure 8 shows the 'squared' profile which can be compared with the 'unsquared' one, Figure 3. What we see is a considerably more peaked profile, more triangular in shape, and, therefore, even more likely to exhibit a spectrum with a substantial  $k^{-4}$  region.

Figures 9 and 10 are the spectra for N and  $N^2$  profiles respectively. Both have an overall  $k^{-4}$  falloff. In the  $N^2$  case the Gaussian falloff is not manifest at as low k-values as in the N case. This follows because the Gaussian 'width' in the squared case has been reduced by  $\sqrt{I}$  and, therefore, constitutes a smaller perturbation on the rest of the profile.

TABLE 1  
ANGULAR VARIATION IN CLOUD MODEL  
(EDGES VARYING BETWEEN 0.1 and 0.3 KM)

<u>Angle</u>	<u>Spectral Index</u> <u>From Least Squares Fit</u>	<u>Wavelength of</u> <u>Gaussian Onset</u>
0°	-6.	-
10°	-6.	-
20°	4.3	-
30°	3.6	-
40°	3.5	0.45 km
50°	3.4	0.35 km
60°	3.5	0.31 km
70°	3.3	0.26 km
80°	3.2	0.26 km
90°	3.2	0.23 km

## 5. COMPARISON WITH CHECKMATE DATA

The Checkmate burst occurred at a high altitude south of Johnston Island (JI). The debris rose and became aligned with the earth's magnetic field and striations were observed. Figure 11 shows the approximate geometrical set up. The plane of the figure is along a north-south geomagnetic longitude determined by the vector from JI to the burst point and the camera axis. Photographs were taken by Chesnut looking north at  $\sim 300$  sec and at other times. At 300 sec the camera elevation angle was such that the center of the photograph was approximately perpendicular to the magnetic field. The component of the ion-neutral relative velocity perpendicular to the field is, thus, aligned with the camera axis and our observation corresponds to a zero angle view (as defined in Figure 2). However, the photograph in Figure 12<sup>(7)</sup> has an angular extent  $\sim 30^\circ$ , and thus striations are observed at various angles. The striations at the extremities may be more than  $15^\circ$  off axis if one accounts for debris motion out of the plane.

In the photograph of Figure 12 we see striations clumped into two major groups associated with our view through the arms of the Checkmate "horseshoe". Figure 13 is the PSD, obtained by Chesnut from scan 2 in Figure 12,

and plotted on a semi-log scale. The PSD has been smoothed by performing an average for each data point of the 31 adjacent data points. Chesnut has shown that if one assumes striations with axial symmetry, e.g. lucite rods or Gaussian rods, it is necessary to assume a range of sizes to adequately fit the data. In the case of Gaussians, for example, it was necessary to include striation sizes ranging from -2 km down to -0.29 km to fit the data. We will show that by using a nonaxially symmetric model of a striation with parameter ratios suggested by numerical simulations it is possible to fit the data well without resorting to a size distribution.

First, we need to establish the shape parameters of our model striation from Checkmate data. We assume that the single striation discussed by Chesnut<sup>(7)</sup> is obtained from one of our striations observed at 10° with an aspect ratio ( $\rho_{F2}/\rho_{C1}$ ) = 10. The mean width of 1.4 km given by Chesnut leads us to choose  $\rho_{F2}$  = 7 km,  $\rho_{C1}$  = 0.7 km,  $\rho_{B1}$  = 0.7 km,  $\rho_{F1}$  = 0.42 km, and edge sizes = 0.1 km. (Edge sizes, in fact, influence higher k values than the Checkmate data can resolve and, thus, are unimportant.)

Next we place 100 of these identical striations at random in two groups associated with the horseshoe. The range covered is 150 km to match roughly the linear extent



in the photographic scan. The groups have a mean separation of 80 km and the left and right groups have half widths of 15 km and 30 km respectively. The random selection is from a normal distribution. To simulate the diverse view angles in the photograph, we rotate striations in various regions along the scan. The resulting profile is shown in Figure 14. Note in obtaining a scan, the minimum transverse dimension of a striation has been sampled by at least 35 points.

To simulate the PSD obtained by Chesnut, Figure 13, we average 8 nearest-neighbor k-space data points of the square of the transform. (This corresponds closely to Chesnut's k space averaging.) The PSD obtained from this is plotted in Figure 15. We have plotted the Chesnut data of Figure 13 on this plot for comparison and indicated the film grain noise level and the fit region on the plot. The region at smaller k than the fit region represents the low level unstructured background which we have not modeled. The exact position of peaks in the Chesnut data is related to the exact placement of striations which we did not attempt to match.

It is clear that in the very limited fit region there is a good match between our model striation PSD and the data. Of course, this shows only that if the data has insufficient spectral range there are at least two distinct

models that can fit it equally well. There are likely to be other combinations of striation parameters that could give equally good fits. In Figure 16 we plot the PSD of Figure 15 on a more standard log-log scale. We plot the  $k^{-4}$  line and indicate the fit region on this plot.

The essential conclusions are: (1) if we accept the results of recent computer simulations and infer from them the approximate shape and dimensions of high-altitude striations we can, at least, match the PSD's obtained from the measured Checkmate data. (2) The region of k-space accessible with the Checkmate data is too small to definitively establish what is the correct model.

## 6. SUMMARY

There is good reason to believe that substantial regions of the ionosphere following HANE events will be characterized by a highly structured plasma and that the structuring will persist for hours. Since defense detectors typically operate in the ir and are sensitive to the nature of the structuring it is important to be able to predict the spatial characteristics of ir emissions. In this paper we have presented a simple analytical model which embodies present knowledge of late-time high altitude striations, based on theory and the simulations being performed at NRL. Those properties still uncertain have been parameterized. Using this model we are able to predict the PSD characteristics that result from striations as a function of shape parameters, edge sizes, and the angle of observation. These results are preliminary. First, there is still imperfect knowledge of some aspects of the physics incorporated in the simulations. Second, simulations to date have been more appropriate to the barium release scenario and need to be repeated for parameters more relevant to the HANE case. Finally, HANE data in the ir is essentially non-existent and available visible data (photographic) has insufficient range to distinguish among alternative models.

We are able to show that available Checkmate data can be fit as well by our nonaxisymmetric striation model, without incorporating a distribution of striation sizes, as it has been by an axially symmetric model with a range of striation sizes. Although the data has insufficient range to distinguish between these models, there is every reason to believe that striations are not axially symmetric and to expect PSD's to be affected substantially by the relative location of detector and striations. We believe it is important that further simulations be performed, more directly relevant to specific HANE events, to determine with greater confidence the essential properties of ionospheric plasma striations. As more sensitive and higher resolution detectors are developed it will become possible and necessary to distinguish among alternative striation models.

#### ACKNOWLEDGMENTS

We thank J. Fedder of NRL and W. Chesnut of SRI for many helpful discussions. This work was supported by the Defense Nuclear Agency.

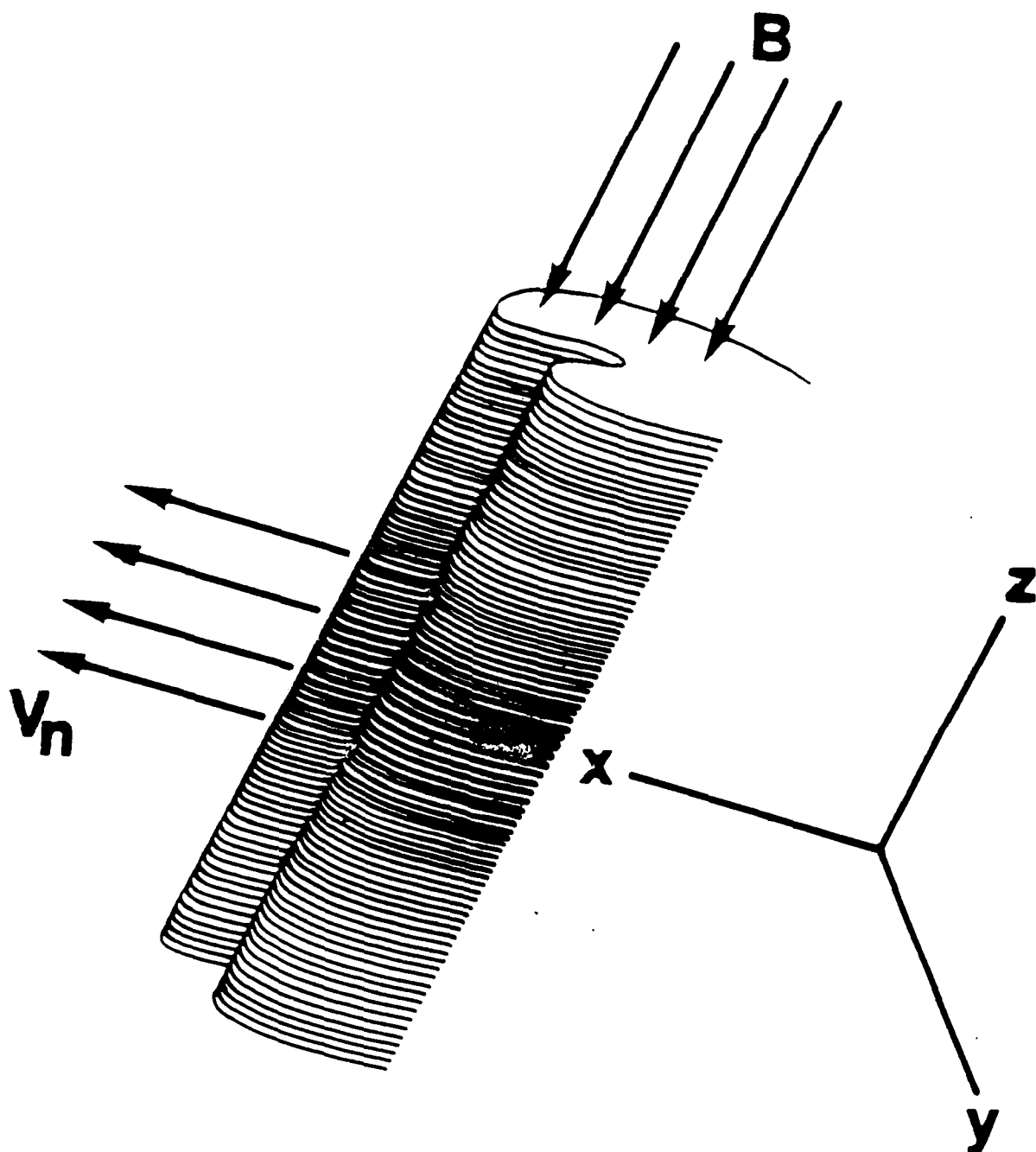


Figure 1 - Schematic view of ionospheric striation showing 'finger like' protuberances forming on the backside. The magnetic field direction,  $B$ , and neutral wind direction,  $V_n$ , are shown.

# ANALYTIC MODEL FOR HANE STRIATION

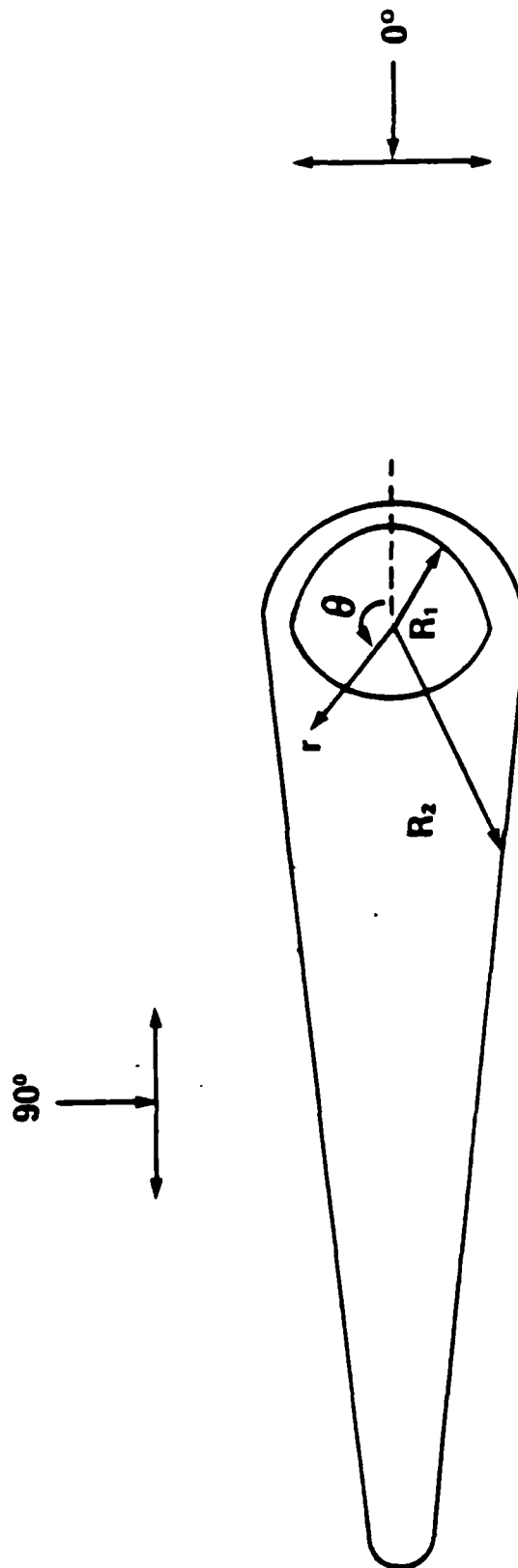


Figure 2 - Model striation in plane perpendicular to the magnetic field.  $R_1(\theta)$  and  $R_2(\theta)$  are given in Equation (1) of text. Scan directions of  $0^\circ$  and  $90^\circ$  are illustrated.

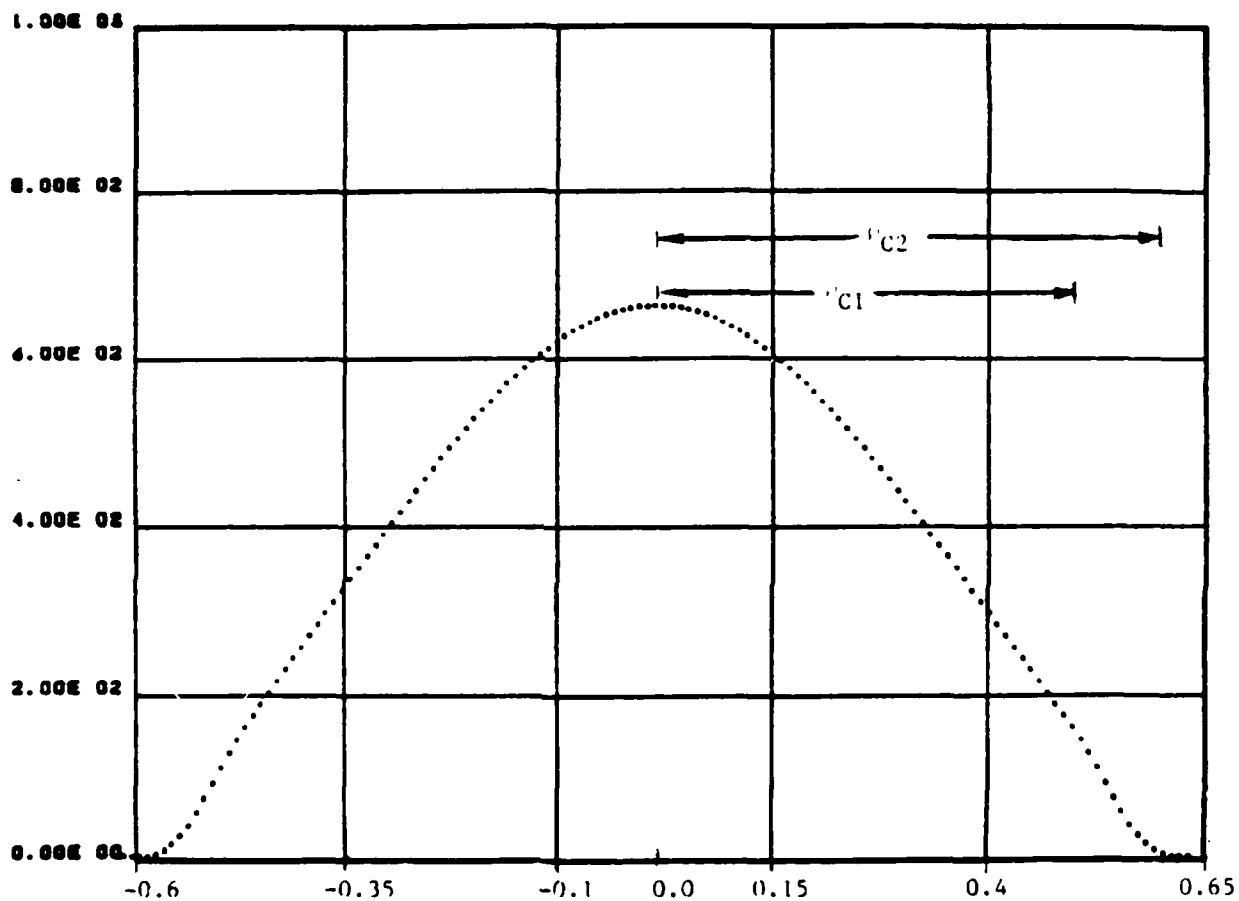


Figure 3 - Profile obtained from 0° scan of Figure 2.  $\rho_{P1} = 0.3$  km,  $\rho_{P2} = 5.0$  km,  $\rho_{B1} = 0.6$  km,  $\rho_{B2} = 0.7$  km,  $\rho_{C1} = 0.5$  km, and  $\rho_{C2} = 0.6$  km. The abscissa is in km and the ordinate is in arbitrary units.

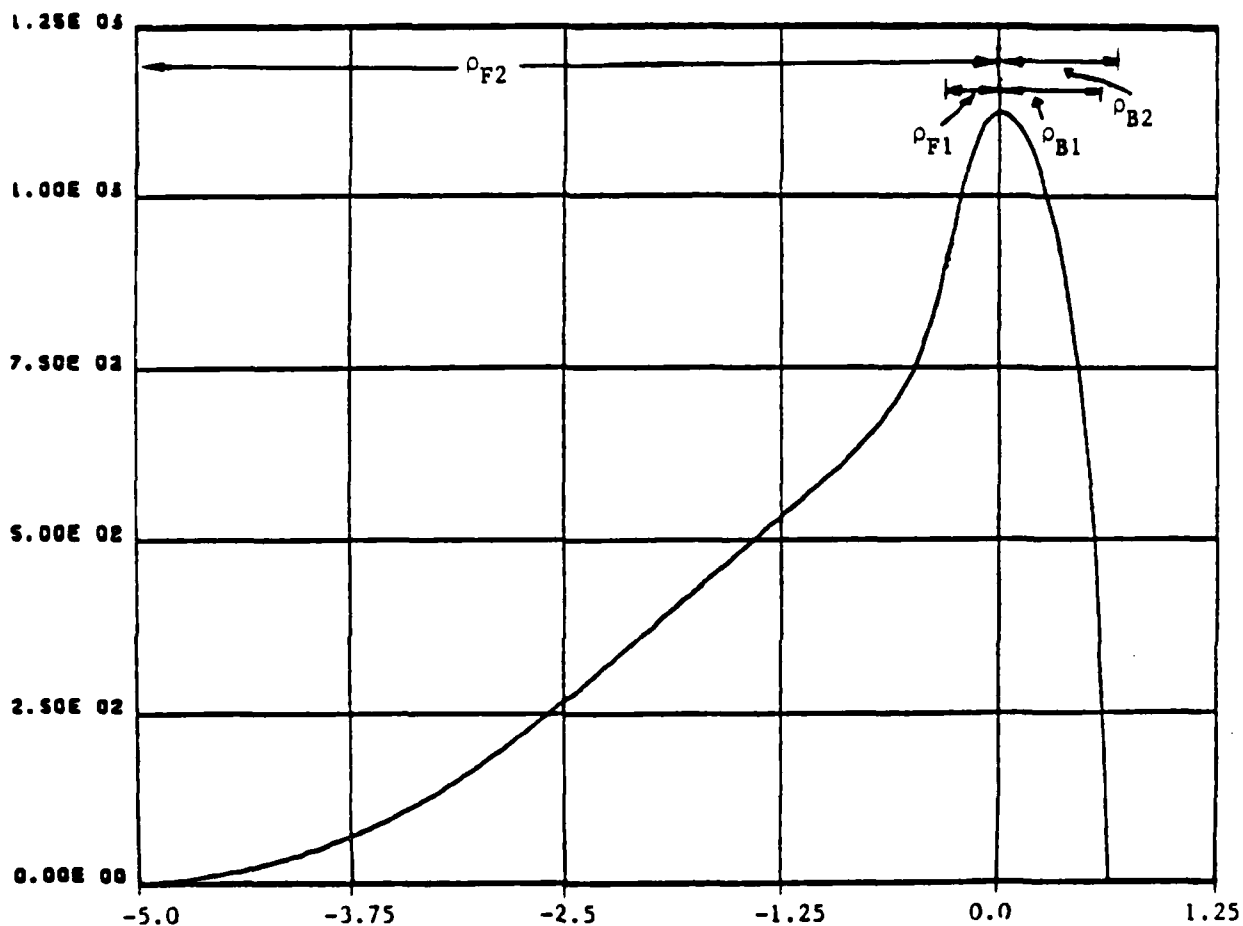


Figure 4 - Profile obtained from 90° scan of Figure 2. Same parameters as in Figure 3. Note the abscissa scale is 5 times that in Figure 3. The ordinate is in arbitrary units.



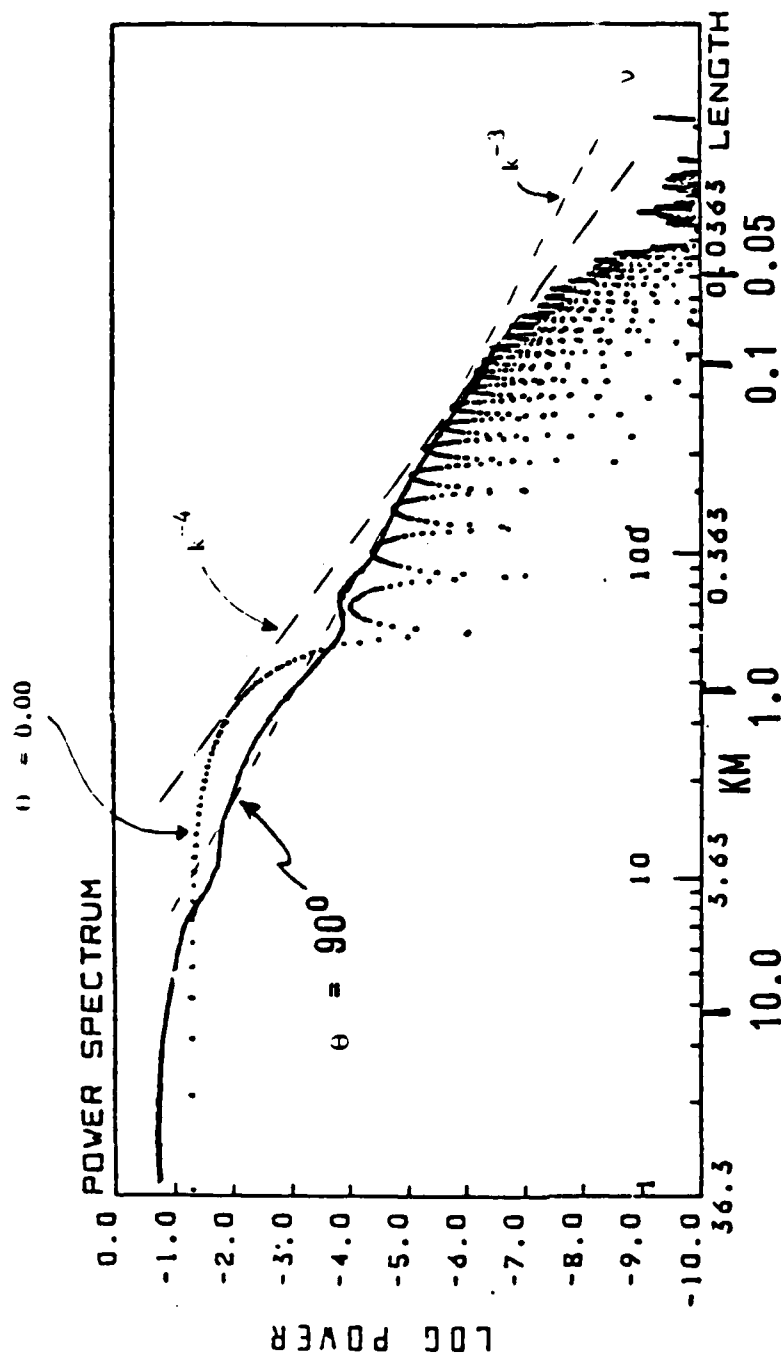


Figure 5 - PSD of 0° profile (unconnected dots) and 90° profile (solid line), with  $k^{-3}$  and  $k^{-4}$  lines added. Parameters are the same as in Figure 3 except  $\rho_{B2} = 0.65\text{km}$  and  $\rho_{C2} = 0.55\text{km}$ . Ordinate is normalized to give unit area. Lower abscissa scale is spatial wavelength. Upper abscissa scale is mode number (applies to 0° case only).

$\rho = 10.00$

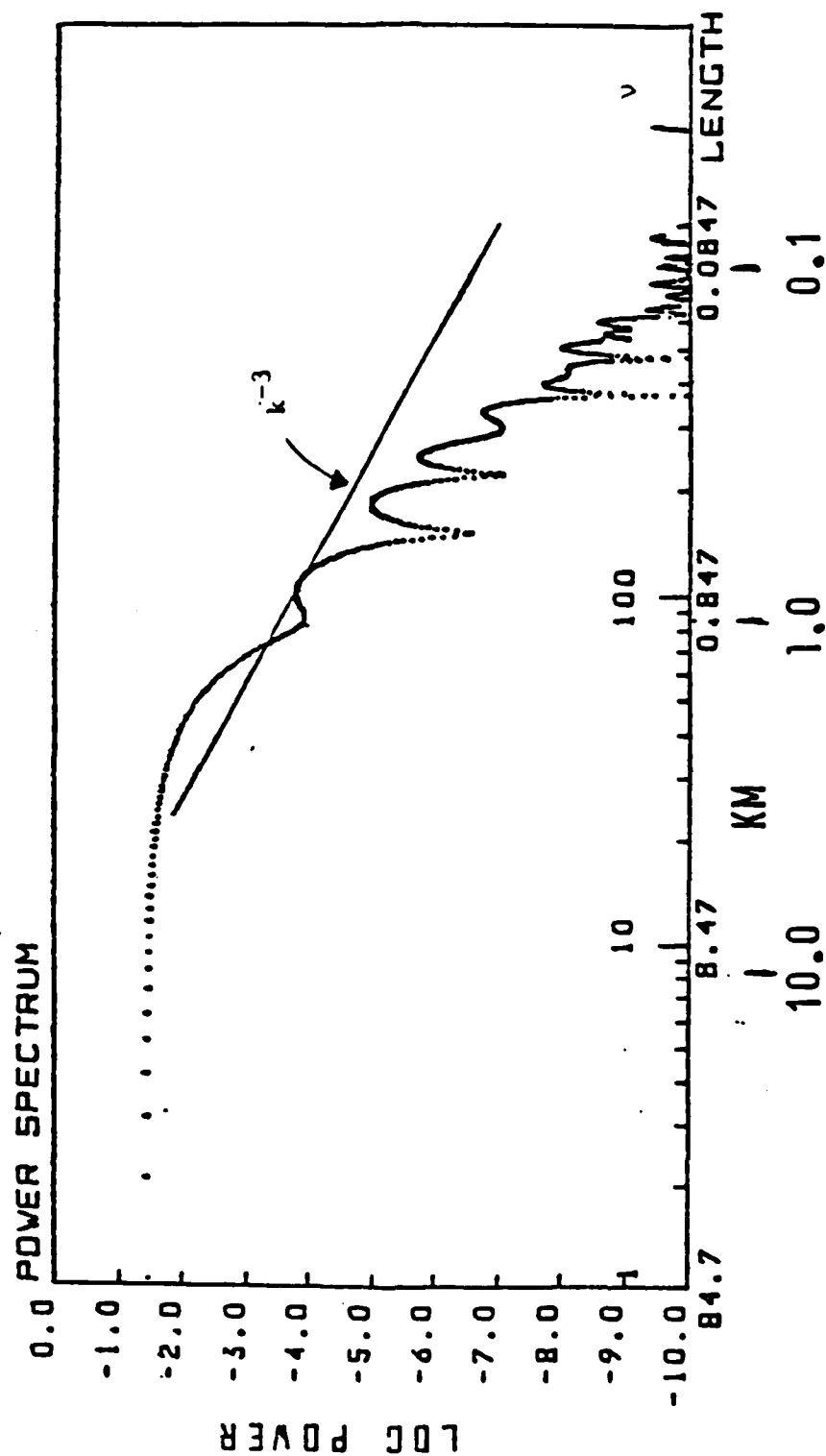


Figure 6 - PSD of 10° profile with  $k^{-3}$  line added. The parameters are the same as in Figure 3 except  $\rho C2 = 0.8\text{km}$ . Scales are defined as in Figure 5.

( ) = 80.00

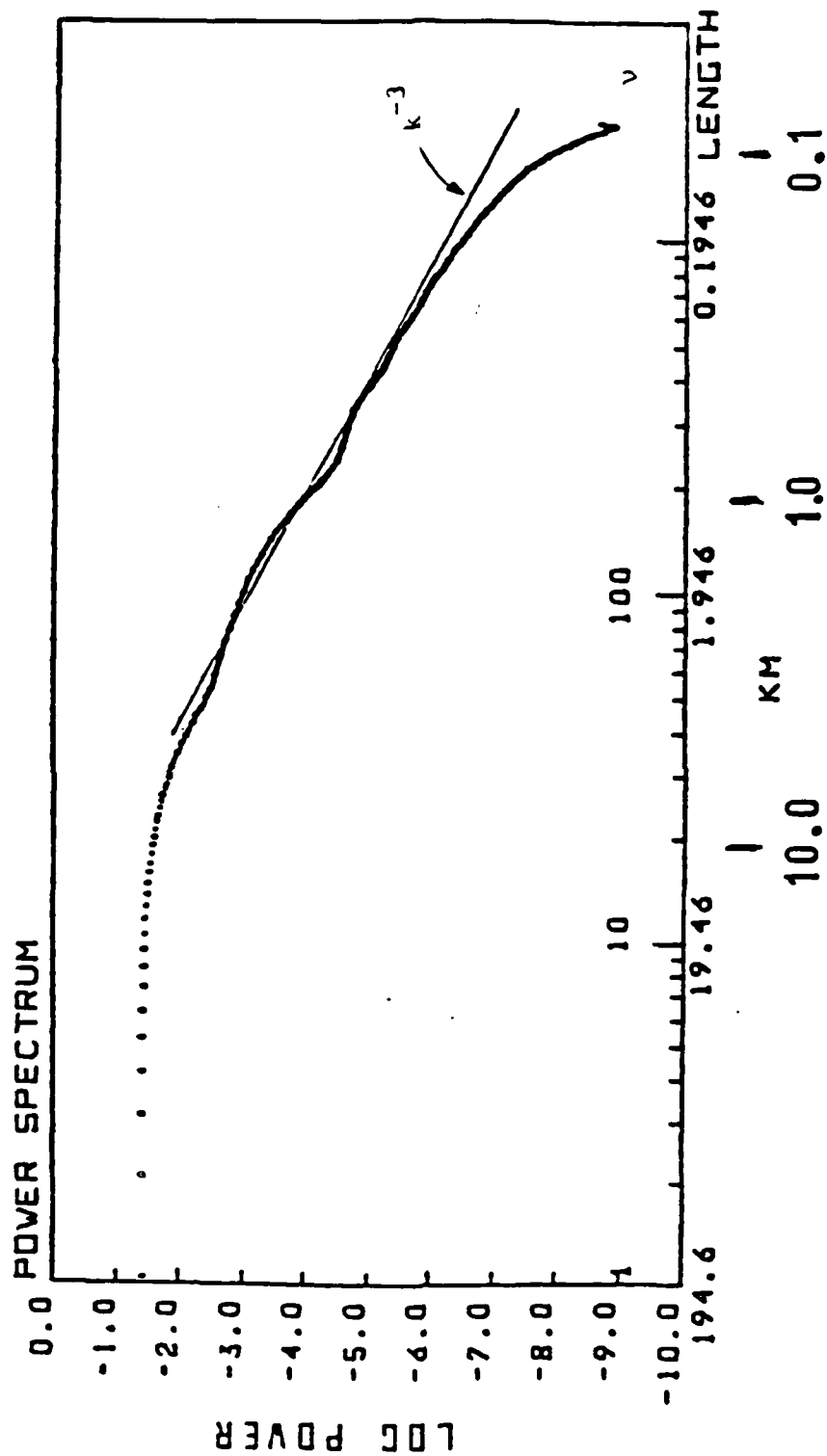


Figure 7 - PSD of 80° profile with  $k^{-3}$  line added. The parameters are the same as in Figure 6 and scales are defined in Figure 5.

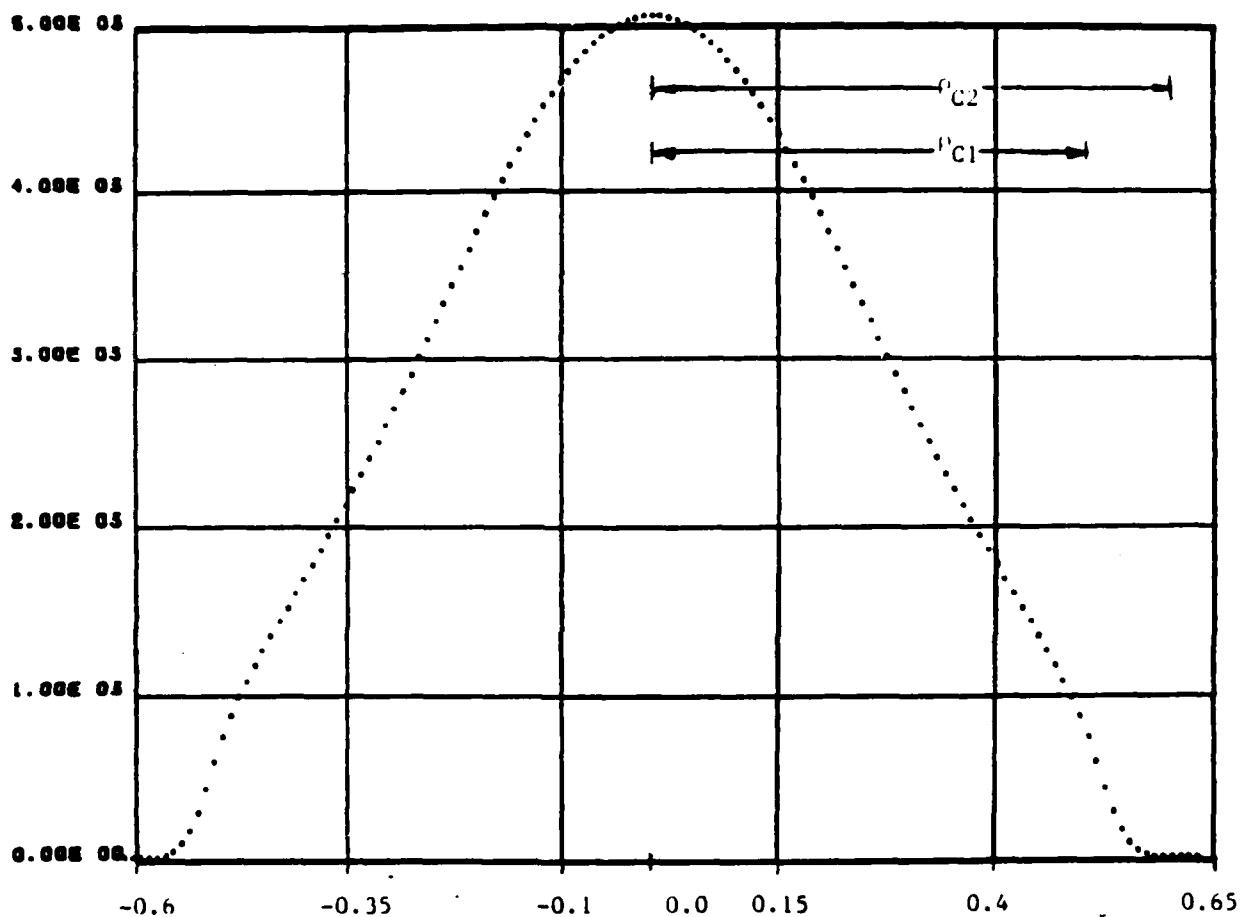


Figure 8 - Profile from 0° scan with parameters as in Figure 3, but radiative emission is assumed proportional to the square of the electron density ( $N^2$ ). The abscissa is in km and the ordinate is arbitrary.

$\theta = 0.00$

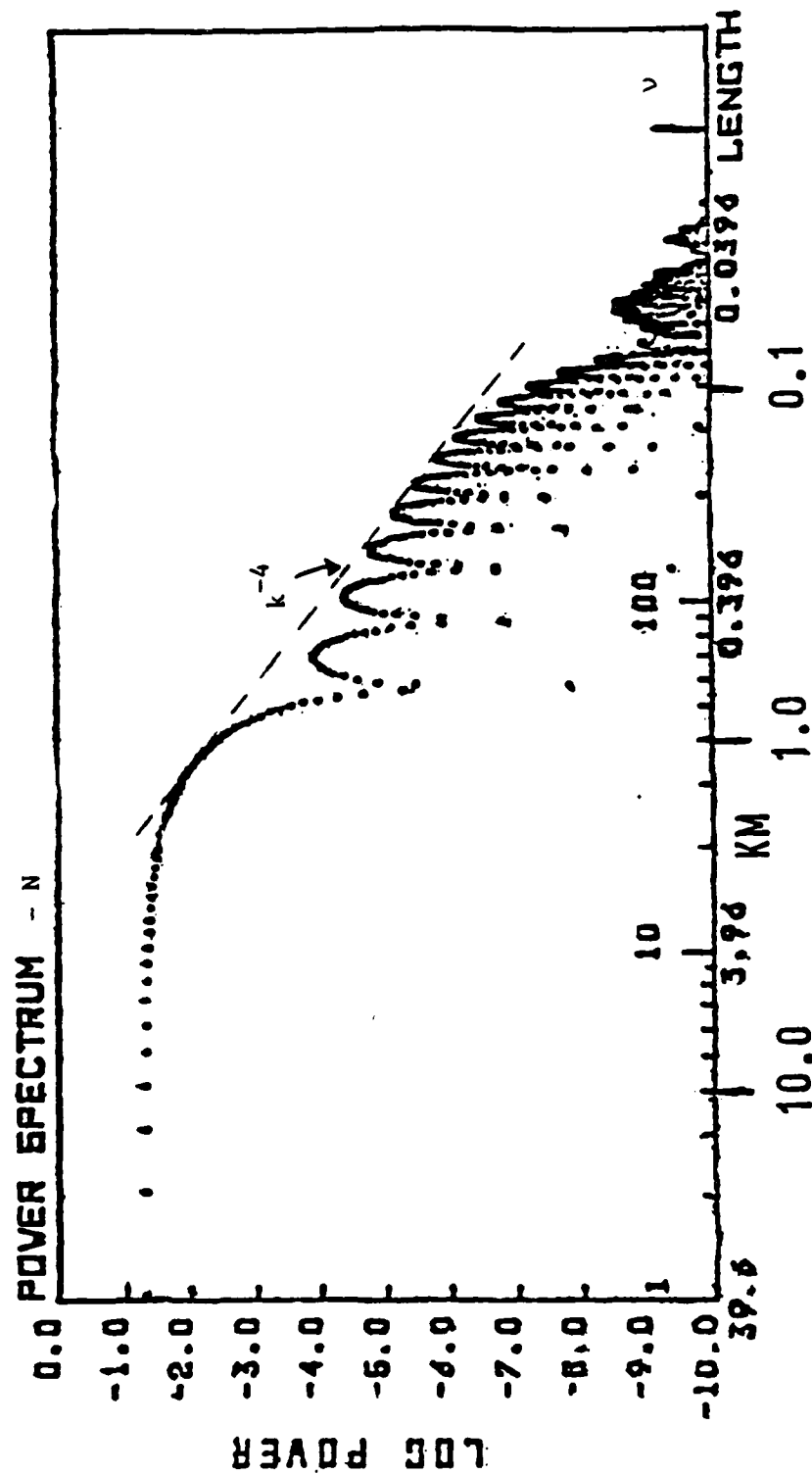


Figure 9 - PSD of 0° profile with parameters of Figure 3.

Scales as defined in Figure 5.

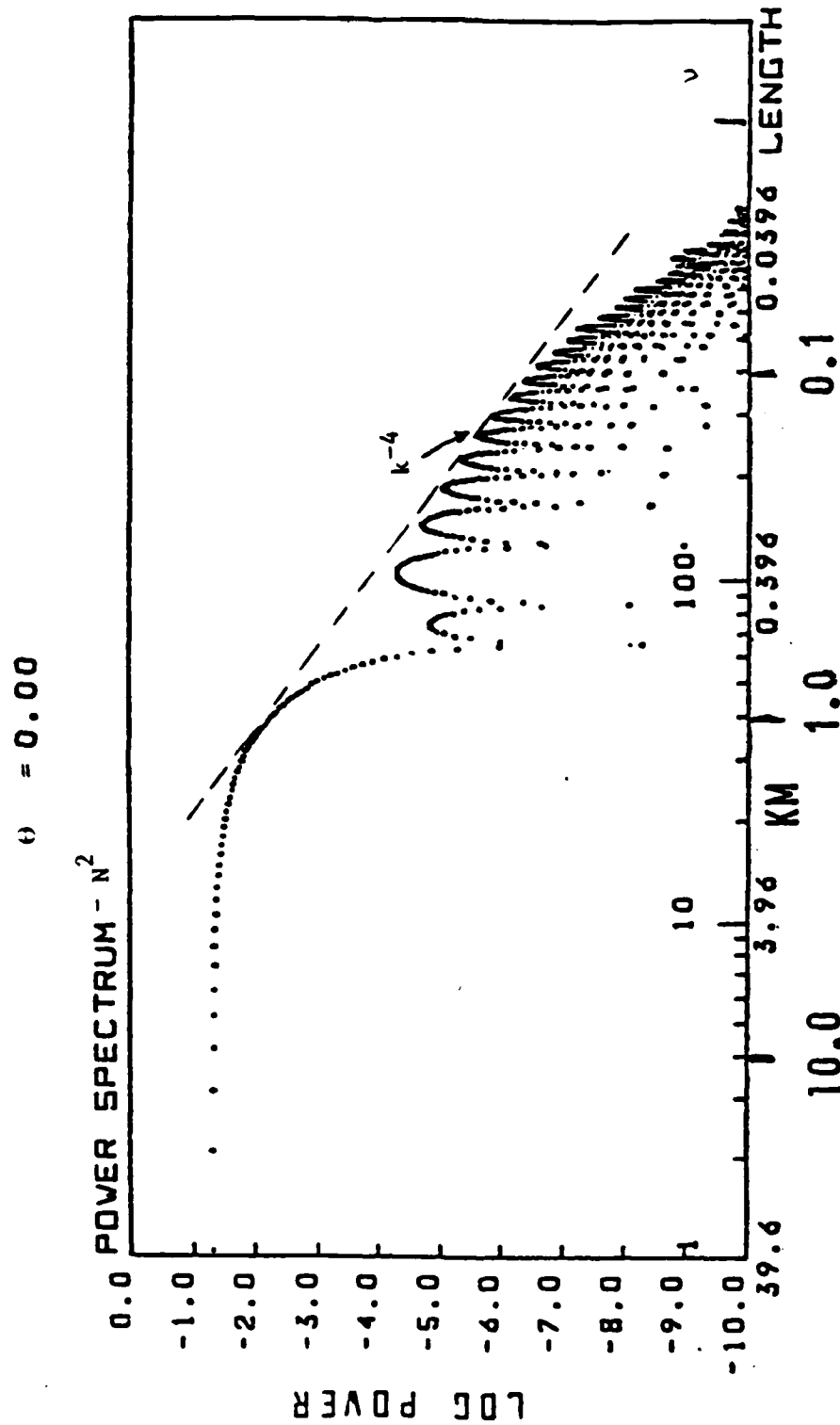


Figure 10- PSD of  $0^\circ$  profile of Figure 8. Parameters are the same as in Figure 3. Scales as defined in Figure 5.

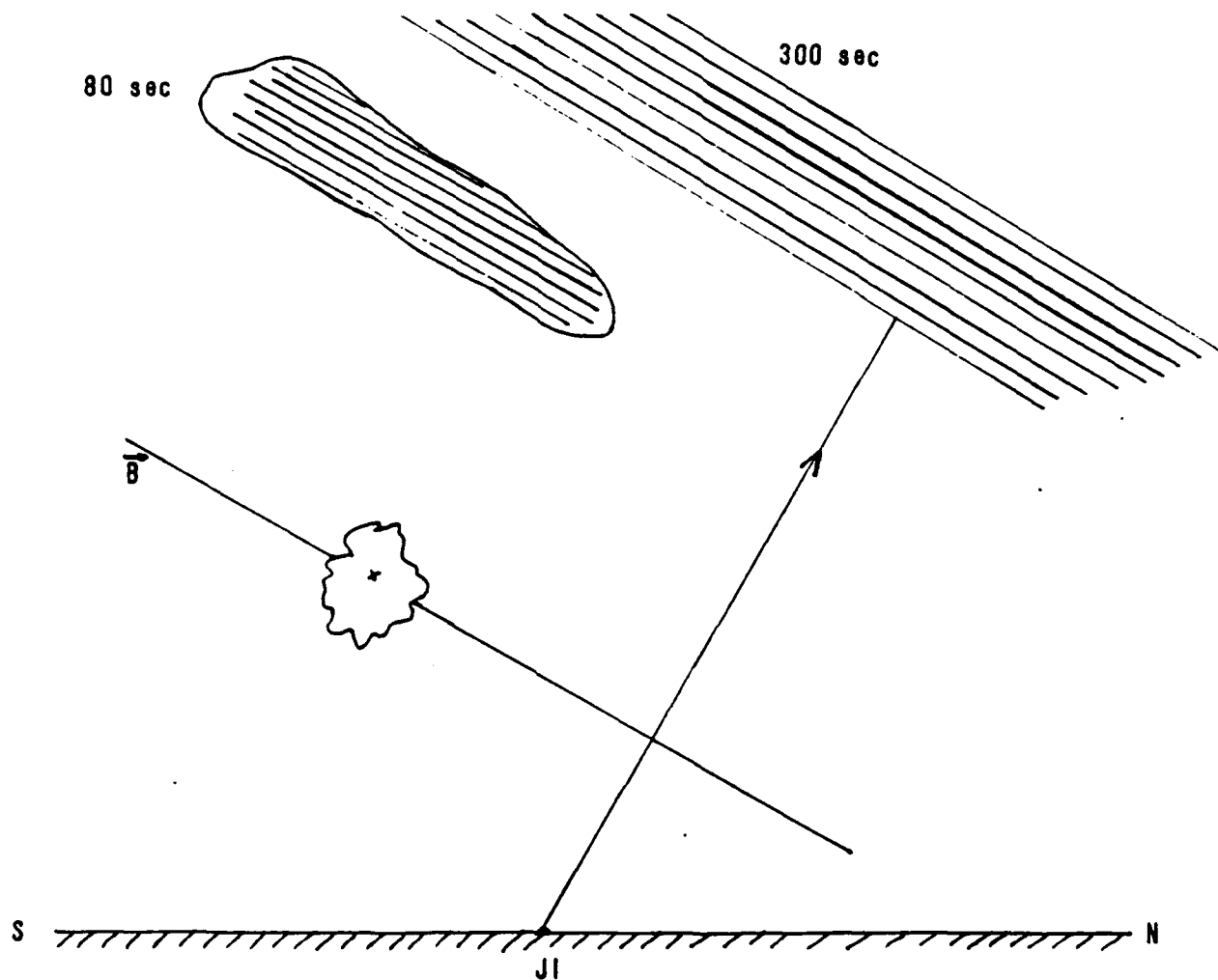


Figure 11- Schematic of Checkmate burst point and striations. Plane is north-south geomagnetic longitude including camera position at Johnston Island (JI), burst point, and camera axis. B is the ambient magnetic field direction.

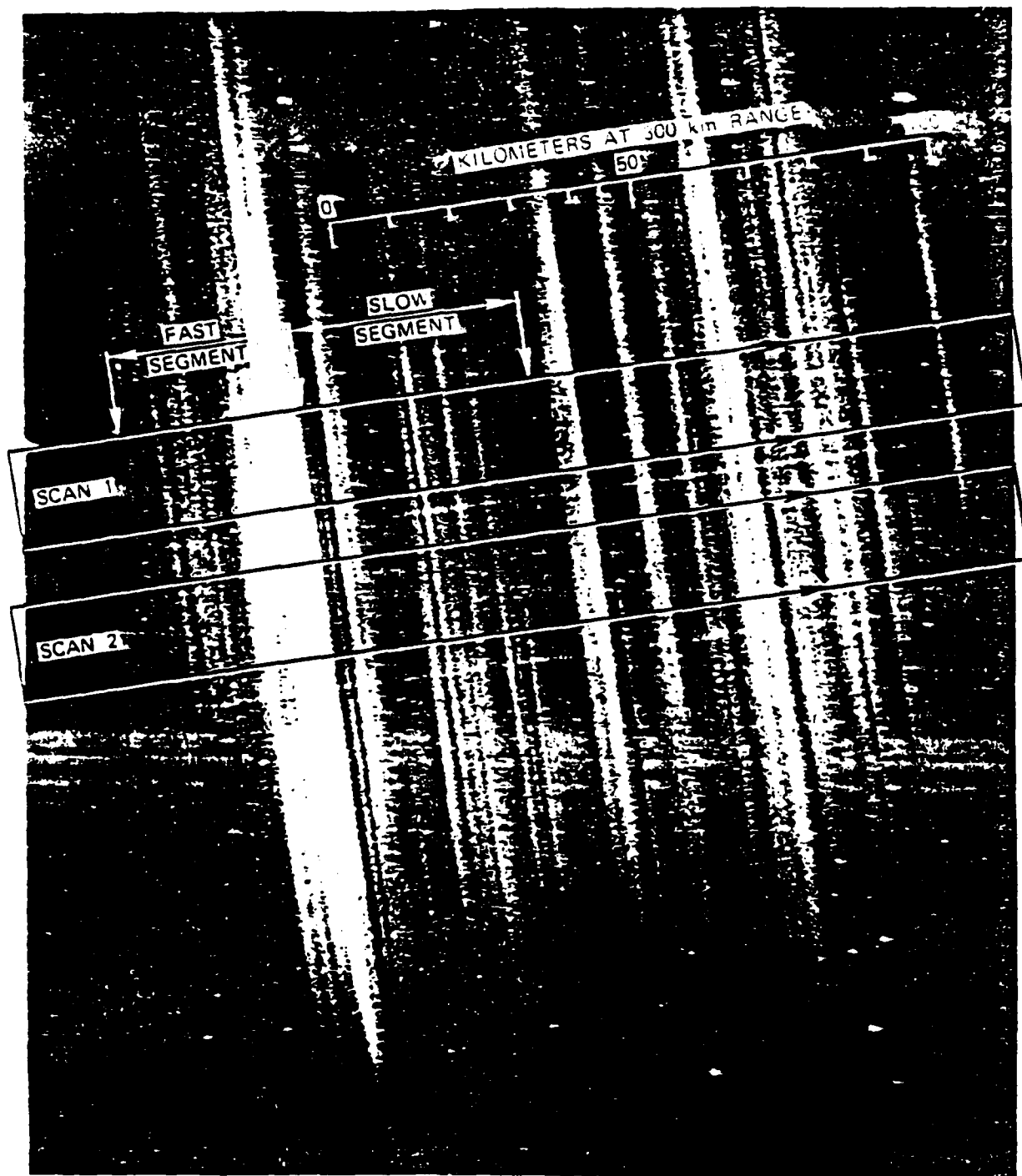


Figure 12- Photograph of Checkmate striations at 300 sec.  
(Reference 7, Figure 2). Various scans are  
illustrated.



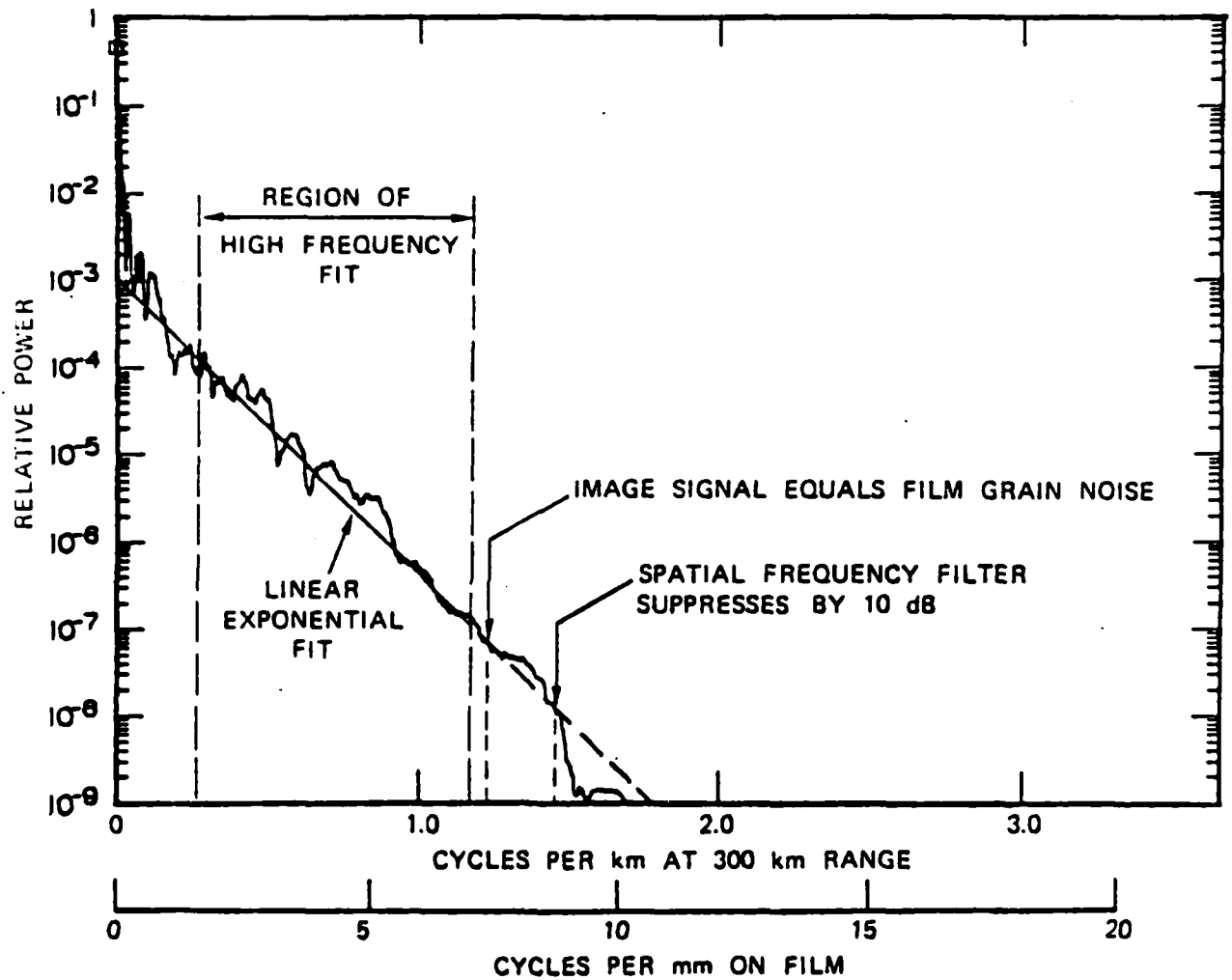


Figure 13- PSD of Scan 2 of Figure 12 (Reference 7, Figure 10) of Checkmate striations, plotted semi-log.

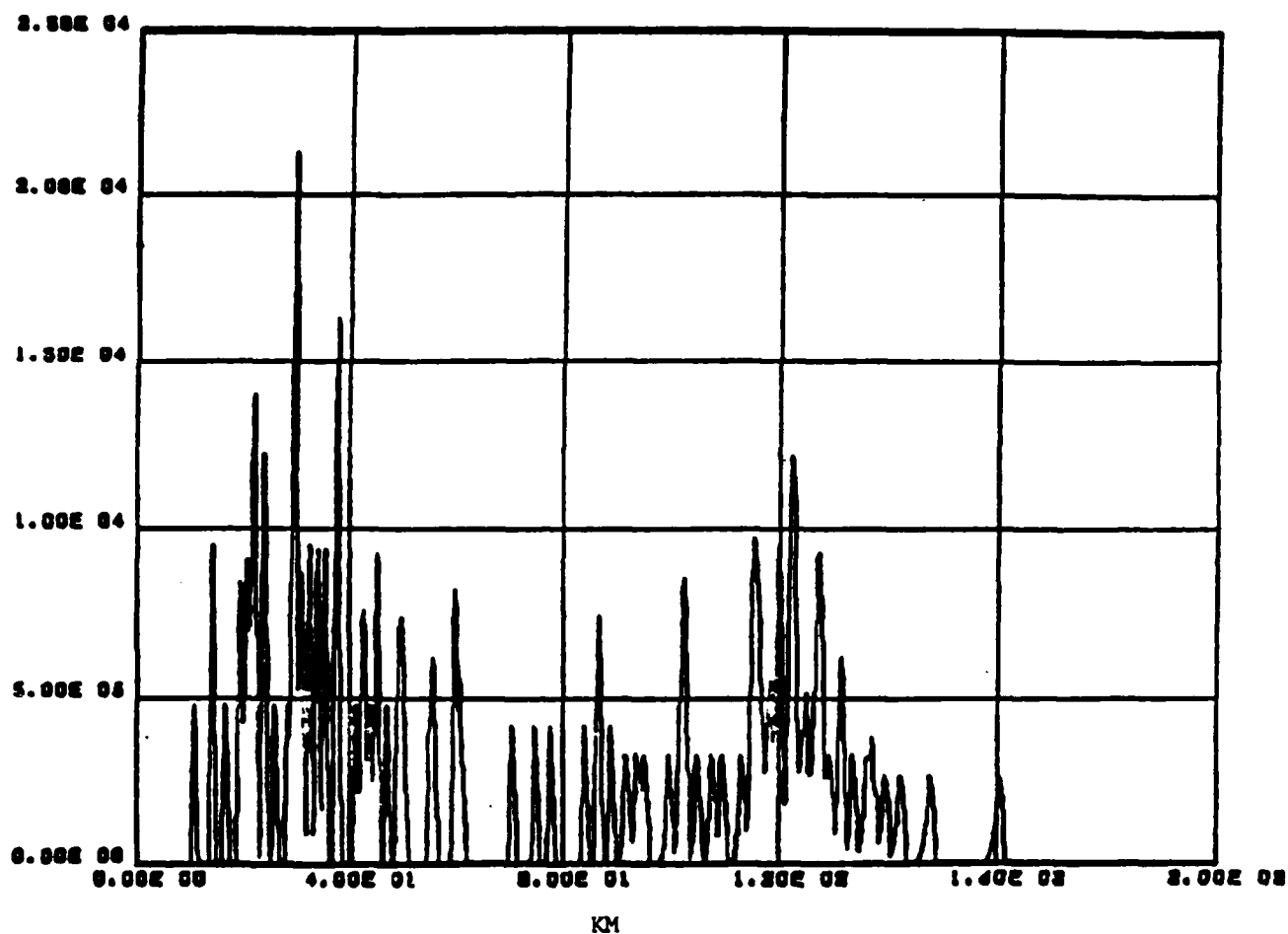


Figure 14- The profile of 100 striations placed to simulate a Checkmate scan. See text for details. The abscissa is in km and the ordinate is arbitrary.

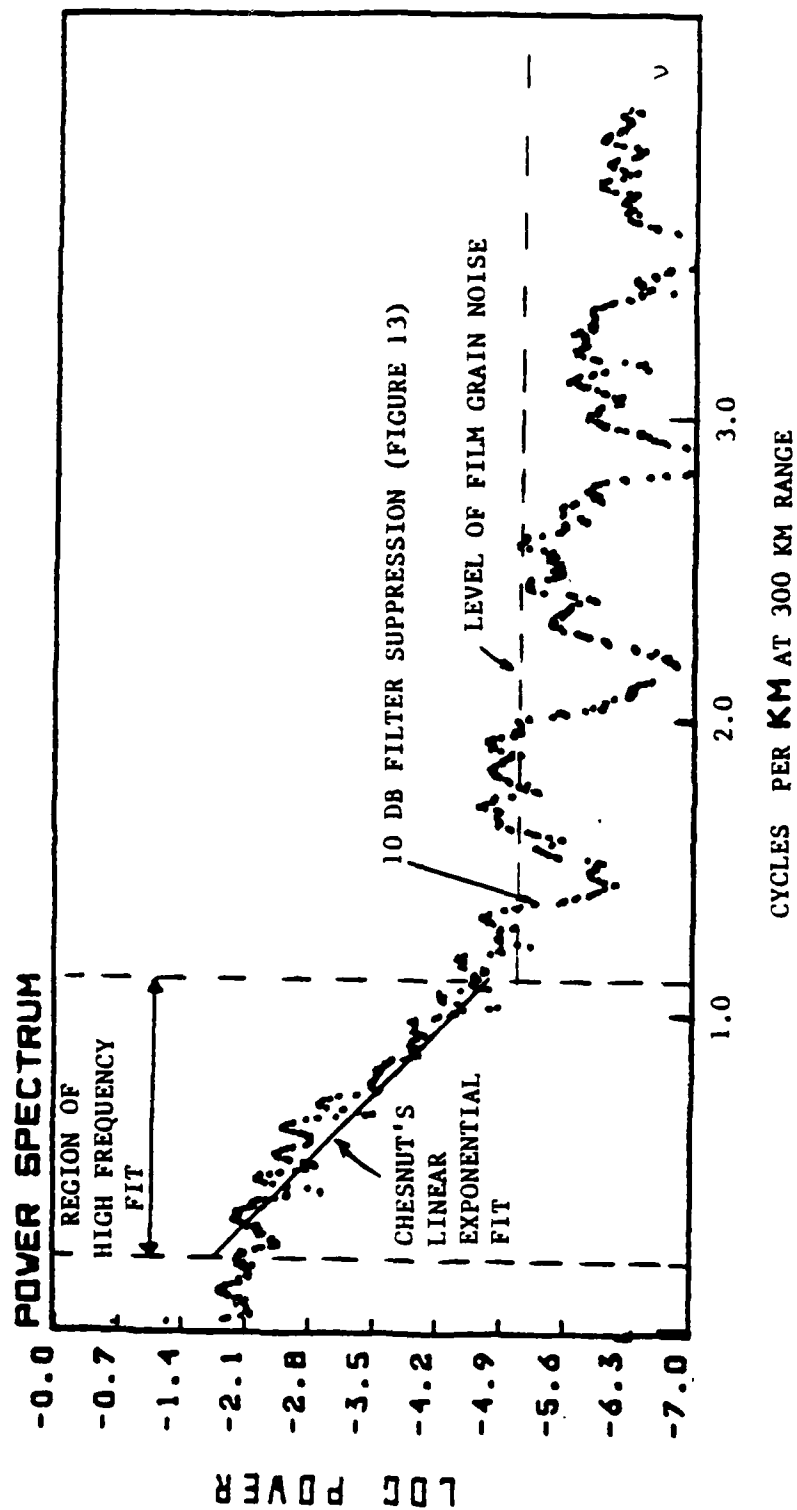


Figure 15- PSD resulting from profile of Figure 14 plotted on semi-log scale. Also shown (from Figure 13) are the region of high frequency fit, Chesnut's linear exponential fit, the film grain noise level, and the point of 10 db filter suppression.

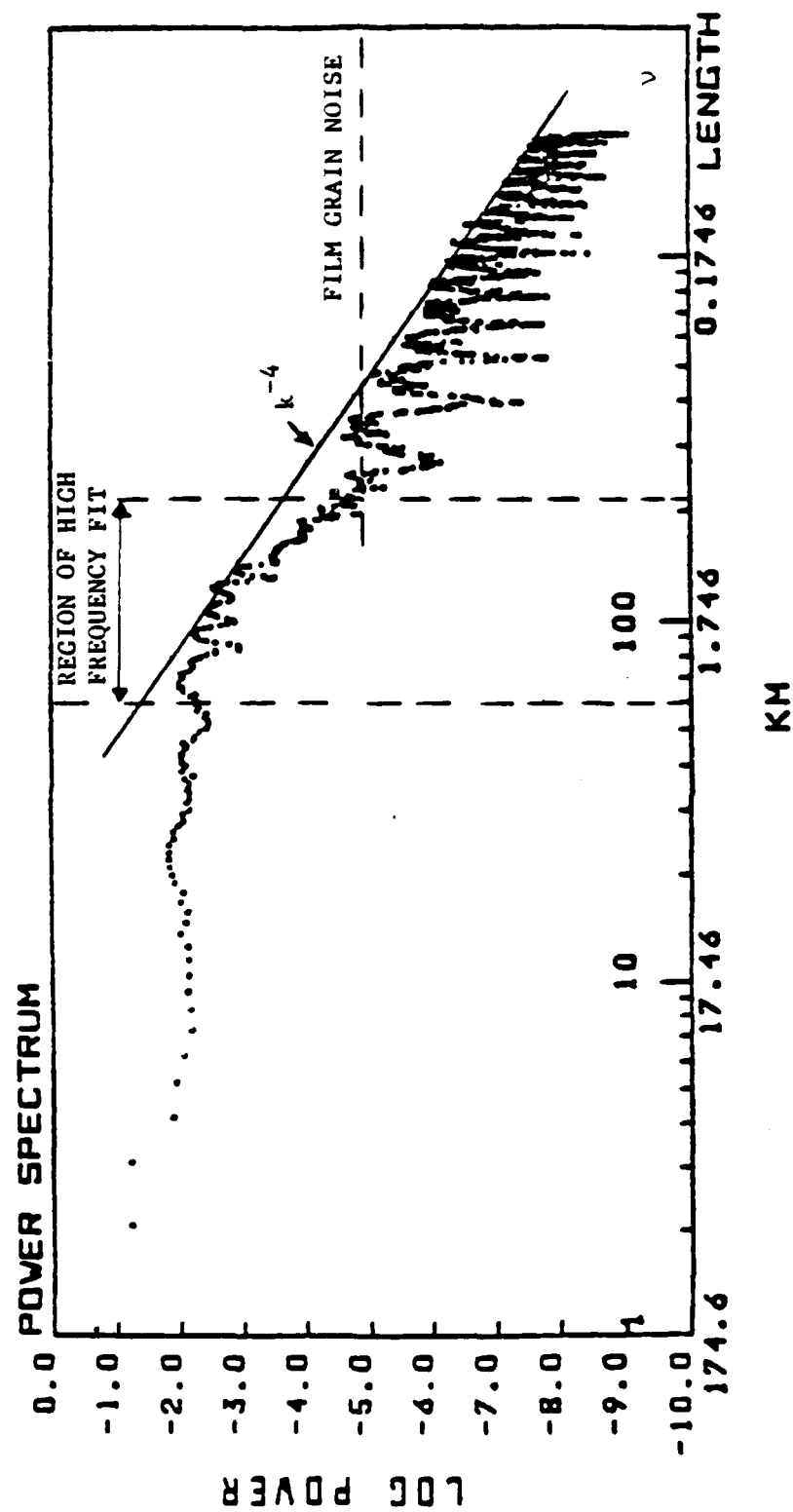


Figure 16- PSD of Figure 15 replotted on standard log-log plot.

## REFERENCES

1. Mulbrandon, M., N.J. Zabusky, and E. Hyman, "Estimating Spectral Indices from Transforms of Discrete Representations of Density Functions, NRL Memorandum Report 5298, March 1984. (AD-A140 164)
2. Zabusky, N.J., E. Hyman, and M. Mulbrandon, "Projections of Plasma Cloud Structures and Their Spectra", NRL Memorandum Report 5561, March 1985.
3. Hyman, E., M. Mulbrandon, S.L. Ossakow, and B.E. McDonald, "Preliminary Numerical Simulation of IR Structure Development in a Hypothetical Uranium Release", NRL Memorandum Report 4659, November 1981. (AD-A107 600)
4. McDonald, B.E., M.J. Keskinen, S.L. Ossakow, and S.T. Zalesak, "Computer Simulation of Gradient Drift Instability Processes in Operation Avefria", J. Geophys. Res. 85, 2143 (1980). (AD-A077 668)
5. Zalesak, S.T., J.A. Pedder, and S.L. Ossakow, "Analysis and Numerical Simulation of the Effect of Ion Pedersen Mobility on Ionospheric Barium Clouds", J. Geophys. Res. 88, 8003 (1983).
6. Zalesak, S.T., P.K. Chalurvedi, S.L. Ossakow, and J.A. Pedder, "Finite Temperature Effects on the Evolution of Ionospheric Barium Clouds in the Presence of a Conducting Background Ionosphere I. A High Altitude Incompressible Background Ionosphere", NRL Memorandum Report 5346, July 1984 (AD-A143 592)

7. Chesnut, W.G., "Spatial-Frequency Analysis of Striated Nuclear Phenomena. Part Two: A Model of the Striated Check Mate Cloud," DNA 2757T-2, April 1972. (AD-522 611)

**APPENDIX S**

**Low Frequency Instabilities Driven by an Ion  
Temperature Anisotropy**

**Y.C. Lee  
Science Applications International Corporation**

**J.D. Huba  
Naval Research Laboratory**





# Low Frequency Instabilities Driven by an Ion Temperature Anisotropy

Y. C. LEE

*Science Applications International Corporation  
McLean, VA 22102*

J. D. HUBA

*Geophysical and Plasma Dynamics Branch  
Plasma Physics Division*

May 8, 1985

This work was sponsored by the Defense Nuclear Agency under Subtask S99QMXBC, work unit 00129 and work unit title "Early Time Dynamics."



NAVAL RESEARCH LABORATORY  
Washington, D.C.

Approved for public release; distribution unlimited.



## REPORT DOCUMENTATION PAGE

1a REPORT SECURITY CLASSIFICATION <b>UNCLASSIFIED</b>		1b RESTRICTIVE MARKINGS	
2a SECURITY CLASSIFICATION AUTHORITY		3 DISTRIBUTION AVAILABILITY OF REPORT Approved for public release; distribution unlimited.	
2b DECLASSIFICATION/DOWNGRADING SCHEDULE		5 MONITORING ORGANIZATION REPORT NUMBER(S)	
4 PERFORMING ORGANIZATION REPORT NUMBER(S) NRL Memorandum Report 5552		7a NAME OF MONITORING ORGANIZATION	
6a NAME OF PERFORMING ORGANIZATION Naval Research Laboratory	6b OFFICE SYMBOL (If applicable) Code 4780	7b ADDRESS (City, State, and ZIP Code)	
8a NAME OF FUNDING/SPONSORING ORGANIZATION Defense Nuclear Agency		9 PROCUREMENT INSTRUMENT IDENTIFICATION NUMBER	
8b ADDRESS (City, State, and ZIP Code) Washington, DC 20305		10 SOURCE OF FUNDING NUMBERS	
		PROGRAM ELEMENT NO 62715H	WORK UNIT ACCESSION NO DN380-296
11 TITLE (Include Security Classification) Low Frequency Instabilities Driven by an Ion Temperature Anisotropy			
12 PERSONAL AUTHOR(S) Lee, Y.C.* and Huba, J.D.			
13a TYPE OF REPORT Interim	13b TIME COVERED FROM 10/84 TO 10/85	14 DATE OF REPORT (Year, Month, Day) 1985 May 8	15 PAGE COUNT 38
16 SUPPLEMENTARY NOTATION *Science Applications International Corporation, McLean, VA 22102 (Continues)			
17 COSATI CODES		18 SUBJECT TERMS (Continue on reverse if necessary and identify by block number)	
FIELD	GROUP	Early time HANE phenomenology Anisotropic ion instabilities	
		Electromagnetic ion cyclotron instability	
19 ABSTRACT (Continue on reverse if necessary and identify by block number)  We present a detailed linear analysis of low frequency ( $\omega \lesssim \Omega_i$ ) instabilities driven by an ion temperature anisotropy ( $T_{\perp i} \neq T_{\parallel i}$ ). In particular we investigate the electromagnetic ion cyclotron instability, the mirror instability, and the firehose instability. These instabilities require a high $\beta$ plasma (i.e., $\beta \gtrsim 1$ ) which is typical of an early time HANE plasma. The electromagnetic ion cyclotron and mirror instabilities also require $T_{\perp i} > T_{\parallel i}$ , while the firehose instability requires $T_{\parallel i} > T_{\perp i}$ . In general, we expect the early time coupling shell to have $T_{\perp i} > T_{\parallel i}$ so that the firehose instability is not obviously relevant to HANE situations but is included for the sake of completeness. We have also included an analysis of the influence of an electron temperature anisotropy on the MHD instability. This is an extension and correction of the work of Basu and Coppi (1984). We discuss the application of this research to HANE phenomena.			
20 DISTRIBUTION AVAILABILITY OF ABSTRACT <input checked="" type="checkbox"/> UNCLASSIFIED UNLIMITED <input type="checkbox"/> SAME AS RPT <input type="checkbox"/> DTIC USERS		21 ABSTRACT SECURITY CLASSIFICATION <b>UNCLASSIFIED</b>	
22a NAME OF RESPONSIBLE INDIVIDUAL J. D. Huba		22b TELEPHONE (Include Area Code) (202) 767-3630	22c OFFICE SYMBOL Code 4780

16. SUPPLEMENTARY NOTATION (Continued)

This work was sponsored by the Defense Nuclear Agency under Subtask S99QMXBC, work unit 00129 and work unit title "Early Time Dynamics."

## CONTENTS

I. INTRODUCTION .....	1
II. DERIVATION OF DISPERSION EQUATION .....	3
III. ANALYSIS OF DISPERSION EQUATION .....	6
IV. DISCUSSION .....	14
ACKNOWLEDGMENTS .....	17
APPENDIX .....	20
REFERENCES .....	24



## LOW FREQUENCY INSTABILITIES DRIVEN BY AN ION TEMPERATURE ANISOTROPY

### I. INTRODUCTION

It is well known that HANE's can have deleterious effects on  $C^3I$  systems (for example, by disrupting satellite communications and radar systems) and it is therefore important to the Defense Nuclear Agency to understand the atmospheric effects of HANE's. The primary cause of these negative effects is the production of long-lasting, large-scale, ionization irregularities in the ionosphere. In order to understand the cause and evolution of these irregularities, the Naval Research Laboratory has developed and is continuing to develop detailed theoretical and computational models of HANE's. Of recent interest to DNA is a thorough re-examination of early time phenomena ( $t \lesssim 1$  sec) which are primarily associated with the deposition of weapon energy in the atmosphere. Aside from radiation processes, the conversion of the kinetic energy of the debris into thermal energy of both the debris and air ions, and its ultimate deposition in the conjugate patches, is of particular importance. The important issues involved are debris-air coupling length and time scales, and thermalization processes. Underlying these issues are a host of complicated plasma physics processes. The ensuing turbulence which results from plasma instabilities can act as a means to thermalize the various ion species and to pitch angle scatter ions.

To date, the most intense effort to understand the role of plasma instabilities in early time HANE evolution has been directed at debris-air coupling. In this regard, NRL performed a series of investigations in the 70's to determine the anomalous transport properties of instabilities which could occur at the debris-air interface (Lampe et al., 1975). The effects of these instabilities on the evolution of the coupling shell were determined by incorporating the appropriate anomalous transport

Manuscript approved February 5, 1985.

Coefficients in a multi-fluid code (Clark, private communication). Subsequently, further advances have been made in this area through the use of a one dimensional hybrid code. This code treats the electrons as a fluid but the ions as particles. This permits the instabilities, and their effects on the plasma, to be studied self-consistently (Goodrich et al., 1984). It has also been recently suggested that microturbulence could impact the evolution of structure causing instabilities (Huba, 1984). Thus, the point to be made is that plasma turbulence can have a significant impact on the early time evolution of a HANE.

The aforementioned studies of plasma instabilities have dealt with high frequency turbulence, i.e.,  $\omega \gg \Omega_i$  where  $\omega$  is the wave frequency and  $\Omega_i = eB/m_i c$  is the ion cyclotron frequency. These instabilities impact very early time processes such as debris-air coupling and plasma thermalization. However, there are many low frequency instabilities (i.e.,  $\omega \lesssim \Omega_i$ ) that can be excited which may be important to early time HANE evolution. Specifically, the electromagnetic ion cyclotron instability ( $\omega \sim \Omega_i$ ) has the capability of pitch angle scattering energetic ions (Davidson and Ogden, 1975). Debris and air ions are energized predominantly in a direction perpendicular to the ambient magnetic field  $B_z$ . Electromagnetic ion cyclotron waves, if excited, can then "transform" this perpendicular energy to parallel energy. This allows energetic ions to stream down the field lines into the upper atmosphere to deposit their energy; an important consideration in HANE events such as Starfish. Recent 1D particle simulations have observed this effect (Ambrosiano and Brecht, 1984). Aside from the electromagnetic ion cyclotron instability, other low frequency hydromagnetic instabilities may be excited which can be important. For example, the mirror or firehose



instabilities (Hasegawa, 1971) generate electromagnetic turbulence which can propagate away from the coupling shell into the magnetosphere. These waves are capable of pitch angle scattering ambient radiation belt protons which can lead to a redistribution of high energy protons in the magnetosphere (Cladis et al., 1970). This issue is germane to satellite survivability since it is believed that Starfish caused the enhancement of high energy proton fluxes at low L shells (Filz, 1967) which affected the operation of several satellites.

One mechanism to generate the instabilities described above is an anisotropic ion distribution. Specifically, a bi-Maxwellian type distribution such that  $T_{\perp\perp} \neq T_{\parallel\parallel}$  where  $T_{\perp\perp}$  and  $T_{\parallel\parallel}$  are the perpendicular and parallel ion temperatures, respectively. The purpose of this report is to investigate in detail the linear stability properties of low frequency waves ( $\omega \lesssim \Omega_i$ ) which are driven unstable by ion anisotropies. Specific application to HANE events will also be discussed.

The organization of the paper is as follows. In the next section we present the basic assumptions of the analysis and derive a general dispersion equation which describes low frequency modes ( $\omega \lesssim \Omega_i$ ). In Section III we present both analytical and numerical results. Finally, in Section IV we summarize our results and apply them to HANE's.

## II. DERIVATION OF DISPERSION EQUATION

We assume a spatially homogeneous plasma with an ion temperature anisotropy ( $T_{\perp\perp} \neq T_{\parallel\parallel}$ ) that is immersed in a uniform static magnetic field  $\mathbf{B} = B_0 \hat{z}$ . The perturbed electric field is taken to be  $\mathbf{E}(\mathbf{x}, t) = \mathbf{\tilde{E}} \exp [i(\mathbf{k} \cdot \mathbf{x} - \omega t)]$  where  $\mathbf{k} = k_{\perp} \hat{x} + k_{\parallel} \hat{z}$  without any loss of generality because of the symmetry of the unperturbed system. The perpendicular wavelength of

the perturbation is assumed to be much larger than the electron Larmor radius  $\rho_e$  ( $k_\perp \rho_e \ll 1$ ) but can be comparable to the ion Larmor radius  $\rho_i$  ( $k_\perp \rho_i \sim 1$ ). The frequency, as well as the growth rate, of the perturbation is taken to be of order of the ion cyclotron frequency ( $\omega \lesssim \Omega_i$ ). For simplicity, we assume that the equilibrium ion distribution is described by a bi-Maxwellian distribution function

$$F_i(v_\perp^2, v_\parallel^2) = \left(\frac{m_i}{2\pi T_{\perp i}}\right)^{1/2} \left(\frac{m_i}{2\pi T_{\parallel i}}\right) \exp\left(-\frac{m_i v_\perp^2}{2T_{\perp i}} - \frac{m_i v_\parallel^2}{2T_{\parallel i}}\right), \quad (1)$$

where  $m_i$  is the mass of the ion species. The electron distribution function is assumed to be isotropic since collisions, as well as high frequency instabilities driven by any electron anisotropy, tend to remove the velocity-space anisotropy in the electron distribution on a very short time scale (i.e.,  $t \ll \Omega_i^{-1}$ ) [see Appendix].

Linearizing the Vlasov equation and using Maxwell's equation, a set of homogeneous equations  $\underline{M} \cdot \underline{E} = 0$  describing the propagation of electromagnetic disturbances at an arbitrary angle with respect to the magnetic field can be obtained (Krall and Trivelpiece, 1973), where

$$\underline{M} = 1 - \frac{k^2 c^2 - c^2 \underline{k} \underline{k}}{\omega^2} + \sum_{\alpha=i,e} \frac{2\omega_p^2}{\omega \Omega_\alpha} \sum_n \langle \underline{p}_n \underline{Q}_n \rangle_\alpha \quad (2)$$

and

$$\langle \quad \rangle_\alpha \equiv 2\pi \int dv_\parallel \int 2v_\perp dv_\perp ( \quad ).$$

$$\underline{p}_n \equiv \frac{n\Omega_\alpha J_n}{k_\perp} \hat{A}_n \hat{x} + i v_\perp J_n \hat{A}_n \hat{y} + v_\parallel J_n \hat{B}_n \hat{z},$$

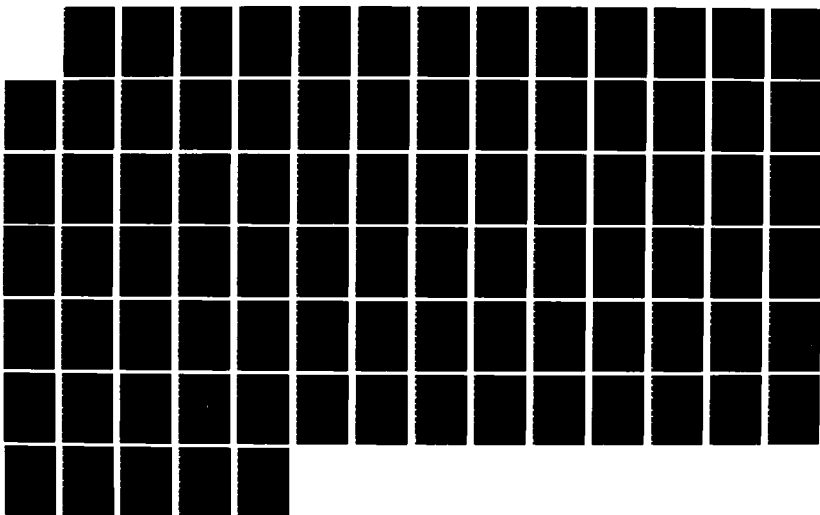
AD-A171 688

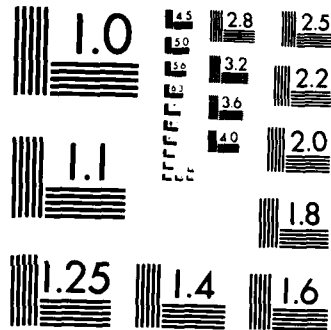
GEOPHYSICAL PLASMAS AND ATMOSPHERIC MODELING(U) SCIENCE 8/8  
APPLICATIONS INTERNATIONAL CORP MCLEAN VA  
E HYMAN ET AL JUL 86 SAIC-86/1781 N00014-85-C-2018

UNCLASSIFIED

F/G 4/1

NL





MICROCOPY RESOLUTION TEST CHART  
NATIONAL BUREAU OF STANDARDS-1963-A

$$\hat{Q}_n \equiv \frac{n\Omega_\alpha J_n}{k_\perp} \hat{x} - i v_\perp J'_n \hat{y} + v_\parallel J_n \hat{z}$$

$$A_n \equiv \left[ \left( 1 - \frac{k_\parallel v_\parallel}{\omega} \right) \frac{\partial f_\alpha}{\partial v_\perp^2} + \frac{k_\parallel v_\parallel}{\omega} \frac{\partial f_\alpha}{\partial v_\parallel^2} \right] (\omega - n\Omega_\alpha - k_\parallel v_\parallel)$$

$$B_n \equiv A_n + (\partial f_\alpha / \partial v_\perp^2 - \partial f_\alpha / \partial v_\parallel^2) / \omega,$$

$J_n = J_n(k_\perp v_\perp / \Omega_\alpha)$  is the Bessel function of order  $n$ ,  $J'_n(x) = dJ_n/dx$ , and  $\Omega_\alpha = e_\alpha B_0 / m_\alpha c$  is the cyclotron frequency of species  $\alpha$  ( $e$ : electrons and  $i$ : ions).

After performing the velocity space integration for both species and taking the appropriate small gyroradius limit for electrons, we obtain the dispersion equation

$$\det [\underline{M}] = 0. \quad (3)$$

The components of  $\underline{M}$  are

$$\begin{aligned} M_{xx} &= 1 - \frac{k_\parallel^2 c^2}{\omega^2} + \frac{1}{2} \frac{\omega_{pe}^2}{\omega^2} (G_{e1} + G_{e-1}) + \frac{\omega_{pi}^2}{\omega^2} \sum_n \frac{n^2 \Gamma_n}{x} G_n \\ M_{xy} &= -M_{yx} = -i \frac{\omega_{pe}^2}{2\omega^2} (G_{e1} - G_{e-1}) + i \frac{\omega_{pi}^2}{\omega^2} \sum_n n \Gamma'_n G_n \\ M_{xz} &= M_{zx} = \frac{k_\parallel k_\perp c^2}{\omega^2} + \frac{\omega_{pe}^2}{2\omega \Omega_e} (H_{e1} - H_{e-1}) + \frac{\omega_{pi}^2}{\omega \Omega_i} \frac{k_\perp}{k_\parallel} \sum_n \frac{n \Gamma_n}{x} H_n \\ M_{yy} &= 1 - \frac{k_\parallel^2 c^2}{\omega^2} + \frac{\omega_{pe}^2}{2\omega^2} (G_{e1} + G_{e-1}) + \frac{\omega_{pi}^2}{\omega^2} \sum_n [ (x \Gamma'_n)' + \Gamma_n ] G_n \\ M_{yz} &= -M_{zy} = -i \frac{\omega_{pe}^2}{\omega \Omega_e} \frac{k_\perp}{k_\parallel} H_{e0} + i \frac{\omega_{pi}^2}{\omega \Omega_i} \frac{k_\perp}{k_\parallel} \sum_n \Gamma'_n H_n \end{aligned} \quad (4)$$

$$M_{zz} = 1 - \frac{k_{\perp}^2 c^2}{\omega^2} + \frac{2\omega_{pe}^2}{k_{\parallel}^2 v_e^2} H_{e0} + \frac{\omega_{pe}^2}{\Omega_i^2} \frac{k_{\perp}^2}{k_{\parallel}^2} \sum_n \frac{\omega - n\Omega_i}{\omega} \frac{\Gamma_n}{x} H_n$$

where

$$G_{en} = \frac{\omega}{k_{\parallel} v_e} Z\left(\frac{\omega - n\Omega_e}{k_{\parallel} v_e}\right); H_{en} = 1 + \frac{\omega - n\Omega_e}{k_{\parallel} v_e} Z\left(\frac{\omega - n\Omega_e}{k_{\parallel} v_e}\right); x = \frac{k_{\perp}^2 v_{\perp i}^2}{2\Omega_i^2},$$

$$G_n = \left[1 - \frac{\omega - n\Omega_i}{\omega} \left(1 - \frac{T_{\perp i}}{T_{\parallel i}}\right)\right] \frac{\omega}{k_{\parallel} v_{\parallel i}} Z\left(\frac{\omega - n\Omega_i}{k_{\parallel} v_{\parallel i}}\right) - \left(1 - \frac{T_{\perp i}}{T_{\parallel i}}\right),$$

$$H_n = \left[\frac{T_{\perp i}}{T_{\parallel i}} + \frac{n\Omega_i}{\omega} \left(1 - \frac{T_{\perp i}}{T_{\parallel i}}\right)\right] \left[1 + \frac{\omega - n\Omega_i}{k_{\parallel} v_{\parallel i}} Z\left(\frac{\omega - n\Omega_i}{k_{\parallel} v_{\parallel i}}\right)\right]; \frac{T_{\perp i}}{T_{\parallel i}} = \frac{v_{\perp i}^2}{v_{\parallel i}^2},$$

$v_e$  is the electron thermal velocity,  $v_{\perp i}$  and  $v_{\parallel i}$  are the ion perpendicular and parallel thermal velocity, respectively,  $Z(\xi)$  is the plasma dispersion function,  $\Gamma_n \equiv e^{-x} I_n(x)$ ,  $I_n(x)$  is the modified Bessel function of order  $n$ , and  $\Gamma'_n = d\Gamma_n/dx$ .

### III. ANALYSIS OF DISPERSION EQUATION

#### A. Electromagnetic Ion Cyclotron Instability

We first consider the excitation of ion cyclotron waves with  $\omega \sim \Omega_i$ . For the case of parallel propagation ( $k_{\perp} = 0$ ), the linear dispersion relation can be greatly simplified to give

$$\det [M_{\pm}] = D_{+} D_{-} \left(1 + \frac{2\omega_{pe}^2}{k_{\parallel}^2 v_e^2} H_{e0} + \frac{2\omega_{pi}^2}{k_{\parallel}^2 v_i^2} H_0\right) = 0, \quad (5)$$

where

$$D_{\pm} = 1 - \frac{k_{\parallel}^2 c^2}{\omega^2} + \frac{\omega_{pi}^2}{\omega^2} G_{\pm 1} + \frac{\omega_{pe}^2}{\omega^2} G_{e\pm 1}.$$

Davidson and Ogden (1975) have shown that the transverse electromagnetic portion of (5) exhibits a strong instability in the presence of an ion temperature anisotropy such that  $T_{\perp i} > T_{\parallel i}$ . This instability has a characteristic frequency at maximum growth rate of  $\omega_r \lesssim \Omega_i$  and  $\gamma \sim (\beta_{\perp i}/2)^{1/2} \Omega_i$  where  $\beta_{\perp i} = 8\pi m_i T_{\perp i}/B_0^2$ , and the corresponding wavelength is such that  $k_{\parallel} c/\omega_{pi} \gtrsim 1$ . The electrostatic branch of the dispersion relation can be shown to be rigorously stable by the Nyquist technique.

The assumption that  $k_{\perp} = 0$  corresponds to an "infinite" wavelength in the direction orthogonal to the ambient magnetic  $B_0$ . For application to HANE's this assumption is violated because the coupling shell has finite dimensions perpendicular to  $B_0$ . Thus, it is necessary to investigate the linear stability properties of ion cyclotron waves for oblique propagation using (3) and (4) if we are to apply this instability to HANE's. Since, in general, (3) and (4) are not amenable to analytical results we solve them numerically for a variety of parameters.

In Fig. 1 we show the growth rate  $\gamma/\Omega_i$  vs. parallel wavenumber  $ck_{\parallel}/\omega_{pi}$  for  $\theta = 0^\circ, 20^\circ, 40^\circ, 60^\circ$ , and  $80^\circ$  where  $\theta = \tan^{-1}(k_{\perp}/k_{\parallel})$ . The other parameters used are  $\omega_{pi}/\Omega_i = 400$ ,  $m_i/m_e = 1836$ ,  $T_{\perp i}/T_{\parallel i} = 20$ ,  $\beta_{\perp i} = 1.0$ , and  $T_e/T_{\perp i} = 0.1$ . There are two major effects of oblique propagation on the excitation of electromagnetic cyclotron waves. First, the growth rate of the instability decreases as the waves become more oblique, i.e., as  $\theta$  increases. However, even for  $\theta$  as large as  $\sim 50^\circ$  the growth rate is only reduced by a factor of two. Thus, the waves have substantial growth rates for a wide range of angles and are not confined to nearly parallel propagation. Second, in general, as  $\theta$  increases the bandwidth of unstable modes in  $k_{\parallel}$  space decreases. The small  $k_{\parallel}$  cutoff remains roughly constant ( $ck_{\parallel}/\omega_{pi} \sim 0.5$ ) for  $0^\circ < \theta < 80^\circ$ , but the large  $k_{\parallel}$  cutoff is reduced by

more than a factor of two. We note that the shape of the  $\theta = 60^\circ$  growth rate is different from the others; namely, there is not a sharp falloff for modes with  $k_{\parallel} > k_{\parallel m}$  where  $k_{\parallel m}$  corresponds to the  $k_{\parallel}$  for maximum growth. There is almost a "plateau" in the growth rate in this region. This parameter regime corresponds to the Harris instability (Soper and Harris, 1965; Gary et al., 1976). The Harris instability only occurs for obliquely propagating waves and, in general, has a maximum growth rate less than the parallel propagating electromagnetic ion cyclotron instability (Gary et al., 1976).

In Fig. 2 we plot  $\gamma_m/\Omega_i$  and  $ck_{\parallel m}/\omega_{pi}$  vs.  $\theta$  where  $\gamma_m$  denotes the maximum growth rate as a function of parallel wavenumber and  $k_{\parallel m}$  is the corresponding wavenumber at maximum growth. The other parameters used are the same as in Fig. 1. These curves emphasize the major points indicated by Fig. 1: (1) maximum growth occurs for  $\theta = 0^\circ$  (or  $k_{\perp} = 0$ , purely parallel propagating waves); (2) there is substantial wave growth for most angles of propagation; and (3) the wavelength of the fastest growing mode increases as the angle of propagation becomes more oblique (i.e., closer to perpendicular propagation).

#### B. MHD Instabilities

We now investigate low-frequency MHD instabilities i.e.,  $\omega \ll \Omega_i$ . However, prior to presenting detailed numerical results, we first make several simplifying assumptions so that analytical results can be given. We assume that  $\Omega_e, \Omega_i \gg \omega, k_{\parallel}v_e, k_{\parallel}v_i$  without any special ordering for  $\omega/k_{\parallel}v_e$  and  $\omega/k_{\parallel}v_i$ . Making use of the approximation  $\xi Z(\xi) = -1 - 1/2\xi^2$ , for  $\xi \gg 1$  the following limiting matrix elements can be derived:



$$M_{xx} = 1 - \frac{\omega_{pi}^2}{\omega_i^2} - \frac{k_{\perp}^2 c^2}{\omega^2} \left[ 1 - \frac{1}{2} (\beta_{\parallel i} - \beta_{\perp i}) \right]$$

$$M_{xy} = M_{yx} = 0$$

$$M_{yy} = M_{xx} - \frac{k_{\perp}^2 c^2}{\omega^2} + \frac{k_{\perp}^2 c^2}{\omega^2} \beta_{\perp i} G_0$$

(6)

$$M_{yz} = -M_{zy} = -i \frac{\omega_{pi}}{\omega \Omega_i} \frac{k_{\perp}}{k_{\parallel}} (H_{e0} - H_0)$$

$$M_{xz} = M_{zx} = \frac{k_{\perp} k_{\parallel}}{\omega^2} c^2 \left[ 1 - \frac{1}{2} (\beta_{\parallel i} - \beta_{\perp i}) \right]$$

$$M_{zz} = 1 - \frac{k_{\perp}^2 c^2}{\omega^2} \left[ 1 - \frac{1}{2} (\beta_{\parallel i} - \beta_{\perp i}) \right] + \frac{2\omega^2}{k_{\parallel}^2 v_e^2} H_{e0} + \frac{2\omega_{pi}^2}{k_{\parallel}^2 v_{\perp i}^2} H_0$$

where  $\beta_{\parallel i} = \omega_{pi}^2 v_{\parallel i}^2 / \Omega_i^2 c^2$ ,  $\beta_{\perp i} = \omega_{pi}^2 v_{\perp i}^2 / \Omega_i^2 c^2 = 8\pi n T_{\perp i} / B^2$ . In deriving (6) we have omitted terms which are smaller by order  $\omega / \Omega_i$  and  $\omega / \Omega_e$ . In addition, we have taken the small ion Larmor radius limit ( $k_{\perp} \rho_{\perp i} \ll 1$ ). For  $\beta_e, \beta_i \approx 1$  we can also neglect the 1 in  $M_{xx}$  as well as  $M_{zz}$  since  $\omega_{pi}^2 / \Omega_i^2$ ,  $k_{\perp}^2 c^2 / \omega^2$ ,  $k_{\perp}^2 c^2 / \omega^2 \gg 1$ . We now show how the well known mirror and firehose instabilities are recovered when subsidiary orderings are made.

Writing  $M_{zy} = i\bar{M}_{zy}$  to make explicit the  $i$  dependence, we can express the dispersion relation (6) in the following compact form:

$$M_{zz} = \frac{n_{\perp}^2 n_{\parallel}^2 \left[ 1 - \frac{1}{2} (\beta_{\parallel i} - \beta_{\perp i}) \right]^2}{M_{xx}} + \frac{\bar{M}_{yy}^2}{M_{yy}}, \quad (7)$$

where  $n_{\perp}^2 \equiv c^2 k_{\perp}^2 / \omega^2$  and  $n_{\parallel}^2 \equiv c^2 k_{\parallel}^2 / \omega^2$ . Further simplification is possible with the introduction of  $\alpha \equiv 1 - \frac{1}{2} (\beta_{\parallel i} - \beta_{\perp i})$ ,  $D_{xx} \equiv M_{xx} + \alpha n_{\parallel}^2$ , and  $D_{zz} \equiv M_{zz} + \alpha n_{\perp}^2$ ,

$$D_{zz} = \frac{\alpha_{\perp}^2 D_{xx}}{D_{xx} - \alpha_{\parallel}^2} + \frac{\bar{M}_{yz}^2}{M_{yy}}. \quad (8)$$

### 1. Mirror Instability

First, let us consider the familiar mirror instability. This corresponds to the limit  $k_{\parallel} v_{\parallel 1}, k_{\parallel} v_e \gg \omega$ . In this limit  $D_{zz}$  becomes very large, hence  $E_{\parallel}(E_z) \sim 0$  which is equivalent to "frozen-in condition" in ideal MHD treatment. Using small argument expansion for  $Z(\xi_e)$  and  $Z(\xi_1)$ , we find

$$\bar{M}_{zy} = \frac{\omega_{pi}^2}{\omega \Omega_1} \frac{k_{\perp}}{k_{\parallel}} \left(1 - \frac{T_{11}}{T_{\parallel 1}}\right) \quad (9a)$$

$$M_{yy} = 1 + \frac{\omega_{pi}^2}{\Omega_1^2} - \alpha_{\parallel}^2 - n_1^2 \left[1 - \beta_{\parallel 1} \left(\frac{T_{11}}{T_{\parallel 1}} - 1\right)\right] \quad (9b)$$

$$D_{xx} = 1 + \frac{\omega_{pi}^2}{\Omega_1^2} \quad (9c)$$

$$D_{zz} = 1 + \frac{2\omega_{pe}^2}{k_{\parallel}^2 v_e^2} + \frac{2\omega_{pi}^2}{k_{\parallel}^2 v_{\parallel 1}^2} \quad (9d)$$

Approximating  $D_{zz} \approx (k_{De}^2/k_{\parallel}^2)(1 + T_e/T_{\parallel 1})$ ,  $k_{De}^2 = 2\omega_{pe}^2/v_e^2$ , and  $D_{xx} \approx \omega_{pi}^2/\Omega_1^2$ , the dispersion relation (8) reduces to

$$1 + \frac{T_e}{T_{\parallel 1}} = \alpha \frac{k_{\perp}^2 \rho_s^2}{\frac{\omega^2}{k_{\parallel}^2 v_A^2} - \alpha} + \frac{\beta_e}{2} \frac{(k_{\perp}^2/k_{\parallel}^2)(1 - T_{11}/T_{\parallel 1})^2}{\frac{\omega^2}{k_{\parallel}^2 v_A^2} - \alpha \frac{k_{\perp}^2}{k_{\parallel}^2} - \frac{k_{\perp}^2}{k_{\parallel}^2} [1 + \beta_{\parallel 1} (1 - \frac{T_{11}}{T_{\parallel 1}})]}, \quad (10)$$

where  $\rho_s^2 = 2c_s^2/\Omega_i^2 = (v_e^2/\Omega_i^2)(m_e/m_i)$ ,  $v_A^2 = c^2\Omega_i^2/\omega_{pi}^2$ ,  $\beta_e = 2c_s^2/v_A^2 = 8\pi nT_e/B^2$  and  $\beta_{ii} = 2v_{ii}^2/v_A^2 = 8\pi nT_{ii}/B^2$ . For  $T_e \sim T_{ii}$ ,  $T_{ii}$ ,  $\rho_s^2 \sim \rho_i^2$ , we find  $k_{\perp}^2 \rho_s^2 \ll 1$ , consistent with our long wavelength ordering. The smallness of  $k_{\perp}^2 \rho_s^2$  immediately yields, for frequencies significantly different from  $\sqrt{\alpha} k_{\parallel} v_A$ , the following approximate dispersion relation

$$(1 + \frac{T_e}{T_{ii}}) \left\{ \frac{\omega^2}{k^2 v_A^2} - \alpha \frac{k_{\parallel}^2}{k^2} - \frac{k_{\perp}^2}{k^2} [1 + \beta_{ii} (1 - \frac{T_{ii}}{T_{ii}})] \right\} = \frac{\beta_e}{2} (1 - \frac{T_{ii}}{T_{ii}})^2 \frac{k_{\perp}^2}{k^2}. \quad (11)$$

The stability condition is given by

$$\omega^2 = v_A^2 [1 - \frac{1}{2} (\beta_{ii} - \beta_{ii}) k_{\parallel}^2] + v_A^2 [1 + \beta_{ii} (1 - \frac{T_{ii}}{T_{ii}}) + \frac{\beta_e (1 - \frac{T_{ii}}{T_{ii}})^2}{2(1 + \frac{T_e}{T_{ii}})}] k_{\perp}^2 > 0 \quad (12)$$

For  $k_{\parallel}^2/k^2 \ll 2/\beta_{ii}$ , the stability condition becomes

$$1 + \beta_{ii} (1 - T_{ii}/T_{ii}) + \frac{T_e [T_{ii}^2 + T_{ii}^2] - 2 T_{ii} T_{ii}}{2 T_{ii} (T_{ii} + T_e)} > 0. \quad (13)$$

It is easy to see that instability can only occur when  $T_{ii}$  is sufficiently larger than  $T_{ii}$ . The stability condition (13) is the same as that of the MHD mirror mode (Hasegawa, 1971) Note that mirror instability only takes place when both  $k_{\parallel}$  and  $k_{\perp}$  are sufficiently nonzero, i.e., for oblique propagation.

## 2. Firehose Instability

In the limit  $k_{\parallel} v_e \gg \omega \gg k_{\parallel} v_{ii}$ ,  $H_{e0} = 1 + i/\pi\omega/k_{\parallel} v_e$ , and  $H_0 = -\frac{1}{2} k_{\parallel}^2 v_{ii}^2/\omega^2$ . We arrive at the following approximate expressions for  $\bar{M}_{yz}$ ,  $M_{zz}$ , and  $M_{yy}$ :

$$\bar{M}_{zy} = \frac{\omega_{pi}^2}{\omega \Omega_i} \frac{k_{\perp}}{k_{\parallel}} \quad (14a)$$

$$M_{zz} = 1 - n_{\perp}^2 \alpha + \frac{k_{De}^2}{k_{\parallel}^2} - \frac{\omega_{pi}^2}{\omega^2} \quad (14b)$$

$$M_{yy} = M_{xx} - n_{\perp}^2 (1 + \beta_{\perp i}), \quad (14c)$$

where we have made use of the identity  $G_0 = H_0 - 1$  to approximate  $G_0$  by  $-1$ .  
 $M_{xx} = D_{xx} - \alpha n_{\parallel}^2$ ,  $D_{xx} = 1 + \omega_{pi}^2 / \Omega_i^2 = \omega_{pi}^2 / \Omega_i^2$  and  $M_{zz} = D_{zz} - \alpha n_{\perp}^2$ .  
 From (14b),  $D_{zz} = 1 + k_{De}^2 / k_{\parallel}^2 - \omega_{pi}^2 / \omega^2 = (k_{De}^2 / k_{\parallel}^2) (1 - \omega_s^2 / \omega^2)$ , where  
 $\omega_s = k_{\parallel} \omega_{pi} / k_{De} = k_{\parallel} c_s$  is the ion sound frequency. The dispersion relation (8) reduces to

$$1 - \frac{\omega_s^2}{\omega^2} = \alpha \frac{k_{\perp}^2 \omega_s^2}{\frac{\omega^2}{k_{\parallel}^2 V_A^2} - \alpha} + \frac{\beta_e}{2} \frac{k_{\perp}^2 / k^2}{\frac{\omega^2}{k_{\parallel}^2 V_A^2} - \frac{k_{\perp}^2}{k^2} (1 + \beta_{\perp i}) - \alpha \frac{k_{\parallel}^2}{k^2}} \quad (15)$$

Here again, the smallness of  $k_{\perp}^2 \omega_s^2$  allows us to drop the first term on the right hand side of (15) provided that  $|\omega^2 - \alpha k_{\parallel}^2 V_A^2| \gg k_{\perp}^2 \omega_s^2$ . The resulting dispersion relation becomes

$$(1 - \frac{\omega_s^2}{\omega^2}) [\frac{\omega^2}{k_{\parallel}^2 V_A^2} - \alpha \frac{k_{\parallel}^2}{k^2} - (1 + \beta_{\perp i}) \frac{k_{\perp}^2}{k^2}] = \frac{\beta_e}{2} \frac{k_{\perp}^2}{k^2} \quad (16)$$

Equation (16) closely resembles the equation derived by Basu and Coppi (1982) with one significant difference: their equation is derived under the assumption of large electron anisotropy and cold ions, whereas ours assumes isotropic electrons but retains temperature anisotropy for ions. Therefore the slow magnetosonic wave and the so-called "field-swelling"

mode which are unstable under conditions discussed in their paper, are no longer so in our isotropic electron limit. In fact it is easy to see that (16) admits real  $\omega^2$  roots (i.e., they are either purely growing or pure oscillatory), and the sole condition for instability is

$$k_{\parallel}^2 (c_s^2 + \alpha v_A^2) + k_{\perp}^2 v_A^2 (1 + \beta_{\perp i} + \beta_e/2) < 0, \quad (17)$$

which can only be satisfied for sufficiently negative values of  $\alpha$ , or

$$\beta_{\parallel i} - \beta_{\perp i} > 2. \quad (18)$$

The instability condition (18) is the same as that of "firehose" instability even though the usual "frozen-in" condition is not imposed, as noted by Basu and Coppi (1982), and the polarization is different from that of the usual firehose mode. A more detailed discussion of this point is given in the Appendix.

To recover the "firehose" instability, we note that (10) can be rewritten in the following form

$$\left( \frac{\omega^2}{k_{\parallel}^2 v_A^2} - \alpha \right) D(\omega, \underline{k}) = \alpha k_{\perp}^2 \rho_s^2 \equiv \epsilon, \quad (19)$$

where  $D(\omega, \underline{k}) = 0$  gives (11), the "mirror" mode dispersion equation. Equation (37) can be considered to be the linear mode-coupling equation between the mirror-type modes and the "firehose" mode

$$\omega^2 = \alpha k_{\parallel}^2 v_A^2 \equiv \left( 1 - \frac{1}{2} (\beta_{\parallel i} - \beta_{\perp i}) \right) k_{\parallel}^2 v_A^2 \quad (20)$$

through the small coupling coefficient  $\epsilon$ . The preceding results derived for mirror instabilities correspond to weak coupling approximation of (10) by treating  $D(\omega, \underline{k})$  to be of the order of  $\epsilon$ . If we assume instead that  $\omega^2 - \alpha k_{\perp}^2 v_A^2 \sim O(\epsilon)$ , then we arrive at the "firehose" dispersion relation (19). It is trivial to see that the firehose stability condition is  $\beta_{\parallel i} - \beta_{\perp i} > 2$ . In fact the stability condition remains unchanged as we change the ordering of  $\omega$ ,  $k_{\parallel} v_e$ , and  $k_{\parallel} v_{\parallel i}$ . Even with the inclusion of the electron temperature anisotropy, the stability condition merely changes to  $\beta_{\parallel} - \beta_{\perp} > 2$ . It therefore seems that the "firehose" mode is a very robust MHD mode which is insensitive to the kinetic effects associated with the parallel motion of electrons and ions. The firehose instability should not be a major concern for HANE since it required  $T_{\parallel} > T_{\perp}$  which is not satisfied under ideal HANE conditions, at least in the coupling region during early time.

#### IV. DISCUSSION

We have presented a detailed linear analysis of low frequency ( $\omega \lesssim \Omega_i$ ) instabilities driven by an ion temperature anisotropy ( $T_{\perp i} \neq T_{\parallel i}$ ). In particular we have studied the electromagnetic ion cyclotron instability, the mirror instability, and the firehose instability. These instabilities require a high  $\beta$  plasma (i.e.,  $\beta \gtrsim 1$ ) which is typical of an early time HANE plasma. The electromagnetic ion cyclotron and mirror instabilities also require  $T_{\perp i} > T_{\parallel i}$ , while the firehose instability requires  $T_{\parallel i} > T_{\perp i}$ . In general, we expect the early time coupling shell to have  $T_{\perp i} > T_{\parallel i}$  so that the firehose instability is not obviously relevant to HANE situations but has been included for the sake of completeness. We have also included an Appendix which describes the influence of an electron temperature

anisotropy on the MHD instability and is an extension (and correction) of the work of Basu and Coppi (1982). Again, this is included for completeness. We now discuss the application of this research to HANE phenomena.

An important reason for this study was to investigate the stability properties of the electromagnetic ion cyclotron instability in order to determine whether or not it would be unstable in the HANE coupling shell. The significance of these unstable waves is that they pitch angle scatter ions, and therefore allow perpendicular energy to be transformed to parallel energy which is germane to debris patch formation. Most earlier studies focussed on parallel propagating modes which have "infinite" transverse wavelengths. However, the coupling shell has finite dimensions transverse to  $B_0$  and one needs to consider oblique propagating modes for application to HANEs. The results of our analysis show that the electromagnetic ion cyclotron frequency has significant growth for a broad range of angles relative to  $B_0$ . Although maximum growth occurs for  $\theta = 0$  (i.e.,  $k_{\perp} = 0$ ), waves have relatively strong growth up to  $\theta \sim 80^\circ$ . This corresponds to transverse wavenumbers in the range  $0 \lesssim k_{\perp} \lesssim 5 k_{\parallel}$ ; since  $k_{\parallel} \sim \omega_{pi}/c$  (see Fig. 1) we can rewrite this inequality as  $0 \lesssim k_{\perp} \lesssim 5\omega_{pi}/c$ . Transforming to wavelength space we find that  $\lambda_{\parallel} \sim c/\omega_{pi}$  and  $\lambda_{\perp} \gtrsim c/5\omega_{pi}$ . For HANE events such as Starfish and Checkmate, we note that the coupling shell width  $L$  is substantially larger than  $c/\omega_{pi}$  at times  $t \sim \text{few } \Omega_i^{-1}$ , which implies  $L \gg \lambda_{\perp}, \lambda_{\parallel}$ . Thus, electromagnetic ion cyclotron waves will easily "fit" into the coupling shell, so that they can play a significant role in pitch angle scattering ions.

In this regard, another important issue is time scale. The instabilities considered in this report require magnetized ions; thus, in

applying these results to HANEs a minimum time scale  $\tau \sim \Omega_i^{-1}$  is required before the instabilities can be excited. However, one expects an instability to e fold several times before the fluctuating fields reach a sufficiently large amplitude to affect the particles. Thus, the time scale on which ion cyclotron waves become important is  $\tau \sim 5\gamma^{-1} \sim 15 \Omega_i^{-1}$ . Note that the ion cyclotron frequency is based on the value of the compressed magnetic field in the coupling shell. Since this value can be as much as an order of magnitude (or larger) than the ambient field, this time scale can be relatively fast. For example, assuming  $m_i = 28$ ,  $B_0 = 5G$ , and  $Z = 1$  we find that  $\Omega_i^{-1} = 0.6$  msec so that  $\tau \sim 9$  msec. Thus, in modeling the effects of electromagnetic ion cyclotron turbulence on debris and air ions (namely, pitch angle scattering) a minimum time scale is required which should be implemented in early time codes which model debris patch formation. We roughly estimate this time scale to be  $\tau_m \sim 15\Omega_i^{-1}$  although it is parameter dependent and specific burst conditions need to be considered to accurately determine  $\tau_m$ . We also add that pitch angle scattering is not the only mechanism which can convert perpendicular ion energy to parallel ion energy. The inverse mirror force associated with the compressed magnetic shell can also cause this energy conversion. The time scale with this process is shorter than pitch angle scattering since it is not associated with wave turbulence.

The waves discussed in this paper can have other important implications for HANE disturbances. First, these waves can also pitch angle scatter high energy ambient radiation belt protons ( $E \gtrsim 1$  MeV). This can cause these high energy radiation belt particles to become trapped at lower L shells where defense and communication satellites reside. Enhanced fluences can then damage or incapacitate these satellites. In fact, this



is believed to have occurred following Starfish (Filz, 1967). And second, these waves (i.e., electromagnetic ion cyclotron) have a significant component of  $\delta E_{\parallel}$  since they propagate obliquely, i.e.,  $k_{\perp} > k_{\parallel}$ . These waves can be resonance with cold magnetospheric electrons which can be heated to 10-50 eV. This can lead to enhanced particle precipitation (Cornwall and Vesecky, 1984).

#### ACKNOWLEDGMENTS

We thank Dan Spicer for helpful discussions. This research has been supported by the Defense Nuclear Agency.

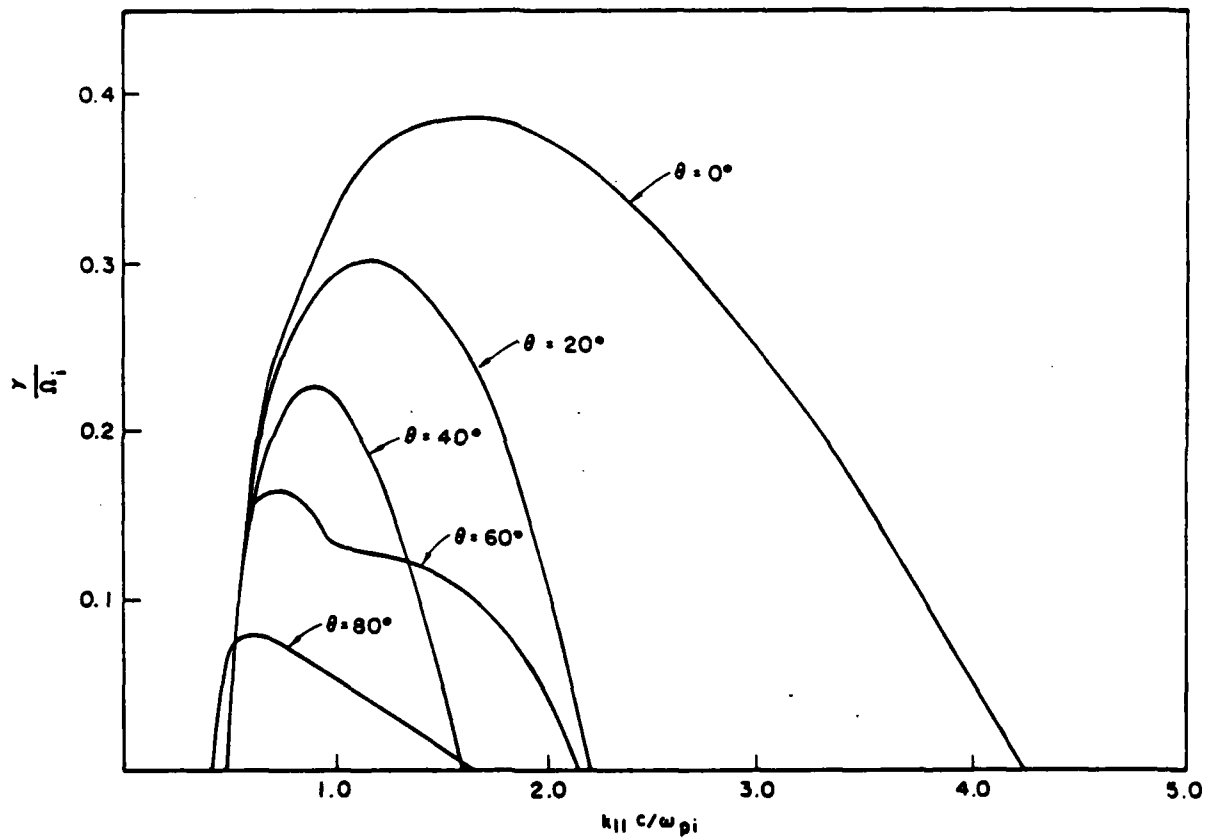


Fig. 1. Plot of  $\gamma/\Omega_i$  versus  $ck_{||}/\omega_{pi}$  for  $\theta = 0^\circ, 20^\circ, 40^\circ, 60^\circ$ , and  $80^\circ$  where  $\theta = \tan^{-1}(k_{\perp}/k_{||})$ . The other parameters used are  $\omega_{pi}/\Omega_i = 400$ ,  $m_i/m_e = 1836$ ,  $T_{ei}/T_{ii} = 20$ ,  $v_{ii} = 1.0$ , and  $T_e/T_{ii} = 0.1$ . Note that although the growth rate is a maximum for  $\theta = 0^\circ$ , it still has an appreciable value for oblique propagation.

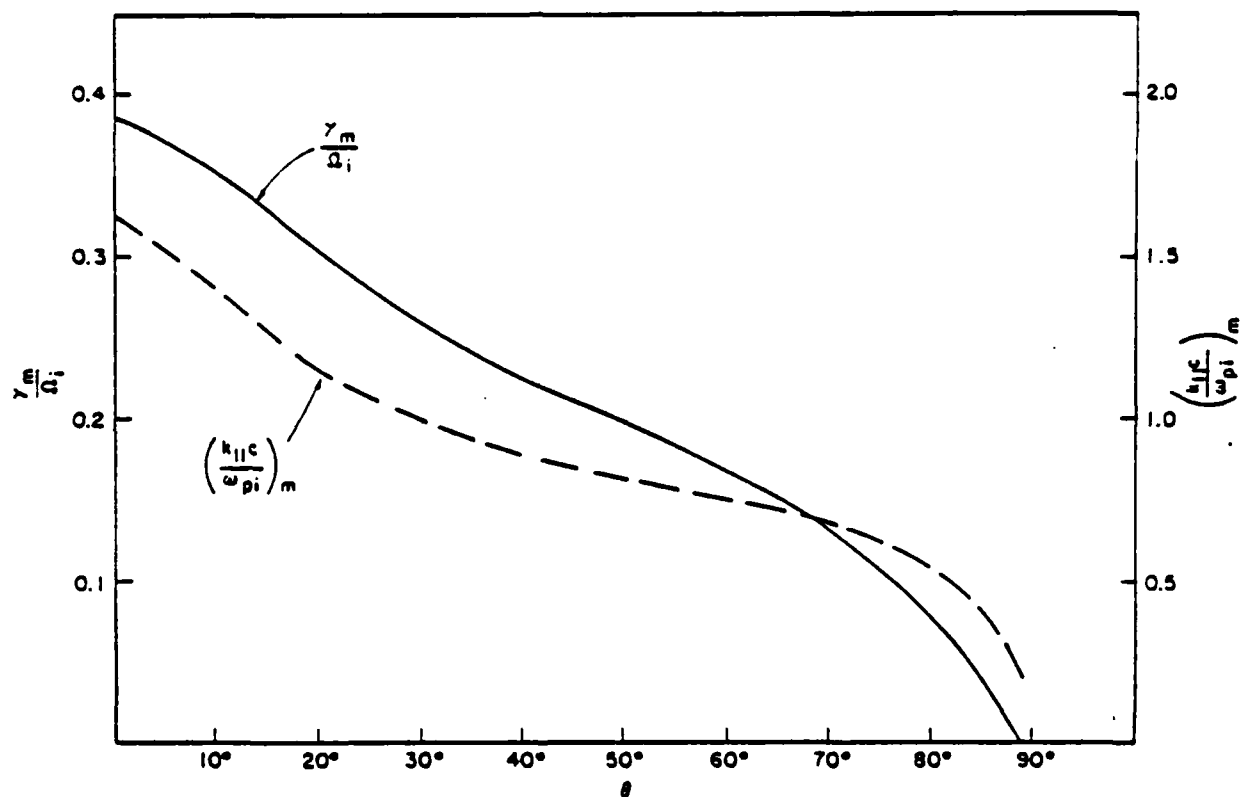


Fig. 2. Plot of  $\gamma_m/\Omega_i$  and  $ck_{||m}/\omega_{pi}$  versus  $\theta$  where  $\gamma_m$  denotes the maximum growth rate as a function of parallel wavenumber and  $k_{||m}$  is the corresponding wavenumber. The other parameters are the same as in Fig. 1.

# APPENDIX

To recover the results of Basu and Coppi (1982), we need to include the electron temperature anisotropy. This can be most simply done by changing  $H_{en}$  to

$$\bar{H}_{en} \equiv \left[ \frac{T_{le}}{T_{\parallel e}} + \frac{n\Omega_e}{\omega} \left( 1 - \frac{T_{le}}{T_{\parallel e}} \right) \right] \left[ 1 + \frac{\omega - n\Omega_e}{k_{\parallel} v_{\parallel e}} Z \left( \frac{\omega - n\Omega_e}{k_{\parallel} v_{\parallel e}} \right) \right] \quad (A1)$$

and using  $\bar{G}_{en} = \omega(\omega - n\Omega_e)^{-1}(\bar{H}_{en} - 1)$  for  $G_{en}$ . In addition, the  $M_{yy}$  element of (4) should be modified as follows

$$M_{yy} = 1 - n^2 + \frac{\omega_{pe}^2}{2\omega^2} \left( \frac{2k_{\perp}^2 v_{\perp e}^2}{\Omega_e^2} \bar{G}_{e0} + \bar{G}_{e1} + \bar{G}_{e-1} \right) + \frac{\omega_{pi}^2}{\omega \Omega_i} \frac{k_{\perp}}{k_{\parallel}} \sum \frac{n \Gamma_n}{x} H_n. \quad (A2)$$

In the low frequency long wavelength limit, the matrix elements become

$$D_{xx} = M_{xx} + n_{\parallel}^2 \bar{\alpha} = 1 + \frac{\omega_{pi}^2}{\Omega_i^2} \quad (A3a)$$

$$M_{yy} = D_{xx} - \bar{\alpha} n_{\parallel}^2 - n_{\perp}^2 (1 - \beta_{\perp 1} G_0 - \beta_{\perp e} \bar{G}_{e0}) \quad (A3b)$$

$$\bar{M}_{zy} = \frac{\omega_{pi}^2}{\omega \Omega_i} \frac{k_{\perp}}{k_{\parallel}} (\bar{H}_{e0} - H_0) \quad (A3c)$$

$$M_{xz} = M_{zx} = n_{\perp} n_{\parallel} \bar{\alpha} \quad (A3d)$$

$$D_{zz} = M_{zz} + \bar{\alpha} n_{\perp}^2 = 1 + \frac{2\omega_{pe}^2}{k_{\parallel}^2 v_{\perp e}^2} \bar{H}_{e0} + \frac{2\omega_{pi}^2}{k_{\parallel}^2 v_{\perp i}^2} H_0. \quad (A3e)$$

where  $\bar{\alpha} = 1 - (\beta_{\parallel} - \beta_{\perp})/2$ ,  $\beta_{\parallel} = \beta_{\parallel e} + \beta_{\parallel i}$ ,  $\beta_{\perp} = \beta_{\perp e} + \beta_{\perp i}$ , and  $M_{xy} = M_{yx} = 0$  as before. Focusing our attention again to the limit  $k_{\parallel} v_e \gg \omega \gg k_{\perp} v_{\parallel i}$ , we find

$$\bar{H}_{e0} = \frac{T_{\perp e}}{T_{\parallel e}} \left( 1 + i\sqrt{\pi} \frac{\omega}{k_{\parallel} v_{\parallel e}} \right). \quad (A4)$$

Hence

$$\bar{M}_{zy} = \frac{\omega_{pi}^2}{\omega \Omega_i} \frac{k_{\perp}}{k_{\parallel}} \frac{T_{\perp e}}{T_{\parallel e}} \quad (A5)$$

$$M_{yy} = D_{xx} - \bar{\alpha} n_{\parallel}^2 - n_{\perp}^2 \left( 1 + \beta_{\perp e} - \beta_{\perp e} \left( \frac{T_{\perp e}}{T_{\parallel e}} - 1 \right) \right) \quad (A6)$$

$$D_{zz} = 1 + \frac{2\omega_{pe}^2}{k_{\parallel}^2 v_{\parallel e}^2} - \frac{\omega_{pi}^2}{\omega^2}. \quad (A7)$$

Redefining  $\omega_s = k_{\parallel} v_{\parallel e} (m_e/m_i)^{1/2} = k_{\parallel} c_{s\parallel}$  to be the parallel ion sound frequency, (8) can be simplified to

$$1 - \frac{\omega_s^2}{\omega^2} = \bar{\alpha} \frac{k_{\perp}^2 \rho_{s\parallel}^2}{\frac{\omega^2}{k_{\parallel}^2 v_A^2} - \bar{\alpha}} + \frac{\beta_{\perp e}}{2} \frac{(k_{\perp}^2/k^2)(T_{\perp e}/T_{\parallel e})}{\frac{\omega^2}{k_{\parallel}^2 v_A^2} - \bar{\alpha} \frac{k_{\parallel}^2}{k^2} - [1 + \beta_{\perp i} - \beta_{\perp e} \left( \frac{T_{\perp e}}{T_{\parallel e}} - 1 \right)] \frac{k_{\perp}^2}{k^2}}, \quad (A8)$$

where  $\beta_{\perp e} = (2c_{s\parallel}^2/v_A^2)(T_{\perp e}/T_{\parallel e})$ , and  $\rho_{s\parallel}^2 = 2c_{s\parallel}^2/\Omega_i^2$ .

Due to the smallness of  $k_{\perp}^2 \rho_{s\parallel}^2$ , (A8) can be simplified by ignoring the  $k_{\perp}^2 \rho_{s\parallel}^2$  term, which results in the following coupled-mode equation

$$\left(1 - \frac{\omega_s^2}{\omega^2}\right) \left[-\frac{\omega^2}{k^2 v_A^2} - \bar{\alpha} \frac{k_{\parallel}^2}{k^2} - \left(1 + \beta_{\perp} - \frac{T_{le}}{T_{li}} \beta_{le}\right) \frac{k_{\perp}^2}{k^2}\right] = \frac{q_{le}}{2} \left(-\frac{k_{\perp}^2}{k^2}\right) \left(\frac{T_{le}}{T_{li}}\right). \quad (A9)$$

Equation (A9) corrects the algebraic error made in Basu and Coppi (1982), as well as extending their result to include ion temperature anisotropy. The instability criterion in this case is

$$k_{\parallel}^2 (c_{s\parallel}^2 + \bar{\alpha} v_A^2) + k_{\perp}^2 v_A^2 \left[1 + \beta_{li} + \beta_{le} \left(1 - \frac{T_{le}}{2T_{li}}\right)\right] < 0. \quad (A10)$$

For  $k_{\parallel}^2/k_{\perp}^2 \ll 2/\beta_{li}$ , one of the mode becomes unstable if

$$\frac{T_{le}}{T_{li}} \beta_{le} > 2(1 + \beta_{li}). \quad (A11)$$

The unstable mode is superficially similar to the wellknown MHD "mirror" instability, but since, as noted by Basu and Coppi (1982), "frozen-in condition" is not imposed, it is not identical to the mirror mode. The other mode is always stable, the reason that Basu and Coppi were able to obtain instability can be traced to the algebraic error they made.

In the other limit,  $k_{\parallel} v_{li}, k_{\parallel} v_{le} \gg \omega$ , we find

$$\bar{M}_{zy} = \frac{\omega_{pi}^2}{\omega \Omega_i} \frac{k_{\perp}}{k_{\parallel}} \left(\frac{T_{le}}{T_{li}} - \frac{T_{li}}{T_{li}}\right) \quad (A12a)$$

$$M_{yy} = D_{xx} - \bar{\alpha} n_{\parallel}^2 - n_{\perp}^2 \left[1 - \beta_{li} \left(\frac{T_{li}}{T_{li}} - 1\right) - \beta_{le} \left(\frac{T_{le}}{T_{li}} - 1\right)\right] \quad (A12b)$$

$$D_{zz} = 1 + \frac{2\omega_{pe}^2}{k_{\parallel}^2 v_{le}^2} + \frac{2\omega_{pi}^2}{k_{\parallel}^2 v_{li}^2} \quad (A12c)$$

The "firehose" branch in this case still remains the same, but the coupled-mode equation becomes

$$\left[ \frac{\omega^2}{k^2 v_A^2} - \frac{\alpha}{k^2} - \left( 1 + \beta_{\perp} - \beta_{\parallel i} \frac{T_{\parallel i}}{T_{\parallel e}} - \beta_{\perp e} \frac{T_{\perp e}}{T_{\parallel e}} \right) \frac{k_{\parallel}^2}{k^2} \right] = \frac{\beta_{\parallel e} \left( \frac{k_{\perp}^2}{k^2} \right)}{2 \left( 1 + \frac{T_{\parallel e}}{T_{\parallel i}} \right)} \left( \frac{T_{\perp e}}{T_{\parallel e}} - \frac{T_{\perp i}}{T_{\parallel i}} \right)^2. \quad (\text{A13})$$

Notice that the parallel ion-sound branch is gone because  $k_{\parallel} v_{\parallel i} \gg \omega$ , which means that both electrons and ions respond adiabatically to parallel electric field. The stability condition is given by

$$\omega^2 = v_A^2 \left[ 1 - \frac{1}{2} (\beta_{\parallel} - \beta_{\perp}) \right] k_{\parallel}^2 + v_A^2 \left[ 1 + \beta_{\perp} - \beta_{\parallel i} \frac{T_{\parallel i}}{T_{\parallel e}} - \beta_{\perp e} \frac{T_{\perp e}}{T_{\parallel e}} + \frac{\beta_{\parallel e} \left( \frac{T_{\perp e}}{T_{\parallel e}} - \frac{T_{\perp i}}{T_{\parallel i}} \right)}{2 \left( 1 + \frac{T_{\parallel e}}{T_{\parallel i}} \right)} \right] k_{\perp}^2 > 0. \quad (\text{A14})$$

For  $k_{\perp}^2/k^2 \ll 2/\beta_{\parallel}$ , the instability condition is the same as that of the MHD mirror instability (Hasegawa, 1971). Note that "frozen-in" condition is satisfied when  $k_{\parallel} v_{\parallel i}, k_{\parallel} v_{\parallel e} \gg \omega$  since the perturbed parallel electric field is completely shielded out by the parallel electron and ion adiabatic response.

## REFERENCES

- Ambrosiano, J. and S.H. Brecht, "Simulation of the Alfvén Ion Cyclotron Instability and Its Relation to a HANE," BRA Report PD-BRA-84-325R, 1984.
- Basu B. and B. Coppi, "Field-swelling Instability in Anisotropic Plasmas," Phys. Rev. Lett., 48, 799, 1982.
- Cladis, J.B., G.T. Davidson, W.E. Francis, R.K. Jaggi, G.H. Nakano, and S.L. Ossakow, "Redistribution of Trapped 55-Mev Protons by Starfish Nuclear Explosion," J. Geophys. Res., 75, 57, 1970.
- Cornwall, J.M. and J.F. Vesky, "Communications Effects of Ionospheric and Magnetospheric Plasma Injection," Jason/Mitre Report JSR-82-401, 1984.
- Davidson, R.C. and J.M. Ogden, "Electromagnetic Ion Cyclotron Instability Driven by Ion Energy Anisotropy in High-Beta Plasmas," Phys. Fl., 18, 1045, 1975.
- Filz, R.C., "Comparison of the Low-Altitude Inner-Zone 55-Mev Trapped Proton Fluxes Measured in 1965 and 1961-1962," J. Geophys. Res., 72, 959, 1967.
- Gary, S.P., M.D. Montgomery, W.C. Feldman, and D.W. Forslund, "Proton Temperature Anisotropy Instabilities in the Solar Wind," J. Geophys. Res., 81, 1241, 1976.
- Goodrich, C., K. Papadopoulos, and J.D. Huba, "Early Time Coupling Studies Using a 1D Hybrid Code," NRL Memo Report (in preparation), 1984.
- Hasegawa, A., "Plasma Instabilities in the Magnetosphere," Rev. Geophys. and Space Phys., 9, 703, 1971.



Huba, J.D., "Influence of Microturbulence on Early Time HANE Structure,"

NRL Memo Rept. 5305, 1984. ADA141244

Krall, N.A. and A.W. Trivelpiece, Principles of Plasma Physics, McGraw-Hill, New York, p. 405, 1973.

Lampe, M., W.M. Manheimer, and K. Papadopoulos, "Anomalous Transport Coefficients for HANE Applications Due to Plasma Micro-instabilities,"

NRL Memo Rept. 3076, 1975. ADA014411

Soper, G.K. and E.G. Harris, "Effect of Finite Ion and Electron Temperatures on the Ion-Cyclotron Resonance Instability," Phys. Fl., 8, 984, 1965.



**APPENDIX T**

**A Linear Model Study of Cross-Equatorial Flow  
Forced by Summer Monsoon Heat Sources**

**Keith D. Sashegyi  
Science Applications International Corporation**



A LINEAR MODEL STUDY OF CROSS-EQUATORIAL FLOW  
FORCED BY SUMMER MONSOON HEAT SOURCES

Keith D. Sashegyi

Science Applications International Corporation  
McLean, Virginia 22102

and

John E. Geisler

Department of Meteorology  
University of Utah  
Salt Lake City, Utah 84112

## ABSTRACT

A linear model of the steady response of a stratified fluid to isolated heat sources on a sphere is developed. The model is used to examine the response to diabatic heating associated with summer monsoon precipitation in India and to low-level diabatic heating along the northeast coast of Africa. In a laterally unbounded, spherical domain the summer monsoon heat source forces a cross-equatorial meridional cell that is about half as strong as the main response feature, which is a cell oriented zonally and situated on the west side of the source. The imposition of a meridional wall concentrates the cross-equatorial flow in the meridional cell into a western boundary current. For representative summer monsoon heating the northward transport in this simple East African Jet is comparable to what is observed. The cross-equatorial flow pattern forced by low-level diabatic heating along the African coast consists of a western boundary current near the equator that turns into a geostrophically balanced sea breeze in low latitudes away from the equator. The northward mass flux in this locally forced jet is about an order or magnitude smaller than that which is forced by the summer monsoon heat source.

## 1. Introduction

The cross-equatorial flow in the East African Jet (EAJ) is commonly viewed as a response to forcing by latent heat release in the Indian monsoon. Much has been learned about the structure and dynamics of the EAJ through the use of barotropic models (Anderson, 1976; Krishnamurti, et al., 1976; Hart, 1977; Bannon, 1979 a,b; Bannon, 1982). Such models have not been used to look at the EAJ and the Indian monsoon as a single dynamical system for the reason that they treat the response to forcing in which both the source and sink for the flow are prescribed. In the dynamical system of EAJ and Indian monsoon together, the sink for the low level flow is upward motion balancing latent heating. It is meaningful to prescribe this heating as a forcing function. The location and distribution of the source for low-level flow, on the other hand, is part of the response and cannot be prescribed. A further limitation on the use of barotropic models is that they cannot be used to assess the affect of local differential heating in East Africa as a source of cross-equatorial mass transport in the EAJ.

In this study, we formulate a simple model of the EAJ and Indian monsoon as a single system of motion responding to an isolated prescribed heat source in a stratified fluid on a sphere. The model is linear, it employs linear damping, and it is steady-state. It differs from other simple models of steady, monsoon-type response to tropical

heating (Webster, 1972; Gill, 1980) in that we sum over many vertical modes in order to calculate, rather than prescribe, the vertical structure of the monsoon response and the flow that constitutes the model EAJ. We also employ a variable horizontal grid point spacing to achieve necessary resolution of features having small horizontal scale.

We use the model to address a specific question that arises from the following considerations. It is possible that the EAJ is a direct response to Indian monsoon heating, by which we mean that the return flow in the upper troposphere across the equator and into a broad entrance region of the EAJ is accomplished primarily by a thermally direct overturning. There is no clear evidence for this in the upper flow pattern of Northern Hemisphere summer. Outflow from the Indian monsoon is the dominant climatological feature in the observed divergent component of the wind (cf, e.g., Krishnamurti, 1985), but the pattern is so broad in longitudinal scale as to suggest that the upper-level, cross-equatorial mass flux compensating the EAJ is accomplished through some global scale dynamics that involves the entire quasistationary wave pattern. The question arising is this: is there present, in the response to a rainfall rate representative of monsoon climatology, a meridional overturning whose mass flux is comparable to what has been observed in the EAJ? In this study we calculate the meridional overturning response using the steady, linear



model. The response is calculated first in the global domain and then in a restricted domain having a western wall that constrains cross-equatorial flow to take place in a western boundary current.

A further objective of the study is to employ the same model to assess the degree to which the EAJ is influenced by a sea-breeze type forcing arising from the existence of a mixed layer over northeast Africa that is several degrees warmer than the air mass off the coast. We treat this mesoscale forcing as a prescribed low-level heating confined to a strip between the western wall and a coastline situated to the east of it.

## 2. Model Description

The primitive equations on a sphere are linearized about a basic state of no motion in an isothermal atmosphere without topography. We are interested in the response to two different prescribed heat sources: one representing latent heat release in the summer monsoon and the other representing low-level sensible heating along the coastal strip of northeast Africa. Damping is in the form of Rayleigh friction (coefficient  $\alpha_R$ ) and Newtonian cooling (coefficient  $\alpha_T$ ) with damping times ( $\alpha^{-1}$ ) of 5 days each. The linearized equations are formulated using log pressure

for the vertical coordinate and the sine of the latitude for the latitudinal coordinate. The steady state equations are

$$\alpha_R u - 2\eta y v = - \frac{1}{a} \frac{\partial \phi}{\partial \lambda} \quad (1)$$

$$\alpha_R v + 2\eta y u = - \frac{(1-y^2)}{a} \frac{\partial \phi}{\partial y} \quad (2)$$

$$\frac{1}{a(1-y^2)} \frac{\partial u}{\partial \lambda} + \frac{1}{a} \frac{\partial v}{\partial y} + e^{z/H} \frac{\partial}{\partial z} (e^{-z/H} w) = 0 \quad (3)$$

$$\alpha_T \frac{\partial \phi}{\partial z} + N^2 w = \frac{R}{H} \frac{Q}{c_p} \quad (4)$$

where the log pressure vertical coordinate  $z = -H \log(p/p_r)$  and  $H$  is the scale height, given by  $H = RT_r/g$ . Here  $p_r = 1000$  mb and  $T_r = 300^\circ K$  are the reference surface pressure and temperature, respectively, providing a scale height of  $H = 8.8$  km. The latitudinal coordinate is  $y = \sin \theta$ , where  $\theta$  is the latitude,  $\lambda$  is the longitude in radians,  $u$  and  $v$  are the perturbation horizontal velocity components multiplied by  $\cos \theta$ ,  $w$  is the perturbation vertical motion with respect to the log pressure coordinate and  $\phi$  is the geopotential perturbation. The basic state stratification is isothermal, with  $N^2 = 1.11 \times 10^{-4} \text{ s}^{-2}$ .

A rigid lid is placed at the upper boundary of the model at a height of  $D = 22.5$  km unless otherwise stated. The rigid lid allows the solution variables and the forcing

to be expanded in a set of vertical modes, following Geisler and Stevens (1982). Then for each vertical mode a forced horizontal structure equation of the form of the shallow water equations, with different equivalent depths for each vertical mode, can be solved.

Prior to separating the vertical dependence of the variables, we introduce the variables  $U, V, \Phi$  such that

$$(u, v, \phi) = (U, V, \Phi) e^{z/2H} \quad (5)$$

and eliminate  $w$  between (3), and (4) to obtain

$$\alpha U - 2\alpha y V = - \frac{1}{a} \frac{\partial \Phi}{\partial \lambda} \quad (6)$$

$$\alpha V + 2\alpha y U = - \frac{(1-y^2)}{a} \frac{\partial \Phi}{\partial y} \quad (7)$$

$$\begin{aligned} \frac{\alpha}{N^2} \left[ \frac{\partial^2}{\partial z^2} - \frac{1}{4H^2} \right] \Phi - \left[ \frac{1}{a(1-y^2)} \frac{\partial U}{\partial \lambda} + \frac{1}{a} \frac{\partial V}{\partial y} \right] \\ = - \frac{RA(\lambda, y)}{C_p N^2 H^2} F(z) \end{aligned} \quad (8)$$

Here we have introduced the vertical forcing function  $F(z)$  given by

$$F(z) = \exp(-z/2H) \left[ B(z) - H \frac{dB}{dz} \right] \quad (9)$$

where the heating function  $Q$  has been assumed to be of the form  $Q(\lambda, y, z) = A(\lambda, y) B(z)$ . The homogeneous form of equations (6), (7) and (8) are separable, and the forcing function  $F$  and solution variables  $U$ ,  $V$  and  $\Phi$  can be expanded onto the set of vertical modes  $G_n(z)$  which satisfy the homogeneous vertical structure equation

$$\left[ \frac{d^2}{dz^2} - \frac{1}{4H^2} + \frac{N^2}{gh_n} \right] G_n(z) = 0 \quad (10)$$

with the boundary conditions

$$\left[ \frac{d}{dz} + \frac{1}{2H} \right] G_n(z) = 0 \text{ at } z = 0, D \quad (11)$$

The boundary conditions (11) express the condition that the geometric vertical velocity and the heating are zero at the surface  $z = 0$  and at the rigid lid  $z = D$  in (4).

We then write

$$(U, V, \Phi, F) = \sum_{n=0}^N (u_n, v_n, \phi_n, f_n) G_n(z) \quad (12)$$

where the amplitudes  $u_n, v_n, \phi_n$  are functions of  $\lambda$  and  $y$ , and the  $f_n$  are constants. Substituting (12) into (6), (7), (8) the equations reduce to the shallow water equations in the variable  $\lambda$  and  $y$  with differing equivalent depths  $h_n$  for each vertical mode:

$$\alpha u_n - 2\Omega y v_n = - \frac{1}{a} \frac{\partial \phi_n}{\partial \lambda} \quad (13)$$

$$\alpha v_n + 2\Omega y u_n = - \frac{(1-y^2)}{a} \frac{\partial \phi_n}{\partial y} \quad (14)$$

$$\begin{aligned} \frac{\alpha}{gh_n} \phi_n + \left[ \frac{1}{a(1-y^2)} \frac{\partial u_n}{\partial \lambda} + \frac{1}{a} \frac{\partial v_n}{\partial y} \right] \\ = \frac{R f_n A(\lambda, y)}{C_p N^2 H^2} \end{aligned} \quad (15)$$

where the amplitude  $f_n$  of the projection of the forcing function  $F$  on the  $n^{\text{th}}$  mode is given by

$$f_n = \frac{\int_0^D F(z) G_n(z) dz}{\int_0^D G_n^2(z) dz} \quad (16)$$

The vertical modes consist of one external mode  $n = 0$  and  $N-1$  internal modes. The external mode is given by

$$G_0(z) = \exp(-z/2H) \quad (17)$$

while the internal modes ( $n \neq 0$ ) are given by

$$G_n(z) = \sin \left[ \frac{n\pi z}{D} - \sigma_n \right] \quad (18)$$

with the phase  $\sigma_n = \tan^{-1} (2n\pi H/D)$ . The equivalent depth  $h_0$  in the case of the external mode is infinite, while for the internal modes the equivalent depth is given by

$$h_n = \frac{N^2 H^2}{8} \left[ \frac{1}{4} + \left( \frac{n\pi H}{D} \right)^2 \right]^{-1} \quad (19)$$

With a depth  $D = 22.5$  km, the first four internal modes have equivalent depths of 498 m, 140 m, 63 m and 36 m, respectively.

The shallow water equations (13), (14) and (15) are solved numerically by finite difference techniques. The solution technique depends on the domain used for each experiment. In the first experiment, in which the monsoon heat source is placed in a global domain without topography, the variables are further Fourier decomposed in longitude. Twenty zonal wavenumbers are used in the Fourier series for each of the variables. The shallow water equations are then only functions of the sine of latitude  $y$ . In latitude 20 grid points are used from pole to pole, with a grid separation of  $\Delta y = 0.1$ . The variables are staggered such that velocity components are defined at the grid points and the heating coefficient and geopotential are defined at the half grid points. The boundary conditions are  $u_n = v_n = 0$ . The resulting difference equations with the boundary conditions form a linear system of equations (for each zonal wavenumber and vertical mode) which are solved by matrix decomposition.

In the second and third experiments, a regional domain is used with rigid boundaries. The longitudinal domain is  $110^\circ$ . In order to resolve the flow along the western boundary and cover the large area required for the monsoon forcing, a stretched grid is used in longitude. The stretching is defined by a coordinate transformation,

$$\lambda(\xi) = \frac{L \sinh \delta \xi}{\sinh \delta} \quad (20)$$

where  $\delta = 3.0$ ,  $L = 110^\circ$  is the domain width,  $\lambda$  is the longitude in degrees and  $\xi$  is a uniform grid of 42 points separated by a distance of  $\Delta\xi = 1/42$ . This stretching provides a grid separation in longitude of  $0.5^\circ$  ( $\sim 50$  km) at the western edge of the domain and  $10^\circ$  at the eastern edge. In the  $\xi$ - $y$  space, the solution variables are staggered in an Arakawa C grid. At the rigid boundaries, the boundary conditions are given by zero normal velocity and a free-slip condition. Choice of the C grid makes the specification of these boundary conditions easy, with  $u_n = 0$  at the western and eastern boundaries and  $v_n = 0$  at the southern and northern boundaries. The resulting block matrix system is solved using the technique described by Lindzen and Kuo (1969).



### 3. Description of Heat Sources

#### a. Summer Monsoon Latent Heating

The time-averaged latent heating due to the convection over India during the summer monsoon is represented by an idealized heating function which is centered at a latitude of 24°N. The heating function is

$$Q_c(\lambda, y, p) = B_c(p) \exp \left[ - \left[ \frac{\lambda - \lambda_o}{\lambda_w} \right]^2 \right] \exp \left[ - \left[ \frac{y - y_o}{y_w} \right]^2 \right] \quad (21)$$

where  $\lambda_o$  is the longitude at the center of the heat source,  $\lambda_w = 20^\circ$  is the halfwidth in longitude,  $y_o = 0.4$  (about 24°N) is the latitude of the center of the heat source and  $y_w = 0.2$  (about 12°) is the halfwidth in latitude. The vertical dependence  $B_c(p)$ , taken from Stevens et al. (1977), is given by

$$B_c(p) = \begin{cases} Q_{co} \frac{(p-p_t)(p-p_a)(p-p_b)}{(p_m-p_t)(p_m-p_a)(p_m-p_b)} & , p_t \leq p \leq p_b \\ 0, & \text{otherwise} \end{cases} \quad (22)$$

Here  $p_t = 140$  mb is cloud top,  $p_b = 908$  mb is cloud base, and the parameter  $p_a = 932$  mb is chosen so that the heating is a maximum of  $Q_{co} = 6^\circ\text{C day}^{-1}$  at  $p_m = 400$  mb. The maximum heating rate of  $6^\circ\text{C day}^{-1}$  provides an integrated latent heating which corresponds to a rainfall rate of  $1 \text{ cm day}^{-1}$ . This vertical heating profile is illustrated in Figure 1.

b. Low Level Sensible Heating Along the East African Coastline

The diurnal-average boundary layer heating over the coastal region of Somalia and Saudi Arabia is represented by an idealized heat source centered at a latitude of  $12^\circ \text{ N}$  ( $y = 0.2$ ). The heat source has a Gaussian dependence in latitude with different halfwidths north and south of the center of the heating. In longitude the heating profile is a tanh function having a relatively constant value over a coastal strip and a sharp decrease to zero at a meridian of  $4.5^\circ$  longitude, which is the position of an idealized north-south coastline. The vertical dependence is represented by another tanh function. The total heating function is then given by

$$Q_s(\lambda, y, z) = \frac{B_s(z)}{2} \left[ 1 - \tanh \left[ \frac{\lambda - \lambda_o}{\lambda_w} \right] \right] \begin{cases} \exp \left[ - \left( \frac{y - y_o}{y_n} \right)^2 \right], & y > y_o \\ \exp \left[ - \left( \frac{y - y_o}{y_s} \right)^2 \right], & y < y_o \end{cases} \quad (23)$$

Here  $\lambda_0 = 4.5^\circ$  longitude (about 500 km east of the longitude where a western boundary wall will be situated) defines the position of the idealized north-south coastline,  $\lambda_w = 0.45^\circ$  (about 50 km) is the halfwidth of the tanh function and  $y_0 = 0.2$  ( $11.5^\circ\text{N}$ ) is the latitude of the center of the heat source. Also,  $y_n = 0.2$  ( $11.5^\circ$ ) is the halfwidth of the Gaussian north of the heating center and  $y_s = 0.1$  ( $5.7^\circ$ ) is the halfwidth to the south of the heating center. The vertical dependence  $B_s(z)$  of the heating is

$$B_s(z) = \frac{Q_{so}}{2} \left[ 1 - \tanh \left[ \frac{z-z_0}{z_w} \right] \right] I(z) \quad (24)$$

where  $z_0 = 3$  km is the center of the tanh function,  $z_w = 1$  km is the halfwidth,  $Q_{so} = 2^\circ\text{C day}^{-1}$  is the maximum heating rate, and  $I(z)$  is the Heaviside unit step function defined by

$$I(z) = \begin{cases} 1, & z > 0 \\ 0, & z = 0 \end{cases} \quad (25)$$

The unit step function ensures that the heating is zero at the surface, as required for use of the homogeneous boundary condition (11) in defining the vertical modes.

The vertical distribution of this sensible heat source is illustrated in Figure 2. The figure shows that the heating rate in the lowest kilometer is a relatively constant  $2^{\circ}\text{C day}^{-1}$  and that most of the heating is confined below 4 km elevation. The maximum heating rate of  $2^{\circ}\text{C day}^{-1}$  is chosen so that the total integrated heating rate is equivalent to a surface sensible heat flux of  $70 \text{ watts m}^{-2}$ . Such values have been observed at the surface over Saudi Arabia in the heat low during the summer months (Ackerman and Cox, 1982). The observations of the thermodynamics of the heat low reported by Blake et al. (1983) show that the boundary layer is convectively mixed from the surface to about 2 km. The potential temperature is observed to be constant from the surface to 650 mb (about 4 km), indicating dry convective mixing to this level.

The contribution of the sensible heat source given by (23) and (24) to the forcing function defined by (9) is

$$F_s(z) = I(z)F_L(z) - H L(z) \delta(z) \exp(-z/2H) \quad (26)$$

Here the vertical dependence  $B_s(z)$  of the heating in (24) has been written as

$$B_s(z) = L(z)I(z) \quad (27)$$

where  $F_L(z)$  is given by

$$F_L(z) = \exp(-z/2H) \left[ L - H \frac{dL}{dz} \right] \quad (28)$$

and  $\delta(z)$  is the Dirac Delta function. The contribution to each coefficient  $f_n$  defined by (16) by the sensible heat forcing function  $F_S$  can then be written as the sum of two parts

$$f_n = l_n + \delta_n \quad (29)$$

where  $\delta_n$  is given by

$$\delta_n = \frac{-H L(0) G_n(0)}{\int_0^D G_n^2(z) dz} \quad (30)$$

Evaluating (30) for the internal modes, as given by (18), we have

$$\delta_n = \frac{2iQ_{so}}{D} \left[ 1 + \left[ \frac{D}{2n\pi H} \right]^2 \right]^{-\frac{1}{2}} \quad (31)$$

while for the external mode ( $n = 0$ ), defined by (17), we have

$$\delta_0 = - Q_0 [1 - \exp(-D/H)]^{-1} \quad (32)$$

#### 4. Results

##### a. Experiment 1: Isolated Monsoon Forcing Without Topography

The global-domain response to the monsoon heat source described in Section 3 is calculated for the heat source centered at  $23.6^{\circ}\text{N}$  ( $y = 0.4$ ) and at an arbitrary longitude of  $180^{\circ}$ . Figure 3 shows a horizontal section at a height of 1.5 km, where the low level response is of maximum intensity. The contours show the geopotential height perturbation, and the arrows indicate the speed and direction of the wind. The figure shows a low situated north-west of the heating center, which is indicated by the letter Q, with the largest winds of some  $11 \text{ m s}^{-1}$  lying about  $10^{\circ}$  south of the low center. A high of almost identical structure (not shown here) is located in the upper troposphere. Similar solutions have been found by others (e.g., Webster, 1972; Gill, 1980) for the linearized response to localized heat sources situated off the equator. The east-west asymmetry of the response is explained by the preferred excitation of longitudinally asymmetric Rossby modes. Gill (1980) has shown that the southerly flow in the region of the heating is consistent with a linear vorticity balance in which negative advection of planetary vorticity balances the positive vorticity tendency generated by convergence.

The field of vertical motion at a height of 7.5 km, which is close to the level of maximum heating (at 400 mb), is shown in Figure 4. Upward vertical motion with a maximum intensity of  $1.4 \text{ cm s}^{-1}$  is seen to be coincident with the region of the heating, consistent with adiabatic cooling balancing the heating. Some of the compensating subsidence is concentrated west of the surface low center. A broader region of weaker subsidence occurs in the Southern Hemisphere. The longitudinal structure of this meridional overturning is illustrated in Figure 5, which shows an equatorial cross-section of meridional wind. A letter Q marks the altitude and longitude of the maximum heating, which is situated at  $23.6^\circ\text{N}$ .

We consider now the question of the relative strength of zonal versus meridional overturning. Figure 6 shows the mass flux streamfunction in the zonal plane integrated from the equator to the north pole. The stronger of the two zonal cells is situated to the west of the heating center. In Figure 7, we show the mass flux streamfunction in the meridional plane integrated around the globe. The meridional overturning south of the heat source has about half the intensity of the zonal overturning west of the heat source. The figure shows that  $22.5 \times 10^{12} \text{ g s}^{-1}$  cross the zonal plane at  $y = 0.2$  (latitude  $12^\circ\text{N}$ ). It also shows that about  $2/3$  of this mass flux, or some  $18 \times 10^{12} \text{ g s}^{-1}$ , crosses the equator from the southern hemisphere.



The mass fluxes in these cells are summarized in the schematic shown in Figure 8. Here the low level fluxes are those integrated from the surface to a height  $z = 6$  km. The global domain is divided into four regions by vertical planes at the equator and at the respective longitudes of maximum eastward and westward mass fluxes. The letters L and Q indicate the locations of the low center and the center of the heating, respectively. Labelled arrows indicate the magnitude and direction of the mass flux across each regional boundary. The compensating total vertical mass fluxes for each region are also shown. The maximum zonal mass flux ( $46.8 \times 10^{12} \text{ g s}^{-1}$ ) crossing the meridional plane at the longitude of the low center is subdivided into two parts and indicated by the two dashed arrows. Most of the mass flux crossing the equator ( $13.1 \times 10^{12} \text{ g s}^{-1}$ ) is in the region west of the low center.

b. Experiment 2: Isolated Monsoon Forcing with Western Boundary Wall

In the second experiment, a meridional wall is placed  $47^\circ$  west of the monsoon heat source of experiment 1. The domain of the model is reduced to  $110^\circ$  of longitude, and another vertical wall is placed at the eastern boundary. The eastern boundary is far enough from the heat source that it has no significant effect on the solution in the interior and along the western boundary wall. A stretched grid of 42

grid points in the longitudinal domain provides a grid resolution of  $0.45^\circ$  (about 50 km) at the western edge and about  $10^\circ$  of longitude at the eastern edge of the domain. As in the first experiment, the 20 grid points used in latitude are separated by a grid distance of  $\Delta y = 0.1$  (about  $6^\circ$  in the tropics), and 16 vertical modes are used to represent the forcing.

The response in the interior of the domain is similar to that found previously (experiment 1) in the absence of the western boundary wall, except that the maximum intensity of the low level circulation now occurs at the surface (rather than at 1.5 km) in a boundary layer flow along the western wall. In Figure 9, we show the geopotential perturbation and the wind field response at the surface in a domain that extends  $75^\circ$  out from near the western boundary. As in the first experiment, a low is situated north-west of the heating center (indicated by the letter Q) and a low level westerly wind maximum of  $10 \text{ m s}^{-1}$  is found south of the low center. The response of the trades in the interior of the domain south of the equator is somewhat stronger in the present experiment, with maximum velocities of  $2 \text{ m s}^{-1}$  (compared to  $1 \text{ m s}^{-1}$  without the wall).

Along the western boundary there is low-level flow concentrated into boundary jets: a northerly jet at the latitude of the low and a southerly jet crossing the equator. These jets separate from the western boundary at

around  $14^{\circ}\text{N}$  ( $y = 0.25$ ) and merge to give a broad westerly jet flowing into the region of the heat source. The abrupt separation of these jets is also a feature of barotropic models of the East African Jet (Anderson, 1976; Bannon, 1982). The observed jet exhibits a more gradual turning away from the topographic barrier of the East African highlands (see, e.g., Findlater, 1977).

The southerly jet is illustrated in more detail in Figure 10. The maximum speed is at the equator. Figure 11 shows a vertical cross-section through the jet at the equator. It can be seen that the vertical structure of this western boundary response consists of a counter jet aloft that has the same horizontal scale as the low-level jet. The velocity is seen to decrease in an exponential fashion away from the boundary, as expected for a linear damping, western boundary layer. In fact, for such damping, the e-folding width of the jet is given by  $\alpha/\beta$ , where  $\alpha$  is the coefficient of Rayleigh friction and  $\beta$  is the latitudinal derivative of the Coriolis parameter (see, e.g., Stommel, 1948). For a damping time ( $\alpha^{-1}$ ) of 5 days this gives a width of 102 km, in agreement with the model result shown in Figure 11.

As previously done for the experiment in the global domain, the mass flux streamfunction was computed and integrated over various sections of the regional domain. The zonal-plane mass flux streamfunction integrated from the

equator to the pole (not shown) has the same structure as that shown in Figure 6 for the global-domain, distinguished from it only by close packing of streamfunction contours along the western boundary. The overturning in the meridional plane is stronger in this experiment by some 50 percent, with an intensity of some  $32 \times 10^{12} \text{ g s}^{-1}$ .

Figure 12 summarizes, in the format of Figure 8, the mass fluxes in this experiment. In the region west of the low center, the mass flux crossing the equator is further partitioned by a broken line into a part occurring within  $5^\circ$  of the boundary and a remainder. The figure shows that the mass flux crossing the equator within  $27^\circ$  of the boundary is some  $22 \times 10^{12} \text{ g s}^{-1}$ . A weak cross-equatorial flow in the interior contributes only a further  $2.5 \times 10^{12} \text{ g s}^{-1}$  to the total mass flux crossing the equator. Of the subsiding mass flux balancing the upward transport in the region of the heating, the largest amount now occurs in the Southern Hemisphere. The effect of the western boundary wall has thus been to increase the subsidence in the Southern Hemisphere and hence the meridional overturning at the expense of the zonal overturning.

c. Experiment 3: Sensible Heating Adjacent to Western Boundary Wall

In this experiment the localized sensible heat source described in Section 3 is placed north of the equator adjacent to the western boundary wall. It is centered at a latitude of  $11.5^{\circ}$  N ( $y = 0.2$ ). This heat source, with a maximum heating rate of  $2^{\circ}\text{C day}^{-1}$  near the surface, represents an idealized differential sensible heating contrast across a meridional coastline situated about 500 km from the western boundary. To adequately resolve this sensible heat source, the latitudinal and vertical resolution is increased in this experiment. To achieve the increased vertical resolution, the model lid is lowered to 11.25 km and the number of vertical modes used is increased to 46, giving a vertical wavelength of 500 meters for the highest mode. A latitudinal grid separation of  $\Delta y = 0.05$  (about  $3^{\circ}$  in the tropics) is used over a reduced latitudinal domain extending from a southern wall at  $17.5^{\circ}$  S ( $y = -0.3$ ) to a northern wall at  $44.4^{\circ}$  N ( $y = 0.7$ ). The boundary condition is one of no flow across these boundaries.

The horizontal distribution of this sensible heating is illustrated in Figure 13. The maximum heating rate of  $2^{\circ}\text{C day}^{-1}$  occurs at a latitude of  $11.5^{\circ}$  N, close to the latitude of the maximum temperature gradient observed during the summer months across the coastline of Somalia (Newell et al., 1974). The heating is maximum at the western boundary

and relatively constant in longitude from the western boundary to near the coastline, where it decreases rapidly in magnitude following a tanh function (see Equation (23)). In the vertical, the heating is essentially confined to the lowest 4 km of the atmosphere, as was shown in Figure 2.

Figure 14 shows the surface horizontal wind field that occurs in response to the sensible heating. There is a low adjacent to the western boundary centered at a latitude of  $16^{\circ}\text{N}$  ( $y = 0.275$ ) indicated in the figure by the letter L. This position is close to that of the Saudi Arabian heat low (van de Boogaard, 1977). The latitude of the maximum heating of  $2^{\circ}\text{C day}^{-1}$  is also indicated by the letter Q in the figure. An easterly flow of about  $4\text{ m s}^{-1}$  along the equator merges into a southerly jet flowing northward across the equator. This low level jet separates from the western boundary around  $9^{\circ}\text{N}$  ( $y = 0.15$ ) to then flow northward along the coastline. The maximum velocity of about  $40\text{ m s}^{-1}$  in the jet at the surface occurs just to the north of the equator at  $3^{\circ}\text{N}$  ( $y = 0.05$ ). Along the coastline, the surface flow in the low level jet forced by this sensible heat source reaches a secondary peak of  $15\text{ m s}^{-1}$  southeast of the low center around  $14^{\circ}\text{N}$  ( $y = 0.25$ ). Upward vertical motion (not shown) balances the heating, with rising motion reaching a maximum of  $0.5\text{ cm s}^{-1}$  in the region of maximum heating. Weaker subsidence occurs in a broad band along the

equator in the region of the low level easterly flow shown in Figure 14.

In Figure 15a, we show a zonal cross-section at the equator of this low-level jet and its upper-level counter jet. Figure 15b is a corresponding cross-section at latitude  $11.5^{\circ}\text{N}$  ( $y = 0.2$ ), the latitude of maximum heating. In these figures, the position of the coastline is indicated by the letter C. At the equator, the low level jet is along the western boundary and has a maximum southerly velocity of  $28 \text{ m s}^{-1}$  at the surface. At latitude  $11.5^{\circ}\text{N}$ , the low level jet is centered on the coastline, with the jet reaching a maximum velocity of  $15 \text{ m s}^{-1}$  at the surface. At all latitudes, the low level jet is confined below 1.5 km in elevation, inside the layer where the heating has a relatively constant magnitude of  $2^{\circ}\text{C day}^{-1}$  (see Figure 2). Above the low level jet, the counter-jet of similar structure is an order of magnitude weaker in intensity, but has greater vertical extent. In Figures 16 a and b we show cross-sections of the zonal flow at the equator and latitude  $11.5^{\circ}\text{N}$ . As in the previous figures, the position of the coastline is indicated by the letter C. The zonal flow at both latitudes is an order of magnitude less than the meridional flow. At the equator, low level easterlies reaching  $4 \text{ m s}^{-1}$  are seen centered at the coastline with weaker, but deeper, westerlies situated above. At the latitude of maximum heating (Figure 16b), weak low level

easterlies lie offshore and do not penetrate across the coastline. Stronger low level westerlies are found inland with a maximum of  $1.5 \text{ m s}^{-1}$  at the surface. The confluence of the westerly and easterly low level flow feed the upward vertical motion balancing the heating.

As in the other experiments, the circulation here can be described by overturnings in the meridional plane and in the zonal plane. The meridional overturning is confined to a narrow region along the western boundary. Due to the shallow nature of the circulation, the mass flux that crosses the equator in the low level jet forced by our sensible heat source is small, only some  $1.8 \times 10^{12} \text{ g s}^{-1}$ . This is an order of magnitude less than that in the jet forced by the monsoon heat source.

To test the sensitivity of our response to the depth of the heating, several runs were made using the same magnitude for the heat source  $Q_{SO}$ , but varying the parameter  $z_0$  in (24) over a range from 1 to 5 km. The horizontal pattern and the amplitude of the maximum wind speed were not too sensitive to such changes in the depth of the heating, but the zero wind level changed in such a way that the counter jet was centered at the height  $z_0$  in all cases.

In a further experiment, the orientation of the coastline was also changed to one more closely matching that of the Somalia and East African coasts. In this case, the heating was assumed to have the same latitudinal and



vertical variation as described above. In longitude, however, the heating was constant from the western boundary out to a coastline inclined from southwest to northeast at an angle of  $35.5^\circ$  to the western boundary. The response was similar to that found above for the meridional coastline, though more intense. The maximum velocity occurring in the low level jet was about  $60 \text{ m s}^{-1}$  just north of the equator along the western boundary, and the secondary maximum of  $12.5 \text{ m s}^{-1}$  occurred at the coastline at latitude  $14.5^\circ\text{N}$ .

The circulation we have just described above is more complicated than a usual sea breeze circulation. In order to contrast the two, a supplementary experiment was carried out in which the Coriolis parameter  $2\Omega y$  in the model was replaced by its value at latitude  $11.5^\circ \text{ N}$  ( $y = 0.2$ ). The response was then found for the same heating distribution that was shown in Figures 2 and 13. The response at the latitude of maximum heating is illustrated in Figures 17 a and b, which show cross-sections of the meridional and zonal wind. In Figure 17a, the meridional wind shows a low level southerly jet with a maximum velocity of  $16 \text{ m s}^{-1}$  centered over the coastline (which is indicated by the letter C in the figure). The northward mass flux here is exactly balanced by the mass flux in the counter flow aloft. These jets are of similar magnitude and position to those shown in Figure 15b, where the Coriolis parameter varies with latitude, but in that experiment this sea breeze jet pair

blended with the pair of jets associated with the western boundary wall. The associated zonal wind pattern (Figure 15a) is considerably more complicated than the simple on-shore component of the sea-breeze circulation shown in Figure 17b.

## 5. Summary and Conclusions

Here we have presented the results of three experiments using a steady, linear model of the response of a stratified fluid on a sphere to an isolated heat source. Forcing in the first experiment was by means of a heat source having a spatial distribution and amplitude representative of condensational heating in the summer monsoon. The second experiment differed from the first in having a rigid wall imposed along a meridian west of the heat source. In the third experiment, the monsoon heating was replaced by a source intended to represent low-level heating over a meridional strip of land situated between the meridional wall and an ocean which exchanges no heat with the atmosphere.

The main feature of the response in the first experiment was a zonal overturning on the west side of the heat source. Of comparable significance was a meridional overturning extending southward from the heat source into the Southern Hemisphere. The mass flux in this cell was about half that in the zonal cell. For a heating amplitude scaled to a  $1 \text{ cm day}^{-1}$  maximum precipitation rate in the summer monsoon, the cross-equatorial mass flux in the meridional cell was  $18 \times 10^{12} \text{ g s}^{-1}$ . With the addition of the wall along a meridian west of the heat source (experiment two), the cross-equatorial mass flux was

concentrated into a western boundary current and was increased by a small amount to  $22 \times 10^{12} \text{ g s}^{-1}$ .

A cross-equatorial jet also characterized the response in experiment three, where the only forcing was low-level differential heating across a meridional coastline situated east of the wall. This jet was a western boundary current at the equator, but migrated away from the wall to become a geostrophically balanced sea breeze at higher tropical latitudes. For low-level heating of  $2^\circ\text{C day}^{-1}$  mixed through the lowest 2.5 km, the maximum windspeed in this jet near the equator was very nearly equal to that in the jet forced by monsoon heating alone (experiment two). Because of the small vertical scale of the low-level heating jet, it carried a cross-equatorial mass flux of only  $1.8 \times 10^{12} \text{ g s}^{-1}$ . This is an order of magnitude smaller than the mass flux carried by the monsoon heating jet.

From an analysis of observational data Findlater (1969) deduced a figure of  $89 \times 10^{12} \text{ g s}^{-1}$  for the northward flux of mass across the equator between longitudes  $35^\circ\text{E}$  and  $75^\circ\text{E}$  during the month of July. The model flux of  $22 \times 10^{12} \text{ g s}^{-1}$  is a factor of four smaller than this figure. This is reduced to a factor of two if we adopt the still-reasonable amplitude of  $2 \text{ cm day}^{-1}$  precipitation rate in the summer monsoon. Adopting this forcing amplitude and noting that the model dissipation (damping time of 5 days) is quite large, we conclude that there is less than a factor of two

discrepancy between observed and model cross-equatorial mass flux. Such agreement in this crude model study supports the hypothesis that a thermally direct meridional overturning is a sufficient mechanism for providing the mass flux carried across the equator by the EAJ.

A firmer conclusion coming from this model study is that the additional cross-equatorial mass forced by low-level differential heating across the east coast of Africa is small. The resulting jet was of very small vertical scale, with a zero wind level well within the heated layer. The maximum wind speed in this jet was, however, comparable to that in the monsoon-heating jet. This suggests that flow in the lowest few hundred meters of the EAJ can be strongly influenced by a flow driven by low-level differential heating.

### Acknowledgments

This work represents part of the first author's requirements for the degree of Doctor of Philosophy at the University of Miami. The research was supported by the National Science Foundation through grant ATM-79-15225. The numerical computations and graphics were performed at the National Center for Atmospheric Research, which is sponsored by the National Science Foundation. Ms. J. Staudinger typed the manuscript.

## REFERENCES

- Ackerman, S.A., and S.K. Cox, 1982: The Saudi Arabian heat low: Aerosol distributions and thermodynamic structure. *J. Geophys. Res.*, 87, 8991-9002.
- Anderson, D.L.T., 1976: The low level jet as a western boundary current. *Mon. Wea. Rev.*, 104, 907-921.
- Bannon, P.R., 1979a: On the dynamics of the East African Jet. I. Simulation of mean conditions for July. *J. Atmos. Sci.*, 36, 2139-2152.
- , 1979b: On the dynamics of the East African Jet II. Jet transients. *J. Atmos. Sci.*, 36, 2153-2168.
- , 1982: On the dynamics of the East African Jet. III. Arabian Sea Branch. *J. Atmos. Sci.*, 39, 2267-2278.
- Blake, D.W., T.N. Krishnamurti, S.V. Low-Nam, and J.S. Fein, 1983: Heat low over the Saudi Arabian desert during May 1979 (Summer MONEX). *Mon. Wea. Rev.*, 111, 1759-1775.
- Findlater, J., 1969: Interhemispheric transport of air in the lower troposphere over the western Indian Ocean. *Quart. J. Roy. Meteor. Soc.*, 95, 400-403.
- , 1977: Observational aspects of the low-level cross-equatorial jet stream of the Western Indian Ocean, *Pure Appl. Geophys.*, 115, 1263-1282.
- Geisler, J.E., and D.E. Stevens, 1982: On the vertical structure of damped steady circulation in the tropics. *Quart. J. Roy. Meteor. Soc.*, 108, 87-93.

- Gill, A.E., 1980: Some simple solutions for heat-induced tropical circulation. Quart. J. Roy. Meteor. Soc., 106, 447-462.
- Hart, J.E., 1977: On the theory of the East African low-level jet stream. Pure. Appl. Geophys. 115, 1263-1282.
- Krishnamurti, T.N., 1985: Summer monsoon experiment - a review. Mon. Wea. Rev., 113, 1540-1626.
- , J. Molinari and H.-L. Pan, 1976: Numerical Simulation of the Somali Jet. J. Atmos. Sci. 33, 2350-2362.
- Lindzen, R.S., and H.L. Kuo, 1969: Reliable method for numerical integration of a large class of ordinary and partial differential equations. Mon. Wea. Rev. 97, 732-734.
- Newell, R.E., J.W. Kidson, D.G. Vincent and G.J. Boer, 1974: The General Circulation of the Tropical Atmosphere, Vol. 2, The MIT Press, 371 pp.
- Stevens, D.E., R. S. Lindzen and L.J. Shapiro, 1977: A new model of tropical waves incorporating momentum mixing by cumulus convection. Dyn. Atmos. Oceans 1, 365-425.
- Stommel, H., 1948: The westward intensification of wind driven ocean currents. Trans. Amer. Geophys. Union 29, 202-206.



van de Boogaard, H., 1977: The mean circulation of the tropical and subtropical atmosphere in July. NCAR Tech. Note, NCAR/TN-118+STR, 48 pp.

Webster, P.J., 1972: Response of the tropical atmosphere to local steady forcing. Mon. Wea. Rev. 100, 518-541.

# FIGURE CAPTIONS

- Fig. 1. The vertical distribution of the monsoon latent heating in  $^{\circ}\text{C day}^{-1}$ .
- Fig. 2. The vertical distribution of the low-level sensible heating in  $^{\circ}\text{C day}^{-1}$ .
- Fig. 3. The contours of geopotential (in units of  $10^5 \text{ cm}^2 \text{ s}^{-2}$ ) and the wind field at  $z = 1.5 \text{ km}$ . Contours every  $25 \times 10^5 \text{ cm}^2 \text{ s}^{-2}$ . The maximum wind vector of  $11 \text{ m s}^{-1}$  is indicated, and the smallest vector plotted is  $1 \text{ m s}^{-1}$ . The center of the heat source is indicated by the letter Q. Along the latitude axis the tick marks show the grid points.
- Fig. 4. The contours of vertical velocity in  $\text{cm s}^{-1}$  at  $z = 7.5 \text{ km}$ . Contours every  $0.2 \text{ cm s}^{-1}$ . Q indicates the heating center as in Fig. 3.
- Fig. 5. A cross-section of the meridional wind (in  $\text{m s}^{-1}$ ) along the equator. Contours every  $0.1 \text{ m s}^{-1}$ . The tick marks are placed every  $9^{\circ}$  in longitude and every  $1.5 \text{ km}$  in  $z$ . Q indicates the height and longitude of maximum heating.
- Fig. 6. Contours of the zonal mass flux (in units of  $10^{12} \text{ g s}^{-1}$ ) integrated from the equator to the north pole. Contours every  $5 \times 10^{12} \text{ g s}^{-1}$ . Q

indicates the height and longitude of maximum heating as in Fig. 5.

Fig. 7. Contours of the meridional mass flux integrated around the globe (in units of  $10^{12} \text{ g s}^{-1}$ ). Contours every  $2.5 \times 10^{12} \text{ g s}^{-1}$ . Latitudinal grid points are indicated.

Fig. 8. A schematic of the low level mass flux balances in several boxes bounded by the equator, longitudes  $162^\circ$ ,  $225^\circ$  and  $360^\circ$  and the north and south pole. The boxes are bounded above at  $z = 6 \text{ km}$ . The large arrows indicate the mass fluxes (in units of  $10^{12} \text{ g s}^{-1}$ ) crossing a particular boundary. The quantities inside each box represent the mass flux leaving the box at  $z = 6 \text{ km}$ .

Fig. 9. The contours of geopotential (in units of  $10^5 \text{ cm}^2 \text{ s}^{-2}$ ) and the wind field at  $z = 0 \text{ km}$  in the limited longitudinal domain. Contours every  $20 \times 10^5 \text{ cm}^2 \text{ s}^{-2}$ . The magnitude of the wind vectors is indicated by the labelled arrow (of  $15 \text{ m s}^{-1}$ ). The grid points are indicated by the inner tick marks. The longitude is measured in degrees from the rigid western boundary at  $0^\circ$ . Lower tick marks are placed every  $5^\circ$  of longitude. Q indicates the center of the heating.

- Fig. 10. The horizontal wind field in the western boundary region and the equator at  $z = 0$  km. The magnitude of the wind vectors is indicated by the labelled arrow (of  $40 \text{ m s}^{-1}$ ). The rigid western boundary is at longitude  $0^\circ$ .
- Fig. 11. A cross-section of the meridional wind (in  $\text{m s}^{-1}$ ) along the equator in the western boundary region. Contour intervals are  $5 \text{ m s}^{-1}$ . The longitude is measured in degrees from the western boundary.
- Fig. 12. A schematic of the low-level mass flux balances in several boxes bounded by the equator, longitude  $27^\circ$  and  $76^\circ$  and the domain boundaries. The boxes are bounded above at  $z = 6$  km. The large arrows indicate the mass fluxes (in units of  $10^{12} \text{ g s}^{-1}$ ) crossing a particular boundary. The quantities inside each box represent the mass flux leaving the box at  $z = 6$  km.
- Fig. 13. The horizontal distribution of the maximum low-level sensible heating (in  $^\circ\text{C day}^{-1}$ ) just above the surface. The inner tick marks show the grid points while the lower tick marks in the longitude scale are shown every  $1^\circ$  longitude measured from the rigid western boundary.
- Fig. 14. The wind field at  $z = 0$  km. The magnitude of the wind vectors is indicated by the labelled arrow.

- Fig. 15a. Cross-section of the meridional wind (in  $\text{m s}^{-1}$ ) in the western boundary region at the equator. Contours start every  $2 \text{ m s}^{-1}$ , becoming every  $4 \text{ m s}^{-1}$ . The upper tick marks on the longitude scale show the grid points while the lower tick marks are placed at every degree of longitude. The letter C shows the position of the coastline.
- Fig. 15b. As in (a) except at a latitude of  $11.5^\circ\text{N}$  ( $y = 0.2$ ) and contours every  $2 \text{ m s}^{-1}$ .
- Fig. 16a. As in Fig. 15a but for the zonal wind at the equator and contours every  $0.5 \text{ m s}^{-1}$ .
- Fig. 16b. As in Fig. 15b except for the zonal wind at a latitude at  $11.5^\circ\text{N}$  and contours every  $0.25 \text{ m s}^{-1}$ .
- Fig. 17a. Cross-section of the meridional wind (in  $\text{m s}^{-1}$ ) in the western boundary region at a latitude of  $11.5^\circ\text{N}$  ( $y = 0.2$ ) in the case of a constant Coriolis parameter (given by the Coriolis parameter at  $11.5^\circ\text{N}$ ). Contours every  $2 \text{ m s}^{-1}$ . The scales are as in Fig. 15a.
- Fig. 17b. As in (a) except for the zonal wind and contours every  $0.25 \text{ m s}^{-1}$ .



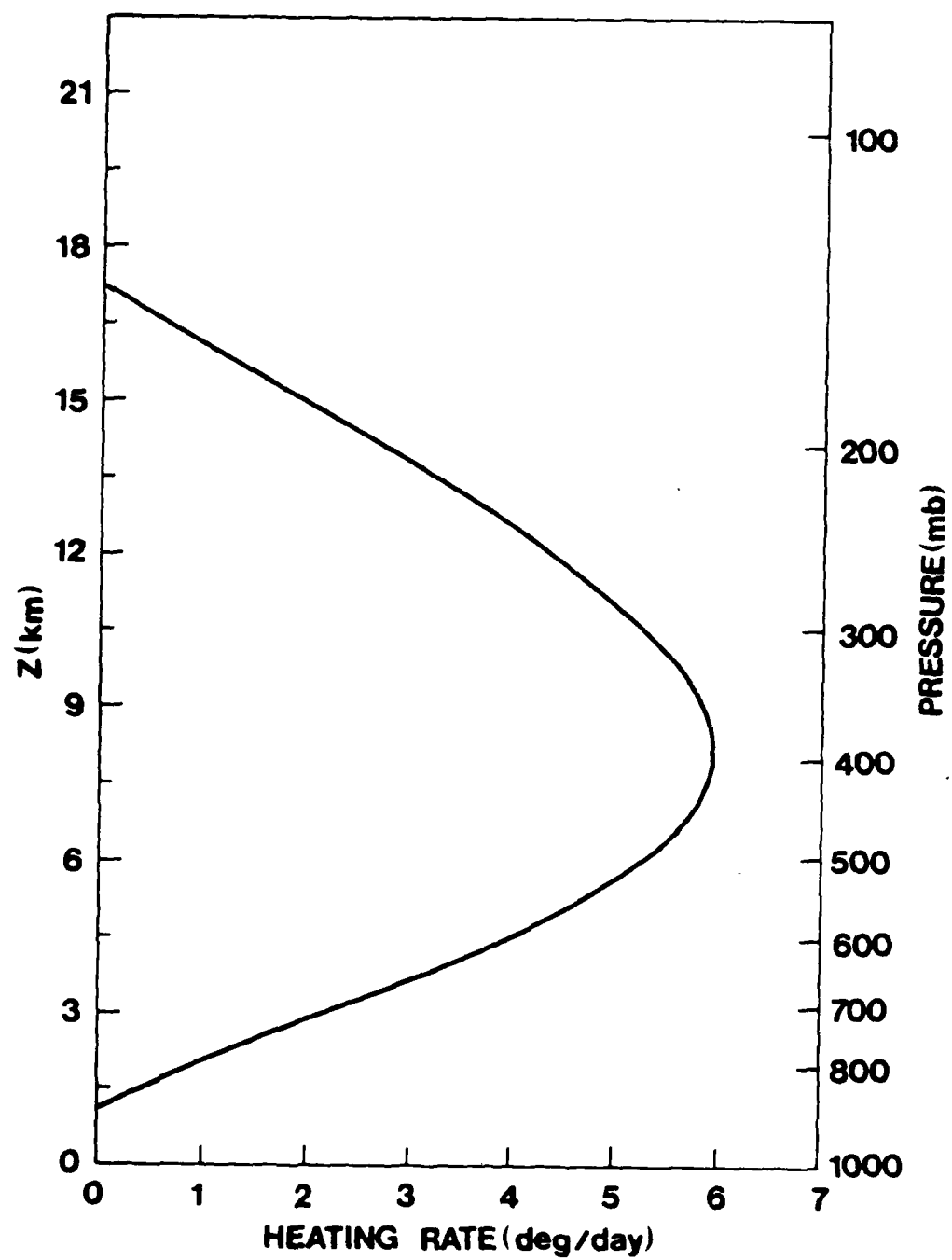


Fig. 1

T-45

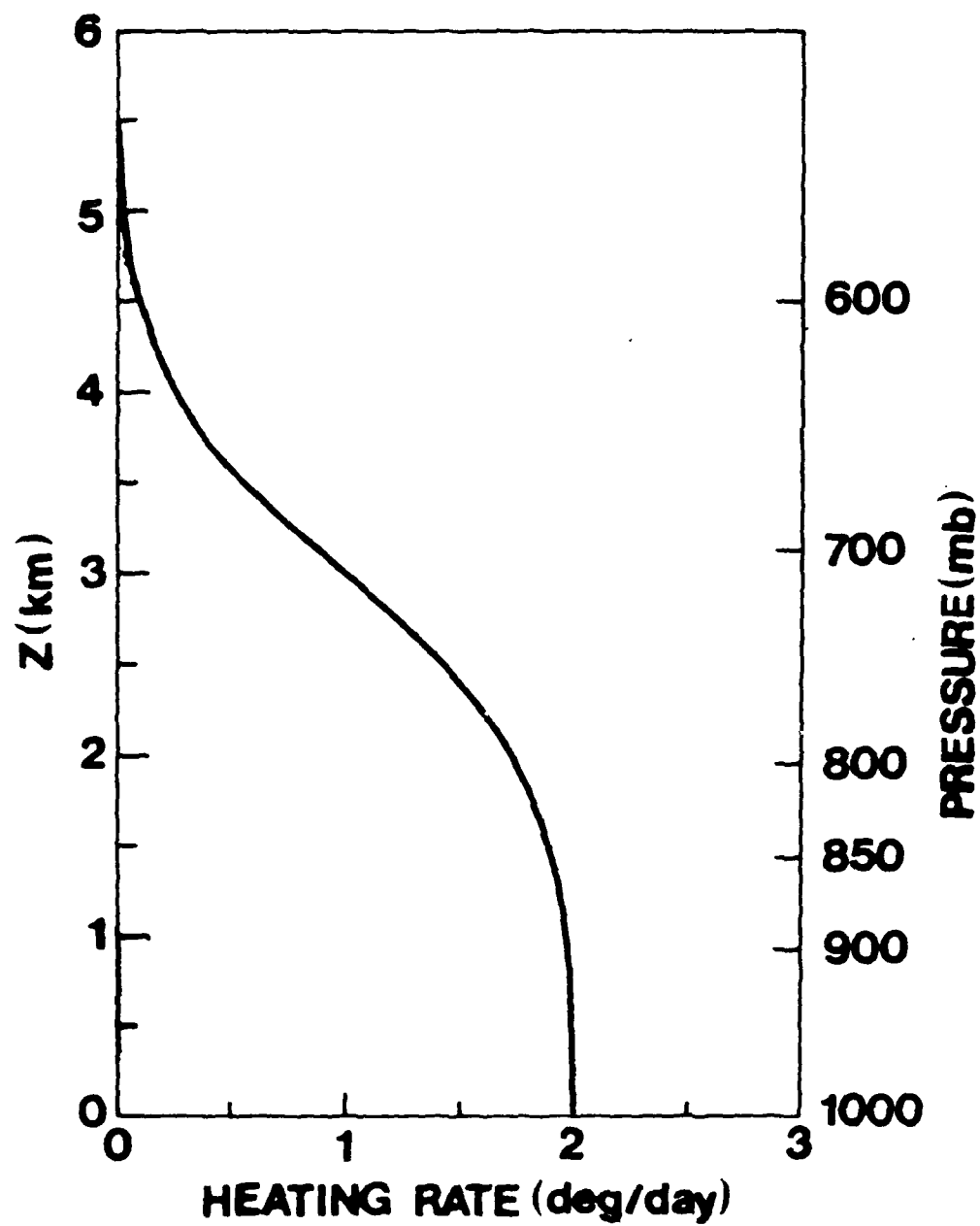


Fig. 2



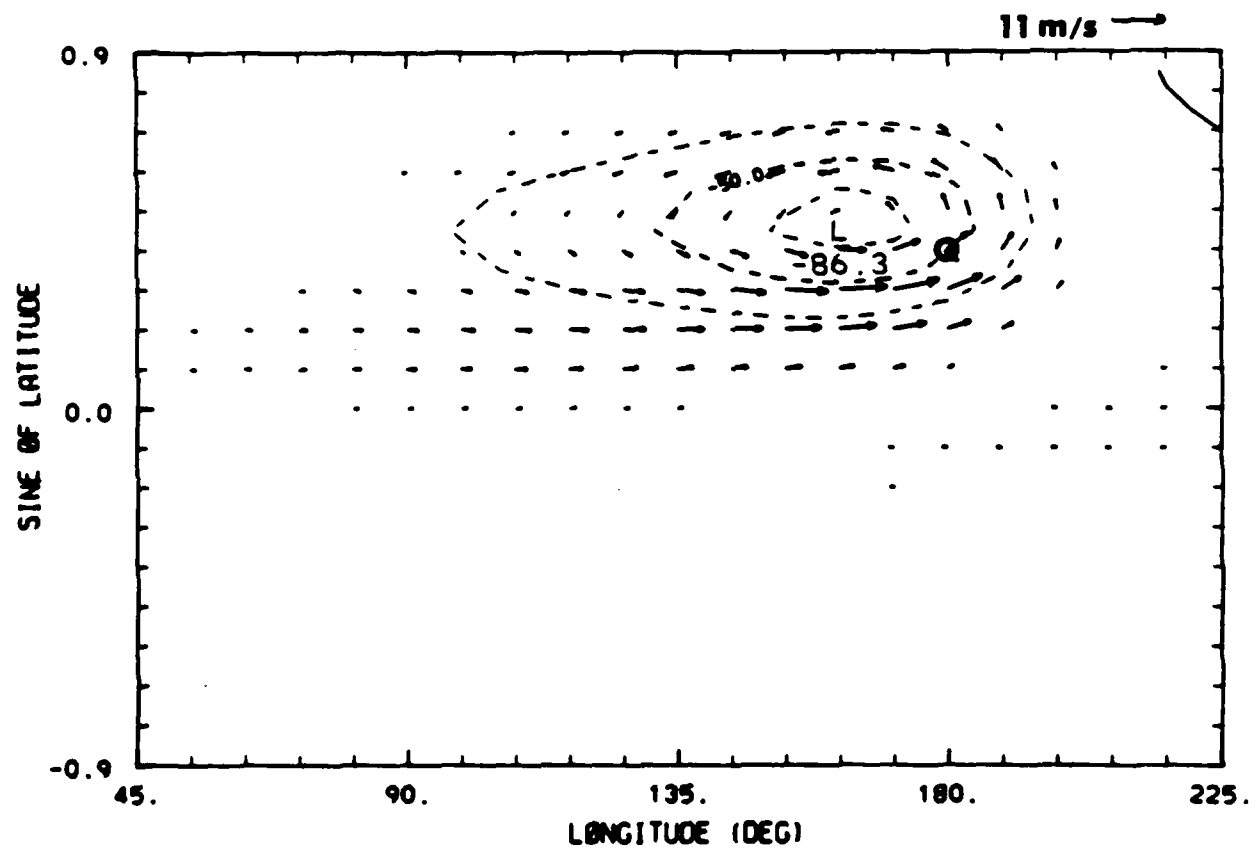


Fig. 3

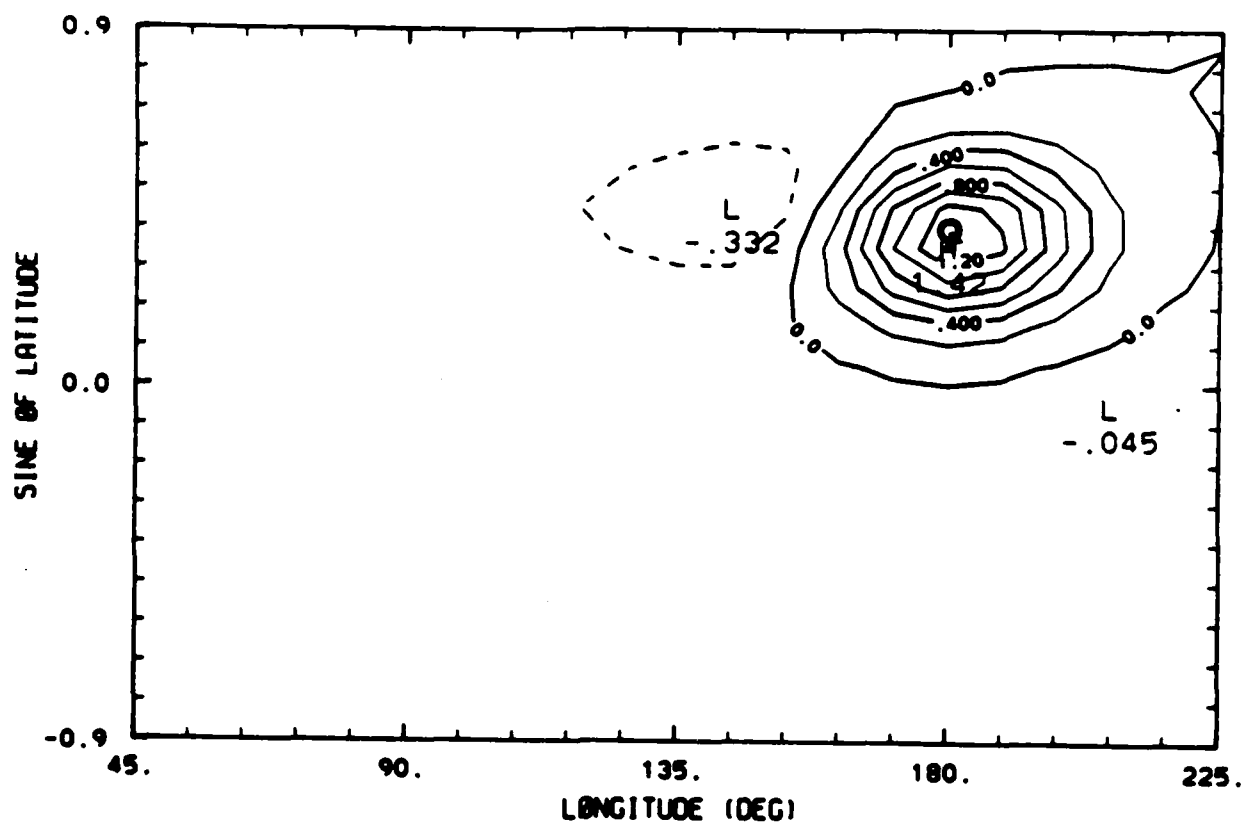


Fig. 4

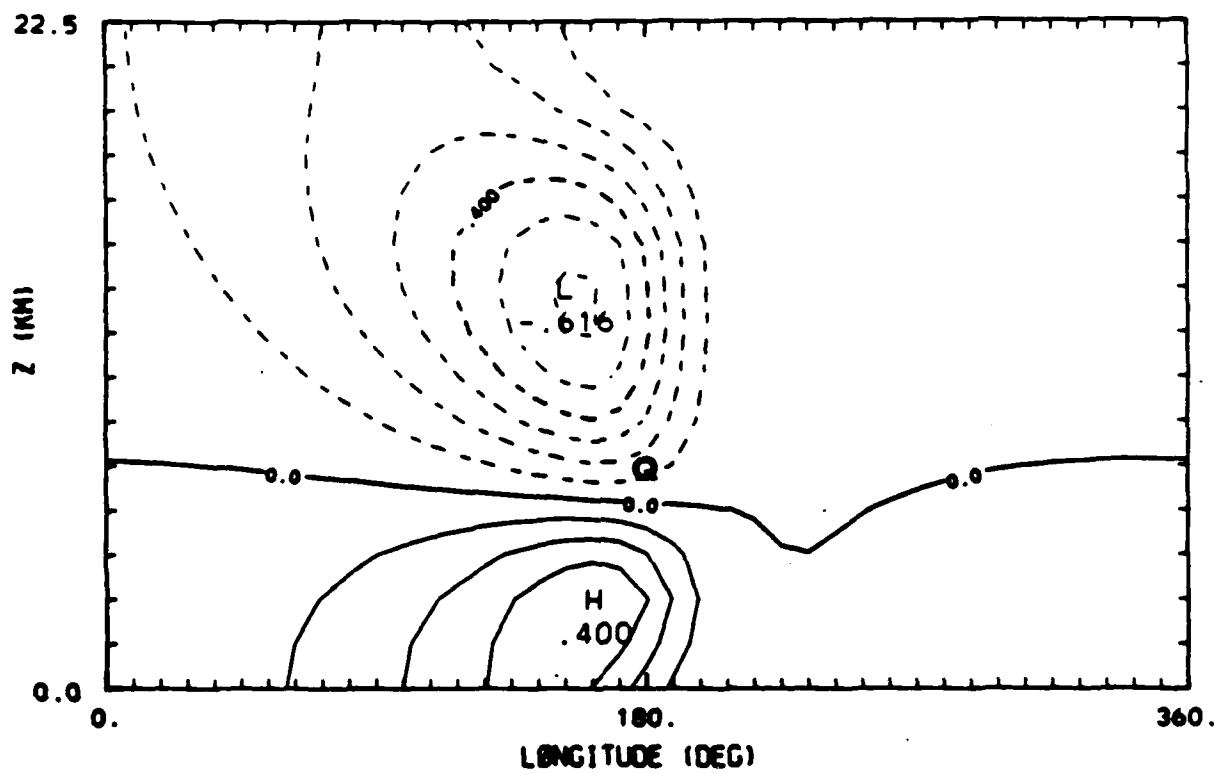


Fig. 5

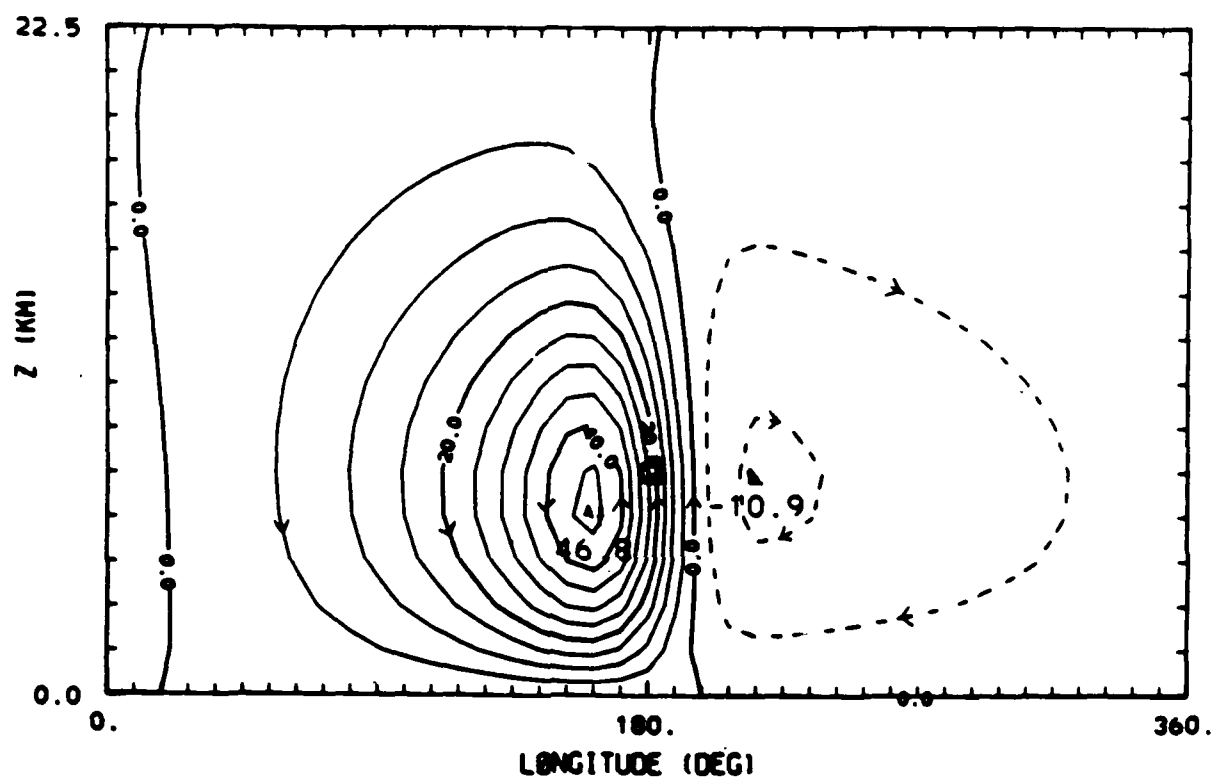


Fig. 6

T-50

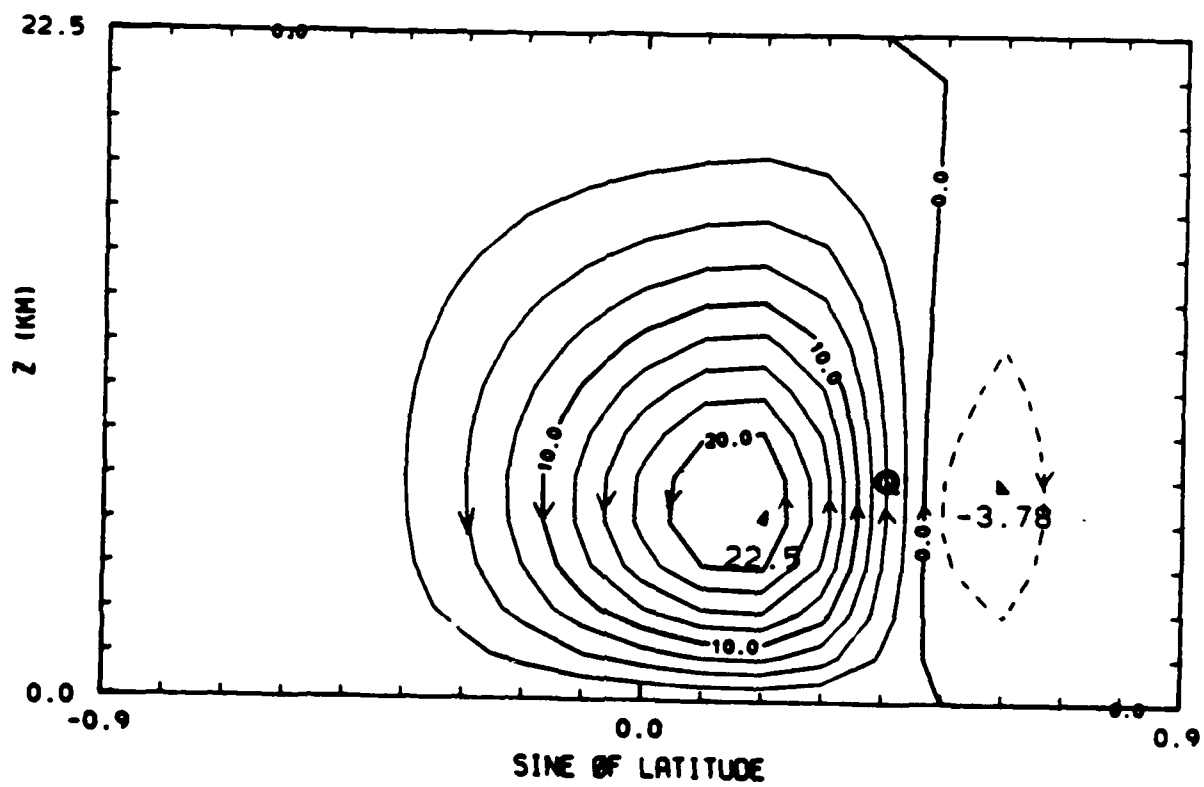


Fig. 7

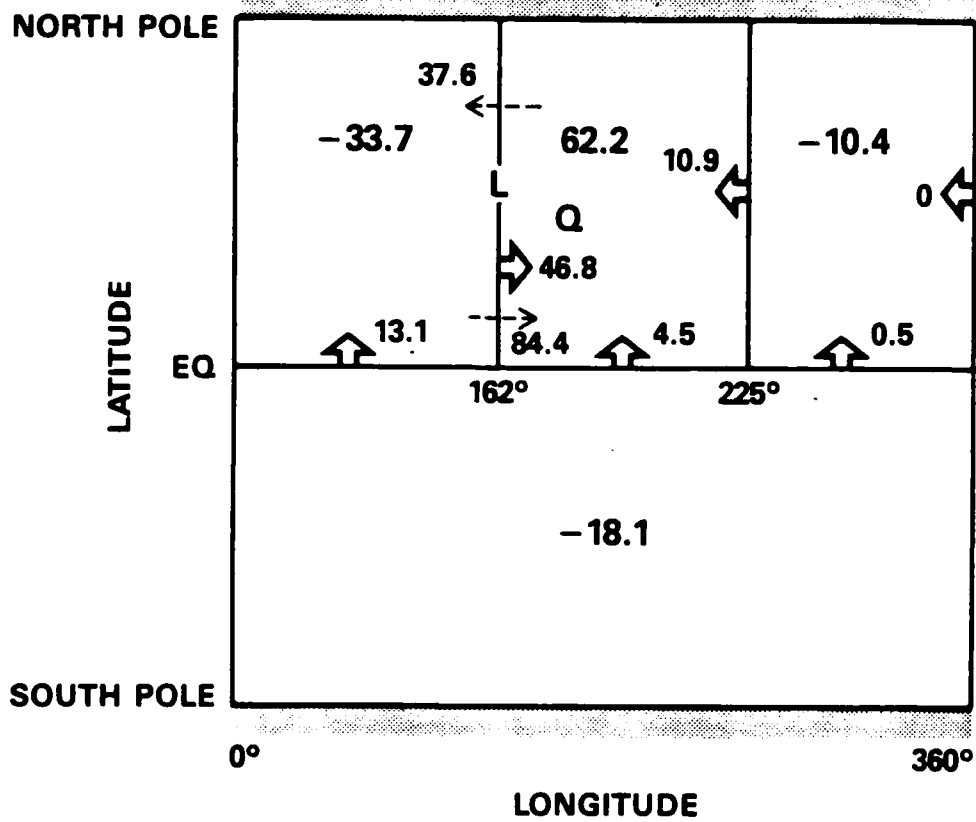


Fig. 8

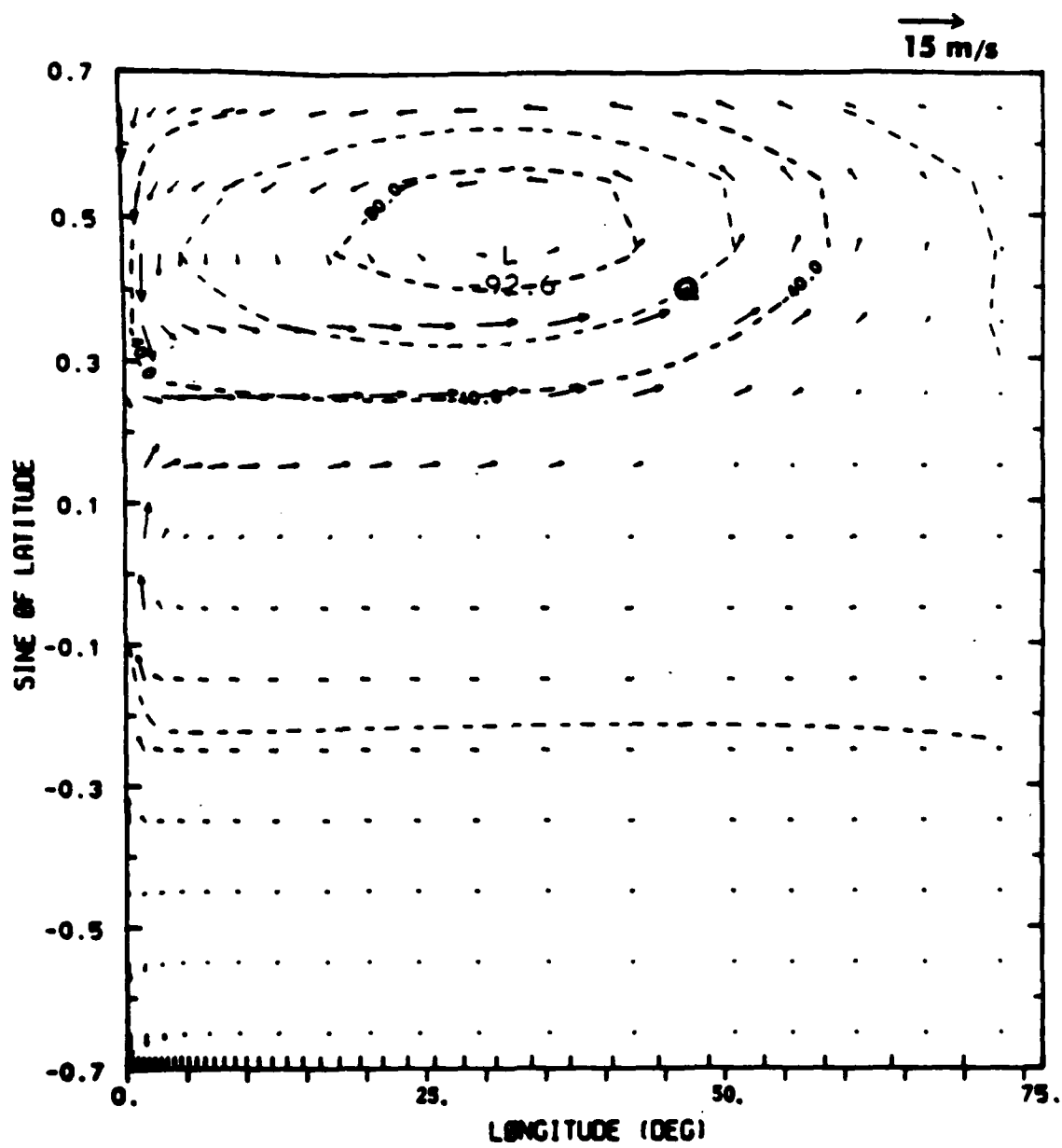


Fig. 9

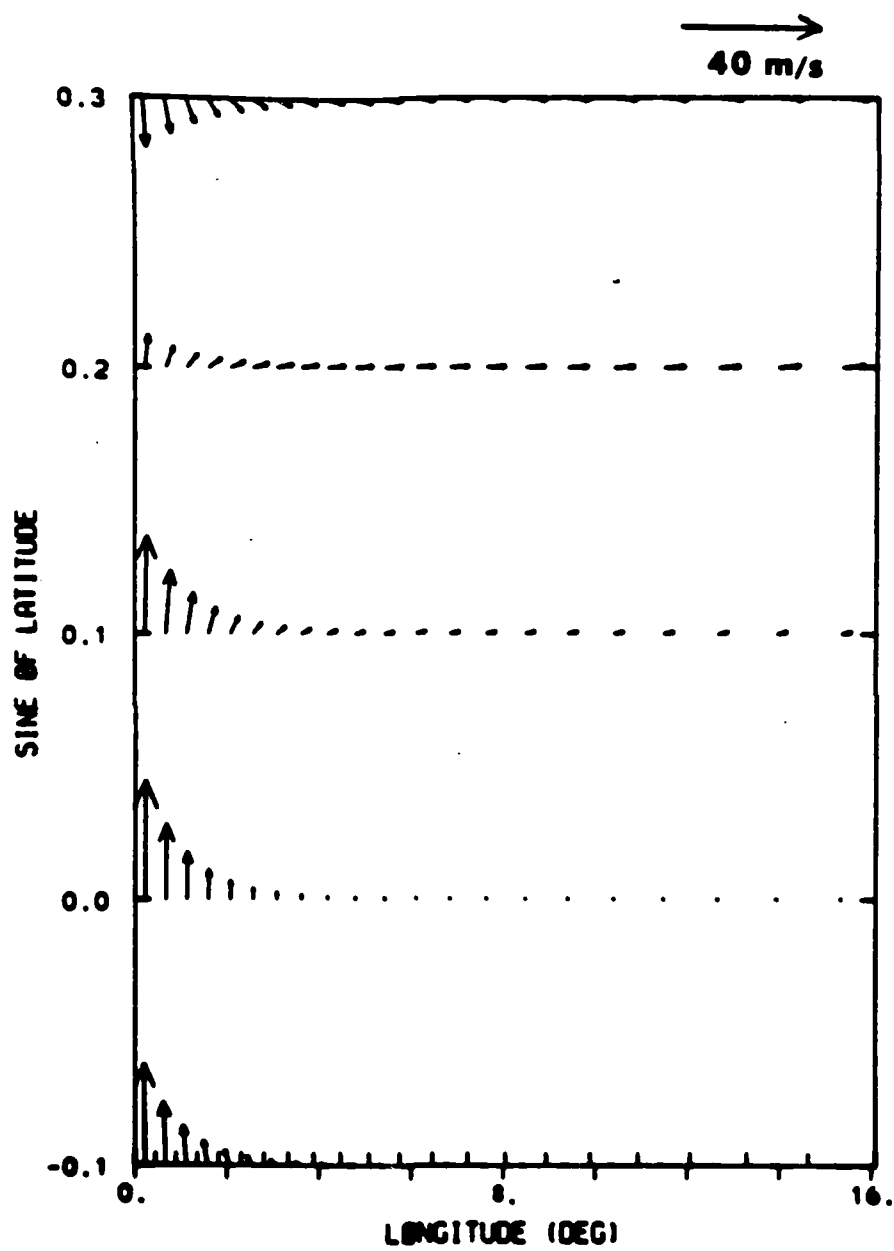


Fig. 10



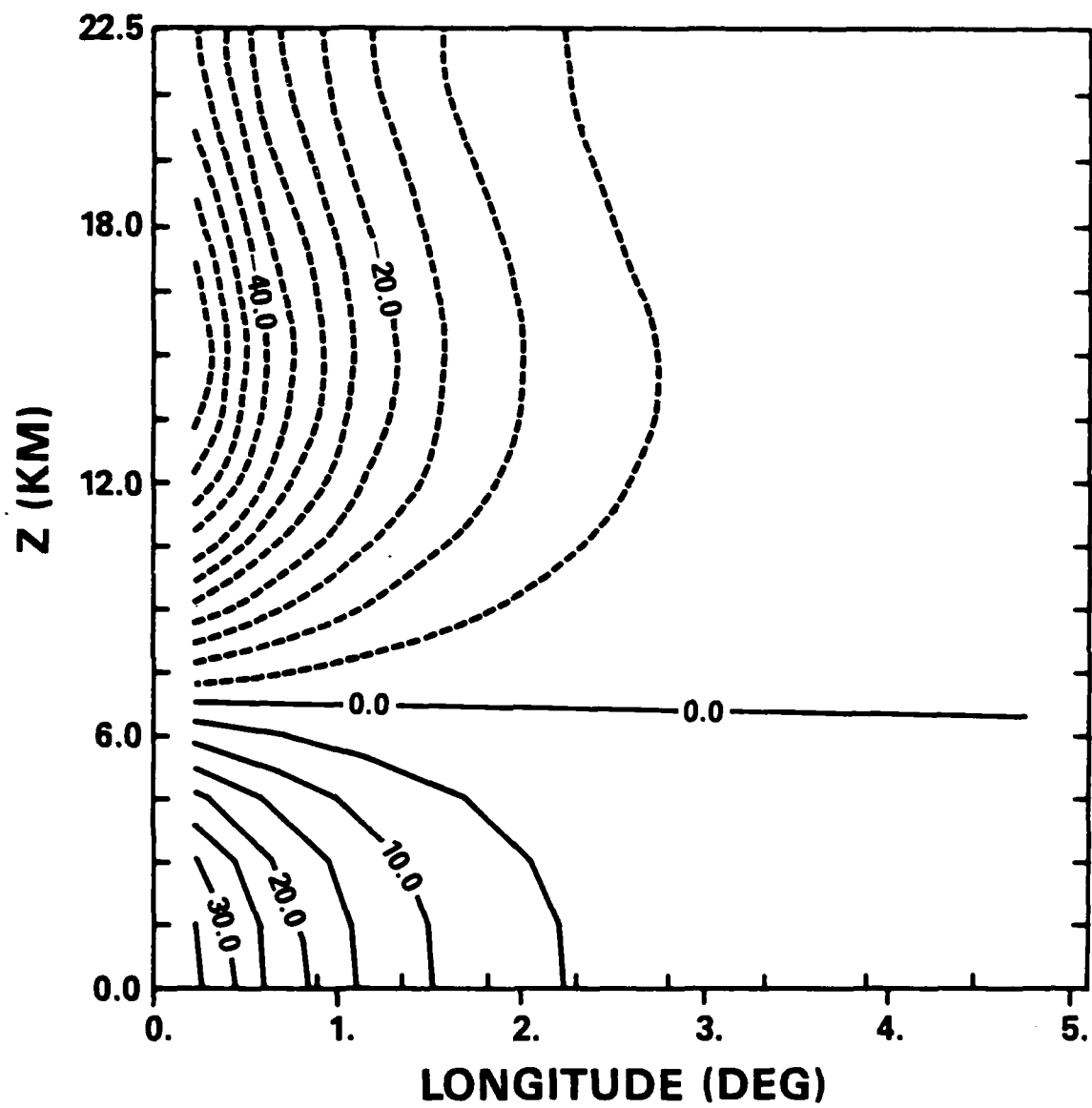


Fig. 11

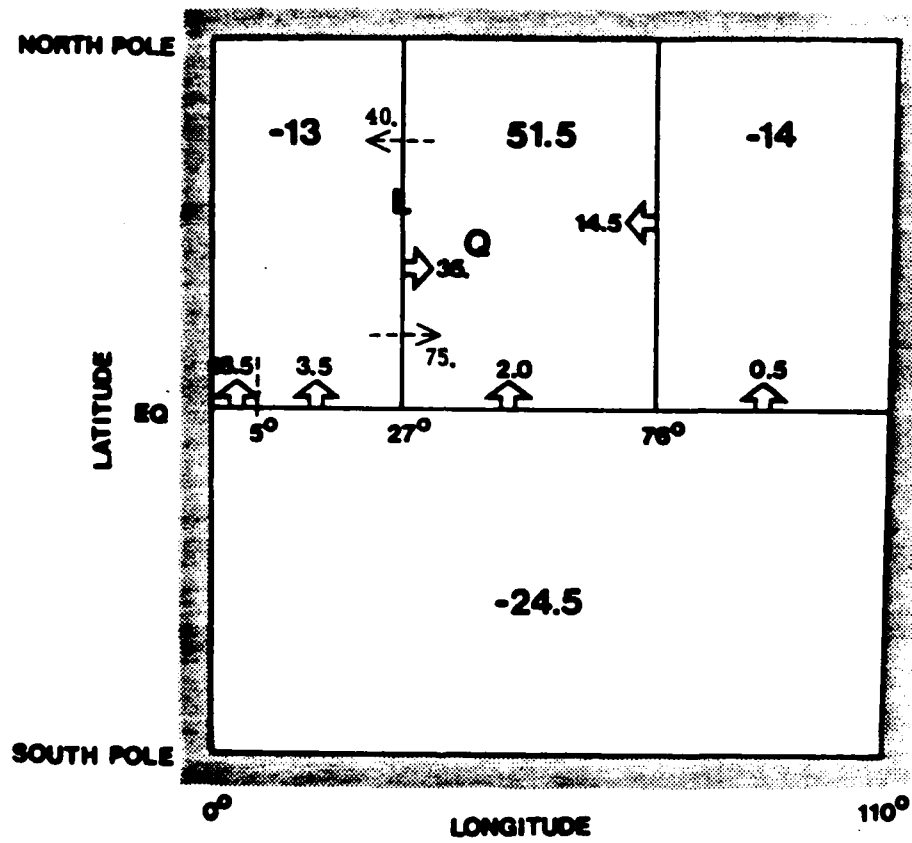


Fig. 12

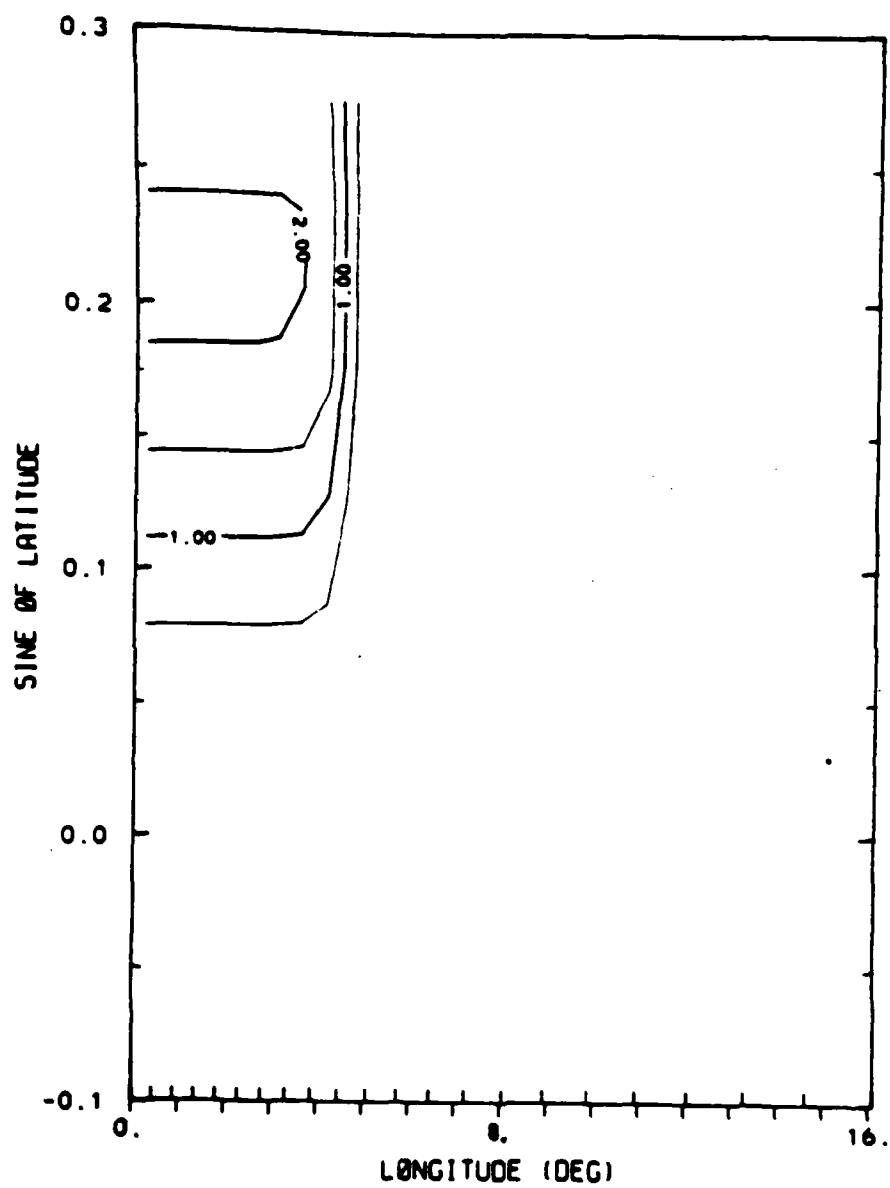


Fig. 13

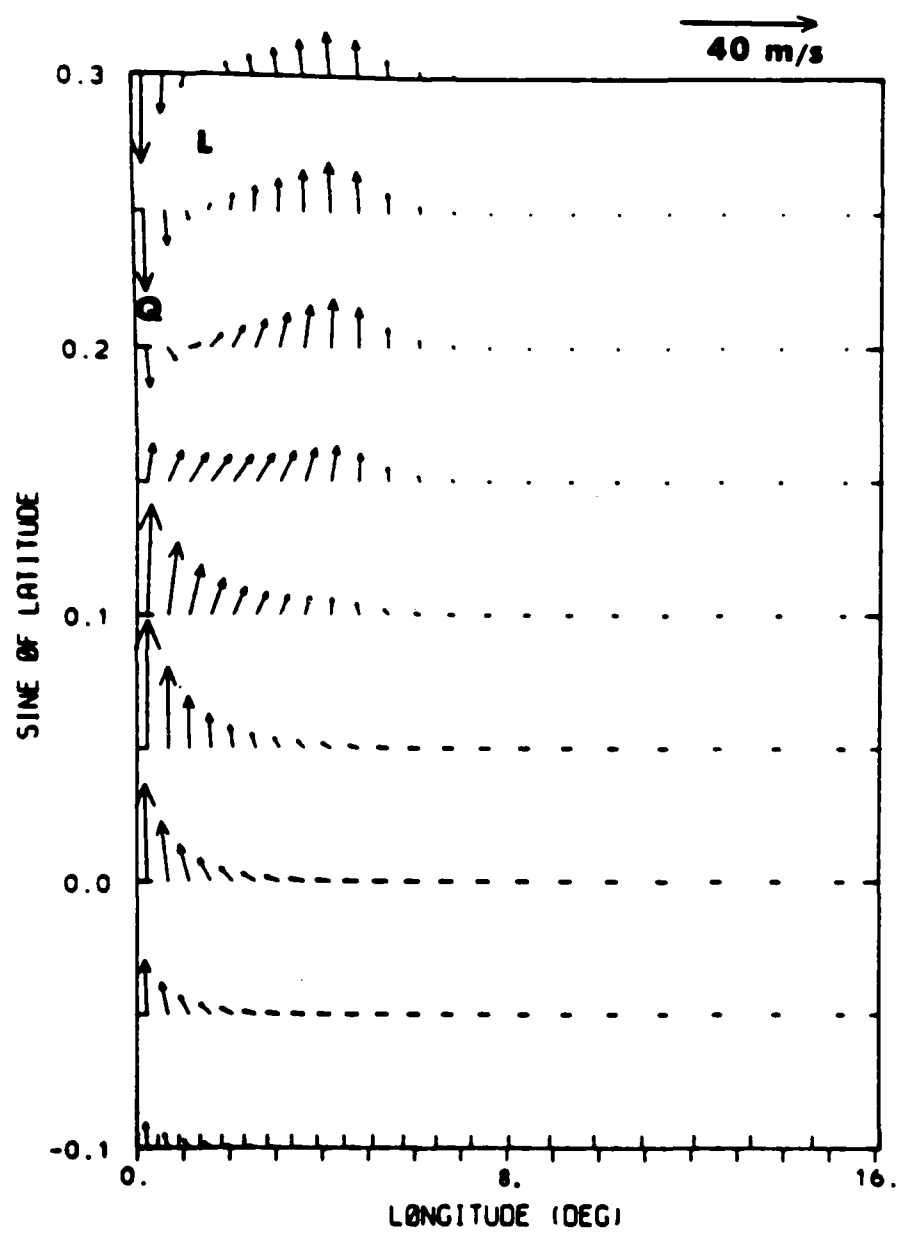


Fig. 14

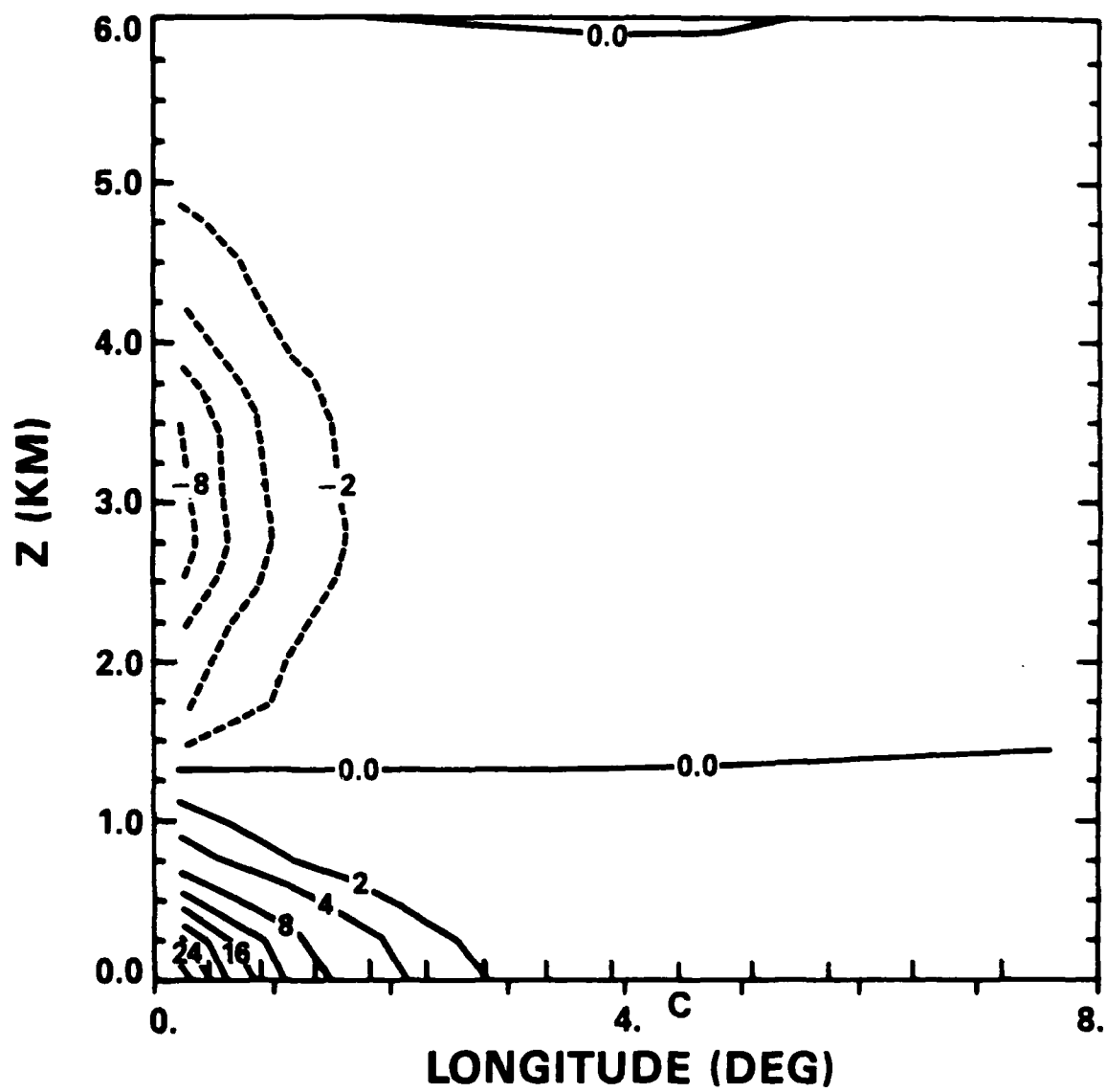


Fig. 15a

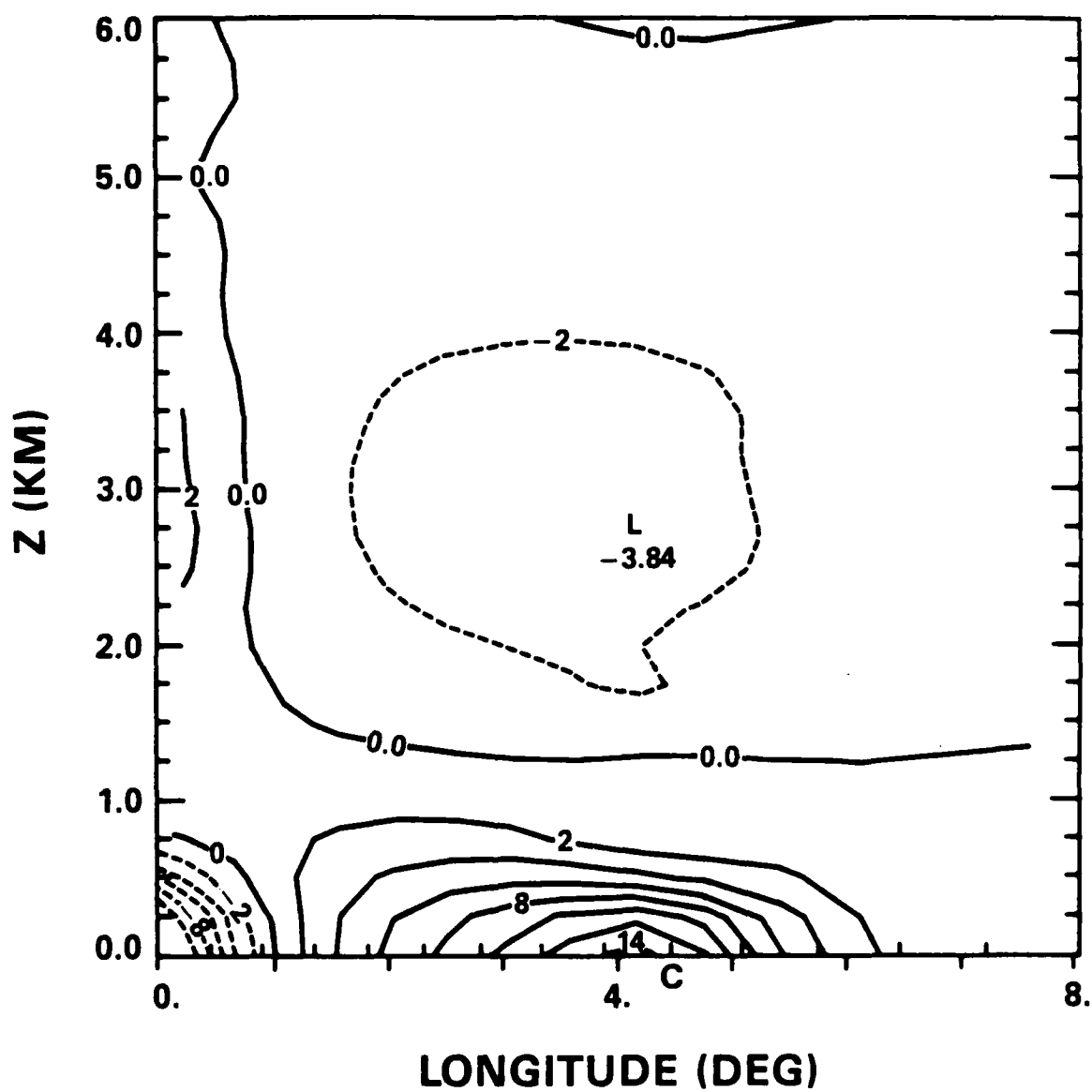


Fig. 15b

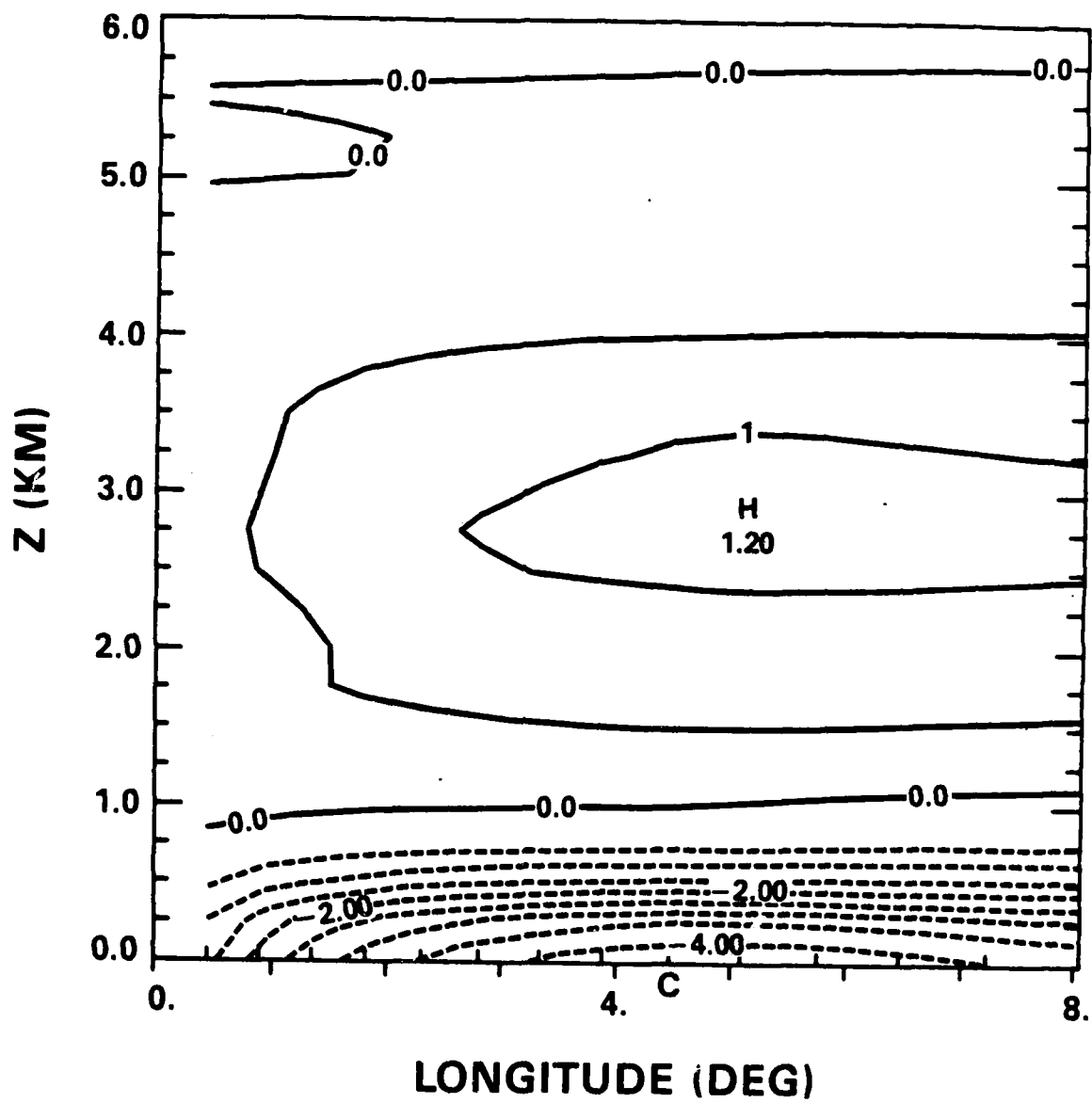


Fig. 16a

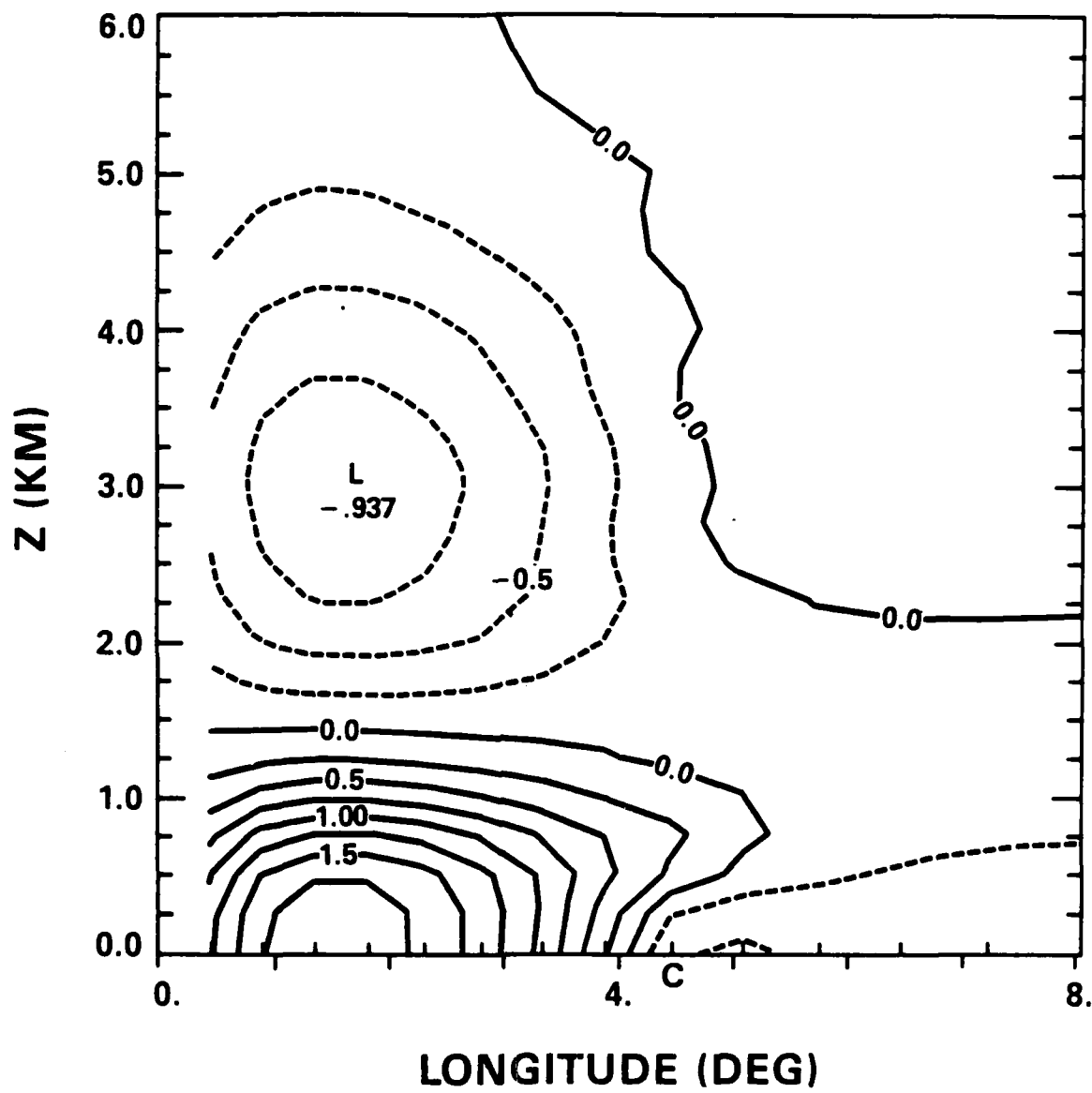


Fig. 16b



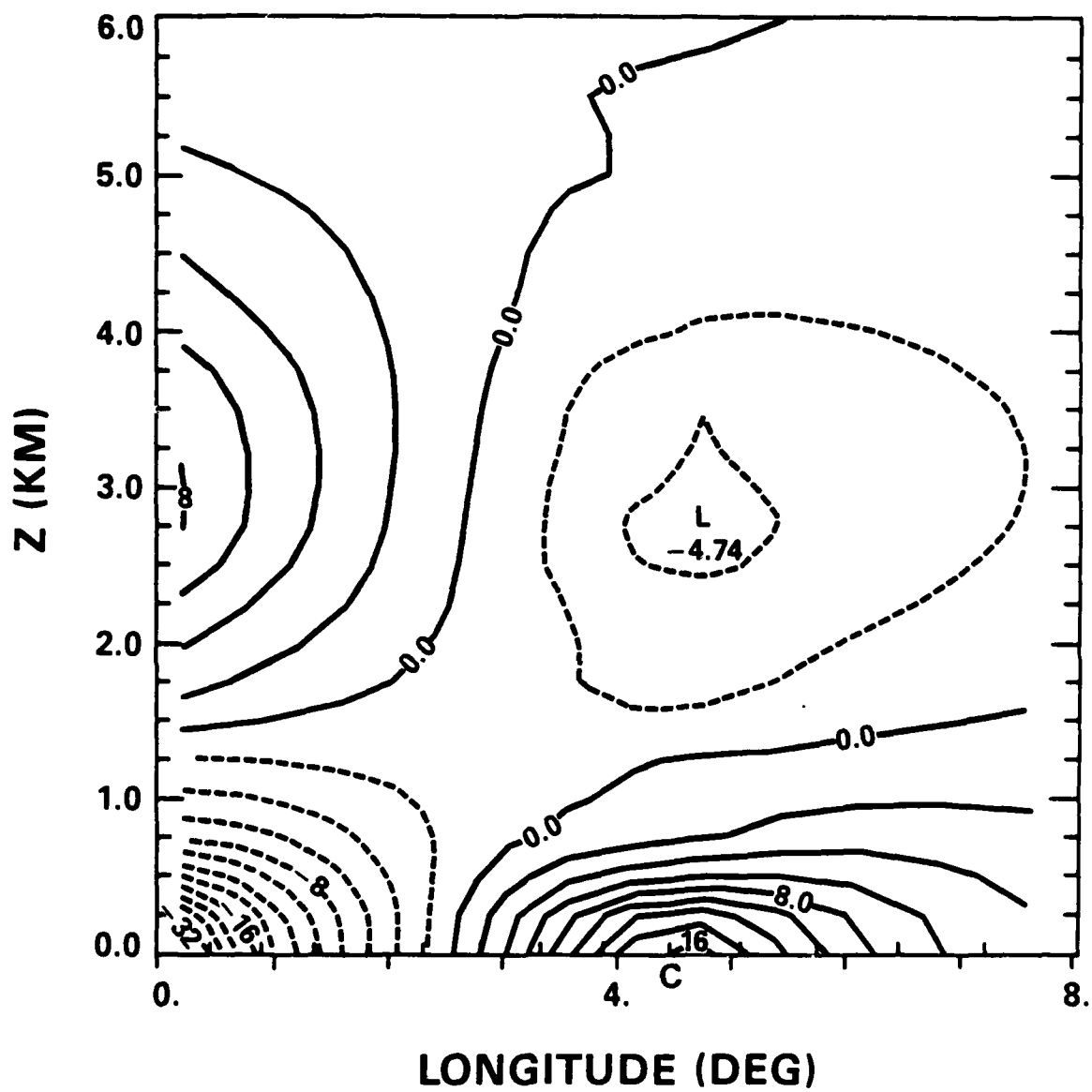


Fig. 17a

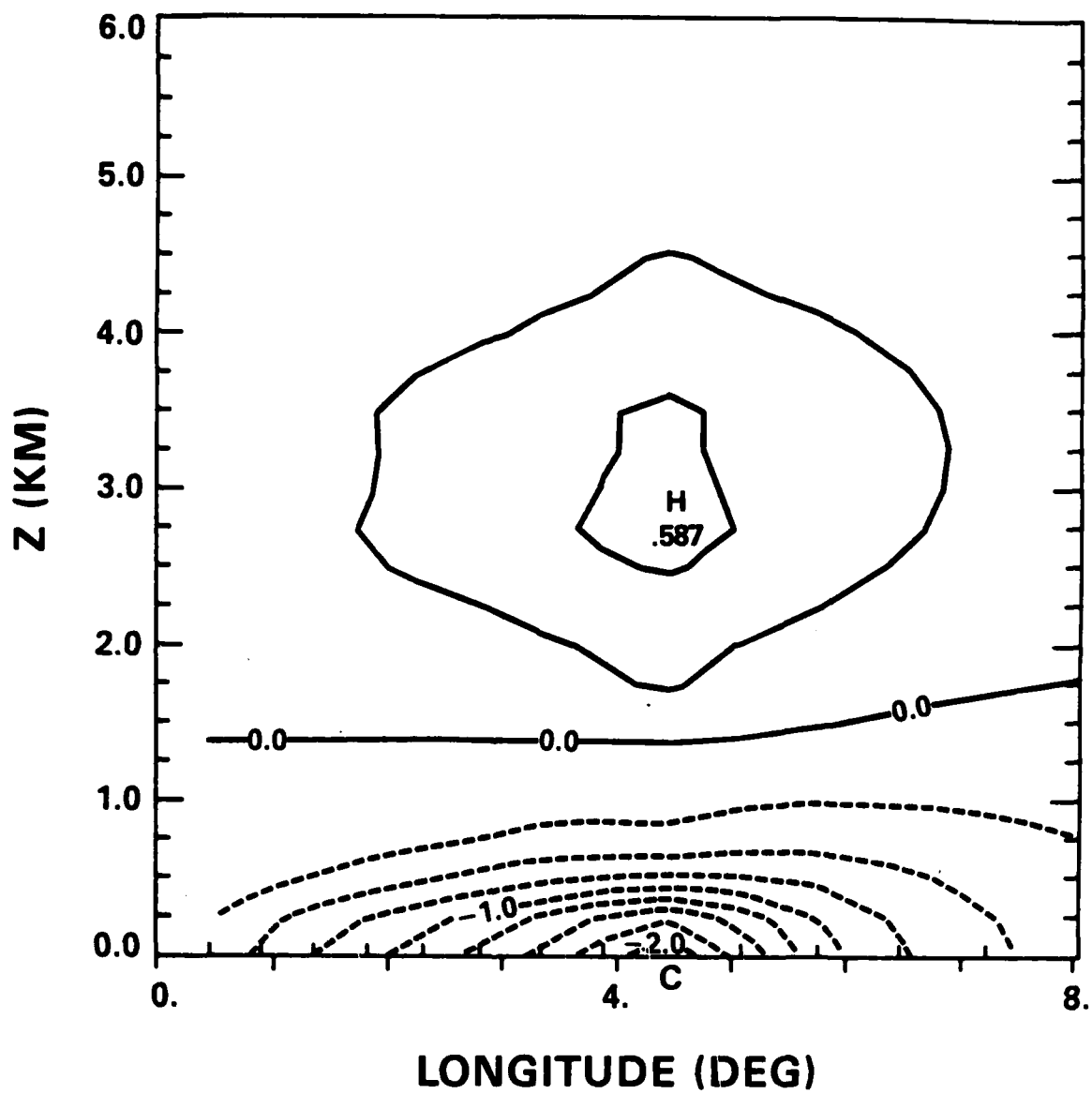


Fig. 17b

END

10-86

DT/C